Towards a Theory for Pattern Formation in Reaction-Diffusion Systems

The Geometrization of Phase Space Flows

Jacob Martin Halatek

Munich 2017

Towards a Theory for Pattern Formation in Reaction-Diffusion Systems

The Geometrization of Phase Space Flows

Jacob Martin Halatek

A dissertation submitted

to the Faculty of Physics at the

Ludwig–Maximilians–Universität München

for the degree of

Doctor rerum naturalium

Munich, 8th August 2017

First referee: Prof. Dr. Erwin Frey

Second referee: Prof. Dr. Ulrich Gerland

Day of the oral examination: 13th September 2017

Zusammenfassung (Summary in German)

Die Theorie der Nichtlinearen Dynamik beschreibt Flüsse im Phasenraum komplexer dynamischer Systeme. In dieser Arbeit wird ein Framework aus Konzepten und Methoden entwickelt um die Struktur von Phasenraumflüssen in musterbildenden Reaktions–Diffusions Systemen zu untersuchen. Das Ziel ist die der selbstorganisierter Musterbildung zugrundeliegenden physikalischen Kernmechanismen aufzudecken. Zu diesem Zwecke eignen sich auf Proteinwechelwirkungen basierende biochemische Reaktions–Diffusions Systeme als idealer Ausgangspunkt. Intrazelluläre Musterbildung spielt eine zentrale Rolle für die Funktion biologischer Systeme, und die jüngsten Fortschritte der quantitativen Biologie haben uns Zugang zu einer Vielzahl quantitativer Informationen über die inneren Arbeitsweisen solcher biologischer Systeme verschafft. Dieser Informationsgewinn erlaubt uns zwar direkt quantitative Modelle für die Kinetik solcher Systeme abzuleiten; die Methoden um solche Modelle analysieren und verstehen zu können sind jedoch auf einfache, planare Systemgeometrie beschränkt. Selbstorganisierte Musterbildung ist aber ein dynamischer Prozess der Anpassung an komplexe Zellgeometrie und kann daher im Rahmen einfacher Systemgeometrie nicht vollständig verstanden werden. Darüberhinaus sind solche quantitativen Modelle zu komplex um auf vereinfachte, effektive Modelle abgebildet zu werden. Nichtsdestotrotz beruht unser Wissen über Musterbildung fast ausschließlich auf der Analyse effektiver Modelle.

In dieser Arbeit werden wir zunähst Methoden der linearen Stabilitätsanalyse auf komplexe Systemgeometrie erweitern, sodass auch nichtlineare Kopplungen zwischen der Dynamik am Systemrand (Zellmembran) und der Dynamik im Systemvolumen (Cytosol) erfasst werden können. Diese Erweiterung wird uns erlauben die Anpassung selbst-organisierter Musterbildung an Zellgeometrien zu untersuchen.

Um die *Dynamik* von Musterbildungsprozessen untersuchen zu können, werden wir von der Tatsache Gebrauch machen, dass Wechselwirkungen zwischen Proteinen Konformationsänderungen darstellen und somit massenerhaltend sind. Dies erlaubt es uns jedes beliebige quantitative Modell in lokale, isolierte Kompartimente zu zerlegen und jeden beliebigen dynamischen Zustand des Systems durch die lokalen Gleichgewichte dieser Kompartimente zu charakterisieren. Die lokalen Gleichgewichte eines jeden Kompartiments sind durch den jeweiligen Wert der lokalen Gesamtproteindichten festgelegt, wobei diese Dichten global streng erhalten sind. Ihre Eigenschaften spiegeln die lokale Topologie des Phasenraumflußes wieder. Als zentrales Ergebnis finden wir, dass die Dynamik jedes Systems im allgemeinen als eine Änderung der lokalen Phasenraumflüsse verstanden werden kann die durch

Umverteilung der lokalen Gesamtdichte und die damit einhergehende Verschiebung und Stabilitätsänderung lokaler Gleichgewichte induziert wird.

Dieses Framework der *Massenumverteilung* ermöglicht uns die Vorhersage sowie Erklärung chemischer Turbulenz nahe des Übergangs zur Musterbildung und der Übergänge von chemischer Turbulenz zu post-chaotischer, langreichweitiger Ordnung fernab des globalen Gleichgewichts. Darüberhinaus sind wir imstande bestehende Konzepte der nichtlinearen Dynamik zu vereinheitlichen und zu erweitern, und allgemeine physikalische Mechanismen selbst-organisierter Musterbildung zu identifizieren und bestehende Prinzipien, wie die wohlbekannte Turing Instabilität, zu verallgemeinern.

Summary

Nonlinear Dynamics is a theory about the phase space flow of complex dynamical systems. In this thesis we will develop a framework of methods and concepts to elucidate the structure of phase space flow of pattern forming reaction-diffusion systems. Our goal is to reveal the physical mechanisms underlying self-organized pattern formation. Biochemical reaction-diffusion systems based on protein interaction are the ideal basis for such an endeavour. Not only does intracellular pattern formation play a crucial role for the function of biological systems, but with the recent advances in quantitative biology we also gained access to a bulk of quantitative information about the inner workings of these systems. While this information immediately allows us to formulate quantitative models for the kinetics of such systems, existing methods to analyse and understand such models are limited to simple planar geometries that do not conform to the complex shape of biological cells self-organized patterns adapt to. Furthermore, quantitative models are too complex to be mapped to the effective models of pattern formation that have been studied in the past. Yet, our understanding of pattern formation is almost exclusively based on the study of such effective models.

In this thesis we will first extend (linear stability analysis) methods from Nonlinear Dynamics to account for complex system geometries and the (nonlinear) coupling of dynamics on the system boundary (membrane) with the system volume (cytosol). This extension will allow us to study the adaption of self-organized pattern formation to cellular geometries.

To understand the *dynamics* of the pattern forming process, we will exploit the fact that protein interactions induce (conformational) state changes, and are as such mass-conserving. This allows us to decompose any quantitative model into isolated local compartments, and characterize any dynamical state of the system by the local equilibria of these compartments. The local equilibria of each compartment are determined by the amount of (globally conserved) total densities contained in the compartment, and serve as a proxy for the topology of the system's local phase space flow. We find that the dynamics of the laterally coupled system can, in general, be understood as the change of local phase space flows caused by lateral redistribution of total density that shifts the local equilibria and potentially changes their stability.

Within this *mass-redistribution framework* we are able to predict and explain the possibility of to chemical turbulence close to (global) equilibrium, and the emergence of post-chaotic long-range order far from (global) equilibrium in a paradigmatic model for biological pattern formation. Furthermore, we will be able to unify and

extend already existing concepts from Nonlinear Dynamics, such as excitability and linear instabilities, and identify the general physical mechanism underlying self-organized pattern formation through lateral instabilities such as the well-known Turing instability.

Contents

I Scope and overview of this thesis

From cellular structures to organisms and populations, biological systems are governed by principles of self-organisation. Self-organized protein pattern formation is essential for spatial organization of many intracellular processes like cell division[1–4], morphogenesis[5], and flagellum positioning[6].

The goal of this thesis is to elucidate the fundamental physical principles underlying self-organized pattern formation in biochemical reaction-diffusion systems. The interacting constituents are proteins - macromolecules that are responsible for the majority of biological function inside cells. A key feature of proteins is the ability to reversibly change their three-dimensional structure (conformation). The conformation of a protein determines its possible interactions with other biomolecules (lipids, nucleotides, or other proteins). Moreover, the conformation can change as a consequence of such interactions with other biomolecules. For example, an intracellular cytosolic protein could be in a conformational state that only enables interactions with cytosolic nucleotides. An interaction with a nucleotide could induce a conformational state change that enables the protein interact with lipids, and thereby bind to the cellular membrane. Upon binding to the membrane the conformation could change again, now, and only now, enabling interactions with other membrane bound or cytosolic proteins. These other proteins could, for instance, stimulate the downstream assembly of some functional machinery responsible for cell division or cell locomotion. The cellular proteome comprises a vast array of protein species that, due to their mutual interactions, give rise to the function of the cell as an individual organism.

The emergence of such function is a remarkable example for self-organization in real world systems: in the majority of cases any intracellular spatial structure arises endogenously as a consequence of the interactions between intracellular biomolecules without the aid of any external cues. Hence, the proper assembly of functional bio-machinery is not only based on robust protein-protein interactions, it also requires mechanisms that guide proteins to specific locations within the cell body. For instance, many (prokaryotic) cells need to divide at midcell to obtain two healthy daughter cells [1–4], flagella that propel the cell through the extracellular medium often need to be assembled exclusively in the polar regions of the cell [6], and the development of multicellular organisms from a single egg cell requires the initial establishment of directionality [5] (e.g. anterior-posterior axis).

In summary, pattern formation is the self-organized transport of proteins to specific locations within the cell body, coming about through the interplay between two distinct physical processes: conformational state changes and molecular diffusion.

To find general physical mechanisms and principles of self-organized pattern formation based on these two processes is the goal of this thesis.

Pattern formation in reaction-diffusion system has been actively studied by the scientific community over the past six decades [7–9]. A succinct review of this field would go beyond the scope of this introductory section. For the purpose of this thesis is important to note that previous efforts to generalize pattern formation mechanisms were either based on a phenomenological analogy between observed patterns (e.g. amplitude equations, see [8, 9]), or the effective molecular interactions (e.g. activator-inhibitor models, see [10–12]). Both approaches account for pattern forming systems by effective models. These effective models cannot, in general, be formally derived from the quantitative microscopic models (mass-action law) of the system under investigation. While these approaches may yield phenomenological agreement with observed patterns in some cases, the inability to map the effective model to the microscopic details of the underlying system makes predictions about the real system ambiguous, if not impossible. That being said, it is crucial to note that at the time when these effective models were developed and studied almost no quantitative data about real pattern forming systems was available for comparison. This situation changed dramatically with the advent quantitative biology in the past two decades, which shifted the focus from the analytical study of effective models to the numerical simulation of quantitative models.

While this purely computational approach allows comparisons between the experimental data and the model on a quantitative level, questions about the mechanisms underlying pattern formation can only be discussed by heuristic interpretation of simulation data that are specific to the particular model and parameter set.

In conclusion, we are faced with the following situation: On one hand, we have a large body of effective models that can be studied analytically, but cannot be related to quantitative models unambiguously. On the other hand, we have a large body of quantitative models that can be compared to experimental data, but that can only be studied by means of computational simulations. This summarizes the starting point of this thesis.

The mathematical foundation of this thesis is the theory of Nonlinear Dynamics, which, in most general terms, deals with the analysis of equilibria (steady states, fixed points, attractors) of nonlinear dynamical system [13–15]. The stability of equilibria is the most fundamental concept of Nonlinear Dynamics. It denotes the response of a system to a perturbation away from an equilibrium state, and can be obtained in general by means of a linear stability analysis. If the system's responses to all possible perturbations of the equilibrium state are known, it becomes possible to reconstruct the topology of the flow in phase space around the equilibrium. In turn,

knowing the topology of phase space around all equilibria one can extrapolate the global topology in phase space, and from this infer the dynamics from any initial condition.

While such a graphical approach is feasible in the low dimensional phase spaces of dynamical systems represented by ordinary differential equations [14, 15], it is, a priori, less applicable to partial differential equations that account for spatiotemporal pattern formation where phase spaces are infinite dimensional [8, 9]. For instance, to calculate the (linear) stability of a spatially uniform state one needs to find a suitable bases within which any perturbation of the uniform state can be represented. In planar geometries (lines, surfaces) such a basis is given by Fourier modes. These growth rates of these modes encode the initial time evolution of any pattern forming process. However, intracellular reaction-diffusion system are not planar but defined in the complex geometries of cells. Moreover, intracellular patterns are mainly membrane-bound patterns that are based on cycling of proteins between membrane-bound and cytosolic conformations, and the pattern forming process is based on cytosolic mass redistribution. Hence, not only needs the cell geometry be taken into account, but also the nonlinear coupling between membrane-bound and cytosolic states. With the classical approach based on Fourier modes this is not possible. Another complication lies in the practical impossibility to construct the patterned (steady) states of quantitative models for biological system in complex cellular geometries. Hence, questions about the maintenance or general characteristics of the patterned state are outside the scope of the classical framework of linear stability analysis.

This thesis is structured in two major parts that seek to address these issues. In the first Part, **"Geometry"**, (based on preliminary work in the author's diploma thesis [16]) we will systematically extend the linear stability framework to include complex cellular geometries and nonlinear bulk-boundary coupling (Chapter III). We will mainly focus on linear stability analysis in elliptical geometry which captures the symmetry of most cells. The extended framework will be used to study a broad range of Min protein patterns in E. Coli in diverse cell shapes (Chapter III), question of pattern selection by cell geometry and multistability of patterns (Chapter IV), symmetry breaking that leads to the loss of the uniform steady state and the emergence of a unique, stable base state that adapts to the geometry of the cell (Chapter V), and questions of axis selection by PAR protein dynamics in the *C. Elegans* embryo (Chapter VI).

The key result of this part will be that the local bulk volume to membrane surface ration is the main feature the pattern forming process adapts to, and that all aspects of pattern selection and multistability are based on an interplay between linear cytosolic, nonlinear membrane processes., and cell geometry. This result is quite surprising, since pattern selection in planar, effective models is typically the consequence of modulation effects induced by the systems nonlinearities. In context of quantitative

biological systems we find that the interplay between linear cytosolic processes and cell geometry play a crucial, non-negligible role.

Where the first part is concerned with the geometry sensitivity of the pattern formation process, the second Part, **"Geometrization"**, deals with the pattern formation process per se. Here, we will identify and discuss the fundamental self organization principles underlying pattern formation that are independent of the molecular details of a particular model, and stem from the most general physical properties all systems have in common alone: dynamics that are driven by (conformational) state changes, and transport that is facilitated by molecular diffusion. In any system driven by state changes the essential dynamics are mass-conserving, and the total particle numbers are key control parameters for the spatiotemporal dynamics. If we take, for instance, a protein that can either be in a membrane-bound or a cytosolic state, the total amount of this protein will, in general, determine the membrane-bound and cytosolic densities of this protein in (chemical) equilibrium.

As we will show in Chapter VIII, the spatial distribution of the conserved quantities (the sums of all state densities that comprise the total density of the protein species) is, in general, spatially nonuniform in any patterned state (where pattern refers to the spatial distribution of the individual states, e.g. the density of membrane-bound protein). By decomposing the spatially extended system into small, isolated compartments, we can calculate the local (chemical) equilibria in all compartments from the amount of conserved quantities in each compartment. The immediate benefit is that the local phase space of these compartmentalized systems is low dimensional and by calculating the linear stability of all local equilibria we can extrapolate the topology of flow in each of the local phase spaces. Strikingly, we find that the pattern of local equilibria (and their stabilities, i.e. the flow in the local phase spaces) characterizes and scaffolds the pattern of the spatially extended system. Since local equilibria can only change endogenously by changing the local amounts of the globally conserved quantities, the key mechanism of pattern formation must lie in the lateral redistribution of these quantities. Indeed, we will show that the lateral diffusive coupling of the local compartments gives, under generic conditions (unequal diffusion coefficients for membrane bound and cytosolic proteins), rise to lateral instabilities that induce lateral redistribution of the conserved quantity. Hence, local and lateral stability will be the fundamental and complementary stability concepts of the proposed framework, with lateral redistribution of (globally conserved) total densities acting as the key physical process driving pattern formation.

Not only will this mass-redistribution framework allow us (in Chapter IX) to generalize mechanisms for the onset of pattern formation from the uniform state (such as the Turing instability), but also to characterize and analyse any dynamical state of the pattern forming system by means of the spatial distribution of local equilibria and their stability (Chapter VIII and IX). The time evolution of any pattern will be characterized by the movement of local equilibria.

In an application of this framework to *in vitro* Min protein dynamics [17] in Chapter VIII we will show that moving local equilibria explain the emergence of chemical turbulence at onset, and quantitatively predict the transition from chemical turbulence to long-range order far from onset. Both of these observations are highly unusual in light our traditional understanding of chemical turbulence, where disorder inducing instabilities arise due to nonlinear mode coupling far from onset but are suppressed near onset. As such, the mass-redistribution framework provides a novel picture of the origin of turbulence and the emergence of order in reaction-diffusion systems driven my mass-conserving interactions. The identification of the (conserved) total densities as the control variables of the self-organized pattern forming process implies that the number of essential degrees of freedom is limited by the number of conserved protein species that comprise a functional reaction-diffusion system. This, in turn, suggests that the core mechanism for pattern formation in any quantitative reaction-diffusion model is encoded in the dependency of local equilibria and their stability on the total density (Chapter VIII). Traditionally on would refer to such a structure as bifurcation diagram, but here it marks the control space where the dynamics take place. This gives rise to the question how many control variables (bifurcation parameters) need to vary dynamically for a certain pattern to emerge.

We will address this question in an investigation of *in vivo* Min protein oscillations (Chapter IX), which is based on two conserved protein species, MinD and MinE [1, 3, 18]. Pole-to-pole Min oscillations in *E. Coli* guide the assembly to the cell division machinery to midcell. Among other biological systems with a similar function (regulation of cell division through polarization) the oscillatory phenomenology of the Min system is highly unusual, superficially implying that Min protein pattern formation is based on a mechanism that is very distinct from mechanisms underlying cell polarity, which is non-oscillatory. Strikingly, we find by application of the mass-redistribution framework that the exact opposite is the case: The self-organization mechanism underlying pattern formation is only based on MinD redistribution and is intrinsically non-oscillatory. In fact, we will even systematically show that the mechanism is strictly equivalent to mechanisms underlying cell polarity. The oscillatory nature of Min protein dynamics arises from the periodic annihilation and reformation polarized states (pattern attractors) due to the spatial redistribution of the second conserved species, MinE. This mechanistic separation of the physical roles of MinD and MinE allows us to systematically reduce the pole-to-pole Min oscillation of the quantitative reaction-diffusion model to a generic relaxation oscillation in control space.

In the final project presented in this thesis we will focus on the bio-molecular details of Min protein dynamics (Chapter X). In particular, we will study how the interplay between cytosolic and membrane processes in combination with the system's geometry affects the sensitivity of the pattern forming process to changes of the average total densities in a system (i.e. acting as control parameters). In

collaboration with experimentalists we will test several model extensions with mutant proteins mimicking the individual model extensions. We will also show that these experiments confirm the predicted emergence of chemical turbulence at onset. In a supplementary section (Chapter XI) we will critically analyse and discuss a recent paper [19] dealing with the geometry sensitivity of the Min system. The results reported in this paper directly contradict a large part of the findings presented in this thesis. Through a thorough and systematic analysis of the simulation data we will show that the reported results are entirely based on undisclosed manipulations of system parameters and details of the numerical implementation enabling the exploitation of numerical artifacts to match the experimental observation and suit a narrative.

While the last part is certainly unpleasant in any respect, it also reinforces an important lesson I learned during my work on this thesis. In the words of Sherlock Holmes:

> "It is a capital mistake to theorize before one has data. Insensibly one begins to twist facts to suit theories, instead of theories to suit facts."
>
> Sir Arthur Conan Doyle, A Scandal in Bohemia

In this thesis we extend the theoretical framework centered around linear stability analysis to include complex system geometries, nonlinear bulk-boundary coupling, and mass-conservation. All these are basic physical properties of biochemical reaction-diffusion system. Our analysis will show that the inclusion of these aspects into our biophysical framework is essential. It reveals that geometry sensitivity results from the interplay between cytosolic processes and the coupling to the reactive membrane. Furthermore, we find that total densities are the essential degrees of freedom of self-organized pattern formation in reaction-diffusion systems based on mass-conserving interactions. This reduction in the complexity of quantitative models for intracellular protein dynamics allows us to identify general mechanisms for pattern formation based on mass-redistribution.

This thesis is structured in chapters, where each chapter represents a self-contained manuscript either prepared for a publication or already published in a peer-reviewed journal. The figures can be found at the end of each manuscript. In the following chapter we will first shortly summarize the scope and key results of each manuscript, and highlight how each manuscript fits into the broader picture outlined above.

II Summaries of all manuscripts

II.1 Reaction-diffusion systems in elliptical geometry: Min protein dynamics *in vivo*

The first manuscript (Chapter III) deals with the extension of the linear stability analysis to elliptical geometry and its application to study Min protein pattern formation in vivo. Here, we introduce the *skeleton* model for Min protein dynamics.

Journal reference

J. Halatek and E. Frey, A highly canalized MinD transfer and MinE sequestration explain the origin of robust MinCDE-protein dynamics, Cell Reports 1, 2012

II.1.1 Abstract

Min-protein oscillations in *Escherichia coli* are characterized by the remarkable robustness with which spatial patterns dynamically adapt to variations of cell geometry. Moreover, adaption, and therefore proper cell division, is independent of temperature. These observations raise fundamental questions about the mechanisms establishing robust Min oscillations, and about the role of spatial cues, as they are at odds with present models. With a conceptually novel and universal approach to cellular geometries, we introduce a robust model based on experimental data, consistently explaining the mechanisms underlying pole-to-pole, striped and circular patterns, as well as the observed temperature-dependence. Contrary to prior conjectures, the model predicts that MinD and cardiolipin domains are not colocalized. The transient sequestration of MinE, and highly canalized transfer of MinD between polar zones, are the key mechanisms underlying oscillations. MinD channeling enhances midcell localization and facilitates stripe formation, revealing the potential optimization process from which robust Min-oscillations originally arose.

II.1.2 Key results

- The theoretical part is based on the construction of an orthonormal basis of eigenfunctions for general reaction-diffusion systems in elliptical geometry. Formally, this basis accounts for reaction-diffusion systems on the elliptical

boundary (membrane), for reaction-diffusion systems in the elliptical bulk volume (cytosol), and reaction diffusion system with bulk-boundary coupling (membrane-cytosol cycling) through reactive (Robin) boundary conditions.

- Due to the broken (rotational) symmetry (of a circle) in elliptical geometry, the eigenfunctions spilt into two groups: even and odd modes. Even modes represent patterns aligned to the long axis of the cell, and odd modes represent patterns aligned to the short axis.

- The investigation of the model for Min protein dynamics shows that long axis alignment of patterns is not generic but parameter dependent. Similarly, the pole-to-pole pattern does not generically gain additional wave nodes as the system length is increased. Hence, a characteristic length scale (wavelength) does not exists generically but only for specific parameter combinations.

- The regime where the experimentally observed phenomenology is reproduced is characterized by an interplay between cytosolic processes and the nonlinear membrane accumulation (recruitment) that optimizes the efficiency of directed transport of proteins from one end of the cell to the other through cytosolic diffusion (which is isotropic on its own, i.e. not directional). This regime has been named canalized transfer.

II.1.3 Relation to other manuscripts

- The linear stability framework in elliptical geometry is the basis for the study of multistability of Min protein patterns in mutant *E. Coli* cells (Chapter IV), and the study of axis selection by PAR protein pattern formation in the *C. Elegans* embryo (Chapter VI).

- The extension of linear stability analysis to include bulk-boundary coupling is the basis for further extensions to other system geometries (Chapters VIII, X, and XI).

- The observation of a non-uniform base state will be further explored in a study of geometry adapted pattern formation without dynamical instability (Chapter V).

- The constrains on the ratio of MinE and MinD particle numbers for pattern formation will motivate further model extensions and experimental tests of model predictions by construction of mutant proteins that mimic these model extensions (Chapter X).

II.1.4 Experimental data supporting the results

- An experimental in vivo study of multistability (Chapter IV) will support the claim that in vivo Min protein dynamics operate in the canalized transfer regime.
- An experimental in vitro study with mutant proteins mimicking the proposed model will confirm the predictions on the ratio of MinE and MinD particle numbers to support pattern formation (Chapter X).

II.2 Geometry adaption: Multistability and geometry induced transitions of intracellular patterns

In Chapter IV we present a combined experimental and theoretical approach where we study the geometry dependence and multistability of Min protein pattern formation *in vivo*.

Journal Reference

F. Wu†, J. Halatek†, M. Reiter, E. Kingma, E. Frey, and C. Dekker, Multistability and dynamic transitions of intracellular Min protein patterns, Molecular Systems Biology 12, 2016 (on the cover)

Author contribution

† F. Wu and J. Halatek contributed equally to this work.

F. Wu, J. Halatek, E. Frey, and C. Dekker designed the work and wrote the paper. F. Wu and E. Kingma carried out the experiments and analyzed the experimental data. J. Halatek performed the analytical and computational analysis of the model. M. Reiter implemented the automated numerical parameter sweeps. F. Wu wrote the scripts for the analysis of experimental data.

II.2.1 Abstract

Cells owe their internal organization to self-organized protein patterns, which originate and adapt to growth and external stimuli via a process that is as complex as it is little understood. Here, we study the emergence, stability, and state transitions of multistable Min protein oscillation patterns in live *Escherichia coli* bacteria during growth up to defined large dimensions. *De novo* formation of patterns from homogenous starting conditions is observed and studied both experimentally and in simulations. A new theoretical approach is developed for probing pattern stability under perturbations. Quantitative experiments and simulations show that, once established, Min oscillations tolerate a large degree of intracellular heterogeneity, allowing distinctly different patterns to persist in different cells with the same geometry. Min patterns maintain their axes for hours in experiments, despite imperfections, expansion, and changes in cell shape during continuous cell growth. Transitions between multistable Min patterns are found to be rare events induced by strong intracellular perturbations. The instances of multistability studied here are the combined outcome of boundary growth and strongly nonlinear kinetics, which are characteristic of the reaction-diffusion patterns that pervade biology at many scales.

II.2.2 Key results

- Due to the absence of a uniform steady state, the base state introduces a bias for modes with an even symmetry (parity). Due to this bias, the basins of attraction corresponding to multistable patterns cannot be inferred from a numerical sampling based on different initial conditions. In this manuscript we introduce an approach based on weak spatial perturbations of linear kinetic rates to guide the initial dynamics towards patterns with a certain symmetry, and to study the stability of these patterns towards perturbations with different symmetries numerically.
- Multistability and adaption to changes of the cell geometry are not generic for reaction-diffusion processes, but specify to parameter choices that enable an interplay between cytosolic and membrane kinetics. In particular, the model supports multistability that is similar to the experimental observation only in the canalized transfer regime.

II.3 Geometry adaption: Pattern formation without instability

In Chapter V we study the possibility of pattern formation by adaption of a stable base state to the cell geometry by linear processes alone, i.e. without any dynamical instability.

Journal reference

D. Thalmeier, J. Halatek, and E. Frey, Geometry-induced protein pattern formation, PNAS 113, 2016

Author contribution

This manuscript is based on the Master thesis by Dominik Thalmeier, supervised by E. Frey and co-supervised by J. Halatek.

D. Thalmeier, J. Halatek, and E. Frey designed research, performed research, and wrote the paper.

II.3.1 Abstract

Protein patterns are known to adapt to cell shape and serve as spatial templates that choreograph downstream processes like cell polarity or cell division. However, how can pattern-forming proteins sense and respond to the geometry of a cell, and what mechanistic principles underlie pattern formation? Current models invoke mechanisms based on dynamic instabilities arising from non- linear interactions between proteins but neglect the influence of the spatial geometry itself. Here, we show that patterns can emerge as a direct result of adaptation to cell geometry, in the absence of dynamical instability. We present a generic reaction module that allows protein densities robustly to adapt to the symmetry of the spatial geometry. The key component is an NTPase protein that cycles between nucleotide-dependent membrane-bound and cytosolic states. For elongated cells, we find that the protein dynamics generically leads to a bipolar pattern, which vanishes as the geometry becomes spherically symmetrical. We show that such a reaction module facilitates universal adaptation to cell geometry by sensing the local ratio of membrane area to cytosolic volume. This sensing mechanism is controlled by the membrane affinities of the different states. We apply the theory to explain AtMinD bipolar patterns in ΔEcMinDE *Escherichia coli*. Due to its generic nature, the mechanism could also serve as a hitherto-unrecognized spatial template in many other bacterial systems. Moreover, the robustness of the mechanism enables self-organized optimization of

protein patterns by evolutionary processes. Finally, the proposed module can be used to establish geometry-sensitive protein gradients in synthetic biological systems.

II.3.2 Key results

- Cytosolic state change that alter the interactions of cytosolic proteins with the membrane are the basis for geometry adaption of patterns.
- The base state is generically non-uniform if both cytosolic states have a different membrane affinity.
- The local membrane to cytosol ratio is the key quantity the dynamics adapt to, which allows to represent the PDE model by an effective ODE system defined on a network that mimics the geometry.

II.4 Geometry adaption: The mechanism for axis selection

In Chapter VI we study long vs. short axis selection in a model for PAR protein polarization in *C. Elegans*.

Journal reference

R. Geßele, J. Halatek, and E. Frey, Cell Polarization in Elliptical Geometry: How does *Caenorhabditis Elegans* Determine its First Axis?, in preparation for publication

Author contribution

This project originated from preliminary work presented in the Master thesis by T. Fehm, and the Bachelor thesis by T. Meinhardt, both supervised by E. Frey and co-supervised by J. Halatek.

J. Halatek, R. Geßele, and E. Frey designed the work. R. Geßele and J. Halatek developed and analyzed the model. R. Geßele performed the numerical simulations and stability analyses. R. Geßele, J. Halatek, and E. Frey analyzed the data and wrote the paper.

This manuscript will also be part of the PhD thesis by R. Geßele.

II.4.1 Abstract

In polarized cells, the accumulation of signaling molecules create axes that guide differentiation, division and proliferation. In the single cell state of the *Caenorhabditis Elegans* embryo, cell polarity determines the future front and back of the worm, and the interface between accumulated signaling proteins defines the division line of the first cleavage. Recent models have indicated mutual binding inhibition of *aPARs* and *pPARs* as the key mechanism of polarity maintenance by the *PAR* reaction-diffusion network. Nevertheless, how polarity stabilizes along the long axis of the elliptical embryo remains an open question. In addition to mutual inhibition of *PAR* proteins (the subject of previous models), we examine polarization in elliptical geometry while accounting for cytoplasmic dynamics in a mass-conserving reaction-diffusion model. We find that mutual inhibition of *aPARs* and *pPARs* by phosphorylation with immediate cytoplasmic dephosphorylation favors short axis polarization. This contradicts polarity maintenance along the long axis in the embryo. This discrepancy, however, is resolved by a more realistic reactivation cycle - in which dephosphorylation (reactivation for attachment) is delayed in the cytosol, and long-axis polarization is

restored. Numerical analysis indicates that a phosphorylated phase and fast diffusion of cytosolic proteins allow for long axis polarization. Furthermore, molecular details in our model (which group species according to their functional role) enable us to investigate how relative densities of proteins with specific functions influence polarization. We show that the relative mutual antagonism, which is determined by antagonistic detachment rates and relative protein densities, determine the robustness of polarity along a specific axis. All together, we find that cell polarity along a specific axis is the result of an interplay of the cell's geometry, a reactivation cycle between membrane and cytosol, and the relative mass of signaling proteins.

II.4.2 Key results

- The selection of the polarity axis is not related to the *characteristic length scale* set by the fastest growing mode in a planar geometry.
- Instead, intracellular reaction-diffusion systems have a *characteristic axis* that depends on (i) the effect cytosolic proteins have on the pattern forming process when they encounter the membrane, and (ii) the position where active cytosolic proteins encounter the membrane most often.
- The effect of membrane encounters is entirely determined by the kinetics of membrane-bound proteins, while the preferred position of membrane encounters only depends on the geometry of the cell and the cytosolic kinetics.
- At the coarsest level, we can distinguish between two types of membrane-kinetics, accumulation and separation based cluster formation: Accumulation is promoted by cooperative attachment. In that case clusters stabilize in the regions of highest encounter frequency of cytosolic proteins (which are active for binding). Antagonistic reactions have the opposite effect: In regions where active proteins reach the membrane most frequently antagonistic interactions promote the establishment of an interface that separates cluster.
- If the cytosol comprises a large reservoir of active proteins the encounter frequency is determined by the local membrane area to cytosol volume ratio alone.
- Otherwise, the position of maximal encounter frequency is regulated by the local ratio of membrane surface to cytosolic volume and the length scale of cytosolic diffusion until reactivation.

II.5 Protein pattern formation on biological membranes

In this chapter we summarize and review the work so far in a broader context, and motivate the second part of this thesis where mass-conservation will be discussed. Beyond that, we review and discuss several key aspects concerning the interpretation of experimental data obtained from in vitro reconstitution of in vivo reaction-diffusion systems. In particular, we focus on the comparison of quantitative experimental data across different experimental setups in relation to quantitative data obtained from theoretical models. In this context we will discuss the importance of unambiguous experimental quantification of key control parameters for proper interpretation of experimental data.

This manuscript is based on a book chapter.

Book reference

E. Frey, J. Halatek, S. Kretschmer, and P. Schwille, Protein Pattern Formation, Physics of Biological Membranes, edited by P. Bassereau and P. C. A. Sens, Springer-Verlag GmbH, Heidelberg, 2017, in print

Author contribution

E. Frey, J. Halatek, S. Kretschmer, and P. Schwille wrote the manuscript.

II.6 Rethinking pattern formation in reaction-diffusion systems: Moving local equilibria

Chapter VIII presents the key part of this thesis. Here, we introduce the *mass-redistribution framework*.

Journal reference

J. Halatek, and E. Frey, Rethinking pattern formation in reaction–diffusion systems, Nature Physics 14, 507-514, 2018

II.6.1 Abstract

The present theoretical framework for the analysis of pattern formation in complex systems is mostly limited to the vicinity of fixed (global) equilibria. Here we present a new theoretical approach to characterize dynamical states arbitrarily far from (global) equilibrium. We show that reaction-diffusion systems that are driven by locally mass–conserving interactions can be understood in terms of local equilibria of diffusively coupled compartments. Diffusive coupling generically induces lateral redistribution of the globally conserved quantities, and the variable local amounts of these quantities determine the local equilibria in each compartment. We find that, even far from global equilibrium, the system is well characterized by its moving local equilibria. We apply this framework to *in-vitro* Min protein pattern formation, a paradigmatic model for biological pattern formation. Within our framework we can predict and explain transitions between chemical turbulence and order arbitrarily far from global equilibrium. Our results reveal conceptually new principles of self-organized pattern-formation that may well govern diverse dynamical systems.

II.6.2 Key results

- Any reaction-diffusion system driven by mass-conserving interactions can be decomposed into isolated (well-mixed) compartments within which the *local total density* (particle number) is conserved.
- In any typical patterned state the spatial distribution of local total density is non-uniform.
- The local total density determines the *local (chemical) equilibria* in each of these compartments.
- The positions and stabilities of local equilibria scaffold and characterize the pattern of the spatially extended system. This has two immediate consequences:

  - The infinite dimensional phase space of the full PDE system can be decomposed into the local phase spaces of the compartments. The local phase space topology of each compartment is low dimensional and has (typically) a simple structure that is well understood within ODE (bifurcation) theory.
  - The local total densities are the only *control variables* that can affect the positions and stabilities of local equilibria dynamically. Hence, local total densities are the essential degrees of freedom that give rise to self-organized pattern formation.

- The only process by which local total density can change is lateral diffusive transport. Lateral diffusive coupling can give rise to lateral instabilities. These instabilities stimulate the growth of (Fourier) modes, which generic action is the lateral redistribution of total density on the corresponding length scales.

- As such, local and lateral stability are the complementary, fundamental stability concepts of self-organized pattern formation:
  - The local positions and stabilities of local equilibria characterize and scaffold the pattern in any dynamical state.
  - Lateral redistribution of total density induced by lateral instabilities shifts the local equilibria and potentially changes their stability. As such, lateral instabilities drive the dynamics (state change) of the pattern forming process.

- The application of this framework to *in-vitro* Min protein dynamics predicts and explains:
  - The observation of chemical turbulence at the onset of the lateral instability due to local destabilization. This comprises a hitherto unknown route to (chemical) turbulence (spatiotemporal chaos) based on generic, model independent properties (local destabilization due to lateral mass redistribution).
  - The observation of post-chaotic (standing-wave) order far from (global) equilibrium due to the concerted mass redistribution by mutually commensurable unstable modes. Here, mode coupling facilitates the *control of spatiotemporal chaos*. This defeats the classical paradigm spatiotemporal chaos originates from mode coupling.
  - A transition from the (*in vivo*) regime (locally stable equilibria) to the *in-vitro* regime where the system can be understood as an oscillatory medium. Hence, the reconstituted Min system is mechanistically distinct from the original *in vivo* system.

II.6.3 Relation to other manuscripts

- The mass-redistribution framework will applied in (Chapter IX) to identify core mechanisms for pattern formation by a systematic reduction of reaction-diffusion systems to their minimal functional form. In this manuscript we will also generalize the mechanism underlying Turing instabilities, and unify the concepts of dynamical instability and excitability within the mass-redistribution framework.
- In (Chapter X) we will test some predictions about *in-vitro* Min protein dynamics experimentally.
- The differences between Min protein pattern formation *in vivo* and *in-vitro* were discussed in (Chapter VII).

II.6.4 Experimental data supporting the results

- In Chapter X we will confirm the prediction of chemical turbulence at onset in a experimental setup with MinE mutants that mimic the minimal function of MinE assumed in the model.
- The work by Caspri and Dekker [20] strongly supports our results that Min protein pattern formation *in-vitro* is mechanistically distinct from Min protein pattern formation *in vivo*.

II.7 Geometrization of pattern formation: From quantitative models to the identification of self-organization mechanisms

In Chapter IX we use the mass-redistribution framework to systematically reduce *in vivo* Min protein dynamics to minimal system and identify the underlying pattern forming mechanism. Furthermore we use the framework to reveal the general physical mechanism underlying Turing instabilities and excitability in mass-conserving reaction diffusion systems.

Journal reference

F. Brauns[†], J. Halatek[†], and E. Frey, From quantitative models to a mechanistic understanding of protein pattern formation, 2017, in preparation for publication

Author contribution

† F. Brauns and J. Halatek contributed equally to this work.

F. Brauns, J. Halatek, and E. Frey designed the research. F. Brauns and J. Halatek performed the research. F. Brauns, J. Halatek, and E. Frey analyzed the data and wrote the manuscript.

This manuscript will also be part of the PhD thesis by F. Brauns.

II.7.1 Abstract

The dynamics of any physical system are encoded in the (flow) structure of the system's phase space. All essential dynamics of a particular system are qualitatively contained in the phase portrait. Unfortunately, phase portraits can, in general, only be derived for low dimensional ODE systems. This strongly limits the applicability of the powerful geometric concepts with which the dynamics of a system can be inferred from the structure phase portraits. Here, we present a systematic theoretical framework to derive the phase portraits of quantitative reaction-diffusion models with mass-conserving interactions. This framework is based on the spatial decomposition of any system into local compartments. The phase space flows of isolated compartments are determined by the positions and stabilities of local equilibria. In turn, local equilibria are uniquely determined by the local amounts of the (globally conserved) total densities n of all protein species in these compartments. The essential effect of diffusive coupling between individual compartments is the lateral exchange of (globally conserved) total densities which changes the structure

of the local phase spaces. Our key results is that the entire pattern forming process can be understood in terms of moving local equilibria, i.e. the dynamically changing structure of local phase spaces caused by lateral diffusive transport. As such, the phase portrait of the pattern forming system is obtained form the local phase spaces and the (linear) effect of diffusive coupling.

The geometrization lets us systematically extend a broad range of concepts from ODE theory (excitability, bifurcations, basins of attraction, nullclines) to pattern formation in mass-conserving reaction-diffusion systems. This, in turn, leads to a natural unification of existing pattern forming mechanisms, such as linear (e.g. Turing) instabilities and excitability. Furthermore, this geometrization approach reveals that the shape of the line of local equilibria (kinetic nullcline) is the central geometric object that universally classifies reaction-diffusion models on a mechanistic level. This classification is based on the topological equivalence classes of kinetic nullclines, which is well-established for dynamical systems theory of ODEs.

To demonstrate the utility of our framework, we apply it to a quantitative model for Min protein patterns *in vivo*. The Min system regulates cell division in *E. Coli* through pole-to-pole oscillations. This lets the Min system appear mechanistically unique among biological systems with similar function (cell polarity), that are typically non-oscillatory. The systematic reduction of Min protein dynamics within our framework reveals that the underlying pattern forming process is intrinsically non-oscillatory and strictly equivalent to mechanisms underlying non-oscillatory polarity patterns in other biological system. MinD generates polarity through phase separation, whereas MinE takes the role of a control variable regulating the existence of polarized MinD patterns. Oscillations are facilitated by MinE redistribution and can be understood mechanistically as relaxation oscillations of the polarization direction.

II.7.2 Key results

- The main physical processes underlying self-organized pattern formation in systems driven by mass-conserving interactions are local reactive flow and diffusive flux–balance.
  - At every point in space, the reactive flows act in the local phase spaces of the system. The local phase spaces are subspaces of the (global) phase space, and are parametrized by the local total densities. The local reactive flow can be extrapolated from the properties of local equilibria, which are also determined by the local total densities.
  - The diffusive processes redistribute local total density and thereby move the system between local phase spaces (shifting local equilibria).

  - A stationary state is reached once diffusive fluxes balance the reactive turnover (accumulated reactive flow).
  - The interplay between reactive and diffusive processes gives rise to the geometrization of phase space. Pattern forming processes can be inferred from three central geometric objects: (i) the line of local equilibria, (ii) the family of local (reactive) phase spaces, and (iii) the (diffusive) flux–balance subspace.

- The geometrization approach provides a fine grained classification of patterns and mechanisms: For stationary polarity patterns it reveals three distinct sub-classes based on regional properties (peaks, plateaus). This classification is based on a regional decomposition of the pattern and a generalization of lateral stability (regional lateral stability).

- Moreover, this approach reveals that the Turing instability and lateral excitability are two manifestations of the same (mass-redistribution) instability.

- The basic requirement for a mass-redistribution instability is an interaction network in which the (chemical) equilibrium density of the faster diffusing component decreases if the total density increases. This leads to a mass-redistribution cascade though cytosolic transport and a continual shifting of local equilibria that scaffold the pattern of the slowly diffusing component.

- Our analysis of Min protein dynamics with the geometrization approach reveals that oscillatory Min protein patterns are based on the same core mechanisms (mass-redistribution instability) as non-oscillatory models for cell polarity. The core pattern forming mechanisms is based on MinD redistribution alone and leads to non-oscillatory polarity patterns. Oscillations are merely a consequence of the purely diffusive redistribution of the MinE total density, which passively follows the pattern forming process of MinD.

- This suggests that pattern formation in complex biochemical interactions networks can be understood by a decomposition into core mechanisms and control mechanisms. For pole-to-pole Min oscillations the core mechanism (MinD polarity by mass-redistribution instability) is controlled by diffusive MinE redistribution: the MinE total density profile *controls* the properties (shape, existence) of MinD polarity attractors.

II.8 Geometry and mass-conservation: The switching paradigm and pattern robustness

In Chapter X we study theoretically and experimentally how cytosolic processes affect pattern robustness with respect to variations of the globally conserved total density of protein species.

Journal reference

J. Denk† , S. Kretschmer† , J. Halatek† , C. Hartl, P. Schwille, and E. Frey, MinE conformational switching confers robustness on self-organized Min protein patterns, PNAS, 201719801, 2018

Author contribution

† J. Denk, S. Kretschmer, and J. Halatek contributed equally to this work.

This project originated from preliminary work presented in the Master thesis by C. Hartl, supervised by E. Frey and co-supervised by J. Halatek.

J. Halatek, J. Denk, S. Kretschmer, P. Schwille, and E. Frey designed the research. J. Denk, J. Halatek, C. Hartl, and E. Frey performed the mathematical analyses. S. Kretschmer and P. Schwille designed and carried out the experiments. J. Denk, S. Kretschmer, J. Halatek, P. Schwille, and E. Frey discussed and interpreted the results, and wrote the manuscript.

This manuscript will also be part of the PhD theses by J. Denk and S. Kretschmer.

II.8.1 Abstract

Robust protein patterning is vital for many fundamental cellular processes. An established motif of intracellular pattern-forming networks is the self-organization of nucleoside triphosphatases (NTPases), which upon interaction with a cognate NTPase activating protein switch between an NTP-bound and nucleoside diphosphate (NDP)-bound form. In the Min system, a prototypical example for pattern formation during bacterial cell division, the adenosine triphosphatase (ATPase) MinD in turn triggers a conformational switch in its activating protein MinE from a latent to a reactive state, although the role of such mutual switching is unclear. By combining nonlinear dynamics analyses and in vitro reconstitution of mutant proteins, we show here that the MinD-dependent switch of MinE is essential for pattern formation in a broad and physiological range of protein concentrations. Our combined theoretical

and experimental approach demonstrates that though simpler reaction networks may suffice to reproduce patterns, interlinking protein switches confers pattern robustness — a fundamental prerequisite for the evolvability of organisms.

II.8.2 Key results

- Fast cytosolic conformational state changes of MinE (from conformations with strong affinity for MinD to conformations with weak affinity for MinD) significantly increase the range of MinE to MinD total density ratios where pattern formation is supported.
- MinE membrane binding has a negligible impact on Min protein pattern formation.

II.8.3 Relation to other manuscripts

- A functionally minimal MinE protein that mimics the MinE action assumed in the skeleton Model confirms the model predictions discussed in (Chapter III).
- At the onset of lateral instability (low MinE/MinD ratio) chemical turbulence is found experimentally, confirming previous model predictions (Chapter VIII).
- The experiments with MinE mutants that are unable to bind to the membrane disprove the claim in the literature, that MinE membrane interactions are essential for pattern formation. This claim is challenged in (Chapter XI) on grounds of the model assumptions and numerical implementation.

II.9 Geometry and mass-conservation: Why a rigorous account for the system geometry and total protein numbers is important

In this chapter we analyze the model by Kruse et. al [19], which has been used to claim that cytosolic dynamics are negligible and that MinE membrane interactions are the primary cause for Min protein pattern formation and geometry sensing.

Journal reference

J. Halatek, and E. Frey, Effective two-dimensional model does not account for geometry sensing by self-organized proteins patterns, PNAS 111, 2014 (Supplementary Material in arxiv:1403.5934)

II.9.1 Abstract

Here we provide a thorough discussion of the model for Min protein dynamics proposed by Schweizer et al. [19]. Our analysis is based on the original COMSOL simulation files that were used for the publication. We show that all computational data in Schweizer et al. rely on exploitation of simulation artifacts and various unmentioned modifications of model parameters that strikingly contradict the experimental setup and experimental data. We find that the model neither accounts for MinE membrane interactions nor for any observed MinDE protein patterns. All conclusions drawn from the computational model are void. There is no evidence at all that persistent MinE membrane binding has any role in geometry sensing.

II.9.2 Key results

- The reported simulation data matching the experiments can only be reproduced by adjusting the system parameters (total densities of MinE and MinD, geometry of the gold layer) for each data-point individually.

- The reported alignment of the pattern to the patch geometry is produced by using a vanishingly small gold layer surrounding the patch (in stark contradiction to the experiment) and periodic boundary conditions. The entire geometric effect (alignment to the aspect ratio) is based on the coupling of the pattern with itself via the periodic boundary. The alignment angle depends on minute details of the implementation (gold layer vs patch geometry, gold layer thickness, i.e. distance from the patch to the periodic boundary) that effects the self-coupling via the periodic boundary.

- For (large) gold layer sizes as used in the experiment no patterns are observed at all.
- For total densities as used in the experiment (and reported in the paper as system parameter) no patterns are observed at all.
- None of the reported simulation data can be reproduced with the parameters and numerical setups as described in the paper.
- The pattern forming mechanism strictly requires MinE membrane binding, in contradiction with several experiments.
- The model assumptions on the molecular interactions deviate from experimental data (residence times) by orders of magnitude.

II.9.3 Experimental data supporting the results

- Our analysis regarding the role of MinE has been confirmed in (Chapter X), disproving the the entire theoretical rational of the commended paper.

II.9.4 Remark about the reply to our comment

We note that the reply by Kruse et al. (arXiv:1406.1347) to our comment has not been published by PNAS, or any other peer reviewed journal. We further note that in this reply, the authors misquote our statements by altering our references to experimental studies that contradict the model assumptions. In their response, the authors blatantly state that the references to not contain the data we were referring to, which, of course, is only due to the fact that the authors altered the references in the first place. As such, the reply is as scientifically sound as the paper it intends to defend. It does not clarify any issues raised by our comment.

Bibliography

[1] D. M. Raskin and P. a. de Boer. Rapid pole-to-pole oscillation of a protein required for directing division to the middle of Escherichia coli. *Proceedings of the National Academy of Sciences of the United States of America* **96**(9), 4971–6, 1999. (Cit. on pp. 1, 5).

[2] L. Rothfield, A. Taghbalout and Y.-L. Shih. Spatial control of bacterial division-site placement. *Nature reviews. Microbiology* **3**(12), 959–68, 2005. DOI: 10.1038/nrmicro1290. (Cit. on p. 1).

[3] S. Kretschmer and P. Schwille. Pattern formation on membranes and its role in bacterial cell division. *Current Opinion in Cell Biology* **38**, 52–59, 2016. DOI: 10.1016/j.ceb.2016.02.005. (Cit. on pp. 1, 5).

[4] L. Merlini, O. Dudin and S. G. Martin. Mate and fuse: how yeast cells do it. *Open biology* **3**(3), 130008, 2013. DOI: 10.1098/rsob.130008. (Cit. on p. 1).

[5] P. Bourgine and A. Lesne. *Morphogenesis : origins of patterns and shapes*. Springer, 2011. (Cit. on p. 1).

[6] B. Kazmierczak and D. Hendrixson. Spatial and Numerical Regulation of Flagellar Biosynthesis in Polarly-Flagellated Bacteria. *Molecular microbiology* **88**(4), 655–663, 2013. (Cit. on p. 1).

[7] A. M. Turing. The chemical basis of morphogenesis. *Philosophical Transactions of the Royal Society of London. Series B, Biological Sciences* **237**(641), 37–72, 1952. DOI: 10.1007/BF02459572. (Cit. on p. 2).

[8] M. Cross and P. Hohenberg. Pattern formation outside of equilibrium. *Reviews of modern physics* **65**(3), 1993. (Cit. on pp. 2, 3).

[9] M. Cross and H. Greenside. *Pattern Formation and Dynamics in Nonequilibrium Systems*. Cambridge University Press, 2009. (Cit. on pp. 2, 3).

[10] A. Gierer and H. Meinhardt. A theory of biological pattern formation. *Kybernetik* **12**(1), 30–9, 1972. (Cit. on p. 2).

[11] S. Kondo and T. Miura. Reaction-diffusion model as a framework for understanding biological pattern formation. *Science (New York, N.Y.)* **329**(5999), 1616–20, 2010. DOI: 10.1126/science.1179047. (Cit. on p. 2).

[12] P. K. Trong, E. M. Nicola, N. W. Goehring, K. V. Kumar and S. W. Grill. Parameter-space topology of models for cell polarity. *New Journal of Physics* **16**, 2014. (Cit. on p. 2).

[13] H. Poincaré. Mémoire sur les courbes définies par une équation différentielle. *Journal de Mathématiques Pures et Appliquées*, 1881. (Cit. on p. 2).

[14] S. H. Strogatz. *Nonlinear Dynamics and Chaos*. 1994. DOI: 9780738204536. (Cit. on pp. 2, 3).

[15] E. M. Izhikevich. *Dynamical Systems in Neuroscience*. MIT Press, 2007. (Cit. on pp. 2, 3).

[16] J. Halatek. *Reaktions-Diffusions Systeme auf Oberflächen*. PhD thesis. 2010. (Cit. on p. 3).

[17] M. Loose, E. Fischer-Friedrich, J. Ries, K. Kruse and P. Schwille. Spatial regulators for bacterial cell division self-organize into surface waves in vitro. *Science (New York, N.Y.)* **320**(5877), 789–92, 2008. DOI: 10.1126/science.1154413. (Cit. on p. 5).

[18] J. Lutkenhaus. Assembly dynamics of the bacterial MinCDE system and spatial regulation of the Z ring. *Annual review of biochemistry* **76**, 539–62, 2007. DOI: 10.1146/annurev.biochem.75.103004.142652. (Cit. on p. 5).

[19] J. Schweizer, M. Loose, M. Bonny, K. Kruse, I. Mönch and P. Schwille. Geometry sensing by self-organized protein patterns. *Proceedings of the National Academy of Sciences of the United States of America* **109**(38), 15283–8, 2012. DOI: 10.1073/pnas.1206953109. (Cit. on pp. 6, 25).

[20] Y. Caspi and C. Dekker. Mapping out Min protein patterns in fully confined fluidic chambers. *eLife* **5**, 1–53, 2016. DOI: 10.7554/eLife.19271. (Cit. on p. 19).

Part I

Geometry

III Reaction-diffusion systems in elliptical geometry: Min protein dynamics *in vivo*

This chapter is based on the following publication:

A highly canalized MinD transfer and MinE sequestration explain the origin of robust MinCDE-protein dynamics

by

J. Halatek and E. Frey

Department of Physics, Arnold Sommerfeld Center for Theoretical Physics and

Center for NanoScience, Ludwig-Maximilians-Universität München,

Theresienstraße 37, 80333 München, Germany

Journal Reference:

***Cell Reports* 1, 2012**

Supplemental Material reproduced on pages 62 to 79.

A highly canalized MinD transfer and MinE sequestration explain the origin of robust MinCDE-protein dynamics

Jacob Halatek and Erwin Frey
Arnold-Sommerfeld-Center for Theoretical Physics
and Center for NanoScience, Department of Physics,
Ludwig-Maximilians-Universität München,
Theresienstraße 37, D-80333 München, Germany

Abstract

Min-protein oscillations in *Escherichia coli* are characterized by the remarkable robustness with which spatial patterns dynamically adapt to variations of cell geometry. Moreover, adaption, and therefore proper cell division, is independent of temperature. These observations raise fundamental questions about the mechanisms establishing robust Min oscillations, and about the role of spatial cues, as they are at odds with present models. With a conceptually novel and universal approach to cellular geometries, we introduce a robust model based on experimental data, consistently explaining the mechanisms underlying pole-to-pole, striped and circular patterns, as well as the observed temperature-dependence. Contrary to prior conjectures, the model predicts that MinD and cardiolipin domains are not colocalized. The transient sequestration of MinE, and highly canalized transfer of MinD between polar zones, are the key mechanisms underlying oscillations. MinD channeling enhances midcell localization and facilitates stripe formation, revealing the potential optimization process from which robust Min-oscillations originally arose.

HIGHLIGHTS

- A conceptually novel formalism predicts protein patterns in realistic cell geometries
- Patterns emerge due to transient MinE sequestration and canalized MinD transfer
- Robust and efficient oscillations originate from optimized MinD-MinD/E interactions
- MinD patterns are not colocalized with cardiolipin domains in the oscillatory regime

INTRODUCTION

Robust spatial patterning was crucial just from the beginning of cellular evolution, and is key to the development of multicellular organisms. The oscillatory pole-to-pole dynamics of MinCDE proteins prevent improper cell divisions apart from midcell [24, 31]. Due to it's critical role for the cell cycle, a robust regulation of Min oscillations is of fundamental importance. As origin of robustness, an efficient mechanism, only depending on a few central molecular processes seems most likely. Indeed, experimental evidence supports a mechanism based on nonlinear reaction-diffusion dynamics. The Min-proteins diffuse through the cytoplasm and the ATPase MinD attaches in its ATP-bound form to the cell membrane, where it recruits MinE, MinC and MinD-ATP from the cytosol [13]. MinC inhibits cell division, but plays no role in establishing oscillations [24, 31]. MinE, which is present as a dimer [9, 21, 30, 34], hydrolyses MinD on the membrane and thereby initiates detachment. As consequence, pole-to-pole oscillations arise in wild type cells, and striped oscillations in filamentous cells [31], revealing the presence of an intrinsic spatial wavelength. Experiments indicate that the temporal and spatial properties of patterns are established independently of each other, as temperature variations strongly affect the oscillation frequency, while leaving the spatial wavelength unchanged [38]. Thereby, proper cell division is ensured in a wide temperature range. In nearly spherical mutant cells one observes predominantly pole-to-pole oscillations along the major or an irregularly wandering axis, as well as circular waves on the membrane [36].
Numerous computational models have been proposed to elucidate Min-protein patterns [19, 23]. Most models are either based on recruitment of cytosolic

proteins to the membrane [1, 7, 14, 22], differing mainly in their assumptions about the involved recruitment processes, or employ phenomenological nonlinearities [2, 11, 25] to reproduce the observed dynamics. The sheer number of conceptually different models accounting for specific observations underlines the generic nature of oscillatory dynamics in nonlinear systems, but leaves the actual underlying mechanisms ambiguous. The only known model which reproduces oscillatory patterns in cells with different shapes is based on recruitment [7]. It was initially formulated in cylindrical geometry by Huang et al. [14], and solely assumes experimentally verified or suggested reactions. However, in this model, striped oscillations only emerge for a nucleotide exchange rate below the experimentally determined lower bound [26], and even then only for specific initial conditions that cannot account for the dynamic transition out of pole-to-pole oscillations [38]. Furthermore, the model could not provide the necessary robustness against parameter variations to account for temperature variations [5, 38], therefore failing to explain proper cell divisions above room temperature. Finally, in contrast to pole-to-pole oscillations, patterns in spherical cells could only be explained by stochastic effects [7] or additionally included saturation terms [16].

The models' sensitivity to initial conditions and parameter variations raised doubts about the validity and completeness of recruitment-based models in general [38]. Moreover, striped patterns rather seem to arise in a small parameter set as a special case of the models possible dynamics, without being of any obvious biological relevance for the wild type division cycle itself. One may therefore wonder why striped patterns arise at all. For the extension of present models, nucleation of MinD polymers at periodically distributed domains enriched with anionic phospholipids was suggested [38]. This would introduce a predetermined spatial template, which might stabilize Min-protein patterns by separating spatial organisation from temporal dynamics. Indeed, some models assert Min oscillations to be induced by the nucleation of MinD filaments at the cell poles [3, 6]. This line of thought is based on the preference of MinD to bind in regions enriched with cardiolipin [27, 28], an anionic phospholipid that clusters in domains of high negative membrane curvature [15, 29, 33], like the cell poles. However, no colocalisation of MinD stripes with cardiolipin domains has been reported so far, leaving the actual role of cardiolipin domains as spatial cue elusive.

As it is ubiquitous in many intracellular biochemical systems, the interactions between Min-proteins are restricted to the lipid membrane, raising interesting questions about the role of cell geometry and spatial organization in spatio-temporal pattern formation. However, so far, a theoretical investigation of

a model's dynamics is restricted to numerical simulations of a few single parameter configurations, leaving the overall parameter and geometry dependent pattern forming abilities largely elusive.
Here, we present a robust minimal model based on recruitment [14] that respects cellular geometry and allows broad parameter studies by linear stability analyses along with the incorporation of membrane diffusion. Employing a nonlinear reactive bulk-boundary coupling and distinct diffusion processes for the cytosol and the membrane, we reformulated the reaction-diffusion system in elliptical coordinates. The use of elliptical geometry was crucial, as it accounts for the various aspect ratios, and captures axial and circular patterns simultaneously, while still being amenable to linear stability analyses. In contrast to one-dimensional reductions [22], this ansatz allows the important distinction between circular waves and pole-to-pole oscillations.
The model reproduces all transitions between oscillatory patterns in wild type, filamentous and nearly spherical cells, as well as the temperature dependence of the temporal period. We find that the pattern forming process neither adapts to spatial templates given by inhomogeneous MinD attachment, nor does it depend on variations of the hydrolysis rate or on initial conditions. In contrast, transitions between patterns are mediated by variations of the cell geometry alone. From the linear stability analysis and extensive numerical simulations, we find that the molecular key mechanisms behind Min oscillations are the transient sequestration of MinE proteins at the cell membrane, and a highly canalized transfer of MinD from old to new polar zones. We argue that robust formation and stabilization of patterns is completely defined by the system's nonlinear bulk-boundary couplings and geometric parameters, and suggest that localized nucleation of MinD polymers is the secondary process guided by the spontaneous oscillations.

RESULTS

Bulk-boundary couplings in cellular geometry

To correctly account for membrane-cytosol exchange dynamics in cellular geometry, we attribute pattern formation to a reactive coupling of distinct species diffusing trough the spatially extended cytosol and the cellular membrane. Previous comparable analytical approaches were restricted to circular geometries and linear bulk-boundary couplings, with spatial patterning relying on bulk degradation [20]. Here, we advance these methods to elliptical geome-

tries and nonlinear reactive boundary conditions, which generally account for possible multimolecular reactions between cytosolic and membrane-bound species. Moreover, we adapted the system parameters to meet recent experiments [21, 26], and disregarded cooperative recruitment of cytosolic MinD [14] or MinE [22] by MinDE complexes, as both processes lack experimental verification [21]. The resulting reaction scheme is based on four molecular processes: attachment, detachment, recruitment and nucleotide exchange. It is described in Fig. 1A. Total particle numbers are conserved, as synthesis and degradation of proteins does not affect the oscillation *in vivo* [31]. We chose orthogonal elliptical coordinates, given by the normal μ and tangential ν components at the boundary, see supplementary Fig. S1. The ensuing set of reaction-diffusion equations reads:

$$\partial_t u_{DT} = D_D \nabla^2 u_{DT} + \lambda u_{DD} \tag{1a}$$

$$\partial_t u_{DD} = D_D \nabla^2 u_{DD} - \lambda u_{DD} \tag{1b}$$

$$\partial_t u_E = D_E \nabla^2 u_E \tag{1c}$$

$$\partial_t u_d = D_d \nabla_\nu^2 u_d + u_{DT}(k_D + k_{dD} u_d) - k_{dE} u_E u_d \tag{1d}$$

$$\partial_t u_{de} = D_{de} \nabla_\nu^2 u_{de} + k_{dE} u_E u_d - k_{de} u_{de}\,, \tag{1e}$$

with nonlinear reactive boundary conditions stating that the reactions equal the flux onto $(-)$ and off $(+)$ the membrane

$$D_D \nabla_\mu u_{DT}|_{\mu=\mu_0} = -u_{DT}(k_D + k_{dD} u_d) \tag{2a}$$

$$D_D \nabla_\mu u_{DD}|_{\mu=\mu_0} = k_{de} u_{de} \tag{2b}$$

$$D_E \nabla_\mu u_E|_{\mu=\mu_0} = k_{de} u_{de} - k_{dE} u_E u_d\,. \tag{2c}$$

Here, u_{DT}, u_{DD} and u_E denote the bulk concentrations of MinD-ATP, MinD-ADP and MinE, respectively, and u_d, u_{de} the membrane concentrations of MinD and MinDE complexes. The limit of instantaneous nucleotide exchange is obtained by replacing both cytosolic MinD species with $u_D = u_{DT} + u_{DD}$. We will also study the implication of this limiting case, as it was assumed in some previous models [19, 22]. In elliptical geometry, patterns along the major or minor axis are expressed by even and odd modes, respectively, see Fig. 1B. The first even mode corresponds to pole-to-pole oscillations. Which modes grow or oscillate can be determined by linear stability analysis, see supplementary document for the technical details.

Conditions on the system parameters for spatial pattern formation

The model parameters are as far as they are available fixed by experimental data: We use the diffusion constants [21, 26] $D_D = 16\mu m^2/s$, $D_E = 10\mu m^2/s$, $D_d = D_{de} = 0.013\mu m^2/s$, and a nucleotide exchange rate $\lambda = 6s^{-1}$ to meet the lower bound [26] of $3s^{-1}$. Regarding particle numbers, we assume a linear scaling with cell size that corresponds to a total number of $N_D = 2000$ MinD monomers and $N_E = 700$ MinE dimers in a wild type elliptical cell of $5\mu m$ length and $1\mu m$ width [34, 39] which yields a MinD/MinE ratio of 2.86. We note that all discussed observations can be reproduced equally well for MinD/MinE ratios of 1.43, where MinD and MinE are both considered as dimers, see supplementary discussion and Fig. S2.
Lacking further *in vivo* measurements, the remaining parameters were adjusted to reproduce all experimentally observed oscillatory patterns [31, 36, 38]. Based on our analytical approach in elliptical geometry, we were able to identify pattern forming instabilities through linear stability analysis already on timescales below 0.1s. This is by order of magnitudes faster than what can be achieved by full simulation runs, which usually take tens of minutes for single parameter configurations. This technical progress allows us to investigate large parameter spaces and thereby make general assessment about a model's validity. By sampling parameter space for pole-to-pole oscillations at cell lengths about $2\mu m$, we were able to determine that, for spatial patterns to emerge in general, MinE needs to be recruited faster to the membrane than MinD (Fig. 1C), while being lower in total particle number:

$$k_{dD} < k_{dE}\,, \tag{3}$$

$$N_E < N_D\,. \tag{4}$$

While the specific ratio of recruitment rates and particle numbers up to which oscillations persist depends on all system parameters, the above conditions were always fulfilled. The implications on the specific mechanism of pattern formation will be discussed in the next section. The model parameters were further refined by accounting for temperature variations, and testing the model for striped and circular patterns with numerical simulations. Regarding the temperature-dependence, we assume an Arrhenius law for the hydrolysis rate k_{de}, with an activation energy $E_A = 16.7kcal/mol$ and normalization $k_{de}(20°C) = 0.4s^{-1}$. The remaining parameters are

$$k_D = 0.1\,\mu m\,s^{-1},\ k_{dD} = 0.108\,\mu m^2 s^{-1},\ k_{dE} = 0.435\,\mu m^2 s^{-1}. \tag{5}$$

These values will serve as reference in further discussions of the model's parameter dependencies.

Min oscillations are caused by transient sequestration of MinE

How do patterns emerge in the minimal model defined by the above reaction-diffusion equations (1a)-(2c)? The conservation of particle numbers ascribes formation and growth of any spatial pattern to a global redistribution of membrane-bound proteins through cytosolic diffusion. MinD is driven off the membrane upon binding MinE through stimulation of ATPase activity. Thereby MinE counteracts the accumulation of MinD at the membrane and drives the displacement of MinD. Polar zones can grow if the local MinE density is sufficiently low, and MinD particles are gradually transferred from MinDE domains to the polar zone. Figure 2 illustrates how the formation and separation of MinD and MinDE domains follows from the conditions on particle numbers and recruitment rates, Eq.(3) and (4), stated above. The higher particle number of MinD (Eq. (4)) enables complete sequestration of MinE in membrane-bound MinDE complexes, still leaving a fraction of MinD available to initiate a new polar zone. Given a sufficiently high MinD membrane concentration and MinE recruitment rate k_{dE}, detaching MinE rebinds immediately, forming the prominent MinE ring [4, 24, 32], see Fig. 2A,C and supplementary movie 1. Continuous MinE cycling locally depletes the membrane from MinD, leading to a slow movement of the MinE ring along the gradient of membrane bound MinD, whereupon a fraction of detaching MinD initiates a weak polar zone in the opposite cell half, see Fig. 2A. The new polar zone grows due to steady redistribution of MinD, while most MinE remains sequestrated in the old polar zone (Fig. 2B) until the remaining MinD are converted into MinDE complexes (Fig. 2B/C). Once this state is reached, the Min proteins rapidly detach, diffuse through the cytosol and rapidly reattach at the new polar zone (cf. supplemental movie 1), leaving behind a region of high MinDE/MinD ratio, where immediate reformation of polar zones is inhibited, cf. Fig. 2C. Due to the faster recruitment of MinE (Eq. (3)) the MinE ring reassembles at the rim of the new polar zone, which provides the crucial separation of MinD and MinDE maxima. Otherwise, MinE would diffuse into the polar zone and accumulate at the MinD maximum, deplete it, and suppress further formation of MinD domains. Moreover, we observed that the MinE recruitment rate k_{dE} regulates the width of the MinE ring and the timescale of polar zone recovery after disintegration. For higher MinE recruitment rates MinE rings narrow

and the recovery timescale increases as MinD reaccumulation is stronger suppressed by sequestrated MinE. The sequestration of MinE is transient, and the system oscillatory, if detaching MinD gradually leaks from polar zones. But how is MinD leakage established and regulated?

Cytosolic MinD transfer is regulated by MinD recruitment

It was argued that oscillations are sustained by the delayed MinD-ATP recovery [14], while the exchange rate λ itself has small impact on the oscillatory dynamics [38]. Indeed, our analysis confirms that the oscillation period depends rather weakly on the exchange rate λ (Fig. 3A). However, while the system stays oscillatory at high MinD recruitment rates k_{dD} even for unrealistically fast but finite exchange rates, it becomes stationary polarized in the limiting case of an instantaneous exchange, if the MinD recruitment rate exceeds a certain low threshold, cf. Fig. 3A. This threshold increases with the MinD attachment rate k_D and decreases with cell length. These results can be understood by considering the spatio-temporal regulation of MinD reattachment by MinD recruitment and recovery.
The MinD recruitment rate k_{dD} defines the "stickiness" of polar zones for cytosolic MinD-ATP. In contrast, a finite nucleotide exchange rate λ uncages MinD from polar zones as MinD only binds to the membrane in its active ATP-form. The faster the nucleotide exchange, and the stronger the recruitment, the less particles leak from polar zones. This is evident from the slowing down of the oscillation with increasing nucleotide exchange and MinD recruitment rates, depicted in Fig. 3A, and agrees with previous findings [14, 38]. With fast nucleotide exchange, MinD does not reaccumulate at the bare membrane before the old pole is depleted, whereas the MinD recruitment rate mainly regulates the reaccumulation position (Fig. 3B). On the other hand, for nucleotide exchange rates close to the experimentally determined lower bound of $3s^{-1}$, reaccumulation always starts in the opposite cell half, and the recruitment of MinD regulates how fast new polar zone grows towards the old one (Fig. 3C). Now, the period peaks at a low MinD recruitment rate $k_{dD} = 0.015\mu m^2/s$ and decreases with MinD recruitment from $41.2s$ to $35.6s$ at the global minimum around $k_{dD} = 0.1\mu m^2/s$, cf. Fig. 3A. This minimum marks parameter configurations where the redistribution of MinD from old to new polar zone is highly canalized, i.e. the total MinD flux is directed towards the opposite cell half immediately after the polar zones starts to shrink (Fig. 3C). Thereby, growth and depletion of polar zones become synchronized. This leads to the

characteristic triangular shape observed in MinD kymographs [23], where new polar zones start growing towards midcell while old polar zones shrink towards the cell pole, cf. Fig. 3C. As rebinding of MinD to the old polar zone is inhibited by delayed ATP recovery, and the growth of new polar zones is promoted by strong MinD recruitment, the oscillation period decreases as a function of the MinD recruitment rate due to a faster redistribution of MinD. Recall that the recovery of polar zones is suppressed by MinE recruitment, which highlights the interdependence of both recruitment processes. Although the system's dynamics is diffusive, which, per se, is an undirected process, the coupling of bulk diffusion and nucleotide exchange with nonlinear recruitment to the membrane enables regulation of the pole-to-pole particle transfer. While the uncaging effect of nucleotide exchange has been noticed previously [14], the role of MinD recruitment has been unknown, so far. Neglecting explicit nucleotide exchange as in earlier models [22] restricts the parameter space to low MinD recruitment rates. In this case, new polar zones do not grow until old polar zones are disassembled, cf. Fig. 3B/C. The following sections will reveal that canalizing MinD transfer enhances the biological function of Min oscillations and enables robust stripe formation in the first place.

Canalized MinD transfer improves the system's efficiency and midcell localization accuracy

The functional purpose of Min oscillations is the inhibition of Z-ring assembly apart from midcell by ongoing consumption of ATP. In this regard it is favourable to establish a high and permanent MinD membrane occupancy at the cell poles, ideally with the smallest number of attachment events during each oscillation cycle. For the localization of Z-ring assembly to be most precise, the mean MinD density should show a pronounced minimum at midcell with a high contrast to the cell poles. As shown in Figure 4A, the mean MinD density is always minimal at midcell, but it's particular shape strongly depends on the MinD recruitment rate k_{dD}. Since the typical environment of *E. coli* is the lower intestine of warm-blooded organisms, oscillations are considered at body temperature. The cell length is set to $5\mu m$.
To measure the optimality of Min oscillations we introduce two quantities. First, and most important, we ask for the accuracy of midcell localization. This depends on the accentuation of midcell in the MinD density profile. We distinguish between the width and the depth of the mean MinD density minimum at midcell, cf. Fig. 4B. If the ratio between width and depth of the

minimum is smallest, midcell is most distinctly accentuated. We find a well-defined and unique optimal value for the MinD recruitment rate k_{dD} (Fig. 4C), which, in addition, is very close to the fitted value (cf. Eq. (5)). The optimum coincides with the value where the MinD transfer is highly canalized. Increasing the MinD recruitment rate accelerates the growth of polar zones towards midcell, such that the mean density decreases at the cell tips, and increases at midcell, cf. Fig. 4A. If the MinD recruitment rate is too low, i.e. much lower than the MinE recruitment rate, recovery of polar zones is suppressed by the predominant rebinding of cytosolic MinE, such that polar zones form at late stages of the oscillation cycle and therefore are constrained to the cell tips, cf. Fig. 3C.

In a previous approach, the precision of midcell localization, depending on the MinD/MinE density ratio, has been investigated for the model by Huang et al. [18]. An acceptable precision could only be obtained at unrealistically high MinD/MinE ratios. Comparing the deterministic data with our results, we find that precision is substantially increased in the present model, even at the protein density ratios determined by experiments.

The second measure describes the efficiency with which MinD occupies the membrane, hence relates the mean membrane occupancy with the ATP consumption per oscillation cycle. While reducing ATP consumption alone might be rather subordinate, a higher MinD membrane density directly affects the probability of recruiting the division inhibitor MinC to the membrane. Again, we find a optimal value for the MinD recruitment rate k_{dD} that corresponds to highly canalized MinD transfer (Fig. 4D). Lower k_{dD} values reduce the mean MinD membrane density, while higher k_{dD} values increase the number of (re-)attachment events during polar zone disassembly but do not increase the mean MinD membrane density much more due to saturation effects.

From the evolutionary perspective, adjusting the pole-to-pole transfer of particles is beneficial and distinguishes favorable configurations out of the large parameter space. A refinement of MinD recruitment increases the accuracy of midcell localization and optimizes the system's ability to occupy the membrane with MinD. Since Min oscillations are highly robust against variations of the recruitment rates (cf. Fig. 1C), it seems plausible that the system was optimized through gradual refinement of the recruitment process.

MinE sequestration explains the persistent binding of MinE observed *in vitro*

Recent experiments revealed a persistent binding of MinE at the rear of MinD domains *in vitro* [21], even without direct MinE membrane interactions. With the transient sequestration of MinE, our model provides an explanation for this observation: The lower particle number of MinE enables sequestration, while fast MinE recruitment confines sequestration spatially, thereby inducing growth of MinD domains. Subsequently, continual leakage of MinD from the polar zones renders sequestration transient, hence the system oscillatory. In particular, the sharp decrease in protein densities at the end of the oscillation cycle is the result of spontaneously suspended sequestration (Fig. 2C). Albeit an extension by explicit MinE membrane interactions was suggested [1, 12, 30], additional sequestration of MinE by transient membrane bonds would merely amplify the argued mechanism, whilst introducing additional experimentally undetermined parameters. However, by implementing the recently proposed "tarzan of the jungle"-mechanism [30] in our model, we found that delayed MinE detachment from the membrane can weaken the condition on the particle numbers, Eq.(4), while additional cycling of MinE on the membrane by rapid recombination with MinD cannot replace the condition on the recruitment rates, Eq.(3). As a consequence, cytosolic cycling remains the key process, showing that the minimal model dynamics comprise a suitable skeleton model where future extensions can be build upon. In this respect it would be highly beneficial to obtain the exact ratio of MinD and MinE densities *in vivo* up to which regular Min oscillations persist, as well as the quantitative aspects of MinE interactions on and with the membrane.

Striped patterns dynamically emerge out of pole-to-pole oscillations

Next we demonstrate that the set of four molecular processes (Fig. 1A) suffices to reproduce all oscillatory patterns, see Fig. 5 and the supplementary material for the corresponding movies. First, we consider the transition of pole-to-pole to striped oscillations. As observed *in vivo* [31, 32], if the cell length exceeds a certain threshold an additional polar zone with an accompanying MinE ring emerges out of pole-to-pole oscillations such that MinD oscillates between both cell poles and midcell. The transition from pole-to-pole to stripe oscillations occurs dynamically as the cell grows, cf. [23]. Hence, for the emergence of stable stripe states, one important precondition is that pole-to-pole

oscillations become unstable first. Otherwise, either no transition would occur at all, or one could expect stochastic switching between both patterns. However, the transition to stripes is very robust and even independent of system temperature [38]. These observations are at odds with previous theoretical studies which found that the formation of stripes depends on initial conditions [38], or that stochastic fluctuations lead to switching between travelling waves and striped oscillations [37]. Therefore, we chose a pole-to-pole wave solution peaking in one cell half as initial condition, and determined the rate constants (Eq. (5)) which yield transitions into stable stripes. This choice of initial conditions was crucial, as the choices made in previous studies [7] proved insufficient for parameter refinement, see supplementary material. We confirm that stable stripes are absent in a reduced one-dimensional geometry with reflecting boundaries [14]. However, we did find stable striped oscillations in the analogous two-dimensional rectangular geometry with reflecting polar caps, indicating that the spatial separation of bulk and membrane is essential for stripe formation. In terms of the scheme in Fig. 2A/B, increasing the cell length promotes the simultaneous formation and depletion of two MinD domains through continuous redistribution of MinD and MinE, leading to colliding unidirectional travelling waves and ultimately the striped pattern, see Fig. 5C and supplementary movie 3. We found that stable stripes emerge out of pole-to-pole waves, only if weak polar zones are enhanced early on by sufficiently strong MinD recruitment, $k_{dD} \gtrsim 0.1\mu m^2/s$. Hence, stripe formation and the optimization of the wild type oscillation cycle are based on the same mechanism. Since striped patterns are irrelevant for the wild type division cycle per se, and are only supported in a small subset of the oscillatory parameter regime (cf. Fig. 1C), they seem to result from an evolutionary optimization of wild type oscillations.

An Arrhenius law for the hydrolysis rate accounts for temperature variations

The reproducibility of temperature dependencies poses a further critical test on the model's robustness. Figure 5A shows the period of pole-to-pole and striped oscillations as a function of temperature, implemented through the hydrolysis rate $k_{de} \propto \exp(-E_A/RT)$, with the activation energy $E_A = 16.7kcal/mol$, the gas constant R, and the absolute temperature T. In agreement with experiments [38], the period-temperature relation is given by an Arrhenius law. Over the complete temperature range, and for all initial conditions, the final pat-

terns stayed qualitatively unchanged, see Fig. 5B. This result highlights the importance of a systematic parameter refinement, as even recent expositions report a loss of oscillations with varying hydrolysis rate [5]. In contrast, our model reveals a strong robustness over a large range of hydrolysis rates. Increasing the temperature leads to faster local cycling of Min-proteins between membrane and cytosol. With each cycle, a fraction of MinD leaks from the polar zone. As a consequence, the temporal period decreases due to a faster redistribution of particles, but the spatial wavelength remains unaffected, as it does not depend on the detachment process. However, oscillations can be lost with increasing hydrolysis rate k_{de} if either attachment or recruitment of MinD is chosen too low. In these cases, an accumulation of MinD at the membrane is impeded by rapid detachment. This provides a possible explanation for the parameter sensitivity observed in previous accounts [5, 38]. Note that the polar zones and MinE rings narrow with increasing temperature (cf. Fig. 5B). This can be explained by the decreased residence time of membrane-bound proteins, which reduces the distance proteins diffuse on the membrane before detachment. Accordingly, we find that the narrowing effect vanishes if membrane diffusion is either turned off, or increased sufficiently along with temperature. Since all diffusion constants depend on temperature, the narrowing of polar zones and MinE rings might be too weak to notice experimentally, or even completely compensated by faster diffusion. Regarding possible temperature dependencies of the remaining parameters the system remains robust: To account for temperature increase ($k_{de} = 2.5s^{-1}$), all other system parameters, i.e. diffusion constants and kinetic rates, can be increased jointly up to a factor of about eight without changing the spatial wavelength. If the upscaling of the diffusion constants is limited to a factor two, the kinetic rates can be increased jointly up to threefold. Due to this robustness we did not include explicit temperature dependencies for the remaining parameters.

Striped patterns do not adapt to cardiolipin domains

The results above demonstrate that spatial cues are not necessary to ensure robust patterns. However, as MinD preferentially binds to anionic phospholipids like cardiolipin found at the cell poles [27, 28], we asked if oscillatory patterns adapt to spatial templates. We considered two different templates in the regime where striped oscillations emerged by restricting MinD attachment to predefined parts of the membrane, see Fig 6C. First, a template for the pole-to-pole oscillation, where direct MinD attachment is restricted to both

cell poles, and second, a periodic template corresponding to the next stripe state given by four separate attachment domains. In both cases, and for various initial conditions, the patterns finally evolved into the original striped oscillation, i.e. no adaption could be observed, see Fig 6C. We find that slow diffusion of membrane-bound MinD, which is is followed by fast recruitment, suffices to promote the formation of robust MinD domains even without foregoing MinD attachment, cf. Fig. 6A,B. This observation demonstrates that the initial position of MinD attachment does not categorically determine the final position of MinD stripes. In contrast to recruitment, the MinD attachment process does not amplify membrane bound patterns, but merely increases the MinD membrane density throughout the cell. Accordingly, we find for the model with spatially homogeneous MinD attachment, that varying the attachment rate k_D rather leads to the loss of instability than to a qualitative change of the spatial pattern.
So, which processes do regulate the characteristic wavelength? From the discussion of the channelling mechanism, we know that the interplay between MinD recruitment and finite nucleotide exchange affects the growth rate of new MinD domains towards the old ones. On the other hand, the MinE recruitment rate k_{dE} defines a minimal distance between MinD stripes, as it determines the width of the MinE ring, and thereby the zone where the accumulation of MinD is suppressed, cf. Fig. 2A,B. Of course, the distance between detachment and re-recruitment also depends on the bulk diffusion coefficients. In contrast, being pronounced membrane-bound structures, MinE rings and MinD stripes widen independently of the recruitment rates with increasing membrane diffusion. In summary, it is the interplay of all processes, and not a specific one, which defines the characteristic wavelength: From the kinetic rates it are the recruitment processes, that affect the pattern's spatial properties most, but, in general, varying these rates alone does not suffice to drive the system into a regular higher order striped state without increasing cell length.

Geometry selects patterns in nearly spherical cells

Patterns in nearly spherical cells result from the additional destabilisation of odd modes, see Fig. 1B. For instance, in cells of $2.4\mu m$ length and $2.2\mu m$ width we observed predominant pole-to-pole oscillations along the major axis over a period of about $535s$ that fade to circular waves and oscillations along a rotating axis for about $175s$, until pole-to-pole oscillations are reestablished

again, see Fig. 5D and supplementary movie 4. Additionally, as a random switching of the travelling direction was observed for circular waves *in vivo* [36], it occurs between consecutive phases of circular waves *in silico*. After the division of nearly spherical cells, one observes a shift of the oscillation axis by 90° towards the cell's new long axis [36]. We employed a deformed mesh technique to increase the cell's width dynamically beyond its length, and likewise observed a shift towards the major axis, see supplementary movie 5. Taken together, our findings indicate that this variety of patterns is primarily caused by weak aberrations from spherical symmetry, and not by stochastic effects or unstable higher order modes, as presumed previously [7, 16].

DISCUSSION

Our analysis identifies transient MinE sequestration to be the key mechanism behind Min oscillations. Sequestration of MinE is based on a lower particle number of MinE or, alternatively, on direct interactions between MinE and the lipid membrane. We find that the faster recruitment of MinE confines sequestration to the rim of polar zones and continual leakage of MinD from old to new polar zones renders sequestration transient. The cellular geometry imposes a nonlinear bulk-boundary coupling, which is key for the selection and stabilisation of spatial patterns.

How do MinD filaments, cardiolipin domains, and irregular patterns fit in this picture? Several models accounting for Min-protein filaments assert the nucleation of MinD polymers to be mediated, and thereby localized, by cardiolipin domains at the cell poles [3, 6]. Consequently, all patterns in filamentous cells ought to be determined by a dynamic periodic template of cardiolipin domains with an intrinsic spatial wavelength. However, neither a presence of periodic templates, nor a colocalization of MinD and cardiolipin domains has been reported in filamentous cells so far. Moreover, as cardiolipin adapts to membrane curvature, so should MinD, but, based on the limited available data, bending filamentous cells does not seem to affect the spatial MinD patterns, cf. e.g. [31, 38]. The mechanism presented in this paper is independent of, and, in fact, robust against spatial cues. This suggests a different origin for MinD nucleation: MinD filaments have been reported in two different setups. *In vivo*, helical MinD filaments only appear along with Min oscillations [35]. In particular, MinD settles in a homogeneous membrane-bound state without any additional ordered structure, if the cell is lacking MinE, and therefore oscillations. This observation immediately follows from our model, as membrane

diffusion removes any potential inhomogeneities caused by spatially restricted MinD attachment. Helical MinD filaments were also observed at high MinD concentrations *in vitro* [13]. In presence of ATP and phospholipid vesicles, MinD assembles in helical structures. Taking both observations together, nucleation of MinD filaments could be promoted at high local MinD densities *in vivo*. In this case, the nonlinear dynamics described by our model provide the primary mechanism, necessary to induce MinD nucleation at the polar zones, suggesting that MinD polymerisation is the consequence and not the origin of spontaneous pattern formation. This scenario resembles the directed assembly of actin cables guided by polar caps of the GTPase Cdc42 in yeast [40].

Irregular patterns, like stochastic pole-to-pole switching in short cells [8], or aberrant oscillations in cells mutant for MinE [12], imply the loss of robustness. In our model, robustness and oscillatory patterns share the same origin. Formation and growth of polar zones and MinE rings is impelled by strong recruitment of MinD and MinE and only constrained by the finite number of available particles. The character of Min oscillations is highly nonlinear, with the cell length acting as natural parameter driving the system from dynamical equilibrium towards highly stable limit cycles corresponding to the individual patterns. Therefore, irregular patterns can only arise in regimes where the system dynamics are moved close to primal bifurcation points. In these regimes close to threshold the system is highly susceptible to fluctuations, such that stochastic dynamics, spatial irregularities, and additional molecular processes that were irrelevant for the regular pattern forming process might play a crucial role. For instance, stochastic pole-to-pole switching were only observed in short cells with lengths below $2.7\mu m$ [8], which is close to the onset of dynamical instability in our model. An investigation of these phenomena, however, is only possible in a stochastic model.

Another example for irregularities is given by the appearance of aberrant oscillations in cell mutant for MinE (MinE C1) [12]. As these mutant MinE lack the ability to bind to the lipid membrane, direct MinE membrane interactions were suggested as an important process for robust Min oscillations. However, the C1 mutant also shows a reduced interaction strength with MinD. Reducing the MinE recruitment rate in our model drives the system towards dynamical equilibrium, suggesting that the reduced MinE-MinD interaction and not the loss of MinE-membrane interactions might have disturbed the oscillatory dynamics in the first place. This example emphasizes that conclusions drawn from irregular dynamics do not necessarily hold for regular Min oscillations, as critical regimes might be dominated by mechanisms not included in the minimal model due to their weak influence on the regular dynamics. Accordingly,

further experiments should be performed in close contact with theoretical modelling. In particular, experiments with the MinE-C1 mutant could validate the sequestration mechanism, as the model predicts that patterns vanish when the MinE concentration approaches the MinD concentration.
Beyond that, a multitude of predictions immediately follows from our results on MinD channelling. For instance, striped patterns should vanish, and accurate cell divisions be compromised, if the MinD recruitment rate could be significantly reduced. Moreover, patterns should vanish, if the MinE recruitment process is weakened severalfold.
The model also predicts an Arrhenius law for the hydrolysis rate with an activation energy about $16.7 kcal/mol$. Quantitative knowledge about the temperature dependencies of the various reactions involved in Min-protein dynamics would improve further theoretical investigations substantially.
Reaching for a complete and coherent account to the Min system as a whole, the next step is to apply the model to *in vitro* dynamics [21, 22] and to verify the sequestration mechanism experimentally. As a preliminary result we note that the current model sustains bands of synchronous travelling waves as observed *in vitro* [21, 22], even without extending the reaction scheme (Fig. 1A) by the suggested nonlinear detachment [21] of Min-proteins or cooperative MinE recruitment [22].
On a broader perspective, the presented theoretical formalism enables the investigation of protein dynamics *in vivo* and *in vitro* with explicit account for the underlying system geometries and nonlinear bulk-boundary couplings. Examples are intracellular polarization mechanisms driven by reaction-diffusion processes, e.g. in *C. elegans* [10] or *S. cerevisiae* [17].

METHODS

Numerical simulations and initial conditions.

All time dependent computations were performed with finite element methods on a triangular mesh using Comsol Multiphysics 3.5a. As initial conditions, linear profiles along the cell's long axis with varying slopes and small random fluctuations at each mesh site were chosen. In these cases all particles were initially located in the bulk. The travelling wave initial condition used in simulations with filamentous cells was obtained by choosing a low MinD recruitment rate about $k_{dD} = 0.03 \mu m^2/s$ and picking the travelling wave solution at a time step where the total MinD concentration was maximal in one

cell half.

ACKNOWLEDGMENTS

The authors thank Andrew Rutenberg and Manfred Jericho for kindly providing their data [38] and Ulrich Gerland for critical reading of the manuscript. This project has been financially supported by the German Excellence Initiative via the program "Nanosystems Initiative Munich" (NIM).

FIGURES

Figure 1

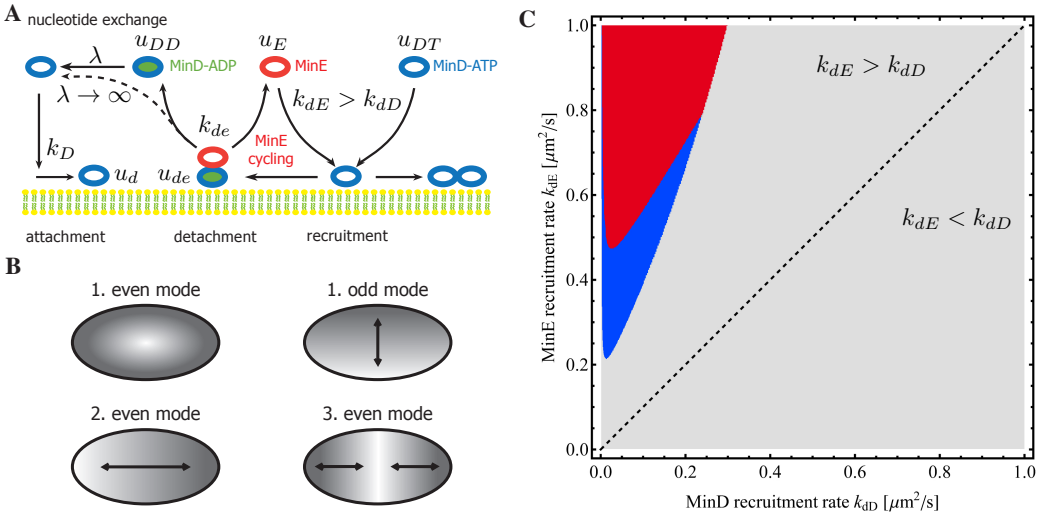

FIG. 1. Minimal model dynamics and dynamical instabilities.

A, Cytosolic MinD-ATP attaches to the membrane with a rate k_D, where it recruits further MinD-ATP and MinE from the cytosol with rates k_{dD} and k_{dE}, respectively. Recruitment of MinE leads to the formation of MinDE complexes, which disintegrate to cytosolic MinD-ADP and MinE with the temperature dependent hydrolysis rate $k_{de} \propto \exp(-E_A/RT)$. Finally, MinD-ADP exchanges nucleotides with rate λ. The scheme highlights the possibility of local MinE cycling, given a sufficiently high density of membrane bound MinD. **B,** Schematic illustration of even and odd modes in elliptical geometry. **C,** Phase portrait for both recruitment processes illustrates the condition on the recruitment rates ((3)) for dynamical instabilities $k_{de} = 0.65s^{-1}$. In the grey domain the system is stable below cell lengths of $2\mu m$. The colored region shows where only even modes (blue) or even and odd modes (red) are unstable at cell lengths below $2.8\mu m$. Numerical simulations determined that only pole-to-pole oscillations are selected in the red domain.

Figure 2

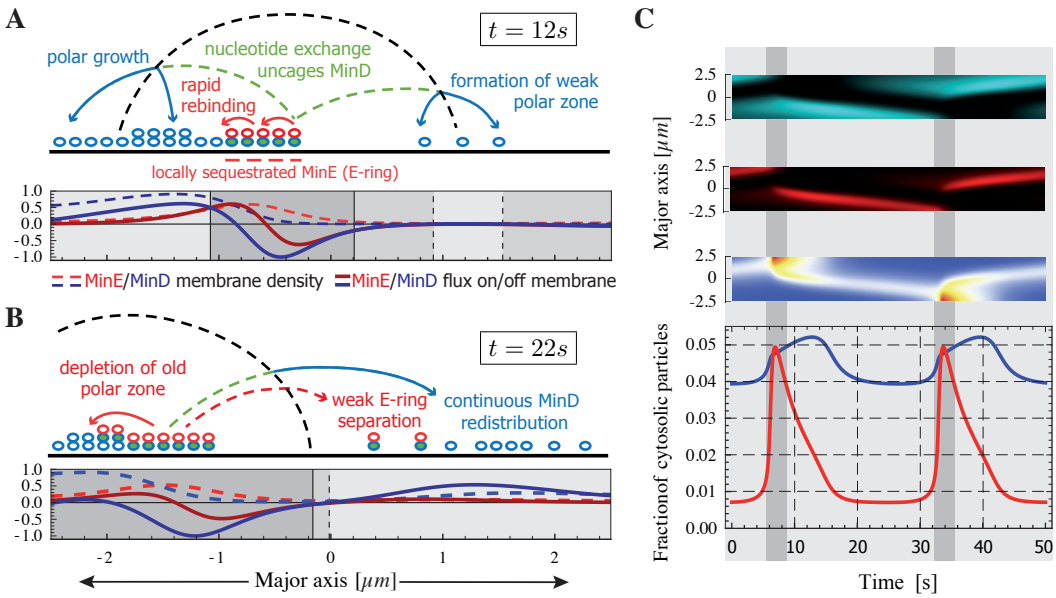

FIG. 2. Key mechanisms underlying Min oscillations.

A, Locally sequestrated MinE constitutes the MinE ring, which moves towards the left pole through local cycling. Detaching MinD rebinds predominately at the left pole and initiates a weak polar zone at the right end. The delayed reattachment due to nucleotide exchange is indicated by dashed lines. The numerical data below corresponds to the timestep $t = 12s$ in Fig. 2C (densities are scaled by a factor $2.5 \times 10^{-3}\mu m^{-1}$, fluxes by a factor $1.8 \times 10^{-2}\mu m^{-1}s^{-1}$). The accentuation shows regions of dominant MinD attachment (light) or MinE attachment (dark). These adjoin to regions (grey) where MinD accumulation is suppressed due to dominant MinE detachment. **B,** MinE depletes the old polar zone of MinD, until only MinDE complexes are left, then reassembles at the rim of the new polar zone, formed by redistributed MinD. The numerical data corresponds to the timestep $t = 22s$ in Fig. 2C (densities are scaled by a factor $2.6\times10^{-3}\mu m^{-1}$, fluxes by a factor $2.2\times10^{-2}\mu m^{-1}s^{-1}$). **C,** Top: Kymographs at $T = 22.5°C$: Membrane densities of MinD+MinDE (turquoise), MinDE (red) and the fraction MinDE/MinD in logarithmic color scale. Bottom: Fractions of total cytosolic particles, MinD (blue) and MinE (red). Accentuated regimes correspond to transient sequestration (light) and rapid relocalization (dark) of MinE. Cf. supplementary movie 1.

Figure 3

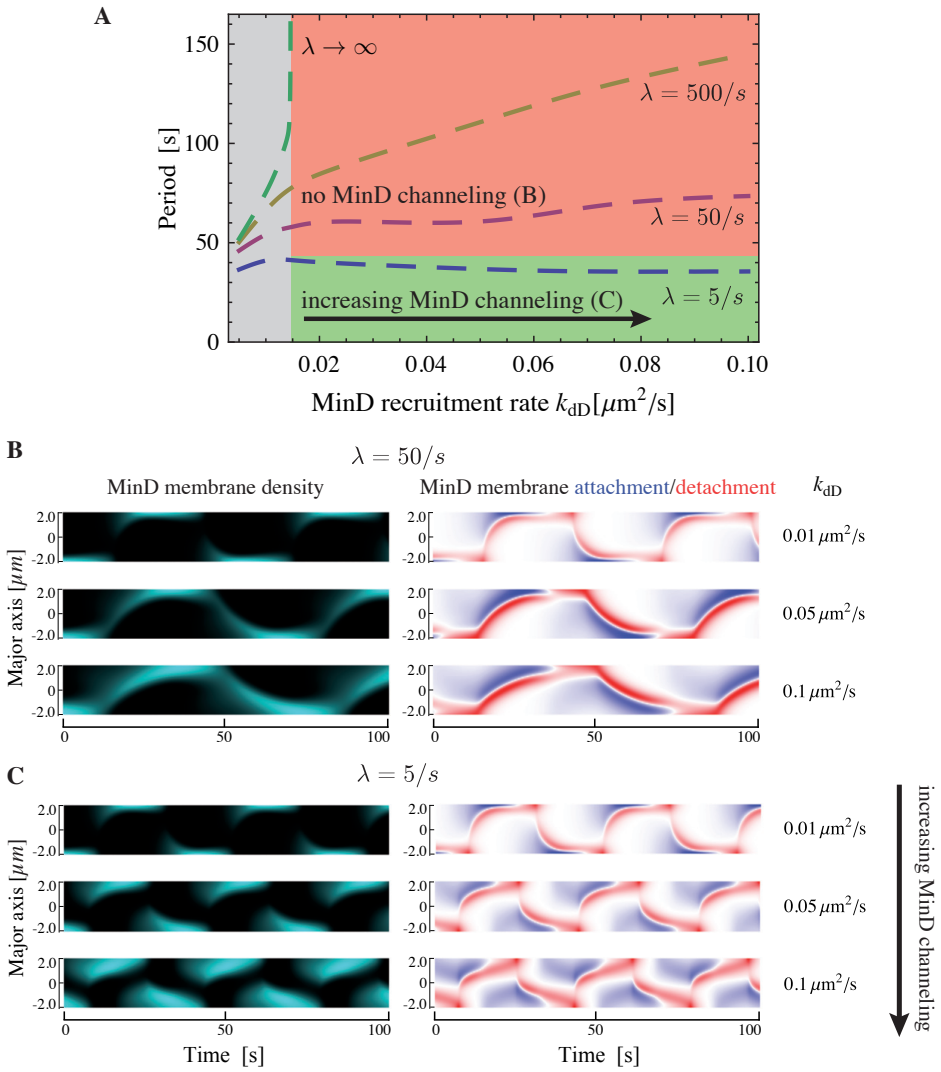

FIG. 3. Canalized MinD transfer and regulation of spatial MinD reattachment by MinD recruitment.

A, Temporal period as function of MinD recruitment k_{dD} and nucleotide exchange λ in cells of $4\mu m$ length at $T = 25°C$. With instantaneous nucleotide exchange, oscillations only exist at low MinD recruitment rates (grey). Beyond this threshold the nucleotide exchange and recruitment rates become control parameters for the spatial distribution of MinD reattachment. At high but finite nucleotide exchange rates the oscillation period increases with the

MinD recruitment rate as MinD reassembles in front of the polar zone, cf. Fig. 3B below. At low nucleotide exchange rates the oscillation period decreases with MinD recruitment as the pole-to-pole particle transfer becomes canalized between both cell halves, cf. Fig 3C below. **B,** Kymographs for $\lambda = 50s^{-1}$ showing the total MinD membrane density $u_d + u_{de}$ and MinD flux $D_D \nabla_\mu (u_{DT} + u_{DD})|_{\mu=\mu_0}$ on (blue) and off (red) the membrane for stepwise increasing MinD recruitment rates. At higher MinD recruitment rates MinD is not depleted but reflected at the cell poles. In this case MinD reattaches in front of a moving MinD wave. **C,** Analogous kymographs for $\lambda = 5s^{-1}$. Here, MinD reaccumulates at the opposite cell pole. Increasing MinD recruitment accelerates the growth of new polar zones towards midcell and synchronizes depletion and formation of polar zones at opposite cell ends by canalizing the MinD flux from old to new polar zones.

Figure 4

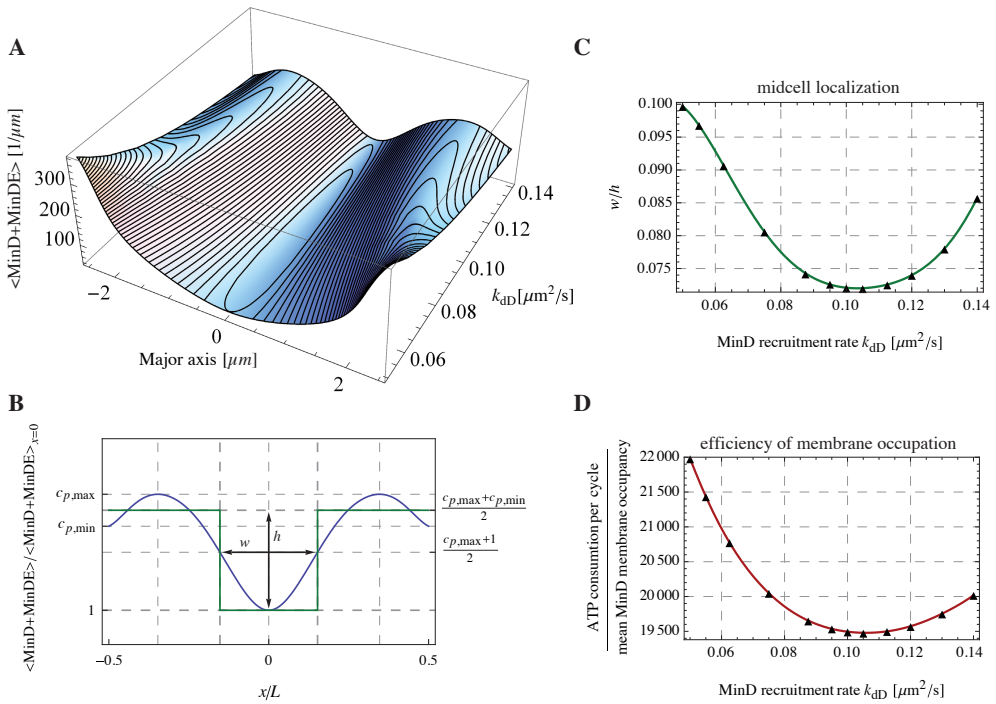

FIG. 4. Optimization of pole-to-pole oscillations by canalized MinD transfer at $T = 37.5°C$.

A, Mean MinD membrane density during one oscillation cycle as function of the MinD recruitment rate k_{dD}. With increasing MinD recruitment, polar zones grow dynamically towards midcell, reflected in a decreased distance between the maxima in the density profile. **B,** Characterisation of the mean MinD membrane density by the width w and depth h of the MinD density minimum at midcell. The axial coordinate x is rescaled by the cell length L. The density is rescaled by its value at $x = 0$. **C,** Optimal midcell localization, defined as the minimum of w/h as a function of the MinD recruitment rate. Optimum at $k_{dD} = 0.103\mu m^2/s$. The solid line shows the interpolation of the numerical data (triangles). **D,** Efficiency of pole-to-pole oscillations, defined as the ratio of ATP consumption per cycle and the mean MinD membrane occupancy as a function of the MinD recruitment rate. Optimum at $k_{dD} = 0.106\mu m^2/s$. The solid line shows the interpolation of the numerical data (triangles).

Figure 5

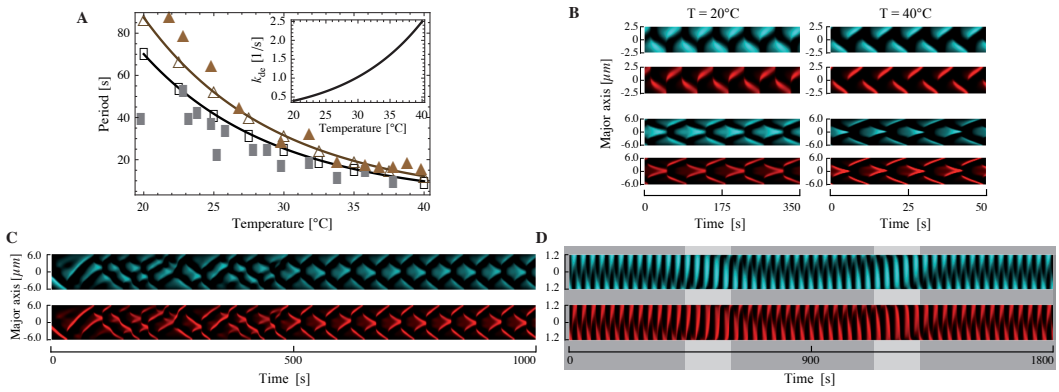

FIG. 5. The temperature dependence and the dynamic adaptation of spatial patterns to cell geometry.

A, Temperature dependent periods of pole-to-pole (open rectangles) and striped (open triangles) oscillations with their according Arrhenius fits ($E_A = 18kcal/mol$), see supplementary material for discussion. Cell lengths are $5\mu m$ and $12\mu m$, respectively. Filled rectangles and triangles show experimental data 38 for cells of $4\mu m - 5\mu m$ and tens of μm length, respectively. Inset shows temperature dependent hydrolysis rate. **B,** Kymographs of membrane densities MinD+MinDE (turquoise) and MinDE (red) for pole-to-pole (top) and striped oscillations (bottom). Cf. supplementary movies 2a-2d.**C,** Example of stripe formation out of travelling waves. Cf. supplementary movie 3. **D,** Kymographs of membrane densities in the upper cell half for nearly spherical cells ($2.4\mu m$ length, $2.2\mu m$ width) show switching between predominant pole-to-pole oscillations (dark) and circular waves (light). Cf. supplementary movie 4.

Figure 6

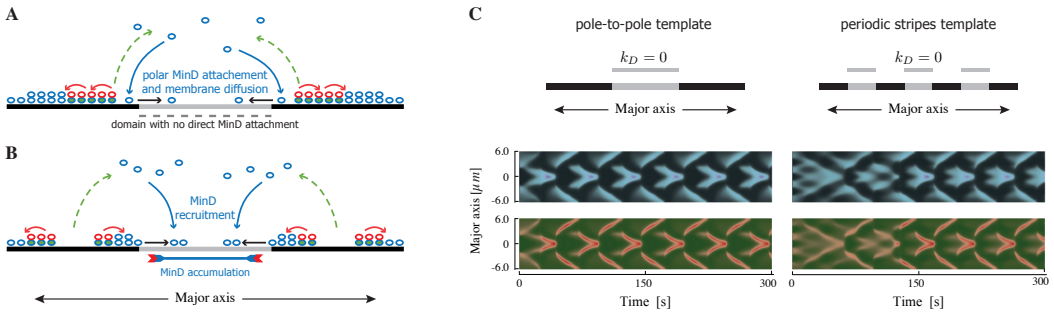

FIG. 6. Effect of spatial cues on spatio-temporal pattern formation.

A, MinD attachment is restricted to the cell poles. Following polar MinD attachment, MinD diffuses towards midcell. **B,** Even without direct MinD attachment, a MinD zone forms at midcell due to slow membrane diffusion and fast MinD recruitment from the cytosol. **C,** Kymographs of Min oscillations in filamentous cells with spatially restricted MinD attachment, MinD (blue), MinE (red/green). Left: Restricting MinD attachment to the cell poles does not jeopardize stripe formation. Right: Adding further attachment domains corresponding to the next striped pattern does not promote additional stripe formation.

[1] Arjunan, A., and Tomita, M. (2010). A new multicompartmental reaction-diffusion modeling method links transient membrane attachment of E. coli MinE to E-ring formation. *Syst. Synth. Biol.*, *4*, 35–53.

[2] de Boer, P., and Meinhardt, H. (2001). Pattern formation in Escherichia coli: A model for the pole-to-pole oscillations of Min proteins and the localization of the division site. *Proc. Natl. Acad. Sci. USA*, *98*, 14202–14207.

[3] Cytrynbaum, E. N., and Marshall, B. D. L. (2007). A multistranded polymer model explains MinDE dynamics in E. coli cell division. *Biophys. J.*, *93*, 1134–1150.

[4] Derr, J., Hopper, J., Sain, A., and Rutenberg, A. (2009). Self-organization of the MinE protein ring in subcellular Min oscillations. *Phys. Rev. E*, *80*, 011922.

[5] Di Ventura, B., and Sourjik, V. (2011). Self-organized partitioning of dynamically localized proteins in bacterial cell division. *Mol. Syst. Biol.*, *7*, 1–13.

[6] Drew, D., Osborn, M., and Rothfield, L. (2005). A polymerization-depolymerization model that accurately generates the self-sustained oscillatory system involved in bacterial division site placement. *Proc. Natl. Acad. Sci. USA*, *102*, 6114–6118.

[7] Fange, D., and Elf, J. (2006). Noise-induced Min phenotypes in E. coli. *PLoS Comput. Biol.*, *2*, e80.

[8] Fischer-Friedrich, E., Meacci, G., Lutkenhaus, J., Chaté, H., and Kruse, K. (2010). Intra- and intercellular fluctuations in Min-protein dynamics decrease with cell length. *Proc. Natl. Acad. Sci. USA*, *107*, 6134–6139.

[9] Ghasriani, H., Ducat, T., Hart, C. T., Hafizi, F., Chang, N., Al-Baldawi, A., Ayed, S. H., Lundström, P., Dillon, J.-A. R., and Goto, N. K. (2010). Appropriation of the MinD protein-interaction motif by the dimeric interface of the bacterial cell division regulator MinE. *Proc. Natl. Acad. Sci. USA*, *107*,

18416–18421.

[10] Goehring, N. W., Trong, P. K., Bois, J. S., Chowdhury, D., Nicola, E. M., Hyman, A. A., and Grill, S. W. (2011). Polarization of PAR proteins by advective triggering of a pattern-forming system. *Science*, *334*, 1137–1141.

[11] Howard, M., Rutenberg, A. D., and de Vet, S. (2001). Dynamic Compartmentalization of Bacteria: Accurate Division in E. Coli. *Phys. Rev. Lett.*, *87*, 1–4.

[12] Hsieh, C.-W., Lin, T.-Y., Lai, H.-M., Lin, C.-C., Hsieh, T.-S., and Shih, Y.-L. (2010). Direct MinE-membrane interaction contributes to the proper localization of MinDE in E. coli. *Mol. Microbiol.*, *75*, 499–512.

[13] Hu, Z., Gogol, E., and Lutkenhaus, J. (2002). Dynamic assembly of MinD on phospholipid vesicles regulated by ATP and MinE. *Proc. Natl. Acad. Sci. USA*, *99*, 6761–6766.

[14] Huang, K., Meir, Y., and Wingreen, N. (2003). Dynamic structures in Escherichia coli: spontaneous formation of MinE rings and MinD polar zones. *Proc. Natl. Acad. Sci. USA*, *100*, 12724–12728.

[15] Huang, K. C., Mukhopadhyay, R., and Wingreen, N. S. (2006). A curvature-mediated mechanism for localization of lipids to bacterial poles. *PLoS Comput. Biol.*, *2*, e151.

[16] Huang, K. C., and Wingreen, N. S. (2004). Min-protein oscillations in round bacteria. *Phys. Biol.*, *1*, 229–235.

[17] Johnson, D. (1999). Cdc42 : An Essential Rho-Type GTPase Controlling Eukaryotic Cell Polarity. *Microbiol Mol Biol R*, *63*, 54–105.

[18] Kerr, R. A., Levine, H., Sejnowski, T. J., and Rappel, W.-J. (2006). Division accuracy in a stochastic model of Min oscillations in Escherichia coli. *Proc. Natl. Acad. Sci. USA*, *103*, 347–352.

[19] Kruse, K., Howard, M., and Margolin, W. (2007). An experimentalists guide to computational modelling of the Min system. *Mol. Microbiol.*, *63*, 1279–1284.

[20] Levine, H., and Rappel, J. (2005). Membrane-bound Turing patterns. *Physical Review E*, *72*, 1–5.

[21] Loose, M., Fischer-Friedrich, E., Herold, C., Kruse, K., and Schwille, P. (2011). Min protein patterns emerge from rapid rebinding and membrane interaction of MinE. *Nat. Struct. Mol. Biol.*, *18*, 577–583.

[22] Loose, M., Fischer-Friedrich, E., Ries, J., Kruse, K., and Schwille, P. (2008). Spatial regulators for bacterial cell division self-organize into surface waves in vitro. *Science*, *320*, 789–792.

[23] Loose, M., Kruse, K., and Schwille, P. (2011). Protein Self-Organization: Lessons from the Min System. *Annu. Rev. Biophys.*, *40*, 315–36.

[24] Lutkenhaus, J. (2007). Assembly dynamics of the bacterial MinCDE system and spatial regulation of the Z ring. *Annu. Rev. Biochem.*, *76*, 539–562.

[25] Meacci, G., and Kruse, K. (2005). Min-oscillations in Escherichia coli induced by interactions of membrane-bound proteins. *Phys. Biol.*, *2*, 89–97.

[26] Meacci, G., Ries, J., Fischer-Friedrich, E., Kahya, N., Schwille, P., and Kruse, K. (2006). Mobility of Min-proteins in Escherichia coli measured by fluorescence correlation spectroscopy. *Phys. Biol.*, *3*, 255–263.

[27] Mileykovskaya, E., and Dowhan, W. (2009). Cardiolipin membrane domains in prokaryotes and eukaryotes. *Biochimica et biophysica acta*, *1788*, 2084–91.

[28] Mileykovskaya, E., Fishov, I., Fu, X., Corbin, B. D., Margolin, W., and Dowhan, W. (2003). Effects of phospholipid composition on MinD-membrane interactions in vitro and in vivo. *The Journal of biological chemistry*, *278*, 22193–8.

[29] Mukhopadhyay, R., Huang, K. C., and Wingreen, N. S. (2008). Lipid localization in bacterial cells through curvature-mediated microphase separation. *Biophysical journal*, *95*, 1034–49.

[30] Park, K.-T., Wu, W., Battaile, K. P., Lovell, S., Holyoak, T., and Lutkenhaus, J. (2011). The Min Oscillator Uses MinD-Dependent Conformational Changes

in MinE to Spatially Regulate Cytokinesis. *Cell*, *146*, 396–407.

[31] Raskin, D. M., and de Boer, P. (1999). Rapid pole-to-pole oscillation of a protein required for directing division to the middle of Escherichia coli. *Proc. Natl. Acad. Sci. USA*, *96*, 4971–4976.

[32] Raskin, D. M., and de Boer, P. a. (1997). The MinE ring: an FtsZ-independent cell structure required for selection of the correct division site in E. coli. *Cell*, *91*, 685–694.

[33] Renner, L., and Weibel, D. (2011). Cardiolipin microdomains localize to negatively curved regions of Escherichia coli membranes. *Proc. Natl. Acad. Sci. USA*, *108*, 6264.

[34] Shih, Y., Fu, X., King, G., Le, T., and Rothfield, L. (2002). Division site placement in E. coli: mutations that prevent formation of the MinE ring lead to loss of the normal midcell arrest of growth of polar MinD membrane domains. *EMBO J.*, *21*, 3347–3357.

[35] Shih, Y., Le, T., and Rothfield, L. (2003). Division site selection in Escherichia coli involves dynamic redistribution of Min proteins within coiled structures that extend between the two cell poles. *Proc. Natl. Acad. Sci. USA*, *100*, 7865–7870.

[36] Shih, Y. L., Kawagishi, I., and Rothfield, L. (2005). The MreB and Min cytoskeletal-like systems play independent roles in prokaryotic polar differentiation. *Mol. Microbiol.*, *58*, 917–928.

[37] Tostevin, F., and Howard, M. (2006). A stochastic model of Min oscillations in Escherichia coli and Min protein segregation during cell division. *Phys. Biol.*, *3*, 1–12.

[38] Touhami, A., Jericho, M., and Rutenberg, A. D. (2006). Temperature dependence of MinD oscillation in Escherichia coli: running hot and fast. *J. Bacteriol.*, *188*, 7661–7667.

[39] Unai, S., Kanthang, P., Junthon, U., Ngamsaad, W., Triampo, W., Modchang,

C., and Krittanai, C. (2009). Quantitative analysis of time-series fluorescence microscopy using a spot tracking method: application to Min protein dynamics. *Biologia*, *64*, 27–42.

[40] Wedlich-Soldner, R., Altschuler, S., Wu, L., and Li, R. (2003). Spontaneous cell polarization through actomyosin-based delivery of the Cdc42 GTPase. *Science*, *299*, 1231–1235.

A highly canalized MinD transfer and MinE sequestration explain the origin of robust MinCDE-protein dynamics

– Supplementary Document –

Jacob Halatek and Erwin Frey
Arnold-Sommerfeld-Center for Theoretical Physics and Center for NanoScience, Department of Physics, Ludwig-Maximilians-Universität München, Theresienstraße 37, D-80333 München, Germany

CONTENTS

LEGENDS FOR SUPPLEMENTARY MOVIES

In all movies, the line height corresponds to the MinD+MinDE concentration at the membrane, line color (left bar) to the MinDE concentration at the membrane, and bulk color (right bar) to the concentration of cytosolic MinE. Parameters are as stated in the article.

movie 1: Illustration of rapid rebinding and transient sequestration of MinE.

Movie shows pole-to-pole oscillations at $T = 22.5°C$ ($k_{de} = 0.51s^{-1}$), in a cell of $5\mu m$ length. In addition to the above quantities, the movie shows the diffusive flux field of cytosolic MinE as a streamline plot. Note the constriction of streamlines in each transient polarized phase, and the burst in cytosolic MinE density in between. The initial condition was taken as a homogeneous state with small fluctuations at each mesh site. Movie corresponds to the kymographs in Fig. 2C, provided in the article.

movie 2a: Pole-to-pole oscillations at $T = 20°C$.

Cell length is $5\mu m$ and the hydrolysis rate is $k_{de} = 0.4s^{-1}$. The initial condition was taken as a homogeneous state with small fluctuations at each mesh site. All particles were initially located in the cytosol. Movie corresponds to the kymographs in Fig. 5B, provided in the article.

movie 2b: Pole-to-pole oscillations at $T = 40°C$.

Cell length is $5\mu m$ and the hydrolysis rate is $k_{de} = 2.5s^{-1}$. The initial condition was taken as a homogeneous state with small fluctuations at each mesh site. All particles were initially located in the cytosol. Movie corresponds to the kymographs in Fig. 5B, provided in the article.

movie 2c: Striped oscillations at $T = 20°C$.

Cell length is $12\mu m$ and the hydrolysis rate is $k_{de} = 0.4s^{-1}$. The initial condition was taken as a travelling wave peaking in one cell half. See movie 3 for details about stripe formation. Movie corresponds to the kymographs in Fig. 5B, provided in the article.

movie 2d: Striped oscillations at $T = 40°C$.

Cell length is $12\mu m$ and the hydrolysis rate is $k_{de} = 2.5s^{-1}$. The initial condition was taken as a travelling wave peaking in one cell half. See movie 3 for details about stripe formation. The observed asymmetry is an imprint of the initial condition. Movie corresponds to the kymographs in Fig. 5B, provided in the article.

movie 3: Stripe formation out of a travelling wave peaking in one cell half.

Cell length is $12\mu m$ and the hydrolysis rate is $k_{de} = 0.65s^{-1}$. The initial condition was generated by choosing a MinD recruitment value about $k_{dD} = 0.03\mu m^2/s$ and picking the timestep where MinD+MinDE are maximal at the membrane in one cell half, and minimal in the other. This solution was chosen as initial condition for all simulations in filamentous cells. Movie corresponds to the first $800s$ of the kymographs in Fig. 5C, provided in the article.

movie 4: Switching between axial oscillations and circular waves in nearly spherical cells.

Cell length is $2.4\mu m$, cell width is $2.2\mu m$, and the hydrolysis rate is $k_{de} = 0.65s^{-1}$. Initial condition was a homogeneous state with small fluctuations at each mesh site. All particles were initially located in the cytosol. Note the switching of travelling direction between consecutive phases of circular waves. Movie corresponds to the first $1500s$ of the kymographs in Fig. 5D, provided in the article.

movie 5: Oscillation aligns to the major axis in nearly spherical cells after cell division.

We used a deformed mesh technique (ALE), provided with COMSOL MULTIPHYSICS 3.5A, to increase the cell width dynamically from $2.2\mu m$ to $2.55\mu m$. The cell length is set to $2.4\mu m$. In agreement with experiments, the oscillations axis shifts towards the cell's long axis. The initial condition was taken as a pole-to-pole oscillation from the simulation in movie 4.

REACTION-DIFFUSION SYSTEMS IN ELLIPTICAL GEOMETRY

Orthogonal elliptical coordinates

For an ellipse with major semi-axis r_a, minor semi-axis r_b, and linear eccentricity $d = \sqrt{r_a^2 - r_b^2}$, we choose orthogonal elliptical coordinates given by

$$x = d\cosh(\mu)\cos(\nu)$$

$$y = d\sinh(\mu)\sin(\nu),$$

with $\mu > 0$ and $0 \leq \nu < 2\pi$. Accordingly, the above ellipse is parametrised at constant $\mu = \mu_0$, given by $\mu_0 = \operatorname{arctanh}(r_b/r_a)$, see supplementary Fig. S1. Differential operators follow in the usual way from the scale factors h_μ and h_ν, given by $h_\mu = h_\nu = d\sqrt{\sinh^2\mu + \sin^2\nu}$.

Construction of orthogonal functions for bulk and membrane diffusion

We solved the linearised system, obtained from the reaction-diffusion equations (1a)-(2c) given in the article, through construction of a mutual orthogonal basis for bulk and membrane diffusion. To simplify matters, we consider in the following only two species u, v, where u accounts for cytosolic particles, and v for membrane particles:

$$\partial_t u = D_c\nabla^2 u - \lambda u, \tag{1}$$

$$\partial_t v = D_m\nabla_\nu^2 v + g(u, v), \tag{2}$$

with boundary conditions:

$$D_c\partial_\mu u|_{\mu=\mu_0} = f(u, v). \tag{3}$$

The degradation term λu in (1) accounts for nucleotide exchange, and can be set to zero in order to obtain the bulk solutions for the different species, e.g. the time evolution of cytosolic MinD $u_D = u_{DT} + u_{DD}$ is governed by diffusion alone as the reaction terms cancel. Then the time evolution of MinD-ATP is obtained from $u_{DT} = u_D - u_{DD}$. The first task is finding an orthogonal set of functions to solve the linearised system. As we aim for a fast computational method to obtain the parameter dependencies of a nonlinear system, our approach is based on approximations and favours computational efficiency and a

satisfactory predictive power over mathematical rigour and highest precision. With the categorically limited predictive power of linear stability analysis in mind, we found this to be the pragmatic choice.

Bulk diffusion

By separation of variables, i.e. $u = \exp(\sigma t)\tilde{u}(\mu,\nu)$, equation (1) can be expressed as an eigenvalue problem in elliptical geometry:

$$\sigma\tilde{u}(\mu,\nu) = D_c \frac{1}{d^2(\sinh^2\mu + \sin^2\nu)}(\partial_\mu^2 + \partial_\nu^2)\tilde{u}(\mu,\nu) - \lambda\tilde{u}(\mu,\nu). \tag{4}$$

With $\tilde{u}(\mu,\nu) = R(\mu)\Psi(\nu)$ we obtain the well known Mathieu equations:

$$0 = \Psi'' + (c - 2q\cos 2\nu)\Psi \tag{5}$$

$$0 = R'' - (c - 2q\cosh 2\mu)R, \tag{6}$$

where c denotes the constant of separation or spatial eigenvalue, and the dimensionless parameter $q = q_\sigma + q_\lambda$ is given by:

$$q_\sigma = -\sigma\frac{d^2}{4D_c},\ q_\lambda = -\lambda\frac{d^2}{4D_c}. \tag{7}$$

Setting the argument in the angular equation (5) complex, i.e. $\nu = i\mu$, yields the radial equation (6). Accordingly, the solutions of the radial equations can be obtained from the solutions of the angular equation. Following the classical procedure, we express the angular Mathieu functions as Fourier series (cf. [3]), and classify the solutions in even Ψe and odd Ψo modes according to the parity wrt. $\nu = 0$:

$$\text{even} : \Psi\text{e}_n(\nu;q) = \sum_{k=0}^{\infty} A^n_{2k+p}(q)\cos(2k+p)\nu,\ n = 0,1,\ldots,\ p = 0,1\ : (a_n(q)) \tag{8}$$

$$\text{odd} : \Psi\text{o}_n(\nu;q) = \sum_{k=1}^{\infty} B^n_{2k+p}(q)\sin(2k+p)\nu,\ n = 1,2,\ldots,\ p = 0,1\ : (b_n(q)) \tag{9}$$

Here, a_n and b_n denote the corresponding spatial eigenvalues, and

$$p = \begin{cases} 0 & \text{for } n \text{ even}, \\ 1 & \text{for } n \text{ odd}. \end{cases} \tag{10}$$

Upon inserting this ansatz into the angular Mathieu equation (5) one obtains recursion equations for the Fourier coefficients, c.f. [3] and [1]:

$$(-m^2 + a_n)A_m^n = q(A_{m+2}^n + (1+\delta_{m,2})A_{m-2}^n + \delta_{m,1}A_m^n) \tag{11}$$

$$(-m^2 + b_n)B_m^n = q(B_{m+2}^n + B_{m-2}^n - \delta_{m,1}B_m^n). \tag{12}$$

As a peculiarity of Mathieu functions, the Fourier coefficients A_m^n, B_m^n and spatial eigenvalues a_n, b_n depend on the dimensionless parameter $q = q_\sigma + q_\lambda$, and thereby, on the growth rates σ we seek. Since this dependence cannot be expressed in a closed form, but the parameter q can be assumed as sufficiently small, we expand the Fourier coefficients and spatial eigenvalues in power series [2]:

$$A_m^n = \sum_{r=0}^{\infty} \alpha_{m,r}^n q^r \qquad a_n = \sum_{j=0}^{\infty} l_j^n q^j, \tag{13}$$

$$B_m^n = \sum_{r=0}^{\infty} \beta_{m,r}^n q^r \qquad b_n = \sum_{j=0}^{\infty} k_j^n q^j. \tag{14}$$

In contrast to previous work [2], we normalize the angular Mathieu functions wrt. the scalar product $\langle f, g\rangle_\nu = \frac{1}{\pi}\int_0^{2\pi} d\nu fg$, i.e.

$$\langle \Psi\mathrm{e}_n(\nu;q), \Psi\mathrm{e}_m(\nu;q)\rangle_\nu = \langle \Psi\mathrm{o}_n(\nu;q), \Psi\mathrm{o}_m(\nu;q)\rangle_\nu = \delta_{n,m}, \tag{15}$$

and express the radial parts as series of hyperbolic functions instead of Bessel functions.

$$\text{even} : \mathrm{Re}_n(\nu;q) = \sum_{k=0}^{\infty} A_{2k+p}^n(q)\cosh(2k+p)\nu,\ n = 0,1,\ldots,\ p = 0,1\ : (a_n(q)) \tag{16}$$

$$\text{odd} : \mathrm{Ro}_n(\nu;q) = \sum_{k=1}^{\infty} B_{2k+p}^n(q)\sinh(2k+p)\nu,\ n = 1,2,\ldots,\ p = 0,1\ : (b_n(q)) \tag{17}$$

Thereby, one obtains approximations in finite order $\mathcal{O}(q^K)$ for the radial $\mathrm{Re}_{n,K}, \mathrm{Ro}_{n,K}$ and angular $\Psi\mathrm{e}_{n,K}, \Psi\mathrm{o}_{n,K}$ Mathieu functions, respectively, where

the expansion coefficients in (13) and (14) are obtained recursively from

$$\alpha^n_{m,K} = \begin{cases} \frac{1}{m^2-n^2}\left[\sum_{s=1}^{K-1} l^n_s \alpha^n_{m,K-s} - \alpha^n_{m+2,K-1} - (1+\delta_{m,2})\alpha^n_{m-2,K-1} - \delta_{m,1}\alpha^n_{m,K-1}\right], & n \neq m \\ -\frac{1}{2}\left(\frac{1}{\sqrt{2}}\delta_{n,0} + 1 - \delta_{n,0}\right) \sum_{k=n-2K\geq 0}^{n+2K} (1+\delta_{k,0}) \sum_{s=1}^{K-1} \alpha^n_{k,s}\alpha^n_{k,K-s}, & n = m \end{cases}$$

$$\alpha^n_{m,0} = \frac{1}{\sqrt{2}}\delta_{n,m}\delta_{n,0} + (1-\delta_{n,0})\,\delta_{n,m},$$

$$l^n_K = \left(\sqrt{2}\delta_{n,0} + 1 - \delta_{n,0}\right)\left[\alpha^n_{n+2,K-1} + (1-\delta_{n,2})\alpha^n_{n-2,K-1} + \delta_{n,1}\alpha^n_{n,K-1} - \sum_{s=1}^{K-1} l^n_s \alpha^n_{n,K-s}\right]$$

$$l^n_0 = n^2, \tag{18}$$

for the even modes, and from

$$\beta^n_{m,K} = \begin{cases} \frac{1}{n^2-m^2}\left(\beta^n_{m+2,K-1} + \beta^n_{m-2,K-1} - \delta_{m,1}\beta^n_{m,K-1} - \sum_{s=1}^{K-1} k^n_s \beta^n_{m,K-s}\right), & n \neq m \\ -\frac{1}{2} \sum_{k=n-2K\geq 1}^{n+2K} \sum_{s=1}^{K-1} \beta^n_{k,s}\beta^n_{k,K-s}, & n = m \end{cases}$$

$$\beta^n_{m,0} = \delta_{n,m},$$

$$k^n_K = \beta^n_{n+2,K-1} + \beta^n_{n-2,K-1} - \delta_{n,1}\beta^n_{n,K-1} - \sum_{s=1}^{K-1} k^n_s \beta^n_{m,K-s},$$

$$k^n_0 = n^2, \tag{19}$$

for the odd modes.

Note that angular Mathieu functions are only orthogonal for the same q, and hence only for equal temporal eigenvalues $\sigma_n = \sigma_m$. As explained in the following, this problem can be resolved by matching the bulk solutions with the orthogonal eigenfunctions for the diffusion process on the membrane.

Membrane diffusion

As $\nabla^2_{\mu_0,\nu} \neq \nabla^2_\nu$, the angular Mathieu functions are not solutions of the diffusion process on the membrane. However, obtaining an orthogonal basis for the one dimensional diffusion process on the membrane is straightforward in arclength parametrisation $s(\nu)$. With

$$s(\nu) = r_b E\left(\nu, 1 - \frac{r_a^2}{r_b^2}\right) = \int_0^\nu d\nu' \sqrt{r_b^2 + (r_a^2 - r_b^2)\sin^2\nu'}, \tag{20}$$

where $E(\phi, k)$ denotes the incomplete elliptic integral of second kind, and

$$\nabla_\nu^2 = \left(\frac{1}{h_{\mu_0,\nu} d\nu}\right)^2 = \partial_s^2, \tag{21}$$

the eigenfunction of membrane diffusion read

$$\Psi \mathrm{e}_n^{\mathrm{mem}}(\mu_0, s) = \cos\left(\frac{2\pi n}{L} s\right), \qquad n = 0, 1, 2, \ldots, \tag{22}$$

$$\Psi \mathrm{o}_n^{\mathrm{mem}}(\mu_0, s) = \sin\left(\frac{2\pi n}{L} s\right), \qquad n = 1, 2, 3, \ldots, \tag{23}$$

where $L = s(2\pi)$ denotes the circumference of the ellipse. It is then possible to expand the membrane modes in series of approximated Mathieu functions:

$$\Psi \mathrm{e}_n^{\mathrm{mem}}(\mu_0, s(\nu)) = \sum_{m=0}^{\infty} \gamma e_{m,K}^n \, \Psi \mathrm{e}_{m,K}(\nu; q_n), \tag{24}$$

$$\Psi \mathrm{o}_n^{\mathrm{mem}}(\mu_0, s(\nu)) = \sum_{m=1}^{\infty} \gamma o_{m,K}^n \, \Psi \mathrm{o}_{m,K}(\nu; q_n). \tag{25}$$

With the abbreviations

$$\kappa e_m^n = \frac{1}{\pi} \int_0^{2\pi} d\nu \cos(m\nu) \cos\left(\frac{2\pi n}{E\left(2\pi, 1 - \frac{r_a^2}{r_b^2}\right)} E\left(\nu, 1 - \frac{r_a^2}{r_b^2}\right)\right), \tag{26}$$

$$\kappa o_m^n = \frac{1}{\pi} \int_0^{2\pi} d\nu \sin(m\nu) \sin\left(\frac{2\pi n}{E\left(2\pi, 1 - \frac{r_a^2}{r_b^2}\right)} E\left(\nu, 1 - \frac{r_a^2}{r_b^2}\right)\right), \tag{27}$$

the Fourier coefficients $\gamma e_{m,K}^n, \gamma o_{m,K}^n$ are given by

$$\gamma e_{m,K}^n = \frac{1}{\pi} \int_0^{2\pi} d\nu \, \Psi \mathrm{e}_{m,K}(\nu; q_n) \, \Psi \mathrm{e}_n^{\mathrm{mem}}(\mu_0, s(\nu)) = \sum_{k=m-2K\geq 0}^{m+2K} \kappa e_k^n \sum_{r=0}^{K} \alpha_{k,r}^m q_n^r, \tag{28}$$

$$\gamma o_{m,K}^n = \frac{1}{\pi} \int_0^{2\pi} d\nu \, \Psi \mathrm{o}_{m,K}(\nu; q_n) \, \Psi \mathrm{o}_n^{\mathrm{mem}}(\mu_0, s(\nu)) = \sum_{k=m-2K\geq 1}^{m+2K} \kappa o_k^n \sum_{r=0}^{K} \beta_{k,r}^m q_n^r. \tag{29}$$

Thereby, one obtains a mutual basis in terms of bulk-membrane modes for both diffusion processes:

$$\Psi\mathrm{e}^{\mathrm{mem}}_{n,K}(\mu,\nu;q^{\mathrm{e}}_n) = \sum_{m=0}^{\infty} \gamma e^n_{m,K} \frac{\mathrm{Re}_{m,K}(\mu;q^{\mathrm{e}}_n)}{\mathrm{Re}_{m,K}(\mu_0;q^{\mathrm{e}}_n)}\, \Psi\mathrm{e}_{m,K}(\nu;q^{\mathrm{e}}_n), \tag{30}$$

$$\Psi\mathrm{o}^{\mathrm{mem}}_{n,K}(\mu,\nu;q^{\mathrm{o}}_n) = \sum_{m=1}^{\infty} \gamma o^n_{m,K} \frac{\mathrm{Ro}_{m,K}(\mu;q^{\mathrm{o}}_n)}{\mathrm{Ro}_{m,K}(\mu_0;q^{\mathrm{o}}_n)}\, \Psi\mathrm{o}_{m,K}(\nu;q^{\mathrm{o}}_n). \tag{31}$$

These modes are orthogonal at the boundary by construction, but not eigenfunctions of the normal flux operator at the boundary, as

$$\nabla_\mu\, \Psi\mathrm{e}^{\mathrm{mem}}_{n,K}(\mu,\nu;q^{\mathrm{e}}_n)|_{\mu=\mu_0} = h^{-1}_{\mu_0,\nu} \sum_{m=0}^{\infty} \gamma e^n_{m,K} \frac{\mathrm{Re}'_{m,K}(\mu_0;q_n)}{\mathrm{Re}_{m,K}(\mu_0;q_n)}\, \Psi\mathrm{e}_{m,K}(\nu;q_n). \tag{32}$$

However, we find that neglecting the coupling of modes induced by boundary flux already yields very good quantitative results, and simplifies further computations substantially. To this end, we approximate the bulk-boundary coupling by

$$\nabla_\mu\, \Psi\mathrm{e}^{\mathrm{mem}}_{n,K}(\mu,\nu;q^{\mathrm{e}}_n)|_{\mu=\mu_0} \approx \left\langle \nabla_\mu\, \Psi\mathrm{e}^{\mathrm{mem}}_{n,K}(\mu,\nu;q^{\mathrm{e}}_n)|_{\mu=\mu_0}, \Psi\mathrm{e}^{\mathrm{mem}}_{n}(\mu_0,s(\nu))\right\rangle_s \Psi\mathrm{e}^{\mathrm{mem}}_{n}(\mu_0,s(\nu)), \tag{33}$$

where

$$\langle f,g\rangle_s = \frac{2}{L}\int_0^L dsfg = \frac{2\pi}{L}\left(\frac{1}{\pi}\int_0^{2\pi} d\nu h_{\mu_0,\nu} fg\right) = \frac{2\pi}{L}\langle h_{\mu_0,\nu} f, g\rangle_\nu \tag{34}$$

denotes the canonical scalar product in arclength parametrisation $s(\nu)$. As both coordinates scale equally, i.e. $h_\mu = h_\nu = h_{\mu,\nu}$, the projections (33) can be expressed in terms of the known coefficients:

$$\left\langle \nabla_\mu\, \Psi\mathrm{e}^{\mathrm{mem}}_{n,K}(\mu,\nu;q^{\mathrm{e}}_n)|_{\mu=\mu_0}, \Psi\mathrm{e}^{\mathrm{mem}}_{n}(\mu_0,s(\nu))\right\rangle_s = \frac{2\pi}{L}\sum_{m=0}^{\infty} \frac{\mathrm{Re}'_{m,K}(\mu_0;q^{\mathrm{e}}_n)}{\mathrm{Re}_{m,K}(\mu_0;q^{\mathrm{e}}_n)} (\gamma e^n_{m,K})^2. \tag{35}$$

The summation can be truncated at a finite value of M such that the approximated bulk-boundary coupling is characterised by the two finite expansions parameters M and K. Having said this, we define the following abbreviations

for the projections on even and odd modes, respectively:

$$\Gamma\mathrm{e}_n^{M,K} = \frac{2\pi}{L}\sum_{m=0}^{M}\frac{\mathrm{Re}'_{m,K}(\mu_0;q_n^{\mathrm{e}})}{\mathrm{Re}_{m,K}(\mu_0;q_n^{\mathrm{e}})}(\gamma e_{m,K}^n)^2, \qquad n=0,1,2,\ldots, \tag{36}$$

$$\Gamma\mathrm{o}_n^{M,K} = \frac{2\pi}{L}\sum_{m=1}^{M}\frac{\mathrm{Ro}'_{m,K}(\mu_0;q_n^{\mathrm{o}})}{\mathrm{Ro}_{m,K}(\mu_0;q_n^{\mathrm{o}})}(\gamma o_{m,K}^n)^2, \qquad n=1,2,3,\ldots. \tag{37}$$

Now, we can proceed with the linear stability analysis, but first, we need to compute a stationary solution.

Approximating the stationary solution

Since the total number of Min proteins is conserved, the following conservation laws apply

$$N_D\frac{r_a r_b}{R_a R_b} = \int_\Omega u_{DD}+u_{DT}+\int_{\partial\Omega} u_d+u_{de}, \tag{38}$$

$$N_E\frac{r_a r_b}{R_a R_b} = \int_\Omega u_E+\int_{\partial\Omega} u_{de}, \tag{39}$$

where N_D and N_E are the numbers of MinD monomers and MinE dimers in an elliptical cell with major semi-axis R_a and minor semi-axis R_b. The integration is taken over the full domain Ω for bulk species, and over the boundary $\partial\Omega$ for membrane species. A homogeneous stationary solution only exists in the limit of instantaneous nucleotide exchange, i.e. when there are no degradation terms in the bulk equation (1). In this limit constant fields solve the stationary bulk equations $0 = D_c\nabla^2_{\mu,\nu}u$. However, this is not the case if nucleotide exchange is taken into account. Here, we compute an approximation of the mean stationary densities at the membrane, which we use as stationary solution in the linearisation. The stationary solutions are of the form $\bar{u}(\mu) \propto \bar{u}(\mu_0)\,\Psi\mathrm{e}_{0,K}^{\mathrm{mem}}(\mu,\nu;q_\lambda) + \text{h.o.t.}$, where h.o.t. denotes higher order modes with even parity wrt. $\nu = 0$ and $\nu = \pi/2$. We neglect these higher order contributions, and approximate the bulk-boundary coupling as described above. Thereby, one retains the stationary gradients across the membrane induced by nucleotide exchange, and constant concentration fields along the membrane. The stationary state $(\bar{u}(\mu),\bar{v}(\mu_0))$ is then obtained numerically from:

$$0 = f(\bar{u},\bar{v}) - D_c\bar{u}\,\Gamma\mathrm{e}_0^{M,K}(q_\lambda), \tag{40}$$

$$0 = g(\bar{u},\bar{v}), \tag{41}$$

where the expansion parameters M, K can be adjusted to obtain results of higher precision.

Linear stability analysis in elliptical geometry

To perform the linear stability analysis, we linearise the reaction-diffusion equations on the membrane (2) and the boundary conditions (3) at the stationary state $(\bar{u}(\mu), \bar{v}(\mu_0))$:

$$D_c h^{-1}_{\mu_0,\nu} \partial_\mu u(\mu,\nu,t)|_{\mu=\mu_0} = f(\bar{u},\bar{v}) + f_u \delta u + f_v \delta v \qquad \text{with} \quad f_i = \partial_i f|_{(\bar{u},\bar{v})}, \tag{42}$$

$$\partial_t v(\mu_0,\nu,t) = D_c \nabla^2_\nu v(\mu_0,\nu,t) + g(\bar{u},\bar{v}) + g_u \delta u + g_v \delta v \qquad \text{with} \quad g_i = \partial_i g|_{(\bar{u},\bar{v})}, \tag{43}$$

and ask for the time evolution of small perturbations $\delta u(\mu,\nu,t), \delta v(\mu_0,\nu,t)$:

$$u(\mu,\nu,t) = \bar{u}(\mu) + \delta u(\mu,\nu,t),$$

$$v(\mu_0,\nu,t) = \bar{v}(\mu_0) + \delta v(\mu_0,\nu,t).$$

We express the small perturbations in terms of the earlier derived membrane-bulk modes $\Psi \mathrm{e}_n^{\mathrm{mem}}$ and $\Psi \mathrm{o}_n^{\mathrm{mem}}$, which yields the linear system:

$$\mathbf{A}_n \begin{pmatrix} \delta\tilde{u}_n \\ \delta\tilde{v}_n \end{pmatrix} = 0, \qquad \mathbf{A}_n = \begin{pmatrix} f_u - D_c \Gamma_n^{M,K}(\sigma_n) & f_v \\ g_u & g_v - \sigma_n - D_m \left(\frac{2\pi n}{L}\right)^2 \end{pmatrix}. \tag{44}$$

Depending on the mode of interest, $\Gamma_n^{M,K}$ denotes either $\Gamma \mathrm{e}_n^{M,K}$ or $\Gamma \mathrm{o}_n^{M,K}$. The growth rates σ_n are then obtained by solving the characteristic equation $\det \mathbf{A}_n = 0$ numerically for each set of parameters. The initial refinement of parameter space was performed by scanning parameter space at cell lengths below $2\mu m$ for oscillatory instabilities (i.e. Hopf bifburcations) of the first even mode $\Psi \mathrm{e}_1^{\mathrm{mem}}$ with critical frequency that corresponds to the typical period of Min oscillations about $40s$ at room temperature.

NOTES ON INITIAL CONDITIONS AND STRIPE FORMATION

As Fange and Elf (Fange and Elf, 2006), we also applied initial conditions, where all particles were located in the cytosol, and distributed unequally between both cell halves. In these cases, we used linear initial profiles along

the major axis in simulations with filamentous cells. For some choices of parameters that differ from the ones reported in the article, we found that the final patterns depend on initial slopes: While stripes emerged for slopes below some certain threshold, travelling pole-to-pole waves were selected for larger slopes. Moreover, even if stripes evolved out of all possible initial slopes, other initial inhomogeneities, such as the travelling wave initial condition (see article), could fail to evolve into stable stripes for the same choice of parameters. These results emphasize that particular attention needs to be paid to initial conditions in models that display dynamical transitions between patterns, as the formation of striped patterns *in vivo* differs substantially from a computational scenario, where initial conditions permit the formation of multiple polar zones and MinE rings from the beginning, e.g. homogeneous or purely cytosolic initial condition. In particular, the connection between stripe formation and MinD canalization only became clear, if pole-to-pole waves were chosen as initial condition.

NOTES ON EXPERIMENTAL DATA AND PARAMETER FITTING

Several difficulties arise in fitting computational models for the Min system to experimental observations. One problem concerns the large variability of oscillation periods observed in wild type cells. For instance, Meacci and Kruse (Meacci and Kruse, 2005) report pole-to-pole oscillations with periods between 30 and 120 seconds at constant room temperature ($22°C$), Unai et al. (Unai et al., 2009) determined a mean pole-to-pole period about $54.6 \pm 8.6s$ at $25°C$, and Hsieh et al. (Hsieh et al., 2010) used a wild type period of 194 seconds as reference for the *in vivo* experiments with MinE mutants. Accordingly, these variations are particularly reflected in the data we used to fit the model to a large temperature range. This makes the identification of the proper parameter set ambiguous. Since previous experiments revealed that the oscillation period depends on the ratio of MinD and MinE densities (Raskin and de Boer, 1999), deviations are mostly ascribed to differences in protein concentrations and ratios. However, it is still unknown how protein numbers change with cell size and age, and there is no quantitative data relating particle numbers and oscillation periods. Nevertheless, as Huang et al. (Huang et al., 2003), we could reproduce the MinD/MinE density dependence of the oscillation period qualitatively.

The choice of particle numbers

The model assumes a wild-type ratio of MinD/MinE particles about 2.86. In this scenario the number of MinE particle is halved as MinE is considered as homodimer. However, MinD-ATP shows enhanced dimerization in presence of phospholipid vesicles, see (Lutkenhaus, 2007) for a review. Therefore, we considered additionally the limiting case where all MinD particles are dimers. This yields a MinD/MinE ratio of 1.43. All results, i.e. pole-to-pole oscillations, striped patterns, circular waves, the temperature dependence, and independence of initial conditions and predefined MinD attachment templates as considered in the main text could be reproduced equally well, see supplementary Fig. S2. The parameters for this case are

$$k_D = 0.18\,\mu m\,s^{-1},\ k_{dD} = 0.515\,\mu m^2 s^{-1},\ k_{dE} = 0.8\,\mu m^2 s^{-1}, \qquad (45)$$

and the hydrolysis rate obeys an Arrhenius law with the same activation energy ($E_A = 16.7\ kcal/mol$) and adjusted normalization $k_{de}(20°C) = 0.145\ s^{-1}$. This demonstrates that the model remains valid for both limiting cases.

The choice of membrane diffusion coefficients

Another ambiguity regards the mobility of Min proteins on the lipid membrane. Using fluorescence correlation spectroscopy (FCS) Meacci et al. (Meacci et al., 2006) determined a mean MinD mobility about $0.17\mu m^2/s$ *in vivo*, however, the larger fraction of observed particles (F=0.77) was cytosolic during measurements. It was argued that a large fraction of membrane bound particles might be incorporated in helical filaments and be therefore inaccessible to FCS measurements. Additionally, the experiments could not distinguish between rapid rebinding and membrane diffusion explicitly. The mobility of MinD was further investigated in recent *in vitro* experiments, giving a mean membrane diffusion about $0.013\mu m^2/s$ at high MinD concentrations ($1.1\mu M$) in the non-oscillatory regime (Loose et al., 2011a). Since our simulations revealed low fractions of cytosolic proteins (see Fig. 2C in the article), and rapid rebinding due to strong recruitment as key mechanism, we used the *in vitro* diffusion constant as model parameter.

SUPPLEMENTARY FIGURES

Figure S1: Orthogonal elliptical coordinates.

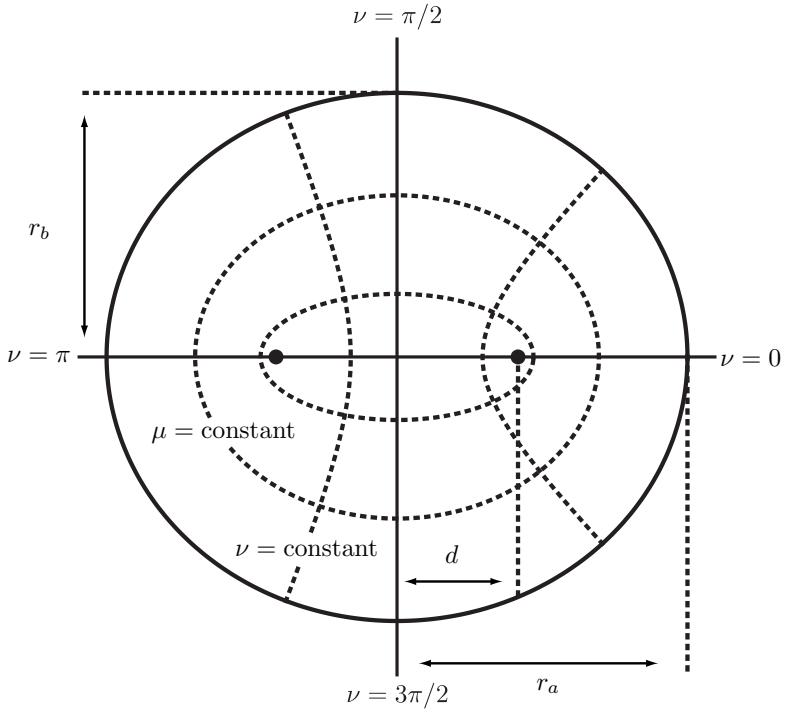

FIG. 1. We use elliptical coordinates given by the normal μ and tangential ν components at the boundary. Ellipses are obtained at constant $\mu = \mu_0$.

Figure S2: Robust pattern formation at low MinD/MinE=1.43 ratio.

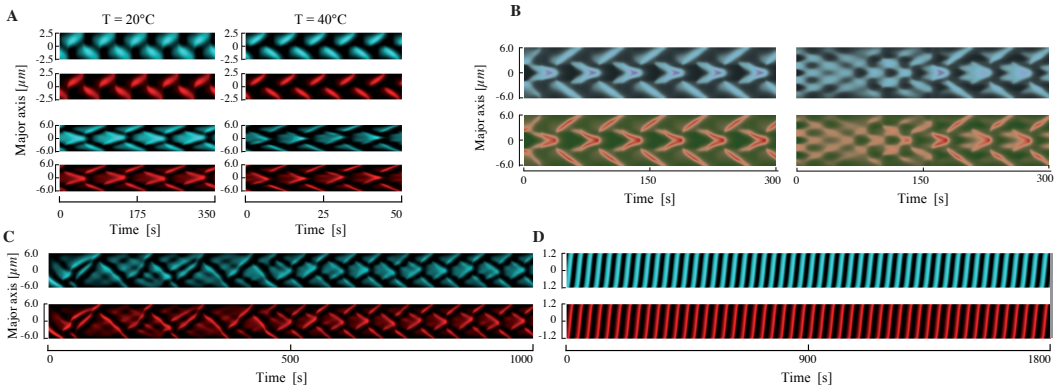

FIG. 2. **A,** Corresponds to data in Fig. 5B in the manuscript. MinD (turquoise) and MinE (red) kymographs for pole-to-pole and striped oscillations at low ($20°C$) and high ($40°C$) temperatures. Inhomogeneous initial condition have been used, cf. Fig. S2C. **B,** Corresponds to data in Fig. 6C in the manuscript. Kymographs of Min oscillations in filamentous cells with spatially restricted MinD attachment, MinD (blue), MinE (red/green). Left: Restricting MinD attachment to the cell poles does not jeopardize stripe formation. Right: Adding further attachment domains corresponding to the next striped pattern does not promote additional stripe formation. **C,** Corresponds to data in Fig. 5C in the manuscript. Kymographs showing stripe formation out of pole-to-pole travelling waves. Hydrolysis rate: $k_{de} = 0.235s^{-1}$. **D,** Corresponds to data in Fig. 5D in the manuscript. Kymographs showing circular waves in nearly spherical cells ($2.4\mu m$ length, $2.2\mu m$ width). Pole-to-pole oscillations are recovered at higher excentricity (not shown). Hydrolysis rate: $k_{de} = 0.235s^{-1}$.

[1] Kokkorakis, G. C., and Roumeliotis, J. A. (2000). Power series expansions for Mathieu functions with small arguments. *Math Comp*, *70*, 1221–1236.

[2] Larsen, T. M., Erricolo, D., and Uslenghi, P. L. E. (2008). New method to obtain small parameter power series expansions of Mathieu radial and angular functions. *Math Comp*, *78*, 255–274.

[3] McLachlan, N. (1964). *Theory and Application of Mathieu Functions*. New York: Dover Publications.

IV Geometry adaption: Multistability and geometry induced transitions of intracellular patterns

This chapter is based on the following publication:

Multistability and dynamic transitions of intracellular Min protein patterns

by

F. Wu[†,1],J. Halatek[†,1], M. Reiter[2], E. Kingma[1], E. Frey[2], and C. Dekker[1]

[1]Department of Bionanoscience, Kavli Institute of Nanoscience, Delft University of Technology, Lorenzweg 1, 2628 CJ, Delft, the Netherlands,

[2]Department of Physics, Arnold Sommerfeld Center for Theoretical Physics and Center for NanoScience, Ludwig-Maximilians-Universität München, Theresienstraße 37, 80333 München, Germany,

† equal contribution

Journal Reference:

***Molecular Systems Biology* 12, 2016, (on the cover)**

Supplemental Material reproduced on pages 136 to 143.

Multistability and dynamic transitions of intracellular Min protein patterns

Fabai Wu[1, †], Jacob Halatek[2, †], Matthias Reiter[2], Enzo Kingma[1], Erwin Frey[*,2], Cees Dekker[*,1] ([†] These authors contributed equally to the work)

[1] Department of Bionanoscience, Kavli Institute of Nanoscience, Delft University of Technology, Lorenzweg 1, 2628 CJ, Delft, the Netherlands
[2] Arnold-Sommerfeld-Center for Theoretical Physics and Center for NanoScience, Ludwig-Maximilians-Universität München, Theresienstrasse 37, D-80333 München, Germany

Abstract

Cells owe their internal organization to self-organized protein patterns, which originate and adapt to growth and external stimuli via a process that is as complex as it is little understood. Here, we study the emergence, stability, and state transitions of multistable Min protein oscillation patterns in live *Escherichia coli* bacteria during growth up to defined large dimensions. *De novo* formation of patterns from homogenous starting conditions is observed and studied both experimentally and in simulations. A new theoretical approach is developed for probing pattern stability under perturbations. Quantitative experiments and simulations show that, once established, Min oscillations tolerate a large degree of intracellular heterogeneity, allowing distinctly different patterns to persist in different cells with the same geometry. Min patterns maintain their axes for hours in experiments, despite imperfections, expansion, and changes in cell shape during continuous cell growth. Transitions between multistable Min patterns are found to be rare events induced by strong intracellular perturbations. The instances of multistability studied here are the combined outcome of boundary growth and strongly nonlinear kinetics, which are characteristic of the reaction-diffusion patterns that pervade biology at many scales.

Introduction

Many cells have characteristic forms. To guide proper assembly of their subcellular structures, cells employ machineries that garner and transmit information of cell shape (Kholodenko & Kolch, 2008; Minc & Piel, 2012; Moseley & Nurse, 2010; Shapiro et al, 2009). But cells are not static objects: they grow, divide, and react to stimuli, and these processes are often accompanied by a change of cell shape. Hence, the means by which a cell gathers spatial information need to be adaptive. One versatile mechanism that is capable of such spatial adaptation is self-organized pattern formation (Cross & Hohenberg, 1993; Epstein & Pojman, 1998; Murray, 2003).

Spontaneous emergence of spatial structures from initially homogeneous conditions is a major paradigm in biology, and Alan Turing's reaction-diffusion theory was the first to show how local chemical interactions could be coupled through diffusion to yield sustained, non-uniform patterns (Turing, 1952). In this way, the symmetry of the starting system can be broken. Reaction-diffusion mechanisms have been shown to account for the generation of many biological patterns (Kondo & Miura, 2010). However, how patterns change in response to noise and perturbations, be they chemical or geometrical, is poorly understood. Resolution of such issues is critical for an understanding of the role of reaction-diffusion systems in the context of the spatial confines and physiology of a cell (or an organism). To include the effects of geometry, the mathematical framework for reaction-diffusion theory has been extended to circular (Levine & Rappel, 2005), spherical (Klünder et al, 2013), and elliptical geometries (Halatek & Frey, 2012). However, focusing on pattern formation from homogeneity is not enough, as was noted by Turing himself at the end of his seminal article in 1952 (Turing, 1952): *'Most of an organism, most of the time, is developing from one pattern into another, rather than from homogeneity into a pattern.'*

Min proteins form dynamic spatial patterns that regulate the placement of division sites in prokaryotic cells and eukaryotic plastids (Colletti et al, 2000; de Boer et al,

1989; Hu & Lutkenhaus, 1999; Leger et al, 2015; Leisch et al, 2012; Makroczyová et al, 2016; Maple et al, 2002; Ramirez-Arcos et al, 2002; Raskin & de Boer, 1999; Szeto et al, 2002). In rod-shaped *Escherichia coli* cells, MinD and MinE form a reaction-diffusion network that drives pole-to-pole oscillations in their local concentrations (Hu & Lutkenhaus, 1999; Huang et al, 2003; Raskin & de Boer, 1999). Membrane-bound MinD binds MinC, which inhibits FtsZ polymerization (Dajkovic et al, 2008). The dynamic Min oscillation patterns thus result in maximal inhibition of FtsZ accumulation at the cell poles and minimal inhibition at the cell center which, together with a nucleoid occlusion mechanism, restricts formation of the division apparatus to mid-cell (Adams & Errington, 2009). Because it exhibits a multitude of complex phenomena which can be explored by experimental and theoretical means, the Min oscillator provides an informative reference system for the quantitative study of geometry-responsive pattern formation.

The dynamic Min oscillations have been explained by reaction-diffusion models based on a minimal set of interactions between MinD, MinE, ATP, and the cell membrane (Fange & Elf, 2006; Halatek & Frey, 2012; Howard et al, 2001; Huang et al, 2003; Kruse, 2002; Loose et al, 2008; Meinhardt & de Boer, 2001; Touhami et al, 2006). MinD, in its ATP-bound form, cooperatively binds to the cytoplasmic membrane (Hu et al, 2002; Mileykovskaya et al, 2003). MinE interacts with membrane-bound MinD, triggering the hydrolysis of its bound ATP and releasing MinD from the membrane (Hsieh et al, 2010; Hu et al, 2002; Loose et al, 2011; Park et al, 2011; Shih et al, 2002). MinD then undergoes a nucleotide exchange cycle in the cytosol, which was initially incorporated into the modeling framework by Huang *et al* (Huang et al, 2003). Further theoretical analysis of the minimal reaction scheme suggested that the interplay between the rate of cytosolic nucleotide exchange and strong preference for membrane recruitment of MinD relative to MinE facilitates transitions from pole-to-pole oscillations in cells of normal size to multi-node oscillations (striped mode) in filamentous cells (Halatek & Frey, 2012). Such transitions occur if proteins that have detached from one polar zone have a greater tendency to re-attach to the membrane in the other half of the cell rather than to the old polar zone – a process which has been termed *canalized transfer*. This leads to synchronized growth and depletion of MinD

from spatially separated polar zones, enabling the simultaneous maintenance of multiple polar zones. Numerical simulations of a reaction-diffusion model based on this canalized transfer of Min proteins successfully explain a plethora of experimentally observed Min oscillations in various geometries (Halatek & Frey, 2012).

Essential for the robust function of Min proteins in ensuring symmetric cell division is their ability to respond to, and thus encode, information relating to cell shape. Upon cell-shape manipulation, Min proteins have been found to exhibit a range of phenotypes under different boundary conditions (Corbin et al, 2002; Männik et al, 2012; Touhami et al, 2006; Varma et al, 2008; Wu et al, 2015b). Recent development of a cell-sculpting technique allows accurate control of cell shape over a size range from 2x1x1 μm^3 to 11x6x1 μm^3, in which Min proteins show diverse oscillation patterns, including longitudinal, diagonal, rotational, striped, and even transverse modes (Wu et al, 2015b). These patterns were found to autonomously sense the symmetry and size of shaped cells. The longitudinal pole-to-pole mode was most stable in cells with widths of less than 3 μm, and lengths of 3-6 μm. In cells of this size range, Min proteins form concentration gradients that scale with cell length, leading to central minima and polar maxima of the average Min concentration. Increasing cell length to 7 μm and above led to the emergence of striped oscillations. In cells wider than 3.5 μm, Min oscillations can align with the short axis of the lateral rectangular shape, yielding a transverse mode (Wu et al, 2015b). The existence of various oscillation modes has also been reconstituted *in vitro* with MinD, MinE, ATP, and lipid bilayers confined to microchambers (Zieske & Schwille, 2014). Numerical simulations based on an established reaction-diffusion model (Halatek & Frey, 2012) successfully recaptured the various oscillation modes in the experimentally sampled cell dimensions (Wu et al, 2015b). This further emphasizes the role of the two above-mentioned factors generic to reaction-diffusion processes in cells: cytosolic nucleotide exchange and membrane recruitment (Halatek & Frey, 2012; Huang et al, 2003). These data provided the first evidence that sensing of geometry is enabled by establishing an adaptive length scale through self-organized pattern formation.

Given that Min proteins in all cells initially adopt the same regime of pole-to-pole oscillations, it is as yet unclear how diverse oscillation modes emerge during cell growth to large dimensions, and whether transitions occur between these patterns. Furthermore, more than one mode of oscillation was often observed in different cells with the same shape, presenting an intriguing example of the multistability of different complex patterns (Wu et al, 2015b). These unexplained phenomena provide us with the rare opportunity to quantitatively explore the basic principles of the dynamics of pattern formation in the context of geometric perturbations and cellular heterogeneities.

In this study, we combine experiments and theory to systematically examine the emergence and dynamic switching of the distinct oscillatory Min protein patterns (longitudinal, transverse, and striped oscillations, cf. Fig. 1A) observed in *E. coli* bacteria that are physically constrained to adopt defined cell shapes. Our primary aim was to investigate the origin of multistability (coexistence of stable patterns), and to further understand its relevance in the context of cell growth (i.e. changing cell shape). Furthermore, we hoped to identify the kinetic regimes and mechanisms that promote transitions between patterns and to probe their robustness against spatial variations in kinetic parameters. One striking discovery is the high degree of robustness of individual modes of oscillation even in the face of significant changes in geometry.

To present our results, we first show experimentally that different patterns can emerge out of near-homogeneous initial states in living cells with different dimensions, thus providing further support for an underlying Turing instability. We then use computational approaches to capture the dependence of pattern selection on geometry. Using stability analysis, we establish kinetic and geometric parameter regimes that allow both longitudinal and transverse patterns to coexist. Furthermore, we evaluate the emergence and stability of these patterns in computer simulations and compare the results with experimental data. Remarkably, we find that the experimentally observed multistability is reproduced by the theoretical model in its original parameter regime characterized by canalized transfer. In experiments, we trace pattern development during the cell-

shape changes that accompany cell growth, and we quantitatively assess the persistence and transition of patterns in relation to cell shape. These analyses reveal that Min patterns are remarkably robust against shape imperfections, size expansion, and even changes in cell axes induced by cell growth. Transitions between multistable patterns occur (albeit infrequently), driving the system from one stable oscillatory pattern to another. Altogether, this study provides a comprehensive framework for understanding pattern formation in the context of spatial perturbations induced by intracellular fluctuations and cellular growth.

Results

1. Symmetry breaking of Min patterns from homogeneity in live *E. coli* cells

One of the most striking examples of the accessibility of multiple stable states observed in shaped *E. coli* cells is the emergence of different - transverse and longitudinal - Min oscillation modes in rectangular cells with identical dimensions (Wu et al, 2015b). The existence of a transverse mode has also been noted in reconstituted *in vitro* systems (Zieske & Schwille, 2014). In live cells, this phenomenon is most prominent in cells with widths of about 5 μm and lengths of between 7 and 11 μm (Wu et al, 2015b). To probe the emergence and stability of these different stable states, we began this study by monitoring the temporal evolution of Min protein patterns in deformable cells growing in rectangular microchambers. Improving upon our previous shaping and imaging method (see Materials and Methods), we recorded cytosolic eqFP670 (a near-infrared fluorescent protein) and sfGFP-MinD fluorescence signals over the entire course of cell growth (~ 6 to 8 h). Owing to the superior brightness and photostability of these two fluorescent probes (Wu et al, 2015a), we were able to image the cells at 2-min intervals without affecting cell growth. Given that an oscillation cycle (or period) takes 68±13 sec (mean ± s.d.) at our experimental temperature (26°C), shorter intervals were subsequently used to capture the detailed dynamics within one oscillation cycle (see below).

We first grew cells with the above-mentioned lateral dimensions (7-11x5x1 μm^3) in microchambers of the appropriate form. Of the 126 cells examined, almost all (n=121) showed clear MinD polar zones in all times prior to cell death or growth beyond the confines of the chambers, demonstrating the striking persistence of the oscillation cycles. In some cells, transition states between different patterns were also captured, which are described below (see Sections 5 and 6). Interestingly, imaging of the remaining 5 cells captured 1-2 frames in which the sfGFP-MinD fluorescence was distributed *homogeneously* (Fig. EV1, Movie EV1). Such a homogeneous state phenomenologically resembles the initial conditions chosen in the majority of chemical and theoretical studies on pattern formation. However, in the present case, Min proteins re-established oscillations *exclusively* in the transverse mode, irrespective of their preceding oscillation mode (Fig. EV1). Why the system should ”revert” to such a homogeneous state in the first place is unknown, although the rapid recovery of patterns leads us to speculate that it most probably results from a transient effect, such as a change in membrane potential or a rearrangement of chromosomes, rather than from a drastic depletion of ATP. Nonetheless, such an intermittent state provides a unique opportunity to study the emergence of patterns from a spatially uniform background.

We therefore explored symmetry breaking by Min proteins over a larger range of cell sizes, and found that different cell dimensions gave rise to different patterns from an intermittent homogeneous state. Because homogeneous distributions of MinD are observed at low frequency, we manually searched for cells in such a state. Once targeted, such cells were subsequently imaged at short time intervals of between 5 and 20 seconds until an oscillation pattern stabilized. As shown in Fig. 1B-D, the uniform distribution of sfGFP-MinD seen in cells of different sizes and shapes became inhomogeneous, and always re-established stable oscillations within a few minutes. In the 6.5x2x1 μm^3 cell shown in Fig. 1B, the homogeneous sfGFP-MinD signal first became concentrated at the periphery of the cell, indicating a transition from the cytosolic state to the membrane-bound form. At t=20 sec, a minor degree of asymmetry was observed. Within the next 30 sec, a clear sfGFP-MinD binding zone developed on the left-hand side of the top cell half. This zone persisted for 40 sec, until a new binding zone was established at

the top cell pole, which then recruited the majority of the sfGFP-MinD molecules. This pattern rapidly evolved into longitudinal pole-to-pole oscillations which lasted for the rest of the time course of our time-lapse imaging (10 min). In an 8.8x2x1 μm^3 cell (Fig. 1C), the initial membrane binding of sfGFP-MinD was accompanied by formation of several local patches of enhanced density (see e.g. t=30 sec), which went on to form one large patch that was asymmetrically positioned in relation to the cell axes (t = 110 sec). This MinD binding zone further evolved into a few cycles of asymmetric oscillations before converging into striped oscillations, with sfGFP-MinD oscillating between two polar caps and a central stripe. In the 8.8x5.2x1 μm^3 cell (Fig. 1D) persistent transverse oscillations emerged within ~2.5 min after clusters of sfGFP-MinD had begun to emerge as randomly localized, membrane-bound patches from the preceding homogeneous state.

To further examine the stability of the transverse mode, we tracked transverse oscillations in 5-μm wide cells with a time resolution of 20 sec. We found that these indeed persisted, with a very robust oscillation frequency, for at least 17 cycles (i.e. the maximum duration of our experiment) under our imaging conditions (Fig. 1E and 1F, Movie EV2). This indicates that, once established, the transverse mode in these large cells is just as robust as the longitudinal pole-to-pole mode in a regular rod-shaped *E. coli* cell.

In order to probe the effect of MinE in the process of symmetry breaking, we engineered a strain that co-expresses sfGFP-MinD and MinE-mKate2 from the endogenous *minDE* genomic locus (see Materials and Methods). In shaped bacteria, MinE-mKate2 proteins oscillate in concert with MinD (Movie EV3). After the loss of oscillatory activities of both sfGFP-MinD and MinE-mKate2, no heterogeneous MinE pattern was observed prior to the emergence of MinD patches that dictate the axis of symmetry breaking (Movie EV2). This is in agreement with the previous finding that MinE relies on MinD for its recruitment to the membrane (Hu et al, 2002).

The observed emergence of Min protein patterns from homogeneous states shows several striking features. First of all, after the early stage of MinD membrane binding, which appears to be rather uniform across the cell, the first patch with enhanced MinD density that forms is neither aligned with the symmetry axes nor does it show a preference for the highly curved polar regions. Secondly, Min patterns converge into a stable pattern within a few oscillation cycles. Emerging patterns align with symmetry axes, and exhibit a preference for the characteristic length range discovered previously (Wu et al, 2015b), confirming that the geometry-sensing ability of Min proteins is intrinsic and self-organized. The fast emergence and stabilization of Min protein patterns indicates an intrinsic robustness of Min oscillations and an ability to adjust oscillatory patterns dynamically to changes in cell geometry.

2. Analytical and computational approach to probe the geometry-dependent symmetry breaking and pattern selection

The experimental observations described above showed that symmetry breaking in spatially almost-homogeneous states can result in stable oscillation patterns of Min proteins. These spatiotemporal configurations are longitudinal and transverse oscillation patterns whose detailed features are dependent on the geometry of the system, in accordance with our previous study (Wu et al, 2015b). We therefore set out to gain a deeper understanding of the mechanisms underlying the phenomenon of multistability and the role of cell geometry in determining, regulating, and guiding the pattern formation process and the ensuing stable spatiotemporal patterns. To this end, we performed a theoretical analysis, building on previous investigations of symmetry breaking induced by the oscillatory Turing instability in bounded geometries (Halatek & Frey, 2012).

The results presented in this Section are based on the observation that the selection of the initial pattern (which does not necessarily coincide with the final pattern) depends on both the Turing instability and the system's geometry. While we focus on the latter aspect in the main text, we review in Box 1 how, more

generally, a Turing instability facilitates symmetry breaking in a planar geometry, which may help the reader to understand why the interconnection between geometry and the classical Turing mechanism is crucial.

BOX 1: Symmetry breaking by the Turing instability in cellular geometries.

The initial phase of a "symmetry-breaking" process in a nonlinear, spatially extended system is determined by a *mode-selection mechanism*. Consider an initial steady state of the corresponding well-mixed system that is weakly perturbed spatially, by some spatially white noise, for instance. For the planar geometry considered in textbooks and review articles, the initial state is typically a spatially uniform state (Cross & Hohenberg, 1993; Epstein & Pojman, 1998; Murray, 2003). The spectral decomposition of this state gives equal weight to all Fourier modes and, therefore, sets no bias for a particular mode. A system is referred to as being "Turing unstable" if any spatially non-uniform perturbation of a uniform equilibrium fails to decay (as expected due to diffusion) but instead grows into a patterned state. The collection of growth rates plotted as a function of the wavenumber of the corresponding Fourier modes is called the dispersion relation, and can be computed by a linear stability analysis. The mode with the fastest growth rate is called the critical mode. It sets the length scale of the initial pattern if there is no other bias for a different mode. Such a bias could, for instance, be provided by a specific initial condition that is non-uniform.

It has been shown recently that, in the context of realistic biological systems, a well mixed state is generically non-uniform for reaction-diffusion systems based on membrane-cytosol cycling and an NTPase activity (Thalmeier et al, 2016). Hence, in this generic case, the symmetry of the stationary state is already broken – in the sense that it is adapted to the geometry of the cell. Consequently, any downstream instabilities – such as the Turing instability – will inherit the symmetry of this spatially non-uniform steady state. In this paper, we discuss how the analysis of the instability of such a non-uniform steady state differs from that of the traditional Turing instabilities of uniform states.

The non-uniformity of the well-mixed state in cell geometries (as noted in Box 1) is not the only salient difference relative to the classical case of a planar geometry. To perform linear stability analysis on a particular system, a set of Fourier modes must be derived that is specific for the boundary geometry of the system. Hence, both the well mixed state and the spectrum of Fourier modes are generically geometry-dependent. Only a few geometries are amenable to an analytical treatment. A recent advance was the derivation of eigenfunctions for reaction-diffusion systems with reactive boundaries (the cell membrane) and diffusive bulks (the cytosol) in an elliptical geometry (Halatek & Frey, 2012). This geometry, being analytically accessible, permits broad, systematic parameter studies. At the same time, it shares the symmetries of interest with rod-shaped, circular, and rectangular cells. The eigenfunctions or modes of the ellipse are classified into even and odd functions by their symmetry with respect to reflections through a plane along the long axis; the lowest-order modes are shown in Fig. 2A. Even functions are symmetric, and odd functions are anti-symmetric with respect to long-axis reflection. As such, even functions correspond to longitudinal modes, and odd functions to transverse modes. More subtle than the separation into two symmetry classes, but no less significant, is the strict absence of any homogeneous steady states in elliptical systems undergoing cytosolic nucleotide exchange (Thalmeier et al, 2016). This can be understood intuitively from a source-degradation picture: Proteins detach from the membrane and undergo cytosolic ADP-ATP exchange. The concentration of ADP-bound MinD drops with increasing distance from the membrane as the diphosphate is replaced by ATP. This yields cytosolic concentration gradients at the membrane that determine the densities of membrane-bound proteins. In an equilibrium state confined to an elliptical geometry, the cytosolic gradients at the membrane cannot be constant, but will vary along the cell's circumference. Hence, a uniform density at the membrane cannot be a steady state of the system, and instead the new basal state of the system is defined by the elliptical eigenfunction of the lowest order (Fig. 2A). This new steady state takes maximal and minimal values at the cell poles and at midcell, respectively. Note that the spatial variation of the density can be very small and may be very difficult to detect experimentally.

So what is the relevance of such a spatially non-uniform basal state? The answer lies in the nonlinear nature of the system. Nonlinearities are known to amplify weak signals. As discussed in Box 1, the selective amplification of parts of a noise spectrum is at the origin of symmetry breaking. The non-uniformity of the well-mixed basal state implies that a spatially uniform initial condition set in a simulation will first adapt to the symmetry of this basal state, even in the absence of any spatial instability. Only after the basal state has been reached can the growth of (linearly) unstable modes begin. In the present case, the geometry of an ellipse imposes a preferred symmetry on the well-mixed state that resembles the symmetry of a striped oscillation (compare the 0th and 2nd even mode in Fig. 2A). Therefore, the initial symmetry adaptation process creates a bias in favor of the 2nd even mode corresponding to striped oscillations, which thus dominates the initial growth of patterns. As shown in Fig. 2B, striped oscillations dominate the early phase of pattern formation in a wide variety of cell shapes. In a 6.5x2x1.1 μm3 cell, the oscillatory stripe mode persists for about 3 oscillation cycles before the dynamics switch to pole-to-pole oscillations. By contrast, the oscillatory stripe mode persists indefinitely in cells with sizes of 9x2x1.1 μm3 and also 9x5x1 μm3. This latter observation differs from our corresponding experimental results in the same geometry, which had revealed the consistent emergence of a transverse mode after the system had passed through a homogeneous phase (Fig. 1D and Fig. EV1) (though striped oscillations were also observed in cells of this size (Wu et al, 2015b)). Clearly, letting the computational system evolve from a uniform configuration introduces a bias towards even modes, which should disfavor the selection of transverse patterns. This difference led us to conclude that we needed to characterize in detail the physiological relevance of the bias imposed by the non-uniformity of the well mixed basal state, i.e. its robustness against other types of intracellular heterogeneities. This issue is addressed in the following.

Realistic cellular systems contain many different factors that induce asymmetries and heterogeneities: the cytosol and the membrane are crowded, cell shape is never perfectly symmetrical, and the lipid distribution (and hence the membrane's affinity for MinD) is sensitive to membrane curvature. All these intrinsic perturbations of the system's symmetry can have an effect on the process of

pattern selection if multiple stable patterns are possible. Previous studies (Halatek & Frey, 2012) have suggested that *stable* Min patterns are not destabilized by spatial heterogeneities in the rate of attachment of MinD to the membrane, as the dynamics are dominated by the recruitment process. Here, faced with a multistable system, we asked whether heterogeneities in MinD membrane attachment might to some extent affect the *initial* selection process. To this end, we spatially perturbed the MinD attachment rate by superimposing a linear gradient. We systematically altered the slope and direction of this gradient, and investigated the effects on initial MinD dynamics. After a few oscillation cycles, we turned the perturbation off again and continued the simulation without any induced bias (i.e. with spatially uniform MinD attachment rates). This procedure provided us with a versatile means of generating a weak spatial perturbation that can break symmetry and is applicable to all cell geometries. In particular, it enabled us to quantify the effects of these intrinsic perturbations on pattern selection and compare them to the impact of the geometric bias discussed above.

Indeed, our simulations showed that an initial MinD attachment gradient with a spatial peak-to-peak amplitude of the spatial variation of as little as 20% indeed compensates for the aforementioned geometric bias for striped oscillations (Fig. 2C). To put this 20% variation in perspective, we note that the affinity of MinD for different lipids can vary by up to one order of magnitude (Mileykovskaya et al, 2003; Renner & Weibel, 2012). Figure 2C shows the onset of pattern formation obtained from computer simulations based on the same geometry as that in Fig. 1B. In contrast to the simulations in Fig. 2B, the MinD attachment gradient is now initially aligned diagonally. Two observations stand out: Firstly, we find that the asymmetric template does not impede the formation of stripes. Hence the template does not dictate the symmetry of possible patterns. Secondly, in the 5 μm wide cells with the weak initial gradient, the transverse mode wins the competition against stripe oscillations, which contrasts with the outcome shown in Fig. 2B. We accordingly conclude that the geometric bias for striped oscillations is rather weak and is presumably of little physiological relevance. However, in the absence of any intrinsic heterogeneity, pattern selection obtained from computer

simulations in cellular geometries will inevitably overemphasize the effect of the geometric bias.

We therefore sought a solution, discussed in the following sections, which explicitly incorporates spatial heterogeneities that compensate for the intrinsic bias, thus effectively restoring unbiased pattern selection based on the Turing instability alone.

3. Computing pattern stability in multistable regimes

Now that we have learned how the initial pattern selection process can be affected by spatial perturbations, we will address how and to what extent the existence and stability of different patterns is affected by the system's geometry, and which molecular processes in the Min reaction circuit control how the system adapts to cell geometry.

Geometry sensing requires the existence of a characteristic length scale. Previous theoretical analysis of Min oscillations has shown that such a length scale is accompanied by synchronization of the depletion and initiation of old and new polar zones, respectively (Halatek & Frey, 2012). A key insight was that a relatively high rate of MinD recruitment (relative to MinE recruitment) is essential for initiation and amplification of the collective redistribution of MinD that leads to such synchronization (Halatek & Frey, 2012). For a broad range of MinD recruitment rates, we found that oscillatory pole-to-pole and striped oscillations could coexist in cells whose length exceeds a certain limit (Halatek & Frey, 2012; Wu et al, 2015b). These earlier studies suggested that the ratio of MinD to MinE recruitment rates is the parameter that allows for geometry-dependent multistability in rectangular cells in which longitudinal and transverse patterns can coexist. The experimental observation of a transverse mode (Wu et al, 2015b) supports the previous theoretical suggestion that circular and aberrant patterns in nearly spherical cells (Corbin et al, 2002) are caused by the additional destabilization and persistence of odd (transverse) modes in an elliptical geometry with increased cell width (Halatek & Frey, 2012). This implies

that the circular and aberrant patterns found experimentally in cells with low aspect ratios, such as nearly spherically shaped cells (Corbin et al, 2002), and the observation of transverse patterns in rectangular shapes (Wu et al, 2015b), are attributable to the same mechanism, namely the additional destabilization of odd modes. The key difference between the nearly spherical and rectangular cases is that, in the former, the choice of modes is reversible (i.e. neither mode is definitively selected), such that the axis of oscillation switches aberrantly, whereas in rectangular cells the high aspect ratio of the geometry leads to the mutually exclusive selection of either longitudinal (purely even) or transverse (purely odd) patterns, but both symmetries of the pattern are initially accessible (i.e. the system exhibits multistability).

To gain further insight into pattern selection, we first computed and compared the growth rates of even and odd modes in a simplified 2D elliptical geometry, and then proceeded to test the results of this linear stability analysis by computer simulations that take the full 3D cell geometry into account. In these computer simulations the pattern stability was then probed by the application of spatial heterogeneities in the MinD attachment rate.

As a first step we performed a linear stability analysis in the elliptical geometry. To characterize the difference between growth rates of even (longitudinal) and odd (transverse) modes, we introduce a quantity which we term the *non-degeneracy*. This is defined as the Euclidian distance between the growth rates of the first three even and the first three odd modes (cf. Materials and Methods section; note that the notion 'growth rates of modes' is not to be associated with the physiological growth rates of cells). Figure 3A shows how the non-degeneracy depends on cell geometry and on the MinD recruitment rate. In agreement with our previous analysis, nearly spherical cells are almost degenerate with respect to even and odd modes (Halatek & Frey, 2012). The effect of a larger MinD recruitment rate is to extend this region of near degeneracy towards larger aspect ratios. Hence, when rates of MinD recruitment are high, we can expect that longitudinal and transverse modes have similar growth rates even in rectangular cells. These results were then tested in 3D computer simulations.

For simulations of realistic 3D cellular geometries, we employ a spatially varying MinD attachment rate, similar to the approach described in Section 2. This allows us to probe the stability of patterns against spatial perturbations, and thereby to test the (nonlinear) stability of the oscillatory pattern. The simulation strategy is schematically shown in Fig. 3B. First, we align the gradient of the MinD attachment profile with one symmetry axis and initialize the simulation. After a few oscillation cycles, we turn the MinD attachment gradient off and allow the simulation to proceed for another ~40 oscillation cycles. If the pattern was stable (i.e. a local attractor of the reaction-diffusion dynamics), it remained aligned with the initially selected axis. In these cases, we used the final state as the initial configuration and ran the simulation for another ~40 oscillation cycles, now with reactivated perturbation of the MinD attachment rate and with the gradient inclined at an angle to the initial oscillation axis. This final step was intended to probe the stability of the pattern against spatial heterogeneities that could potentially switch pattern symmetry from longitudinal to transverse or vice versa. We repeated this simulation to cover all possible alignments (i.e. angles from 0 to 90 degrees) and slopes of the MinD attachment perturbation (i.e. spatial variations from 0 to 100% of the average MinD attachment rate). Together, these simulations enabled us to quantify the stability of each initialized pattern based on the degree of perturbation that it can sustain without losing its alignment to the initial axis. We performed this stability analysis for a broad range of experimentally probed geometries as well as recruitment rates. Note that we only distinguished transverse oscillations from longitudinal oscillations, but not between pole-to-pole and stripe modes within the longitudinal oscillations. In all probed configurations (cell geometries, spatial heterogeneities), we observed that longitudinal patterns are stable, independently of the MinD recruitment rate (Fig. 3C). In contrast, the number of cell geometries that support stable transverse patterns turned out to be strongly dependent on the relative rate of MinD recruitment (Fig. 3D). In agreement with the above linear stability analysis in the 2D elliptical geometry, we found that an increasing MinD recruitment rate extends the domain of stable transverse patterns towards cell geometries with larger aspect ratios. Furthermore, our simulations show that the degree of pattern

stability is surprisingly high. Almost all configurations were able to withstand more than 90% of all applied perturbations (slopes and angles) to the MinD attachment profile (Fig. 3C and D).

These findings lead to several important conclusions. First, the simulation data show that stability analysis in the two-dimensional elliptical geometry is able to account well for the patterns of behavior observed in realistic three-dimensional geometries. Second, our findings indicate that a gradient in the MinD attachment rate affects the initial selection of the axis of oscillation by guiding the dynamics into the basin of attraction of the corresponding pattern. Moreover, spatial gradients of MinD attachment rate typically cannot drive a system from one pattern into the orthogonal alternative once the system has settled down into a stable oscillation. This suggests that the spatiotemporal patterns are in general very robust against spatial heterogeneities in the MinD attachment rate. The above analysis provides a way to probe the basins of attraction of different oscillatory patterns systematically, which will be introduced and discussed in the following.

4. Basins of patterns are controlled by geometry and recruitment strength

In the preceding Section, we demonstrated that highly stable longitudinal and transverse patterns can be initialized in a broad range of geometric configurations. Knowing that these patterns exist, we turned to the question of which patterns can be plausibly reached by the system dynamics, i.e. without having to tune the initial conditions in any particular fashion. To approach this issue, we began our simulations with a homogeneous initial configuration. As discussed in Section 2, adaptation to the non-uniform well-mixed state (adaptation to geometry) introduces a preference for striped oscillations, and hence a bias for even patterns. To include other potential effects that weakly break the system's symmetry (but not the symmetry of the stable patterns, cf. Section 3) and neutralize the weak bias for stripe selection, we imposed a fixed, weak spatial gradient on the rate of MinD attachment. The relative magnitude of the variation was again set to 20%, which, as mentioned above, is well below the typical range of variation in MinD's

affinity for different lipids in the *E. coli* membrane. We examined all alignments of the MinD attachment gradient interpolating between purely longitudinal and purely transversal states. After ~100 oscillation cycles, we recorded the final pattern, distinguishing between transverse pole-to-pole, longitudinal pole-to-pole, and longitudinal striped oscillations. Following this procedure, we separately studied the effects of varying geometry and MinD recruitment rates on multistability and pattern selection.

To study the effect of system geometry, we fixed the value of the MinD recruitment rate to a high value (k_{dD}=0.1) such that the number of coexisting stable longitudinal and transverse patterns is largest. Sampling over all alignments of the gradient led to the distributions of the final patterns shown in the histograms in Fig. 4A. Cell length was varied from 7 μm to 10 μm, cell width from 3 μm to 5 μm. We observed a critical cell length of between 9 and 10 μm for the selection of striped oscillations. This coincides with the length scale for which the model parameters were initially adjusted in the 2D elliptical geometry (Halatek & Frey, 2012). Surprisingly, this length scale translates directly to realistic 3D cell shapes. We found that the fraction of oscillatory striped patterns decreased in favor of transverse patterns as the cell width was increased. Overall, these results show that cell width, and not cell length, is the main determinant for the onset of transverse modes. All these observations are remarkably consistent with previous experimental data based on random sampling of live *E. coli* cells after they have reached a defined shape (Wu et al, 2015b). Given this level of agreement, we expected to gain further insight into the molecular origin of the observed pattern distribution by studying its dependence on the kinetic parameters in the theoretical model.

To investigate the effect of MinD recruitment rate, we focused on data from the cell sizes that show the greatest number of coexisting patterns, as determined by the previous numerical stability analysis. The corresponding histograms are shown in Fig. 4B. The cell lengths for which the data was collected were 9 and 10 μm, and the cell width varied from 1.1 to 5 μm. In narrow cells we recovered our previous results on the onset of striped oscillations: The fraction of stripes

increased with the MinD recruitment rate (Halatek & Frey, 2012). Remarkably, this was no longer the case when cells reached a width of 5 μm: Here, the fraction of stripes was zero below some threshold MinD recruitment rate, and took on a constant value above this threshold. On the other hand, the fraction of transverse patterns did increase with MinD recruitment rate in these 5 μm wide cells, as does that of the stripe fraction in narrower cells. Hence, we conclude that multistability is indeed promoted by high rates of MinD recruitment. We attribute this feature to the ability of the reaction-diffusion system to operate in the regime in which a characteristic length scale is established through synchronized growth and depletion of spatially separated polar zones ("canalized transfer") (Halatek & Frey, 2012). Notably, the same mechanism that enables striped oscillations in filamentous cells also facilitates transverse oscillations in wide cells.

In all examples discussed so far, the height of the cell was fixed at 1.1 μm, well below the minimal span required to establish a Min oscillation (Halatek & Frey, 2012). Therefore, no oscillations occur along the z-axis. While the present study focuses on competition between longitudinal and transverse patterns, we also used our computational model to explore patterns along the z-direction. In a representative simulation with a 3.1 μm high chamber (cell dimensions 5x4x3.1 μm^3) we found oscillations aligned with the z-axis in addition to oscillations aligned with the x- and y-axes. This shows that increased headroom in the third dimension extends the number of accessible stable patterns even further.

5. Persistent directionality traps Min oscillations in a stable state during cell growth

Experiments (Fig. 1B-F) and simulations have shown that both longitudinal and transverse modes are stable over a range of rectangular shapes once they have been established. However, it is still unclear how patterns evolve during cell growth, which can involve an increase in volume of over 10-fold. Particularly intriguing is the fact that different patterns emerge during the growth of cells that reach the same final shape. This prompted us to study the development of patterns throughout the growth history of a cell. We captured around 200 successive MinD

binding patterns per cell at intervals of 2 min during the geometrical changes that accompanied cell growth. Here, we focused on the cells that reach a final width of between 5 and 5.5 μm and a final length of 8-10 μm, taking advantage of their very long growth history of 6-8 h and the previously detected co-existence of two longitudinal modes and a transverse mode in such cells. The final data set comprised 97 cells.

Spatially constrained by microchambers, the cells adopted growth patterns that can be categorized into several types, based on the difference in alignment of the cell axes with the axes of the chambers (Fig. 5A, D, and G). Under the combined effects of exposure to A22 and cephalexin, cells are initially elliptical in shape (Fig. 5A and 5D). When cell widths were small, Min oscillations almost exclusively aligned along the longest elliptical axis of the cell, with a certain degree of lateral-axis fluctuation (Fig. 5B and E). As a result, with respect to the rectangular chamber axes, the initial Min patterns were aligned in accordance with the orientations of the cells. Fig. 5A and D, for example, show two cells whose long axes are initially aligned with the long axis and short axis of the chambers, respectively. In Fig. 5B, Min oscillations remained aligned close to the vertical (long) axis for the entire 7.8 h of cell growth, from an initial size of 2.1x1.5x1 μm^3 (at t = 0) to a final size of 9x5x1 μm^3 (Fig. 5A; for other examples see Movie EV4). In contrast, Min oscillations in Fig. 5E aligned close to the horizontal (short) axis of the chamber over the whole 8 h taken to reach the same dimensions (Fig. 5D; for more examples see Movie EV4). Note that in the latter scenario, the long and short axes exchanged identity at t=5.8 h, but this did not affect the persistence of horizontal Min oscillations (Fig. 5D and E). These observations suggest that Min oscillations have a strong tendency to remain faithful to their existing orientation for as long as the length scale allows. In addition, some pattern transitions were observed during instances of drastic switching of cell axes that are associated with a low aspect ratio of the cell shapes (Fig. 5G, Movie EV5), similar to examples shown previously (Corbin et al, 2002; Männik et al, 2012). This phenomenon was explained previously by invoking theoretical predictions that low aspect ratios should lead to a transient coupling between longitudinal and transverse modes (Halatek & Frey, 2012) and Min patterns in these shapes are

more sensitive to stochastic perturbations (Fange & Elf, 2006; Schulte et al, 2015). The above scenarios show that pattern multistability can emerge through adaptation of persistent Min oscillations during different modes of cell growth.

To quantitatively characterize the evolution of Min patterns during cell growth, we wrote a data analysis program that automatically quantifies cell shape and Min patterns (see Materials and Methods, Fig. EV2). We used Feret's statistical diameters to parameterize cell shape. Feret's diameter measures the perpendicular distance between two parallel tangents touching the opposite sides of the shape (Walton, 1948). This can be measured along all angles, and the maximum and minimum values are used here to define the smallest and largest cell dimensions. In general, the minimum Feret diameter aligns with the short (symmetry) axis of the cell; the maximum Feret diameter aligns with the long axis of a near-elliptical shape and the diagonal of a near-rectangular shape. We defined the angle of oscillations by connecting the center of the MinD patch to the cell center. Note that all angles were calculated relative to the horizontal plane. With these measurements, we can now compare the length scale that Min oscillations adopt with the lengths of the cell's dimensions (top panels in Fig. 5C, F and H). We can also correlate the angle of the Min oscillations with the planes along which these cell dimensions are measured (bottom panels in Fig. 5C and 5F). Indeed, Fig. 5C and Fig. 5F show that Min patterns aligned with either the long (symmetry) axis or the short (symmetry) axis of the cell shapes, albeit with some degree of fluctuation. In addition, the frequent switching of Min oscillation angles in cells with low aspect ratios is well captured by the automated analysis (Fig. 5H).

For statistical analyses of the robustness of Min oscillations against cell-axis switching, we evaluated Min patterns 20 min before and 20 min after the time point at which cell width reaches the limit of 5 μm imposed by the width of the chamber (marked by the black arrows in all plots in Fig. 5C and F). At the beginning of this period, all Min patterns were in longitudinal pole-to-pole mode. Over the following 40 min, 41 of the 97 cells analyzed showed no large-scale axis shift, with the long axes remaining above 75° and the short axes below 15°. In all these cells, Min oscillations were sustained along the vertical (long) axes, as

shown in Fig. 5A-C. Maintenance of the oscillations along the long axis was also observed in 18 cells in which the long axis did not undergo a drastic switch but the short axis did. In total, 60% of the cells exhibited continuous alignment with the long axis during adaptation of the cell to the width of the chamber. The other 40% of the cells showed a switch in the mode of oscillations, including 28 cells that followed a similar pattern of growth to those shown in Fig. 5D-F and 10 cells that grew as in Fig. 5G-H.

These observations reveal several features. First of all, a robust long-axis alignment of Min patterns in narrow cells determines the initial oscillation direction. Second, the directions of established oscillations are sustained for as long as the corresponding cell dimension along this direction falls within the characteristic symmetry and scale preferred by the oscillation mode (e.g., a 5-μm horizontal dimension in Fig. 5D). Third, Min oscillations show a notable degree of tolerance to asymmetries in cell shape during growth. These properties largely agree with our previous conclusion that the propensity to adopt a given pattern is set by the length scale and the symmetry of the cell shape (Wu et al, 2015b). Hence, in a cell shape that allows for multistability, the selection of Min pattern mode depends largely on (and thus is deducible from) the growth history of the cell.

6. Experimental observations of pattern transitions between multi-stable states

In large cells, 5 μm in width, we observed transitions from longitudinal pole-to-pole modes to transverse modes and vice versa (Fig. 6A and B, Movie EV6). These transitions occurred after the long and short axes of the cell had aligned with the respective axes of the chambers due to confinement, and were characteristically different from the transitions caused by low aspect ratio and shape asymmetry shown in Fig. 5G. For instance, Fig. 6A shows a transition from the longitudinal to the transverse mode. This transition initiated with a large and unexpected displacement of the MinD polar zone from the longitudinal axis of the

cell (9x5x1 μm^3) after several hours of persistent longitudinal oscillations. This perturbation gradually shifted the axis of oscillation towards the short axis of the cell over the course of 10 oscillation cycles. An example of the inverse transition is shown in Fig. 6B for a 6x5x1 μm^3 cell. We note here that this type of spontaneous rearrangement of the oscillation mode occurred rather infrequently, considering the 6- to 8-h lifetime of a bacterium on the chip. To distinguish this type of transition from the previously discussed transitions induced by small aspect ratio or apparent asymmetry (cf. Fig. 4H), we restricted the further statistical analysis to data from the growth phase after the point at which the maximum cell width of 5 μm had been attained. This phase spanned the last 2-3 h of cell growth, i.e. encompassed 120-180 Min oscillation cycles. We found that the majority of cells that eventually came to occupy a volume of 9x5x1 μm^3 (n=47, excluding the few cells that went through a transient homogeneous state such as that shown in Fig. 1B) only exhibited one transition in their Min patterns (Fig. 6C). Transitions rarely occurred more than once in any given cell. On average, 0.3 transitions occurred per cell per hour during growth from a size of 6x5x1 μm^3 to a size of 9x5x1 μm^3, and this observation holds true for cells grown in both nutrient-rich and nutrient-poor media (see Materials and Methods). The average number of transitions per cell did however increase in nutrient-poor medium (see Fig. 6C, inset), which correlates well with the fact that it took them longer to fill out the custom-designed shapes. Altogether, the rarity of such transitions again confirms that different pattern modes are robust against intracellular fluctuations.

Automatic angle tracking of the sfGFP-MinD clusters reveals that most of the transitions between longitudinal and transverse modes involve an intermediate state in which the axis of oscillation deviates from the symmetry axes of the cell shape (Fig. 6D). This suggests that the transitions are due to a strong perturbation of a stable oscillation that pushes the system into the domain of attraction of another stable oscillatory mode. Most of these gradual transitions took place on time scales of 4-8 min in both nutrient-rich and nutrient-poor growth medium (Fig. 6E and inset).

The types of transitions occurring in these cells are length dependent (Fig. 6F). In our data set, transitions from transverse to longitudinal mode were only found in cells with lengths around 6 and 7 μm, whereas the inverse transition was only observed at cell lengths of around 8 to 9 μm. In such cells, the longitudinal striped oscillation mode was observed to evolve from either longitudinal or transverse pole-to-pole oscillations at lower frequencies.

To explore the effect of cell width on pattern stability, we carried out long-term time-lapse imaging of cells shaped into rectangles with lengths of 9 to 10 μm and widths of 3 to 6 μm (Fig. 6G). Unlike previous experiments, in which we had randomly sampled cells that had already attained the desired shape and imaged them at 2-min intervals (Wu et al, 2015b), here we were able to determine the final pattern before cell death or before cells grew out of the chamber. In agreement with the trend seen in previous experiments, increase in cell width resulted in a reduction of the fraction of cells displaying oscillations in the longitudinal pole-to-pole mode and a corresponding increase in the proportion of the transverse mode. Strikingly, we find that the incidence of oscillatory stripe patterns decreases dramatically as cell width increases from 4 to 5 μm. This feature was also well captured by the simulation data in Fig. 4A. Hence, while the precise pattern mode in a cell depends on various factors including growth history and large intracellular perturbations, the statistical trend in pattern composition with respect to cell size is compatible with the basins of attractions probed through small spatial perturbations in our simulations (Fig. 4A).

When cell widths reached more than 5 μm, more complex oscillation modes were observed, including diagonally striped, zig-zag and other asymmetric patterns. These modes often appeared to represent transient, intermediate states between two symmetric modes (Fig. 6H, Movie EV6), but could occasionally persist for several cycles before cell death or overgrowth, as presented in the statistics in Fig. 6G. Thus increasing cell width expands the number of intermediary metastable states available for transitions between stable oscillation modes (Fig. 6H). In addition, a transverse-stripe mode has also been observed (albeit infrequently) in

cells with widths of slightly over 6 μm (Movie EV6), further demonstrating that the 3- to 6-μm adaptive range dictates mode selection in Min pattern formation.

Discussion

Combining experiments and theory to study the time evolution of Min oscillations in shaped bacteria, this work sheds new light on the origin of multistability in biological Turing patterns and on transitions between different patterned states. The experiments described here show how a stable pattern can emerge from a homogeneous state via direct symmetry breaking. Moreover, these patterns exhibit persistent adaptation during cell growth, as well as dynamic transitions induced by strong spatial perturbations. Systematic stability analyses of multistable states *in silico* revealed that the underlying Min pattern dynamics is set by (i) the sensitivity of initial pattern selection to cellular heterogeneity and (ii) the robustness of the established oscillations in the face of perturbations. Overall, this study establishes a framework for understanding Turing reaction-diffusion patterns in the context of fluctuating cellular environments and boundary growth.
Any study on the emergence of patterns within a cellular boundary must take cellular heterogeneity into account. Homogeneous initial states have been broadly used to probe the emergence of spatial patterns in computational simulations. While such an approach has been shown to capture the symmetry breaking of unbounded reaction-diffusion systems, we demonstrate that computing pattern selection in *bounded* systems from such a homogeneous initial state can lead to an intrinsic (but physiologically irrelevant) bias. For example, in this study, a bias towards striped modes impedes computer simulations that employ a homogeneous initial state from reaching a transverse pattern, even if the stability of such a transverse pattern is comparable to that of a longitudinal pattern. The new theoretical methods outlined in this study provide a framework for realistically predicting symmetry breaking in biological systems through linear stability analysis in an elliptical geometry, and probing the basins of attraction of different stable patterns by numerical simulations. Our examples demonstrate the importance of taking spatial heterogeneity into account when studying symmetry breaking within biological boundaries.

Multistability in Min patterns is not determined by either kinetic parameters or cell geometry alone, but originates from the interdependence between the geometric properties of the cell's form and the kinetic regimes of the pattern-forming system. Some limited examples of multistability in reaction-diffusion systems have previously been analyzed in very large systems (Ouyang et al, 1992), where the system size exceeded the length scale of the pattern by two orders of magnitude and the system geometry was rotationally symmetrical. Here, the various stable states of Min patterns are defined with reference to the axes of cell shape, and boundary confinement is thus required by definition, without being a sufficient condition (see below), for the emergence of the class of multistability phenomenon characterized in this study. For instance, an increase of cell width beyond 3 μm is required to enable the transverse mode to be sustained in addition to a longitudinal pole-to-pole oscillation. Most interestingly, our theoretical analysis of the underlying model shows that increasing the size of a Turing-unstable system alone does not in itself facilitate the existence of multiple stable patterns that can be reached from a broad range of initial conditions. In our previous theoretical work we had found that the emergence of a pole-to-pole oscillation in a short cell does not generically imply the existence of a stable striped oscillation with a characteristic wavelength in a long filamentous cell (Halatek & Frey, 2012). Instead, the emergence of a characteristic length scale (which becomes manifest in striped oscillations) is restricted to a specific regime of kinetic parameters, where growth and depletion of spatially separated polar zones become synchronized such that multiple, spatially separated polar zones can be maintained simultaneously. A key element among the prerequisites that permit this regime to be reached is that the nonlinear kinetics of the system (MinD cooperativity) must be particularly strong. Here we find the same restriction on the parameters for the emergence and selection of stable transverse patterns in addition to longitudinal pole-to-pole and striped oscillations. For example, weak nonlinear (cooperative) kinetics can readily give rise to longitudinal Min oscillations in 2-μm-long cells, but cannot sustain a transverse mode of oscillation in cells as wide as 4 μm. These findings hint at an exciting connection between multistability, the ability of patterns to sense and adapt to changes in system geometry, and the existence of an intrinsic length scale in the underlying reaction-

diffusion dynamics. Remarkably – and contrary to the treatments in the classical literature – the existence of an intrinsic length scale is not generic for a Turing instability *per se*. One example is the aforementioned selection of pole-to-pole patterns in arbitrarily long cells where MinD recruitment is weak. In this case, irrespective of the critical wavenumber of the Turing instability, the final pattern is always a single wave traveling from pole to pole. The selection of a single polar zone is also characteristic in the context of cell polarity (Klünder et al, 2013; Otsuji et al, 2007), where it has been ascribed to the finite protein reservoir and a winner-takes-all mechanism. It will be an interesting task for further research to elucidate the general requirements for the emergence of an intrinsic length scale in mass-conserved reaction-diffusion systems. Here we have defined the requirements for geometry sensing and multistabilty in the underling model for Min protein dynamics.

The dynamic relationship between multistable states is determined by the robustness of individual stable states when exposed to large-scale intracellular fluctuations. Our computer simulations suggest that the Min system can tolerate various degrees of spatial perturbations imposed by a heterogeneous profile of MinD's binding affinity for the membrane. This is consistent with our experimental observation that a Min oscillation mode can persist in a living cell for tens of oscillation cycles, even within cell shapes where other stable states exist. Such persistence was also found to tolerate a large degree of asymmetry in cell shape, except for cases with low aspect ratios. Multistable states in the Min system are in essence independent stable states that do not toggle back and forth except under the influence of large spatial perturbations. This is experimentally verified by our observation that instances of switching between multistable states are extremely rare in large rectangular cells. These properties show that biological patterns driven by a reaction-diffusion mechanism can exhibit behaviors similar to classical bistable systems, in which two states switch from one to the other upon surmounting an activation energy barrier.

Pattern selection among multistable states can be dependent on cell growth. Turing patterns have rarely been analyzed in the context of growth, either experimentally or computationally, largely due to technical challenges. A recent example is the study of digit formation during embryonic development

(Raspopovic et al, 2014), where a 3-node Turing network was simulated in a 2D growing mesh to verify experimental findings. In the present paper, our study of the Min oscillations throughout the growth history of the cells revealed a remarkable persistence in in the face of boundary changes induced by cell growth. This phenomenon could not be deduced from previous studies on the Min system, which showed various degrees of fluctuations in cells with certain degrees of asymmetry and enlargement (Corbin et al, 2002; Fange & Elf, 2006; Hoffmann & Schwarz, 2014; Männik et al, 2012; Schulte et al, 2015; Varma et al, 2008). Indeed, although Min oscillations do fluctuate in our experimental settings, they rarely undergo drastic switches even during periods of growth that increase the cell volume by up to 20 fold. One essential finding of this study is the persistent directionality of the oscillations in the case where the long axis and short axis of a cell have switched during adaptation to the chamber boundaries. This provides strong evidence that the Min patterns do not respond to boundary changes *per se*, but are dictated by the history and the scale of the cell dimensions. With such a strong tolerance for physiological and geometrical fluctuations, the patterns are thus found to be largely predictable when the growth history of the cell is known, even without explicit computer simulations involving stochastic effects and boundary growth.

Nonlinear kinetics and boundary confinement are general to Turing patterns in cells and organisms (Goryachev & Pokhilko, 2008; Klünder et al, 2013; Kondo & Miura, 2010; Raspopovic et al, 2014; Vicker, 2002), implying that the multistability phenomenon can be probed in other reaction-diffusion systems as well. Using the framework employed in this study to understand the effect of fluctuations and growth in these other systems may facilitate the discovery of general rules governing the spatial adaptation of patterns in biology.

Materials and Methods

Bacterial strains

In this study, all MinD and MinE proteins or their fluorescent fusions were expressed from the endogenous genomic *minDE* locus. Bacterial strain BN1590 (W3110 [*ΔleuB :: eqFP670 :: frt aph frt*, *ΔminDE :: sfGFP-minD minE :: frt*]), constructed and characterized previously (Wu et al, 2015a; Wu et al, 2015b), was used for all the experiments in this study, with the exception of the co-imaging of MinD and MinE.

The double-labeled *minDE* strain used in this study, FW1919 (W3110 [*ΔminDE :: exobrs-sfGFP-minD minE-mKate2 :: frt*]), was constructed using the λ RED recombination method (Datsenko & Wanner, 2000) after we had observed that plasmid-borne MinDE fusions are prone to overexpression in long-term experiments, and that imaging of CFP rather easily leads to photobleaching and photodamage to the cells. To obtain this strain, strain FW1554 (W3110 [*ΔminDE :: exobrs-sfGFP-minD minE :: frt*]) (Wu et al, 2015a) was transformed with pKD46, and made electro-competent. A linear fragment containing the chloramphenicol gene amplified from pKD3 was transformed into the resulting strain to replace the *frt* scar, thus yielding strain FW1626 (W3110 [*ΔminDE :: exobrs-sfGFP-minD minE:: cat*]). FW1626 was then transformed with pKD46, made competent, and transformed with a linear fragment containing a *mKate2::aph frt* sequence amplified from plasmid pFWB019 to produce strain FW1639 (W3110 [*ΔminDE :: exobrs-sfGFP-minD minE-mKate2:: aph frt*]). FW1639 was then cured of kanamycin resistance using a pCP20 plasmid as described previously (Datsenko & Wanner, 2000) to yield the final strain FW1919. This strain grows in rod shape in both M9 minimal medium and LB rich medium, and produces no minicells, indicating that MinE-mKate2 is fully functional. However, both its fluorescence intensity and photostability in the cells are much lower than those of sfGFP-MinD, and thus less suitable for long-term imaging than the latter.

Growth conditions

The M9 rich medium used previously (Wu et al, 2015b) and in the majority of the experiments in this study (unless specified) contained M9 salts, 0.4% glucose, and

0.25% protein hydrolysate amidase. The M9 poor medium contained M9 salts, 0.4% glucose, and 0.01% leucine. At 30°C, the doubling time of BN1590 cells during exponential growth was 104±9 minutes in M9 poor liquid medium, and 69±3 minutes in M9 rich liquid medium.

For cell shaping, cells were first inoculated into M9 liquid medium supplemented with 4 μg/ml A22 and incubated at 30 °C for 3.5 h (rich medium) or 6 h (poor medium). The agarose pad used to seal the microchambers contained M9 medium supplemented with 4 μg/ml A22 and 25 μg/ml cephalexin as described previously. All cell-shaping experiments were carried out at 26 °C.

Cell shaping

The cell sculpting method was used as described previously (Wu & Dekker, 2015; Wu et al, 2015b), with the following modifications. Prior to inoculation of the cells, the cover glass with the PDMS structures was treated with O_2 plasma for 10 sec to make the surface hydrophilic, which facilitates wetting of the surface and allows for more homogeneous inoculation of the cells into the microchambers. After the cells had settled into the microchambers, these were sealed with a small piece of agarose pad, as described previously (Wu et al, 2015b). We then poured 1 ml of warm agarose onto the existing agarose, which prevented the agarose from drying out during the long time course of the imaging. These two modifications in the cell-sculpting process increased the throughput of the shaping method, as well as minimizing the movement of the cells in the chambers due to drag of the drying agarose.

Fluorescence microscopy

Fluorescence imaging was carried out with the same set-up as previously described (Wu et al, 2015b), but the following modifications were introduced to facilitate long-term tracking. We used an upgraded perfect focus system (PFS3) on the Nikon Ti microscope, which has a larger z-range than the PFS2 system. While PFS3 was optimized for detecting the glass-water interface, we find that it

can be used to locate the interface between glass and PDMS, which was then used to correct for the drift in z over time and keep the cells in focus. The PDMS layer with a thickness of 5-10 μm is within the sampling range for the PFS3, such that we can define the position of the cell with reference to to the glass-PDMS interface. To track sfGFP-MinD during the whole course of cell growth, we used a time interval of 2 min. To monitor in detail the symmetry-breaking process that permits sfGFP-MinD patterns to emerge from homogeneity, we took fluorescence images sfGFP-MinD at intervals of 5 - 20 sec, and only imaged the cytosol before and after this acquisition period. To examine the stability of the transverse oscillations, we used a 20-sec time interval. To sample the effect of cell width on the final oscillation patterns in cells, we imaged every 5 min to obtain a larger dataset per experiment. Despite the fact that sfGFP is relatively resistant to photobleaching, it is critical to use low-intensity light for excitation in order to avoid photodamage to the cells, which reduces oscillation frequencies and eventually causes cell lysis.

Image analysis

The cytosolic fluorescence images of the cells were processed in *Matlab* as described previously for boundary determination (Wu et al, 2015b). The binary image was used to define the lengths of the Feret diameters along the full 360° angular coordinates. From these data, the maximum and minimum Feret diameters were determined. The center of the MinD cluster was determined as described previously using a *Matlab* script, and its angle was determined from its location relative to the cell center. The Feret diameter along this angle was used to compare the oscillation distance with the Feret diameters. Note that we use the Feret diameter along the oscillation angle as a measure of how well oscillations align with long or short axes, but this does imply that it represents a fair estimate of the distance traversed by each MinD protein. All the angle values extracted above are folded to between 0° and 90° due to the multifold symmetry of rectangles. Note that this MinD tracking method is restricted to the analysis of two-node oscillations and is not suitable for striped oscillations. The analyses of the final patterns in cells with various widths were carried out manually. After

publication of the manuscript, the *Matlab* script used in this study will be made available on the webpage [http://ceesdekkerlab.tudelft.nl/downloads/].

Analytical and numerical methods

All simulations were performed using the FEM method as implemented in the software *Comsol Multiphysics 4.4*. The linear stability analysis was performed with Wolfram *Mathematica 10* in elliptical geometry as introduced in (Halatek & Frey, 2012). We define the non-degeneracy of even and odd modes as:

$$d = \sqrt{\sum_{i=1}^{3} \left(Re(\sigma_i^e) - Re(\sigma_i^o) \right)^2}$$

where $Re(\sigma_i^e)$ and $Re(\sigma_i^o)$ denote the growth rate of the i-th even and odd mode respectively.

The model is based on bulk-boundary coupling through a reactive boundary condition as introduced in (Halatek & Frey, 2012). For the cytosol, model equations read:

$$\begin{aligned} \partial_t u_{DD} &= D_D \nabla^2 u_{DD} - \lambda u_{DD} \\ \partial_t u_{DT} &= D_D \nabla^2 u_{DT} + \lambda u_{DD} \\ \partial_t u_E &= D_E \nabla^2 u_E \end{aligned}$$

Here u_{DD} denotes the density of cytosolic MinD-ADP, u_{DT} cytosolic MinD-ATP, and u_E cytosolic MinE; ∇ the Nabla/Del operator in the cytosol (coordinate-free); D_D the diffusion coefficient for cytosolic MinD, D_E the diffusion coefficient for cytosolic MinE, and λ the cytosolic nucleotide exchange rate.
At the membrane we have

$$\begin{aligned} \partial_t u_d &= D_m \nabla_m^2 u_d + (k_D + k_{dD} u_d) u_{DT} - k_{dE} u_d u_E \\ \partial_t u_{de} &= D_m \nabla^2 u_{de} + k_{dE} u_d u_E - k_{de} u_{de} \end{aligned}$$

Here u_d denotes the density of membrane-bound MinD, and u_{de} membrane-bound MinDE complexes; ∇_m the Nabla/Del operator on the membrane (coordinate-free); D_m the diffusion coefficient for the membrane, k_D the MinD attachment rate constant, k_{de} the MinDE detachment rate, k_{dD} the MinD recruitment rate constant, k_{dE} the MinE recruitment rate constant. Membrane and cytosolic dynamics are coupled by a system of reactive boundary conditions:

$$D_D \nabla_n u_{DD} = k_{de} u_{de}$$
$$D_D \nabla_n u_{DT} = -(k_D + k_{dD} u_d) u_{DT}$$
$$D_E \nabla_n u_E = -k_{dE} u_d u_E + k_{de} u_{de}$$

Here ∇_n denotes the (outer) normal derivative at the boundary of the cytosol (membrane). Unless noted otherwise, all system parameters are taken from (Halatek & Frey, 2012), cf. listing in the Appendix.

Acknowledgements

F.W. and C.D thank Rutger Hermsen, Jacob Kerssemakers, Felix Hol, and Juan Keymer for valuable discussions in the early stage of the research. F.W. and C.D. are supported by the ERC Advanced Grant SynDiv (No. 669598), the Netherlands Organization of Scientific Research (NOW/OCW) as part of the Frontiers of Nanoscience program, and the NanoNextNL program 3B Nanomedicine. J.H. and E.F. are supported by the German Excellence Initiative via the NanoSystems Initiative Munich, and by the Deutsche Forschungsgemeinschaft (DFG) via Project B02 within SFB 1032 (Nanoagents for Spatio-Temporal Control of Molecular and Cellular Reactions).

Author Contribution

F.W., J.H., E.F., and C.D. designed the work and wrote the paper. F.W. and E.K. carried out the experiments and analyzed the experimental data. J.H. performed the analytical and computational analysis of the model. M.R. implemented the

automated numerical parameter sweeps. F.W. wrote the scripts for the analysis of experimental data.

The authors declare no competing financial interest.

References

Adams DW, Errington J (2009) Bacterial cell division: assembly, maintenance and disassembly of the Z ring. *Nat Rev Micro* **7:** 642-653

Colletti KS, Tattersall EA, Pyke KA, Froelich JE, Stokes KD, Osteryoung KW (2000) A homologue of the bacterial cell division site-determining factor MinD mediates placement of the chloroplast division apparatus. *Curr Biol* **10:** 507-516

Corbin BD, Yu X-C, Margolin W (2002) Exploring intracellular space: function of the Min system in round-shaped *Escherichia coli*. *EMBO J* **21:** 1998-2008

Cross MC, Hohenberg PC (1993) Pattern formation outside of equilibrium. *Reviews of Modern Physics* **65:** 851-1112

Dajkovic A, Lan G, Sun SX, Wirtz D, Lutkenhaus J (2008) MinC Spatially Controls Bacterial Cytokinesis by Antagonizing the Scaffolding Function of FtsZ. *Curr Biol* **18:** 235-244

Datsenko KA, Wanner BL (2000) One-step inactivation of chromosomal genes in *Escherichia coli* K-12 using PCR products. *Proc Natl Acad Sci USA* **97:** 6640-6645

de Boer PAJ, Crossley RE, Rothfield LI (1989) A division inhibitor and a topological specificity factor coded for by the minicell locus determine proper placement of the division septum in E. coli. *Cell* **56:** 641-649

Epstein IR, Pojman JA (1998) *An Introduction to Nonlinear Chemical Dynamics*: Oxford University Press.

Fange D, Elf J (2006) Noise-induced Min phenotypes in *E. coli*. *PLoS Comput Biol* **2:** e80

Goryachev AB, Pokhilko AV (2008) Dynamics of Cdc42 network embodies a Turing-type mechanism of yeast cell polarity. *FEBS Letters* **582:** 1437-1443

Halatek J, Frey E (2012) Highly canalized MinD transfer and MinE sequestration explain the rigin of robust MinCDE-protein dynamics. *Cell Rep* **1:** 741-752

Hoffmann M, Schwarz US (2014) Oscillations of Min-proteins in micropatterned environments: a three-dimensional particle-based stochastic simulation approach. *Soft Matter* **10:** 2388-2396

Howard M, Rutenberg AD, de Vet S (2001) Dynamic compartmentalization of bacteria: accurate division in *E. coli*. *Phys Rev Lett* **87:** 278102

Hsieh C-W, Lin T-Y, Lai H-M, Lin C-C, Hsieh T-S, Shih Y-L (2010) Direct MinE–membrane interaction contributes to the proper localization of MinDE in E. coli. *Mol Microbiol* **75:** 499-512

Hu Z, Gogol EP, Lutkenhaus J (2002) Dynamic assembly of MinD on phospholipid vesicles regulated by ATP and MinE. *Proc Natl Acad Sci USA* **99:** 6761-6766

Hu Z, Lutkenhaus J (1999) Topological regulation of cell division in *Escherichia coli* involves rapid pole to pole oscillation of the division inhibitor MinC under the control of MinD and MinE. *Mol Microbiol* **34:** 82-90

Huang KC, Meir Y, Wingreen NS (2003) Dynamic structures in *Escherichia coli*: Spontaneous formation of MinE rings and MinD polar zones. *Proc Natl Acad Sci USA* **100:** 12724-12728

Kholodenko BN, Kolch W (2008) Giving Space to Cell Signaling. *Cell* **133:** 566-567

Klünder B, Freisinger T, Wedlich-Söldner R, Frey E (2013) GDI-Mediated Cell Polarization in Yeast Provides Precise Spatial and Temporal Control of Cdc42 Signaling. *PLoS Comput Biol* **9:** e1003396

Kondo S, Miura T (2010) Reaction-diffusion model as a framework for understanding biological pattern formation. *Science* **329:** 1616-1620

Kruse K (2002) A Dynamic Model for Determining the Middle of *Escherichia coli*. *Biophysical Journal* **82:** 618-627

Leger MM, Petrů M, Žárský V, Eme L, Vlček Č, Harding T, Lang BF, Eliáš M, Doležal P, Roger AJ (2015) An ancestral bacterial division system is widespread in eukaryotic mitochondria. *Proc Natl Acad Sci USA* **112:** 10239-10246

Leisch N, Verheul J, Heindl NR, Gruber-Vodicka HR, Pende N, den Blaauwen T, Bulgheresi S (2012) Growth in width and FtsZ ring longitudinal positioning in a gammaproteobacterial symbiont. *Curr Biol* **22:** R831-R832

Levine H, Rappel W-J (2005) Membrane-bound Turing patterns. *Physical Review E* **72:** 061912

Loose M, Fischer-Friedrich E, Herold C, Kruse K, Schwille P (2011) Min protein patterns emerge from rapid rebinding and membrane interaction of MinE. *Nat Struct Mol Biol* **18:** 577-583

Loose M, Fischer-Friedrich E, Ries J, Kruse K, Schwille P (2008) Spatial regulators for bacterial cell division self-organize into surface waves *in vitro*. *Science* **320:** 789-792

Makroczyová J, Jamroškovič J, Krascsenitsová E, Labajová Na, Barák I (2016) Oscillating behavior of Clostridium difficile Min proteins in Bacillus subtilis. *MicrobiologyOpen***:** n/a-n/a

Männik J, Wu F, Hol FJH, Bisicchia P, Sherratt DJ, Keymer JE, Dekker C (2012) Robustness and accuracy of cell division in *Escherichia coli* in diverse cell shapes. *Proc Natl Acad Sci USA* **109:** 6957-6962

Maple J, Chua N-H, Møller SG (2002) The topological specificity factor AtMinE1 is essential for correct plastid division site placement in Arabidopsis. *The Plant Journal* **31:** 269-277

Meinhardt H, de Boer PAJ (2001) Pattern formation in *Escherichia coli*: A model for the pole-to-pole oscillations of Min proteins and the localization of the division site. *Proc Natl Acad Sci USA* **98:** 14202-14207

Mileykovskaya E, Fishov I, Fu X, Corbin BD, Margolin W, Dowhan W (2003) Effects of phospholipid composition on MinD-membrane interactions *in vitro* and *in vivo*. *Journal of Biological Chemistry* **278:** 22193-22198

Minc N, Piel M (2012) Predicting division plane position and orientation. *Trends Cell Biol* **22:** 193-200

Moseley JB, Nurse P (2010) Cell division intersects with cell geometry. *Cell* **142:** 184-188

Murray JD (2003) Mathematical Biology II Spatial Models and Biomedical Applications, 3 edn.: Springer-Verlag New York.

Otsuji M, Ishihara S, Co C, Kaibuchi K, Mochizuki A, Kuroda S (2007) A Mass Conserved Reaction–Diffusion System Captures Properties of Cell Polarity. *PLoS Comput Biol* **3:** e108

Ouyang Q, Noszticzius Z, Swinney HL (1992) Spatial bistability of two-dimensional Turing patterns in a reaction-diffusion system. *The Journal of Physical Chemistry* **96:** 6773-6776

Park K-T, Wu W, Battaile KP, Lovell S, Holyoak T, Lutkenhaus J (2011) The Min oscillator uses MinD-dependent conformational changes in MinE to spatially regulate cytokinesis. *Cell* **146:** 396-407

Ramirez-Arcos S, Szeto J, Dillon J-AR, Margolin W (2002) Conservation of dynamic localization among MinD and MinE orthologues: oscillation of Neisseria gonorrhoeae proteins in Escherichia coli. *Mol Microbiol* **46:** 493-504

Raskin DM, de Boer PAJ (1999) Rapid pole-to-pole oscillation of a protein required for directing division to the middle of *Escherichia coli*. *Proc Natl Acad Sci USA* **96:** 4971-4976

Raspopovic J, Marcon L, Russo L, Sharpe J (2014) Digit patterning is controlled by a Bmp-Sox9-Wnt Turing network modulated by morphogen gradients. *Science* **345:** 566-570

Renner LD, Weibel DB (2012) MinD and MinE Interact with Anionic Phospholipids and Regulate Division Plane Formation in Escherichia coli. *Journal of Biological Chemistry* **287:** 38835-38844

Schulte JB, Zeto RW, Roundy D (2015) Theoretical Prediction of Disrupted Min Oscillation in Flattened *Escherichia coli*. *PLoS ONE* **10:** e0139813

Shapiro L, McAdams HH, Losick R (2009) Why and how bacteria localize proteins. *Science* **326:** 1225-1228

Shih Y-L, Fu X, King GF, Le T, Rothfield L (2002) Division site placement in *E.coli*: mutations that prevent formation of the MinE ring lead to loss of the normal midcell arrest of growth of polar MinD membrane domains. *EMBO J* **21:** 3347-3357

Szeto TH, Rowland SL, Rothfield LI, King GF (2002) Membrane localization of MinD is mediated by a C-terminal motif that is conserved across eubacteria, archaea, and chloroplasts. *Proc Natl Acad Sci USA* **99:** 15693-15698

Thalmeier D, Halatek J, Frey E (2016) Geometry-induced protein pattern formation. *Proc Natl Acad Sci USA* **113:** 548-553

Touhami A, Jericho M, Rutenberg AD (2006) Temperature dependence of MinD oscillation in *Escherichia coli*: running hot and fast. *J Bacteriol* **188:** 7661-7667

Turing AM (1952) The chemical basis of morphogenesis. *Philos Trans R Soc London Ser B* **237:** 37-72

Varma A, Huang KC, Young KD (2008) The Min system as a general cell geometry detection mechanism: branch lengths in Y-shaped *Escherichia coli* cells affect Min oscillation patterns and division dynamics. *J Bacteriol* **190:** 2106-2117

Vicker MG (2002) F-actin assembly in *Dictyostelium* cell locomotion and shape oscillations propagates as a self-organized reaction–diffusion wave. *FEBS Letters* **510:** 5-9

Walton WH (1948) Feret's statistical diameter as a measure of particle size. *Nature* **162:** 329-330

Wu F, Dekker C (2015) Nanofabricated structures and microfluidic devices for bacteria: from techniques to biology. *Chemical Society Reviews*

Wu F, van Rijn E, van Schie BGC, Keymer JE, Dekker C (2015a) Multicolor imaging of bacterial nucleoid and division proteins with blue, orange and near-infrared fluorescent proteins. *Frontiers in Microbiology* **6:** 607

Wu F, van Schie BGC, Keymer JE, Dekker C (2015b) Symmetry and scale orient Min protein patterns in shaped bacterial sculptures. *Nature Nanotechnology* **10:** 719-726

Zieske K, Schwille P (2014) Reconstitution of self-organizing protein gradients as spatial cues in cell-free systems. *Elife***:** 03949

Figures

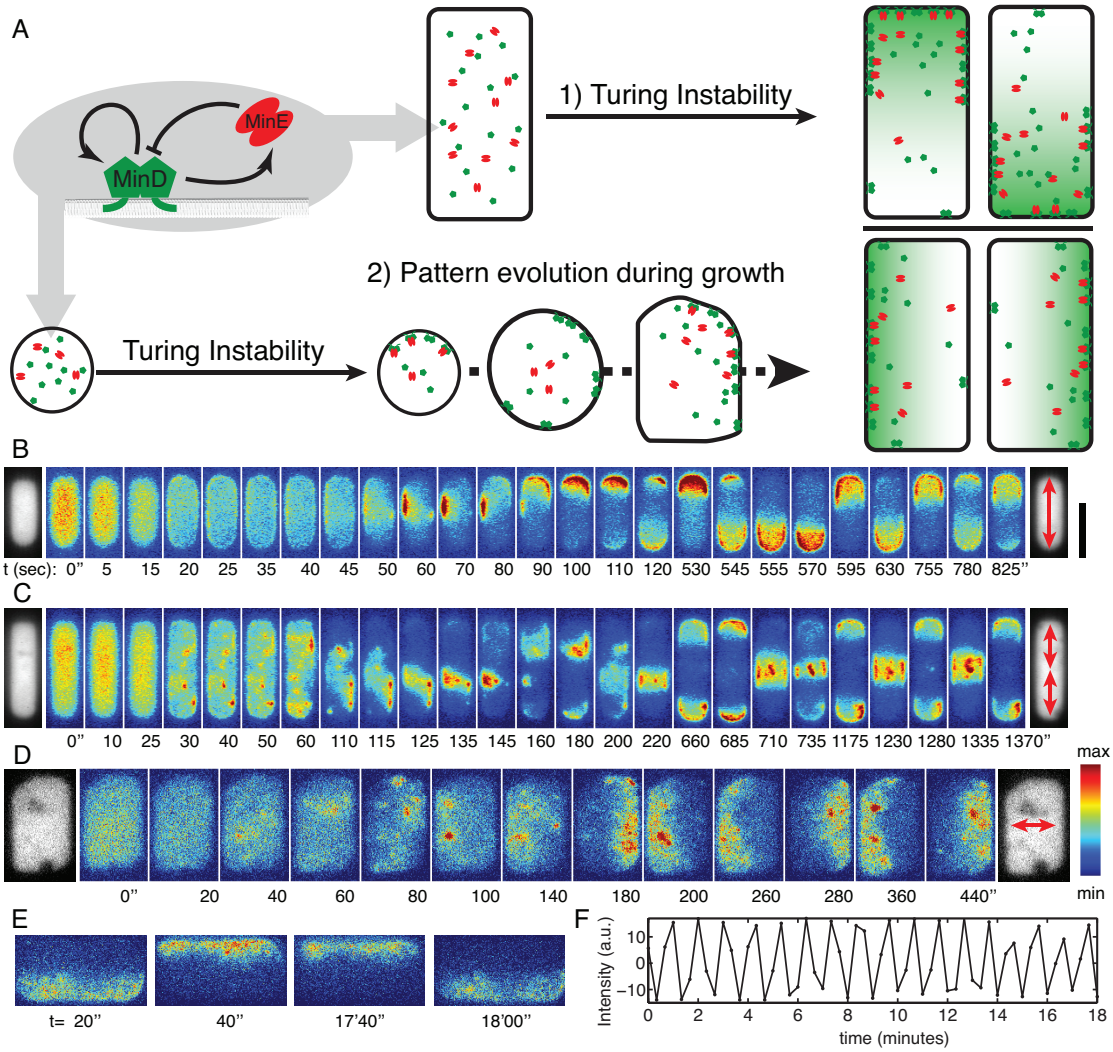

Figure 1. Symmetry breaking of Min protein patterns *in vivo*.

A. Schematic showing Min protein patterns in a defined geometry originating from 1) a dynamic instability arising from an equilibrium state, or 2) dynamic transitions from a pre-existing pattern associated with cell growth. Green and red particles represent MinD and MinE proteins, respectively. The green gradient depicts the MinD concentration gradient.

B-D. Examples of Min protein patterns emerging from nearly homogeneous initial conditions in *E. coli* cells of different sizes. Lateral dimensions (in µm) from top to bottom: 2x6.5, 2x8.8, and 5.2x8.8 respectively. The gray-scale images show

cytosolic near-infrared fluorescence emitted by the protein eqFP670 at the first (left) and last (right) time points. The color montages show the sfGFP-MinD intensity (indicated by the color scale at the bottom right) over time. The scale bar in panel B corresponds to 5 μm. Red arrows show the oscillation mode at the respective time point.

E. Two early and two late frames depicting sfGFP-MinD patterns in a cell exhibiting stable transverse oscillations. The images share the scale bar in B.

F. Difference in sfGFP-MinD intensity between the top half and bottom half of the cell plotted against time.

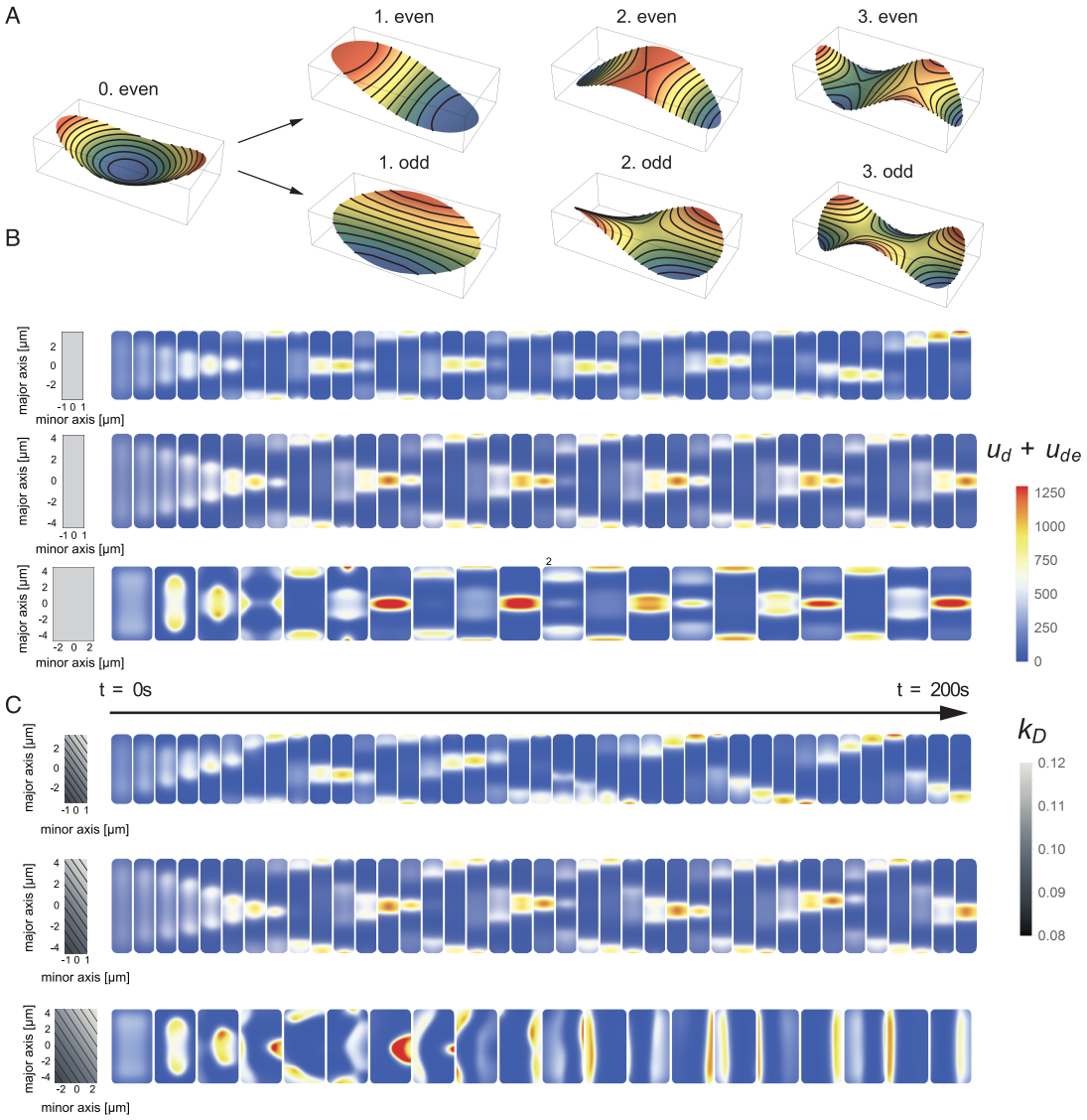

Figure 2 Pattern emergence upon spatial perturbation.

A. Even and odd Mathieu functions in an elliptical geometry. The 0.even mode shows the symmetry of the basal state of the system. Here no homogeneous steady state exists. Note the similarity between the 0th and the 2nd even mode.
B. Simulations of Min pattern formation from an initially homogeneous state. Dimensions of the cells shown are 6.5x2x1 µm^3, 9x2x1 µm^3, and 9x5x1 µm^3. All cells show an initial striped pattern, which persists in both cells of 9 µm length throughout the simulation period.

C. Simulations analogous to the experiments shown in Fig. 1B, with the same cell dimensions as in Fig. 2B. The left-hand column depicts the spatially perturbed MinD attachment profile, showing gradients along the diagonal lines of the rectangles. With these attachment profiles, the Min distributions in the three cells quickly evolve into longitudinal, striped, and transverse patterns, respectively.

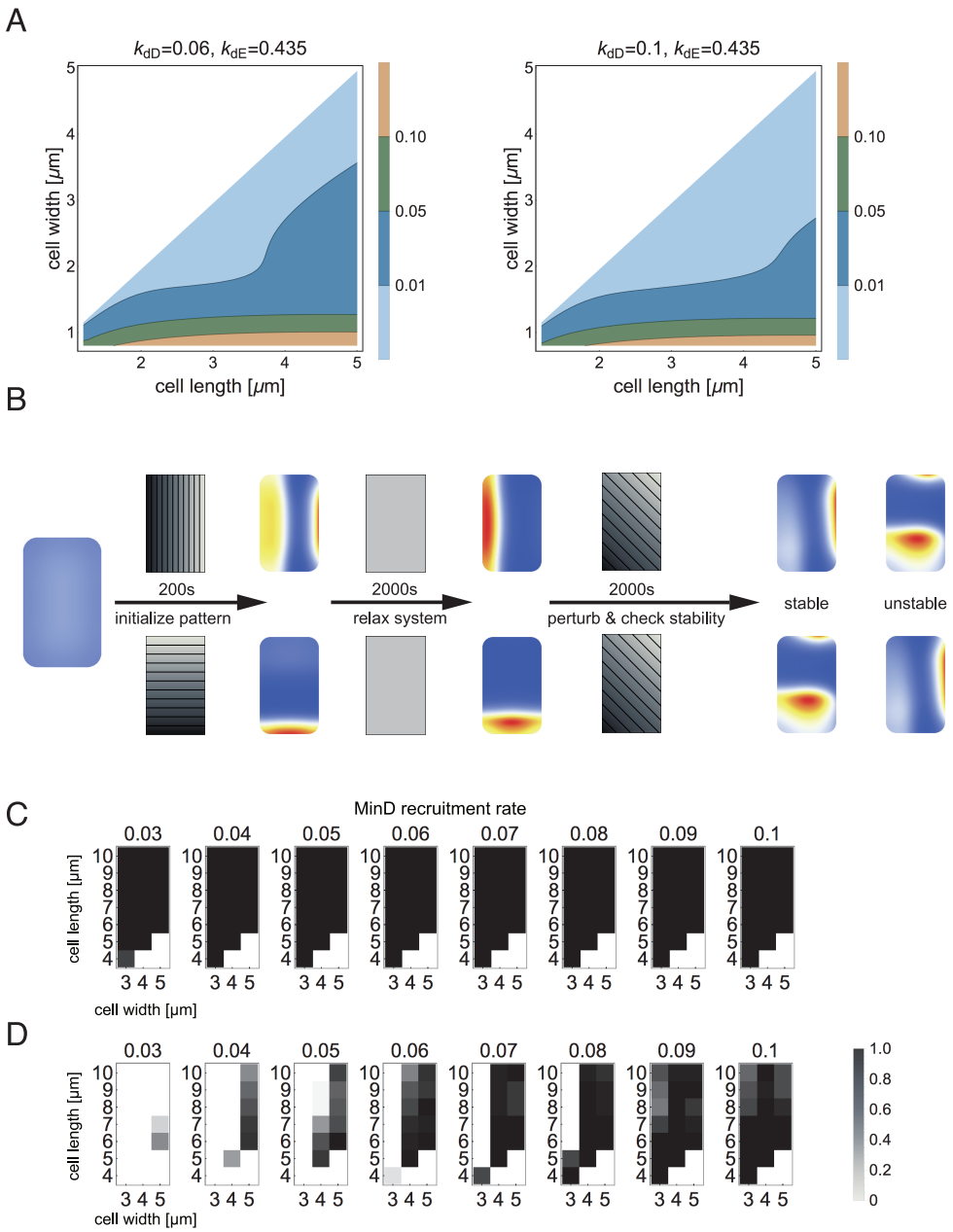

Figure 3. Computing stability in multistability regimes.

A. Two plots that show the non-degeneracy of even and odd modes in an elliptical geometry for varying cell geometry and MinD recruitment rate. The degeneracy (light blue area) increases with the MinD recruitment rate.

B. Schematic representation of the simulation process used to probe the stability of longitudinal and transverse patterns. The system is initialized with a homogeneous configuration and the gradient of the MinD attachment rate is aligned with the major or minor axis to direct pattern selection. After initialization the MinD attachment rate is equalized to allow the system to relax into the initialized state. If the initialized pattern persists in the absence of a stabilizing gradient, the gradient is reapplied to deflect the pattern from its preset alignment and study its stability vis-a-vis spatial inhomogeneities that break its symmetry. The stability towards all possible deflections with linear MinD attachment profiles is probed and the persistence of the initialized pattern is checked.

C-D. Stability diagrams of the simulation procedure outlined in (B) for longitudinal (C) and transverse (D) patterns. White areas represent configurations where the respective mode was not initialized. The grey values show the fraction of all simulations (with different attachment templates) in which the respective pattern mode is sustained.

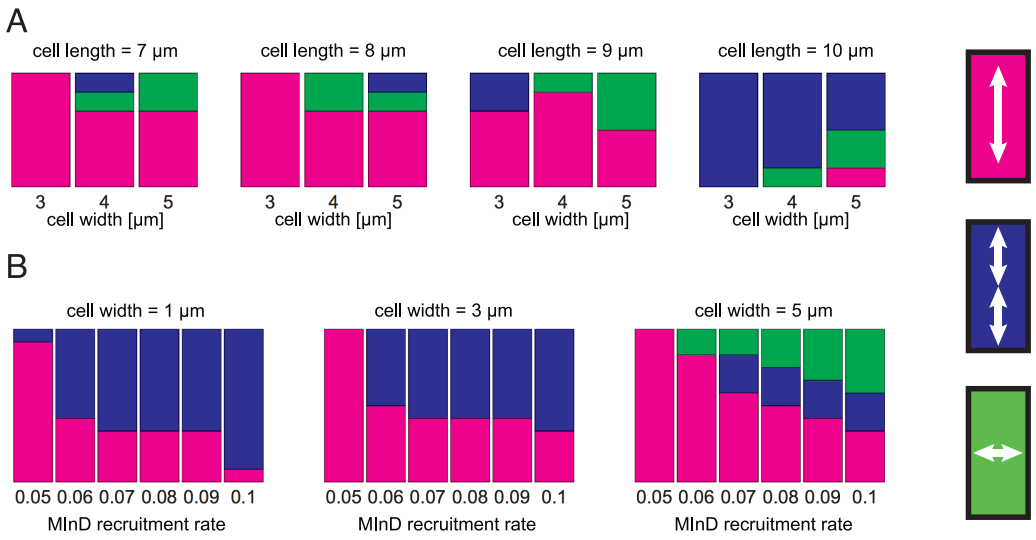

Figure 4. Basins of attraction predicted from systematic perturbations of patterns with shallow attachment gradients.

A. Relative distribution of the final patterns (indicated on the right) observed after sampling all alignment angles of the MinD attachment template from 0 to 90 degrees. The MinD recruitment rate was set to a constant value $k_{dD} = 0.1$. The data shows the increase in the incidence of multistability as the cell size is increased beyond minimal values for cell length and cell width.

B. Fractions of the final patterns in cells of 9- and 10-µm length after sampling all alignment angles of the MinD attachment template from 0 to 90 degrees. The data shows that increasing the MinD recruitment rate facilitates multistability.

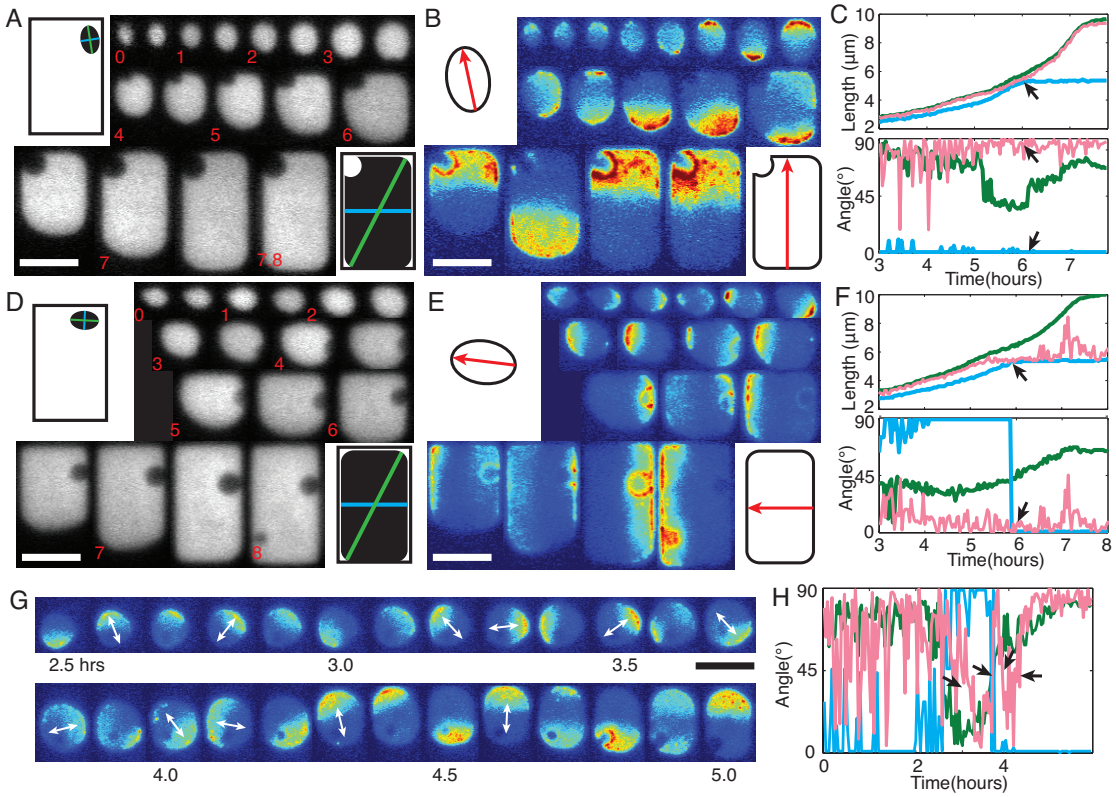

Figure 5. The effect of cell-shape change during growth on the stability of Min protein patterns.

A. Cytosolic fluorescence during growth of a cell from a small elliptical form into a large rectangular shape. Numbers in red indicate time in hours. Illustrations show the positions and orientations of the cell in the first and last time frames. Green and blue lines indicate the maximum and minimum Feret diameters, respectively.

B. sfGFP-MinD patterns during the growth of the cell shown in A. Illustrations indicate the cell boundaries and oscillation angles observed in the first and last frames (not to scale).

C. Quantitative data obtained from the cell shown in A and B. The maximum and minimum Feret diameters (green and blue), and the measured MinD oscillations (red) were expressed in terms of length (top) and angle (bottom) and plotted against time. The number of cells that fit this category was 41/97. Arrows indicate the time when cell width reached the chamber width of 5 μm.

D-F. Data are presented as in A-C for another cell that showed persistent oscillations along the horizontal axis throughout growth. The number of cells that fit this category was 28/97.

G. Time-lapse images of sfGFP-MinD that reveal stochastic switching of patterns in a cell with an asymmetric shape and a low aspect ratio. White arrows indicate the oscillation axes.

H. The angles of the maximum and minimum Feret diameters (green and blue), and the measured MinD clusters (red) for the cell shown in panel G plotted against time. The number of cells that fit this category was 10/97. All scale bars correspond to 5 μm.

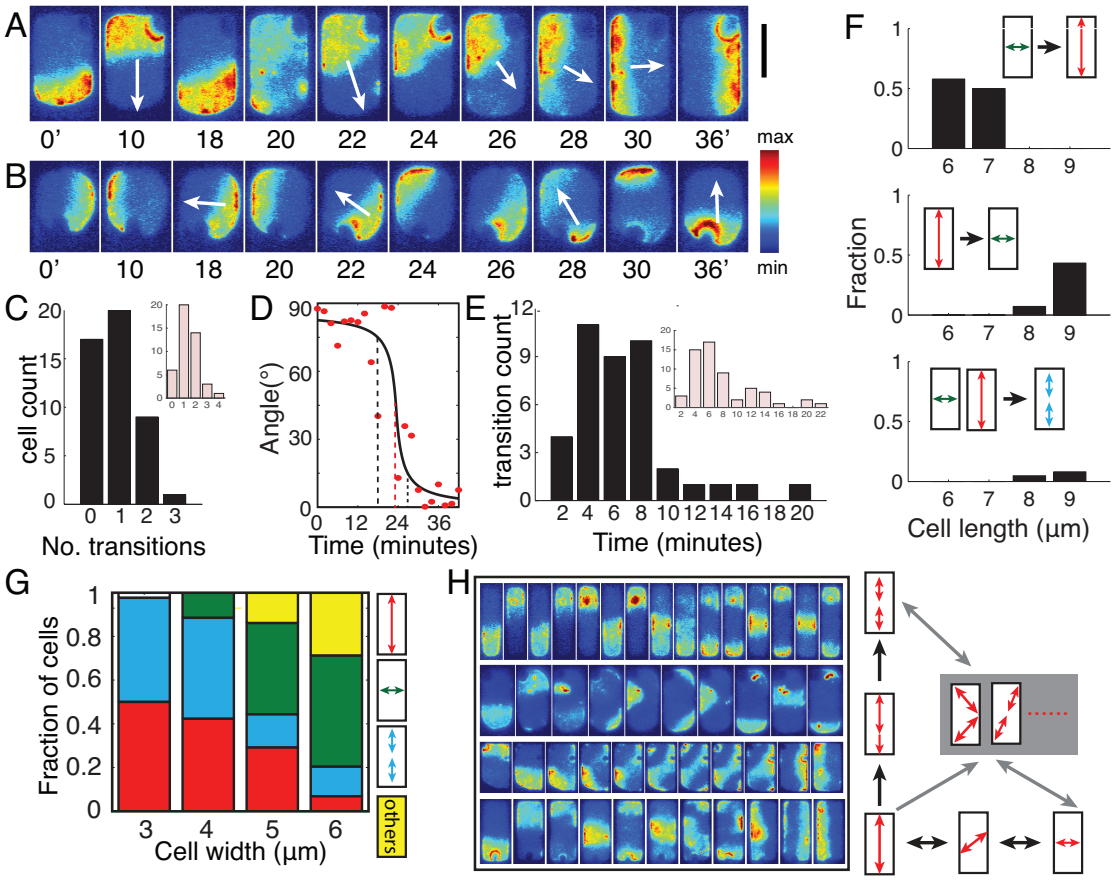

Figure 6. Transitions between various modes of Min protein patterns.

A. Time-lapse images showing the transition from a longitudinal pole-to-pole mode to the transverse mode. Scale bar, 5 μm.

B. Time-lapse images showing the transition from a transverse mode to a longitudinal pole-to-pole mode.

C. Bar plot showing the distribution of the number of transitions. Inset: Data from experiments carried out under nutrient-poor conditions in which growth rates are reduced.

D. Representative time-course of a change in the mode of sfGFP-MinD oscillation. The black line is a sigmoidal fit. The dashed black lines indicate 15° and 75° and the dashed red line indicates 45°.

E. Bar plot showing the time scale of the switch in the oscillations. Inset: Data from experiments carried out in nutrient-poor conditions.

F. Bar plots showing the relative numbers of the indicated transitions that occur at different cell lengths. All cells have a width of 5 μm.
G. Distribution of final patterns in cells of the indicated widths as indicates, and lengths of 9-10 μm.
H. Time-lapse images of various modes of transitions between patterns. Cell sizes from top to bottom are respectively 10x2x1, 10x6x1, 9x5x1, 10x4x1 μm^3. Note that the cells are scaled differently. On the right is an illustration showing Min pattern transitions through intermediate states.

Extended View Figures and Movies

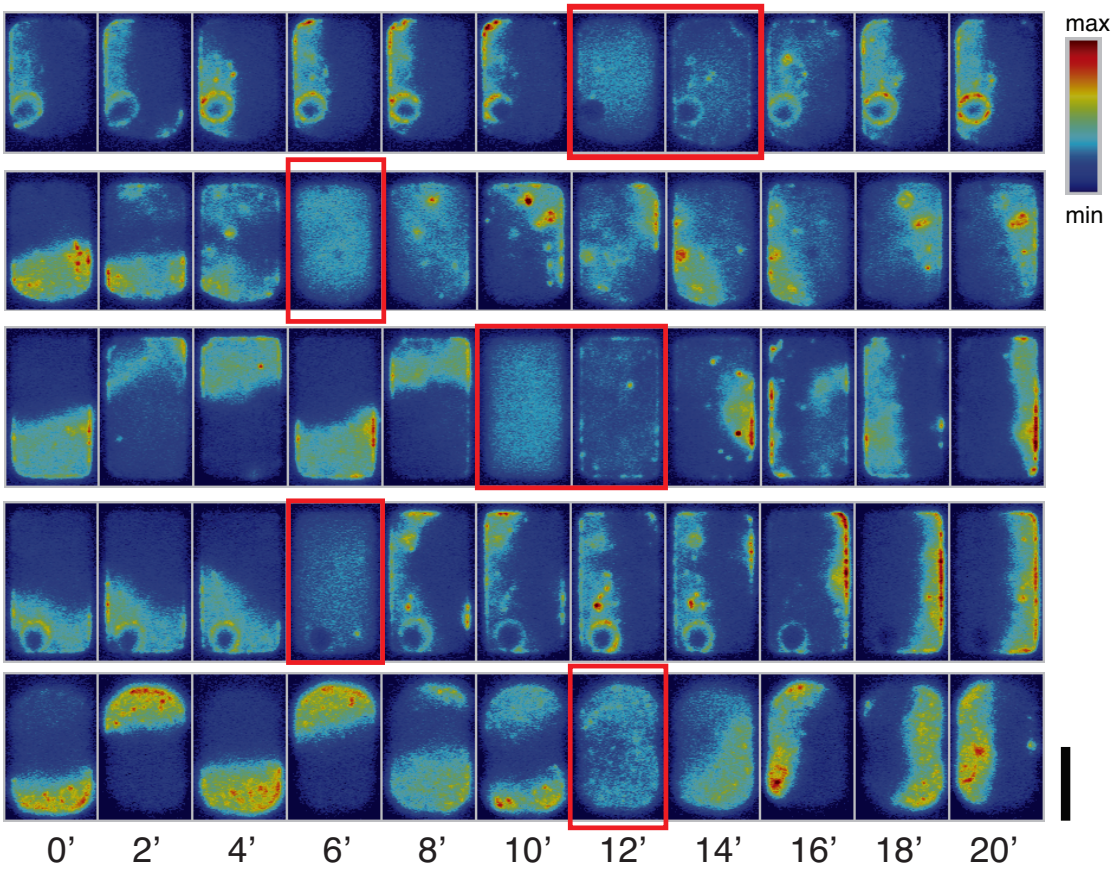

Fig. EV1. Disruption and re-emergence of Min patterns in cells of 5 µm in width. Scale bar = 5 µm. The red boxes show the near homogeneous state. The color scale indicates MinD concentration.

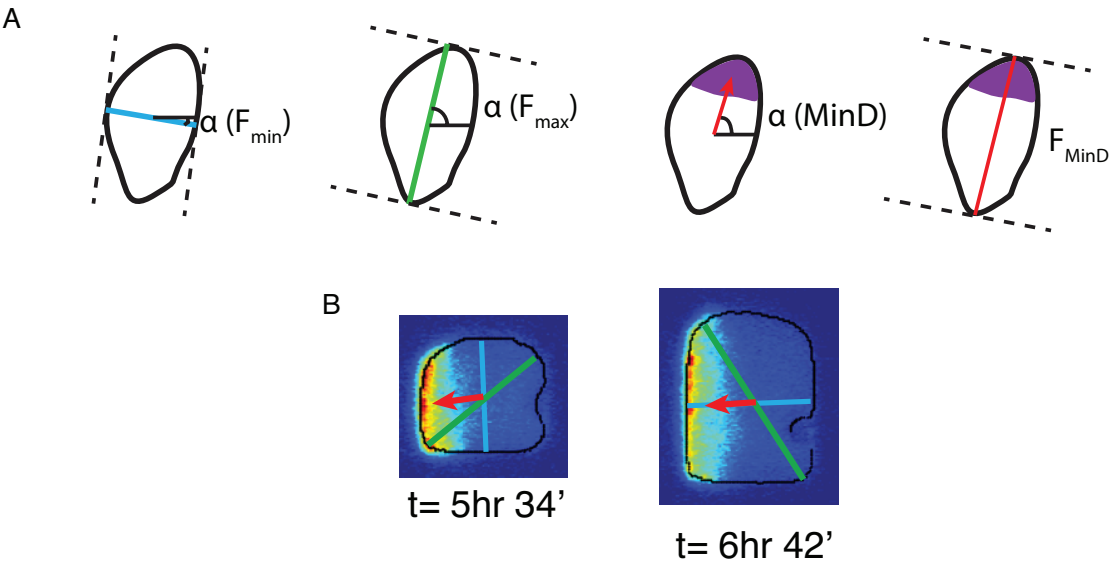

Fig. EV2. Illustrations of maximum/minimum Feret diameters.

A. From left to right showing the minimum Feret diameter and its angle, the maximum Feret diameter and its angle, the angle of the MinD polar zone, and the Feret diameter corresponding to this angle.
B. Two examples of Feret diameters and angles in the cell shown in Fig. 2D-F

Movie EV1. Disruption and re-emergence of Min patterns in cells of 5 μm in width imaged at 2-min intervals.

Movie EV2. Robust transversal oscillations imaged at 20-sec intervals.

Movie EV3. Co-imaging of sfGFP-MinD and MinE-mKate2 during a symmetry-breaking process.

Movie EV4. Time evolution of patterns in cells that adopt different pattern modes due to different constraints on their growth, imaged at 2-min intervals.

Movie EV5. An example of stochastically switching Min patterns in cells with low aspect ratios.

Movie EV6. Various examples of pattern transitions in cells with different dimensions.

Multistability and dynamic transitions of intracellular Min protein patterns

– Supplementary Document –

Fabai Wu[†],[1] Jacob Halatek[†],[2] Matthias Reiter,[2]
Enzo Kingma,[1] Erwin Frey,[2] and Cees Dekker[1]

[1]*Department of Bionanoscience,*
Kavli Institute of Nanoscience,
Delft University of Technology, Lorenzweg 1,
2628 CJ, Delft, the Netherlands
[2]*Arnold-Sommerfeld-Center for Theoretical Physics*
and Center for NanoScience, Department of Physics,
Ludwig-Maximilians-Universität München,
Theresienstraße 37, D-80333 München, Germany

NUMERICAL STABILITY ANALYSIS OF MIN OSCILLATION PATTERNS

This section describes how the stability of Min oscillation patterns in rectangular-shaped 3D cell geometries is determined numerically.
We analyse the stability with respect to spatial variations in the MinD attachment rate. For the sake of simplicity such variations will be restricted to linear profiles of the attachment rate k_D,

$$k_D(x, y, z) = \bar{k}_D \left(1 + 2s \frac{x \cos a + y \sin a}{|l_x \cos a + l_y \sin a|}\right). \quad (1)$$

Here l_x and l_y denote cell length and width ($|x| < l_x/2$, $|y| < l_y/2$), $\bar{k}_D$ the mean attachment rate, s characterizes the slope of the profile ($0 \leq s \leq 1$) and a denotes the direction of rate variation with respect to the x-axis ($0 \leq a \leq \pi/2$).
In order to investigate how the stability of oscillation patterns depends on cell size, geometry and the MinD recruitment rate k_{dD}, we define 18 different rectangular-shaped cell bodies with varying length and width, but identical height $2r$. The cell lengths were increased from $4\mu m$ to $10\mu m$, the cell width from $3\mu m$ to $5\mu m$, both in steps of $1\mu m$. For each of these geometries, we perform the following procedure independently for all MinD recruitment rates $k_{dD} \in \{0.03, 0.035, \ldots 0.1\mu m^3/s\}$:

1. The system is prepared in a transversal oscillation pattern in y-direction by solving the nonlinear equations (c.f. Materials and Methods) numerically for 200s with an attachment rate variation in y-direction using parameters $s = 1$, $a = \pi/2$ in Equ. (1).

2. Subsequently the spatial variation of k_D is removed by setting $s = 0$ and the pattern is observed for a simulation time of 2000s with spatially homogeneous attachment rate.

   We then determine if the pattern remains stable during this period by comparing the evolution of the concentration u_{DD} at two points $\mathbf{p_1}$ and $\mathbf{p_2}$ in the cell interior which are located axisymmetrically with respect to the y-axis. We here choose $\mathbf{p_1} = [0.95(-lx/2 + r), 0, r/2]$ and $\mathbf{p_2} = [0.95(lx/2 - r), 0, r/2]$.
   If the pattern is stable, $u_{DD}(\mathbf{p_1}, t)$ and $u_{DD}(\mathbf{p_2}, t)$ will, apart from small numerical errors, not deviate from each other. However, if the pattern exists only transiently and switches into a longitudinal oscillation, the concentration in $\mathbf{p_1}$ and $\mathbf{p_2}$ will loose its symmetry and the signals will

deviate.
We therefore apply the following criterion for stability:

$$\max_{t\in\{0,100s,\ldots,2000s\},i\in\{1,2\}} \left\{ \frac{|u_{DD}(\mathbf{p_1},t) - u_{DD}(\mathbf{p_2},t)|}{u_{DD}(\mathbf{p_i},t)} \right\} \begin{cases} \geq \alpha \Rightarrow & \text{pattern not stable} \\ < \alpha \Rightarrow & \text{pattern stable} \end{cases} \tag{2}$$

Eq. 2 states that a pattern is only considered stable if the maximum relative deviation of the concentration u_{DD} between $\mathbf{p_1}$ and $\mathbf{p_2}$ over the solution interval does not exceed a threshold α. By inspection we find that $\alpha = 0.05$ is a reasonable choice.
An example for the application of Eq. (2) is shown in Fig. 1.

3. In the case that a stable pattern is found in the previous step, we use its final system state as initial configuration for independent simulations in which the stability is tested against perturbations given by spatial attachment rate variations with different slopes s and directions a (cf. Eq. (1)).

   Specifically, for each combination

$$(s,a) \in \{0.2, 0.4, \ldots 1.0\} \times \{0, pi/18, \ldots, pi/2 - pi/18\}$$

   we compute the solution for an interval of 2000s and determine the type of the final pattern. We here distinguish between three different pattern types: transversal pole-to-pole oscillation, longitudinal pole-to-pole oscillation and longitudinal stripe-shaped oscillations. The following recipe describes how this evaluation is automated:

   - The three pattern types are distinguishable by their different spatial symmetries. We therefore measure and compare the values of all concentrations $u \in \{u_{DD}, u_{DT}, u_E\}$ on 6 different straight lines

located in the cell interior (cf. Fig. 2) :

$$\begin{aligned}
\gamma_1 &= \{(x,y,r/2) : x = -0.95(l_x/2-r) \quad \wedge |y| \le 0.95(l_y/2-r)\},\\
\gamma_2 &= \{(x,y,r/2) : x = 0 \qquad\qquad\quad \wedge |y| \le 0.95(l_y/2-r)\},\\
\gamma_3 &= \{(x,y,r/2) : x = 0.95(l_x/2-r) \quad \wedge |y| \le 0.95(l_y/2-r)\},\\
\eta_1 &= \{(x,y,r/2) : |x| \le 0.95(l_x/2-r) \quad \wedge y = -0.95(l_y/2-r)\},\\
\eta_2 &= \{(x,y,r/2) : |x| \le 0.95(l_x/2-r) \quad \wedge y = 0.95(l_y/2-r)\}.
\end{aligned} \tag{3}$$

- Using the notation $\langle u\rangle_\gamma \equiv |\gamma|^{-1}\int_\gamma u\mathrm{d}s$, we define the following three measures for the symmetry of the pattern, again for all $u \in \{u_{DD}, u_{DT}, u_E\}$:

$$\begin{aligned}
p_L(u) &= \frac{|\langle u\rangle_{\gamma_1} - \langle u\rangle_{\gamma_3}|}{\langle u\rangle_{\gamma_1\dot{+}\gamma_3}}.\\
p_T(u) &= \frac{|\langle u\rangle_{\eta_1} - \langle u\rangle_{\eta_2}|}{\langle u\rangle_{\eta_1\dot{+}\eta_2}},\\
p_S(u) &= \frac{|\langle u\rangle_{\gamma_1\dot{+}\gamma_3} - \langle u\rangle_{\gamma_2}|}{\langle u\rangle_{\gamma_1\dot{+}\gamma_2\dot{+}\gamma_3}}.
\end{aligned} \tag{4}$$

  The line integrals in $\langle u\rangle_\gamma$ are here approximated by the value of u at three points, the two endpoints and the midpoint of the line γ. The concentrations are evaluated at the last time step, $t = 2000s$.

  In case of a longitudinal pole-to-pole oscillation, the signals at γ_1 and γ_3 oscillate in opposition, resulting in a large p_L. Similarly, transversal pole-to-pole oscillations yield large values of p_T. Finally, in case of a longitudinal stripe pattern (with two nodes of oscillation) the concentrations at γ_1 and γ_3 are in phase with each other and in opposition with the signal at γ_2. Therefore large values of p_S characterize longitudinal stripe oscillations.

- Taken these considerations together, we conclude that the type of the oscillation pattern can be determined reliably by the following

rule:

$$\text{if} \quad p(u) = \max\{p_L(u), p_T(u), p_S(u)\} = \begin{cases} p_L(u) & \Rightarrow \quad \text{long. pole-to-pole} \\ p_T(u) & \Rightarrow \quad \text{trans. pole-to-pole} \\ p_S(u) & \Rightarrow \quad \text{long. stripe.} \end{cases} \tag{5}$$

To obtain a single, final result for the pattern type we take the vote over the independent evaluations for $u \in \{u_{DD}, u_{DT}, u_E\}$. The unspecified case that the three concentrations yield all three different pattern types did not occur.

For fixed cell geometry, this procedure firstly provides us with a threshold for the MinD recruitment rate k_{dD}^* above which the initiated transversal oscillation persists in step 2. Secondly, for each $k_{dD} > k_{dD}^*$ one obtains thresholds in direction and slope of the perturbation above which the pattern switches.
Interchanging the role of cell length and cell width enables us analyse the stability of longitudinal oscillations analogously to steps 1 to 3. Since all non-perturbed longitudinal oscillations are found stable in step 2 for the considered range of k_dD, no critical recruitments rates are determined in this case.
The numerical solution of the model equations (c.f. Materials and Methods) was computed using *Comsol Multiphysics 4.4*. To reduce the number of necessary simulations for the parametric sweep in step 3, we utilised the observation that the stability of a pattern decreases with the slope of the perturbation and (partly) skipped parameter sets where the stability or de-stability could be inferred from previous runs.

CHARACTERIZATION OF MIN OSCILLATION PATTERNS

The goal of this study is to investigate how the occurrence of specific types of oscillation patterns depends on cell geometry and MinD recruitment rate k_{dD}. As opposed to the previous section, the Min system is not prepared in a specific solution. Instead, the initial condition is a spatially homogeneous configuration.
We again impose a linear variation of the attachment rate k_D with different slopes and directions according to Eq. (1). The solution is calculated for $0 \leq t \leq 4000s$. We subsequently determine the final pattern that the Min

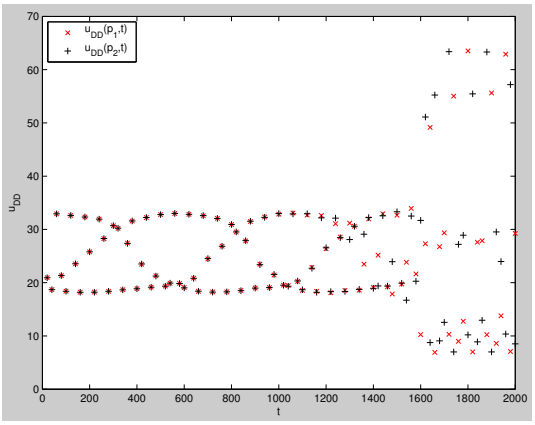

(a)

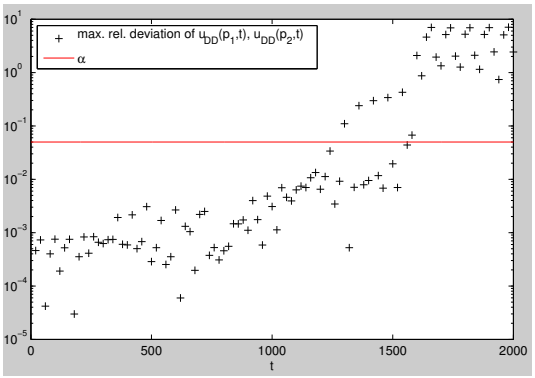

(b)

FIG. 1: Example for a transversal oscillation pattern that is found unstable using Eq. (2). The concentrations $u_{DD}(\mathbf{p_1}, t)$ and $u_{DD}(\mathbf{p_2}, t)$ deviate considerably at $t \approx 1600s$, since the pattern changes into a longitudinal oscillation (**a**). The relative deviation therefore exceeds the threshold α and the pattern is found unstable (**b**). Parameters:
$l_x = 8, l_y = 3, k_{dD} = 0.07\mu m^3/s$

system settles into with the procedure explained in step 3 of section , in which we evaluate the concentrations at the last time step $t = 4000s$.
This analysis is performed independently for the cell geometries and MinD recruitment rates reporded in Fig. 4 of the main text, and for parameters $a \in \{0, \pi/10, \ldots, \pi/2\}$ and $s = 0.2$ in the attachment rate profile.

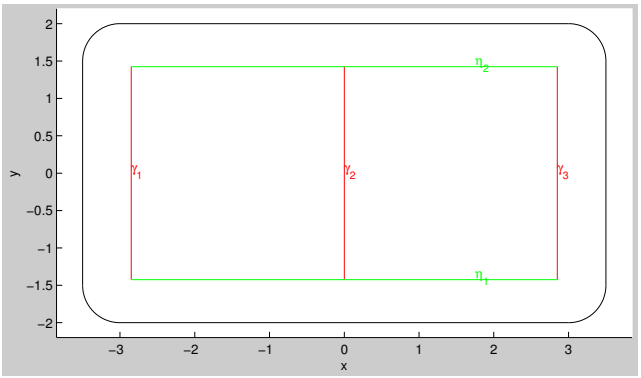

FIG. 2: Illustration of the straight lines along which u_{DD} is evaluated in order to determine the type of the final oscillation pattern. The contour indicated in black is the shape of a cell with parameters $l_x = 7$ and $l_y = 4$ in topview. The straight lines γ_i and η_i for pattern determination are indicated in red and green, respectively. The position of the lines in z-direction is $z = r/2$.

With width specified:

Parameter	Value	Description
D_D	$16\mu m^2 s^{-1}$	Cytosolic Diffusion coefficient MinD
D_E	$10\mu m^2 s^{-1}$	Cytosolic Diffusion coefficient MinE
D_m	$0.013\mu m^2 s^{-1}$	Membrane Diffusion coefficient MinDE
λ	$6s^{-1}$	Cytosolic nucleotide exchange rate
k_{de}	$0.5s^{-1}$	MinDE Detachment rate
k_D	$0.1\mu m s^{-1}$	MinD attachment rate constant
k_{dD}	$0.1\mu m^3 s^{-1}$	MinD recruitment rate constant
k_{dE}	$0.435\mu m^3 s^{-1}$	MinE recruitment rate constant
C_D	$602/\mu m^3$	total MinD density
C_E	$301/\mu m^3$	total MinE density

TABLE I: Parameter values used in numerical simulations

V Geometry adaption: Pattern formation without instability

This chapter is based on the following publication:

Geometry induced protein pattern formation

by

D. Thalmeier[1,2]**, J. Halatek**[1]**, and E. Frey**[1]

[1]Department of Physics, Arnold Sommerfeld Center for Theoretical Physics and Center for NanoScience, Ludwig-Maximilians-Universität München, Theresienstraße 37, 80333 München, Germany,

[2]Donders Institute, Department of Biophysics, Radboud University, Nijmegen, The Netherlands

Journal Reference:

***Proc. Natl. Acad. Sci. U.S.A.* 113, 2016**

Supplemental Material reproduced on pages 168 to 187.

Geometry induced protein pattern formation

Dominik Thalmeier,[1,2] Jacob Halatek,[1] and Erwin Frey[1]

[1]*Arnold-Sommerfeld-Center for Theoretical Physics and Center for NanoScience, Department of Physics, Ludwig-Maximilians-Universität München, Theresienstraße 37, D-80333 München, Germany*

[2]*Donders Institute, Department of Biophysics, Radboud University, Nijmegen, The Netherlands*

Abstract

Protein patterns are known to adapt to cell shape and serve as spatial templates that choreograph downstream processes like cell polarity or cell division. But how can pattern-forming proteins sense and respond to the geometry of a cell, and what mechanistic principles underlie pattern formation? Current models invoke mechanisms based on dynamic instabilities arising from nonlinear interactions between proteins but neglect the influence of the spatial geometry itself. Here we show that patterns can emerge as a direct result of adaptation to cell geometry, in the absence of dynamical instability. We present a generic reaction module that allows protein densities robustly to adapt to the symmetry of the spatial geometry. The key component is an NTPase protein that cycles between nucleotide-dependent membrane-bound and cytosolic states. For elongated cells we find that the protein dynamics generically leads to a bipolar pattern, which vanishes as the geometry becomes spherically symmetrical. We show that such a reaction module facilitates universal adaptation to cell geometry by sensing the local ratio of membrane area to cytosolic volume. This sensing mechanism is controlled by the membrane affinities of the different states. We apply the theory to explain AtMinD bipolar patterns in ΔEcMinDE *E. coli*. Due to its generic nature, the mechanism could also serve as a hitherto unrecognized spatial template in many other bacterial systems. Moreover, the robustness of the mechanism enables self-organized optimization of protein patterns by evolutionary processes. Finally, the proposed module can be utilized to establish geometry-sensitive protein gradients in synthetic biological systems.

INTRODUCTION

Protein patterns serve to initiate and guide important cellular processes. A classic example is the early patterning of the *Drosophila* embryo along its anterior-posterior axis [1]. Here maternal morphogen gradients initiate a complex patterning process which subsequently directs cell differentiation. However, protein patterns play a regulatory role even at the single cell level. For example, they determine cell polarity and the position of the division plane. In the yeast *Saccharomyces cerevisiae*, the GTPase Cdc42 regulates cell polarization which in turn determines the position of a new growth zone or bud site. This pattern-forming process is driven by the interaction between a set of different proteins that cycle between the plasma membrane and the cytoplasm [2, 3]. In the rod-shaped bacterium *Escherichia coli*, Min proteins accumulate at the ends of the cell to inhibit the binding of the division proteins [4, 5]. Here, the main player in the pattern-forming process is the ATPase MinD. It attaches to the membrane in its ATP-bound state and recruits MinE and further MinD-ATP from the cytosol [6]. Cycling of proteins between membrane and cytosol is mediated by the action of MinE, which stimulates the intrinsic ATPase activity of MinD and thereby initiates its detachment. The ensuing oscillatory pattern directs the division machinery to mid-cell, enabling proper cell division in two viable daughter cells.

In all of these processes, regulatory proteins establish chemical gradients or patterns that reflects aspects of cell shape. But how is it achieved in the absence of an external template? Many possible mechanisms have been proposed and they are by no means fully classified yet [7, 8]. Establishing a pattern involves definition of preferred accumulation points and requires that the symmetry of the homogeneous state is broken. In *Bacillus subtilis*, there is good evidence suggesting that DivIVA recognizes negative membrane curvature directly by a mechanism which is intrinsic to this cell division protein [7, 9]. In contrast, enrichment of MinD at the cell poles in *E. coli* is an emergent property of the collective dynamics of several proteins. As shown in Refs. [10–16], the non-linear dynamics of the Min system leads to a polar pattern, which oscillates along the long axis and is clearly constrained by cell geometry. A clear disadvantage of such self-organized symmetry-breaking through a dynamical instability is that the kinetic parameters must be fine-tuned in order to allow the establishment of a stable polar pattern.

Here we show that cell geometry itself can enforce a broken symmetry under generic conditions without any need for fine-tuning. We introduce a class of geometry-sensing protein systems whose only stable state is a spatial pattern

that is maintained by energy consumption through an ATPase or GTPase (NTPase). The proposed mechanism is based on a generic property of diffusion: The probability that a protein diffusing through the cytosol will strike (and attach) to the membrane scales with the area of membrane accessible to it. Thus, close to the poles of a rod-shaped cell most of the trajectories available lead to the membrane. Close to mid-cell, where the membrane is almost flat, about half of the the possible paths lead away from the membrane. However, on its own, this mechanism only produces *transient* patterns on the membrane, as the system approaches a stable, uniform equilibrium in finite time [17]. Moreover, patterns only emerge from specific initial conditions. In this paper we ask: How can this generic property of diffusion be complemented by a minimal set of biomolecular processes to robustly maintain patterns? We show that the NTPase activity of a single protein that cycles between membrane and cytosol is sufficient to achieve this goal. Our analysis shows that an inhomogeneous density profile is established on the membrane in the generic case where the affinities of NTP-and NDP-bound forms differ. Moreover, these membrane-bound patterns are amplified if the proteins are able to bind cooperatively to the membrane (e.g. due to dimerization). This mechanism is highly robust because the stable, uniform equilibrium is simply replaced by a unique, stable patterned state. In particular, the mechanism involves no dynamical instability and requires no fine-tuning of parameters.
Experimental support for the proposed mechanism comes from *E. coli* mutants in which both EcMinD and EcMinE were replaced by chloroplastic AtMinD (MinD homologue from Arabidopsis) [18]. With this single ATPase [20] the system establishes a bipolar pattern along the long axis, rescuing the ΔMinDE mutant from cell division pathologies. Mutation studies of the Walker-A binding module show that AtMinD (unlike EcMinD) can form dimers on the membrane even in its ADP-bound form [19–21], suggesting that both forms can cooperatively bind to the membrane. Our study shows that such cooperativity leads to a bipolar pattern along the long axis of the cell, as observed. Furthermore, we suggest that due to its generic nature, the binding module might also play an essential role in other bacterial pattern-forming systems.

A GENERIC REACTION MODULE FOR SENSING OF CELL GEOMETRY

We consider a reaction module comprised of a single type of NTPase which cycles between an NDP-bound (P_{NDP}) and a NTP-bound (P_{NTP}) state (Fig.1A).

Both forms are allowed to freely diffuse in the cytosol and the membrane with *diffusion constants* D_c and D_m, respectively. For the biochemical reaction kinetics we assume that (i) cytosolic P_{NDP} undergoes *nucleotide exchange* with a rate λ; (ii) both protein species can bind to the membrane with respective *attachment rates* ω_D^+ and ω_T^+; (iii) in addition to direct membrane attachment, each protein species can also bind cooperatively to the membrane, forming homodimers, with corresponding recruitment rates k_{dD} for P_{NDP} and k_{tT} for P_{NTP}; (iv) *hydrolysis* of P_{NTP} triggers *detachment* with rate ω_t^- which is thus converted into cytosolic P_{NDP}; (v) membrane-bound P_{NDP} is released to the cytosol with *detachment rate* ω_d^-. For a mathematical formulation in terms of reaction-diffusion equations please refer to Eqs.(1-6) in the SI Appendix.
This reaction module serves as a model for the bipolar pattern of AtMinD in *E. coli* cells [18]: AtMinD is an ATPase [20] which has been reported to dimerize [20, 21]. This process thus provides for cooperative membrane binding. Unlike EcMinD [19], AtMinD dimerizes even when its Walker-A binding module is inactivated [20], locking the protein in its ADP-bound state. This strongly suggests that also the ADP-bound form of AtMinD exhibits cooperative membrane binding, as we have assumed in the above reaction scheme by introducing a recruitment rate k_{dD} for P_{NDP}. Overall, there is strong evidence that AtMinD shows the same interactions with the membrane as EcMinD but with additional cooperative membrane binding in its ADP-bound state.
If not mentioned otherwise, we use the following model parameters, which are set to experimental values acquired for *E. coli* if available. The diffusion constants in the cytosol and on the membrane are set to D_c=16μm^2/s and D_m=0.013μm^2/s, respectively [22, 23]. The nucleotide exchange rate is set to λ=6s^{-1} [15] to meet the lower bound of $3s^{-1}$ [22]. The kinetic parameters, are chosen to be of the order of 1μm/s for attachment, 1s^{-1} for detachment and 0.1μm^2/s for recruitment [15]; for the specific values see Table I in the SI Appendix. In the numerical studies, the cell shape is modeled as a two-dimensional ellipse. *(Remark: For the sake of clarity we will still use the terms of cytosolic volume and membrane area instead of areas and lines.).* This reduced geometry has the same basic symmetries as the real geometry of an *E. coli* cell. Importantly, in contrast to a one-dimensional model, it fully accounts for the different dimensionalities of cytosol and membrane. This will turn out to be essential for the ability of the system to generate protein patterns that reflect cell geometry. The overall protein density is set to a physiologically typical value of the order of 1μM [24]. For a cell which is 5μm long and has a width of 1μm this gives a fixed protein number of about 2000 MinD molecules. Specifically, in our numerical studies we set the protein density in the bulk

to be ρ=500μm^{-2} if all proteins are in the cytosol. To accommodate changes in cell size, we keep this mean density constant and change the number of proteins as appropriate.

RESULTS

The impact of cell geometry on protein gradients in elongated cells

We performed a numerical analysis of this reaction module, paying particular attention to the effect of varying the cell geometry and the degree of cooperativity in membrane binding (Fig.1B). Our simulations show that in elongated cells the protein density on the membrane is *always* inhomogeneous and reflects the local cell geometry. Indeed, one can show analytically that the homogeneous steady state ceases to exist as one passes from circular to elliptical geometry (c.f. SI Appendix). We observe two distinct types of pattern: membrane-bound proteins either accumulate at mid-cell or form a bipolar pattern with high densities at both cell poles. The polarity of these patterns is quantified by the ratio of the density of membrane-bound proteins located at the cell poles (u_{pole}) to that at mid-cell ($u_{\text{mid-cell}}$): P=$u_{\text{pole}}/u_{\text{mid-cell}}$. First, we investigated the impact of preferetial recruitment of either P_{NTP} or P_{NDP} to the membrane, defined as R=$(k_{dD}-k_{tT})/(k_{dD}+k_{tT})$, on cell polarity. We find that proteins accumulate at the cell poles (P>1) if there is a preference for cooperative binding of P_{NDP} (R>0). Moreover, the polarity P of this bipolar pattern becomes more pronounced with increasing R. This scenario corresponds to the strongly bipolar pattern of AtMinD observed in mutant *E. coli* cells lacking EcMinD and EcMinE [18]. In contrast, when cooperative binding favors P_{NTP} (R<0), proteins accumulate at mid-cell (P<1). Thus, the sign of the recruitment preference R for a protein in a particular nucleotide state controls the type, while its magnitude determines the amplitude of the pattern. Next, we investigated how cell geometry affects the pattern, while keeping R fixed. Upon varying the length of the long axis, L, while keeping the length of the short axis fixed at ℓ=1μm, we find that the aspect ratio L/ℓ controls the amplitude of the pattern, but leaves the type of pattern unchanged. With increasing eccentricity of the ellipse, the respective pattern becomes more sharply defined; for a spherical geometry the pattern vanishes. In summary, cell geometry controls the definition of the pattern, and the preference for membrane recruitment of a certain nucleotide state determines the location on the cell membrane where the proteins accumulate and how pronounced this accumulation becomes.

Why geometry influences patterning

Our finding that recruitment is a major determinant of cell polarity suggests that there is some underlying intrinsic affinity of the two protein species for either the cell poles or the mid-zone. This affinity can not be encoded in the attachment or recruitment rates alone, since these are position-independent. Instead, it must emerge from the interplay between these reactions, cell geometry, and diffusion. To uncover the underlying mechanism we first performed a numerical study from which all cooperative membrane binding processes were omitted, such that the dynamics became linear. Interestingly, we observed that although the overall protein density is homogeneous in the cytosol (see SI Appendix), P_{NDP} and P_{NTP} are nevertheless spatially segregated, accumulating in the vicinity of the cell poles and close to mid-cell, respectively (Fig.2A). This observation, the origin of which will be discussed later, explains how patterns of membrane-bound proteins arise: These inhomogeneities in protein densities in the cytosol serve as seeds for the polarization of the protein pattern on the membrane and their respective impact is regulated by the attachment rates ω_D^+ and ω_T^+. The pattern of the protein species with the higher membrane affinity determines the type of the pattern (Fig.2C). If P_{NDP} has the larger membrane affinity, a bipolar pattern emerges, whereas one observes enrichment of membrane-bound proteins at mid-cell if attachment of P_{NTP} dominates. Note that the detachment rates have the inverse effect (c.f. SI Appendix).
Next, to analyze the additional nonlinear effects of membrane recruitment we considered a situation, illustrated in Fig.2D, where both nucleotide states have the same membrane affinity. As a result the steady-state membrane density becomes uniform (see SI Appendix). Since cooperative membrane binding effectively increases the affinity of a protein species just like an increase in the respective attachment rate, we expected that membrane patterns could be restored by switching the recruitment processes back on. Indeed, we found a strong increase in polarity upon raising the recruitment rate k_{dD} for fixed k_{tT}=0 (Fig.2E). Moreover, for large recruitment rates, not only does the relative level of the two species on the membrane change, but the pattern of P_{NDP} becomes highly polar (Fig.2F). The reason is the positive feedback facilitated by cooperative membrane binding: In membrane regions facing a cytosolic region with an enhanced P_{NDP} concentration, binding leads to a locally increased concentration which in turn increases the net attachment rate. Recruitment strongly amplifies the slight dominance of P_{NDP} already existing at the cell poles in the absence of cooperative membrane binding, and thereby leads to the observed strongly bipolar P_{NDP} membrane pattern.

In summary, the above analysis shows that the mechanism underlying the pattern-forming process is intrinsic to the protein dynamics: An inhomogeneous protein density in the cytosol together with unequal membrane affinities of the two forms leads to a spatially nonuniform accumulation of membrane-bound proteins. Nonlinear dynamics in the form of cooperative membrane binding (recruitment) serves to amplify these weakly nonuniform profiles into pronounced membrane patterns.

Cytosolic reaction volume determines the pattern

After investigating the phenomenology of geometry dependent pattern formation we were left with the key question: What is the origin of the observed spatial segregation of P_{NTP} and P_{NDP} in the cytosol? Since these patterns form without cooperative membrane binding, the mechanism must be based on the combined effect of membrane attachment and detachment, diffusion, and nucleotide exchange. Moreover, as all chemical processes are spatially uniform, the key to understanding the impact of cell geometry must lie in the diffusive coupling of these biochemical processes.
Consider the situation where the attachment rates for P_{NDP} and P_{NTP} are equal, such that the total protein density on the membrane becomes spatially homogeneous (see Fig.2D). Only P_{NDP} is released from the membrane. Hence, the latter acts as a source of cytosolic P_{NDP}. Because, in addition, cytosolic P_{NDP} is transformed into cytosolic P_{NTP} by nucleotide exchange, we have all the elements of a source-degradation process. The ensuing density profile for P_{NDP} in the cytosol is exponential with the decay length set by $l_\lambda = \sqrt{D_c/\lambda}$. Due to membrane curvature these reaction volumes overlap close to the cell poles (Fig.2B bottom), which implies an accumulation of P_{NDP} at the cell poles. The effect becomes stronger with increasing membrane curvature. Moreover, there is an optimal value for the penetration depth l_λ, roughly equal to a third of the length l of the short cell axis, that maximizes accumulation of P_{NDP} at the cell poles (Fig.2B top). As l_λ becomes larger than l, the effect weakens, because the reaction volumes from opposite membrane sites also overlap at mid-cell. In the limit where l_λ is much smaller than the membrane curvature at the poles, the overlap vanishes and with it the accumulation of P_{NDP} at the poles.
Expressed differently, these heuristic arguments imply that the local ratio of the reaction volume for nucleotide exchange to the available membrane surface is the factor that explains the dependence of the protein distribution on cell

geometry. To put this hypothesis to the test we performed numerical simulations that are in the spirit of a minimal system approach taken by in-vitro experiments [23, 25]. In our numerical setup we considered a cytosolic volume adjacent to a flat membrane, as illustrated in Fig.3. We were interested in how alterations in the volume of cytosol available for protein diffusion and/or nucleotide exchange would affect the density profile on the membrane.
In accordance with our hypothesis, we find that excluding volume for diffusion in the vicinity of a flat membrane reduces the available reaction volume locally and leads to accumulation of proteins at the membrane (Figs.3A,C, and D). The larger the volume excluded, the more proteins accumulated at the membrane. To focus on reaction volume explicitly we considered a situation where nucleotide exchange was disabled in a given region of the cytosolic area but proteins could still diffuse in and out of it. Again, we found protein accumulation at the nearby membrane but with reduced amplitude (Fig.3B). Hence, these numerical studies strongly support our heuristic arguments and lead us to conclude that it is indeed exclusion of the reaction volume for nucleotide exchange that provides for the adaptation of the pattern to the geometry of the setup. Likewise, the membrane patterning in a cell could be effected by the nucleoid if the DNA material acts as a diffusion barrier, though at present this is debated [26]. In the SI Appendix we study how different sizes of effective excluded volume changes the membrane pattern. While bipolarity is still obtained for a broad parameter range, the complex geometry gives rise to a richer spectrum of possible patterns: For large sizes of excluded volume, accumulation at the poles occurs for $R<0$ (preferential recruitment for $\mathrm{P_{NTP}}$) while for $R>0$ the proteins accumulate at mid-cell. For intermediate sizes, there are parameter ranges where patterns with several maxima, not necessarily at the poles or mid-cell, are observed.

Pattern formation does not require a dynamical instability

The above analysis shows that the difference in local reaction volume for cytosolic nucleotide exchange is the key element of the mechanism underlying geometry sensing. To put this result in perspective with pattern formation mechanisms based on dynamical instabilities we consolidated the key properties of the spatially extended model in a spatially discretized version amenable to rigorous analytical treatment (Fig.4A):
Diffusion in the cytosol and on the membrane is treated in terms of exchange processes between a network of nodes. A minimal set comprises four nodes

on the membrane, two at the poles and two at mid-cell, and a distribution of nodes in the cytosol which ensures that the ratio of membrane area to bulk volume at the cell poles is higher than at mid-cell. Since all observed stationary patterns are symmetrical with respect to both symmetry axes, we can further reduce the network to one quadrant of the ellipse (see Fig.4B). We are now left with a network of one membrane node at a pole and one at mid-cell, two nodes serving as the interface between membrane and cytosol, and three cytosolic nodes whose distribution reflects the asymmetry in the cytosolic reaction volume between the cell poles and mid-cell.
We have analyzed the ensuing mathematical model, a system of coupled ordinary differential equations, in the context of dynamic systems theory; for mathematical details and the model parameters used please refer to the SI Appendix. Confirming our previous reasoning, we found that the reduced network model indeed leads to polarization between cell pole and mid-cell (Fig.4B). Moreover, from a bifurcation analysis we learn that generically the dynamic system does *not* exhibit a bifurcation: There is only one physically possible solution with positive protein density on the membrane and this density increases with recruitment rate (Fig.4C). Only in the special (non-generic) case where the attachment rate of P_{NDP} vanishes, $\hat{\omega}_D^+=0$, do we find a transcritical bifurcation. Then, there is a critical recruitment rate $\hat{k}_{dD}^*$ below which the membrane is depleted of P_{NDP}. In other words, generically the system shows an imperfect transcritical bifurcation, which implies robustness of the mechanism linking protein distribution to cell geometry.

DISCUSSION

How does protein patterning adapt to cell geometry? Dynamic models for pattern formation often reduce the cytosolic volume to the same dimension as the membrane and focus on the role of non-linear protein interactions; see e.g. Ref. [11, 27]. At first sight this appears to make sense, since diffusion coefficients are generically much higher in the cytosol than on the membrane. Indeed, if only attachment and detachment processes are involved, any transient geometry-dependent pattern is rapidly washed out [17].
Here we have shown that the assumption of a well-mixed cytosolic protein reservoir becomes invalid as soon as cytosolic processes like nucleotide exchange, which alter protein states become involved. We have introduced a minimal reaction module with a single NTPase that cycles between membrane and cytosol. The fact that cytosolic nucleotide exchange may take place on

a diffusive length scale far below cell size has been noted previously [13], and it has been show that this can be critical for robust, intracellular pattern formation [15]. Our analysis reveals that nucleotide exchange leads to an inhomogeneous protein distribution in the cytosol, which is stably maintained and depends strongly on the geometry of the cytosolic space. As a consequence, proteins accumulate on certain membrane regions, depending on the local ratio of membrane area to cytosolic volume. In an elongated cell this serves as a robust mechanism for proper cell division by facilitating protein accumulation at the poles. The proposed reaction module operates through implicit curvature sensing and does not require that the relevant protein themselves respond to membrane curvature [7, 9] or lipids [28]. The degree and the axis of polarization depend on the level of cooperativity in membrane binding, which can be regulated by enzymes.

Our theoretical analysis suggests that evolutionary tuning of this simple reaction module is feasible: Because there is no threshold involved, polarity can be improved stepwise starting from *any* parameter configuration. This lack of a threshold can at the same time also be a disadvantage: without a trigger pattern formation is difficult to induce as response to an upstream event. Another distinctive element of the mechanism is the lack of a characteristic length scale (e.g. as striped Min-patterns in *E. coli*), instead the pattern scales with the size of the cell. Depending on the functional role this might be desired or disadvantageous.

The reaction module gives a possible explanation for the bipolar patterns of AtMinD observed in mutant *E. coli* cells [18]. Several experimental tests could be performed to validate the proposed reaction module: One route would be to study spherical *E. coli* cells. For this geometry, we predict that the polarization of AtMinD should vanish, since the membrane curvature is uniform. This, however, would also be the case if the kinetics of AtMinD binding is directly dependent on membrane curvature, as in the case of DivIVa [7, 9]. To rule out this scenario an in-vitro experiment could be conducted, as described in Fig.3. In-vitro experiments might also serve as a proof of concept for the use of the suggested reaction module in nano-scale self-organization. By enzymatically regulating the kinetic rates of the process one could induce protein patterns on a membrane which then serve as templates for the localization of nano-scale structures, e.g. similar to the formation of actin cables close to Cdc42 protein caps in yeast. Localization could either be self-organized or target specific curvatures or be externally controlled by volume exclusion in the cytosolic space. If, in addition, such nano-structures exert forces on the membrane this self-organization principle could be used to regulate the shape of membranes.

Thus the proposed minimal module might serve as a core network for the design of other geometry sensing protein networks.
On a more speculative note, geometry sensing protein networks like the one discussed here would enable a cell to gradually optimize its biological function, since the underlying mechanism does not involve a bifurcation threshold. For example, one could envision a biochemical network containing a protein which is able to trigger hydrolysis-driven detachment. Such a catalytic process could act selectively on the P_{NTP} or the P_{NDP} species. This would create an imbalance between the effective membrane affinities of P_{NTP} and P_{NDP}, and thus regulate polarity. Moreover, the copy number of such a catalyst would become an evolutionary tunable modulator of the effective imbalance. MinE in E. Coli which stimulates the hydrolysis of membrane bound MinD-ATP is a possible instance of such a factor.
Finally, due to its generic nature the proposed mechanism might be involved in many bacterial pattern-forming systems. For instance, the sensitivity to cytosolic reaction volume provides a way to sense large cytosolic structures. This could, for instance, be part of the mechanism that guides PomZ to mid-cell in *M. xanthus* [29]. One could also imagine direct feedback mechanisms between force-exerting proteins that regulate cell shape (e.g. FtsZ ring contraction) and proteins that adapt to local cell shape by sensing the local reaction volume, and which guide the downstream accumulation of further force-exerting proteins. In this scenario cell shape could be controlled (even in a self-organized fashion) by balancing these two processes.

MATERIALS

Computational methods and initial conditions

The model is mathematically described as a set of reaction diffusion equations (see SI Appendix). All simulations were performed with finite-element methods on a triangular mesh using Comsol Multiphysics 4.3. As initial condition all proteins where in the NDP state and located in the bulk of the ellipse. In Fig.3, the particles are initially located on the membrane in the NDP state. For Figs.1 and 2 the simulation time was 1000s, and for Fig.3 it was 2000s. A steady state is reached after approximetely 100s.
This research was supported by the German Excellence Initiative via the program 'NanoSystems Initiative Munich', and the Deutsche Forschungsgemeinschaft (DFG) via project B02 within the SFB 1032 "Nanoagents for Spatio-

Temporal Control of Molecular and Cellular Reactions".

FIGURES

Figure 1

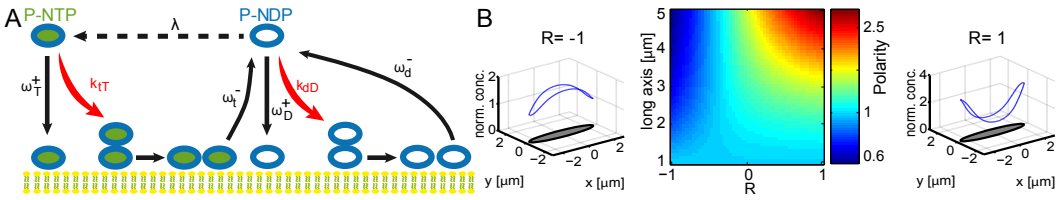

FIG. 1. **Minimal reaction module for geometry-induced cell polarity**.

(A) Illustration of the reaction module: Cytosolic P_{NDP} can exchange its nucleotide, $P_{NDP} \rightarrow P_{NTP}$, with rate λ. P_{NTP} attaches to the membrane with rate ω_T^+ where it recruits further P_{NTP} with rate k_{tT}. At the membrane, hydrolysis triggers detachment with rate ω_t^- such that membrane-bound P_{NTP} is converted to cytosolic P_{NDP}. Cytosolic P_{NDP} attaches to the membrane with rate ω_D^+ where it recruits further P_{NDP} with rate k_{dD} or detaches with rate ω_d^-. **(B)** Membrane-bound proteins accumulate either at mid-cell (left) or form a bipolar pattern with high protein densities at the cell poles (right). The left and right plot show the normalized concentration of the membrane density (blue curve) and the corresponding geometry of the cell (grey ellipse). The membrane density of the protein is divided by its minimum concentration (left: $113\mu m^{-1}$, right: $100\mu m^{-1}$) such that the minimum of the normalized density is 1. The polarity P (color bar in plot is logarithmically spaced) of the pattern strongly depends on cell geometry and preference R for the recruitment of a certain nucleotide state (middle); the length of the short axis is fixed at l=1μm, and we have used k_{dD}+k_{tT}=0.1μm/s. While for large R (preferential recruitment of P_{NDP}) the proteins form a bipolar pattern on the membrane, the membrane-bound proteins accumulate at mid-cell for small R (preferential recruitment of P_{NTP}) If the recruitment processes are balanced (R=0) the pattern is flat and polarity vanishes. The cell geometry determines how pronounced a pattern becomes: The more elongated the ellipse, the more sharply defined the pattern, while it vanishes completely when the ellipse becomes a circle.

Figure 2

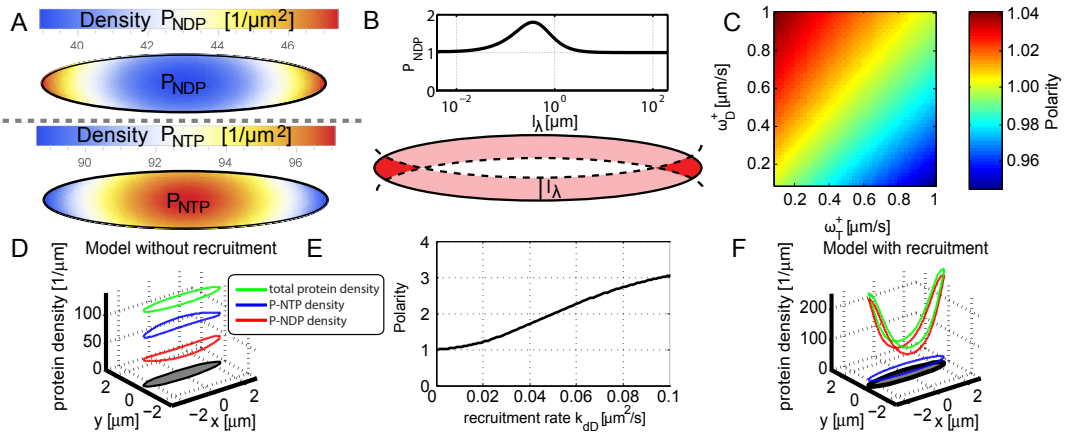

FIG. 2. **Membrane affinity controls, and recruitment amplifies geometry adaption.**

The cells used for the numerical studies have a length of L=5μm and a width of l=1μm. **(A)** Even when recruitment is turned off, $\mathrm{P_{NTP}}$ and $\mathrm{P_{NDP}}$ form inhomogeneous density profiles in the cytosol. $\mathrm{P_{NDP}}$ accumulates close to the poles and is depleted at mid-cell. In contrast, $\mathrm{P_{NTP}}$ exhibits high concentration at mid-cell and a low concentration at the poles. The attachment and detachment rates are set to 1μm/s and 1s^{-1}, respectively, which gives a penetration depth l_λ≈1.6μm. **(B)** Illustration of the source-degradation mechanism for the spatial segregation of cytosolic $\mathrm{P_{NDP}}$ and $\mathrm{P_{NTP}}$. All proteins that detach from the membrane are in an NDP-bound state and can undergo nucleotide exchange, the range of $\mathrm{P_{NDP}}$ in the cytosol is limited to a penetration depth l_λ (dashed lines); here l_λ=0.35μm. At the poles this reaction volumes receives input from opposing faces of the membrane resulting in an accumulation of cytosolic $\mathrm{P_{NDP}}$ (dark red). The magnitude of this accumulation depends on the penetration depth. The polarity P_{NDP}=$u_d^{\text{pole}}/u_d^{\text{mid-cell}}$ of membrane-bound $\mathrm{P_{NDP}}$ plotted as a function of l_λ shows a maximum at l_λ≈0.35μm and vanishes in the limits of large as well as small penetration depths. **(C)** Polarity P of membrane -bound proteins as a function of the attachment rates, ω_D^+ and ω_T^+, with cooperative binding (recruitment) turned off. While for $\omega_D^+ > \omega_T^+$ membrane-bound proteins form a bipolar pattern (P>1), they accumulate at mid-cell (P<1) for ω_D^+<ω_T^+. **(D)** Density profiles of membrane-bound proteins in the limit where the attachment rates of the two species are equal, ω_D^+=ω_T^+ = 1μm/s, and re-

cruitment is switched off. The membrane profile of the total protein density (green) is flat, while membrane-bound P_{NTP} (blue) accumulates at mid-cell and P_{NDP} (red) forms a bipolar pattern. **(E)** Polarity P of the membrane-bound proteins as a function of k_{dD} for $\omega_D^+ = \omega_T^+$. Increasing the recruitment rate restores polarity. **(F)** Density profiles of membrane-bound proteins for $k_{dD} = 0.1 \mu m^2/s$. The density of P_{NDP} (red) as well as the overall protein density (green) exhibit strongly bipolar patterns, which are much more pronounced than the corresponding patterns in the absence of cooperative membrane binding. The density of P_{NTP} (blue) is comparatively flat, and there are much less membrane-bound proteins in this nucleotide state than in the P_{NDP} state. The overall protein pattern is strongly dominated by P_{NDP}.

Figure 3

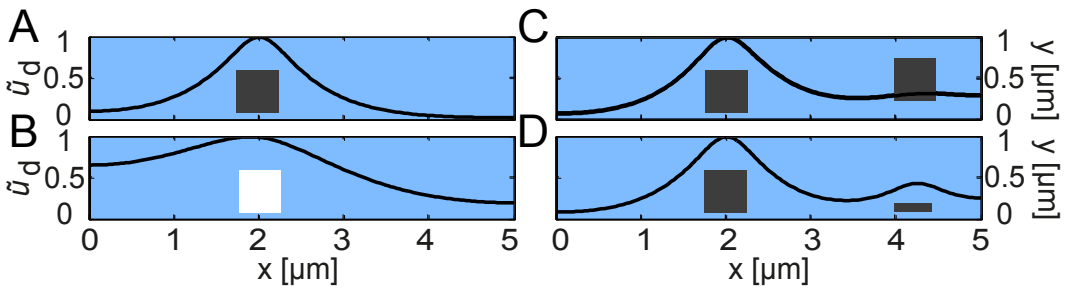

FIG. 3.

Two-dimensional planar geometry with cytosolic volume (blue) above a membrane at y=0. The left, right and top boundaries of the cytosolic regime are reflecting boundaries. Diffusion and nucleotide exchange rates are set to their standard values, the total number of proteins is set to N=50. Black boxes indicate areas which are not accessible to the proteins and thereby generate excluded reaction volumes; the boundaries of the boxes are assumed to be reflecting. Solid curves show the normalized density of $\mathrm{P_{NDP}}$ bound to the membrane: $\tilde{u}_d{=}u_d/u_d^{\max}$. Generally, $\mathrm{P_{NDP}}$ accumulates at membrane regions in the vicinity of the cytosolic areas with excluded reaction volumes with the effect being stronger with larger excluded reaction volumes and closer to the membrane (A,C,D). In (B) the white box indicates that within its volume all proteins are allowed to diffuse but they do not undergo nucleotide exchange. This has a similar but weaker effect to that observed in the other panels: The proteins accumulate at the membrane near the excluded reaction volume. The parameters used in these numerical experiments are summarized in Table I of the SI Appendix.

Figure 4

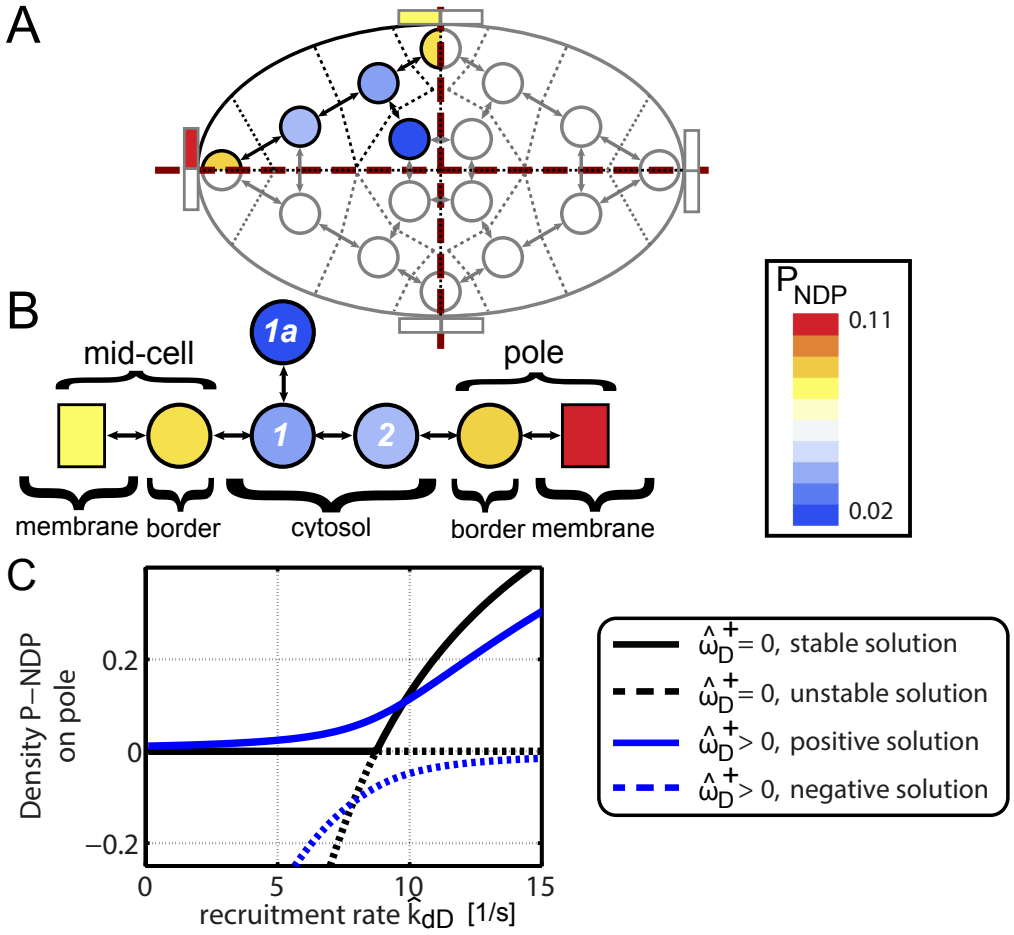

FIG. 4. **Reduced network model and bifurcation analysis.**

(A) The full spatio-temporal dynamics in an ellipse is reduced to the nonlinear dynamics of a *network of coupled nodes*. We take the minimal possible number of nodes reflecting the asymmetry in the ratio of membrane area to bulk volume at the cell poles and mid-cell. Diffusion in the cytosol is modeled as particle exchange processes between the nodes. The network equations are derived from a discrete time jump process. Since the symmetry of the pattern reflects the symmetry of the ellipse there is no flux of particles through either midplanes (red dashed lines). Therefore, the network can be further reduced to a single quadrant (black) with the other quadrants (gray) simply mirroring its behaviour. **(B)** The reduced model comprises two membrane nodes at the pole and at mid-cell, two border nodes connecting membrane and cytosol, as

well as three cytosolic nodes. Node $1a$ captures the increased ratio of membrane area to bulk volume at mid-cell. As illustrated by the colored nodes, this minimal network model polarizes: the density of P_{NDP} at the pole node is higher than on the membrane node. **(C)** Density of P_{NDP} at the pole node as a function of the recruitment rate $\hat{k}_{dD}$. The density is given relative to the total number of particles located at the membrane node of the pole. For vanishing attachment rate of P_{NDP}, $\hat{\omega}_D^+=0$, there is a transcritical bifurcation at a critical rate $\hat{k}_{dD}^*\approx 8.7s^{-1}$ where a polarized state exchanges stability with an unpolarized state (black lines). In contrast, for the generic case of finite membrane attachment, $\hat{\omega}_D^+>0$, there is only one positive fixed point solution which is always stable (blue lines).

[1] Ephrussi A, Johnston DS (2004) Seeing is believing: The bicoid morphogen gradient matures. *Cell* 116(2):143–152.

[2] Wedlich-Soldner R, Altschuler S, Wu L, Li R (2003) Spontaneous cell polarization through actomyosin-based delivery of the Cdc42 GTPase. *Science* 299(5610):1231–5.

[3] Klünder B, Freisinger T, Wedlich-Söldner R, Frey E (2013) GDI-mediated cell polarization in yeast provides precise spatial and temporal control of Cdc42 signaling. *PLoS Comput Biol* 9:e1003396.

[4] Lutkenhaus J (2007) Assembly dynamics of the bacterial MinCDE system and spatial regulation of the Z ring. *Annu Rev Biochem* 76:539–562.

[5] Raskin DM, de Boer PA (1999) Rapid pole-to-pole oscillation of a protein required for directing division to the middle of Escherichia coli. *Proc Natl Acad Sci USA* 96(9):4971–4976.

[6] Hu Z, Gogol EP, Lutkenhaus J (2002) Dynamic assembly of MinD on phospholipid vesicles regulated by ATP and MinE. *Proc Natl Acad Sci USA* 99(10):6761–6766.

[7] Strahl H, Hamoen LW (2012) Finding the corners in a cell. *Curr Opin Microbiol* 15(6):731–736.

[8] Zamparo M, *et al.* (2015) Dynamic membrane patterning, signal localization and polarity in living cells. *Soft Matter* 11:838–849.

[9] Lenarcic R, *et al.* (2009) Localisation of DivIVA by targeting to negatively curved membranes. *EMBO J* 28(15):2272–2282.

[10] Meinhardt, H., de Boer, P.A. (2001) Pattern formation in Escherichia coli: a model for the pole-to-pole oscillations of Min proteins and the localization of the division site. *Proc Natl Acad Sci USA* 98(25): 1420214207.

[11] Howard M, Rutenberg AD, de Vet S (2001) Dynamic compartmentalization of

bacteria: accurate division in E. coli. *Phys Rev Lett* 87(27):278102.

[12] Meacci, G. and Kruse, K. (2005) Min-oscillations in Escherichia coli induced by interactions of membrane-bound proteins. *Phys. Biol.* 2(2): 8997.

[13] Huang KC, Meir Y, Wingreen NS (2003) Dynamic structures in Escherichia coli: spontaneous formation of MinE rings and MinD polar zones. *Proc Natl Acad Sci USA* 100(22):12724–12728.

[14] Varma A, Huang KC, Young KD (2008) The Min system as a general cell geometry detection mechanism: branch lengths in Y-shaped Escherichia coli cells affect Min oscillation patterns and division dynamics. *J Bacteriol* 190(6):2106–2117.

[15] Halatek J, Frey E (2012) Highly canalized MinD transfer and MinE sequestration explain the origin of robust MinCDE-protein dynamics. *Cell Rep* 1(6):741–752.

[16] Fange D, Elf J (2006) Noise-induced Min phenotypes in E. coli. *PLoS Comput Biol* 2(6):e80.

[17] Rangamani P, *et al.* (2013) Decoding information in cell shape. *Cell* 154(6):1356–1369.

[18] Zhang M, Hu Y, Jia J, Gao H, He Y (2009) A plant MinD homologue rescues Escherichia coli HL1 mutant (ΔMinDE) in the absence of MinE. *BMC Microbiol* 9(1):101.

[19] Zhou H, *et al.* (2005) Analysis of MinD mutations reveals residues required for MinE stimulation of the MinD ATPase and residues required for MinC interaction. *J Bacteriol* 187(2):629–638.

[20] Aldridge C, Moeller SG (2005) The plastid division protein AtMinD1 is a Ca^{++}-ATPase stimulated by AtMinE1. *J Biol Chem* 280(36):31673–31678.

[21] Fujiwara MT, *et al.* (2004) Chloroplast division site placement requires dimerization of the ARC11/AtMinD1 protein in Arabidopsis. *J Cell Sci* 117(11):2399–2410.

[22] Meacci G, *et al.* (2006) Mobility of Min-proteins in Escherichia coli measured by fluorescence correlation spectroscopy. *Phys Biol* 3(4):255.

[23] Loose M, Fischer-Friedrich E, Herold C, Kruse K, Schwille P (2011) Min protein patterns emerge from rapid rebinding and membrane interaction of MinE. *Nat Struct Mol Biol* 18(5):577–583.

[24] Shih YL, Fu X, King GF, Le T, Rothfield L (2002) Division site placement in E. coli: mutations that prevent formation of the MinE ring lead to loss of the normal midcell arrest of growth of polar MinD membrane domains. *EMBO J* 21(13):3347–3357.

[25] Loose M, Mitchison TJ (2014) The bacterial cell division proteins FtsA and FtsZ self-organize into dynamic cytoskeletal patterns. *Nat Cell Biol* 16(1):38–46.

[26] Sanamrad, A. et al. (2014) Single-particle tracking reveals that free ribosomal subunits are not excluded from the Escherichia coli nucleoid. *Proc Natl Acad Sci USA* 111(31):11413-11418.

[27] Alonso S, Baer M (2010) Phase separation and bistability in a three-dimensional model for protein domain formation at biomembranes. *Phys Biol* 7(4):046012.

[28] Huang KC, Mukhopadhyay R, Wingreen NS (2006) A curvature-mediated mechanism for localization of lipids to bacterial poles. *PLoS Comput Biol* 2(11):1357–1364.

[29] Treuner-Lange A, Sogaard-Andersen L (2014) Regulation of cell polarity in bacteria. *J Cell Bio* 206(1):7–17.

Geometry induced protein pattern formation

– Supplementary Document –

Dominik Thalmeier,[1,2] Jacob Halatek,[1] and Erwin Frey[1]

[1] *Arnold Sommerfeld Center for Theoretical Physics and Center for NanoScience, Department of Physics, Ludwig-Maximilians-University, Munich, Germany*
[2] *Donders Institute, Department of Biophysics, Radboud University, Nijmegen, Netherlands*

MODEL EQUATIONS

Using orthogonal elliptical coordinates (for mathematical details please refer to the following section), given by the normal μ and tangential ν components at the boundary as in Ref.[1], the reaction module is mathematically described by the following set of reaction-diffusion equations:

$$\partial_t u_T = D_c\,\Delta u_T + \lambda\,u_D\,, \tag{1}$$

$$\partial_t u_D = D_c\,\Delta u_D - \lambda\,u_D\,, \tag{2}$$

$$\partial_t u_t = k_{tT}\,u_t u_T + \left(\omega_T^+\,u_T - \omega_t^-\,u_t\right) + D_m\,\Delta_\nu u_t\,, \tag{3}$$

$$\partial_t u_d = k_{dD}\,u_d u_D + \left(\omega_D^+\,u_D - \omega_d^-\,u_d\right) + D_m\,\Delta_\nu u_d\,. \tag{4}$$

Here u_D and u_T denote for the bulk concentrations of $\mathrm{P_{NDP}}$ and $\mathrm{P_{NTP}}$, respectively, and u_d and u_t the membrane concentrations of $\mathrm{P_{NDP}}$ and $\mathrm{P_{NTP}}$, respectively. The equations account for particle conservation. The exchange of particles between the cytosol and the membrane is determined by a reactive boundary condition [1, 4] stating that the reactions equal the flux onto and off the membrane

$$D_c\,\nabla_\mu u_T = -k_{tT}\,u_t u_T - \omega_T^+\,u_T\,, \tag{5}$$

$$D_c\,\nabla_\mu u_D = -k_{dD}\,u_d u_D - \omega_D^+\,u_D + \omega_d^-\,u_d + \omega_t^-\,u_t\,. \tag{6}$$

For Fig.3 we use orthogonal cartesian coordinates with (μ, ν) replaced by (y, x).

ORTHOGONAL ELLIPTICAL COORDINATES AND DIFFERENTIAL OPERATORS

The model equations of the diffusion-reaction system (Eqs.1-4) with reactive boundary conditions is formulated in elliptical coordinates μ and ν (Fig. S1). In the following we introduce this coordinate system and give the differential operators used in the model equations (see also [1]).
For an ellipse with major semi-axis r_a, minor semi-axis r_b, and linear eccentricity $d{=}\sqrt{r_a^2 - r_b^2}$, we choose orthogonal elliptical coordinates given by

$$x = d\,\cosh\mu\,\cos\nu\,, \tag{7}$$

$$y = d\,\sinh\mu\,\sin\nu\,, \tag{8}$$

with $\mu > 0$ and $0 \leq \nu \leq 2\pi$.
To obtain the differential operators in a curved orthogonal coordinate system one needs the lengths of the basis vectors, h_μ and h_ν, also called scale factors; see e.g. [2]. In elliptical coordinates they are given by

$$h_\mu = h_\nu = d\sqrt{\sinh^2\mu + \sin^2\nu}\,. \tag{9}$$

Then the gradient operator in μ-direction reads

$$\begin{aligned}\nabla_\mu =& \frac{1}{h_\mu}\,\mathbf{e}_\mu\,\partial_\mu \\ =& \frac{1}{d\sqrt{\sinh^2\mu + \sin^2\nu}}\,\mathbf{e}_\mu\,\partial_\mu.\end{aligned} \tag{10}$$

with $\mathbf{e}_\mu$ being the basis vector for the μ direction. The corresponding diffusion operator (see [2] page 137) in the cytosol is given by

$$\begin{aligned}\Delta =& \frac{1}{h_\mu h_\nu}(\partial_\mu^2 + \partial_\nu^2) \\ =& \frac{1}{d^2(\sinh^2\mu + \sin^2\nu)}(\partial_\mu^2 + \partial_\nu^2).\end{aligned} \tag{11}$$

Diffusion on the cell membrane is constrained to a fixed value of μ: μ_0=arctanh(r_b/r_a). We formulate the diffusion operator on the membrane Δ_ν in arclength parametrization $s(\nu)$:

$$s(\nu) = \int_0^\nu d\tilde{\nu}\sqrt{r_b^2 + (r_a^2 - r_b^2)\sin^2\tilde{\nu}}\,. \tag{12}$$

The Laplacian then simply becomes

$$\Delta_\nu = \partial_s^2\,. \tag{13}$$

For Fig.3 in the main text we used cartesian coordinates such that the diffusion operators are given by Δ=∂_x^2+∂_y^2 for the cytosol, and Δ=∂_x^2 for the membrane.

SUPPLEMENTARY DETAILS FOR THE FIGURES

The parameters for Figs.1-3 can be found in Table I.

Fig.	ω_D^+	k_{dD}	k_{tT}	ω_d^-	ω_T^+	ω_t^-	D_c	D_m	λ	ρ
1	1 μm/s	- μm^2/s	-	1 s^{-1}	1 μm/s	1s^{-1}	16 μm^2/s	0.013 μm^2/s	6 s^{-1}	500 μm^{-2}
2A	1 μm/s	0 μm^2/s	0	1 s^{-1}	1 μm/s	1s^{-1}	16 μm^2/s	0.013 μm^2/s	6 s^{-1}	500 μm^{-2}
2B	1 μm/s	0 μm^2/s	0	1 s^{-1}	1 μm/s	1s^{-1}	16 μm^2/s	0.013 μm^2/s	- s^{-1}	500 μm^{-2}
2C	- μm/s	0 μm^2/s	0	1 s^{-1}	- μm/s	1s^{-1}	16 μm^2/s	0.013 μm^2/s	6 s^{-1}	500 μm^{-2}
2D	1 μm/s	0 μm^2/s	0	1 s^{-1}	1 μm/s	1s^{-1}	16 μm^2/s	0.013 μm^2/s	6 s^{-1}	500 μm^{-2}
2E	1 μm/s	- μm^2/s	0	1 s^{-1}	1 μm/s	1s^{-1}	16 μm^2/s	0.013 μm^2/s	6 s^{-1}	500 μm^{-2}
2F	1 μm/s	0.1 μm^2/s	0	1 s^{-1}	1 μm/s	1s^{-1}	16 μm^2/s	0.013 μm^2/s	6 s^{-1}	500 μm^{-2}
3	1 μm/s	0.7 μm^2/s	0	0.65 s^{-1}	2.2 μm/s	3s^{-1}	16 μm^2/s	0.013 μm^2/s	6 s^{-1}	10 μm^{-1}
S4B	1 μm/s	0.5 μm^2/s	0	1 s^{-1}	1 μm/s	1s^{-1}	16 μm^2/s	0.013 μm^2/s	- s^{-1}	see text
S4C	1 μm/s	0.5 μm^2/s	0	1 s^{-1}	1 μm/s	1s^{-1}	16 μm^2/s	0.013 μm^2/s	- s^{-1}	see text
S4D	1 μm/s	0	0.5 μm^2/s	1 s^{-1}	1 μm/s	1s^{-1}	16 μm^2/s	0.013 μm^2/s	- s^{-1}	see text
S4E	1 μm/s	0	0.5 μm^2/s	1 s^{-1}	1 μm/s	1s^{-1}	16 μm^2/s	0.013 μm^2/s	- s^{-1}	see text

TABLE I. Parameters used to create the simulations used in Figs.1-3. Cells marked with a "-" denote that this parameter was varied in the corresponding figure, details are found in the corresponding *Supplementary details* section.

Supplementary details for Figure 1

For Fig.1, the recruitment rate k_{dD} was sampled in the range $0-0.1\mu m^2/s$ with 50 uniformly spaced parameter values. k_{tT} was chosen as k_{tT}=$0.1\mu m^2/s - k_{dD}$ such that $k_{dD} + k_{tT}$=$0.1\mu m^2/s$. The major semi-axis of the ellipse was varied in the range from $0.5\mu m$ to $2.5\mu m$ with 50 equally spaced parameter values. The minor semi-axis was kept constant at $0.5\mu m$.

Supplementary details for Figure 2

For Fig.2 we used an elliptic geometry for the cell with a length of 5μm and a width of 1μm. For Fig.2B, the penetration depth l_λ was varied between 10^{-3} and 10^7; the values are equally spaced on a logarithmic scale. For Fig.2C, the parameters ω_D^+ and ω_T^+ were varied between $0.11/s$ and $11/s$ with 50 uniformly spaced parameter values.

Supplementary details for Figure 3

The quadratic boxes in Fig.3 have side length 0.5μm. In panel A and B, the position of the lower left point of the square is at x=1.75μm and y=0.05μm. In

panel C the position of the left box is also x=1.75μm and y=0.05μm, while the position of the right box is x=4μm and y=0.15μm. In panel D, the position of the left box is also x=1.75μm and y=0.05μm; the right box has side lengths 0.5μm and 0.1μm, its lower left point is at x=4μm and y=0.05μm.

Supplementary details for Figure 4

The parameters for the bifurcation plot Fig.4D can be found in Table .

Figure	N	λ	$\hat{\omega}_D^+$	$\hat{\omega}_d^-$	$\hat{k}_{dD}$	$\hat{\omega}_t^-$	$\hat{\omega}_T^+$	ϵ
4B	1	1 s^{-1}	1 s^{-1}	10 s^{-1}	$100s^{-1}$	$1s^{-1}$	$1s^{-1}$	$1s^{-1}$
4C	1	1 s^{-1}	0 s^{-1} and 0.05 s^{-1}	1 s^{-1}	-	$1s^{-1}$	$1s^{-1}$	$1s^{-1}$

TABLE II. Parameters used in Fig.4. Cells marked with a "-" denote that this parameter was varied in the corresponding figure, details are found in the corresponding *Supplementary details of* section.

EQUATIONS OF THE MINIMAL SYSTEM

To frame the coarse-grained model we use the following nomenclature: The quantities u_A^X denote the number of the proteins in state A, which may be cytosolic $\mathrm{P_{NDP}}$ (A=D), cytosolic $\mathrm{P_{NTP}}$ (A=T), membrane bound $\mathrm{P_{NDP}}$ (A=d) or membrane bound $\mathrm{P_{NTP}}$ (A=t). The superscript X signifies the spatial position in the coarse-grained network. Here, membrane nodes are denoted with m for mid-cell and p for pole, respectively. The neighboring cytosolic nodes of these membrane nodes are also denoted by m and p. The remaining nodes in the bulk of the cytosol are denoted by 1, 1a and 2 (see Fig.4B).
The dynamic processes for the membrane nodes in the coarse-grained model comprise, as in the spatially extended model, attachment and detachment as well as recruitment processes. The ensuing nonlinear equations read

$$\partial_t u_d^m = \hat{k}_{dD} u_d^m u_D^m + \hat{\omega}_D^+ u_D^m - \hat{\omega}_d^- u_d^m \,, \tag{14}$$
$$\partial_t u_d^p = \hat{k}_{dD} u_d^p u_D^p + \hat{\omega}_D^+ u_D^p - \hat{\omega}_d^- u_d^p \,, \tag{15}$$
$$\partial_t u_t^p = -\hat{\omega}_t^- u_t^p + \hat{\omega}_T^+ u_T^p \,, \tag{16}$$
$$\partial_t u_t^m = -\hat{\omega}_t^- u_t^m + \hat{\omega}_T^+ u_T^m \,, \tag{17}$$

where a hat on the rates indicates that the rates are for the discrete model. For the sake of simplicity we omit in the minimal model the cooperative membrane binding of the P_{NTP} species, since this process is not necessary to obtain a bipolar pattern. In section we will perform a continuum limit and show how these rates are related to the corresponding rates of the continuum model. For the bulk cytosolic nodes we have

$$\partial_t u_D^1 = -\epsilon(3u_D^1 - u_D^m - u_D^{1a} - u_D^2) - \lambda u_D^1 \,, \tag{18}$$
$$\partial_t u_T^1 = -\epsilon(3u_T^1 - u_T^m - u_T^{1a} - u_T^2) + \lambda u_D^1 \,, \tag{19}$$
$$\partial_t u_D^{1a} = -\epsilon(u_D^{1a} - u_D^1) - \lambda u_D^{1a} \,, \tag{20}$$
$$\partial_t u_T^{1a} = -\epsilon(u_T^{1a} - u_T^1) + \lambda u_D^{1a} \,, \tag{21}$$
$$\partial_t u_D^2 = -\epsilon(2u_D^2 - u_D^1 - u_D^p) - \lambda u_D^2 \,, \tag{22}$$
$$\partial_t u_T^2 = -\epsilon(2u_T^2 - u_T^1 - u_T^p) + \lambda u_D^2 \,, \tag{23}$$

where ϵ is the hopping rate between nodes, and λ the nucleotide exchange rate in the cytosol. Finally, the dynamics for the cytosolic nodes neighboring the membrane nodes are given by

$$\begin{aligned}\partial_t u_D^p = &-\epsilon(u_D^p - u_D^2) + \hat{\omega}_t^- u_t^p \\ &-(\hat{k}_{dD} u_d^p u_D^p + \hat{\omega}_D^+ u_D^p - \hat{\omega}_d^- u_d^p) \,,\end{aligned} \tag{24}$$
$$\begin{aligned}\partial_t u_D^m = &-\epsilon(u_D^m - u_D^1) + \hat{\omega}_t^- u_t^m \\ &-(\hat{k}_{dD} u_d^m u_D^m + \hat{\omega}_D^+ u_D^m - \hat{\omega}_d^- u_d^m) \,,\end{aligned} \tag{25}$$
$$\partial_t u_T^p = -\epsilon(u_T^p - u_T^2) - \hat{\omega}_T^+ u_T^p \,, \tag{26}$$
$$\partial_t u_T^m = -\epsilon(u_T^m - u_T^1) - \hat{\omega}_T^+ u_T^m \,. \tag{27}$$

In addition, since the total number of particles is conserved, we have the constraint

$$\begin{aligned}N = &\, u_d^m + u_d^p + u_t^p + u_t^m + u_D^1 + u_T^1 + u_D^{1a} + u_T^{1a} \\ &+ u_D^2 + u_T^2 + u_D^p + u_T^p + u_D^m + u_T^m \,.\end{aligned} \tag{28}$$

To analyze the fixed point structure of this minimal system (see Fig.4C) we set all time derivatives in Eqs.(14-27) to zero and solved the corresponding system of equations for the particle occupation numbers u_A^X. To solve the systems of equations we used Mathematica 10.0. Next we performed a linear stability analysis of those fixed points for the two cases $\hat{\omega}_D^+$=0 and $\hat{\omega}_D^+$>0.

In both cases the system has three fixed points. The main observation is that for $\hat{\omega}_D^+$=0 there is a transcritical bifurcation from a homogeneous P_{NDP} distribution on the membrane to a polarized P_{NDP} distribution when varying $\hat{k}_{dD}$; while for $\hat{\omega}_D^+$>0 the stability of the fixed points does not change and the polarized state is always stable (see Fig.4B main text).
Interestingly in the case of $\hat{\omega}_D^+$>0 the polarized state is the only fixed point with only positive particle occupation numbers u_A^X. Thus the other two fixed points cannot be reached when starting with an initial condition with only positive particle occupation numbers u_X^Y which leaves the polarized fixed point as the only physically possible steady state solution of the system.

BALANCE OF MEMBRANE AFFINITIES

In this section we show how equal membrane affinities of the P_{NDP} and P_{NTP} species lead to the reestablishment of a spatially uniform steady state. To this end we consider the dynamics of the linear diffusion-reaction equations where the recruitment rates are set to zero, k_{dD}=k_{tT}=0. We will specify the conditions leading to spatially uniform protein densities in the cytosol and on the membrane.
The diffusion-reaction equations in the cytosol read

$$\partial_t u_T = D_c \, \Delta u_T + \lambda \, u_D \,, \tag{29}$$

$$\partial_t u_D = D_c \, \Delta u_D - \lambda \, u_D \,, \tag{30}$$

Because of the nucleotide exchange term, the density distribution of a protein in a given nucleotide state can not be spatially homogeneous, quite independent from the boundary conditions at the membrane. In contrast, since the equation for the total protein density, u_c=u_T+u_D, reads

$$\partial_t u_c = D_c \, \Delta u_c \,, \tag{31}$$

a spatially uniform density u_c in the cytosol is possible. To see what conditions need to be satisfied for that to be the case, consider the boundary conditions specifying the coupling between the membrane and the cytosol

$$D_c \, \nabla_\mu u_T = -\omega_T^+ \, u_T \tag{32}$$

$$D_c \, \nabla_\mu u_D = -\omega_D^+ \, u_D + \omega_d^- \, u_d + \omega_t^- \, u_t \,. \tag{33}$$

Note that these boundary conditions are constant along the membrane only if the normal derivatives are. In general, this is not the case (We will discuss

the case of broken circular geometry in the next section). However, reactive boundary conditions do admit stationary solutions that are uniform along the membrane if the normal fluxes vanish altogether, i.e. if the cytosolic density in steady state is constant.
Upon adding both boundary conditions (32) and (33) one obtains

$$D_c \nabla_\mu u_c = -\omega_T^+ u_T - \omega_D^+ u_D + \omega_d^- u_d + \omega_t^- u_t \,. \tag{34}$$

Hence, there is a reflective boundary condition, $\nabla_\mu u_c$=0, and thereby a homogeneous cytosolic total protein density u_c, if the following balance equation is satisfied

$$\omega_T^+ u_T + \omega_D^+ u_D = \omega_d^- u_d + \omega_t^- u_t \,. \tag{35}$$

Inversely, this condition is satisfied if the cytosolic total protein u_c density is homogeneous. Hence, the question whether a spatially uniform cytosolic protein density is a steady state of the nonlinear dynamics reduces to the question whether the balance equation, Eq.35, is consistent with the stationary solutions of the diffusion-reaction equations on the membrane:

$$\partial_t u_t = D_m \Delta u_t + \omega_T^+ u_T - \omega_t^- u_t \,, \tag{36}$$

$$\partial_t u_d = D_m \Delta u_d + \omega_D^+ u_D - \omega_d^- u_d \,. \tag{37}$$

First, let us neglect membrane diffusion. If the membrane diffusion constant would be zero, D_m=0, the steady state conditions read

$$0 = \omega_T^+ u_T - \omega_t^- u_t \,, \tag{38}$$

$$0 = \omega_D^+ u_D - \omega_d^- u_d \,, \tag{39}$$

and hence the balance equation is satisfied. This implies that the overall protein density in the cytosol is spatially uniform. However, this does not imply that the membrane density is homogeneous as well. To the contrary, upon inserting u_c=u_D+u_T into Eqs.38 and 39 one obtains

$$u_t = \frac{\omega_T^+}{\omega_t^-} u_T \,, \tag{40}$$

$$u_d = \frac{\omega_D^+}{\omega_d^-} (u_c - u_T) \,. \tag{41}$$

and hence for the overall protein density on the membrane

$$u_m = \frac{\omega_D^+}{\omega_d^-} u_c + \left(\frac{\omega_T^+}{\omega_t^-} - \frac{\omega_D^+}{\omega_d^-} \right) u_T \,. \tag{42}$$

Since u_T is always spatially heterogeneous (for $\lambda \neq 0$ and a non-spherical cell geometry), the protein density on the membrane can become uniform only if the membrane affinities for the two different nucleotide states balance each other[**?**]

$$\frac{\omega_T^+}{\omega_t^-} = \frac{\omega_D^+}{\omega_d^-} \,. \tag{43}$$

If the diffusion constant on the membrane is finite, $D_m{>}0$, spatially uniform membrane densities in the cytosol and on the membrane are possible for the special case where $\omega_T^+{=}\omega_D^+{=}\omega^+$ and $\omega_t^-{=}\omega_d^-{=}\omega^-$. Then one also obtains a diffusion-reaction equations for overall protein density on the membrane

$$\partial_t u_m = D_m \, \Delta u_m + \omega^+ \, u_c - \omega^- \, u_m \,. \tag{44}$$

with the boundary condition for the membrane-cytosol coupling

$$D_c \, \nabla_\mu u_c = \omega^+ \, u_c - \omega^- \, u_m \,, \tag{45}$$

For the steady state, the overall protein density on the membrane as well as in the cytosol become uniform if

$$\omega^+ \, u_c = \omega^- \, u_m \,, \tag{46}$$

i.e. there is detailed balance between the overall membrane and cytosolic protein densities. This corresponds to the situation shown in Fig.2C of the main text, where we observe that $P = 1$ if the attachment rates and detachment rates of the two nucleotide states balance each other precisely ($\omega_T^+{=}\omega_D^+{=}\omega^+$ and $\omega_t^-{=}\omega_d^-{=}\omega^-$).
If however recruitment is switched on one typically does not get a spatially homogeneous solution (see main text Fig.2E for the membrane and Fig. S2 for the cytosol).
Remark: Since the diffusion dynamics on the membrane is in general very slow as compared to attachment and detachment processes, we expect that the diffusion-reaction dynamics on the membrane is dominated by the reaction terms. Therefore, already Eq.43 should be a good criterion for a spatially uniform overall protein density on the membrane.

BREAKING THE HOMOGENOUS STEADY STATE IN THE CIRCULAR LIMIT

In this section we take a closer look at the cytosolic steady state in the circular limit. In coordinate free notation, the stationary cytosolic equations read

$$0 = D_c\,\Delta u_T + \lambda\, u_D\,, \tag{47}$$

$$0 = D_c\,\Delta u_D - \lambda\, u_D\,. \tag{48}$$

As mentioned earlier $u_c{=}u_D{+}u_T$ decouples both equations as the combined species u_c satisfies the Laplace equation

$$0 = D_c\,\Delta u \tag{49}$$

which always admits a constant (i.e. spatially homogenous) solution for no flux boundary conditions irrespective of the specific boundary geometry. Hence, whether the system admits a homogenous solution depends on the stationary diffusion-degradation equation (48) which we will now consider in elliptical coordinates $u_D{=}u_D(\mu,\nu)$ as outlined in section . With an ansatz employing separation of variables $u_D(\mu,\nu){=}R(\mu)\Psi(\nu)$ one obtains the well known Mathieu equations:

$$0 = \Psi'' + (c - 2q\cos 2\nu)\Psi \tag{50}$$

$$0 = R'' - (c - 2q\cosh 2\mu)R, \tag{51}$$

where c is a constant of separation and q a dimensionless parameter given by

$$q = -\lambda\frac{d^2}{4D_c}. \tag{52}$$

Note that q vanishes in the circular limit $d{\to}0$, or if the cytosolic degradation length scale $\sqrt{D_c/\lambda}$ becomes infinite. The solutions of the Mathieu equations are the Mathieu functions which form an orthonormal basis for the diffusion-degradation problem in elliptical geometry, c.f. the supplementary material in Ref.[1] and references therein. Note that only in the limit $q{\to}0$ the angular Mathieu equation (50) admits a constant solution $\Psi_0(\nu){=}\Psi_0{=}$const. For small q, i.e. in the nearly circular case, one can express the Mathieu functions perturbatively in powers of q [1]. For the expansion of the homogenous solution one obtains

$$\Psi_0(\nu) \approx 1 - \frac{q}{2}\cos(2\nu) + \mathcal{O}(q^2), \tag{53}$$

which has the characteristic symmetry of the bipolar patterns we observe. The amplitude of this new base state scales with q in the circular limit. Of course, since the Mathieu functions form an orthonormal basis we can construct a solution that is constant at the boundary. However, one finds that the normal derivative of this solution is not constant in angular direction (see supplementary material of [1] for the detailed derivation) and as such it is incompatible with the boundary conditions (33) that assume spatially uniform densities at the membrane. Hence, a spatially uniform solution at the membrane is lost as steady state as soon as circular geometry is broken.

CONTINUUM LIMIT OF THE BOUNDARY CONDITIONS OF THE MINIMAL SYSTEM

In this section we show how the reactive boundary conditions, as given by Eqs.(1-5) in the main text, can be obtained as a continuum limit from the boundary conditions used in the coarse-grained network model in Eqs.(24-27). For simplicity, we will illustrate the calculation for a one-dimensional model with only one protein species (Fig.S3), and refer the reader for a more elaborate description of the continuum limit to [3]
The proteins are performing a symmetric random walk on this one-dimensional grid with hopping rate ϵ. Hence, the dynamics for the occupation number u_c^x of each node x in the bulk is given by

$$\partial_t u_c^x = \epsilon(u_c^{x+a} + u_c^{x-a} - 2\,u_c^x)\,, \tag{54}$$

where a is the distance between the nodes. Furthermore, we assume that the bulk is reactively coupled (by attachment and detachment processes) with the membrane node via the boundary node at position x=0:

$$\partial_t u_m = \hat{\omega}^+ u_c^0 - \hat{\omega}^- u_m\,, \tag{55}$$

$$\partial_t u_c^0 = \epsilon(u_c^a - u_c^0) - \hat{\omega}^+ u_c^0 + \hat{\omega}^- u_m\,. \tag{56}$$

Here u_m is the occupation number of the membrane node, and $\hat{\omega}^-$ and $\hat{\omega}^+$ signify the detachment and attachment rate, respectively.
In the continuum limit $a\to 0$, the number of grid nodes increases, and concomitantly its occupation number u_c^x decreases such that the particle (line) density $u_c(x){:=}u_c^x/a$ remains finite. Then, the bulk dynamics, Eq.(54), becomes a diffusion equation

$$\partial_t u_c(x) = D_c \partial_x^2\, u_c(x) \tag{57}$$

with the macroscopic diffusion constant D_c and the hopping rate ϵ related by $D_c{=}\epsilon a^2$. Note that in the continuum limit, the occupation number of the membrane node, u_m, remains a zero-dimensional quantity. It constitutes a reservoir of particles. Therefore, in the continuum limit, Eq.(55) simply becomes

$$\partial_t u_m = \omega^+ u_c(0) - \omega^- u_m \,, \tag{58}$$

where we have defined the macroscopic attachment rate as $\omega^+{=}\hat{\omega}^+ a$, and the macroscopic detachment rate as $\omega^-{=}\hat{\omega}^-$. Finally, the equation for the boundary node, Eq.(56), in the continuum limit reduces to

$$-D_c \partial_x u_c(0) = -\omega^+ u_c(0) + \omega^- u_m \,. \tag{59}$$

where we have used that $\lim_{a\to 0} \partial_t u_c(0)\, a{=}0$; since the time scale on the boundary scales with a the node right next to the membrane is in equilibrium with the membrane. The reactive boundary condition, Eq.(59), states that the diffusive flux on and off the membrane $-D_c\partial_x u_c(0)$ is balanced by attachment and detachment processes $-\omega^+ u_c(0){+}\omega^- u_m^0$. Note that in the boundary equations 5 and 6 in the main text the gradient ∇_μ is the normal derivative pointing towards the membrane. Here the corresponding normal derivative is $-\partial_x$, which also point towards the membrane.

Remark: For the elliptic geometry mapping of microscopic to macroscopic rates becomes position dependent since the volumina represented by the different grid nodes are not uniform. The minimal model in Fig. 4 main text is not meant to exactly map back to the elliptic geometry in a continuum limit, rather to illustrate and analyze the effect of an inhomogeneous geometry on the reaction diffusion dynamics in a minimal model.

THE EFFECT OF VOLUME EXCLUSION BY THE NUCLEOID

In this section we analyze the effect of volume exclusion which might potentially be caused by a nucleoid if the DNA material acts as a diffusion barrier. Although it has been reported that the nucleoid does not necessarily influence protein diffusion [5] it might still be possible that the diffusion of AtMinD is effected by interaction with the DNA material. For simplicity and as a reference for later studies, we here assume that the effect of this DNA material can be modeled as an effective excluded volume of different sizes.

We consider an elliptic diffusion barrier with the same proportions as the cell (see Fig. S4 A). This volume resides in the middle of the cell and is modeled as an obstacle with reflecting boundary conditions. We studied the impact of

such an effective excluded volume for two different scenarios: when the P_{NDP} species shows finite recruitment (Fig. S4 B,C) and when the P_{NTP} species shows finite recruitment (Fig. S4 D,E). In both scenarios we changed the size of the elliptic volume as well as the nucleotide exchange rate which defines the typical length-scale of the pattern. We observe that as the excluded volume is increased the necessary minimal diffusion length l_λ to obtain a finite polarity shrinks. The reason becomes evident when we look at the local reaction volume defined by the diffusion length l_λ at mid cell vs. the equivalent reaction volume at the poles: If there is a diffusion barrier at a distance smaller than l_λ away from the membrane at mid-cell, the local reaction volume becomes smaller. If this reaction volume at midcell is smaller then the reaction volume at the poles the P_{NDP} particles start accumulating at mid-cell while the P_{NTP} species avoids mid-cell. However, if we decrease the diffusion length below the distance of the excluded volume from the membrane this reaction volume is not longer influenced by the volume exclusion effect and only dependent on the local curvature of the membrane. Thus, P_{NDP} is avoiding mid-cell while P_{NTP} is accumulating there. Depending on which pattern is amplified by the recruitment rates k_{dD} or k_{tT} the overall pattern resembles the pattern of the P_{NDP} respectively P_{NTP} species.
Taken together, for a small effective excluded volume (a geometry factor smaller than 40%) k_{dD} should be high in order to obtain accumulation of proteins on the poles, while for a large excluded volume (a geometry factor larger than 85%) k_{tT} should be higher. For intermediately sized proteins the diffusion length scale needs to be adapted such that the necessary local reaction volume ratios are obtained. This is possible by an adjustment of the nucleotide exchange rate λ or by changing the diffusion coefficient.
Here we considered the nucleoid as an effective static excluded volume with reflecting boundary conditions in two dimensions. The actual nucleoid is, however, a dynamic density distribution of DNA material in three dimensions [6]. How the diffusion of AtMinD is effected by this is yet unknown to the best of our knowledge. Here we studied the possible case that it is acting as an effective diffusion barrier. However, we want to stress that the size of this diffusion barrier is most likely not the same as the extension of the nucleoid since for low densities of DNA material the interaction might be negligible. It might even very well be that AtMinD is small enough such that its diffusion is not influenced by the nucleoid at all. Hence, it is currently not possible to make quantitative predictions about the effect of the nucleoid on the proposed pattern forming mechanism. Yet we can say that bipolarity can be obtained for a broad spectrum of possibilities.

Once more data about the interaction of the nucleoid with AtMinD becomes available a full study taking into account those parameters can be performed. Then it would be possible to make quantitative predictions about the influence of the nucleoid. In that case one needs to conduct the theoretical analysis in three dimensions since the ratio of membrane area to cytosolic volume changes in the full dimensional case. A nucleoid of the same dimensions as in a two dimensional study would take less volume and thus we would expect that its impact on the final pattern is smaller then in a two dimensional study.
The parameters can be found in table I. The initial conditions where different than in the previous cases: we started with a homogeneous protein density of $500 * 4/10.5\mu\text{m}^{-1}$ on the membrane which is approximately equivalent to a homogeneous protein density of $500\mu\text{m}^{-2}$ in the cytosol in the absence of an excluding volume. The reasoning behind this choice is to keep the amount of particles constant in the cell when its inner volume becomes reduced due to the volume exclusion. The simulation time was set to $150k$s to ensure that it reaches equilibrium.

SUPPLEMENTARY FIGURES

Figure 1

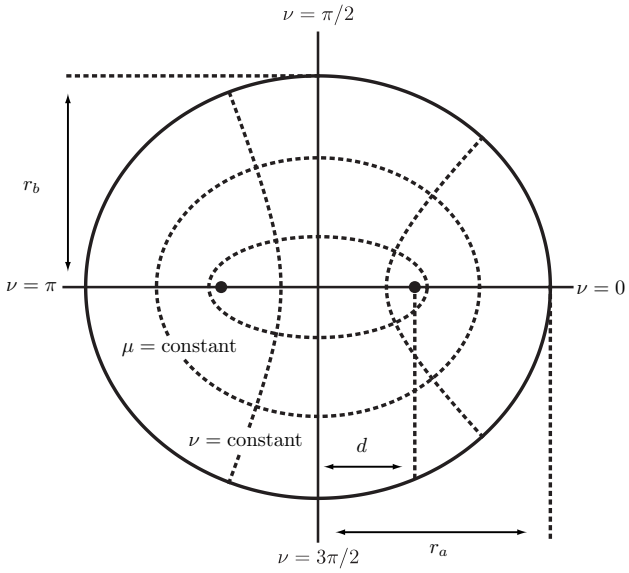

FIG. S1. **Orthogonal elliptical coordinates.**

We use elliptical coordinates given by the normal μ and tangential ν components at the boundary. Ellipses are obtained at constant μ=μ_0.

Figure 2

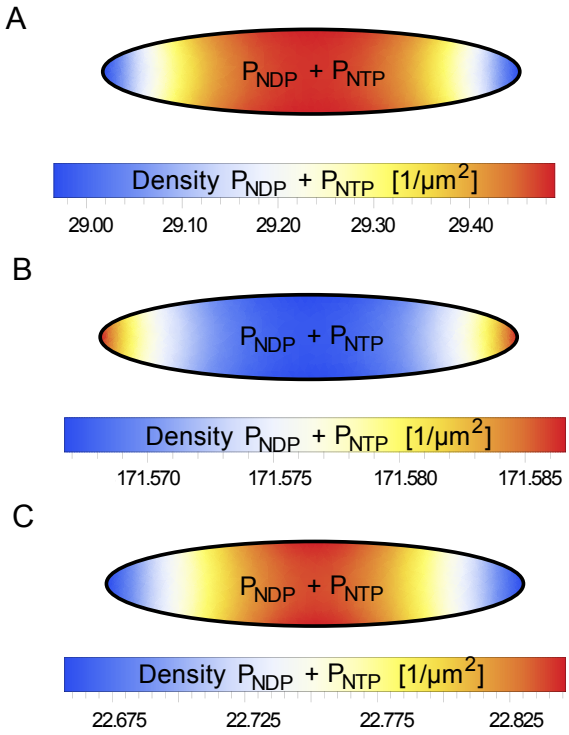

FIG. S2. **Overall protein density in the cytosol.**

(A) Overall cytosolic protein density, u_c=u_D+u_T, for the same parameters as in Fig.2F where recruitment is switched on. The protein density is enhanced at mid-cell and depleted at the poles. **(B)** Overall cytosolic protein density, u_c=u_D+u_T, for the same parameters as in Fig.2C, where recruitment is switched off but the attachment rates are unbalanced with P_{NTP} having the higher membrane affinity: ω_D^+=0.1μm/s and ω_T^+=1μm/s. The protein density exhibits maxima at both cell poles and a minimum at mid-cell. The profile is inhomogeneous but much less pronounced than in panel A. **(C)** Overall cytosolic protein density, u_c=u_D+u_T, for the same parameters as in Fig.2C, where recruitment is switched off but the attachment rates are unbalanced with P_{NDP} having the higher membrane affinity: ω_D^+=1μm/s and ω_T^+=0.1μm/s. The protein density exhibits maxima at mid-cell and minima at both cell-poles. The profile is inhomogeneous but much less pronounced than in panel A.

Figure 3

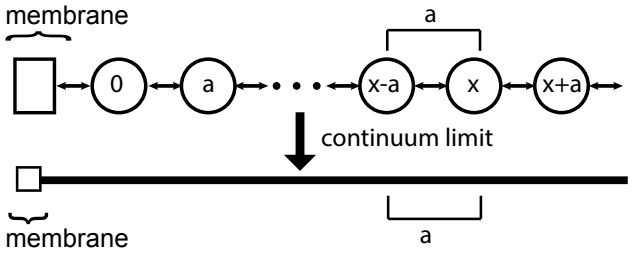

FIG. S3. A hopping process on a one-dimensional grid with bulk nodes x at a distance a (open circles), and with a membrane node on the left (square). In the continuum limit $a \to 0$, one obtains diffusion in the bulk which is coupled to the membrane by a reactive boundary conditions which balances diffusive flux on and off the membrane with the attachment and detachment processes.

Figure 4

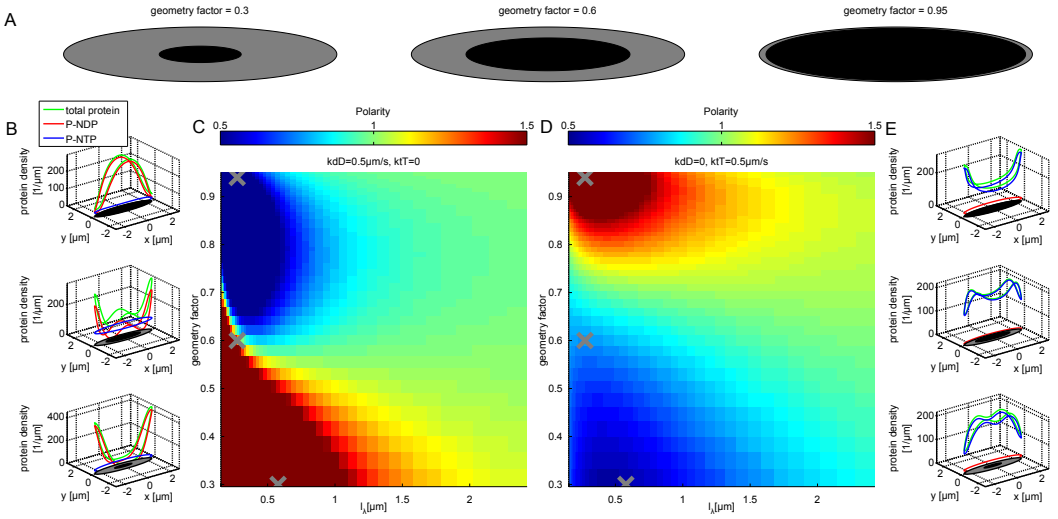

FIG. S4. **Volume exclusion by the nucleoid.**

(A) We model effective volume exclusion by the nucleoid by placing an ellipse with reflecting boundary conditions in the middle of the cell. This inner ellipse has the same proportions as the cell: the axes of the inner axis are obtained by multiplying the axis of the cell by a geometry factor. We show here three examples where this geometry factor is $0.3, 0.6$, and 0.95, respectively. **(B)** Three examples for the pattern of the total protein density (green), the density of $\mathrm{P_{NDP}}$ (red) and of $\mathrm{P_{NTP}}$ (blue) for different sizes of the excluded volume and different values of the diffusion length scale (values marked by grey crosses in C)). The recruitment rate of $\mathrm{P_{NDP}}$ is k_{dD}=$0.5\mu\mathrm{m/s}^2$ while the recruitment of $\mathrm{P_{NTP}}$ is switched off. The polarity here is significantly smaller than one. The upper plot corresponds to a large excluded volume (geometry factor=0.95) and a small diffusion length scale (l_λ=$\sqrt{(16\mu\mathrm{m}^2/\mathrm{s})/213\mathrm{s}^{-1}}$ $\approx$ $0.27\mu\mathrm{m}$)). In this plot the proteins accumulate at mid-cell. The middle plot shows the results for an intermediate excluded volume (geometry factor=0.6) and a small diffusion length scale (l_λ=$\sqrt{(16\mu\mathrm{m}^2/\mathrm{s})/213\mathrm{s}^{-1}}$ $\approx$ $0.27\mu\mathrm{m}$)). In this plot the protein density peaks at the poles as well as at mid-cell. Thus the effective polarity is close to one. The lower plot shows the results for a small excluded volume (geometry factor=0.3) and a larger diffusion length scale (l_λ = $\sqrt{(16\mu\mathrm{m}^2/\mathrm{s})/48\mathrm{s}^{-1}}$$\approx$$0.58\mu\mathrm{m}$)). In this plot the protein density peaks strongly at the cell poles. Thus the polarity is significantly larger than one.

(C) For P_{NDP} being the species with the higher recruitment dominance, small excluded volume leads to the accumulation of the proteins at the poles (polarity larger than 1) while large excluded volume leads to accumulation at mid-cell (polarity smaller than 1). For intermediate excluded volumes both phases are possible depending on the magnitude of the diffusion length l_λ. Small length scales lead to a polarity larger than one while larger length scales lead to a polarity smaller than one. For l_λ large enough, the polarity becomes equal to 1. The recruitment rate of P_{NDP} is k_{dD}=0.5μm/s^2 while the recruitment of P_{NTP} is switched off. For visualization purposes the color bar for the polarity is clipped at a value of 1.5 from above and at a value of 0.5 from below (same holds for D)). The grey crosses show the parameter values for the three examples in B). The sweep was performed for 50 logarithmically spaced values of the geometry factor between 0.2953 and 0.9502, and for 46 logarithmically spaced values of λ between $2.7s^{-1}$ and $671.9s^{-1}$ (same holds for D)). **(D)** If P_{NTP} is the species with the higher recruitment dominance the behavior for different sizes of excluded volume is inverted with respect to (C). Here accumulation at the poles is obtained for large excluded volumes while small excluded volumes lead to accumulation at mid-cell. For intermediate value the polarity is close to one thus neither the poles nor mid-cell is preferred. As for the case with $k_{dD}>0$ large values of l_λ lead to a polarity close to one. The recruitment rate of P_{NTP} is k_{tT}=0.5μm/s^2 while the recruitment of P_{NDP} is switched off. The grey crosses show the parameter values for the three examples in E). **(E)** Similar to B) three examples of the protein pattern are shown but now for k_{dD}=0 and k_{tT}=0.5μm/s^2. The parameter values of λ and the geometry factor correspond to the plots in B): The upper plot shows that the proteins accumulate at the poles for a large excluded volume. The pattern originates from the spatial P_{NTP} distribution, whereas the P_{NDP} species shows no significant pattern. The polarity in this case is larger than one. The center plot shows a depletion of the proteins at mid-cell and the poles for an intermediate excluded volume. The polarity is close to one. The lower plot shows strong depletion of proteins at the poles (but not at mid-cell) and thus a polarity smaller than one.

[1] Halatek J, Frey E (2012) Highly canalized MinD transfer and MinE sequestration explain the origin of robust MinCDE-protein dynamics. *Cell Rep* 1(6):741–752.

[2] Spiegel MR (1959) Schaum's outline of theory and problems of vector analysis and an introduction to tensor analysis .

[3] Erban R, Chapman SJ (2007) Reactive boundary conditions for stochastic simulations of reactiondiffusion processes. *Physical Biology* 4(1):16.

[4] Levine H, Rappel WJ (2005) Membrane-bound Turing patterns. *Phys Rev E* 72(6):061912.

[5] Sanamrad, A. et al. (2014) Single-particle tracking reveals that free ribosomal subunits are not excluded from the Escherichia coli nucleoid. *Proc Natl Acad Sci USA* 111(31):11413-11418.

[6] Fisher, Jay K. et al. (2013) Four-Dimensional Imaging of E. coli Nucleoid Organization and Dynamics in Living Cells. *Cell* 153(4):882-895.

VI Geometry adaption: The mechanism for axis selection

This chapter is based on the following manuscript:

Cell Polarization in Elliptical Geometry: How does *Caenorhabditis Elegans* Determine its First Axis?

by

R. Geßele[1,2], J. Halatek[1], and E. Frey[1]

[1]Department of Physics, Arnold Sommerfeld Center for Theoretical Physics and Center for NanoScience, Ludwig-Maximilians-Universität München, Theresienstraße 37, 80333 München, Germany,

[2]Graduate School of Quantitative Biosciences, Ludwig-Maximilians-Universität München, Feodor-Lynen-Str. 25, 81337 München, Germany

Journal Reference:

in preparation for publication

Supplemental Material reproduced on pages 213 to 224.

Cell Polarization in Elliptical Geometry: How does *Caenorhabditis Elegans* Determine its First Axis?

Raphaela Geßele,[1,2] Jacob Halatek,[1] and Erwin Frey[1]

[1] *Arnold-Sommerfeld-Center for Theoretical Physics and Center for NanoScience, Department of Physics, Ludwig-Maximilians-Universität München, Theresienstraße 37, D-80333 München, Germany*

[2] *Graduate School of Quantitative Biosciences, Ludwig-Maximilians-Universität München, Feodor-Lynen-Str. 25, 81337 München, Germany*

Abstract

In polarized cells, the accumulation of signaling molecules create axes that guide differentiation, division and proliferation. In the single cell state of the *Caenorhabditis Elegans* embryo, cell polarity determines the future front and back of the worm, and the interface between accumulated signaling proteins defines the division line of the first cleavage. Recent models have indicated mutual binding inhibition of *aPARs* and *pPARs* as the key mechanism of polarity maintenance by the *PAR* reaction-diffusion network. Nevertheless, how polarity stabilizes along the long axis of the elliptical embryo remains an open question. In addition to mutual inhibition of *PAR* proteins (the subject of previous models), we examine polarization in elliptical geometry while accounting for cytoplasmic dynamics in a mass-conserving reaction-diffusion model. We find that mutual inhibition of *aPARs* and *pPARs* by phosphorylation with immediate cytoplasmic dephosphorylation favors short axis polarization. This contradicts polarity maintenance along the long axis in the embryo. This discrepency, however, is resolved by a more realistic reactivation cycle - in which dephosphorylation (reactivation for attachment) is delayed in the cytosol, and long-axis polarization is restored. Numerical analysis indicates that a phosphorylated phase and fast diffusion of cytosolic proteins allow for long axis polarization. Furthermore, molecular details in our model (which group species according to their functional role) enable us to investigate how relative densities of proteins with specific functions influence polarization. We show that the relative mutual antagonism, which is determined by antagonistic detachment rates and relative protein densities, determine the robustness of polarity along a specific axis. All together, we find that cell polarity along a specific axis is the result of an interplay of the cell's geometry, a reactivation cycle between membrane and cytosol, and the relative mass of signaling proteins.

INTRODUCTION

Signaling molecules are a crucial determinant of cell development; perhaps most prominently, they detect the shape of cells themselves. Here, the self-organized formation of polarized patterns of protein concentrations can promote the formation of intrinsic axes, and symmetry-breaking. In turn, cell polarization establishes a template for proliferation, migration and further differentiation -for example, the localization of bud sites in yeast, apico-basal asymmetry in mammalian epithelial cells and the first cell division in the Caenorhabditis Elegans (*C. Elegans*) embryo [2, 3].

In the nematode worm *C. Elegans*, the anterior-posterior axis (APA) is determined in the single cell state of the embryo. In this state, the embryo has the approximate shape of a prolate spheroid with long axis $a = 27\mu m$ and short axis $b = 15\mu m$ [4]. Before the first cell division, a polarized distribution of membrane bound signaling proteins establishes and characterizes the future front and back of the worm until the first cleavage. For this reason, the relevant signaling molecules are called *aPARs* to denote anterior *partitioning defective* proteins and *pPARs* for the posterior *partitioning defective* protein group. Before fertilization, the *aPAR* proteins cover the cell cortex while *pPARs* remain evenly distributed in the cytoplasm [5]. Upon fertilization, the cell cortex contracts towards the anterior, and consequently *aPARs* detach from the posterior part of the cortex where *pPARs* start to accumulate (see also Fig. 1**A** top). The two accumulations of *PAR* proteins establish a polarized distribution along the long axis of the ellipsoidal cell. This determines the anterior and posterior parts of the cell which later on divides into two daughter cells of different size. Once the opposing protein clusters are formed (during the 'establishment phase)', they persist for several minutes through the 'maintenance' phase until cell division (see also Fig. 1**A** bottom) [3, 5]. Several independent *in vivo* experiments on *C. Elegans* have demonstrated that maintaining the *PAR* protein polarity is independent from an intact actomyosin network [5–8]. Rather, it appears that the contractions of the cortical actomyosin serve as a temporary trigger for the establishment of the *PAR* protein pattern [4, 9]. This, of course, raises the questions 'how is the pattern robustly formed and how is it maintained on the long term'? Given the evidence that *aPARs* and *pPARs* mutually inhibit each others binding to the membrane by phosphorylation [10, 11], as well as the fact that mutually inhibiting reactions promote distinct cluster formation [12–14], previous studies have outlined the means by which self-organization of *PAR* proteins maintain polarization until cell division [8, 9, 11]. These previous studies established minimal reaction-diffusion

models for the reactions of the *PAR* proteins [4, 8, 15]. These models have shown that polarization is obtained through *PAR* protein complex formation and mutual inhibition of membrane-bound *aPARs* and *pPARs* [4, 8]. However, the cytosolic proteins were assumed to be homogeneously distributed, omitting the influence of cell geometry. Thus, the question remains how the long axis for polarization is maintained by reaction and diffusion of the *PAR* proteins in the single cell state of the *C. Elegans* embryo. Which mechanism stabilizes cell polarity along the long instead of the short axis?

Studies of other protein systems have revealed that even rapid cytosolic diffusion does not enforce homogeneous protein concentrations in the cytosol [16, 17]. For any finite cytosolic diffusion, patterns are sensitive to the geometry of the cell. However, patterns need not align to the long axis of the cell. Recently, it has been shown that patterns can align to the short axis of the cell as well; which pattern arises is determined by the reaction kinetics of the underlying reaction-diffusion system [18]. Furthermore, it has been shown that delayed reattachment to the cell membrane (due to cytosolic nucleotide exchange) is key to geometry sensing [17, 18].

These results strongly suggest that the protein dynamics in the cytoplasm of the *C. Elegans* embryo may also influence sensing long versus short axis for axis alignement during polarity maintenance. Are complex formation and mutual binding inhibition the only *PAR* reactions needed to maintain polarity along the long axis in the *C. Elegans* embryo? In order to investigate axis alignment, we developed a model of the single cell state of the embryo that takes its elliptical (prolate spheroidal) shape into account.

Central to our model is mutual binding inhibition by phosphorylation on the membrane. Mutual inhibition is based on mass-action law kinetics. The requirement for heuristic nonlinearities has been eliminated by taking complex formation and cytosolic dephosphorylation into account. Strikingly, our extended model in elliptical geometry reveals that the cytosolic dephosphorylation is crucial to long-axis polarization. Without it, polarity stabilizes only along the short axis. Furthermore, we identified the roles mutual inhibition and overall protein numbers play for stable long-axis polarization: While the inhibition rates determine how well one axis is selected over the other, relative protein numbers primarily affect the robustness of pattern formation to fluctuations in the length scale of cytosolic dephosphorylation. Most importantly, our analysis indicates that these findings are not system- or model-specific, but rather, are based on the generic dependence of pattern forming processes on the local ratio of cytosolic volume to membrane area. This ratio determines the frequency with which cytosolic proteins reach the membrane, while the

kinetics determine the affect this arrival frequency has on pattern formation.

A model including dephosphorylation in elliptical geometry

The *aPAR* family of proteins can be subdivided into 3 types: *PAR-3, PAR-6* and *PKC-3*. Only complexes containing *PKC-3* (an atypical protein kinase C) can phosphorylate *pPARs*, disabling membrane binding of *pPARs*. How exactly complexes of *PAR-3, PAR-6* and *PKC-3* form is not fully understood, however, there is evidence that *PAR-6* acts as a linker between *PKC-3* and *PAR-3*, the latter of which binds directly to the membrane. Without *PAR-6*, *PKC-3* remains diffuse in the cytosol [8, 19–21]. Hence, in the reaction network our model is based around we simplify the formation of trimeric complexes to a complex formation of two mass-conserved species of *aPARs*: A_1 and A_2. A_1 attaches directly to the membrane, while A_2 can then bind to it, forming the hetero-dimer A_{12}, see *aPARs* in the network in Fig. 1**C** on the left. In our model, only the dimer A_{12} can phosphorylate, i.e. drive *pPARs* off of the membrane, with rate $k_{Pa} \cdot A_{12}$. The choice of hetero-dimerization among A_1 and A_2 captures the separation of labor, among different *aPARs*. A_1 models the binding and linking function of *PAR-3, PAR-6* complexes whereas A_2 phosphorylates *PKC-3* when included in a hetero-dimer on the membrane. Thus, we can investigate the effect of *scaffold* proteins and proteins which inactivate other species.
As with *aPARs*, there are different species of *pPARs*, although less is known about *pPAR* complex formation. While *PAR-2* binds directly to the membrane, and *PAR-1* phosphorylates *PAR-3*, it remains unclear if *PAR-2* also helps maintain anterior-posterior polarity by excluding the *aPAR* complex from the membrane [5, 11, 12, 22]. In light of this uncertainty, we treat the *pPARs* simply as a single species P that antagonizes *aPARs*. The *pPAR* model is illustrated on the right in Fig. 1**C**. Similar to the *aPARs*, P unbinds A_1 and A_{12} with rate $k_{Ap} \cdot P$.
While previous models emphasize the role of mutual inhibition and relied on higher-order nonlinearities to produce polarity, we consider the geometry of the embryo and account for reaction kinetics and diffusion along its membrane, as well as throughout its cytosol. The shape of the real single cell embryo is approximately a prolate spheroid with long axis a; it is along this axis that polarization aligns in the healthy embryo. In order to understand how the long axis is robustly selected we investigate the appearance and direction of cell polarization in *C. Elegans*, assuming two-dimensional elliptical geometry

with long axis a and short axis b. The boundary and interior of the ellipse represent the membrane and cytosolic region respectively. In addition to cytosolic diffusion, our model also introduces a protein dephosphorylation reaction in the cytosol. This creates a cytosolic reactivation cycle, as proteins that were phosphorylated on the membrane are then reactivated for membrane-binding (Fig. 1**B,C**). We introduce the reactivation rate λ for both cytosolic, deactivated *pPARs* (P) and *aPARs* (only A_1). Protein densities also play an important role in mass-conserving reaction-diffusion systems. Thus we also perform simulations to investigate the dependence of axis selection on relative protein densities ρ_{A_1}, ρ_{A_2} and ρ_P.

RESULTS

Cytosolic dephosphorylation is important for axis determination

Given the above assumptions, a number of heuristic arguments can be made for how proteins distribute themselves on the membrane and in the cytosol. In the *PAR* system, cluster formation is driven by mutual antagonism between membrane-bound *aPARs* and *pPARs*. As each *PAR* species dominates the mutual phosphorylation competition in a given region, it evicts the other species from the membrane locally, and an interface arises between clusters of the two species along the membrane.

Clusters -and the interfaces between them- maintain their location and shape through a balance of mutual phosphorylation. This entails detachment from the membrane, spontaneous detachment and attachment of both species between cytosol and membrane. Dynamic equilibrium is eventually established between protein concentrations in the cytosol and on the membrane (Fig. 1**B**), however this does not establish where the interface between *aPAR* and *pPAR* clusters should localize in an elliptical embryo -nor what role the embryo's geometry might play. We argue that the availability of nearby membrane surface plays a major role in determining cluster localization -and, thereby, axis alignment in cell polarization. Due to the curvature of an elliptical cell, the ratio of available surface area to cytosolic volume is highest at the cell poles, and lowest at midcell (Fig. 2**A**). Thus, for finite diffusion and a dephosphorylation that requires time, this geometric constraint can influence the distribution of actively binding proteins. Moreover, the effect of the geometric constraints depends on the dephosphorylation time; a longer reactivation time implies that a protein that detached from the membrane diffuses further away from the

membrane before it can reattach. We refer to this length scale as the *reactivation length* and it is approximately defined by the cytosolic diffusion constant D_{cyt} and the dephosphorylation rate λ:

$$\ell = \sqrt{\frac{D_{cyt}}{\lambda}}.$$

To illustrate the effect of this length scale on protein dynamics, consider a short inactive phase (i.e. $\ell <$ cell size). In this scenario, proteins are able to rebind to the membrane quickly after detachment by phosphorylation and the inactive layer is vanishingly small (Fig. 2**A**). Furthermore the elliptical shape of the embryo affects the likelihood of the proteins to reencounter the membrane nearby immediately following their detachment. Near the cell poles, the large ratio of membrane surface to cytosolic bulk facilitates reencountering here of recently detached proteins, increasing the likelihood of polar reattachment (Fig. 2**A left pole**). Conversely, proteins detached from the membrane at midcell have more cytosol in their vicinity than those detached at the poles and, thus, tend to diffuse longer and further away before encountering are less likely to encounter the the membrane again (Fig. 2**A midcell**). The increased reencountering frequency of proteins detached at the poles (relative to those detached at midcell) translates into high local rebinding rates of actively binding proteins, hence a stronger *caging* effect. For antagonistic protein interactions such as in the PAR system, protein clusters are separated by an interface where the mutual detachment dominates. For an interface (and the clusters it separates) to be maintained, the amount of proteins that detached needs to be resupplied to the interface, otherwise the antagonism would deplete the membrane. Unless there is a large cytosolic reservoir of proteins that can take the place of the detached proteins, the mass-conserving nature of the protein interactions requires that detached proteins quickly rebind. In that case, an interface can be best maintained in a region where rebinding after detachment is most likely. This heuristic picture suggests that cluster interfaces preferentially form at the cell poles, and, that polarity is established along the short axis (Fig. 2**A bottom left**).

Alternatively, if dephosphorylation requires more time, the mean distance a protein diffuses away from the membrane upon reactivation ℓ increases (Fig. 2**B**). Thus, the effect of the geometry (membrane surface to cytosolic volume ratio) becomes weaker, leading to increasing *uncaging* of detaching proteins from their detachment position as the reactivation length approaches the dimension of the cell ($\ell \lesssim$ cell size). Ultimately, if the reactivation length exceeds the dimension of the cell ($\ell \lesssim$ cell size, cf. Fig. 2**C**) the protein becomes com-

pletely delocalized (its position uniformly distributed) throughout the cell due to the diluting effect of cytosolic diffusion. Due to the elliptical geometry, the accumulated density of homogeneously distributed proteins along the long axis reaches its maximum at midcell, see Fig. 2**C** . Thus, a completely delocalized but activated protein will reach the membrane most likely in the midcell area. This translates into most disturbance of antagonistic protein clusters in interfaces at midcell, and eventually leads to long axis polarization.
Altogether, while fast reactivation biases reattachment in favor of the region near the point of detachment, longer delays promote a redistribution throughout the cell before reactivation. Thus, a delay in binding reactivation moves the preferred reattachment position of proteins from the poles to midcell membrane, creating greater instability to cluster growth there, and thus promoting interface formation. Consequently, we expect cell polarization induced by antagonism along the long axis, only if the delay induced by dephosphorylation is long enough.

Numerical analysis

It was discovered by Turing [23] that with different diffusion constants in a reaction-diffusion system, homogeneous protein concentrations can become unstable, leading to spontaneous patterns such as stripes or polarized concentrations. To see this mathematically, firstly spatially-homogeneous steady state solutions of the reaction-diffusion equations are computed. From these homogeneous solutions, one can then linearize the time-dependent reaction-diffusion equations to determine the growth rates σ of a set of eigenfunctions (typically called 'modes') corresponding to different patterns. The mode with the largest positive growth rate from an unstable homogeneous solution describes the pattern that will arise from small perturbations initially. Here we use a recently extended method based on linear stability analysis to bounded geometries ([16, 18]) in order to test for lateral (Turing) instabilities along the long (*even*) and short (*odd*) axis. The first and second mode aligning to each axis are depicted in Fig. 3**A**. The first *even* and first *odd* mode resemble a polarized protein distribution on the membrane along short and long axis respectively. For system with cytosolic reactivation, no perfectly homogeneous steady state exists, (cf. [16–18]). Thus, an approximation of the near homogenous base state was used (see. **SI**), which, for simplicity, is referred to as the 'homogeneous' solution in the following and thus we can compute σ for these modes: if $\Re(\sigma) > 0$ for one or more modes, then the homogeneous solution

is unstable; the pattern corresponding to the mode with largest growth rate will emerge. Otherwise, if the growth rates of all modes are negative, small perturbations of the homogeneous protein distribution will dissipate and the homogeneous solution will remain stable. For the natural cell size and typical cytosolic diffusion constants ($O(1-10)\mu m^2/s$) we observe only negligibly small growth rates for the second or higher modes. In some parameter regimes, however, the growth rates of the first *even* and *odd* modes are positive and similar. To quantify the growth competition among modes, we define the gap term $\Delta := \frac{\sigma_e - \sigma_o}{\sqrt{\sigma_e^2+\sigma_o^2}}$, and probe the dependence of this difference on cytosolic diffusion and dephosphorylation rates, to see how these effect influence polarity-axis selection (for illustration of Δ see Fig. 3**B**). Stability analysis is a good method to detect parameter regimes where patterns form and it predicts which patterns arise firstly from homogeneous starting points. Which pattern eventually forms the steady state cannot securely be predicted. Thus, we also run simulations of the full nonlinear system according to finite-element method (FEM) to test and verify results from stability analysis.

The cytosolic reactivation length selects the polarization axis

We computed Δ as a function of λ and D_{cyt} (see Fig. 3**C**) and found it to be negative for small D_{cyt}/λ (blue in Fig. 3**C**), and positive otherwise (red in Fig. 3**C**). This is consistent with our hypothesis that reactivation must be slow and D_{cyt} fast to obtain polarity along the long axis. Furthermore, we ran FEM sweeps of λ and D_{cyt} and found the boundary dividing steady state long and short axis polarization in the D_{cyt}-λ diagramme. This divison can be expressed as a straight line $\ell^2 = D_{cyt}/\lambda = (11.18\mu m)^2$. Taken together, the results from stability analysis and FEM indicate that diffusion (parameterized by D_{cyt}) and reactivation (λ) in the cytosol have inverse effects on the selection of the axis of polarity; the net effect of these cytosolic processes can be expressed using the reactivation length ℓ.

The relative antagonistic rates facilitate fast establishment of the stFig.able polarity axis

So far, our results have shown that the length scale of cytosolic reactivation determines the axis along which polarity is maintained, as it influences where actively-binding A_1 and P proteins tend to reach the membrane. If ℓ is suf-

ficiently long, active A_1 and P encounter the membrane more often at midcell, leading to greater competition there. An interface separating $aPAR$- and $pPAR$-dominant regions on the membrane - if existent - then stabilizes at midcell. The persistent coexistence of clusters of both protein groups on the membrane rather than uniform domination of one group over the other, depends on the antagonistic rates k_{Ap} and k_{Pa}, as well as the relative numbers of each protein type which are defined by the ratios of ρ_{A_1}, ρ_{A_2} and ρ_P. In the following we refer to such a persistent coexistence as 'balance of mutual antagonism'. To determine the necessary conditions for balanced mutual antagonism we performed a stability analysis, using k_{Ap} and k_{Pa} as control parameters for various reactivation rates λ. For any λ that satisfies $\ell \leq 2a$ (where $2a = 54\mu m$ is the full cell length) we observe polarity only within a fixed range of ratios k_{Pa}/k_{Ap}; outside of this range, no patterns emerge (Fig. 4**A,B** top). For large k_{Pa}/k_{Ap}, λ determines which of the first *even* or *odd* modes dominates pattern formation from a homogeneous base state, and thereby determines the axis of polarization. For low k_{Pa}/k_{Ap}, however, Δ approaches zero, implying no preference between either orientation. FEM simulations, however, show that also for low k_{Pa}/k_{Ap} and $-0.1 < \Delta < 0.1$ one specific polarity axis depending on λ is obtained in steady state. We performed FEM simulations that were initialized with their homogeneous base state and randomly perturbed by $\pm 0.1\%$. Here, $\lambda = 1/s$ and $\lambda = 0.05/s$ leads to polarization along the short and long axes respectively for all ratios k_{Pa}/k_{Ap} that satisfy balance of mutual antagonism. Further simulations show that even if an initial concentration gradient is established perpendicular to the preferred direction, polarity is eventually re-established as described above. Only the time required for polarity to change axes depends on the ratio k_{Pa}/k_{Ap} (see kymographs for each λ in Fig. 4**A,B** on the bottom). However, a slight correlation between the steady state polarity axis and the ratio k_{Pa}/k_{Ap} does exist. FEM simulation sweeps of λ show that the transition from a steady state polarity along long or short axis lies in the range $0.07/s < \lambda < 0.25/s$ depending on k_{Pa}/k_{Ap}. Still, while λ mainly determines the polarization axis in steady state, the ratio k_{Pa}/k_{Ap} sets the timescale with which steady state is reached. More generally, this suggests that cytosolic processes can control axis alignment of patterns while the nonlinear membrane kinetics determines the robustness of a single pattern against others.

Relative protein numbers vary the range of ratios allowing for polarity

Since the balance of mutual antagonism depends not only on the phosphorylation rates but also on the relative global densities of each protein type, we computed Δ as a function of k_{Pa}/k_{Ap} and ℓ for varying average protein densities of each species, ρ_{A_1}, ρ_{A_2}, and ρ_P. Among *aPARs* A_1 represents a *scaffold* protein, while A_2, plays an *antagonistic* role against P. Changing the relative densities of these two protein types, several observations and interpretations can be made. Lowering ρ_{A_2}/ρ_{A_1} by increasing ρ_{A_1}, i.e. relative numbers of *aPARs* versus *pPARs* are increased only by ρ_{A_1}, widens the range of ratios k_{Pa}/k_{Ap} that admit a polarized *aPAR-pPAR* protein distribution on the membrane (note range in Fig. 5**A** versus **B,C,D**). We explain this as follows: With an overabundance of A_1 but not A_2, the maximum number of hetero-dimers is limited by A_2. Since A_2 is responsible for antagonism, P is still able to compete. Thus, high k_{Pa}/k_{Ap} (the phosphorylation rate of P by A_{12} is comparably high) still admit polarity (see Fig. 5**A** with $\rho_{A_1} > \rho_P > \rho_{A_2}$). However, for low k_{Pa}/k_{Ap} A_1 acts as a buffer for re-dimerization. When a hetero-dimer detaches from the membrane in a cell with abundant A_1, another A_1 can quickly catalyze the re-dimerization of A_2 on the membrane. Consequently, even with lower k_{Pa}/k_{Ap}, mutual antagonism can still balance with sufficient A_1.
With increasing ρ_{A_2}/ρ_{A_1} (see Fig. 5**B,C,D**), polarity is observed within a narrower range of k_{Pa}/k_{Ap}. We rationalize this with the argument that there is comparably less active A_1 left in the cytosol, not only because their global relative amounts are shortened but also, more of them are locked in dimers with A_2 on the membrane. When the relative number of *aPAR* proteins is significantly larger than that of *pPAR*, the minimal k_{Pa}/k_{Ap} range approaches unity from above (Fig. 5 **A,D**, $(\rho_{A_1} + \rho_{A_2})/\rho_P > 2$). Thus, overabundance of all *aPARs* compensates for the additional step of dimerization that is necessary for phosphorylation of *pPAR*.
In summary, we conclude that an abundance of the *scaffold* protein (A_1) widens the range of antagonistic rates that allow for polarization, while high numbers of all *aPARs* lowers the minimal range of ratios k_{Pa}/k_{Ap} towards unity.

Relative protein numbers change the sensitivity to ℓ

The results above show that the maintenance of polarity depends on not only the relative global densities of *aPARs* and *pPARs* in the cell, but also the relative densities within each functional group. We now consider the signifi-

cance of relative global densities of proteins with different functions - namely, *scaffolding* and *antagonistic* phosphorylation.
The Δ values obtained for various k_{Pa}/k_{Ap} and ℓ show that increasing the abundance of A_1 desensitizes the dynamics to elongation of ℓ (Fig. 5**A**). For $\rho_{A_1} > \rho_P > \rho_{A_2}$ only short axis polarization is observed for $\ell \leq 2a$. It seems that the transient inactivity of A_1 can be compensated for by simple over-abundance, making cell polarization less sensitive to ℓ. Furthermore, A_2 can immediately re-dimerize with A_1 when reencountering the membrane since the former is not dephosphorylated. As argued in section this leads to stable cluster interfaces at the poles, and thus, short-axis polarity (cf. SI movies of simulations).
For high ρ_{A_2} we find the opposite effect, i.e. short ℓ stabilizes polarity along the long axis (see Fig. 5**C,D** relative global densities of A_2 increase from left to right):
As described above, with sufficient A_2 in the cell, many active A_1 proteins are locked as hetero-dimers on the membrane, leaving fewer active A_1 available in the cytosol. Thus, the inactive A_1 and P comprise a large fraction of cytosolic proteins and many proteins in the cell have an inactive diffusion environment ℓ after their detachment. Therefore, the cell is more sensitive to already small ℓ. For equal amounts of all species ($\rho_{A_1} = \rho_P = \rho_{A_2}$) $\ell \approx 1/6 \cdot (2 \cdot a)$, i.e. an inactive layer of one fifth of the cell length, leads to stable long axis polarization. Conclusively, the relative global densities of each functional protein type (e.g. *scaffold*, *dimerizing* or *inactive*) plays a role in axis selection.

DISCUSSION

Cell polarization has been studied in many organisms. However most models neglect the geometric effects, such that the orientation of polarization cannot be predicted. For models where polarization emerges due to an instability of the uniform state (e.g. Turing instability) in a planar system geometry (e.g. a line) each length scale is associated with the growth rate of the Fourier mode with the corresponding wave length. A major property of Turing instabilities is the notion of a *characteristic length scale* given by the fastest growing Fourier mode. This length scale supposedly dominates any (Turing) pattern. Based on this notion, one may have expected that patterns align with the axis that is closer to the (characteristic) length scale of the fastest growing mode. Strikingly, our results show that this is not the case: An intracellular pattern forming system is not only characterized by the (traditional) wavelength of

the pattern, but also by a preferential axis. The selection of this *characteristic axis* is not related to the *characteristic length scale*, but depends on the effect cytosolic proteins have on the pattern forming process when they encounter the membrane. At the coarsest level, we can distinguish between two types of processes: accumulation and separation of membrane-bound protein clusters. Accumulation is promoted by cooperative attachment, i.e. when the local attachment rate is increased by similar proteins. An example would be Min protein dynamics. In that case clusters stabilize in the regions of highest encounter frequency of cytosolic proteins (which are active for binding). Antagonistic reactions, as displayed, for instance, by PAR proteins, have the opposite effect: In regions where active proteins reach the membrane most frequently antagonistic interactions promote the establishment of an interface that separates cluster.
In any mass-conserving reaction-diffusion system dynamics comprise an ongoing cycling between membrane-bound and cytosolic states. Therefore, axis selection mainly depends on the position where cytosolic proteins re-encounter the membrane most often after detachment once they have been reactive for binding. As we have shown, this position is regulated by the local ratio of membrane surface to cytosolic volume and the length scale ℓ of cytosolic diffusion until reactivation. The only other case is when the cytosol comprises a large reservoir of active proteins. In that case the reactivation length scale ℓ has a negligible effect such that the encounter frequency is determined by the local membrane to cytosol ratio alone.
These findings suggest several experiments to test pattern dependencies on the cytosolic volume to membrane area ratios. An *in vitro* setup could be comprised of a flat membrane, buffer (cytosol) including the *PAR* proteins (*PAR-3, PAR-6, PKC-3* and *PAR-1,2*) and an exclusive volume, such as a stamp. Here, our analysis predicts stable interfaces of *PAR* clusters depending on several experimental parameters:

- the viscosity of the buffer, which determines the speed of cytosolic diffusion
- the cytosolic phosphatase concentration, which determines the rate of dephosphorylation in the cytosol
- and the ratios of *PAR* proteins in the system.

A *minimal in vitro cell* would also offer a suitable, if more elaborate, setup. It would be comprised of an ellipsoidal or rectangular membrane, buffer and the *PAR* proteins. The same parameters as in the flat environment could be

varied. An artificial slowing of cytosolic diffusion (obtained by increasing the buffer viscosity) should lead to a switch of the polarity axis.
For the *PAR* system, *in vivo* investigations have been established for decades now. Thus, we suggest the following experiments in a living one-cell state of the *C. Elegans* embryo: Our model predicts that an increased number of *PAR-3* and *PAR-6* (such as A_1 in the model) destabilize long axis polarization in favor of short axis polarization. However, in order to only investigate the ability of the *PAR* system to maintain polarity, a deactivation of the actomyosin network might be necessary.

ACKNOWLEDGMENTS

We thank Brendan Ozberg for the great help to formulate the article. We also thank Tim Meinhardt and Thomas Fehm for their preliminary work, and Laeschkir Hassan for discussions. R.G., J.H. and E.F. are supported by the German Excellence Initiative via the NanoSystems Initiative Munich, and by the Deutsche Forschungsgemeinschaft (DFG) via Project B02 within SFB 1032 (Nanoagents for Spatio?Temporal Control of Molecular and Cellular Reactions). Furthermore R.G. is supported by a DFG fellowship through QBM.

FIGURES

Figure 1

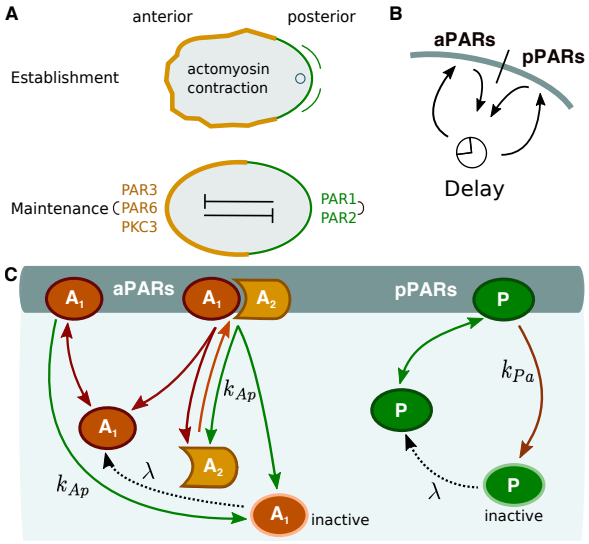

FIG. 1.

(A) Cell polarization in the C. Elegans embryo during establishment phase (top) and maintenance phase (bottom). Sketch adopted from [3]. **(B)** Sketch of the flux between cytosol and membrane: As proteins detach from the membrane they are phosphorylated and can therefore not immediately rebind to the membrane. There is an intrinsic time delay before rebinding due to a phosphorylated phase. **(C)** The reaction model: *aPARs* are treated as two species, A_1 and A_2 (red oval and orange sharp cut cylindrical shape), *pPARs* with one species P (green oval). A_1 and P can attach to and detach from the membrane with constant on and off rates. Complex formation of *aPARs* is accounted for by introducing hetero-dimerization of A_1 and A_2 with rate k_d: A_1 can directly attach to the membrane whereas A_2 can only attach to the membrane indirectly when recruited from A_1 building the hetero-dimer A_{12}. The model further includes mutual phosphorylation as detaching and inactivating process of A_{12} hetero-dimers and A_1 by P with rate $k_{Ap} \cdot P$ and of P by the hetero-dimer A_{12} with rate $k_{Pa} \cdot A_{12}$. Inactive A_1 and P are signed with a light boundary. Dephosphorylation, i.e. reactivation for binding, is integrated for A_1 and P with rate λ. The corresponding reaction-diffusion equations are provided in the supplement (eq. [1-16]).

Figure 2

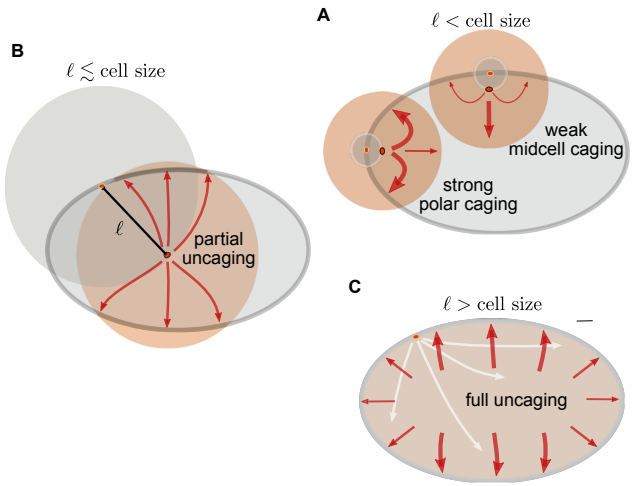

FIG. 2.

(A) If the reactivation length ℓ is small compared to the cell size, the local membrane area to cytosolic volume ratio strongly affects the position where detaching proteins reattach. A protein detaching from a cell pole is more likely to reattach to the cell pole than a protein detaching from midcell is to reattach at midcell. In that case dynamics that are based on membrane-cytosol cycling (such as antagonistic reactions that maintain an interface) are enhanced at the cell poles. **(B)** As the reactivation length ℓ approaches the dimension of the cell size, this geometry effect becomes weaker, and the detaching proteins become increasingly *uncaged* from the position of membrane detachment. **(C)** This geometric effect is completely lost if the reactivation length ℓ exceeds the dimension of the cell size. In that case the position of a detaching protein becomes uniformly distributed throughout the cell before it is reactivated. In that case it will reencounter the membrane most likely near midcell after reactivation, since a delocalized protein (uniformly distributed position) will most likely be found in the midcell area.

Figure 3

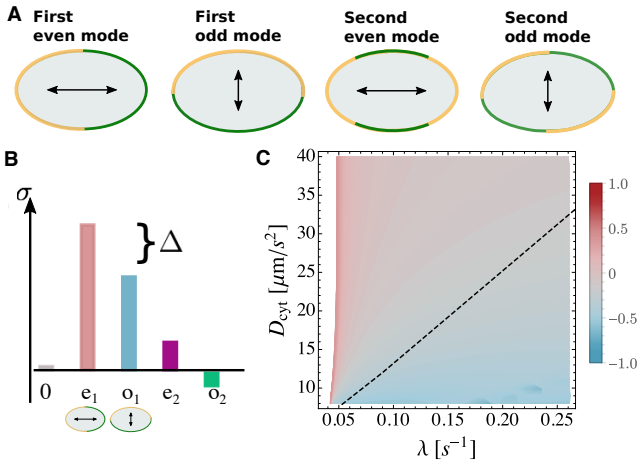

FIG. 3.

Mode selection and the polarity axis. (A) Illustration of the first and second modes (*even* on the left, *odd* on the right). These modes represent solutions to the diffusion equation in elliptical geometry. Homogeneous protein concentrations that solve the steady state equations of the model (cf. SI) are disrupted by these spatial modes. Each mode has a corresponding growth rate $\sigma^{1/2/...}_{even/odd}$ away from (positive) or towards (negative) the steady state solution. The largest positive growth rate corresponds to the pattern which forms out of the homogeneous concentration after perturbation. Here we define the normalized difference between the largest growing even and odd mode as the growth rate gap: Δ. **(B)** Illustration of the gap Δ of the growth rates. **(C)** Δ is shown in red to blue scale for a sweep of D_{cyt} versus λ. For small λ and large D_{cyt} Δ is clearly above zero (red), which predicts long axis polarization, whereas for large λ and small D_{cyt} Δ is clearly below zero (blue). These findings are validated using FEM simulations. Since for parameter sets which lead to Δ close to zero the steady state of the system is unclear, we perform a FEM simulation with an initial concentration gradient along the long axis. In the regime where D_{cyt} and λ define $\ell < 11,2\mu m$ an initial long axis polarization switches to the short axis and the steady state exhibits short axis polarization. Whereas for $\ell > 11,2\,\mu m$ the long axis polarity arising from the initial gradient stabilizes forever. This confirms that the reactivation length $\ell = \sqrt{D_{cyt}/\lambda}$, which is the square root of the slope of a line in this diagram, is a key parameter for axis selection.

Figure 4

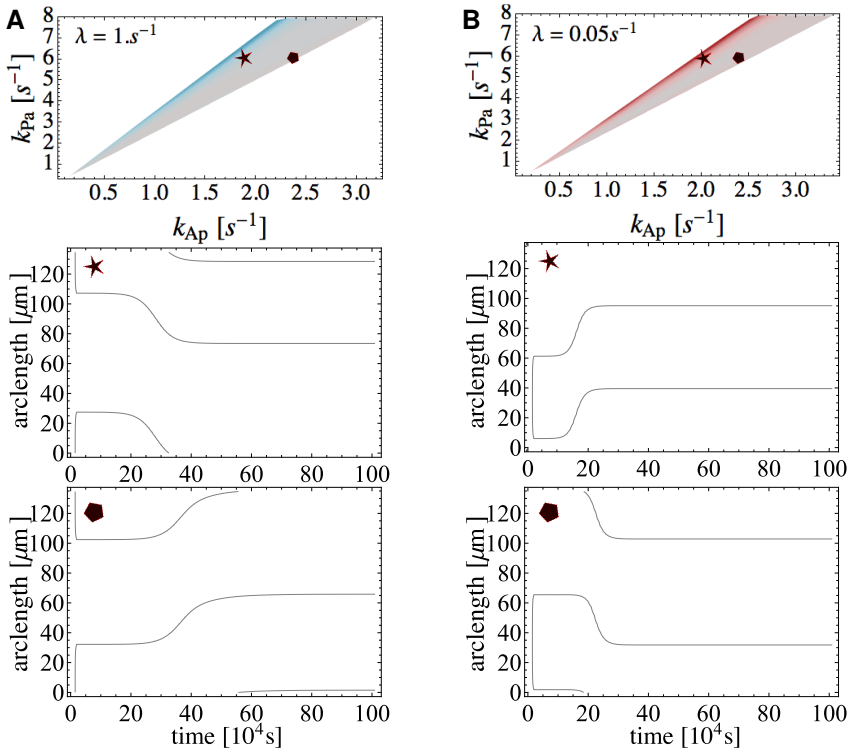

FIG. 4.

λ determines the polarity axis, while the phosphorylation rates facilitate the establishment of the steady state axis polarity. A cone of polarization can be seen in the $k_{Ap} - k_{Pa}$ diagram (left and right top). Each cone was found sweeping k_{Ap} and k_{Pa} for one value of λ using stability analysis. Inside of each cone the $aPAR$-dominant fixed point is unstable against the first even and odd modes. For each λ also sample kymographs from FEM simulations at the upper bound (upper kymos) and lower bound (lower kymos) of the $k_{Ap} - k_{Pa}$ cone are shown. **(A)** For $\lambda = 1/s$, polarization always occurs along the short axis. This is confirmed numerically (FEM) by kymographs of the membrane concentration of P. Here, simulations are initiated with a perpendicular concentration gradient of A_1, A_2 and P along the long axis. In the left kymograph the values $k_{Ap} = 6.$ and $k_{Pa} = 2.4$ are chosen along the region $\Delta \approx 0$ - here, stability analysis indicates no preference with regard to polarization. Although the initial long axis polarization persists for some time, short axis polarization is ultimately established and maintained in

steady state. In the right kymograph $k_{Ap} = 6./s$ and $k_{Pa} = 2./s$ are chosen from the regime where Δ is clearly below zero and thus predicts short axis polarization. The kymograph shows that an initial long axis polarization turns into short axis polarization faster than for $k_{Ap} = 6.$ and $k_{Pa} = 2.4$. **(B)**: k_{Ap} versus k_{Pa} for $\lambda = 0.05/s$. Stability analysis predicts long axis polarization for high k_{Pa}/k_{Ap}. This is also confirmed by FEM simulations in the region of $\Delta \approx 0$ (low k_{Pa}/k_{Ap}). As in to **(A)** kymographs reveal that phosphorylation rates only influence the time taken for polarization to change alignment.

Figure 5

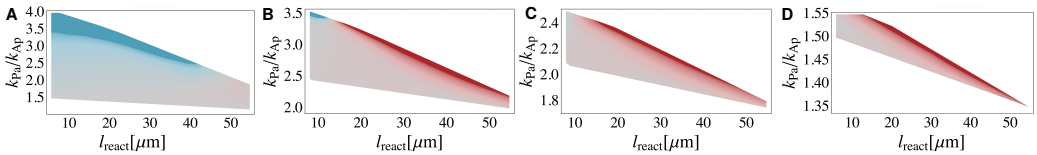

FIG. 5.

Relative protein numbers regulate the robustness of polarity. From left to right the relative densities are varied: **(A)** $\frac{\rho_{A_1}}{\rho_{A_2}} = 6.$, $\frac{\rho_{A_1}+\rho_{A_2}}{\rho_P} = 2.1875$; Long axis polarization vanishes with excess A_1. **(B)** $\frac{\rho_{A_1}}{\rho_{A_2}} = 3.2$, $\frac{\rho_{A_1}+\rho_{A_2}}{\rho_P} = 1.3125$; With increasing ρ_{A_2}, we observe a minimum ℓ to allow polarization along the long axis.**(C)** $\frac{\rho_{A_1}}{\rho_{A_2}} = 2.28571$;$\frac{\rho_{A_1}+\rho_{A_2}}{\rho_P} = 1.4375$; An excess of A_2 allows for even lower ℓ. **(D)** $\frac{\rho_{A_1}}{\rho_{A_2}} = 0.761905$, $\frac{\rho_{A_1}+\rho_{A_2}}{\rho_P} = 2.3125$.

[1] M. Lee and V. Vasioukhin, "Cell polarity and cancer–cell and tissue polarity as a non-canonical tumor suppressor.," *Journal of cell science*, vol. 121, no. Pt 8, pp. 1141–50, 2008.

[2] B. Klünder, T. Freisinger, R. Wedlich-Söldner, and E. Frey, "GDI-Mediated Cell Polarization in Yeast Provides Precise Spatial and Temporal Control of Cdc42 Signaling," *PLoS Computational Biology*, vol. 9, no. 12, 2013.

[3] B. Goldstein and I. G. Macara, "The PAR Proteins: Fundamental Players in Animal Cell Polarization," *Developmental Cell*, vol. 13, no. 5, pp. 609–622, 2007.

[4] N. W. Goehring, P. K. Trong, J. S. Bois, D. Chowdhury, E. M. Nicola, A. A. Hyman, and S. W. Grill, "Polarization of PAR Proteins by Advective Triggering of a Pattern-Forming System," vol. 334, no. November, pp. 1137–1141, 2011.

[5] A. A. Cuenca, A. Schetter, D. Aceto, and K. Kemphues, "Establishment and Maintenance Phases," vol. 130, no. 7, pp. 1255–1265, 2007.

[6] D. P. Hill and S. Strome, "An analysis of the role of microfilaments in the establishment and maintenance of asymmetry in ¡i¿Caenorhabditis elegans¡/i¿ zygotes.," *Developmental biology*, vol. 125, no. 1, pp. 75–84, 1988.

[7] Z. Petrásek, C. Hoege, A. Mashaghi, T. Ohrt, A. a. Hyman, and P. Schwille, "Characterization of protein dynamics in asymmetric cell division by scanning fluorescence correlation spectroscopy.," *Biophysical journal*, vol. 95, no. 11, pp. 5476–5486, 2008.

[8] A. T. Dawes and E. M. Munro, "PAR-3 oligomerization may provide an actin-independent mechanism to maintain distinct par protein domains in the early Caenorhabditis elegans embryo," *Biophysical Journal*, vol. 101, no. 6, pp. 1412–1422, 2011.

[9] N. W. Goehring, C. Hoege, S. W. Grill, and A. a. Hyman, "PAR proteins diffuse freely across the anterior-posterior boundary in polarized C. elegans embryos," *Journal of Cell Biology*, vol. 193, no. 3, pp. 583–594, 2011.

[10] A. Traweger, G. Wiggin, L. Taylor, S. a. Tate, P. Metalnikov, and T. Pawson, "Protein phosphatase 1 regulates the phosphorylation state of the polarity scaffold Par-3.," *Proceedings of the National Academy of Sciences of the United States of America*, vol. 105, no. 30, pp. 10402–10407, 2008.

[11] C. Hoege and A. A. Hyman, "Principles of PAR polarity in Caenorhabditis elegans embryos," *Nature Reviews Molecular Cell Biology*, vol. 14, no. 5, pp. 315–322, 2013.

[12] Y. Hao, L. Boyd, and G. Seydoux, "NIH Public Access," vol. 10, no. 2, pp. 199–208, 2007.

[13] S. Zonies, F. Motegi, Y. Hao, and G. Seydoux, "Symmetry breaking and polarization of the C. elegans zygote by the polarity protein PAR-2.," *Development (Cambridge, England)*, vol. 137, pp. 1669–1677, 2010.

[14] F. Motegi, S. Zonies, Y. Hao, A. A. Cuenca, E. Griffin, and G. Seydoux, "Microtubules induce self-organization of polarized PAR domains in Caenorhabditis elegans zygotes.," *Nature cell biology*, vol. 13, no. 11, pp. 1361–7, 2011.

[15] P. K. Trong, E. M. Nicola, N. W. Goehring, K. V. Kumar, and S. W. Grill, "Parameter-space topology of models for cell polarity," *New Journal of Physics*, vol. 16, no. 6, p. 65009, 2014.

[16] J. Halatek and E. Frey, "Highly Canalized MinD Transfer and MinE Sequestration Explain the Origin of Robust MinCDE-Protein Dynamics," *Cell Reports*, vol. 1, no. 6, pp. 741–752, 2012.

[17] D. Thalmeier, J. Halatek, and E. Frey, "Geometry-induced protein pattern formation.," *Proceedings of the National Academy of Sciences of the United States of America*, vol. 113, no. 3, pp. 548–553, 2016.

[18] F. Wu, J. Halatek, M. Reiter, E. Kingma, and E. Frey, "Multistability and dynamic transitions of intracellular Min protein patterns," pp. 1–18, 2016.

[19] T.-j. Hung and K. J. Kemphues, "PAR-6 is a conserved PDZ domain-containing protein that colocalizes with PAR-3 in Caenorhabditis elegans embryos," vol. 135, pp. 127–135, 1999.

[20] P. Z. Gatzeva-topalova, L. R. Warner, A. Pardi, and M. Carlos, "NIH Public Access," vol. 18, no. 11, pp. 1492–1501, 2011.

[21] D. D. Of, a. T. Different, and T. In, "NIH Public Access," *Development*, vol. 344, no. 2, pp. 745–757, 2011.

[22] L. Boyd, S. Guo, D. Levitan, D. T. Stinchcomb, and K. J. Kemphues, "PAR-2 is asymmetrically distributed and promotes association of P granules and PAR-1 with the cortex in C. elegans embryos.," *Development (Cambridge, England)*, vol. 122, pp. 3075–3084, 1996.

[23] B. Y. a. M. Turing and a. M. Turing, "the Chemical Basis of Mokphogenesis," *Philosophical Transactions of the Royal Society B: Biological Sciences*, vol. 237, no. March, pp. 37–72, 1952.

Cell Polarization in Elliptical Geometry: How does *Caenorhabditis Elegans* Determine its First Axis – Supplementary Document –

Raphaela Geßele,[1,2] Jacob Halatek,[1] and Erwin Frey[1]

[1] *Arnold Sommerfeld Center for Theoretical Physics and Center for NanoScience, Department of Physics, Ludwig-Maximilians-University, Munich, Germany*

[2] *Graduate School of Quantitative Biosciences, Ludwig-Maximilians-Universität München, Feodor-Lynen-Str. 25, 81337 München, Germany*

GEOMETRY

The natural shape of the *C. Elegans* embryo resembles a prolate spheroid with approximate axis lengths a and b. a is the distance from centre to pole along the symmetry axis and thus the major axis, while b is the semi-major axis, which is the equatorial radius of the spheroid. Since we are interested in distinguishing between long and short axis polarization, here the geometry is simplified to a two dimensional ellipse with major axis a and minor axis b. In the following we abbreviate the area of the ellipse with $\Omega := \pi \cdot a \cdot b$ which contains the cytosolic bulk in the model and $\partial\Omega$ for its perimeter, which resembles the membrane.

MODEL EQUATIONS

The model is mathematically described as a set of reaction-diffusion equations for the cytosolic bulk and for the membrane species (see below).

Cytosolic equations

The dynamics of the bulk species according to the model depicted in Fig.1 of the main text is given by the following reaction- diffusion equations restricted to Ω:

$$\partial_t c_{A_1} = \lambda c_{A_1^*} + D_{cyt}\nabla^2 c_{A_1} \tag{1}$$

$$\partial_t c_{A_1^*} = -\lambda c_{A_1^*} + D_{cyt}\nabla^2 c_{A_1^*} \tag{2}$$

$$\partial_t c_{A_2} = D_{cyt}\nabla^2 c_{A_2} \tag{3}$$

$$\partial_t c_P = \lambda c_{P^*} + D_{cyt}\nabla^2 c_P \tag{4}$$

$$\partial_t c_{P^*} = -\lambda c_{P^*} + D_{cyt}\nabla^2 c_{P^*}. \tag{5}$$

Membrane equations

Membrane species react and diffuse on the perimeter $\partial\Omega$. The ensuing set of equations is:

$$\partial_t m_{A_1} = k_{aon} c_{A_1} - k_{aoff} m_{A_1} - k_{Ap} m_P m_{A_1} \tag{6}$$
$$- k_d m_{A_1} c_{A_2} + D_{am} \nabla_T^2 m_{A_1}$$
$$\partial_t m_{A_{12}} = k_d m_{A_1} c_{A_2} - k_{aoff} m_{A_{12}} - k_{Ap} m_P m_{A_1}$$
$$+ D_{am} \nabla_T^2 m_{A_1} \tag{7}$$
$$\partial_t m_P = k_{pon} c_P - k_{poff} m_P - k_{Pa} m_{A_{12}} m_P + D_{pm} \nabla_T^2 m_P \tag{8}$$

Reactive boundary conditions

$\partial\Omega$ is connected to Ω via reactive boundary conditions. These describe the particle flux between membrane and cytosolic bulk. The boundary equations are:

$$D_{cyt} \nabla_N c_{A_1} = -k_{aon} c_{A_1} + k_{aoff} m_{A_1} \tag{9}$$
$$D_{cyt} \nabla_N c_{A_2} = k_{Ap} m_P m_{A_{12}} - k_d c_{A_2} m_{A_1} \tag{10}$$
$$D_{cyt} \nabla_N c_P = -k_{pon} c_P + k_{poff} m_P \tag{11}$$
$$D_{cyt} \nabla_N c_{A_1^*} = k_{Ap} m_P \left(m_{A_1} + m_{A_{12}} \right) \tag{12}$$
$$D_{cyt} \nabla_N c_{P^*} = k_{Pa} m_P m_{A_{12}} \tag{13}$$

Mass conservation

On the time scales of polarization establishment and maintenance in *C. Elegans PAR* protein production and degradation is negligible. Therefore, mass conservation can be assumed. In the model the species are conserved in the

finite space Ω for the bulk and the boundary region $\partial\Omega$ according to:

$$\begin{aligned} N_{A_1} &= \int_\Omega \rho_{A_1}\Omega \\ &= \int_\Omega \left(c_{A_1} + c_{A_1^*}\right) d\Omega + \int_{\partial\Omega} \left(m_{A_1} + m_{A_{12}}\right) d\partial\Omega \qquad (14) \\ N_{A_2} &= \int_\Omega \rho_{A_2} d\Omega \\ &= \int_\Omega c_{A_2} d\Omega + \int_{\partial\Omega} m_{A_{12}} d\partial\Omega\partial \qquad (15) \\ N_P &= \int_\Omega \rho_P d\Omega \\ &= \int_\Omega \left(c_P + c_{P^*}\right) d\Omega + \int_{\partial\Omega} m_P d\partial\Omega \qquad (16) \end{aligned}$$

COMPUTATIONAL METHODS

In this model many parameters are unknown. In order to perform the analysis efficiently, but also investigate the full protein dynamics in polarizing parameter regimes accurately, we perform two different computational methods: 1. Linear stability analysis to identify computationally efficiently in which parameter regimes polarization can arise out of homogeneous starting conditions. 2. FEM simulations on a triangular mesh using Comsol Multiphysics 5.1. to understand the full protein dynamics and to find out for which parameter sets a polarized protein distribution along the long axis forms a steady state.

Linear stability analysis in elliptical coordinates

The model equations of the reaction-diffusion system (Eqs.1-4) with reactive boundary conditions are formulated in elliptical coordinates similar to the formulation of reaction-diffusion systems in elliptical geometry describing the *Min* protein dynamics introduced in [1]). Here we shortly recall how to obtain a set of orthogonal eigenfunctions solving the bulk equations. The equations are rewritten in elliptical coordinates. The transformation from Cartesian (x, y) to elliptical coordinates (μ, ν) reads:

$$x = d\,\cosh\mu\,\cos\nu\,, \qquad (17)$$

$$y = d\,\sinh\mu\,\sin\nu\,, \qquad (18)$$

with $d = \sqrt{a^2 - b^2}$ and variables $\mu > 0$ and $0 \leq \nu \leq 2\pi$ An equation for an inactive cytosolic species reads

$$\partial_t c^* = -\lambda c^* + D_{cyt} \nabla^2 c^* \,, \tag{19}$$

where $\lambda \to 0$ for a species without an inactive phase. Also for the total concentrations of active and inactive species of the same kind, $C := c^* + c$, one obtains the describing equation by setting $\lambda = 0$. The solutions for the active species alone can then be calculated by exploiting $c = C - c^*$. To solve equation (19) in bounded elliptical geometry the Laplace operator is transformed to elliptical coordinates:

$$\nabla^2 = \frac{1}{d^2(\sinh^2 \mu + \sin^2 \nu)} (\partial_\mu^2 + \partial_\nu^2). \tag{20}$$

Using this the transformed equation (19) becomes:

$$\partial_t c = \lambda c^* + D_{cyt} \frac{1}{d^2(\sinh^2 \mu + \sin^2 \nu)} (\partial_\mu^2 + \partial_\nu^2) c \,. \tag{21}$$

Exploiting an ansatz of separation for time and space variables $c(t, \mu, \nu) = e^{\sigma t} R(\mu) \Psi(\nu)$ one obtains separate equations for all variables:

$$\begin{aligned} \partial_t c(t, \mu, \nu) &= \sigma \cdot c(t, \mu, \nu) \\ \Rightarrow 0 &= \partial_\mu^2 R(\mu) - (\alpha - 2q cosh(2\mu)) R(\mu) && (22) \\ 0 &= \partial_\nu^2 \Psi(\nu) + (\alpha - 2q cos(2\nu)) \Psi(\nu) && (23) \end{aligned}$$

where α is the constant of separation and $q = -(\sigma + \lambda) \frac{d^2}{4 D_{cyt}}$. An orthogonal set of eigenfunctions solves these so called Mathieu equations. We used this set of functions, the Mathieu functions, to construct a set of eigenfunctions for the diffusion equations on the membrane, here the circumference of an ellipse. This approach is based on previous work by Halatek and Frey [1], where a detailed description of this construction can be found.
The membrane equations describing diffusion and reaction of a general species m have the form:

$$\partial_t m = D_{mem} \nabla^2 m + g(c, m) \,. \tag{24}$$

The boundary condition is further described by

$$D_{cyt} \nabla c = f(c, m), \tag{25}$$

where the flux and diffusion operators are constrained to the membrane or mathematically to a constant $\mu = \mu_0$ giving the perimeter $\partial\Omega$. By parameterizing $\partial\Omega$ one finds the Laplace operator constrained to the membrane:

$$s(\nu) = \int_0^\nu d\tilde{\nu}\sqrt{b^2 + (a^2 - b^2)\sin^2\tilde{\nu}}\,. \tag{26}$$

The Laplace operator then reads

$$\Delta_\nu = \partial_s^2\,. \tag{27}$$

In previous work [1] we constructed a set of orthogonal eigenfunctions as functions of q as linear combination of the Mathieu functions. This set of eigenfunctions, which we will now call membrane-bulk modes, solves the cytosolic bulk and membrane diffusion simultaneously. With it we could further approximate the flux operator acting on the membrane-bulk modes. In the following we use the same notation for the membrane-bulk modes

$$\Psi_n e_n^{mem}(\mu, \nu, q_n^e)\,, \Psi_n o_n^{mem}(\mu, \nu, q_n^o)\,, \tag{28}$$

where e/o denotes even and odd modes. Furthermore the approximated flux operator is abbreviated

$$\partial_\mu \Psi e/o_n^{mem}|_{\mu=\mu_0} = \Gamma e/o_n \Psi e/o_n^{mem}|_{\mu=\mu_0}\,. \tag{29}$$

Thus, all ingredients to perform a linear stability analysis are described mathematically.

Near homogeneous fixed points

As mentioned in the main text, for a finite λ a perfectly homogeneous base state for which to start the stability analysis does not exist. However, near homogeneous fixed points can be approximated by

$$\bar{c}(\mu) = \bar{c}(\mu_0)\Psi_0 e_n^{mem}(\mu, \nu, q_0^e)\,, \tag{30}$$

where q_0^e depends only on λ ($\sigma = 0$). The near homogeneous cytosol ($\bar{c}(\mu)$) and membrane ($\bar{m}(\mu_0) = const.$) concentrations are then obtained by solving the stationary membrane equation and the approximated boundary conditions:

$$0 = g(\bar{c}, \bar{m})\,, \tag{31}$$

$$0 = f(\bar{c}, \bar{m}) - D_{cyt}\Gamma e/o_n(q_0^e)\,, \tag{32}$$

Linearized system

The linearized system is described by matrix A_n.

$$\begin{pmatrix}
D_1 & \partial_{m_{A_{12}}} g_{A_1} & \partial_{m_P} g_{A_1} & \partial_{c_{A_1}} g_{A_1} & \partial_{c_{A_2}} g_{A_1} & \partial_{c_P} g_{A_1} & \partial_{c_{A_1^*}} g_{A_1} & \partial_{c_{P^*}} g_{A_1} \\
\partial_{m_{A_1}} g_{A_{12}} & D_2 & \partial_{m_P} g_{A_{12}} \partial_{c_{A_1}} g_{A_{12}} & \partial_{c_{A_2}} g_{A_{12}} & \partial_{c_P} g_{A_{12}} & \partial_{c_{A_1^*}} g_{A_{12}} & \partial_{c_{P^*}} g_{A_{12}} & \\
\partial_{m_{A_1}} g_P & \partial_{m_{A_{12}}} g_P & D_3 & \partial_{c_{A_1}} g_P & \partial_{c_{A_2}} g_P & \partial_{c_P} g_P & \partial_{c_{A_1^*}} g_P & \partial_{c_{P^*}} g_P \\
\partial_{m_{A_1}} f_{A_1} & \partial_{m_{A_{12}}} f_{A_1} & \partial_{m_P} f_{A_1} & D_4 & \partial_{c_{A_2}} f_{A_1} & \partial_{c_P} f_{A_1} & \partial_{c_{A_1^*}} f_{A_1} & \partial_{c_{P^*}} f_{A_1} \\
\partial_{m_{A_1}} f_{A_2} & \partial_{m_{A_{12}}} f_{A_2} & \partial_{m_P} f_{A_2} & \partial_{c_{A_1}} f_{A_2} & D_5 & \partial_{c_P} f_{A_2} & \partial_{c_{A_1^*}} f_{A_2} & \partial_{c_{P^*}} f_{A_2} \\
\partial_{m_{A_1}} f_P & \partial_{m_{A_{12}}} f_P & \partial_{m_P} f_P & \partial_{c_{A_1}} f_P & \partial_{c_{A_2}} f_P & D_6 & \partial_{c_{A_1^*}} f_P & \partial_{c_{P^*}} f_P \\
\partial_{m_{A_1}} f_{A_1^*} & \partial_{m_{A_{12}}} f_{A_1^*} & \partial_{m_P} f_{A_1^*} & \partial_{c_{A_1}} f_{A_1^*} & \partial_{c_{A_2}} f_{A_1^*} & \partial_{c_P} f_{A_1^*} & D_7 & \partial_{c_{P^*}} f_{A_1^*} \\
\partial_{m_{A_1}} f_{P*} & \partial_{m_{A_{12}}} f_{P*} & \partial_{m_P} f_{P*} & \partial_{c_{A_1}} f_{P*} & \partial_{c_{A_2}} f_{P*} & \partial_{c_P} f_{P*} & \partial_{c_{A_1^*}} f_{P*} & D_8
\end{pmatrix}$$

with

$$\begin{aligned}
g_{A_1} &= k_{aon} c_{A_1} - k_{aoff} m_{A_1} - k_{Ap} m_P m_{A_1} - k_d m_{A_1} c_{A_2} \\
g_{A_{12}} &= k_d m_{A_1} c_{A_2} - k_{aoff} m_{A_{12}} - k_{Ap} m_P m_{A_1} \\
g_P &= k_{pon} c_P - k_{poff} m_P - k_{Pa} m_{A_{12}} m_P \\
f_{A_1} &= -k_{aon} c_{A_1} + k_{aoff} m_{A_1} \\
f_{A_2} &= k_{Ap} m_P m_{A_{12}} - k_d c_{A_2} m_{A_1} \\
f_P &= -k_{pon} c_P + k_{poff} m_P \\
f_{A_1^*} &= k_{Ap} m_P \left(m_{A_1} + m_{A_{12}} \right) \\
f_{P^*} &= k_{Pa} m_P m_{A_{12}} \,,
\end{aligned}$$

and

$$
\begin{aligned}
D_1 :=& \partial_{m_{A_1}} g_{A_1} - \sigma_n - D_m \frac{2\pi n}{L}^2 \\
D_2 :=& \partial_{m_{A_{12}}} g_{A_{12}} - \sigma_n - D_m \frac{2\pi n}{L}^2 \\
D_3 :=& \partial_{m_P} g_P - \sigma_n - D_m \frac{2\pi n}{L}^2 \\
D_4 :=& \partial_{c_{A_1}} f_{A_1} - D_{cyt} \Gamma_n(q(\sigma_n)) \\
D_5 :=& \partial_{c_{A_2}} f_{A_2} - D_{cyt} \Gamma_n(q(\sigma_n)) \\
D_6 :=& \partial_{c_P} f_P - D_{cyt} \Gamma_n(q(\sigma_n)) \\
D_7 :=& \partial_{c_{A_1^*}} f_{A_1^*} - D_{cyt} \Gamma_n(q(\sigma_n)) \\
D_8 :=& \partial_{c_{P^*}} f_{P*} - D_{cyt} \Gamma_n(q(\sigma_n)) \,.
\end{aligned}
$$

To perform the linear stability analysis the membrane equations and the boundary conditions are linearized around the fixed point $(\bar{c}, \bar{m})$. The stability of the fixed point is tested by adding small perturbations $(\delta m, \delta c)$ which are expressed in terms of the membrane eigenfunctions $\Psi e/o_n^{mem}$ and an exponential function for the time dependency. This way we can also write out the flux operator in a linear fashion. The final minimal version for the membrane equation and boundary condition for $(m, c) = (\bar{m} + \delta m, \bar{c} + \delta c)$ reads:

$$
A_n \begin{pmatrix} \delta m \\ \delta c \end{pmatrix} = 0 \,, \tag{33}
$$

with

$$
A_n = \begin{pmatrix} \partial_m g|_{(\bar{c},\bar{m})} - \sigma_n - D_m \frac{2\pi n}{L}^2 & \partial_c g|_{(\bar{c},\bar{m})} \\ \partial_m f|_{(\bar{c},\bar{m})} & \partial_c f|_{(\bar{c},\bar{m})} - D_{cyt} \Gamma_n(q(\sigma_n)) \end{pmatrix} , \tag{34}
$$

where $L = s(2\pi)$ is the full circumference. All steps above can be performed similarly for equations [1-14]. This results in matrix A_n shown in Fig. .

COMSOL 5.1 simulations

Setup for FEM simulations

The time dependent solver in COMSOL 5.1 was chosen PARDISO with a multithreaded nested dissection. The time stepping was performed with a relative tolerance of 10^{-6} between time steps and solved with a multistep method (BDF). In all simulations we used triangular meshing (COMSOL 5.1 setting "finer") with additional refinement at the boundary, i.e. along the membrane.
For the standard parameter sets given in table [I] we tested the stability of the steady state up to $5 \cdot 10^6 s$. In order spare time and memory other simulation times were limited to $1 \cdot 10^6 s$

Initial conditions

For the density profiles in Fig. 2 and also in the Movie we used homogeneous starting concentrations with $aPAR$ species dominant on the membrane. The initial concentration of each species was found by solving the time and space independent model equations. Also the FEM sweep of λ versus D_{cyt} was initialized with homogeneous starting concentrations with $aPAR$ species dominant on the membrane. We further performed a test simulation of λ versus D_{cyt} which was initialized with gradients to see if the final steady state pattern, i.e. here long or short axis polarization, depends on the initial perturbation. This was not the case. Although the initial concentration gradients lead to a temporary polarization along the same axis as the original gradient, the steady state polarization was the same as with homogeneous starting concentrations. Similar observations were made when varying the initial conditions for the kymographs in Fig. 4.

SUPPLEMENTARY DETAILS FOR THE FIGURES

Supplementary details for Figure 2

The parameters for Fig. 2 can be found in Table I. The homogeneous initial concentrations are in Table II. Each FEM simulation was initially perturbed by multiplying the membrane concentration of A_1 and A_{12} with

$1 + 0.01 \cdot rand(x, y)$, where $rand(x, y)$ is a random number drawn from a normal distribution with zero mean and variance 1.

Fig.	$a[\mu m]$	$b[\mu m]$	$D_{cyt}[\mu m^2/s]$	$k_{a/pon}[\mu m/s]$	$k_{a/poff}[s^{-1}]$	$k_{Ap}[\mu m/s]$	$k_{Pa}[\mu m/s]$
2A left	27	15	30	0.1	0.005	2.	6.
2A right	27	15	30	0.1	0.005	2.	6.

Fig.	k_d	$D_{am}[\mu m^2/s]$	$D_{pm}[\mu m^2/s]$	$\lambda[s^{-1}]$	$\rho_{A_1}[\mu m^{-2}]$	$\rho_{A_2}[\mu m^{-2}]$	$\rho_P[\mu m^{-2}]$
2A left	0.17	0.28	0.15	10	1.6	0.5	1.6
2A right	0.17	0.28	0.15	0.05	1.6	0.5	1.6

TABLE I. Parameters used to obtain the density profiles in Fig. 2. The units are numbers of particles per μm on the membrane and numbers of particles per μm^2 in the cytosol.

Supplementary details for Figure 3

For the sweep using linear stability analysis in Fig. 3 **C** all parameters but λ and D_{cyt} where chosen as in I. λ was varied between $5^{-3}s^{-1}$ and $0.26s^{-1}$; the values are uniformly spaced with distance 5^{-3}. D_{cyt} was varied from 7 to 40 with a uniform spacing of 1.

Supplementary details for Figure 4

For the sweep using linear stability analysis in Fig. 4 **A,B** all parameters but λ and k_{Ap} and k_{Pa} where chosen as in Table I. k_{Ap} was varied between $0.1\mu m/s$ and $4.0\mu m/s$ and k_{Pa} was varied between $0.3\mu m/s$ and $8.0\mu m/s$; for both parameters values are uniformly spaced with distance 0.1. D_{cyt} was varied from $7\mu m^2/s$ to $40\mu m^2/s$ with a uniform spacing of $1\mu m^2/s$.
For each kymograph we ran a COMSOL 5.1 simulation for $1000000s$ initialized with concentration gradients of the membrane species. The gradient was chosen along the long axis for fast λ, i.e. $m_{A_1}(x, y) = m_{A_1}^{fp}(1 + y/b), m_{A_{12}}(x, y) =$

Fig.	initial m_{A_1}	initial $m_{A_{12}}$	initial m_P	initial c_{A_1}	initial c_{A_2}	initial c_P	initial $c_{A_1^*}$	initial c_{P^*}
2A left	1.83055	2.69718	0.00987737	1.12083	0.214555	1.59895	0	0
2A right	1.80934	2.91656	0.00758949	0.953638	0.191338	1.32849	0.146215	0.270707

TABLE II. Initial concentrations used for the density profiles in Fig. 2. The units are numbers of particles per μm on the membrane and numbers of particles per μm^2 in the cytosol.

$m^{fp}_{A_{12}}(1+y/b), m_P(x,y) = m^{fp}_P(1-y/b)$ where fp denotes the fixed point concentration. For the fast $\lambda = 1s^{-1}$ k_{Pa} and k_{Ap} were chosen $(6.0, 2.4)$ and $(6.0, 1.9)$ for lower and upper regions of the polarity cone, respectively. For $\lambda = 0.05s^{-1}$ the gradient was chosen along the short axis, i.e. $m_{A_1}(x,y) = m^{fp}_{A_1}(1+x/a), m_{A_{12}}(x,y) = m^{fp}_{A_{12}}(1+x/a), m_P(x,y) = m^{fp}_P(1-x/a)$. k_{Pa} and k_{Ap} were set $(6.0, 2.4)$ and $(6.0, 2.0)$.

Supplementary details for Figure 5

For the sweeps using linear stability analysis in Fig. 5 **A,B,C,D** all parameters but the densities ρ_{A_1}, ρ_{A_2} and ρ_P, λ and k_{Ap} were set as in Table I.The simultaneous sweep of ℓ and k_{Pa}/k_{Ap} was obtained by varying λ and k_{Ap} for fixed $D_{cyt} = 30\mu m^2/s$ and $k_{Pa} = 6.0\mu m/s$. The values of λ were uniformly spaced with distance $0.01s^{-1}$ from $0.01s^{-1}$ to $1.0s^{-1}$, and k_{Ap} was varied from $0.5\mu m/s$ to $9.0\mu m/s$ with uniform steps of $0.05\mu m/s$.

[1] J. Halatek and E. Frey, "Highly Canalized MinD Transfer and MinE Sequestration Explain the Origin of Robust MinCDE-Protein Dynamics," *Cell Reports*, vol. 1, no. 6, pp. 741–752, 2012.

[2] D. Thalmeier, J. Halatek, and E. Frey, "Geometry-induced protein pattern formation.," *Proc Nat Acad Sci USA*, vol. 113, no. 3, pp. 548–553, 2016.

[3] Spiegel MR (1959) Schaum's outline of theory and problems of vector analysis and an introduction to tensor analysis .

[4] Erban R, Chapman SJ (2007) Reactive boundary conditions for stochastic simulations of reactiondiffusion processes. *Physical Biology* 4(1):16.

VII Protein pattern formation on biological membranes

This chapter is based on the following publication:

Protein pattern formation

by

E. Frey[1], J. Halatek[1], S. Kretschmer[2,3], and P. Schwille[3]

[1]Department of Physics, Arnold Sommerfeld Center for Theoretical Physics and Center for NanoScience, Ludwig-Maximilians-Universität München, Theresienstraße 37, 80333 München, Germany,

[2]Graduate School of Quantitative Biosciences, Ludwig-Maximilians-Universität München, Feodor-Lynen-Str. 25, 81337 München, Germany,

[3]Department of Cellular and Molecular Biophysics, Max-Planck-Institute of Biochemistry, Am Klopferspitz 18, D- 82152 Martinsried, Germany

Book Reference:

***Physics of Biological Membranes*, edited by P. Bassereau and P. C. A. Sens, Springer-Verlag GmbH, Heidelberg, 2017, in print**

Protein Pattern Formation

Erwin Frey,[1] Jacob Halatek,[1] Simon Kretschmer,[2,3] and Petra Schwille[2]

[1]*Arnold-Sommerfeld-Center for Theoretical Physics and Center for NanoScience, Department of Physics, Ludwig-Maximilians-Universität München, Theresienstraße 37, D-80333 München, Germany*

[2]*Department of Cellular and Molecular Biophysics, Max-Planck-Institute of Biochemistry, Am Klopferspitz 18, D- 82152 Martinsried, Germany*

[3]*Graduate School of Quantitative Biosciences, Ludwig-Maximilians-Universität München, Feodor-Lynen-Str. 25, 81337 München, Germany*

CONTENTS

INTRODUCTION

From cellular structures to organisms and populations, biological systems are governed by principles of self-organisation. The intricate cycles of autocatalytic reactions that constitute cell metabolism, the highly orchestrated processes of nucleic acid transcription and translation, the replication and segregation of chromosomes, the cytoskeletal assemblies and rearrangements that mechanically drive important cellular processes like cell division and cell motility, the morphogenesis of complex tissue from a single fertilised egg - all of these processes rely on the generation of structures and gradients based on molecular self-organisation. Frequently, the assembly and maintenance of these structures is accompanied by spatial and temporal protein patterning.

What are the principles underlying self-organising processes that result in protein patterns? Though the term 'self-organisation' is frequently employed, as it is here, in the context of complex systems, it needs to be emphasised that there is no generally accepted theory of self-organisation that explains how internal molecular processes are able to coordinate the interactions between a system's components such that order and structure emerge. The field which has arguably contributed most to a deeper understanding of emergent phenomena is 'nonlinear dynamics', especially with concepts such as 'catastrophes' [1], 'Turing instabilities' [2], and 'nonlinear attractors' [3]. However, although pattern formation and its underlying concepts have found their way into textbooks [4], we are far from answering the above question in a comprehensive and convincing way. This chapter will highlight some of the recent progress in the field, but also address some of the fascinating questions that remain open.

In contrast to the conventional representation of pattern–forming systems in classical texts, our exposition will be closely tied to the analysis of quantitive models for specific biological systems. At first, this might appear to involve a loss of generality. However, as we will see, only by studying the actual physical processes that give rise to what we call self-organisation will we be able to uncover its key features in the first place. These key aspects can then be generalised again by identifying the according processes in other systems. Here, we will mainly, but not exclusively, focus on a model for Min protein dynamics, a system of self-organising proteins that is essential for cell division in the bacterium *Escherichia coli*. The Min system offers an ideal combination of a broad and rich phenomenology with accessibility to theoretical and experimental analyses on a quantitative level. As we will see, a major finding from the study of the Min system is the role of mass-conserved interactions and of system geometry in the understanding of self-organised pattern formation.

INTRACELLULAR PROTEIN PATTERNS

The formation of protein patterns and the localisation of protein clusters is a fundamental prerequisite for many important processes in bacterial cells. Examples include Min oscillations that guide the positioning of the Z-ring to midcell in *Escherichia coli*, the localisation of chemotactic signalling arrays and the positioning of flagella, as well as chromosome and plasmid segregation. In all these examples, experimental evidence supports mechanisms based on reaction-diffusion dynamics. Moreover, the central elements of the biochemical reaction circuits driving these processes are P-loop NTPases. These proteins are able to switch from an NTP-bound 'active' form that preferentially binds to an intracellular interface (membrane or nucleoid) to an inactive, freely diffusing, NDP-bound form in the cytosol.

Interestingly, these types of pattern–forming–mechanisms are not restricted to prokaryotic cells, but are found in eukaryotic cells as well. An important example is cell polarisation, an essential developmental process that defines symmetry axes or selects directions of growth. Signalling molecules accumulate in a restricted region of the inner surface of a cell's plasma membrane where they initiate further downstream processes. For example, in the yeast *Saccharomyces cerevisiae*, cell polarisation determines the position of a new growth or bud site. The central polarity regulator responsible for this process is Cdc42, a small GTPase of the Rho family [5]. Similarly, cell polarity plays an important role in proper stem cell division [6] and in plant growth processes such as pollen tube or root hair development [7, 8]. Another intriguing example of self-organised polarisation occurs in the *Caenorhabditis elegans* zygote through the action of mutually antagonistic, so called partitioning-defective (PAR) proteins [9]. Moreover, the crucial role of protein pattern formation in animal cell cytokinesis is highlighted by cortical waves of Rho activity and F-actin polymerization, recently observed in frog and starfish oocytes and embryos [10].

Yet another system where protein patterns play an important role is the transport of motor proteins along cytoskeletal filaments. We will not elaborate on this system in this review, but would like to note that pattern formation in these systems is based on similar principles as for the other systems. For instance, microtubules are highly dynamic cytoskeletal filaments, which continually assemble and disassemble through the addition and removal of tubulin heterodimers at their ends [11]. It was recently shown that traffic jams of molecular motors on microtubules play a key regulatory mechanism for the length control of microtubules [12, 13].

MinCDE oscillations in *E. coli*

Proteins of the Min system in the rod-shaped bacterium *E. coli* show pole-to-pole oscillations [14–17]. A combination of genetic, biochemical, and cell biological studies has identified the following key features of the underlying interaction network: (1) The ATPase MinD, in its ATP-bound dimeric form, cooperatively binds to the cytoplasmic membrane [18–21], and forms a complex with MinC that inhibits Z-ring formation [22]. (2) MinD then recruits its ATPase Activating Protein (AAP) MinE to the membrane, triggering MinD's ATPase activity and thereby stimulating detachment of MinD from the membrane in its monomeric form [23]. (3) Subsequently, MinD undergoes nucleotide exchange in the cytosol and rebinds to the membrane [24]. (4) Notably, MinE's interaction with MinD converts it from a latent to an active form, by exposing a sequestered MinD–interaction region as well as a cryptic membrane targeting sequence [25, 26].

All of these biochemical features give us highly valuable molecular information, but in themselves they do not suffice to explain the emergent phenomenon of Min oscillations. There are basically two unknowns. First, the detailed dynamic processes underlying, for example, cooperative membrane binding of MinD, as well as the MinE conformational switch are poorly understood on a mechanistic molecular level. At present, one can only speculate on them based on structural data. For example, Hill coefficients have been measured for MinD ATP (~ 2) and ADP (~ 1) [21], indicating that recruitment may be associated with dimerisation. Secondly, and perhaps even more importantly, even if all the details of the molecular processes were known, one would still not know which is responsible to what degree for any specific macroscopic property of the dynamic Min pattern. Furthermore, how these processes are affected by changing protein expression levels and cell geometry is unclear, *a priori*. Both of these obstacles represent major challenges for the field, and can be overcome only by a combined experimental and theoretical approach.

The main biological function of Min oscillations is to regulate formation and positioning of the Z-ring [17], comprised of curved, overlapping FtsZ filaments, which interact with a range of accessory proteins that together make up the cytokinetic machinery [27]. The pole-to-pole oscillations of the MinD-ATP/MinC complex result in a time-averaged density profile of MinC that is highest at the cell poles and lowest at midcell. Since MinC acts as an antagonist of FtsZ assembly, Min oscillations inhibit Z-ring formation at the poles and restrict it to midcell [22]. How self-organisation into the Z-ring occurs remains unknown and is subject to extensive research [28–30].

Cell polarity in yeast

Polarity establishment in budding yeast relies on crosstalk between feedback loops, one based on the actin cytoskeleton, the other on a reaction-diffusion system [5]. Both are regulated by the Rho-type GTPase Cdc42. To fulfil its functions, it must constantly cycle between a GTP-bound (active) and a GDP-bound (inactive) state. In budding yeast, activation of Cdc42 is controlled by a single guanine nucleotide exchange factor (GEF), Cdc24, and the hydrolytic activity of Cdc42 is promoted by several GTPase-activating proteins (GAPs). In addition, Cdc42 is extracted from membranes by a single Rho-guanine nucleotide dissociation inhibitor (GDI), Rdi1 [31]; see Fig. 2 for an illustration of the biochemical network.

Initially two independent feedback loops were identified: one based on the actin cytoskeleton and one based on a reaction-diffusion system that *in vivo* depends on the scaffold protein Bem1 [31]. A combined experimental and theoretical study has shown that a combination of actin- and GDI-dependent recycling of the GTPase Cdc42 is required to achieve rapid, robust and focused polarisation [32]. However, there are still many open issues on the detailed interplay between these two mechanisms.

The GDI-mediated polarisation in itself is reasonably well understood. Theoretical models differ in how they describe the recruitment of the GEF (Cdc24) towards active Cdc42 on the membrane [33, 34]. Experimental data [32] support a reaction network where recruitment of Cdc24 is mediated by Bem1 (Fig. 2): Cytosolic Bem1 is targeted to the membrane by interaction with active Cdc42 or other Cdc42-GTP-bound proteins such as Cla4 and subsequent binding of Bem1 to the membrane [35–37]. Once bound to the membrane it recruits the Cdc24 from the cytosol to the membrane [35, 36]. Membrane-bound Cdc24 then enhances both the attachment and activation of cytosolic Cdc42-GDP to the membrane and the nucleotide-exchange of membrane-bound Cdc42-GDP [32, 34]. A mathematical model [34] based on this reaction scheme accurately predicts phenotypes associated with changes in Cdc42 activity and recycling, and suggests design principles for polarity establishment through coupling of two feedback loops. Recently, there has even been evidence for a third feedback loop [38].

In a recent *in vivo* study the essential component Bem1 was deleted from the reaction-diffusion feedback loop [39]. Interestingly, after the mutant was allowed to evolve for about $1,000$ generations, a line was recovered that had regained the ability to polarise, despite the absence of Bem1. Moreover, the newly evolved network had actually lost more components, resulting in a sim-

pler reaction-diffusion system. The structure of this minimal network has yet to be identified [40].

Protein pattern formation in animal cell polarisation and cytokinesis

As we have seen for the Min system in *E. coli* and Cdc42 in budding yeast, protein patterns are an elegant way to convey intracellular positional information. Thus, it is not surprising that more complex organisms also employ protein pattern formation to control essential processes including cell polarisation, cytokinesis, embryogenesis and development.

An animal's body plan is typically specified during embryogenesis. In this context, the establishment and stable maintenance of cell polarity is a fundamental feature of developmental programs. So-called partitioning defective (PAR) proteins are key molecular players that promote symmetry breaking and establish intracellular polarity in diverse animal cells [41]. Here, we focus on the PAR network in the nematode worm *C. elegans*, as this system has been particularly well studied.

C. elegans PAR proteins are required for asymmetric cell division of the zygote, which they achieve by generating two distinct and complementary membrane domains with the aid of actomyosin flows [9, 42]. Several "design principles" of the PAR network have been established by a combination of experiments and theory [43]. A core feature of PAR polarity is the mutual antagonism between anterior and posterior PAR components (Fig. 3), which preferentially accumulate on the anterior and posterior halves of the membrane respectively while being excluded from the opposite half.

The maintenance of this polarity is highly dynamic and involves mobility of PAR proteins in the cytosol, their cross-inhibition via phosphorylation as well as additional feedback loops [43]. Importantly, the mutual antagonism in the PAR network relies on reversible switching of PAR proteins between "inactive", rapidly diffusing cytosolic and "active", slowly diffusing membrane-bound states [43], one of the key features of the pattern-forming protein networks discussed in this chapter.

Another intriguing example of protein pattern formation occurs during animal cell cytokinesis. This process involves the small GTPase Rho, whose localised activation directs assembly of the cytokinetic machinery, consisting of F-actin and myosin-2, in the equatorial cortex [44]. Recently, cortical waves of Rho activity and F-actin polymerisation were discovered in frog and echinoderm oocytes and embryos [10]. These protein patterns exhibited excitable dynamics

and were proposed to emerge through a reaction-diffusion mechanism involving positive feedback during Rho activation and delayed negative feedback exerted by F-actin (Fig. 4). In this view, Rho attaches to the plasma membrane in its inactive GDP-bound form. On the membrane, Rho is then converted to its GTP-bound active form in an autocatalytic manner, dependent on the Rho GEF Ect-2. Subsequently, F-actin is assumed to mediate a negative feedback on Rho, converting it back to its inactive form [10]. Remarkably, this reaction-diffusion network shares many similarities with our previous examples, such as reversible protein attachment to a lipid membrane, switching between different NTP-bound states and coupling of feedback loops.

The switch paradigm

The molecular mechanisms underlying the spatio-temporal organisation of cellular components in bacteria are frequently linked to P-loop ATPases such as ParA and MinD [27, 45, 46]. ParA and MinD proteins belong to a family of proteins known as the ParA/MinD superfamily of P-loop ATPases [27]. Both are known to form self-organised dynamic patterns at cellular interfaces, ParA on the nucleoid and MinD on the cell membrane. The nucleotide state of these ATPases determines their subcellular localisation: While the ATP-bound form dimerises and binds to the appropriate surface, the ADP-bound form is usually a monomer with a significantly reduced affinity for surface binding that freely diffuses in the cell. Importantly, both ParA and MinD have a partner protein (ParB and MinE, respectively) that stimulates their ATPase activity and causes them to detach from their respective surfaces. Moreover, there is a delay due to nucleotide exchange between the release of the ADP-bound form from the surface and its subsequent rebinding in the dimeric ATP-bound form. These interactions enable proteins to cycle between surface-bound and cytosolic states, depending on the phosphorylation state of their bound nucleotide. The surface-bound state is typically associated with spatially localised function (e.g. the downstream regulation of other proteins on the surface), whereas the cytosolic state enables spatial redistribution and formation of surface bound patterns of these proteins. Despite the striking similarities on a molecular level, the biological functions of ParA and MinD differ significantly. The Min system directs the placement of the division site at midcell by inhibiting the assembly of FtsZ into a ring-like structure (Z-ring) close to the cell poles. In contrast, ParA is involved in chromosome and plasmid segregation. Several other ParA-like proteins have been identified that are also important for the

correct localisation of large cellular structures at the cell poles, at midcell or along the cell length [27]. One of these is PomZ in *M. xanthus*. PomZ is part of a protein system that – like the Min system – is important for Z-ring formation. However, in contrast to the Min system, the Pom system positively regulates the formation of the FtsZ ring at midcell [47] Apart from the cell division and the chromosome partitioning machineries, there are various other multiprotein complexes that are positioned by self-organising processes based on P-loop NTPases. For example, the GTPase FlhF and the ATPase FlhG constitute a regulatory circuit essential for defining the distribution of flagella in bacterial cells [46, 48].

MASS-CONSERVING REACTION-DIFFUSION SYSTEMS

All of the examples of intracellular pattern-forming systems discussed in the previous section share some common features. They are reaction-diffusion systems in confined intracellular space, where proteins cycle between the cytosol and the cell membrane. On the time scale on which these patterns form, net change in the levels of the proteins involved is negligible and thus the *copy number within each protein species is conserved*. The reactions correspond to transitions of each protein species between a finite number of different states (membrane-bound, cytosolic, active, inactive, etc.), and these states play different functional roles in the corresponding biochemical circuit. For example, only membrane-bound MinD induces positive and negative feedback by recruiting MinD and MinE from the cytosol to the membrane. Hence, the protein dynamics can be understood as a reaction-diffusion system where diffusion takes place in different compartments (membrane and cytosol), and where reactions are sequences of state changes induced by protein-nucleotide, protein-protein, and protein-membrane interactions.

Mass-conserving dynamics is the generic case for intracellular dynamics. Because the production of proteins is a resource-intensive process, any mechanism that utilises production and degradation as pattern forming mechanisms would be highly inefficient and wasteful[49]. This excludes activator-inhibitor mechanisms [50], since they are based on the interplay between autocatalytic production of a (slow diffusing) activator and its degradation by a (fast diffusing) inhibitor. Though such a mechanism is frequently invoked as a paradigm in biological pattern formation [51], it is actually irreconcilable with the fundamental physical processes on which intracellular pattern formation is based on. This in turn implies that the study of biological systems should reveal hitherto

unknown mechanisms for pattern formation. In particular, explicit account for mass-conservation yields the total protein densities as system control parameters. As we will see, these are crucial for the theoretical understanding of the experimentally observed phenomena.

Cellular geometry: membrane and cytosol

Figure 5 illustrates the geometry of a rod-shaped prokaryotic cell. It is comprised of three main compartments: the cell membrane, the cytosol, and the nucleoid. There are two major facts that are relevant for intracellular pattern formation. First, the diffusion constants in the cytosol and on the cell membrane are vastly different. For example, currently accepted values for Min proteins in *E. coli* are of the order of $D_c \approx 10\,\mu\mathrm{m}^2/\mathrm{s}$, and $D_m \approx 0.01\,\mu\mathrm{m}^2/\mathrm{s}$, respectively. Second, due to the rod-like shape, the ratio of cytosolic volume to membrane area differs markedly between polar and midcell regions. Beyond this local variation of volume to surface ratio, the overall ratio of cytosol volume to membrane area depends on the shape of the cell.

Reaction-diffusion equations for the Min system

The biochemical reactions of the Min system outlined in section are summarised in Fig. 6. In the following we will refer to this scheme as the *skeleton network*, as it accounts only for those molecular interactions that are (presently) believed to be essential for Min protein phenomenology. For a quantitative analysis, this skeleton biochemical network has to be translated into a mathematical model [52, 53].
We denote the volume concentrations of MinE, MinD-ADP, and MinD-ATP in the cytosol by c_E, c_{DD}, and c_{DT}. Since the only reaction that takes place in the cytosol is reactivation of cytosolic MinD-ADP by nucleotide exchange (with rate λ) to MinD-ATP, the ensuing reaction-diffusion equations read:

$$\partial_t c_{DD} = D_c \nabla^2 c_{DD} - \lambda\, c_{DD}\,, \tag{1a}$$

$$\partial_t c_{DT} = D_c \nabla^2 c_{DT} + \lambda\, c_{DD}\,, \tag{1b}$$

$$\partial_t c_E = D_c \nabla^2 c_E\,, \tag{1c}$$

The diffusion coefficients are typically distinct for all protein configurations, for simplicity, we only distinguish between cytosolic (D_c) and membrane bound

(D_m) states.

Only the active form of MinD, c_{DT}, can attach to the membrane, either spontaneously with a rate k_D or facilitated by MinD-ATP already bound to the membrane (recruitment) with a rate $k_{dD}m_d$, where m_d denotes the areal density of MinD-ATP on the membrane. Overall then, the reaction term reads $R_D^+ = (k_D + k_{dD}\, m_d)\, \tilde{c}_{DT}$, where the tilde on the cytosolic concentration of MinD-ATP indicates that the value must be taken in the immediate vicinity of the membrane. Membrane bound MinD-ATP can also recruit cytosolic MinE to the membrane and thereby form MinDE complexes. The corresponding reaction term reads $R_E^+ = k_{dE}\, m_d\, \tilde{c}_E$. Finally, MinE in the MinDE complexes stimulates ATP hydrolysis by MinD and hence facilitates detachment and decay of membrane bound MinDE complexes into cytosolic MinD-ADP and MinE, c_E, with rate k_{de}. This process is described by the reaction term $R_{DE}^- = k_{de}\, m_{de}$ where m_{de} denotes the areal density of MinDE complexes on the membrane. Taken together, the reaction-diffusion equations on the membrane read

$$\partial_t m_d = D_m \nabla_m^2 m_d + R_D^+(m_d, \tilde{c}_{DT}) - R_E^+(m_d, \tilde{c}_E), \tag{2a}$$

$$\partial_t m_{de} = D_m \nabla_m^2 m_{de} + R_E^+(m_d, \tilde{c}_E) - R_{DE}^-(m_{de})\,, \tag{2b}$$

where the index m denotes the Laplacian for membrane diffusion.

These two sets of reaction-diffusion equations, Eq. 1 and Eq. 2, are complemented by nonlinear reactive boundary conditions at the membrane surface that guarantee local particle number conservation. In other words, the chemical reactions involving both membrane-bound and cytosolic proteins equal the diffusive flux onto ($-$) and off ($+$) the membrane (the index $\perp$ denoting the outward normal vector at the boundary):

$$D_c \nabla_\perp c_{DD}|_m = +R_{DE}^-(m_{de})\,, \tag{3a}$$

$$D_c \nabla_\perp c_{DT}|_m = -R_D^+(m_d, \tilde{c}_{DT})\,, \tag{3b}$$

$$D_c \nabla_\perp c_E|_m = +R_{DE}^-(m_{de}) - R_E^+(m_d, \tilde{c}_E)\,. \tag{3c}$$

For example, Eq. 3a states that detachment of MinD-ADP following hydrolysis on the membrane is balanced by gradients of MinD-ADP in the cytosol. In general, any exchange of proteins between the membrane and the cytosol leads to diffusive fluxes and thereby to protein gradients in the cytosol since the membrane effectively acts as a sink or source of proteins. These gradients are essential for understanding the mechanisms underlying intracellular pattern

formation, and preclude a naive interpretation of the cytosol as a spatially uniform particle reservoir.
For the model to be complete, one needs to know the values of all of the reaction rates. However, the estimation and choice of system parameters is a highly nontrivial problem. Nonlinear systems are generically very sensitive to parameter changes, whereas biological function has to be sufficiently robust against variations in the kinetic rates and diffusion coefficients (e.g. caused by temperature changes). In addition, only rarely are the system parameters known quantitatively from experiments. For the Min system only the diffusion coefficients have been measured and estimates for the nucleotide exchange rate λ [54] and the Min protein densities exist [55]. However, a theoretical investigation of the skeleton model by means of linear stability analysis and numerical simulations was able to identify parameter regimes where the experimentally observed patterns are formed [53].

Basic mechanisms underlying Min oscillations in *E. coli* cells

From the analysis of the skeleton model [53], quantified by the reaction-diffusion equations in the previous section, one can now learn how Min proteins self-organize to give rise to pole-to-pole oscillations *in vivo*.
The basic theme of the protein dynamics is the cycling of proteins between the membrane and the cytosol. This cycling is driven by the antagonistic roles of MinD and MinE: Membrane-bound active MinD facilitates flux of MinD and MinE from the cytosol to the membrane (recruitment). This accumulation of proteins at the membrane is counteracted by MinE's stimulation of MinD's ATPase activity, which triggers detachment of both MinD and MinE. In concert with redistribution of proteins through cytosolic diffusion, spatio-temporal patterns may emerge on the membrane.
However, the formation of pole-to-pole oscillations is by no means generic in the context of the above reaction scheme.[56] In general, there are conditions on the values of the reaction rates, as well as on the relative abundances of the proteins which have to be met. An exhaustive parameter scan for model equations Eq. 1, 2, and 3 has shown that, for spatial patterns to emerge in the skeleton model, MinE needs to be recruited faster to the membrane-bound protein layer than MinD, while being lower in total particle number [53]

$$k_{dD} < k_{dE}\,, \quad N_E < N_D\,. \tag{4}$$

These conditions give rise to the formation and separation of MinD and MinDE

domains, the *polar zone* and *MinE ring*, as the two basic emergent structures of pole-to-pole oscillations.

As illustrated in Fig.7, this is (heuristically) understood as follows [53]. The higher particle number of MinD enables complete sequestration of MinE in membrane-bound MinDE complexes, while leaving a fraction of MinD available to initiate a new polar zone.[57] Given a sufficiently high MinD membrane concentration and MinE recruitment rate k_{dE}, detaching MinE rebinds immediately, forming the prominent MinE ring. Continuous MinE cycling locally depletes the membrane of MinD, leading to a slow poleward progression of the MinE ring along the gradient of membrane bound MinD, whereupon a fraction of detaching MinD initiates a weak polar zone in the opposite cell half, see Fig.7A. The new polar zone grows due to steady redistribution of MinD, while most MinE remains sequestrated in the old polar zone until the remaining MinD molecules are converted into MinDE complexes, see Fig.7B. Once this state is reached, the Min proteins rapidly detach, dissociate and diffuse through the cytosol and rapidly reattach at the new polar zone, leaving behind a region of high MinDE/MinD ratio, where immediate reformation of polar zones is inhibited. Due to the faster recruitment of MinE, the MinE ring reassembles at the rim of the new polar zone, which provides the crucial separation of MinD and MinDE maxima, i.e. a polar zone and a MinE ring.

There is one element of the above argument which needs further consideration: The sequestration of MinE is transient, and hence the system is oscillatory, only if detaching MinD gradually leaks from the old to the new polar zone. But, how is this process established and regulated? Leakage from the old polar zone is determined by the balance between two opposing factors: the ATPase cycle of MinD, and the propensity of cytosolic MinD to bind to the membrane. MinE stimulates ATPase activity of MinD and thereby initiates detachment of ADP-bound MinD. The inactive MinD cannot reattach to the membrane until it is reactivated by nucleotide exchange. This delay implies that the zone near the membrane is depleted of active MinD, i.e. active MinD has time to diffuse further away from the membrane into the cytosol. Taken together, these factors effectively suppress immediate reattachment of MinD and promote its leakage from the polar zone: The slower the nucleotide exchange the more particles leak from polar zones. This is counteracted by MinD recruitment: The stronger the recruitment, the "stickier" the membrane and hence the fewer particles leak from polar zones. Clear evidence for this reasoning comes from the slowing down of the oscillation with increasing nucleotide exchange and MinD recruitment rates, depicted in Fig.8A.

Numerical simulation of the reaction-diffusion equations, Eq.1–3, reveals fur-

ther functional characteristics of Min oscillations. For nucleotide exchange rates $\lambda = 5\,s^{-1}$, close to the experimentally determined lower bound of $3\,s^{-1}$, reaccumulation of the polar zone always starts in the opposite cell half, and the recruitment rate k_{dD} of MinD regulates how fast new polar zone grows towards the old one (Fig. 8B). Notably, at $k_{dD} = 0.1\,\mu\text{m}^2/\text{s}$ in Fig. 8B, the redistribution of MinD from old to new polar zone is highly canalised, i.e. the total MinD flux is directed towards the opposite cell half immediately after the polar zones start to shrink (Fig.8B). This implies that growth and depletion of polar zones are synchronised. This is also reflected in the characteristic triangular shape observed in MinD kymographs [58], where new polar zone start growing towards midcell while old polar zones shrink towards the cell pole (Fig. 8B).
Although most of the Min protein patterns (like stripe patterns) observed in filamentous mutant *E. coli* have no biological function, the theory is able to account for their occurrence. This argues strongly that they too arise from the mechanism that optimises the spatial profile of pole-to-pole oscillations for midcell localisation. In other words, the rich phenomenology in mutant cells appears to be a byproduct of the evolutionary optimisation of the wild-type dynamics.

Cell geometry and pattern formation

To ensure robustly symmetrical cell division, one would expect Min patterns to scale with cell size and shape, at least within the biologically relevant range. Indeed, recent experiments using 'cell-sculpting' techniques [59] have shown that longitudinal pole-to-pole oscillations are highly stable in cells with widths below 3μm, and lengths in the range of $3 - 6\,\mu$m. Interestingly, however, outside of this range of cell geometries, Min proteins show diverse oscillation patterns, including longitudinal, diagonal, rotational, striped, and even transverse modes [15, 59–65]. What is the origin of the simultaneous robustness of Min oscillations inside the biologically relevant regime and the bewildering diversity of patterns and multistability outside of it? In what sense are these seemingly contradictory features two faces of the same coin?
To answer these questions one has to address how and to what extent the existence and stability of different patterns is affected by a cell's geometry, and which specific biomolecular processes in the Min reaction circuit control how the system adapts to cell geometry. This has recently been achieved by a combination of numerical studies, based on the reaction-diffusion model

discussed in section , and experimental studies, in which the geometry of *E. coli* bacteria was systematically varied [61].

There are basically two types of randomness that may affect the process of pattern selection, or transitions between patterns if multiple stable patterns are possible. First, the inherent randomness of any chemical reaction may cause stochastic transitions between patterns. Though such stochastic effects are possible in principle [66], given the large copy number of Min proteins, they are unlikely to be the major source for transitions between patterns; factors like heterogeneities and asymmetries are expected to be far more important. Second, there are many different factors which cause realistic cellular systems to be asymmetric or heterogeneous. For example, the membrane affinity of MinD depends on the lipid composition, which in turn is sensitive to membrane curvature. Hence, small asymmetries of the cell shape translate to variations of MinD membrane attachment. While these asymmetries and heterogeneities are intrinsic to ensembles of cells, they need to be specifically emulated in numerical simulations. A natural choice are gradients in the MinD attachment rate that are inclined at all possible angles to the long axis of the cell. The magnitude of these gradients must be sufficiently large to significantly affect the pattern selection process, but at the same time small enough not to cause any asymmetry in the final stable pattern. A relative magnitude of variation in the range of 20% (well below the natural variability of MinD affinity to different lipids [21, 67]) fulfills these requirements.

Figure 9 shows histograms of the final stable patterns obtained by sampling over all directions of the gradient, as a function of cell width and length, and of the MinD recruitment rate [61]. For a recruitment rate fixed to the value that facilitates canalised transfer, $k_{dD} = 0.1$, the following observations are of note. (i) As cell length is increased, striped oscillations become more frequent patterns. (ii) The fraction of oscillatory striped patterns tends to decrease in favour of transverse patterns as the cell width increases, indicating that cell width, and not cell length, is the main determinant for the onset of transverse modes. Both observations are remarkably consistent with experimental data based on random sampling of live *E. coli* cells after they have reached a defined shape [59]. Numerical simulations allow us to go beyond the analysis of cell geometry, and investigate the effect of MinD recruitment rate, see Fig.9B. In narrow cells with widths ranging from $1\,\mu$m to $3\,\mu$m, one observes that the fraction of stripes increases with the MinD recruitment rate [53, 61]. In contrast, for cells that reach a width of 5 μm, stripe patterns are absent below some threshold MinD recruitment rate. With increasing MinD recruitment rate, transverse patterns appear first and increase in frequency, while the

fraction of striped patterns takes on a constant value.
There are several conclusions one can draw from these observations. The most obvious one is that multistability in Min patterns is not determined by either kinetic parameters or cell geometry alone, but originates from the interdependence between these two factors. In addition, increasing the size of a Turing-unstable system alone does not in itself facilitate the existence of multiple stable patterns [68]. This is clearly evident from the observation that the emergence of a pole-to-pole oscillation in a short cell does not generically imply the existence of a stable striped oscillation with a characteristic wavelength in a long filamentous cell [53]. Instead, the emergence of a characteristic length scale (which becomes manifest in striped oscillations) is restricted to a specific regime of kinetic parameters, where growth and depletion of spatially separated polar zones become synchronised such that multiple, spatially separated polar zones can be maintained simultaneously ("canalised transfer" regime) [53]. A key element among the prerequisites that permit this regime to be reached is that the degree of nonlinearity in the kinetics of the system (MinD cooperativity) must be particularly strong. Notably, the same mechanism that enables striped oscillations in filamentous cells also facilitates transverse oscillations in wide cells.
These findings hint at an exciting connection between multistability, the ability of patterns to sense and adapt to changes in system geometry, and the existence of an intrinsic length scale in the underlying reaction-diffusion dynamics. Remarkably – and contrary to the treatments in the classical literature – the existence of an intrinsic length scale is not generic for a Turing instability per se. One example is the aforementioned selection of pole-to-pole patterns in arbitrarily long cells where MinD recruitment is weak. In this case, irrespective of the critical wavenumber of the Turing instability, the final pattern is always a single wave traveling from pole to pole. The selection of a single polar zone is also characteristic in the context of cell polarity [34, 69], where it has been ascribed to the finite protein reservoir and a winner-takes-all mechanism. It will be an interesting task for further research to elucidate the general requirements for the emergence of an intrinsic length scale in mass-conserved reaction-diffusion systems.

Principles of adaption to geometry in reaction-diffusion systems

How does the geometry of a cell affect the formation of spatio-temporal patterns? This question may be rephrased in more mathematical terms as follows:

What are the inherent features of a reaction-diffusion system in confined geometry that promote or impede the adaptation of the ensuing patterns to the size and shape of that confining space[70]? In previous sections, we have seen two recurrent themes: nucleotide exchange and positive feedback through recruitment. To elucidate the role of these two factors we will in this section study a minimal pattern-forming system comprised of a single NTPase only.
As illustrated in Fig.10, the NTPase cycles between an NDP-bound inactive (D) and an NTP-bound active state (T). Both protein species are able to bind to the membrane spontaneously; for simplicity we take the rates to be identical and given by k_+. In addition, to direct membrane attachment, each protein species may also bind cooperatively to the membrane with corresponding recruitment rates k_{mD} for the inactive and k_{mT} for the active protein species. Detachment of the membrane-bound species is asymmetric: While the inactive species is simply released to the cytosol with *detachment rate* k_-, detachment of the active species is triggered by NTP hydrolysis which is thereby converted into cytosolic inactive D; again, for simplicity, we assume the corresponding detachment rates to be equal and given by k_-. Reactivation of cytosolic inactive D through nucleotide exchange occurs at rate rate λ. Both protein forms are allowed to freely diffuse in the cytosol and the membrane with diffusion constants D_c and D_m, respectively.
Denoting the concentrations of D and T in the cytosol by c_D and c_T and by m_D and m_T on the membrane, respectively, the reaction-diffusion equations read

$$\partial_t c_T = D_c \,\Delta\, c_T + \lambda\, c_D\,, \tag{5a}$$

$$\partial_t c_D = D_c \,\Delta\, c_D - \lambda\, c_D\,, \tag{5b}$$

$$\partial_t m_T = D_m \,\Delta_m\, m_T + (k_+\, \tilde{c}_T - k_-\, m_T) + \, k_{mT}\, m_T\, \tilde{c}_T\,, \tag{5c}$$

$$\partial_t m_D = D_m \,\Delta_m\, m_D \, + (k_+\, \tilde{c}_D \, - k_-\, m_D) + k_{mD}\, m_D \, \tilde{c}_D\,. \tag{5d}$$

As before, reactive and diffusive fluxes balance at the membrane-cytosol boundary

$$D_c\, \nabla_\perp c_T|_m = -(k_+ \, + \, k_{mT}\, m_T)\, \tilde{c}_T \tag{6a}$$

$$D_c\, \nabla_\perp c_D|_m = -(k_+ \, + \, k_{mD}\, m_D)\, \tilde{c}_D + k_-\, (m_D + m_T)\,. \tag{6b}$$

Solving this set of equations numerically in elliptical geometry reveals a series of striking features (Fig.11): (i) In elongated cells the protein density on the

membrane and in the cytosol is *always* inhomogeneous, and reflects the local cell geometry. (ii) There are two distinct types of patterns: membrane-bound proteins either accumulate at midcell or form a bipolar pattern with high densities at both cell poles. (iii) The protein gradients scale with the size of the cell, i.e. fully adapt to the geometry of the cell.

The type of polarity of these patterns is quantified by the ratio of the density of membrane-bound proteins located at the cell poles to that at midcell: $\mathcal{P} = m_{\mathrm{pole}}/m_{\mathrm{midcell}}$. Accumulation occurs either at the cell pole or at midcell depending on the value of the preferential recruitment parameter $\mathcal{R} = (k_{mD}-k_{mT})/(k_{mD}+k_{mT})$: One finds that proteins accumulate at the cell poles ($\mathcal{P} > 1$) if there is a preference for cooperative binding of D ($\mathcal{R} > 0$). Moreover, the polarity $\mathcal{P}$ of this bipolar pattern becomes more pronounced with increasing $\mathcal{R}$. In contrast, when cooperative binding favours T ($\mathcal{R} < 0$), proteins accumulate at midcell ($\mathcal{P} < 1$). Thus, the sign of the recruitment preference $\mathcal{R}$ for a protein in a particular nucleotide state controls the type, while its magnitude determines the amplitude of the pattern. With increasing eccentricity of the ellipse, the respective pattern becomes more sharply defined; for a spherical geometry the pattern vanishes. In summary, cell geometry controls the definition of the pattern, and the preference for membrane recruitment of a certain nucleotide state determines both the location on the cell membrane where the proteins accumulate and how pronounced this accumulation becomes.

What is the origin of these polar patterns and their features? To answer this question in the clearest possible way, it is instructive to consider the limiting case where positive feedback effects on recruitment are absent and the dynamics hence is fully linear. Then, Eqs.5-6 imply that both the total concentration of proteins on the membrane, $m = m_D + m_T$, and in the cytosol, $c = c_D + c_T$, are spatially uniform if the detailed balance condition $k_+ \tilde{c} = k_- m$ holds for the exchange of proteins between the cytosol and the membrane. This uniformity in total protein density, however, does not imply uniformity in the densities of the active and inactive protein species, either on the cell membrane or in the cytosol! The origin of this effect is purely geometrical, and it is linked to the finite time required for nucleotide exchange in the cytosol. Heuristically, this can be seen as follows. As only inactive proteins D are released from the membrane they act as a source of cytosolic proteins. In the cytosol they are then reactivated through nucleotide exchange, which is effectively equivalent to depleting the cytoplasmic compartment of inactive proteins. This in turn implies the formation of a gradient of inactive protein and a corresponding, oppositely oriented gradient of active proteins as one moves away from the

membrane into the cytosol. As is known from standard source-degradation processes, the ensuing density profile for D in the cytosol is exponential, with the decay length being set by $\ell_\lambda = \sqrt{D_c/\lambda}$.
Due to membrane curvature these reaction volumes overlap close to the cell poles (Fig. 12B, bottom), which implies an accumulation of D at the cell poles. The effect becomes stronger with increasing membrane curvature. Moreover, there is an optimal value for the penetration depth ℓ_λ, roughly equal to a third of the length l of the short cell axis, that maximises accumulation of D at the cell poles (Fig.12B, top). As ℓ_λ becomes larger than l, the effect weakens, because the reaction volumes from opposite membrane sites also overlap at mid-cell. In the limit where ℓ_λ is much smaller than the membrane curvature at the poles, the overlap vanishes, and with it the accumulation of D at the poles.
More generally, these heuristic arguments imply that the local ratio of the reaction volume for nucleotide exchange to the available membrane surface is the factor that explains the dependence of the protein distribution on cell geometry.

IN VITRO RECONSTITUTION AND THEORETICAL ANALYSIS OF MIN PROTEIN PATTERN FORMATION

A key step towards understanding pattern-formation mechanisms in biological systems is the identification of the essential functional modules that facilitate the formation of certain patterns. In living systems, such an identification is strongly impeded by the vast amount of potentially interacting and, therefore, interdependent components. A common strategy for tackling the complexity of biological systems is mathematical modelling, which has been discussed in the previous section of this chapter. While mathematical analysis is able to identify possible mechanisms of pattern formation, it is also based on a priori assumptions about the biological system under consideration. However, these assumptions need to be tested by suitable experiments. Ideally, a conclusive comparison between theory and experiment requires the ability to isolate the essential players of the pattern forming dynamics and reconstitute them in a minimal system lacking any other potential interactions and allowing for precise control of parameters, such as protein concentrations or geometric boundaries.
A major breakthrough in this regard was the successful *in vitro* reconstitution of Min protein patterns in a lipid bilayer assay [71]. These experiments demon-

strated that a flat lipid bilayer surface coupled to a cytosolic solution containing only MinD, MinE, and ATP is sufficient for the formation of membrane bound Min protein patterns. However, the patterns observed in reconstituted systems significantly differed from the intracellular patterns found *in vivo*. While the majority of patterns found *in vivo* can be viewed as standing waves with a wavelength matching the cell length, the patterns on the flat membrane are travelling and spiral waves with wavelengths one order of magnitude greater than the typical length of *E. coli*.

A kaleidoscope of *in vitro* patterns

The successful reconstitution of Min protein patterns on flat lipid bilayers stimulated a plethora of *in vitro* experiments that studied Min protein dynamics under various circumstances and revealed a true kaleidoscope of patterns. On flat lipid bilayers one observed spiral and travelling wave patterns, and a varying degree of spatial coherence sometimes verging on chemical turbulence [72]. Other experiments constrained the Min protein dynamics geometrically to small membrane patches [73], semi-open PDMS grooves with varying lipid composition [74], lipid-interfaced droplets [75], and bilayer coated three-dimensional chambers of various shapes and sizes [76]. Strikingly, the observed patterns show a very broad range of characteristics and varying degrees of sensitivity to the geometry of the enclosing membrane. Other experiments were performed in large, laterally extended flow cell devices with a flat lipid bilayer of varying lipid composition attached at the bottom [77]. These experiments showed that Min protein patterns are formed even when there is hydrodynamic flow in the cytosol. Furthermore, these experiments revealed the capability of Min protein dynamics to form exotic patterns sharing characteristics of travelling waves and stationary patterns alike [77].
Despite these intensive experimental efforts, a quantitative reconstitution of Min protein patterns observed *in vivo* has not been achieved. Instead a broad range of different patterns has been found, all of which exhibit wavelengths that are several times larger than that of the *in vivo* pattern. The pole-to-pole patterns that are observed in (semi-)confined compartments [76, 78] most closely resemble those seen *in vivo*. Interestingly, this resemblance is limited to geometries with dimensions below the typical wavelength of the pattern. In these systems the characteristic pole-to-pole oscillation is observed *in vivo* as well as in vitro. If the length and width of the confined system are increased, the reconstituted *in vitro* experiments [76] predominantly show traveling and spiral

wave patterns, whereas *in vivo* experiments show longitudinal and transversal standing waves [59, 61]. This suggests that the underlying mechanisms (dynamic instabilities) are actually not the same[79]. While longitudinal and transversal standing waves have also been observed in semi-confined PDMS grooves of specific sizes [78], the patterns became chaotic in these experiments when the system size was increased [78].
Given these ambiguous results, how can we reconcile the kaleidoscope of *in vitro* patterns and the range of *in vivo* patterns? In the following, we discuss how theory can shed some light on these bewildering results. As we will see, a key problem with the interpretation of recent *in vitro* reconstitution experiments and their comparison to *in vivo* dynamics lies in the lack of the ceteris paribus condition, i.e. conditions where only one control parameter is varied while the rest are held constant. Achieving quantitative control over all parameters will be the key goal for future experiments.

The polychotomy of Min protein patterns

All experimental evidence supports the assumption that the Min system can be understood as a reaction-diffusion system driven by nonlinear (cooperative) protein interactions. Therefore, we can expect that Min protein dynamics will share generic features of such nonlinear systems. In particular, as is well known in the field of nonlinear dynamics, even very simple models can produce a broad variety of patterns [80–84]. Moreover, which patterns are observed depends on the parameters of the system. In the classical mathematical theory these parameters are the coefficients of the (non-)linear interactions (representing the "kinetics"), as well as the diffusion coefficients.
Diffusion coefficients (in the cytosol) have been measured *in vivo* [54] and *in vitro* [71, 72], and they can be controlled experimentally by the addition of crowding agents [73, 76]. Kinetic parameters of the Min system are much more difficult to measure and to control. However, diffusion coefficients and kinetic rates are not the only control parameters. Most of the classical literature in nonlinear dynamics neither accounts for system geometry nor for the mass-conserving nature of bio-molecular interactions. This might explain why the fact that system geometry as well as protein densities can be key control parameters of the system's dynamics is often overlooked. The effect of changes in these parameters is not necessarily restricted to changes in the length- and time-scales of the dynamics (e.g. wavelength, wave speed, and oscillation period), but can also induce qualitative changes and transitions

between patterns.
One clear difference between the reconstituted Min system on flat lipid bilayers and the intracellular system in E. coli is the vastly increased ratio of cytosolic volume to membrane surface in the *in vitro* system, where the height of the system is of the order of milimetres, instead of μm, in the living system. A recent theoretical analysis [85] has shown that increasing this volume–to–surface ratio leads to an increased wavelength of the pattern. This prediction agrees with the experimental observation of a reduced wavelength of the Min protein patterns in fully confined geometries [76] that mimic the *in vivo* membrane-to-cytosol ratio more closely than does the flat lipid bilayer. Strikingly, even when cytosolic diffusion was reduced to *in vivo* levels, these experiments still showed a 3- to 4-fold increased wavelength in confined compartments compared to the intracellular patterns – emphasising an apparent dichotomy between patterns observed *in vivo* and *in vitro*.
However, the surface–to–volume ratio is not the only difference between the intracellular and the reconstituted Min systems. Another is the particle number or effective density of MinD as well as MinE. At first glance there is no apparent difference between the protein concentrations *in vivo* and *in vitro*, since the concentrations in all reconstituted systems are adjusted to the intracellular concentrations which are about $1\,\mu$M for MinD and MinE. However, it is important to note that these are the average cytosolic densities with no proteins attached to the membrane. Since all cytosolic proteins are able to bind to the membrane[86], the total number of cytosolic proteins determines the upper bound for the maximal membrane densities. Hence, even if the average cytosolic densities in the reconstituted system are identical to typical intracellular concentrations, the crucial control parameter is the ratio of cytosolic volume to membrane surface. In vivo, a cytosolic density of about 1μM yields a number of proteins that can easily be absorbed by the membrane and still remain up to two orders of magnitude below the saturation limit.[87] However, in the reconstituted system with flat lipid bilayer the volume to surface ratio is given by the bulk height h. For the typical bulk height on the order of millimetres, less than 1% of all proteins can bind to the membrane before saturation due to volume exclusion is reached. As a consequence, the protein densities at and on the membrane are highly increased in the reconstituted system compared to the situation in vivo, despite the average cytosolic densities being identical. Note that the densities of membrane-bound proteins are directly involved in the recruitment process which represents the only intrinsically nonlinear interaction in the Min system (cf. section). As such, one can expect that changes in the average protein densities on the membrane affect

the system dynamics in a significant way. Indeed, estimates of the concentration on the flat lipid bilayer show that the density across a wave profile is about two orders of magnitude higher than the typical protein densities on the intracellular membrane [72]. The same can be assumed to be the case for reconstituted Min oscillations in semi-open PDMS grooves [74, 78], since the dynamics are initialised with a high cytosolic column above the grooves which is only removed after the onset of pattern formation (and therefore membrane accumulation). Elevated protein densities were also found for the reconstituted Min patterns in confined chambers [76] since these are based on a microfluidic device. As proteins accumulate on the membrane while the flow is still active, the density at the inlet is merely a lower bound for the actual protein densities in the individual chambers. Measurements of the protein fluorescence inside the confined chambers after careful calibration show that the total densities of MinD and MinE and the MinE/MinD ratios are increased and are broadly distributed [76]. A similar result can be expected for Min protein dynamics in large, laterally extended flow cells where diverse wave patterns are observed [77, 88].

To put these findings from the *in vitro* reconstruction of Min protein pattern in the context of the theoretical framework, the broad variation of volume to surface ratios, total protein numbers, and MinE/MinD density ratios, is a crucial aspect to consider (cf. [89]). The theoretical analysis of the skeleton model, Eqs.1–3, has shown that all these quantities are key control parameters for the system dynamics. An increase in any of these values (total density, density ratio, volume/surface ratio) can lead to a Turing- or Hopf-instability [85]. In the latter case, each point on the membrane can be considered to be an individual chemical oscillator, and the laterally extended system a field of diffusively coupled oscillators [85]. Such dynamics describe a broad class of systems well documented in the classic nonlinear dynamics literature [90]. Key characteristics of oscillatory media are spiral and travelling patterns, as well as various manifestations of chemical turbulence. All these phenomena can be observed in the reconstituted Min system. From this point of view, the observed dichotomy rather appears as a polychotomy, not only between *in vivo* and *in vitro*, but between the many different experimental setups. Its origin lies in the broad distribution of control parameters and emphasises the diversity of Min protein dynamics on a phenomenological and mechanistic level.

DISCUSSION AND OUTLOOK

As outlined in this chapter, the recent focus on the quantitative study of pattern formation in biological systems has led to conceptually new approaches in theory and experiments. Among the important milestones are the inclusion of cell geometry and a explicit distinction between cell membrane and cytosolic volume in theoretical models, as well as the identification of particle numbers and cell geometry as major control parameters of the self-organisation processes that lead to pattern formation. While these efforts enabled the quantitative study of biological pattern formation within the theoretical framework of nonlinear dynamics, experimental advances in *in vitro* reconstitution opened new ways to probe, study, and design protein pattern formation as well controlled minimal systems. Due to its simplicity, the *E. coli* Min system has been the subject of intensive theoretical and experimental investigation, establishing it as a paradigm for protein pattern formation. In contrast, the eukaryotic systems discussed here remain far less well understood. In part, this is due to a higher degree of complexity and redundancy in these systems. For example, PAR networks involve several different molecular players in the anterior and posterior PAR components respectively, and also interact with dynamic cytoskeletal structures and physical triggers [43]. Accordingly, the in vitro reconstitution of eukaryotic pattern-forming systems is typically more challenging compared to bacterial systems. Yet, efforts to experimentally reconstitute even basic aspects of such pattern-forming systems in vitro could substantially enhance our understanding of their underlying mechanisms via control and perturbation of the experimental conditions.

For the Min system, several key questions remain to be answered. Central is the experimental control over system parameters that gives rise to the multitude of observed patterns. Future research may reveal additional chemical states of MinD as well as MinE or additional chemical reactions that refine the hitherto identified skeleton network. While this will affect the number of chemical components and reaction terms one has to take into account in the mathematical model, it does not change the overall structure of the set of reaction-diffusion equations: (1) Fast cytosolic diffusion is coupled to slow membrane dynamics by chemical reactions that conserve protein number. (2) Nucleotide exchange in the cytosol implies that active MinD is spatially separated from the reactive membrane. As a consequence, the cytosol serves as a repository for active MinD. (3) MinD and MinE remain the only conserved species. The sum of individual components of each species, regardless of the number of components, will always be a conserved quantity.

Open questions relating to molecular details of Min protein interaction concern the roles of membrane binding and conformational state switching of MinE [25]. Only a combined approach, in which the theoretical model is constrained and supported by unambiguous experimental data, has the potential to truly relate molecular "design" features of Min proteins to defined roles in pattern formation.

In summary, protein pattern formation plays key roles in many essential biological processes from bacteria to animals, including cell polarisation and division. Combined theoretical and experimental approaches have established important principles of pattern-forming protein systems. Perhaps the most crucial feature that has emerged from these research efforts is the identification of the cytosol as a depot. This depot enables the system to store proteins and redistribute them throughout the system. Cytosolic diffusion is the key process that detects the local shape of the membrane, and it is this explicit dependence on geometry that is imprinted on membrane-bound protein patterns.

ACKNOWLEDGEMENT

We thank Fridtjof Brauns, Yaron Caspi, Cees Dekker, Jonas Denk, and Fabai Wu for helpful discussions. This research was supported by the German Excellence Initiative via the program "NanoSystems Initiative Munich" (NIM), and the Deutsche Forschungsgemeinschaft (DFG) via project A09 and B02 within the Collaborative Research Center (SFB 1032) "Nanoagents for spatiotemporal control of molecular and cellular reactions".

FIGURES

Figure 1

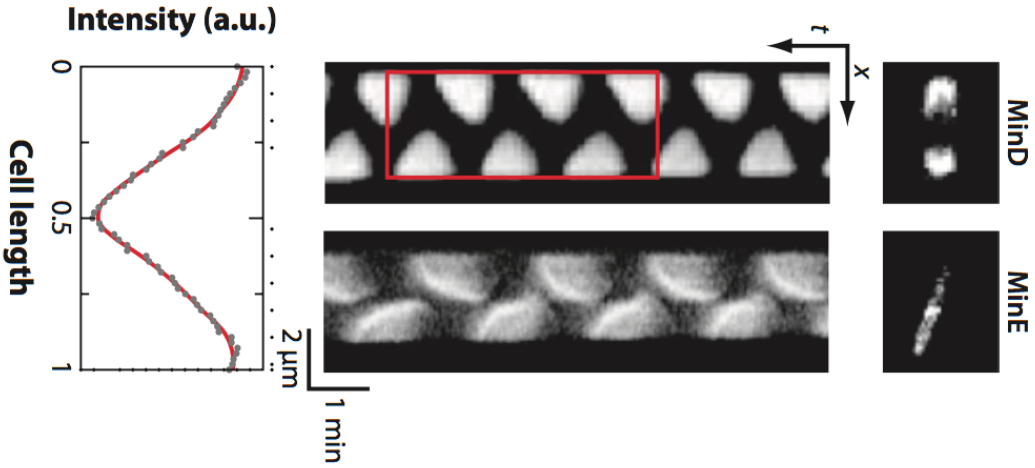

Figure 1. **Oscillatory patterns of Min proteins in vivo.** *Left:* Time-averaged MinD fluorescence intensity profile along the red rectangle shown in the kymograph. Adopted from Ref. [72]. *Middle:* Kymograph of pole-to-pole oscillations of MinD and MinE in cells of normal length (shorter than 5 μm). *Right:* Micrographs of GFP-MinD and MinE-GFP in vivo.

Figure 2

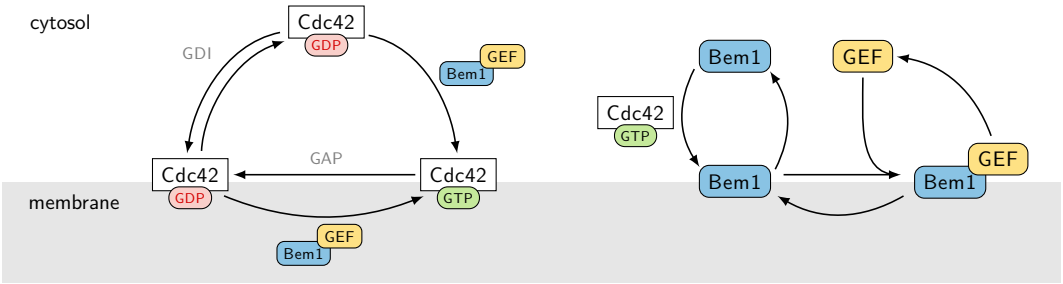

Figure 2. **Reaction network of the Cdc 42 system in yeast** with a guanine exchange factor (Cdc24) and GAPs controlling the hydrolytic activity of Cdc42. The polarisation relies on activation of Cdc42 through a Bem1-Cdc24-Cla4 complex and on extraction of Cdc42 from membranes by the GDI Rdi1.

Figure 3

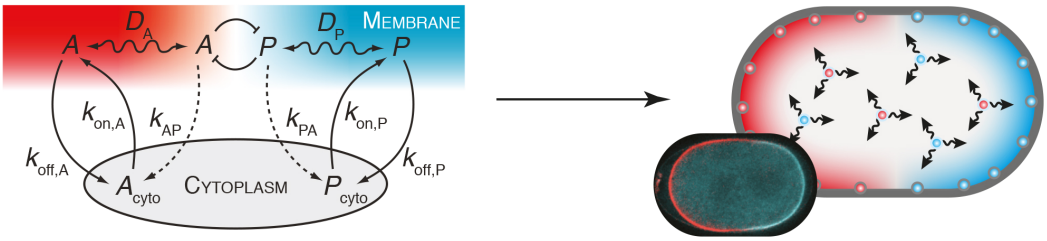

Figure 3. **Cell polarisation in the *C. elegans* embryo.** A reaction-diffusion network of mutually antagonistic anterior and posterior PAR proteins, switching between "active" membrane-bound and "inactive" cytosolic states, sustains opposing membrane domains in the *C. elegans* embryo. Anterior and posterior PAR components are shown in red and blue, respectively. Adapted from Ref. [9, 91].

Figure 4

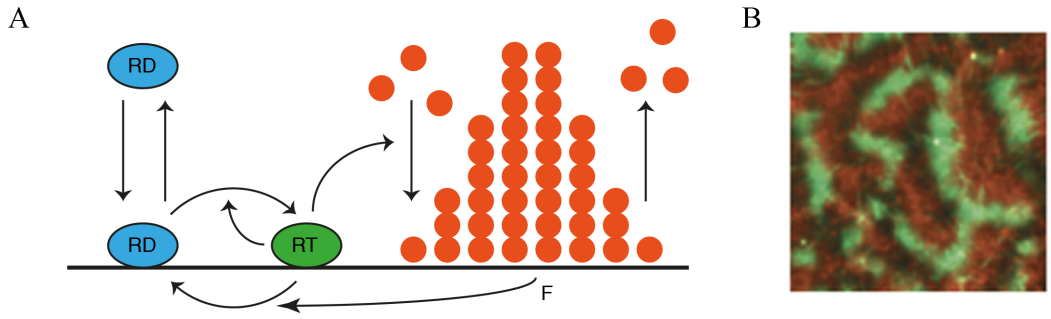

Figure 4. **Cortical waves of Rho activity and F-actin polymerisation involved in animal cell cytokinesis. A**, Possible scheme of interactions underlying wave formation. Inactive GDP-bound Rho (RD) binds to the membrane, where it is activated to GTP-bound Rho (RT) via nucleotide exchange in an autocatalytic, GEF-dependent manner. Subsequently, the theoretical model assumes that coupled F-actin polymerisation (F) exerts a negative feedback on Rho activity converting it back into its inactive form [10]. **B**, Fluorescence image of cortical waves of Rho (malachite) and F-actin (copper) in an Ect2-overeexpressing starfish oocyte. Adapted from Fluorescence image of cortical waves of Rho (malachite) and F-actin (copper) in an Ect2-overexpressing starfish oocyte. Adapted from Ref. [10] by permission from Macmillan Publishers Ltd: Nature Cell Biology [10], copyright 2015.

Figure 5

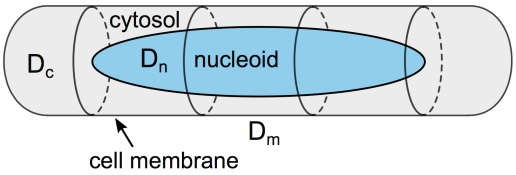

Figure 5. **Schematic representation of the geometry of a rod-shaped bacterial cell.** There are three main compartments: cell membrane, cytosol, and nucleoid. The diffusion constants in these compartments will, in general, be different.

Figure 6

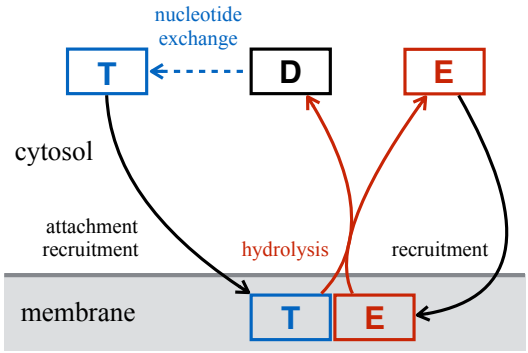

Figure 6. **Skeleton MinCDE network:** Cytosolic MinD-ATP (T) attaches to the membrane, and recruits MinD-ATP and MinE (E) from the cytosol. Recruitment of MinE leads to the formation of MinDE complexes. MinE in the MinDE complexes stimulates ATP hydrolysis by MinD and thereby triggers detachment and dissociation of membrane-bound MinDE complexes into cytosolic MinD-ADP (D) and MinE.

Figure 7

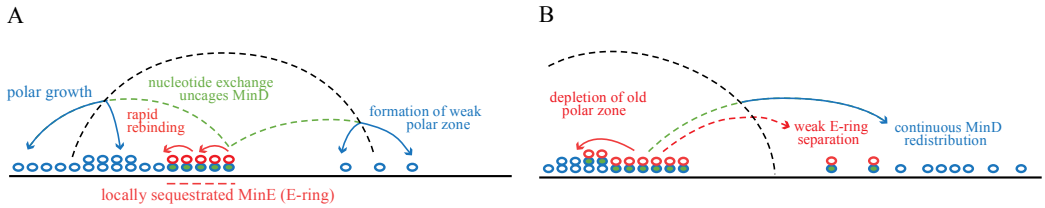

Figure 7. **Key mechanism underlying Min oscillations. A,** Locally sequestrated MinE constitutes the MinE ring, which moves toward the left pole through local cycling. Detaching MinD rebinds predominantly at the left pole and initiates formation of a weak polar zone at the right end. The delay in reattachment caused by the need for nucleotide exchange is indicated by dashed lines. **B,** MinE depletes the old polar zone of MinD, until only MinDE complexes are left, then reassembles at the rim of the new polar zone, formed by redistributed MinD.

Figure 8

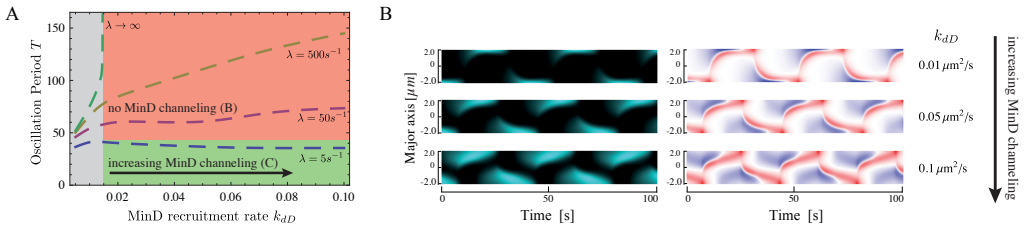

Figure 8. **Canalised MinD transfer and regulation of spatial MinD reattachment by MinD recruitment. A**, Temporal period of Min oscillations as a function of the MinD recruitment rate k_{dD}, and nucleotide exchange rate λ in cells of 4 μm length. With instantaneous nucleotide exchange, oscillations only exist at low MinD recruitment rates (grey). Beyond this threshold the nucleotide exchange and recruitment rates become control parameters for the spatial distribution of MinD reattachment. At high but finite nucleotide exchange rates the oscillation period increases with the MinD recruitment rate, as MinD reassembles in front of the polar zone. At low nucleotide exchange rates the oscillation period decreases with MinD recruitment, as the pole-to-pole particle transfer becomes canalised between the two cell halves. **B**, Kymographs for $\lambda = 5s^{-1}$ showing the total MinD membrane density, $m_d + m_{de}$, and MinD flux $J_D = D_D \nabla_\perp (c_{DT} + c_{DD})|_m$ on (blue) and off (red) the membrane, for a set of increasing MinD recruitment rates k_{dD}. MinD reaccumulates at the opposite cell pole while the old pole is still present. Increasing MinD recruitment accelerates the growth of new polar zones towards midcell and synchronises depletion and formation of polar zones at opposite cell ends by canalising the MinD flux from old to new polar zones.

Figure 9

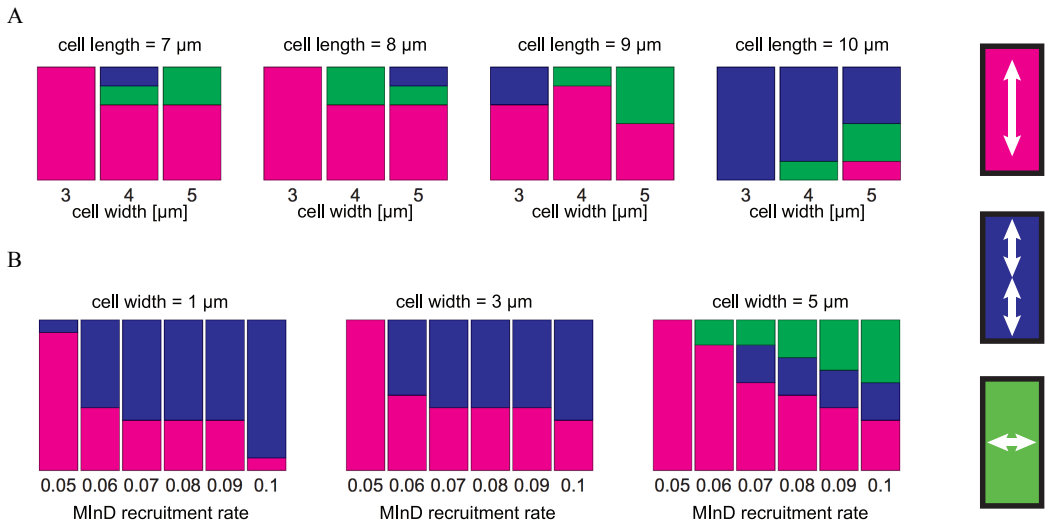

Figure 9. **Basins of attraction predicted from systematic perturbations of patterns with shallow attachment gradients. A,** Relative distribution of the final patterns (indicated on the right) observed after sampling all alignment angles of the MinD attachment template from 0 to 90 degrees. The MinD recruitment rate was set to a constant value $k_{dD} = 0.1$. The data shows the increase in the incidence of multistability as the cell size is increased beyond minimal values for cell length and cell width. **B,** Fractions of the final patterns in cells of 9- and 10-μm length after sampling all alignment angles of the MinD attachment template from 0 to 90 degrees. The data shows that increasing the MinD recruitment rate facilitates multistability. Adpated from [61].

Figure 10

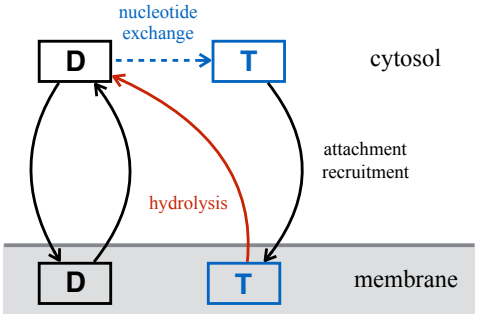

Figure 10. The NTPase can bind to the membrane in both of its states with *attachment rate* k_+, or cooperatively with corresponding *recruitment rates* k_{mD} for D and k_{mT} for T. NTP *hydrolysis* by T triggers *detachment* with rate k_-, converting membrane-bound T into cytosolic D. Membrane-bound D is also spontaneously released to the cytosol with *detachment rate* k_-. Cytosolic D undergoes *nucleotide exchange* with a rate λ.

Figure 11

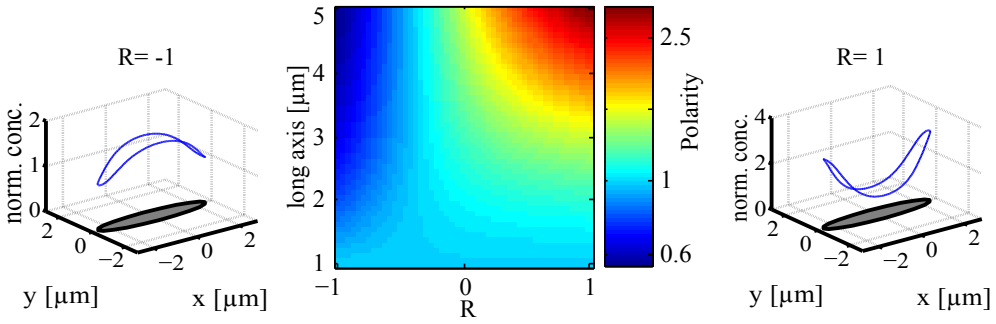

Figure 11. Membrane-bound proteins accumulate either at midcell (left) or form a bipolar pattern with high protein densities at the cell poles (right). The left and right plots show the normalised concentration of the membrane density (blue curve) and the corresponding geometry of the cell (grey ellipse). The membrane density of the protein is divided by its minimum concentration (left: $113\mu\text{m}^{-1}$, right: $100\mu\text{m}^{-1}$) such that the minimum of the normalised density is 1. The polarity $\mathcal{P} = m_{\text{pole}}/m_{\text{midcell}}$ (colour bar in plot is logarithmically spaced) of the pattern strongly depends on cell geometry and preference $\mathcal{R} = (k_{mD} - k_{mT})/(k_{mD} + k_{mT})$ for the recruitment of a certain nucleotide state (middle); the length of the short axis is fixed at $l = 1\,\mu$m, and we have used $k_{mD}+k_{mT} = 0.1\,\mu$m/s. While for large $\mathcal{R}$ (preferential recruitment of D) the proteins form a bipolar pattern on the membrane, the membrane-bound proteins accumulate at midcell for small R (preferential recruitment of T). If the recruitment processes are balanced ($\mathcal{R} = 0$) the pattern is flat and polarity vanishes. The cell geometry determines how pronounced a pattern becomes: The more elongated the ellipse, the more sharply defined the pattern, which vanishes completely when the ellipse becomes a circle.

Figure 12

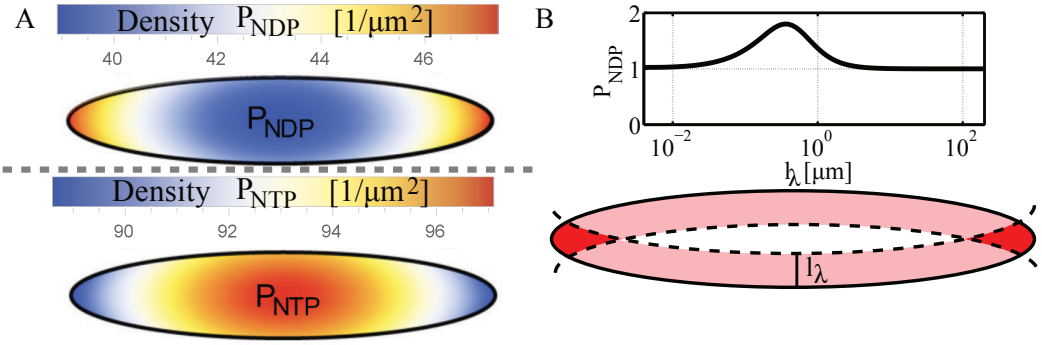

Figure 12. **Membrane affinity controls, and recruitment amplifies adaptation to geometry.** The cells used for the numerical studies have a length of $L = 5\,\mu$m and a width of $l = 1\,\mu$m. **A,** Even when recruitment is turned off, T and D form inhomogeneous density profiles in the cytosol. D accumulates close to the poles and is depleted at mid-cell. In contrast, T exhibits high concentration at mid-cell and a low concentration at the poles. The attachment and detachment rates are set to $1\,\mu$m/s and 1s^{-1}, respectively, which gives a penetration depth $\ell_\lambda \approx 1.6\,\mu$m. **B,** Illustration of the source-degradation mechanism for the spatial segregation of cytosolic D and T. All proteins that detach from the membrane are in an NDP-bound state and can undergo nucleotide exchange, the range of D in the cytosol is limited to a penetration depth ℓ_λ (dashed lines); here $\ell_\lambda = 0.35\,\mu$m. At the poles this reaction volume receives input from opposing faces of the membrane resulting in an accumulation of cytosolic D (dark red). The magnitude of this accumulation depends on the penetration depth. The polarity $\mathcal{P}_{\text{NDP}} = m_d^{\text{pole}}/m_d^{\text{mid-cell}}$ of membrane-bound D plotted as a function of ℓ_λ shows a maximum at $\ell_\lambda \approx 0.35\,\mu$m and vanishes in the limits of large as well as small penetration depths.

Figure 13

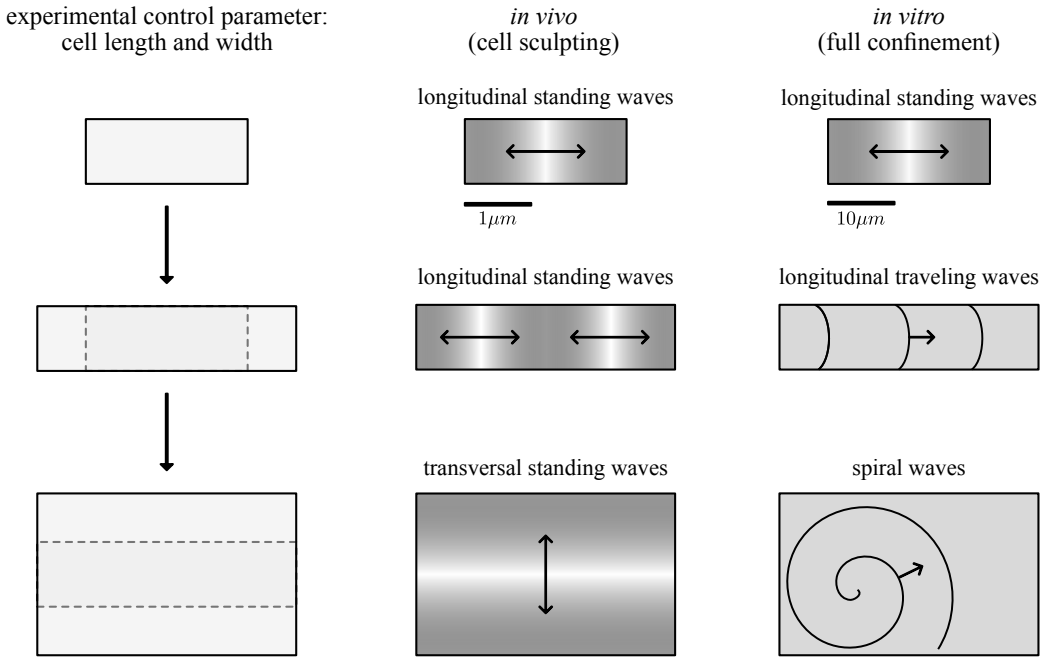

Figure 13. **Min protein patterns *in vivo* vs *in vitro***. Schematic depiction of the phenomenology observed in experiments when the system geometry is changed. For small systems the patterns in reconstituted systems [76] are similar to intracellular dynamics [59], showing pole-to-pole oscillations (with different length scales) in both cases. However, as the system length and width are increased, patterns appear that are not normally seen in vivo.

Figure 14

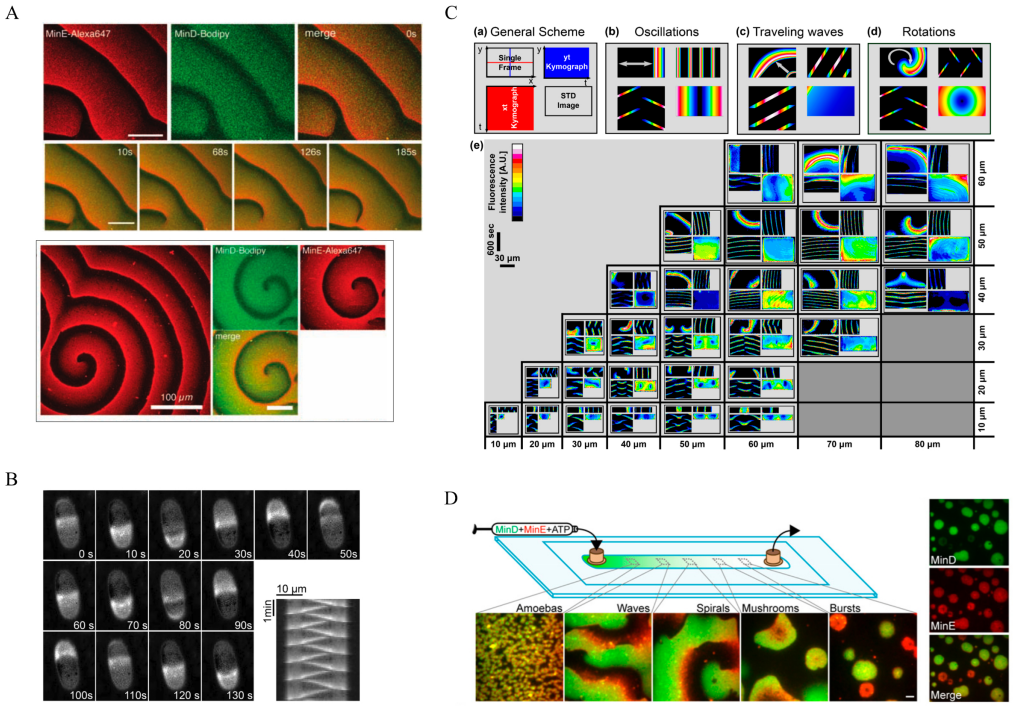

Figure 14. **Min patterns in vitro. A,** Spiral- and travelling-wave patterns observed on flat lipid bilayers. Taken from [71]. **B,** Pole-to-pole oscillations in semi-confined PDMS grooves. Taken from [74]. **C,** Standing waves, travelling waves, and spiral waves observed in fully confined microfluidic chambers with different lateral dimensions. Taken from [76]. **D,** Exotic Min protein patterns on flat lipid bilayers in large laterally extended flow cells showing different phenomenology depending on the distance to the outlet and inlet of the flow cell device. Taken from [88].

[1] R. Thom, *Mathematical models of morphogenesis* (1983).

[2] A. M. Turing, Philosophical Transactions of the Royal Society of London. Series B, Biological Sciences **237**, 37 (1952).

[3] J. Guckenheimer and P. J. Holmes, *Nonlinear Oscillations, Dynamical Systems, and Bifurcations of Vector Fields* (Springer Science & Business Media, 2013).

[4] M. Cross and H. Greenside, *Pattern Formation and Dynamics in Nonequilibrium Systems* (Cambridge University Press, 2009).

[5] R. Wedlich-Soldner, S. Altschuler, L. Wu, and R. Li, Science **299**, 1231 (2003).

[6] M. C. Florian and H. Geiger, Stem Cells **28**, 1623 (2010).

[7] A. J. Molendijk, F. Bischoff, C. S. Rajendrakumar, J. Friml, M. Braun, S. Gilroy, and K. Palme, EMBO J **20**, 2779 (2001).

[8] Y. Gu, V. Vernoud, Y. Fu, and Z. Yang, J Exp Bot **54**, 93 (2003).

[9] N. W. Goehring, P. K. Trong, J. S. Bois, D. Chowdhury, E. M. Nicola, A. A. Hyman, and S. W. Grill, Science (New York, NY) **334**, 1137 (2011).

[10] W. M. Bement, M. Leda, A. M. Moe, A. M. Kita, M. E. Larson, A. E. Golding, C. Pfeuti, K.-C. Su, A. L. Miller, A. B. Goryachev, and G. von Dassow, Nature Cell Biology **17**, 1471 (2015).

[11] A. D. and and T. J. Mitchison, dx.doi.org.emedien.ub.uni-muenchen.de (2003).

[12] L. Reese, A. Melbinger, and E. Frey, Biophysical journal **101**, 2190 (2011).

[13] A. Melbinger, L. Reese, and E. Frey, Physical review letters **108**, 258104 (2012).

[14] D. M. Raskin and P. A. de Boer, Journal of Bacteriology **181**, 6419 (1999).

[15] D. M. Raskin and P. A. de Boer, Proceedings of the National Academy of Sciences **96**, 4971 (1999).

[16] Z. Hu and J. Lutkenhaus, Molecular Microbiology **34**, 82 (1999).

[17] J. Lutkenhaus, Annual review of biochemistry **76**, 539 (2007).

[18] T. H. Szeto, S. L. Rowland, L. I. Rothfield, and G. F. King, Proceedings of the National Academy of Sciences **99**, 15693 (2002).

[19] Z. Hu and J. Lutkenhaus, Molecular Microbiology **47**, 345 (2003).

[20] L. L. Lackner, D. M. Raskin, and P. A. J. de Boer, Journal of Bacteriology **185**, 735 (2003).

[21] E. Mileykovskaya, I. Fishov, X. Fu, B. D. Corbin, W. Margolin, and W. Dowhan, Journal of Biological Chemistry **278**, 22193 (2003).

[22] Z. Hu, A. Mukherjee, S. Pichoff, and J. Lutkenhaus, Proceedings of the National Academy of Sciences **96**, 14819 (1999).

[23] Z. Hu and J. Lutkenhaus, Molecular Cell **7**, 1337 (2001).

[24] Z. Hu, E. P. Gogol, and J. Lutkenhaus, Proceedings of the National Academy of Sciences **99**, 6761 (2002).

[25] K.-T. Park, W. Wu, K. P. Battaile, S. Lovell, T. Holyoak, and J. Lutkenhaus, Cell **146**, 396 (2011).

[26] Y.-L. Shih, K.-F. Huang, H.-M. Lai, J.-H. Liao, C.-S. Lee, C.-M. Chang, H.-M. Mak, C.-W. Hsieh, and C.-C. Lin, PLoS ONE **6**, e21425 (2011).

[27] J. Lutkenhaus, Trends In Microbiology **20**, 411 (2012).

[28] M. Loose and T. J. Mitchison, Nature Cell Biology **16**, 38 (2014).

[29] J. Denk, L. Huber, E. Reithmann, and E. Frey, Physical Review Letters **116**, 178301 (2016).

[30] D. Ramirez, D. A. Garcia-Soriano, A. Raso, M. Feingold, G. Rivas, and P. Schwille, biorxiv (2016).

[31] E. Bi and H.-O. Park, Genetics **191**, 347 (2012).

[32] T. Freisinger, B. Klünder, J. Johnson, N. Müller, G. Pichler, G. Beck, M. Costanzo, C. Boone, R. A. Cerione, E. Frey, and R. Wedlich-Soldner, Nature communications **4**, 1807 (2013).

[33] A. B. Goryachev and A. V. Pokhilko, FEBS Lett. **582**, 1437 (2008).

[34] B. Klünder, T. Freisinger, R. Wedlich-Soldner, and E. Frey, Plos Computational Biology **9**, e1003396 (2013).

[35] I. Bose, J. E. Irazoqui, J. J. Moskow, E. S. Bardes, T. R. Zyla, and D. J. Lew, J. Biol. Chem. **276**, 7176 (2001).

[36] A.-C. Butty, N. Perrinjaquet, A. Petit, M. Jaquenoud, J. E. Segall, K. Hofmann, C. Zwahlen, and M. Peter, EMBO J. **21**, 1565 (2002).

[37] L. Kozubowski, K. Saito, J. M. Johnson, A. S. Howell, T. R. Zyla, and D. J. Lew, Curr. Biol. **18**, 1719 (2008).

[38] F. O. Bendezu, V. Vincenzetti, D. Vavylonis, R. Wyss, H. Vogel, and S. G. Martin, PLoS biology **13** (2015).

[39] L. Laan, J. H. Koschwanez, and A. W. Murray, eLife **4** (2015).

[40] F. Brauns, J. Halatek, L. Laan, and E. Frey,.

[41] B. Goldstein and I. G. Macara, Developmental Cell **13**, 609 (2007).

[42] E. Munro, J. Nance, and J. R. Priess, Developmental Cell **7**, 413 (2004).

[43] N. W. Goehring, Experimental Cell Research **328**, 258 (2014).

[44] R. A. Green, E. Paluch, and K. Oegema, Annual review of cell and developmental biology **28**, 29 (2012).

[45] K. Gerdes, M. Howard, and F. Szardenings, Cell **141**, 927 (2010).

[46] G. Bange and I. Sinning, Nature structural & molecular biology **20**, 776 (2013).

[47] A. Treuner-Lange and L. Søgaard-Andersen, The Journal of Cell Biology **206**, 7 (2014).

[48] J. S. Schuhmacher, K. M. Thormann, G. Bange, and S.-V. Albers, **39**, 812 (2015).

[49] Of course, such a process would also be limited by the duration of protein synthesis.

[50] L. A. Segel and J. L. Jackson, Journal of Theoretical Biology **37**, 545 (1972).

[51] S. Kondo and T. Miura, Science (New York, NY) **329**, 1616 (2010).

[52] K. C. Huang, Y. Meir, and N. S. Wingreen, Proceedings of the National Academy of Sciences of the United States of America **100**, 12724 (2003).

[53] J. Halatek and E. Frey, Cell Reports **1**, 741 (2012).

[54] G. Meacci, J. Ries, E. Fischer-Friedrich, N. Kahya, P. Schwille, and K. Kruse, Physical biology **3**, 255 (2006).

[55] Y.-L. Shih, X. Fu, G. F. King, T. Le, and L. Rothfield, The EMBO journal **21**, 3347 (2002).

[56] In general, a given reaction-diffusion equation can generate a plethora of spatio-temporal patterns, as is well known from classical equations like the complex Ginzburg-Landau equation [90] or the Gray-Scott equation [80–84]. Conversely, a given pattern can be produced by a vast variety of mathematical equations. Hence, one must be careful to avoid falling into the trap: "Cum hoc ergo propter hoc" (correlation does not imply causation).

[57] It should be noted that the condition on the particle numbers mainly serves to emphasise the sequestration mechanism. In order for MinD to accumulate in polar zones the action of MinE must be disabled, and specifying that there are fewer MinE particles permits them to be spatially confined. Outside of this zone MinD can accumulate on the membrane. It has been speculated [53] that other mechanisms, such as transient MinE membrane binding, might provide alternative ways to transiently disable the action of MinE, removing the requirement from the particle numbers. The exact mechanism needs to be investigated in future experiments as well as in the framework of theoretical models.

[58] M. Loose, K. Kruse, and P. Schwille, Annual Review Of Biophysics **40**, 315 (2011).

[59] F. Wu, B. G. C. van Schie, J. E. Keymer, and C. Dekker, Nature Nanotechnology **10**, 719 (2015).

[60] Y.-L. Shih, I. Kawagishi, and L. Rothfield, Molecular Microbiology **58**, 917 (2005).

[61] F. Wu, J. Halatek, M. Reiter, E. Kingma, E. Frey, and C. Dekker, Molecular Systems Biology **12**, 642 (2016).

[62] B. D. Corbin, X.-C. Yu, and W. Margolin, The EMBO journal **21**, 1998 (2002).

[63] A. Touhami, M. Jericho, and A. D. Rutenberg, Journal of Bacteriology **188**, 7661 (2006).

[64] A. Varma, K. C. Huang, and K. D. Young, Journal of Bacteriology **190**, 2106 (2008).

[65] J. Männik, F. Wu, F. J. H. Hol, P. Bisicchia, D. J. Sherratt, J. E. Keymer, and C. Dekker, Proceedings of the National Academy of Sciences of the United States of America **109**, 6957 (2012).

[66] D. Fange and J. Elf, Plos Computational Biology **2**, e80 (2006).

[67] L. D. Renner and D. B. Weibel, The Journal of biological chemistry **287**, 38835 (2012).

[68] This is surprising, because Turing instabilities are generically associated with the existence of a *characteristic* (or intrinsic) wave length in the literature. This is evidently not the case here.

[69] M. Otsuji, S. Ishihara, C. Co, K. Kaibuchi, A. Mochizuki, and S. Kuroda, PLoS Comput. Biol. **3**, e108 (2007).

[70] In 1966 Mark Kac published an article entitled "Can one hear the shape of a drum?"[**?**]. As the dynamics (frequency spectrum) of an elastic membrane whose boundary is clamped is described by the Helmholtz equation $\nabla^2 u + \sigma u = 0$ with Dirichlet boundaries, $\nabla u \mid_\perp = 0$, this amounts to asking how strongly the eigenvalues σ depend on the shape of the domain boundary. Here we ask a much more intricate question, as the dynamics of pattern forming systems is nonlinear and we would like to know the nonlinear attractor for a given shape and size of a cell.

[71] M. Loose, E. Fischer-Friedrich, J. Ries, K. Kruse, and P. Schwille, Science (New York, NY) **320**, 789 (2008).

[72] M. Loose, E. Fischer-Friedrich, C. Herold, K. Kruse, and P. Schwille, Nature structural & molecular biology **18**, 577 (2011).

[73] J. Schweizer, M. Loose, M. Bonny, K. Kruse, I. Mönch, and P. Schwille, Proceedings of the National Academy of Sciences **109**, 15283 (2012).

[74] K. Zieske and P. Schwille, Angewandte Chemie (International ed. in English) **52**, 459 (2013).

[75] K. Zieske, G. Chwastek, and P. Schwille, Angewandte Chemie **128**, 13653 (2016).

[76] Y. Caspi and C. Dekker, eLife **5**, e19271 (2016).

[77] V. Ivanov and K. Mizuuchi, Proceedings of the National Academy of Sciences of the United States of America **107**, 8071 (2010).

[78] K. Zieske and P. Schwille, eLife **3** (2014), 10.7554/eLife.03949.

[79] We note that travelling wave patterns have also been observed *in vivo* [**?**], albeit only upon massive over-expression of MinD and MinE, leading to highly elevated intracellular protein densities and pathological phenomenology [**?**] relative to the wild type. While the exact protein densities in the experiments have not been measured, this observation is consistent with the observation of travelling waves in fully confined compartments, where the protein densities inside microfluidic chambers were also elevated [76]. For further discussion of the effect of protein densities we refer the reader to section .

[80] P. Gray and S. K. Scott, Chemical Engineering Science **38**, 29 (1983).

[81] P. Gray and S. K. Scott, Chemical Engineering Science **39**, 1087 (1984).

[82] P. Gray and S. K. Scott, The Journal of Physical Chemistry **89**, 22 (1985).

[83] J. E. Pearson, Science (New York, NY) **261**, 189 (1993).

[84] K. J. Lee, W. D. McCormick, Q. Ouyang, and H. L. Swinney, Science (New York, NY) **261**, 192 (1993).

[85] J. Halatek and E. Frey, (2017).

[86] Either directly, or by complex formation as for MinDE complexes.

[87] Assuming a cylindrical geometry for simplicity, the volume to surface ratio is $\sim r/2$, i.e. well below $1\,\mu$m for typical cell radii r.

[88] A. G. Vecchiarelli, M. Li, M. Mizuuchi, L. C. Hwang, Y. Seol, K. C. Neuman, and K. Mizuuchi, Proceedings of the National Academy of Sciences of the United States of America **113**, E1479 (2016).

[89] J. Halatek and E. Frey, Proceedings of the National Academy of Sciences **111**, E1817 (2014).

[90] I. Aranson and L. Kramer, Reviews of Modern Physics **74**, 99 (2002).

[91] N. W. Goehring and S. W. Grill, Trends in cell biology **23**, 72 (2013).

Part II

Geometrization

VIII Rethinking pattern formation in reaction-diffusion systems: Moving local equilibria

This chapter is based on the following publication:

Rethinking pattern formation in reaction-diffusion systems

by

J. Halatek and E. Frey

Department of Physics, Arnold Sommerfeld Center for Theoretical Physics and

Center for NanoScience, Ludwig-Maximilians-Universität München,

Theresienstraße 37, 80333 München, Germany

Journal Reference:

***Nature Physics*, 14, 2018**

Supplemental Material reproduced on pages 300 to 381.

Rethinking pattern formation in reaction–diffusion systems

J. Halatek and E. Frey*
Arnold-Sommerfeld-Center for Theoretical Physics and Center for NanoScience, Department of Physics, Ludwig-Maximilians-Universität München, Theresienstraße 37, D-80333 München, Germany

Abstract

The present theoretical framework for the analysis of pattern formation in complex systems is mostly limited to the vicinity of fixed (global) equilibria. Here we present a new theoretical approach to characterize dynamical states arbitrarily far from (global) equilibrium. We show that reaction-diffusion systems that are driven by locally mass–conserving interactions can be understood in terms of local equilibria of diffusively coupled compartments. Diffusive coupling generically induces lateral redistribution of the globally conserved quantities, and the variable local amounts of these quantities determine the local equilibria in each compartment. We find that, even far from global equilibrium, the system is well characterized by its moving local equilibria. We apply this framework to *in-vitro* Min protein pattern formation, a paradigmatic model for biological pattern formation. Within our framework we can predict and explain transitions between chemical turbulence and order arbitrarily far from global equilibrium. Our results reveal conceptually new principles of self-organized pattern-formation that may well govern diverse dynamical systems.

INTRODUCTION

Equilibria and their stability are crucial concepts for the characterization of dynamic systems. The stability of an equilibrium is defined as the response of the system to a perturbation away from an equilibrium position. In pattern-forming systems any perturbation of a spatially uniform equilibrium can be represented by Fourier modes [1]. How the amplitudes of these modes grow or decay is encoded in the growth rates (dispersion relation) of these modes.
For more than two decades the shape of dispersion relations has served as the only general characteristic for the classification of pattern forming systems [2], including Turing instabilities [3], oscillatory media, and hydrodynamic instabilities. However, this characterization, which was introduced by Cross and Hohenberg [2], is meaningful only if the system concerned conforms to certain restrictions. First, the system needs to be near the threshold of the instability, which requires fine-tuning of (control) parameters. Second, the nonlinear interactions are required to have a purely stabilizing effect that keeps the system close to the unstable uniform equilibrium (supercriticality). These restrictions made possible a tremendous advance in the mathematical analysis of pattern attractors and their stability. Unfortunately most real systems are rarely found close to the threshold of an instability. Moreover, catastrophes and discontinuous state changes are quite common in many complex dynamical systems (morphogenesis and cell polarity [4], epidemics, endogenous and exogenous tipping events in climatic [5], economic [6], and ecological [7–9] systems). In such cases, nonlinear interactions amplify deviations from an equilibrium position. They are therefore excluded from the Cross-Hohenberg classification.
Here we propose an alternative approach. Our primary goal is to dissect complex dynamical systems into elementary building blocks that are conceptually accessible, physically well–defined, and likely to reveal some general physical mechanisms underlying self–organization. To this end, we introduce the concept of moving local equilibria. The idea is based on the observation that in mass–conserving systems the available amount of each conserved quantity determines the nature (number, position, and stability) of all equilibria. As these conserved quantities will, generally speaking, not be distributed in a spatially uniform manner, neither will be the corresponding equilibria (Fig. 1A). This suggests that spatially extended systems can best be viewed as being partitioned into local compartments that can be considered as well–mixed reactors, whose individual (local) equilibria are characterized by the respective local values of conserved quantities. This information serves as a proxy for the local dynamics, and the set of all local equilibria across all compartments

characterizes the dynamic state of the whole system.
We show that many self–organization phenomena can be traced back to changes in the positions (and possibly stabilities) of local equilibria, caused by lateral mass redistribution that is facilitated by unstable (Fourier) modes. Further, we find that Turing patterns are scaffolded by patterns of local equilibria. Based on this insight we also reveal the mechanistic connection between Turing instabilities and seemingly unrelated excitability phenomena that arise in the context of cell polarity ("wave-pinning") [10, 11].
Of course, the value of a novel theoretical framework is not only measured by its ability to generalize beyond existing concepts, but also by its predictive power. Therefore, we tested our framework on a concrete model of oscillatory Min protein patterns [12, 13] which, owing to their complex phenomenology [14–17], present a particularly difficult challenge for current theoretical approaches. We show that an analysis based on moving local equilibria quantitatively predicts and mechanistically explains a transition from chemical turbulence to long–range order, in a regime that is far from onset of the instability, but where nonlinearities have a strongly destabilizing effect. Our results indicate that these phenomena are not specific to the Min system, but that (catastrophic) local destabilization is a generic consequence of lateral mass redistribution.

RESULTS

Diffusive coupling moves local equilibria

To illustrate our main conceptual ideas, we consider the simplest possible case, a reaction–diffusion system over a one-dimensional spatial domain for one chemical *species* that is interconvertible between two diffusing *components* a and b:

$$\partial_t a(x,t) = D_a \partial_x^2 a + f(a,b), \tag{1}$$

$$\partial_t b(x,t) = D_b \partial_x^2 b - f(a,b), \tag{2}$$

Here f accounts for all chemical reactions, $a(x,t)$ and $b(x,t)$ are the local densities, and D_a and D_b are the diffusion constants.
Let us first disregard any lateral coupling by diffusion and focus on the local dynamics driven by the chemical reactions encoded in $f(a,b)$ at any point x in space. These reactions conserve the local value of the *total density*, $n_x(t) := a(x,t) + b(x,t)$, which determines the *local phase space* of the system at any

point x in space (see Fig. 1A,B). Within each of these subspaces, the local dynamics are characterised by the positions and stability of the *local equilibria* (a_x^*, b_x^*), determined by $f(a_x^*, b_x^*) = 0$ with $a_x^* + b_x^* = n_x$. If no mass is exchanged laterally the spatial distribution n_x is time independent and so too are the local equilibria.

Now let us add lateral diffusive coupling to the picture. Once the dynamics have reached a stationary state (pattern) $(\tilde{a}(x), \tilde{b}(x))$ (determined by $\partial_t a(x) = 0$ and $\partial_t b(x) = 0$ in Eq. (1), (2)) the diffusive fluxes are balanced, i.e. $0 = D_a \partial_x \tilde{a} + D_b \partial_x \tilde{b}$ (see Methods). This balance of diffusive fluxes confines any stationary pattern to a linear subspace given by $\eta = D_a \tilde{a}(x) + D_b \tilde{b}(x)$ (Fig. 1B, cf. [18]), where η is a constant of integration. Hence, for unequal diffusion constants the mass distribution of the pattern $\tilde{n}_x = \tilde{a}(x) + \tilde{b}(x)$ is incompatible with a spatially uniform mass distribution $n_x = \bar{n}$, where $\bar{n}$ denotes the spatial average of n_x (Fig. 1B). Therefore, the spatial distribution of local equilibria (a_x^*, b_x^*) (determined by n_x) is non–uniform for any pattern $(\tilde{a}(x), \tilde{b}(x))$ as well. How spatial patterns $(\tilde{a}, \tilde{b})$ are related to the local equilibria (a_x^*, b_x^*) is one major question we will address in this article. In this context we study the relation between pattern forming mechanisms and lateral redistribution of the total density n_x.

Since Alan Turing's seminal discovery we know that pattern formation can be self–organized [3]: A spatially uniform and *locally stable* system can become *laterally unstable* such that random fluctuation are amplified, which leads to the growth of certain Fourier modes $\propto e^{\sigma_q t} \cos(qx)$ with *growth rates* $\mathrm{Re}[\sigma_q]$ (the amplitude of the mode $\cos(qx)$ grows for $\mathrm{Re}[\sigma_q] > 0$ and decays otherwise, Fig. 1C).

Here, linear stability analysis (Fig. 1B,C, see Supplementary Section I) reveals that *any* lateral instability with unequal diffusion coefficients (including the Turing instability) endogenously induces lateral redistribution of total density, i.e. $n_x(t) \propto e^{\sigma_q t} \cos(qx)$ (cf. Fig. 1A). Taken together this shows that the displacement of local equilibria by lateral mass redistribution is the key mechanism of self–organized pattern formation in mass–conserved systems. In Supplementary Section II we explain how this mechanism unifies and generalizes excitability ("wave–pinning", [10, 19]) and dynamical instability ("Turing patterns") phenomena which have hitherto been treated as mechanistically distinct in the literature.

From a broader perspective this result immediately suggests a way to dramatically reduce the complexity of large multi–component dynamical systems: If pattern formation can be understood in terms of a displacement of local equilibria, the total densities become the *essential degrees of freedom*, since

these are the only *control variables* that *dynamically* affect the properties of local equilibria. Hence, the essential dynamics of a multi–component system should be captured by the number of control variables (conserved quantities) and their overall effect on local equilibria. We will refer to the space spanned by the control variables as *control space*.

To test this theoretical framework we considered the *in vitro* Min protein system, which is known for its rich phenomenology and has eluded theoretical characterization so far [14, 20]. *In vivo* the proteins MinD and MinE self-organise into standing wave patterns that act as spatial regulators for cell division [21, 22]. *In-vitro* a variety of wave patterns has been observed on supported lipid bilayers [14, 17]. MinD mediates both its own accumulation and that of MinE on the membrane, MinE drives both itself and MinD off the membrane, and cytosolic diffusion facilitates their spatial redistribution. Biochemically the process is driven by ATP consumption [23]. The biochemical reaction circuit contains five chemical components (see Supplementary Information) of the *two globally conserved chemical species*, MinD ($D = [\mathrm{MinD}]/\overline{[\mathrm{MinD}]}$) and MinE ($E = [\mathrm{MinE}]/\overline{[\mathrm{MinE}]}$), both normalised with respect to their time-independent spatial averages $\overline{[\mathrm{MinE}]}$ and $\overline{[\mathrm{MinD}]}$. Since the dynamics involve competition between MinD-driven accumulation and MinE-driven depletion, we use the ratio $\Delta := E/D$ and the sum $\Sigma := \sqrt{\frac{1}{2}(E^2 + D^2)}$ as our set of dynamic control variables, and define a vector-valued amplitude in control space as $\boldsymbol{n}(x,t) = (\Sigma, \Delta)$, with $\overline{\boldsymbol{n}}(x,t) = \big(\Sigma(\overline{E}, \overline{D}), \Delta(\overline{E}, \overline{D})\big) = (1, 1)$.

Onset dynamics is slaved to moving local equilibria

For our analysis we considered the box geometry as used in experimentally reconstituted Min systems [14]. The membrane is located at the bottom of the box, and we use the height h of the cytosolic volume as a control parameter. To begin with, we adjusted the height to a value $h = 20\,\mu m$ just above the point of onset of a lateral instability (of oscillatory Turing type) at $h_{\mathrm{Lat}} \approx 19.85\,\mu m$ (Fig. 2A , see Supplementary Information). In this regime, starting from a spatially uniform protein distribution, our numerical simulations initially showed a standing wave pattern of MinD on the membrane with an exponentially growing amplitude $\overline{A}_{\mathrm{pattern}}$ (Fig. 2B,C, see Methods).

Strikingly, we find that the local distance between the pattern and the local equilibria $\overline{A}_{\mathrm{state}}$ (see Methods) remains constant and small relative to the amplitude of the pattern $\overline{A}_{\mathrm{pattern}}$ (Fig. 2B,C). The standing wave pattern follows the oscillatory time evolution of local equilibria, i.e. $\boldsymbol{u}(x,t) \sim \boldsymbol{u}^*(x,t)$, and

can therefore be identified as a *pattern of local equilibria*. In the Supplementary Material we show that this *scaffolding* of the pattern by local equilibria is a generic property of non-oscillatory patterns in cell polarity models. This further suggests that *scaffolding* is a generic property of (locally stable) mass–conserved dynamics and is not related to specific phenomenology (oscillatory vs. non–oscillatory). In both cases the movement of local equilibria is caused by the lateral redistribution of total density (control variable) stimulated by the lateral instability. This is reflected in the exponential increase of the amplitude $\overline{A}_{\text{control}}$ (Fig. 2C) in *control space* (Σ, Δ).

Loss of structural control induces a transition to chemical turbulence

These findings merely mark the beginning of an intriguing story, for the local equilibria not only shift positions upon variation of the control variables, their stabilities may also change (Fig. 2D). Indeed, our simulations (Fig. 2E) showed that the control variables Σ_x and Δ_x will, at some set (cluster) of points x in space, eventually enter a regime where the moving local equilibria become unstable (dark grey shaded area in Fig. 2D). Concomitantly with this local destabilisation at $t = t_c$, we observe that the distance between the pattern and the moving local equilibria abruptly increases by several orders of magnitude (Fig. 2C, 3A), which precipitates the formation of a propagating wavefront at the cluster position (Fig. 3B, Movie 1). The rear of this wavefront remains structurally within the domain of unstable equilibria as it propagates. Hence, the passage of the front triggers a cascade of transiently destabilized local equilibria throughout the system, which facilitates the formation of additional propagating wavefronts. We observe that all waves finally annihilate each other in aberrant collisions and the dynamics settles into a turbulent state in which the dynamics in control space, the change in local stability, and the dynamics of the observed patterns are spatially uncorrelated (Fig. 3C, Supplementary Figure 3).

Overall, the transition to turbulence shows that the observed dynamics sensitively react to changes in position and stability of local equilibria. This further emphasises that the essential dynamics take place in control space (Σ, Δ); hence, the control variables Σ_x and Δ_x are the essential degrees of freedom.

Establishment of structural control through the lateral instability

In supercritical reaction–diffusion systems nonlinearities have a stabilizing effect that suppresses jumps in amplitude upon lateral destabilization [1, 2]. In these classical cases, turbulence originates from the production of incoherent spatial structures at increasingly shorter length scales due to nonlinear coupling of unstable modes. Here, turbulence only arises far from onset where the band of unstable modes is wide. In contrast, we observe chemical turbulence at the very onset of a lateral instability. In this regime the band of unstable modes is too narrow to facilitate mode coupling and induce turbulence. Instead, the lateral instability is subcritical (see Supplementary Material), such that the inflation in control space (mass redistribution) does not saturate immediately. This allows local equilibria to be destabilized even at onset of the lateral instability, which leads to chemical turbulence. Strikingly, we find that spatially coherent patterns are reestablished far from onset through a concerted interplay between mutually commensurable, unstable modes in control space, as we shall see below.

To keep the discussion of this mechanism clear and concise we restrict the presentation to a conceptual level. However, we emphasise that this conceptual presentation is entirely based on empirical data extracted from systematic simulations (see Supplementary Information).

In the preceding sections we established that the lateral instability drives the spatial redistribution of total mass densities, which in turn act as control variables for the local equilibria (Fig. 1). Increasing the bifurcation parameter h beyond the critical value h_{Lat} broadens the band of unstable modes responsible for mass redistribution (Fig. 4A). Hence, mass redistribution can occur on a broader range of length scales, and we find that a larger average fraction of the system is driven into the locally unstable domain in control space (Fig. 4B, Supplementary Fig. 9A). As the control parameter h passes a critical value $h_{\mathrm{SW}} \approx 23.5\ \mu m$, we observe a transition from chemical turbulence to a spatially coherent standing wave pattern (Fig. 4C, Movie 2). Strikingly, this transition occurs when the unstable mode q_{max} with the shortest wavelength becomes commensurable with the critical (fastest growing) mode q_c, i.e. when $q_{\mathrm{max}} = 2q_c$ (Fig. 4D, bottom right).

For $h > h_{\mathrm{SW}}$, we find that two unstable commensurable modes q_c and $q_r = 2q_c \geq q_{\mathrm{max}}$ have distinct but interdependent roles in the establishment of global coherence: The critical mode q_c coordinates synchronised destabilisation of local equilibria at distances $l_c = 2\pi/q_c$ (see $t = t_1$ in Fig. 4D). Upon local destabilisation the dynamics undergo a large amplitude excursion in control

space (Supplementary Fig. 9B), first accumulating, then releasing mass synchronously at distances l_c. We know that redistribution of mass is mediated by unstable modes. Assume that this mass is redistributed symmetrically to the left and right of each cluster at a distance $l < l_c/2$ ($t = t_1$ in Fig. 4D). This directional redistribution will lead to the formation of wavefronts propagating away from their source towards points of mutual annihilation in collisions midway between the original sources ($t = t_2$ in Fig. 4D). The mass contained in the propagating wavefronts, i.e. the mass that has been accumulated during the original excursion, is released again in the annihilation event at a distance $l_c/2$ from the original cluster ($t = t_3$ in Fig. 4D). If this mass is again redistributed symmetrically to the left and right of each cluster by the distance $l < l_c/2$, it will return to its origin and complete the cycle ($t = t_4$ in Fig. 4D). To achieve this synchronised redistribution of released mass, the mode redistributing mass q_r must be commensurable with the distance between mass sources, i.e. $q_r = 2q_c$. In this case the length scale of mass redistribution is $l_r/2 = \pi/q_r$. Our simulations show that the transition to standing waves occurs when the commensurable mode becomes unstable. Additionally, we find that mass redistribution takes place on a well defined length scale $l_r/2$ throughout the standing wave regime (Fig. 4D, Supplementary Section 8). The scenario outlined here is further supported by the observation of phase-slip defects in the vicinity of the commensurable–incommensurable transition (Supplementary Section 8).

The observed emergence of order due to destabilization of additional modes is in stark contrast to the classical case where turbulence originates from mode coupling [2]. However, it is not unusual for chaotic systems to become regular if external driving is strong enough (cf. the prominent chaotic waterwheel [24]); indeed, this effect is utilized in control theory [25]. In that case, the control of chaotic dynamics is based on external forcing, but our results demonstrate that such control can emerge endogenously as a new mechanism for self–organisation.

A chimera state marks the transition from short to long-range correlated patterns

So far we have identified regimes and mechanisms for chemical turbulence and standing–wave patterns. *In-vitro* experiments performed at large bulk heights $h \approx 5\ mm$ show travelling-, and spiral-wave patterns [14] . Such patterns are generic phenomena observed in oscillatory media. Indeed, if we

increase h beyond a certain point $h_{\mathrm{Loc}} \approx 37\ \mu m$ all local equilibria become oscillatory unstable (Fig. 4A,B) in the uniform state, i.e. the system becomes an oscillatory medium. Accordingly, simulations of the 3D system with a large bulk height (e.g. $h = 100\ \mu m \gg h_{\mathrm{Loc}}$) reproduce the experimentally observed wave patterns (Fig. 5A, Movie 3).

In fact, the standing wave pattern discussed in the last section arises because source defects periodically emit propagating wavefronts. However, in this regime mass sources were depleted after emitting a single pair of propagating wavefronts, such that the local equilibria remain non–oscillatory until the arrival of the returning wavefronts (Fig. 4D). Surprisingly, at a bulk height $h_{\mathrm{TW}} = 33\ \mu m$ (well below the threshold h_{Loc} where the system becomes an oscillatory medium globally), our simulations show that a single source defect remains oscillatory after emitting wavefronts (Fig. 5B, Movie 4). This enables the source to emit a periodic band of travelling waves, which expands into the domain of the standing waves. Since this expansion occurs on a time scale much longer than the local oscillation period (Fig. 5C), the whole pattern is an example of a chimera state [26, 27], with long-range correlated oscillators in the travelling–wave phase, and short-range correlated oscillators in the standing wave phase. In contrast to the sources in the standing wave regime, the source of travelling waves redistributes mass on a length scale $l_c/2$ set by the defect control mode q_c (Fig. 5D,E, cf. Fig. 1B,4D). This length scale therefore sets the wavelength of the travelling and spiral waves which we observe for $h > h_{\mathrm{TW}}$ (Fig. 5F). The matching of these length scales suggests that the experimentally observed patterns are based on the spatiotemporal control of local stability. Moreover, the *in-vitro* patterns are based on local oscillations, and therefore mechanistically distinct from the (Turing) patterns observed *in vivo* (see Supplementary Material).

Finally we note that the dispersion relation assumes all forms listed in the Cross-Hohenberg classification as the control parameter h is increased from $h < h_{\mathrm{Loc}}$ (Type I) through $h = h_{\mathrm{Loc}}$ (Type II) to $h > h_{\mathrm{Loc}}$ (Type III), yet the phenomenology remains invariant. In the Supplementary Material we discuss how a control space analysis for ($h > h_{\mathrm{Loc}}$) identifies the local dynamics as relaxation oscillations and, in turn, suggests a mechanistic connection between patterns in the Min protein and the CO–Pt system [28–30].

DISCUSSION

Taken together, these results indicate that local equilibria and their dynamics constitute elementary concepts in a theory of complex dynamical systems driven by mass–conserving interactions. This encompasses chemical systems based on cyclical state changes such as biochemical reaction networks driving intracellular dynamics, and could potentially be extended to catalytic surface reactions with a conserved number of binding sites (cf. our discussion in the Supplement). We also note that lateral coupling is not limited to spatial coupling but can be extended to general network topologies.
Our findings also offer unexpected insight into possible causes of spatiotemporal chaos (chemical turbulence) and mechanisms for its control. The origin of chemical turbulence and its control can both be linked to an endogenous destabilization of local equilibria due to lateral coupling. These mechanisms are surprisingly distinct from known causes of weak or fully developed turbulence, but due to their generic origin (redistribution of mass) they could apply in many complex systems.

ACKNOWLEDGMENTS

This research was supported by the German Excellence Initiative via the program 'NanoSystems Initiative Munich', and by the Deutsche Forschungsgemeinschaft (DFG) via project B02 within the SFB 1032 "Nanoagents for Spatio-Temporal Control of Molecular and Cellular Reactions". The authors thank Fridtjof Brauns, Cees Dekker, and Greg Pawlik for detailed feedback on the manuscript. We thank Fridtjof Brauns, Jonas Denk, and Dominik Thalmeier for many helpful discussions. We thank Fridtjof Brauns for his preliminary work on the CO-Pt system, which has significantly advanced our understanding of the mass-redistribution framework presented here.

METHODS

Glossary

Chemical species: A chemical that is conserved in chemical reactions, e.g. a protein.
Chemical component: A state of a chemical species that is susceptible to

change in chemical reactions, e.g. the conformation of a protein.
Total density/mass: The summed density of all components of a chemical species. The average total density is conserved, while the local total density can change though lateral mass redistribution.
Control space: The space spanned by the total densities of a system. Its dimension equals the number of conserved species.
Control variable: A spatiotemporal variable that represents a coordinate of control space and specifies the values of the local total densities at any point in space and time.
Control parameter: Any system parameter that does not change endogenously (in contrast to control variables) but is set by the microscopic physics (kinetic rates, diffusion coefficients) or by the experimentalist (system size, average total densities).
Local equilibria: The chemical equilibria at any fixed point in time and space considered as a spatially isolated (and well-mixed) subsystem. Determined by the local total densities.
Local stability: The linear stability of local equilibria with respect to perturbations that do not change the local total densities.
Lateral stability: The linear stability of a spatially uniform state with respect to non-uniform spatial perturbations.
Turing instability: A lateral instability of a locally stable uniform state that arises as a consequence of diffusive coupling.

Subspace of the stationary pattern

We set the left-hand sides of Eq.1 and 2 to zero and add the two equations to obtain

$$0 = D_a \partial_x^2 a + D_b \partial_x^2 b. \tag{3}$$

Integration shows that the stationary state is characterized by a balance of diffusive fluxes $0 = D_a \partial_x \tilde{a} + D_b \partial_x \tilde{b}$. Another integration shows that the pattern is confined to a subspace $\eta = D_a \tilde{a}(x) + D_b \tilde{b}(x)$, where η is a constant of integration.

Amplitudes

In the following we define the three amplitudes $A_{\text{pattern}}(x,t)$, $A_{\text{control}}(x,t)$, and $A_{\text{state}}(x,t)$ used to characterize the dynamics. For illustration purposes the

definitions are given here for the general two-component model. The specific definitions for the Min system can be found in the Supplementary Information. The three amplitudes reveal how the observed pattern, the movement of local equilibria, and the dynamics in control space are interrelated. The "classical" amplitude of the pattern

$$A_{\text{pattern}}(x,t) = \|\boldsymbol{u}(x,t) - \overline{\boldsymbol{u}}(x,t)\|, \tag{4}$$

denotes the euclidian distance between the concentration vector $\boldsymbol{u}(x,t) = \Big[a(x,t) \ , \ b(x,t)\Big]^T$ and the vector that represents the spatial averages of all concentrations $\overline{\boldsymbol{u}}(t) = \Big[\bar{a}(t) \ , \ \bar{b}(t)\Big]^T$.
Similarly, we define the amplitude in control space

$$A_{\text{control}}(x,t) = \|n(x,t) - \overline{n}\|, \tag{5}$$

as the local distance between the control variable and its (conserved) spatial average. For systems with multiple conserved species (such as the Min system) the control variables will be combined into a vector and the distance is defined analogously to $A_{\text{pattern}}(x,t)$.
Finally, we trace the local distances between the concentration $\boldsymbol{u}(x,t)$ and the local equilibria $\boldsymbol{u}^*(x,t) = \Big[a^*(x,t) \ , \ b^*(x,t)\Big]^T$:

$$A_{\text{state}}(x,t) = \|\boldsymbol{u}(x,t) - \boldsymbol{u}^*(x,t)\|. \tag{6}$$

FIGURES

Figure 1

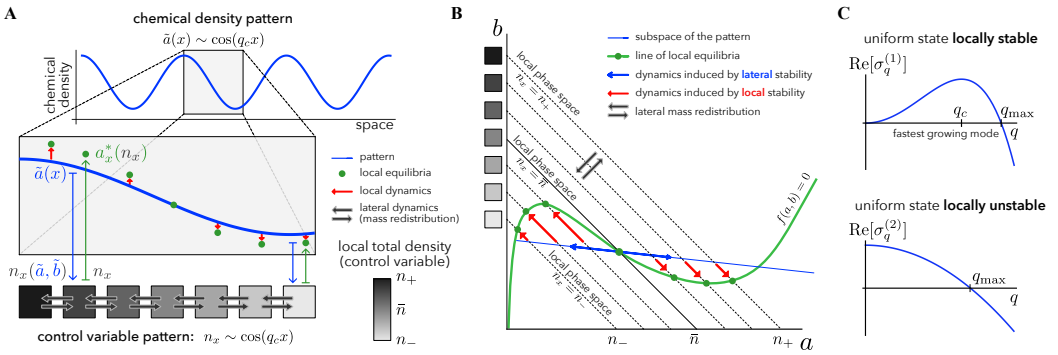

FIG. 1.

A, A schematic of the compartmentalization concept: Any multi–component pattern $\big(\tilde{a}(x), \tilde{b}(x)\big)$, here represented by $\tilde{a}(x)$ (blue line) can be spatially decomposed in its local equilibria (a_x^*, b_x^*) (green dots). If all local equilibria are stable, the pattern is *scaffolded* by the pattern of local equilibria, i.e. the pattern is locally driven (red arrows) towards the pattern of local equilibria. The local total density $n_x = \tilde{a}(x) + \tilde{b}(x)$ is the only quantity that *dynamically controls* the properties (position and stability) of local equilibria. The essential dynamics of the pattern forming process are therefore encoded in the spatio-temporal variation of the *control variable* n_x. **B**, A schematic projection onto the *global phase space* (a, b) of two-component reaction-diffusion systems (Eq. 1,2). At each point in space x and time t the local dynamics (red arrows) are restricted to the *local phase spaces* $n_x(t) := a(x,t) + b(x,t)$ (cf. Fig. 1A). A representative line of local equilibria $(f(a,b) = 0)$ is shown in green. It can be seen that for any typical $f(a,b)$ the positions of local equilibria change as $n_x(t)$ is varied. All stationary patterns are confined to the subspace $\eta = D_a\tilde{a}(x) + D_b\tilde{b}(x)$ (blue line) which is spanned by the unstable mode $q_{\max}$ (blue arrow) for dispersion relations of any type (Fig. 1C, cf. supplementary material). **C**, Top: Schematic dispersion relations $\max(\mathrm{Re}[\sigma_q^{(1,2)}])$ for lateral instabilities with locally stable (top, $\mathrm{Re}[\sigma_{q=0}^{(2)}] < \mathrm{Re}[\sigma_{q=0}^{(1)}] = 0$) and unstable (bottom, $\mathrm{Re}[\sigma_{q=0}^{(2)}] > \mathrm{Re}[\sigma_{q=0}^{(1)}] = 0$) steady state; q_c denotes the fastest growing mode and $q_{\max}$ the growing mode with the shortest wavelength. The detailed definitions of these quantities are given in the Supplementary Material.

Figure 2

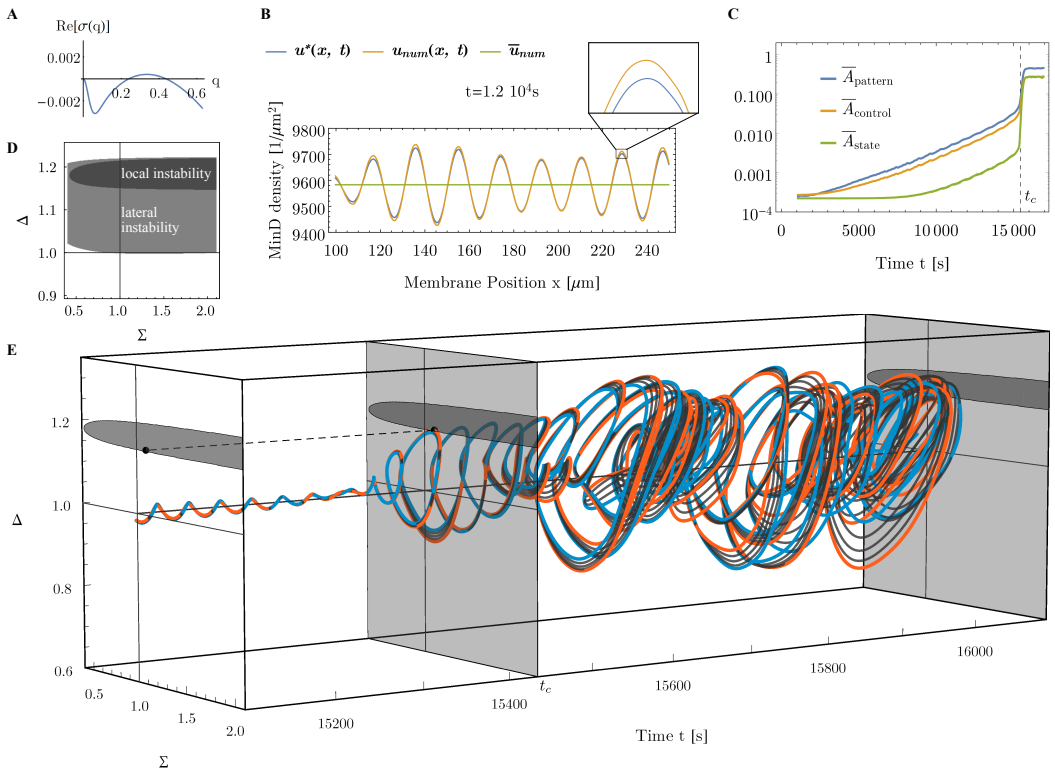

FIG. 2.

A, Dispersion relation for the Min system model at the onset of the lateral instability (oscillatory, Turing) at $h = 20\ \mu m$; note that only the real part of the largest eigenvalue is shown.
B, A section of the standing wave pattern of membrane-bound MinD at $t = 1.2 \cdot 10^4\ s$. Total system size is 500 μm with periodic boundary conditions. We observe that the densities $u_{\text{num}}(x,t)$ (the subscript indicates that this data is extracted from the numerical simulation) are closely tied to their local equilibria $u^*(x,t)$ (the exact definition of u^* from u_{num} is provided in the Supplementary Information).
C, Time evolution of the spatially averaged amplitudes $A_{\text{pattern}}(x,t)$, $A_{\text{state}}(x,t)$, and $A_{\text{control}}(x,t)$. As implied by the data in Fig. 2B, the distances to the local equilibria are small compared to the amplitudes of the pattern and the control variables, i.e. $\overline{A}_{\text{state}} \ll \overline{A}_{\text{pattern}} \sim \overline{A}_{\text{control}}$, until all amplitudes undergo a sudden jump at $t = t_c = 15434\ s$. This shows that the dynamics of all densities are globally slaved to the time evolution of the local equilibria set by

the evolution of the control variables Σ and Δ.
D, Stability diagram of the system in control space (Σ, Δ) at $h = 20\ \mu m$ (see the Supplementary Information for the underlying computation). All values are normalised to the global averages used in the simulations (all parameter values are listed in the Supplementary Information). The grey areas highlight all laterally unstable configurations, with the global average being locally stable (Turing-type instability) in the light grey area, and locally unstable (oscillatory medium) in the dark grey area. Here, the global average is at the onset of a Turing-type instability (see Fig. 2A).
E, Trajectories of the control variables (Σ, Δ) at five adjacent ($\Delta x = 0.2\ \mu m$) and fixed points in space during the transition through the jump at $t = t_c$. The two outer trajectories are highlighted in orange ($x = 90\ \mu m$) and blue ($x = 91\ \mu m$), the trajectories in-between in black. For $t < t_c$ all trajectories are entrained and the corresponding local equilibrium remains in the stable regime. At $t = t_c$, all five trajectories enter the locally (oscillatory) unstable regime (dark grey) for the first time. From this point onward, their trajectories begin to diverge from each other, and their amplitude in control space $A_{\text{control}}(x, t)$ becomes large and irregular.

Figure 3

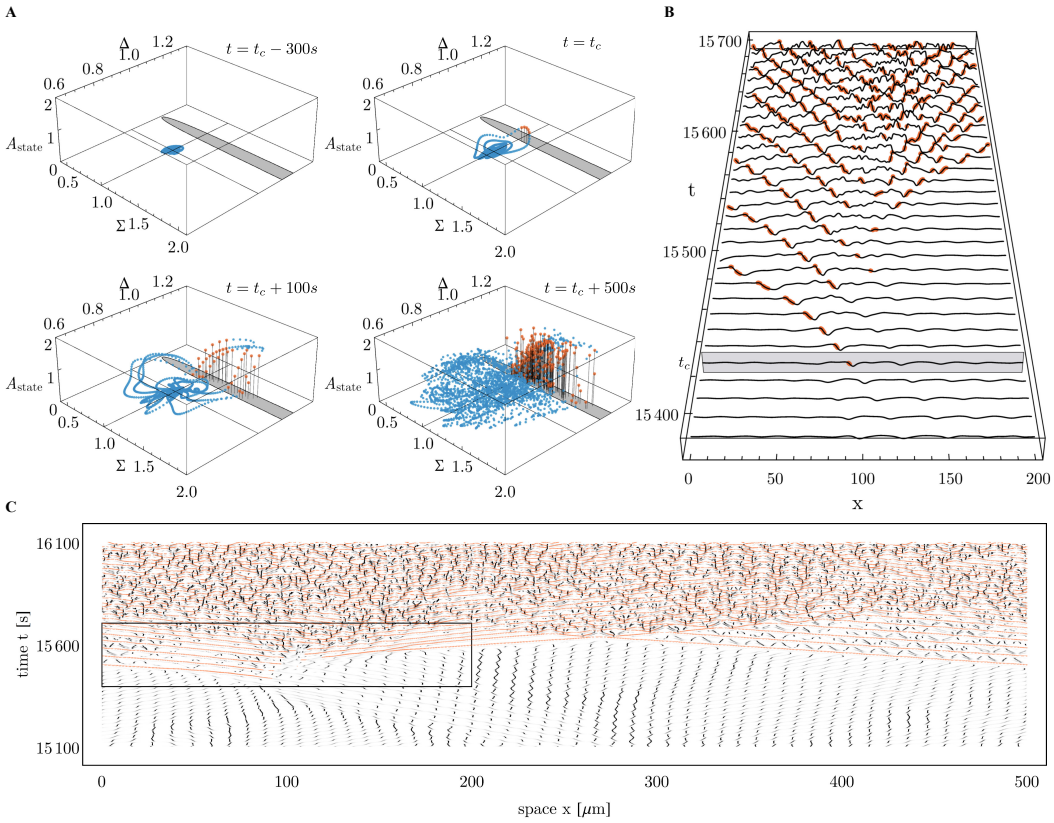

FIG. 3.

A, Distribution of the whole simulated system (system size 500 μm, sampling $\Delta x = 0.2\ \mu m$) in control space (Σ, Δ) and corresponding distances to local equilibria $A_{\text{state}}(x,t)$ before, at, and after the jump at $t = t_c$. The stability of the local equilibria is encoded by the color, orange for unstable spirals, blue for stable spirals. $A_{\text{state}}(x,t)$ immediately increases by several orders of magnitude as a local reactor enters the regime of local instabilities. This supports our proposed notion of local stability. The final state is characterised by a broad distribution in control space.

B, Section of the density profiles of membrane-bound MinD during the transition at $t = t_c$. All points with locally unstable equilibria are highlighted as red dots. Local destabilisation leads to the formation of laterally propagating wavefronts that leave behind a spatially increasingly disordered pattern.

C, Kymograph showing the correlation of the time series ($T = 10\ s, \Delta t = 1\ s$) of spatially adjacent MinD membrane signals ($\pm\Delta x = 0.2\ \mu m$) for the whole system (see the Supplementary Information for the underlying definitions). Correlation is indicated in greyscale with black indicating no correlation, i.e. stationary signals on the timescale T. Spatial disorder originates from the sources and sinks of local instability highlighted in orange. The inset highlights the section shown in Fig. 3B.

Figure 4

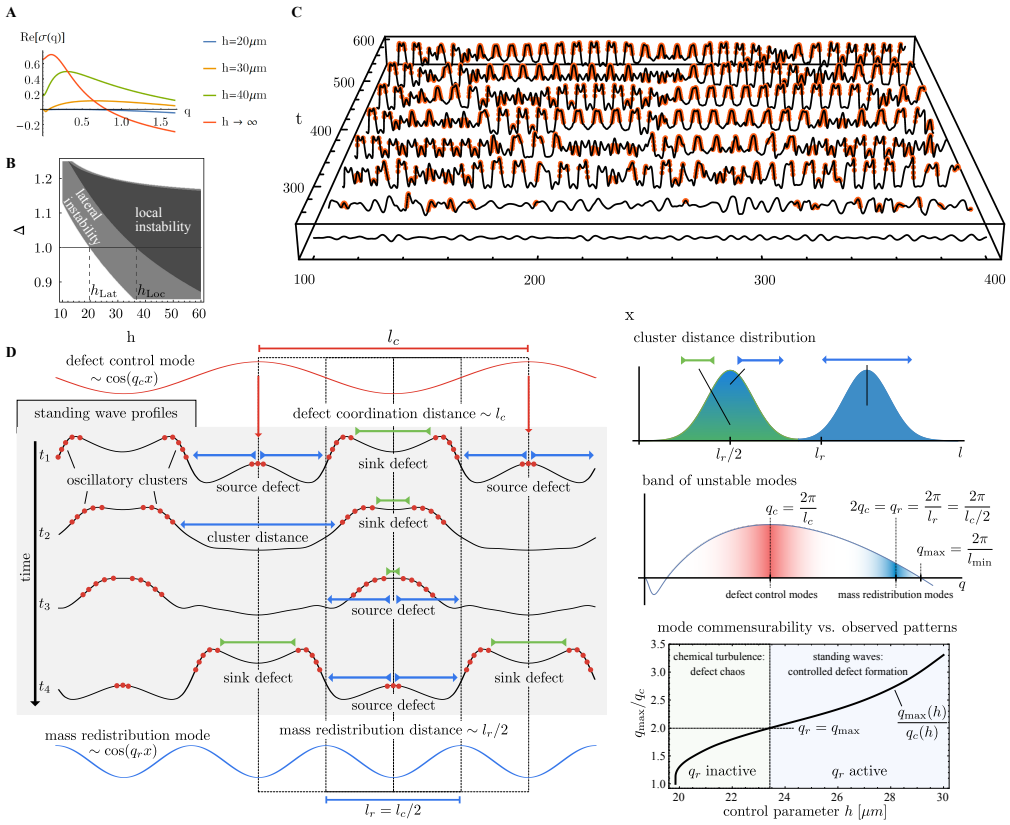

FIG. 4.

A, Dispersion relations for increasing bulk height h, showing the destabilisation of the zero mode and the preservation of the finite sized critical mode q_c as $h \to \infty$.
B, Stability diagram of the system in (Δ, h) space, with $\Sigma = 1$ kept constant. As h increases, the regime of local instability (dark grey) approaches the spatial average $\Delta = 1$ until the uniform system becomes locally unstable at $h = h_{\mathrm{Loc}}$ (zero mode instability in Fig. 4A). The diagram shows that Δ and h have similar effects on local and lateral stability.
C, Sections of the MinD membrane profile with clusters of locally unstable equilibria highlighted as red dots, showing the emergence of a standing-wave pattern for $h = 25\ \mu m$ (source-sink defect cycle) starting from a spatially uniform initial condition (at $t = 0\ s$, not shown).

D, Schematic representation of the mechanism that establishes spatially coherent standing wave patterns. Left: Schematic standing-wave profiles for successive time steps, overlaid with the defect control mode $\sim \cos(q_c x)$ (red, top) and the mass redistribution mode $\sim \cos(q_r x)$ (blue, bottom). Both control modes are defined in the schematically represented dispersion relation (right, middle). Red dots indicate clusters of local oscillatory unstable equilibria. Blue unidirectional arrows indicate distances of mass redistribution as indicated by cluster distances. Bidirectional arrows indicate distances between clusters that move away from (blue arrows) or towards (green arrows) each others. The length scales corresponding to different arrows can be inferred from the distribution statistics of cluster distances as schematically represented in the histogram (top right). The corresponding simulation data can be found in the Supplementary Material. In the bottom right Figure we plot the mode commensurability $q_{\min}/q_c$ as a function of the control parameter h. Comparison with the simulation data (coloured background) shows that the transition from chemical turbulence to spatially coherent standing waves coincides with the activation of the commensurable mode q_r.

Figure 5

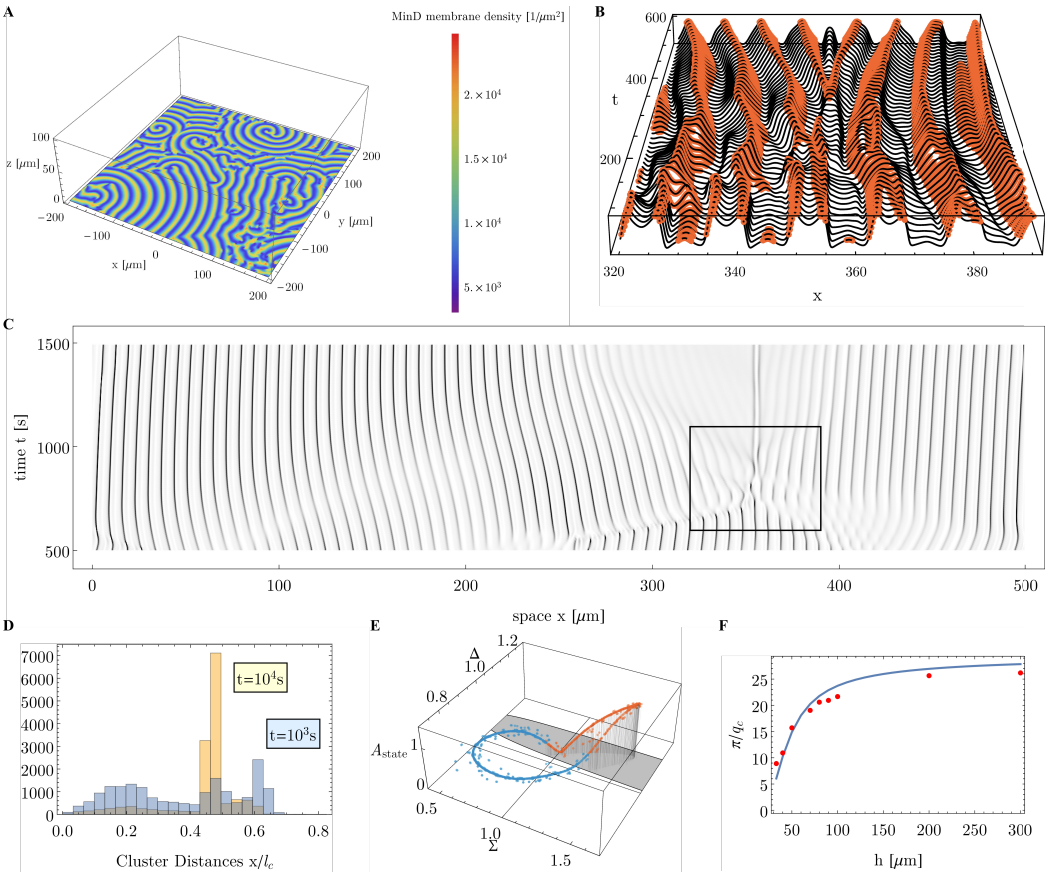

FIG. 5.

A, Snapshot ($t = 1.2 \cdot 10^3\ s$) of the simulation in full three-dimensional box geometry for $h = 100\ \mu m$ showing spiral- and travelling wave patterns on the two-dimensional membrane.
B, Sections of the MinD membrane profile with clusters of locally unstable equilibria highlighted as red dots, showing the transition from the standing-wave pattern (source-sink defect cycle) to a travelling wave pattern (maintained central source defect) for $h = 33\ \mu m$.
C, Kymograph with the correlation of adjacent MinD membrane signals (c.f. Fig. 3C, 4E) at $h = 33\ \mu m$, showing the chimera transition from standing-wave patterns to travelling waves. Black lines show the positions of stationary standing wave nodes, the blank area the domain of (uniformly correlated) travelling waves with the maintained source defect at the center. The inset

highlights the section shown in Fig. 5B.
D, Histogram with the distance-distribution of local instability clusters for $h = 33\ \mu m$. Distance is rescaled to the length scale set by the fastest growing mode $q_c = 2\pi/l_c$. The data shows that the travelling wave pattern consists of instability clusters separated by a sharply defined distance that corresponds to the length scale of control variable transport set by the fastest growing mode π/q_c (c.f. Fig 1A).
E, Distribution of the whole system in control space (Σ, Δ) and corresponding distances to local equilibria $A_{\text{state}}(x,t)$ (c.f. Fig. 3A) for $h = 33\ \mu m$ at $t = 40^4\ s$. With the formation of travelling waves the distribution of the whole system condenses on a sharply defined two-dimensional circle in control space (Σ, Δ) with only the point corresponding to the remaining source and sink defect lying outside.
F, Comparison of the wavelengths extracted from simulations (red dots) with the length scale π/q_c set by the lateral instability for the respective bulk height h. The data shows that the length scale set by the lateral instability controls the pattern for any h outside the turbulent regime, i.e. the lateral instability sets the length scale arbitrarily far away from onset but not at onset $h \approx 20\ \mu m$.

* frey@lmu.de

[1] M. Cross and H. Greenside, *Pattern Formation and Dynamics in Nonequilibrium Systems* (Cambridge University Press, 2009).

[2] M. Cross and P. Hohenberg, Reviews of modern physics **65** (1993).

[3] A. M. Turing, Philosophical Transactions of the Royal Society of London. Series B, Biological Sciences **237**, 37 (1952).

[4] P. Bourgine and A. Lesne, *Morphogenesis : origins of patterns and shapes* (Springer, 2011).

[5] P. J. Menck, J. Heitzig, N. Marwan, and J. Kurths, Nature Physics **9**, 89 (2013).

[6] S. Gualdi, M. Tarzia, F. Zamponi, and J. P. Bouchaud, Journal of Economic Dynamics and Control **50**, 29 (2015), arXiv:1307.5319.

[7] M. Scheffer, S. Carpenter, J. a. Foley, C. Folke, and B. Walker, Nature **413**, 591 (2001).

[8] L. Dai, K. S. Korolev, and J. Gore, Nature **496**, 355 (2013).

[9] M. Anstey, S. Rogers, S. Ott, M. Burrows, and S. Simpson, Science , 627 (2009).

[10] Y. Mori, A. Jilkine, and L. Edelstein-Keshet, Biophysical journal **94**, 3684 (2008).

[11] P. K. Trong, E. M. Nicola, N. W. Goehring, K. V. Kumar, and S. W. Grill, New Journal of Physics **16** (2014).

[12] K. C. Huang, Y. Meir, and N. S. Wingreen, Proceedings of the National Academy of Sciences of the United States of America **100**, 12724 (2003).

[13] J. Halatek and E. Frey, Cell reports **1**, 741 (2012).

[14] M. Loose, E. Fischer-Friedrich, J. Ries, K. Kruse, and P. Schwille, Science (New York, N.Y.) **320**, 789 (2008).

[15] F. Wu, B. G. C. van Schie, J. E. Keymer, and C. Dekker, Nature Nanotechnology (2015).

[16] F. Wu, J. Halatek, M. Reiter, E. Kingma, E. Frey, and C. Dekker, Molecular Systems Biology **12**, 642 (2016).

[17] Y. Caspi and C. Dekker, eLife **5**, 1 (2016).

[18] S. Ishihara, M. Otsuji, and A. Mochizuki, Physical Review E **75** (2007), 10.1103/PhysRevE.75.015203.

[19] Y. Mori, A. Jilkine, and L. Edelstein-Keshet, SIAM Journal on Applied Mathematics **71**, 1401 (2011).

[20] J. Halatek and E. Frey, Proceedings of the National Academy of Sciences **111** (2014), 10.1073/pnas.1220971111.

[21] D. M. Raskin and P. a. de Boer, Proceedings of the National Academy of Sciences of the United States of America **96**, 4971 (1999).

[22] S. Kretschmer and P. Schwille, Current Opinion in Cell Biology **38**, 52 (2016).

[23] J. Lutkenhaus, Annual review of biochemistry **76**, 539 (2007).

[24] S. H. Strogatz, *Westview Press* (1994).

[25] E. Schöll and H. G. Schuster, *Handbook of Chaos Control*, 2nd ed. (Wiley-VCH, 2008).

[26] Y. Kuramoto and D. Battogtokh, Nonlinear Phenomena in Complex Systems **5**, 380 (2002).

[27] D. M. Abrams and S. H. Strogatz, Physical Review Letters **93** (2004).

[28] G. Eigenberger, Chemical Engineering Science **33**, 1263 (1978).

[29] M. Kim, M. Bertram, M. Pollmann, a. von Oertzen, a. S. Mikhailov, H. H. Rotermund, and G. Ertl, Science (New York, N.Y.) **292**, 1357 (2001).

[30] A. S. Mikhailov and K. Showalter, Physics Reports **425**, 79 (2006).

Rethinking pattern formation in reaction–diffusion systems - Supplementary Document

J. Halatek and E. Frey*
Arnold Sommerfeld Center for Theoretical Physics and Center for NanoScience, Department of Physics, Ludwig-Maximilians-Universität München, Theresienstraße 37, D-80333 München, Germany

* frey@lmu.de

CONTENTS

I. TWO-COMPONENT REACTION-DIFFUSION MODEL

To illustrate our main ideas and to place our exposition in a sufficiently general framework, we consider the simplest possible reaction-diffusion system: a chemical system comprises two chemical components A and B confined to a finite one-dimensional domain of length L. Let $a(x,t)$ and $b(x,t)$ denote the local densities of components A and B, respectively. We are interested in dynamical systems that conserve the total mass $N = \int n_x(t)\,dx$, where $n_x(t) := a(x,t) + b(x,t)$ is the local value of the *total mass density*. Our goal in this supplementary section is to show that lateral instabilities generically induce mass redistribution and thereby shift local equilibria. The most general reaction-diffusion equation describing such a dynamics reads

$$\partial_t a = D_a \partial_x^2 a + f(a,b)\,, \tag{1a}$$

$$\partial_t b = D_b \partial_x^2 b - f(a,b)\,, \tag{1b}$$

where the function $f(a,b)$ accounts for all chemical reactions, and D_a and D_b are the diffusion constants of the chemical components A and B, respectively. The boundary conditions can be open, periodic, no-flux, or Dirichlet type.

A. Dynamics without diffusive coupling

For a *well-mixed system*, the dynamics reduces to

$$\partial_t a = f(a,b)\,, \tag{2a}$$

$$\partial_t b = -f(a,b)\,, \tag{2b}$$

with spatially uniform densities $a(t)$ and $b(t)$. The equilibria (fixed points) of the reactive dynamics, a^* and b^*, are given by the stationarity condition $f(a^*,b^*)=0$ supplemented by the mass conservation constraint $a^* + b^* = \bar{n}$, where $\bar{n} = N/L$ is the invariant total mass density. To study the *linear stability* of these equilibria one defines the displacement vector $\delta\boldsymbol{a} = \begin{bmatrix} a-a^* & , & b-b^* \end{bmatrix}^T$, and considers the linearised system corresponding to Eq. (2),

$$\partial_t\, \delta\boldsymbol{a} = \mathcal{J}\, \delta\boldsymbol{a}\,, \tag{3}$$

with the Jacobian given by

$$\mathcal{J} = \begin{bmatrix} f^a & f^b \\ -f^a & -f^b \end{bmatrix}, \tag{4}$$

where $f^a := \frac{\partial f}{\partial a}|_{(a^*,b^*)}$ and $f^b := \frac{\partial f}{\partial b}|_{(a^*,b^*)}$ are the first order Taylor coefficients evaluated at the fixed point (a^*, b^*). With the ansatz $\delta\boldsymbol{a}(t) = \mathrm{e}^{\sigma t}\,\boldsymbol{e}$ one finds the eigenvalues

$$\sigma^{(1)} = 0\,, \tag{5a}$$

$$\sigma^{(2)} = f^a - f^b\,, \tag{5b}$$

and the corresponding eigenvectors,

$$\boldsymbol{e}^{(1)} = \Big[-f^b/f^a \;,\; 1\Big]^T\,, \tag{6a}$$

$$\boldsymbol{e}^{(2)} = \Big[-1 \;,\; 1\Big]^T\,. \tag{6b}$$

The first eigenpair defines a *center space*, where the eigenvector $\boldsymbol{e}^{(1)}$ is tangent to the line of fixed points given by $f(a, b) = 0$, which explains why the associated eigenvalue $\sigma^{(1)}$ is zero. The second eigenpair defines the stability of the equilibrium (fixed point) against perturbations that preserve the total particle density $\bar{n}$; note that the eigenvector $\boldsymbol{e}^{(2)}$ spans a 1-simplex in phase space defined by the mass conservation constraint $a + b = \bar{n}$, whereas $\boldsymbol{e}^{(1)}$ breaks mass conservation (c.f. main text Fig. 1).

Before continuing with the stability analysis of these spatially uniform equilibria (a^*, b^*) against spatially non-uniform perturbations, we first study a particular system where the initial mass distribution is spatially non-uniform, $n_x(0)$, but there is no mass transport through diffusion. This is equivalent to the following 'Gedankenkonstrukt' (notional construct), whose significance for the spatiotemporal dynamics will become clear as we proceed: Imagine the one-dimensional system be divided up into a set of (infinitesimal) compartments (*reactors*) where each of them is considered as well-mixed but they are separated from each other by walls which inhibit any diffusive flux; for an illustration see main text Fig. 1A. Then, for a compartment at position x, we have the same well-mixed dynamics as above,

$$\partial_t a_x = f(a_x, b_x)\,, \tag{7a}$$

$$\partial_t b_x = -f(a_x, b_x)\,, \tag{7b}$$

but with the difference that each of these compartments contains a different amount of mass as specified by the local value of the total mass density $n_x(0)$. Since there is no diffusion we have $\partial_t n_x(t) = 0$, i.e. the total mass density remains locally invariant in time: $n_x(t) = n_x(0) =: n_x$. As a consequence, each

spatial position x is characterised by a different fixed point, (a_x^*, b_x^*), which we term *local equilibrium*. It is obtained from the conditions of local stationarity $f(a_x^*, b_x^*) = 0$, and local mass conservation $a_x^* + b_x^* = n_x$. Upon defining the displacement vector $\delta\boldsymbol{a}_x(t) = \left[a_x(t) - a_x^* \ , \ b_x(t) - b_x^*\right]^T$, one can study the stability of these local equilibria. The linearised systems corresponding to Eq. (7a) reads

$$\partial_t \, \delta\boldsymbol{a} = \mathcal{J}_x \, \delta\boldsymbol{a} \tag{8}$$

with the local Jacobian given by

$$\mathcal{J}_x = \begin{bmatrix} f_x^a & f_x^b \\ -f_x^a & -f_x^b \end{bmatrix}, \tag{9}$$

where $f_x^a \equiv \frac{\partial f}{\partial a}|_{(a_x^*, b_x^*)}$ and $f_x^b \equiv \frac{\partial f}{\partial b}|_{(a_x^*, b_x^*)}$. For each space point x, the linear system, Eq.(8), is solved by the ansatz $\delta\boldsymbol{a}_x(t) = e^{\sigma_x t} \, \boldsymbol{e}_x$. Depending on the values n_x, this ansatz gives a local eigensystem with the two eigenvalues

$$\sigma_x^{(1)} = 0 \, , \tag{10a}$$

$$\sigma_x^{(2)} = f_x^a - f_x^b \, , \tag{10b}$$

and the corresponding eigenvectors

$$\boldsymbol{e}_x^{(1)} = \left[-f_x^b / f_x^a \ , \ 1\right]^T \ , \tag{11a}$$

$$\boldsymbol{e}_x^{(2)} = \left[-1 \ , \ 1\right]^T \ , \tag{11b}$$

spanning the *phase space* (a, b) of the system (c.f. main text Fig. 1B). The first eigenpair again defines a local *center space*, where the eigenvector $\boldsymbol{e}_x^{(1)}$ is tangent to the line of fixed points. The second eigenpair now defines the *local* stability of fixed points against perturbations that locally preserve the respective total mass density n_x. For each fixed n_x, the eigenvector $\boldsymbol{e}_x^{(2)}$ spans a 1-simplex defined by $a_x + b_x = n_x$. This is the *local phase space* of the compartment at position x to which its dynamics remains confined due to mass conservation (in the absence of diffusion). The eigenvalue $\sigma_x^{(2)}$, which is a function of n_x, defines the stability of these local equilibria. Taken together, this identifies the *local mass density* n_x as a *local control parameter*: For any point x in space we can reduce the local dynamics to the local phase space via $f(a, b) = f(a, n_x - a) =: f(a; n_x)$ such that the nonlinear dynamics reduces to

that of a general one-dimensional dynamical system with the control parameter n_x. Hence, all co-dimension one bifurcation scenarios can be realised by variation of n_x, depending on the choice of the nonlinear function $f(a,b)$.
All of the above considerations on local equilibria are in a straightforward fashion generalised to systems with s conserved chemical species with respective conserved mass densities $n_x^{(\alpha)}(t)$, $\alpha \in S$. The corresponding local equilibria are then controlled by S independent local mass densities which grants access to co-dimension S bifurcations. For the Min dynamics (and similar intracellular protein dynamics) the notion of local equilibria needs to be further generalised as it couples dynamics on a reactive surface (membrane) with some bulk (cytosol). The subtleties arising in such cases will be discussed in Sec. VI A.

B. Dynamics with diffusive coupling

Next we analyse the effect of diffusion on the system's dynamics. Since lateral diffusion induces spatial redistribution of n_x, its role becomes that of a *dynamic control variable* which we will now investigate in the context of lateral instabilities. Returning to the full reaction-diffusion system, Eq. (1), and assuming a spatially uniform initial distribution of the total mass density, $n_x(0) = \bar{n}$, we can generalise the Jacobian to contain the diffusive part:

$$\mathcal{J}_x \to \mathcal{J}_q = \begin{bmatrix} f^a - D_a q^2 & f^b \\ -f^a & -f^b - D_b q^2 \end{bmatrix} . \tag{12}$$

The corresponding linearised system reads $\partial_t\, \delta\boldsymbol{a}_q = \mathcal{J}_q\, \delta\boldsymbol{a}_q$, and is solved by the separation ansatz $\delta\boldsymbol{a}_q \propto e^{\sigma_q t} \cos qx$. The eigenvalues are given by

$$\sigma_q^{\pm} = \frac{1}{2}\left(\tau_q \pm \sqrt{\tau_q^2 - 4\delta_q}\right) , \tag{13}$$

where τ_q and δ_q denote the trace and determinant of the Jacobian, respectively:

$$\tau_q := \operatorname{tr} \mathcal{J}_q = (f^a - f^b) - (D_a + D_b)\, q^2 , \tag{14a}$$

$$\delta_q := \det \mathcal{J}_q = (D_a f^b - D_b f^a)\, q^2 + D_a D_b\, q^4 . \tag{14b}$$

For wavenumber $q = 0$, one recovers the results of the well-mixed case discussed above, Eq. (5): $(\sigma_q^+, \sigma_q^-)|_{q=0} = (\sigma^{(1)}, \sigma^{(2)})$ for $\sigma^{(2)} < 0$, and $(\sigma_q^+, \sigma_q^-)|_{q=0} = (\sigma^{(2)}, \sigma^{(1)})$ for $\sigma^{(2)} > 0$ (note that σ_q^+ is always the larger of the two eigenvalues). Now

we are interested in the stability of a spatially uniform state against spatially non-uniform perturbations, i.e. the dynamics of modes with $q>0$. There are special wave vectors where the stability is marginal, $\sigma_q^{\pm}=0$, or equivalently $\det \mathcal{J}_q=0$. They are given by

$$q_{\min}=0,\ q_{\max}=\sqrt{\frac{D_b f^a - D_a f^b}{D_a D_b}}\,, \tag{15}$$

provided that $D_b f^a - D_a f^b > 0$; otherwise the spectrum is marginal only at $q_{\min}=0$. From Eq. (13) one reads off that the condition on the determinant of the Jacobian, $\det \mathcal{J}_q \leq 0$, defines a band $[0, q_{\max}]$ of unstable modes, where $\mathrm{Im}\,[\sigma_q^{\pm}]=0$ and $\sigma_q^{+}\geq 0$; see Supplementary Fig. 1 A for examples of dispersion relations. By solving $\frac{d}{dq}\det \mathcal{J}_q=0$ at $q_{\min}$ and $q_{\max}$ we find that the lateral instability always occurs first at the critical wavenumber $q_c=0$, c.f. [1].
We have to distinguish between the cases $\sigma^{(2)}<0$ and $\sigma^{(2)}>0$, where the uniform state is stable and unstable with respect to spatially uniform perturbations (conserving mass), respectively. The dispersion relations for these two cases are illustraded in Supp. Fig. 1 A. For $\sigma^{(2)}<0$, where all (spatially uniform) local equilibria are stable, the lateral instability is of type-II in the classification scheme of Cross and Hohenberg [2] with the growth rate at $q=0$ always zero: $\sigma^{+}_{q=0}=\sigma^{(1)}=0$, see Supp. Fig. 1 A (left). In contrast, for $\sigma^{(2)}>0$, where all (spatially uniform) local equilibria are unstable, the lateral instability is of type-III with the growth rate at $q=0$ positive: $\sigma^{+}_{q=0}=\sigma^{(2)}\geq 0$, see Supp. Fig. 1 A (right). As discussed next, both linear instabilities, despite of belonging to different classes, induce dynamics facilitated by the spatial redistribution of total mass density.
Let us first consider the case where the local equilibria are spatially uniform and stable. In this case the local eigenvalue (encoding *local stability* in *local phase space*) is negative: $\sigma^{(2)}<0$. Then, the eigenvalue $\sigma^{(1)}=0$, with the corresponding eigenvector $\boldsymbol{e}^{(1)}$ tangent to the line of fixed points (nullcline), determines the stability of the uniform state ($\sigma^{+}_{q=0}=\sigma^{(1)}=0$) with respect to uniform perturbations that alter the total mass in the system such that the system is shifted along the line of fixed points. Once shifted by a perturbation that breaks mass conservation the system remains in the local phase space, within which the stability is given by the eigenvalue $\sigma^{(2)}<0$. This case corresponds to the classical lateral instability as considered by Turing: The system is stable without diffusive coupling, and lateral diffusive coupling leads to the formation of a finite band $[0, q_{\max}]$ of unstable modes for $f_a/D_a > f_b/D_b$. Since the instability occurs first at $q_c=0$, we can assume q to be small at onset, and

expand the eigenvector in orders of q^2. We find

$$\boldsymbol{e}^{(1)} = \boldsymbol{e}^{+}_{q=0} \rightarrow \boldsymbol{e}^{+}_{q} = \boldsymbol{e}^{(1)} - \frac{f^b}{f^a}\frac{D_b - D_a}{|\sigma^{(2)}|}\, q^2 \begin{pmatrix} 1 \\ 0 \end{pmatrix} + \mathcal{O}(q^4), \tag{16}$$

where $\boldsymbol{e}^{(1)}$ is tangent to the line of fixed points (center space).
What does the direction of this eigenvector reveal about the spatial redistribution of mass? The growth of any unstable mode q implies an increase of the densities $a(x,t)$ and $b(x,t)$ at the maxima and a reduction at the minima. If the growth of one density (say $a(x,t)$) at some point in space x is not balanced by the same decrease of the other density ($b(x,t)$) mass is being redistributed in space, and the local total density $n_x(t)$ becomes a dynamical *control variable*. The distance of redistribution is then given by the distances between minima and maxima of the unstable mode q, i.e. by half a wavelength π/q. The entries of the eigenvector of a mode q are the coefficients (pre-factors) of the modes for both species. Only if the sum of coefficients is zero no mass is being redistributed, in this case the eigenvector reads $\boldsymbol{e} = \begin{bmatrix} -1 & , & 1 \end{bmatrix}^T = \boldsymbol{e}^{(2)}$ and spans the 1-simplex $a + b = \bar{n}$. We can summarise the meaning of the eigenvector as follows (see also Supp. Fig. 1 B for an illustration of the eigenvectors): **The eigenvector parametrises, in the vicinity of the uniform steady state, the flow of density $(\mathbf{a}, \mathbf{b})$ in phase space induced by diffusive coupling between two reactors separated by half a wavelength $\pi/\mathbf{q}$ in space.**
For $\boldsymbol{e}^{+}_{q}$, two things are important to note: First, for $q > 0$, the eigenvector points away from the line of stable fixed points spanned by $\boldsymbol{e}^{(1)}$. Hence, as expected for a Turing instability, each reactor is driven away from the stable local reactive fixed point. However, as the eigenvector also points away from the local phase space (1-simplex) in which total mass density $\bar{n}$ is conserved, the total mass density becomes time- and concomitantly also space-dependent, i.e. $\bar{n} \rightarrow n_x(t)$. Therefore, as each reactor is driven away form its local equilibrium, the equilibrium (its position and potentially its stability) also changes dynamically. As a consequence, the flow field representing the dynamical system (reactor) becomes nonuniform in time and space, and the local control parameter n_x becomes a dynamic control variable $n_x(t)$ with dynamics driven by the lateral instability. As we will see in the following, this result is not specific to the scenario of a Turing type instability but rather generic for mass-conserved reaction-diffusion systems.
The second type of instabilities that can occur in the two-component reaction-diffusion system considerer here is defined by locally unstable equilibria, see

Supp. Fig. 1 A (right). In this case the destabilisation occurs locally such that $\sigma^{+}_{q=0} = \sigma^{(2)} > 0$. By expanding the eigenvectors in orders q^2 we find a remarkably similar result as in Eq. 16:

$$\boldsymbol{e}^{(2)} = \boldsymbol{e}^{+}_{q=0} \rightarrow \boldsymbol{e}^{+}_{q} = \boldsymbol{e}^{(2)} + \frac{D_b - D_a}{|\sigma^{(2)}|}\, q^2 \begin{pmatrix} 1 \\ 0 \end{pmatrix} + \mathcal{O}(q^4). \tag{17}$$

For $D_a \neq D_b$, the spatial coupling induces a change in the total mass density $n_x(t)$ as well. Hence, even if the destabilisation of the uniform state occurs locally, we find that a lateral instability ($q > 0$) still induces dynamics in the local equilibria, just as in the previously discussed case of the Turing instability. For the particular case where the diffusion constants are equal, we note that the total density obeys the simple diffusion equation, $\partial_t n_x(t) = D\partial_x^2 n_x(t)$, and hence will relax to a spatially uniform distribution for no-flux boundary conditions. However, in the presence of an external mass flux, the total density will tend towards some spatial gradient whose magnitude depends on the strength of this external flux. In this paper we will restrict ourselves to closed systems without external fluxes. We suppose that generalisations to include the additional effects of external fluxes are highly interesting and deserve further study.

C. Type-II instabilities in mass–conserved reaction diffusion systems

The type-II instability in the classification scheme by Cross and Hohenberg [2] is associated with the presence of conservation laws. It is important to realize that a lateral instability of type-II only implies that the system will most likely satisfy a conservation law of some sort. However, in the literature on pattern formation one often finds statements of the reverse, namely that the presence of a conservation law *necessitates* any lateral instability of the system to be of type-II. In particular, it is often assumed that in any system with a conservation law the eigenvalues of the zero mode $q = 0$ need to be zero, i.e. the system needs to be neutrally/marginally stable with respect to spatially uniform perturbations. As we have shown mathematically in the previous section there is indeed a zero eigenvalue for the mode $q = 0$. Its eigenvector is tangent to the line of fixed points ($f = 0$). However, we have also shown that the other eigenvalue of the zero mode ($q = 0$) is not generally zero but encodes the *local stability* of the system. Its corresponding eigenvector spans the local phase space where mass is conserved. Hence, spatially uniform perturbations

in this direction do not break mass–conservation. If the mass–conserved system is locally unstable the dispersion relation takes the shape shown in Supp. Fig. 1 A (right), which is a type-III instability in the Cross-Hohenberg classification scheme.
For mass–conserved reaction–diffusion systems with two components the shape of the dispersion relation is limited to type-II and type-III instabilities. However, mass–conserved systems with more than two components (such as the Min system and most other intracellular pattern–forming systems) can also show lateral instabilities of type-I, see main text Fig. 2A (note that the zero mode ($q = 0$) is still marginally stable but the band of unstable modes is bound from below at a finite wavenumber). Hence, our findings show that mass–conservation does not impose any restrictions on the Type of the dispersion relation within the Cross-Hohenberg classification.
Strikingly, we find that the phenomenology of the Min dynamics does not appear to be related to the type of the dispersion relation in any way (see main text).

II. WAVE–PINNING IN THE MASS–REDISTRIBUTION FRAMEWORK

A. The concept of wave–pinning in the literature

The term wave-pinning refers to the mathematical construction of a polarized stationary state in a certain class of models for cell polarity [3, 4]. The concept originated from the study of propagating wavefronts in the classical nonlinear dynamics literature. For general bistable systems without mass–conservation such wavefronts are interfaces between two (uniform) stable states and propagate at a constant speed. The general idea underlying wave–pinning is that a propagating wavefront is *pinned* at a fixed location in space due to global mass constraints. The concept was introduced for mass-conservative two-component systems as considered in section I. The mathematical construction is based on two assumptions: First, the faster diffusing component (cytosolic) is considered in the limit of infinitely fast diffusion. The density profile of this component is therefore assumed to be spatially uniform. Second, the ensuing system is assumed to be bistable when the faster diffusing component is considered as a parameter. The wavefront solution of this system is constructed with the well-known rolling–ball–analogy (e.g. see [1]), where both stable states mark

the start- and end-point of a fictitious ball's trajectory.
A main claim in the literature is that a wave–pinning pattern is distinct from any mechanism related to Turing instabilities or Turing patterns. In the following we will study the original wave-pinning model [3] within our mass–redistribution framework, discuss the origin of the aforementioned statement, and argue that it is based on a conceptual misinterpretation of local stability in the limit of infinite cytosolic diffusion.

B. Wave–pinning is based on mass–redistribution

The wave–pinning phenomenon has been introduced for a Rho GTPase model by Mori et al. [3]. The model considers two diffusive components in a one–dimensional domain (representing the cell) of length L:

$$\partial_t a(x,t) = D_a \partial_x^2 a + f(a,b), \tag{18}$$

$$\partial_t b(x,t) = D_b \partial_x^2 b - f(a,b). \tag{19}$$

The authors consider a reaction term with positive feedback described by a Hill term

$$f(a,b) = b\left(k_0 + \frac{\gamma a^2}{K^2 + a^2}\right) - \delta a. \tag{20}$$

The parameters with their corresponding biological meaning and values are given in Table I. Due to mass conservation we additionally need to specify the total mass in the system:

$$\int_0^L (a+b)\,\mathrm{d}x = \int_0^L n_x\,\mathrm{d}x = N. \tag{21}$$

Note that we are using our naming conventions here, in the original model [3] total mass is denoted by C.
With the model definition in place, we can now proceed with the analysis of the underlying mechanism. To this end we first look at the $f = 0$ nullcline in the phase space (a, b). For the given reaction term (Eq. 20), the nullcline has a characteristic N-shape (Supp. Fig. 1B). In the limit of infinite cytosolic diffusion ($D_b \to \infty$) the spatial distribution of the b component is uniform, i.e. $b(x,t) = b(t)$. In the phase space (a, b) the whole system will, therefore, be constrained to lines with constant b. We will refer to these lines as the subspace of the polarized state.

D_a	0.1 $\mu m^2 s^{-1}$	membrane diffusion
D_b	10 $\mu m^2 s^{-1}$	cytosolic diffusion
L	10 μm	cell length
δ	1 s^{-1}	inactivation rate (GAP hydrolysis)
γ	1 s^{-1}	GEF activation rate
k_0	0.0.67 s^{-1}	baseline GEF activity
K	1 μm^{-1}	saturation parameter

TABLE I: Parameters of the wave–pinning model [3].

The construction of the wave–pinning pattern is based on the concept of bistabilty. For the N-shape of the $f = 0$ nullcline there is a range of b values for which the system admits three intersections between the subspace of the polarized state and the nullcline. Let us denote these intersections by $a^*_-(b^*) < a^*_m(b^*) < a^*_+(b^*)$. In the wave–pinning literature, bistabilty refers to the existence of these three intersections. It is important to realize that these states are local equilibria for *different* values of the local total density n_x. One part of the system is in the high density state $a^*_+(b^*)$ where the local total density is $n_+ = a^*_+ + b^*$. The other part of the system is in a low density state $a^*_-(b^*)$ with $n_- = a^*_- + b^*$. Since b^* is constant and $a^*_-(b^*) < a^*_+(b^*)$, it follows that this construction is based on a spatially non-uniform distribution of total mass density n_x: the wave–pinning pattern is a pattern of local equilibria by construction, see Supp. Fig. 2 C (bottom). Moreover, since there is only one fixed point for each spatially uniform $n_x = \overline{n}$, there is no bistabilty in the local phase space $a + b = \overline{n}$. Hence, redistribution of total mass density is explicitly required to reach the wave–pinning pattern. In the wave–pinning literature one assumes that an external perturbation facilitates this mass redistribution. The perturbation induces formation of a propagating wave front that stops (becomes "pinned") due to global mass conservation. However, in stark contrast to known wave propagation phenomena in bistable media, the states (a^*_-, b^*) and (a^*_+, b^*) do no exist a priori, but are created by externally induced mass redistribution. Considering that mass redistribution is the main feature of a lateral (Turing) instability, it is surprising that wave–pinning is supposed to be unrelated to any mechanism based on Turing instability.
To shed light on this matter let us analyse the model and its local and lateral

stability in full detail. First, let us remind the reader that a Turing instability is defined by the local stability of the system and induced by lateral diffusive coupling alone. Because the Turing instability is an instability of a spatially uniform state, we will denote spatially uniform states by (a^*, b^*) instead of $a^*(b^*)$. The latter notation that is used by the authors of the wave–pinning model (cf. [3]) implies that b^* is the control parameter, while the actual control parameter is $\overline{n}$. From the previous discussion in section I we know that any lateral instability (regardless of the local stability) is based on redistribution of total density which leads to a movement of local equilibria. The main requirement for redistribution of total density are unequal diffusion coefficients. This is clearly fulfilled for the wave–pinning model, in particular, in the case of infinitely fast cytosolic diffusion.
Next, we need to check the local stability of the uniform steady state for all values of the control parameter $\overline{n}$. For any two–component system a local equilibrium (a^*, b^*) is unstable iff

$$\sigma^{(2)} = f^a - f^b \geq 0, \tag{22}$$

where $f^a = \partial_a f|_{(a^*,b^*)}$ and $f^b = \partial_b f|_{(a^*,b^*)}$. In this case all parameters except the total mass N (which is related to the total density $\overline{n}$ through $\overline{n} = N/L$) determining the position of the local equilibria are given. A computation of $\sigma^{(2)}$ as a function of $\overline{n}$ shows that the local equilibrium $(a^*(\overline{n}), b^*(\overline{n}))$ (which is unique for any fixed choice of $\overline{n}$) is always locally stable, including the "middle" steady state (a^*_m, b^*) in the subspace of the polarized state (constant b). Therefore, a Turing instability cannot be ruled out *a priori* for the uniform steady state (a^*_m, b^*). For a locally stable two–components system a band of unstable modes (type-II instability) exists iff (see Eq. 15)

$$D_b f^a - D_a f^b > 0. \tag{23}$$

To check this condition let us first note that $-f^a/f^b$ denotes the slope of the f nullcline in the phase space (a, b), i.e.

$$\partial_a b^*(a)|_{a=a^*} = -f^a/f^b. \tag{24}$$

In addition, from Eq. 20 we obtain $f^b = k_0 + \frac{\gamma a^2}{K^2+a^2} > 0$ for all parameter choices. Then we can immediately read off from the N-shape of the nullcline that $f^a > 0$ in general for all middle steady states (a^*_m, b^*), see Supp. Fig. 2 A. In addition, note that f^a and f^b are independent of the diffusion coefficients D_b and D_a. For the assumption of infinite b diffusion ($D_b \to \infty$), on which the construction of the wave–pinning solution is based, it immediately follows from

Eq. 23 that (a_m^*, b^*) is always laterally (Turing) unstable, and from Eq. 15 that there is a band of unstable modes that extends to $q_{\max} = \sqrt{f^a/D_a}$. Hence, the assumptions on which wave–pinning is based (bistability for constant b) guarantees a Turing instability for this type of models (characterized by the N-shape of the f nullcline), cf. Supp. Fig. 2 A.

Up to this point we have clearly established that the wave–pinning model does admit a Turing instability. Moreover, wave–pinning relies on mass–redistribution in order to create bistability of local equilibria in the subspace of the polarized state (constant b, see Supp. Fig. 2 A). Our findings also show that any lateral instability generically leads to the redistribution of local total density and thereby the movement of local equilibria. Taken together, this implies that the possibility of wave–pinning and the presence of a Turing instability is not a mere coincidence, but that both phenomena are based on the same self–organization mechanism. Our previous analysis of the general two–component model (Eq. 1) revealed that any unstable mode $\cos(qx)$ causes the redistribution of local total density, and that the ensuing mass transport is associated with a *direction* in phase space (a, b) given by the eigenvector $\boldsymbol{e}_q^+$ (Eq. 16) of the mode, i.e. $\begin{bmatrix} a(x,t) & , & b(x,t) \end{bmatrix}^T \sim \boldsymbol{e}_q^+ \exp(\sigma_q^+ t) \cos(qx)$ at onset of the lateral instability. In this previous section we have mainly used this result to show that any unstable mode causes the redistribution of local total density n_x, as $\boldsymbol{e}_q^+$ points away from the subspace where mass is conserved $a^* + b^* = \overline{n}$ (local phase space). The particular direction of $\boldsymbol{e}_q^+$ had no specific relevance in this general discussion. However, we know that (for $D_b \to \infty$) the subspace containing the final pattern is a line for constant b in the phase space. Hence, the subspace for the polarized state is spanned by the vector $\begin{bmatrix} 1 & , & 0 \end{bmatrix}^T$. Let us assume that the system is initially in the uniform (Turing unstable) steady state (a_m^*, b^*). To reach the polarized state the local total density needs to be redistributed such that the dynamics approach the states (a_-^*, b^*) and (a_+^*, b^*). Since we assume infinite diffusion of component b ($D_b \to \infty$) it only matters how the eigenvectors $\boldsymbol{e}_q^+$ depend on D_b. From Eq. 16 we directly read off $\boldsymbol{e}_q^+ \sim \begin{bmatrix} D_b q^2 & , & 1 \end{bmatrix}^T$. Hence, in the limit $D_b \to \infty$ the normalized eigenvector $\boldsymbol{e}_q^+$ spans the subspace of the polarized state, i.e.

$$\lim_{D_b \to \infty} \boldsymbol{e}_q^+ = \begin{bmatrix} 1 & , & 0 \end{bmatrix}^T, \ \forall q. \tag{25}$$

We conclude that the polarized state originates from a lateral (Turing) instability, and note that this analytical result is supported by simulations, see Supp. Fig. 2 C.

Of course, this does not imply that a Turing unstable uniform steady state is strictly required for the polarized state to exist. It has already been pointed out by Goryachev and Leda [5] (also see [6]) that a Turing stable uniform state near a subcritical Turing instability should admit a polarized state, since subcritical bifurcations are a sign for excitability. Indeed the authors of the original wave–pinning model consider a Turing stable uniform solution (a^*_-, b^*) as the initial base state, and observe that the polarized state is reached if this state is sufficiently perturbed. Heuristically speaking, this is possible if a perturbation of the local total density n_x puts a sufficiently large part of the system in the basin of attraction of the state (a^*_+, b^*) by increasing $n_x(0)$ locally beyond $n_m = a^*_m + b^*$, i.e. $n_x(0) > n_m$ for some range of x values at time $t = 0$. It is important to realize that such a choice of initial conditions where the system is spatially distributed between the basins of attraction of (a^*_-, b^*) $(n_x(0) < n_m)$ and (a^*_+, b^*) $(n_x(0) > n_m)$ is exactly the action of the lateral (Turing) instability at the uniform steady state (a^*_m, b^*). The only difference is that in the excitable case, an external stimulus guides the system into the basin of attraction of the polarized state, whereas in the second case, this guidance is self–organized by the Turing instability. However, even if the system is in an excitable state, a variation of system parameters (e.g. a change of total density $\bar{n}$) will *always* (due to the shape of the nullcline) be able to render the excitable state laterally unstable such that pattern formation becomes self-organized.
Now that we have established the mechanistic connection between the Turing instability and the wave–pinning phenomenon, two main question remain. The first questions concerns the length scale of the fastest growing mode which sets the length scale at onset. The second question concerns the misunderstanding on which basis the uniform solution (a^*_m, b^*) has been identified as unstable and therefore ruled out as a candidate for a Turing instability. Because the answers to both questions turn out to be connected we will discuss them together in the following section. Again, the realization that the key physical process for pattern formation is mass redistribution will turn out to be crucial.

C. Local and lateral stability in the limit of infinitely fast diffusion

The fastest growing mode q_c from the band of unstable modes ($q_{\min} < q_c < q_{\max}$) always sets the initial length scale of the pattern forming process in the linear regime. For lateral instabilities in mass–conserving two–component models with a locally stable uniform state (Turing) the band of unstable modes always extends down to the zero mode, i.e. $q_{\min} = 0$ (cf. Eq. 15). It has been

previously been realized by Trong et al. [6] that the position of the fastest growing mode q_c strongly depends on the value of the fast diffusion coefficient (D_b in our case). Indeed, one can analytically derive from the q-dependent spectrum of the Jacobian (Eq. 12) that q_c approaches the zero mode as D_b approaches infinity, i.e.

$$\lim_{D_b \to \infty} q_c = 0, \tag{26}$$

while maintaining a positive growth rate, i.e.

$$\lim_{D_b \to \infty} \sigma^+_{q_c} = f^a > 0. \tag{27}$$

Hence, in the limit $D_b \to \infty$ the mode with longest wavelength (which is infinite in an infinite system) becomes the fastest growing mode. The growth rate $\sigma^+_{q \to 0} > 0$ converges towards f^a, and not towards zero. The system remains neutral stability for any finite $D_b < \infty$. Only for $D_b = \infty$ does the dispersion obtain the characteristic shape with a maximum at $q = 0$, i.e.

$$\lim_{D_b \to \infty} \sigma^+_q = f^a - D_a q^2, \tag{28}$$

which represents a prototypical type-III instability within the Cross-Hohenberg classification scheme, see Supp. Fig. 2 B. It is absolutely crucial to realize that this *discontinuously displaced zeroth Fourier mode* [6] does not represent nor alter the local stability of the system which is still determined by $\sigma^{(2)} = f^a - f^b$, and is independent of any lateral diffusion process (e.g. D_b) by definition of locality (fixed x). However, the pathological shape of the dispersion relation (Supp. Fig. 2 B) in the limit $D_b \to \infty$ with an unstable zero mode appears to be the reason why the middle fixed point (a^*_m, b^*) has been ruled out as a candidate for a Turing instability. This also emphasizes that local stability and therefore the condition for a Turing instability cannot be inferred from the dispersion relation (at $q = 0$) in such limiting cases, but has to be considered explicitly by calculating the local stability in the local phase space of the uniform state (Eq. 22).

Furthermore, we note that the shape of the dispersion relation in the limit $D_b \to \infty$ does reveal additional insight about the mechanism underlying wave–pinning, when considered in the context of mass redistribution. As discussed in the previous sections, any laterally unstable mode induces a redistribution of local total density on the length scale π/q (the distance between minima and maxima of a mode $\sim \cos qx$). Let us consider a system with length L ($-L/2 < x < L/2$) and no–flux boundary conditions at $x = \pm L/2$. Then the spectrum of modes with finite wave length will be limited to the discrete set

$\{\sin(n\pi/Lx) \mid n = 1, 2, ...\}$. Note that the polarized pattern is represented by the mode with the longest wave length ($n = 1$) with a minimum at $x = -L/2$ and a maximum at $x = +L/2$ (or vice versa). As the wave length of the fastest growing mode increases with D_b we can guarantee for any system length L that the the first mode ($n = 1$) will be the fastest growing mode for sufficiently high D_b, i.e. that local total density is redistributed the fastest from $x = -L/2$ to $x = +L/2$ (or vice versa). This is *exactly* the requirement needed for the uniform system to approach the polarized wave–pinning state.

This discussion also reveals the physically correct interpretation of the dispersion relation at $q = 0$ in the (pathological) limit $D_b \to \infty$ (Supp. Fig. 2). In this limit the fastest growing mode transports local total density from $x = -L/2$ to $x = +L/2$ (or vice versa) for any system length L. Only in this limit the latter remains to be the case for $L \to \infty$, where the fastest growing mode $q_c = \pi/L$ induces mass-redistribution from $x = -\infty$ to $x = +\infty$. Clearly this cannot represent any meaningful physical process. Hence, it becomes evident that the dispersion relation at $q = 0$ defines a lateral instability (from $x = -\infty$ to $x = +\infty$) and does not represent the local stability of the uniform state (which is independent of diffusion by definition, and still encoded by 22). This example shows that the distinction between these two physically distinct properties of a system (local and lateral stability) needs to be carefully considered. In this case the distinction was obfuscated by the limit $D_b \to \infty$, where system becomes laterally coupled on an instantaneous time scale ($\sqrt{D_b/L^2}$), i.e. lateral mass transport can be instantaneous across any distance and the dynamics is effectively "delocalized".

III. MIN PROTEIN DYNAMICS AND THE EFFECT OF SYSTEM GEOMETRY

A. Reaction-diffusion equations for the skeleton model of Min dynamics

We use a mathematical model [7, 8] for the Min system that accounts for the molecular interactions that are believed to be essential for the Min protein dynamics. This model includes the following set of chemical reactions:

1. The attachment of cytosolic MinD-ATP, u_{DT}, to the membrane with rate constant k_D.

2. The recruitment of cytosolic MinD-ATP, u_{DT}, to the membrane by membrane bound MinD, u_d, with rate constant k_{dD}.

3. The formation of membrane bound MinDE complexes, u_{de}, through the recruitment of cytosolic MinE, u_E, by membrane bound MinD, u_d, with rate constant k_{dE}.

4. The detachment and decay of membrane bound MinDE complexes, u_{de}, into cytosolic MinD-ADP, u_{DD}, and MinE, u_E, with rate k_{de}.

5. The reactivation of cytosolic MinD-ADP, u_{DD}, by nucleotide exchange to MinD-ATP, u_{DT}, with rate λ.

All components are able to diffuse in their respective domains (cytosol or membrane). Since only the distinction between cytosolic and membrane diffusion is important for the dynamics, and since the diffusion coefficients with a domain (cytosol or membrane) are very similar for different proteins, we only distinguish between cytosolic and membrane diffusion with diffusion constants D_c for the cytosol and D_m for the membrane, respectively.
In previous work [8], the mathematical model has been generalised to complex system geometries with bulk-boundary coupling (this will be discussed in this section below), and subsequently applied to account for

- the transition from pole-to-pole oscillations to (multi-node) stipe oscillation in filamentous cells [8],

- oscillations with rotating oscillation axis in nearly spherical cells [8],

- the temperature dependence of the oscillation period [8],

- robustness of the intracellular pattern agains inhomogeneities in the lipid composition (affecting the attachment process) [8],
- optimisation of the time-average membrane density profile for mid-cell localisation [8],
- traverse oscillations in broad rectangular cells [9, 10],
- multi-stability of various longitudinal and transversal patterns in large rectangular cells [9, 10].

This success to consistently reproduce and explain a broad range of experimentally observed features of the Min system suggests that the underlying molecular interaction are indeed essential for the Min protein dynamics. As new experimental data on the molecular interactions of Min proteins becomes available, the kinetic processes assumed in the model can be further refined (e.g. by replacing one-step processes with multi-step processes). In the latter case we would expect that the original network would be contained in a detailed model as a limiting case. For this reason we refer to the reaction network outlined above as the *skeleton network*, and *skeleton model* respectively.
In coordinate free form (with index c or m denoting that an operator acts in the cytosol or at the membrane, respectively) the ensuing system of partial differential equations for the skeleton model reads:

$$\partial_t u_{DD} = D_c \nabla_c^2 u_{DD} - \lambda u_{DD}\,, \tag{29a}$$

$$\partial_t u_{DT} = D_c \nabla_c^2 u_{DT} + \lambda u_{DD}\,, \tag{29b}$$

$$\partial_t u_E = D_c \nabla_c^2 u_E\,, \tag{29c}$$

$$\partial_t u_d = D_m \nabla_m^2 u_d + f_d(u_d, \tilde{u}_{DT}, \tilde{u}_E), \tag{29d}$$

$$\partial_t u_{de} = D_m \nabla_m^2 u_{de} + f_{de}(u_{de}, u_d, \tilde{u}_E)\,, \tag{29e}$$

where the chemical reactions on the membrane are given by the nonlinear functions

$$f_d(u_d, \tilde{u}_{DT}, \tilde{u}_E) := (k_D + k_{dD} u_d)\, \tilde{u}_{DT} - k_{dE}\, u_D\, \tilde{u}_E\,, \tag{30a}$$

$$f_{de}(u_{de}, u_d, \tilde{u}_E) := k_{dE}\, u_D\, \tilde{u}_E - k_{de}\, u_{de}\,, \tag{30b}$$

with $\tilde{u}_i$ denoting the respective cytosolic densities right at the membrane. These equations are complemented by nonlinear reactive boundary conditions

at the membrane surface stating that the chemical reactions involving both membrane-bound and cytosolic proteins equal the diffusive flux onto (−) and off (+) the membrane (the index n denoting the outward normal vector at the boundary)

$$D_c \nabla_n u_{DD}|_m = k_{de}\, u_{de} =: f_{DD}\,, \tag{31a}$$

$$D_c \nabla_n u_{DT}|_m = -(k_D + k_{dD} u_d)\, \tilde{u}_{DT} =: f_{DT}\,, \tag{31b}$$

$$D_c \nabla_n u_E|_m = k_{de}\, u_{de} - k_{dE}\, u_D\, \tilde{u}_E =: f_E\,, \tag{31c}$$

and no-flux boundary condition at any non-reactive surfaces (denoted by the index s)

$$D_c \nabla_n u_{DD}|_s = 0\,, \tag{32a}$$

$$D_c \nabla_n u_{DT}|_s = 0\,, \tag{32b}$$

$$D_c \nabla_n u_E|_s = 0\,. \tag{32c}$$

The above set of reaction-diffusion equations locally conserve the total mass of MinD as well as MinE. This implies that the spatial averages, $\overline{[\mathrm{MinD}]}$ and $\overline{[\mathrm{MinE}]}$, of the total densities of MinD and MinE obey the relation

$$\overline{[\mathrm{MinD}]}\,\Omega = \int_\Omega \mathrm{d}c\ (u_{DD} + u_{DT}) + \int_{\delta\Omega} \mathrm{d}m\ (u_d + u_{de})\ , \tag{33a}$$

$$\overline{[\mathrm{MinE}]}\,\Omega = \int_\Omega \mathrm{d}c\ u_E + \int_{\delta\Omega} \mathrm{d}m\ u_{de}\,, \tag{33b}$$

where $\int_\Omega \mathrm{d}c$ and $\int_{\delta\Omega} \mathrm{d}m$ signify integration over the whole cytosolic volume Ω and membrane surface $\delta\Omega$, respectively. The values of the overall masses of these conserved quantities needs to be specified (in the simulation through the initial condition).

The advantage of such a general (coordinate-free) model definition is that it can be adjusted to any system geometry, allowing to consistently use the same model for different experimental setups. For the *in-vitro* experiments a simple box geometry is typically used, where the reactive lipid bilayer (membrane) is located at the bottom of the box, and all other boundaries are reflective. Since the lateral extension of *in-vitro* box geometries is typically very large $\mathcal{O}(10^3 \mu m)$ compared to the wave length of the pattern $\mathcal{O}(10\,\mu m)$, we will perform simulations in an intermediate sized computational box $\mathcal{O}(10^2 \mu m)$ and employ periodic boundary conditions. The height h of the experimental

box geometry is similarly very large $\mathcal{O}(10^3 \mu m)$ such that the dynamics perpendicular to the membrane cannot be neglected for two main reasons that we will discuss in the following subsection.

The parameter values used in the simulations are given in Table II.

TABLE II: **System parameters**. The values of the diffusion coefficients and protein densities are chosen in accordance with experimental data [11]. The kinetic rate constants are chosen within the order of magnitude of the values fitted to the *in vivo* dynamics [8, 10] to reproduce the *in-vitro* phenomenology qualitatively and the wavelengths and -velocities quantitatively within the order of magnitude of the experimental data.

Parameter	Symbol	Value
MinD and MinE cytosol diffusion	D_c	$60\,\mu m^2 s^{-1}$
MinD and MinDE membrane diffusion	D_m	$0.013\,\mu m^2 s^{-1}$
MinD mean total density	$\overline{[\mathrm{MinD}]}$	$638\,\mu m^{-3}$
MinE mean total density	$\overline{[\mathrm{MinE}]}$	$410\,\mu m^{-3}$
MinD attachment rate constant	k_D	$0.065\,\mu m s^{-1}$
MinD recruitment rate constant	k_{dD}	$0.098\,\mu m^3 s^{-1}$
MinE recruitment rate constant	k_{dE}	$0.126\,\mu m^3 s^{-1}$
MinDE detachment rate	k_{de}	$0.34\,s^{-1}$
Nucleotide exchange rate	λ	$6\,s^{-1}$

B. Relevance of the cytosolic bulk for the spatiotemporal membrane dynamics

The dynamics of most intracellular processes, and in particular the Min dynamics, involves a coupling between dynamics on a membrane surface and a cytosolic volume. Biochemical interactions, with the exception of nucleotide exchange, are confined to the vicinity of the membrane. At first sight, one might therefore suppose that it is straightforward to eliminate the cytosolic bulk from the dynamics and consider it simply as a passive particle reservoir. Though there are certain limits where this is indeed possible, in general, however, the bulk dynamics plays a key role for the spatiotemporal dynamics and can not be disregarded. In the following we will illustrate the underlying physics for two simple analytically tractable cases, and discuss general implications for reaction–diffusion systems with bulk–boundary coupling.

1. The attachment rate constrains the reduction of the bulk dimension

Consider a diffusion process normal to the membrane in a one-dimensional column of height h. Then for a single protein species with line density $c(z,t)$ and diffusion constant D_c, the dynamics are given by a one-dimensional diffusion equation

$$\partial_t c(z,t) = D_c \nabla_z^2 c(z,t)\,. \tag{34}$$

At one end of the column (the reactive membrane) we consider an attachment process where cytosolic particles attach to the membrane with a rate k_{on}. Then local mass conservation implies a (Robin) boundary condition which accounts for the balance of reactive flux on the membrane with diffusive in the cytosol flux due to ensuing density gradients,

$$-k_{\mathrm{on}}\, c(0,t) + D_c \nabla_z c(z,t)|_{z=0} = 0\,. \tag{35}$$

This 'reactive' boundary condition is complemented by reaction kinetics on the membrane

$$\partial_t m(t) = k_{\mathrm{on}}\, \tilde{c}(t)\,, \tag{36}$$

where $m(t)$ denotes the membrane density and we have introduced $\tilde{c}(t) = c(0,t)$ for the cytosolic density right at the membrane. Note that the Robin boundary condition, Eq.(35), clearly shows that inevitably any reactive coupling between the cytosol and the membrane (here attachment to the membrane) leads to

gradients in the cytosolic bulk. The corresponding length scale can be read off (by simple dimensional analysis) from Eq.(35) as

$$\ell_{\rm on} := D_c/k_{\rm on}\,. \tag{37}$$

At the other end (the surface of the cytosolic solution), the system is assumed to be closed which implies a reflective boundary condition

$$D_c\nabla_z c|_{z=h} = 0\,. \tag{38}$$

We now ask under what conditions one may disregard the diffusive dynamics normal to the membrane. To this end, we define the spatial average of the cytosolic protein density as

$$\bar{c}(t) = \frac{1}{h}\int_0^h dz\, c(z,t)\,. \tag{39}$$

Combining Eq.(34) with the boundary conditions, Eq.(35) and (38), one obtains

$$\partial_t\bar{c}(t) = -\frac{k_{\rm on}}{h}\,c(0,t)\,. \tag{40}$$

This reduces to an equation for the concentration at the membrane $c(0,t) = \tilde{c}(t)$ only if one can approximate the average density by the density at the membrane, $\bar{c}(t)\approx\tilde{c}(t)$. Then one gets

$$\partial_t\tilde{c}(t) = -\frac{k_{\rm on}}{h}\,\tilde{c}(t)\,, \tag{41}$$

which is solved by $\tilde{c}(t) = \tilde{c}(0)\,e^{-t/\tau_{\rm on}}$ where the relaxation time is given by

$$\tau_{\rm on} := \frac{h}{k_{\rm on}}\,. \tag{42}$$

However, one can approximate the average density by the density at the membrane only if there are no significant gradients in the bulk. Heuristically, this requires that the penetration depth $\ell_{\rm on}$ is much *larger* that the height h of the column, $h\ll\ell_{\rm on}$. As the above reaction-diffusion equation is exactly solvable this can also been seen explicitly. With the separation ansatz $c(z,t) = \varphi(t)\zeta(z)$, and the separation parameter σ one gets

$$\partial_t\varphi(t) = -\sigma\,\varphi(t)\,, \tag{43a}$$

$$D_c\nabla_z^2\zeta(z) = -\sigma\,\zeta(z)\,. \tag{43b}$$

These linear equations are solved by $\varphi(t) = \varphi(0)\, e^{-\sigma t}$ and $\zeta(z) = \zeta(h)\, \cos(q(h-z))$, and linear combinations of these solutions $c(z,t)$; note that we have chosen the spatial part $\zeta(z)$ such that it already respects the reflective boundary condition at $z = h$, Eq.(38). The relaxation rate σ is related to the wave vector q by the dispersion relation (Eq.(43b))

$$\sigma = D_c\, q^2\,, \tag{44}$$

and the set of possible wave vectors $\{q_i\}$ is determined by the eigenvalue condition

$$hq_i \tan(hq_i) = \frac{h}{\ell_{\text{on}}}\,, \tag{45}$$

which is obtained from the Robin boundary condition, Eq.(35). This transcendental equation may be solved graphically (or numerically). Analytic solutions are obtained in asymptotic limits only. If $h \ll \ell_{\text{on}}$, we may approximate $\tan(hq) \approx hq$ to find the smallest eigenvalue as $q_1 = 1/\sqrt{h\ell_{\text{on}}}$. The corresponding relaxation rate is $\tau_1 = \frac{1}{\sigma_1} = \frac{h\ell_{\text{on}}}{D_c} = \frac{h}{k_{\text{on}}}$, which is identical to τ_{on} defined above. All other relaxation times, corresponding to larger wave vectors, are smaller and hence correspond to faster decay. Therefore, after initial transients (resulting from some prepared initial state) have decayed, the dominant wave length is $\lambda_{\max} = \frac{2\pi}{q_1} = 2\pi\sqrt{h\ell_{\text{on}}} \gg 2\pi h$, i.e. gradients on the scale of the column can be neglected. The dynamics of the longest wave length mode then corresponds to the dynamics of the average cytosolic concentration, Eq.(41), $c(z,t) \propto e^{-t/\tau_1} \cos(q_1(h-z))$; note that $\cos(q_1(h-z))$ hardly shows any z-dependence as $q_1 \ll h$. In the opposite limit, $h \gg \ell_{\text{on}}$, the eigenvalues are approximately given by $hq_i = (2i-1)\frac{\pi}{2}$ with $i \in \{1, 2, 3, \ldots\}$ such that the largest wave length is $\lambda_{\max} = 4h$ and gradients are significant. We conclude that for the dominant slow modes (largest wave length modes) the bulk dynamics may be neglected if the penetration depth ℓ_{on} is much larger than the column height h. For fast modes and for columns with a height larger than the penetration depth, there are significant density gradients in the bulk whose dynamics show an intricate interplay with the membrane dynamics. Hence, the cytosolic dynamics is an integral part of the system's dynamics and can not effectively be described as some passive reservoir.

All of the above may also be summarised by a simple scaling argument: The diffusive dynamics normal to the reactive membrane can be neglected if the time scale of cytosolic mixing, $\tau_{\text{diff}} \sim h^2/D_c$, is much smaller than the typical time a protein suspended in the bulk needs to attach to the membrane, $\tau_{\text{on}} \sim h/k_{\text{on}}$. This yields the condition

$$h \ll \frac{D_c}{k_{\text{on}}} = \ell_{\text{on}}\,, \tag{46}$$

which the ratio of the cytosolic diffusion coefficient, D_c, and the attachment rate, $k_{\rm on}$, need to satisfy in order to justify assuming a well-mixed cytosolic volume and neglect any density gradients.

For the dynamics of the Min system *in-vitro* an upper bound for the penetration depth can be estimated from the experimental data. MinD accumulation within a traveling wave takes place on a timescale $\Delta t \approx 40s$ during which the membrane density increases by the amount $\Delta m(t) \approx 1.5 \cdot 10^4 \mu m^{-2}$. With the upper bound for the cytosolic MinD density set by the mean total density $\overline{[\mathrm{MinD}]} \approx 600\,\mu m^{-3}$, one can estimate (employing Eq.(36)) a minimal attachment rate constant $k_{\rm on,\,min} \approx \frac{\Delta m/\Delta t}{\overline{[\mathrm{MinD}]}} \approx 0.625\,\mu m/s$. With the diffusion constant $D_c \approx 60\,\mu m^2 s^{-1}$ one obtains an upper bound for the penetration depth: $\ell_{\rm on}^{\rm max} \approx 96\,\mu m$. Since this value is much smaller than the typical bulk height $h_{\rm exp}$ used in *in-vitro* experiments $h_{\rm exp} \approx 5 \cdot 10^3 \mu m$, one must conclude that the bulk dynamics can not be neglected. In the above crude estimate we have mot accounted for the fact that attachment is actually a nonlinear process, and that there is also constant detachment of MinD induced by MinE recruitment. Therefore, any measured effective attachment rate $k_{\rm on}$ is actually the net difference between ongoing attachment and detachment of proteins. In terms of the skeleton model, the total attachment rate is explicitly given by $k_{\rm on} = k_D + k_{dD} u_d$, where the values for the rates k_D and k_{dD} are given in Table II. Extracting the MinD membrane density u_d from our simulations (that reproduce the order of magnitude of experimental time scales) we find values ranging from a minimal value $u_{d,\rm min} \approx 2\,\mu m^{-2}$ to a maximal value $u_{d,\rm max} \approx 2.7 \cdot 10^3\,\mu m^{-2}$, and an average value of $\bar{u}_d \approx 8.3 \cdot 10^2 \mu m^{-2}$. For the penetration depth this corresponds to an upper bound $\ell_{\rm on,\,max} \approx 200\,\mu m$, a lower bound $\ell_{\rm on,\,min} \approx 0.2\,\mu m$, and an average value $\overline{\ell_{\rm on}} \approx 0.7\,\mu m$. Besides giving estimates for the value of the penetration depth, this analysis also shows several additional aspects: (i) The nonlinear nature of an attachment process has to be taken into account when a reduction of the bulk dimension is being considered. (ii) The penetration depth is a dynamic quantity which varies as the concentration of proteins on the membrane varies. Upon combining experimental data with our computational analysis we conclude that the attachment rates of Min proteins clearly forbid the reduction of the bulk dimension when accounting for *in-vitro* experiments.

2. Reduction of the bulk dimension with nucleotide exchange

A second reason why the bulk dimension cannot be reduced easily is cytosolic nucleotide exchange. MinD is released from the membrane into the cytosol in its ADP form, and is transformed back into its ATP form by nucleotide exchange with a rate that can be estimated to $\lambda \approx 6\, s^{-1}$ (c.f. [8]). This corresponds to a source-degradation process with the membrane as an MinD-ADP source, and implies that the MinD-ADP density decays exponentially into the cytosol with a *penetration depth* given by

$$\ell := \sqrt{D_c/\lambda}\,. \tag{47}$$

Since typical values of the cytosolic diffusion constant D_c for proteins is *in-vitro* of the order $60\,\mu m^2\, s^{-1}$, one estimates $\ell \approx 3\,\mu m$, which is much smaller than typical system heights h used experimentally. Hence there are protein density gradients normal to the membrane due to nucleotide exchange, and we will show next that they critically influence the chemical equilibrium at the membrane.

Consider a one-dimensional column of height h where the dynamics of MinD-ATP and Mind-ADP in the bulk is given by the following reaction-diffusion equations

$$\partial_t u_D(z,t) = D_c \nabla_z^2 u_D - \lambda u_D\,, \tag{48a}$$

$$\partial_t u_T(z,t) = D_c \nabla_z^2 u_T + \lambda u_D\,, \tag{48b}$$

where $u_D(z,t)$ and $u_T(z,t)$ denote the cytosolic density of MinD-ADP and MinD-ATP, respectively. We further assume that MinD-ATP may bind to the membrane through some nonlinear attachment process specified by an arbitrary function $f_{\text{on}}(u_m, \tilde{u}_T)$ where $\tilde{u}_T = u_T|_{z=0}$ denotes the value of the cytosolic MinD-ATP concentration at the membrane, and $u_m(t)$ signifies the MinD-ATP membrane concentration. Membrane bound MinD-ATP is assumed to transform into MinD-ADP upon detaching from the membrane through a linear process specified by the rate constant k_{off}. Then, the membrane dynamics reads

$$\partial_t u_m(t) = f_{\text{on}}(u_m, \tilde{u}_T) - k_{\text{off}}\, u_m\,. \tag{49}$$

and the corresponding reactive boundary condition at the membrane ($z = 0$), respecting local mass conservation, is given by

$$k_{\text{off}}\, u_m + D_c \nabla_z u_D|_{z=0} = 0\,, \tag{50a}$$

$$-f_{\text{on}}(u_m, \tilde{u}_T) + D_c \nabla_z u_T|_{z=0} = 0\,. \tag{50b}$$

The column is assumed to be closed at $z = h$, which yields the reflective boundary conditions

$$D_c \nabla_z u_D|_{z=h} = 0\,, \tag{51a}$$

$$D_c \nabla_z u_T|_{z=h} = 0\,. \tag{51b}$$

In the following we consider the steady state. Solving the stationary diffusion equation and stationary membrane kinetics subject to the reactive and reflective boundary conditions yields for the stationary density profiles in the bulk,

$$u_D^*(z) = \tilde{u}_D^* \, \frac{\cosh\left(\frac{h-z}{\ell}\right)}{\cosh\left(\frac{h}{\ell}\right)}\,, \tag{52a}$$

$$u_T^*(z) = \tilde{u}_T^* + \tilde{u}_D^* \left[1 - \frac{\cosh\left(\frac{h-z}{\ell}\right)}{\cosh\left(\frac{h}{\ell}\right)}\right]\,, \tag{52b}$$

where $\tilde{u}_D^*$ and $\tilde{u}_T^*$ denote the stationary densities of MinD-ADP and MinD-ATP, respectively, right at the membrane ($z = 0$). These bulk profiles explicitly show that ℓ plays the role of a penetration depth into the bulk. The MinD-ADP concentration has its largest value at the membrane, decays exponentially into the bulk and levels off at a value $\tilde{u}_D^*/\cosh(h/\ell)$. In turn, the MinD-ATP concentration increase from $\tilde{u}_T^*$ to $\tilde{u}_T^* + \tilde{u}_D^*[1 - 1/\cosh(h/\ell)]$, i.e. the ATP-form which is the one that can attach to the membrane is depleted close to the membrane. The latter suggest to call ℓ a 'recycling length' as it binds the active form of MinD (ATP-bound form) away from the membrane. The equilibrium values of the protein concentrations at the membrane, $\tilde{u}_D^*$, $\tilde{u}_T^*$, and u_m^*, are determined by the reactive boundary condition, Eq.(50a)-(50b), and the stationarity condition for the membrane dynamics, Eq.(49),

$$\frac{\ell_{\text{off}}^2}{\ell} \, \tanh\left(\frac{h}{\ell}\right) = \frac{u_m^*}{\tilde{u}_D^*}\,, \tag{53a}$$

$$f_{\text{on}}(u_m^*, \tilde{u}_T^*) = k_{\text{off}}\, u_m^*\,, \tag{53b}$$

where we have defined the length scale $\ell_{\text{off}} := \sqrt{D_c/k_{\text{off}}}$, together with mass conservation,

$$\bar{n} = \tilde{u}_T^* + \tilde{u}_D^* + u_m^*/h\,, \tag{54}$$

where $\bar{n}$ represents the mean total mass density.

If the penetration depth is much smaller than the column height, $\ell \ll h$ (i.e. $h \to \infty$), Eq.(53a) this reduces to

$$\frac{\ell_{\text{off}}^2}{\ell} = \frac{u_m^*}{\tilde{u}_D^*} \,. \tag{55}$$

Since the total mass density is an upper bound for the bulk densities, $\bar{n} > \tilde{u}_D$, this implies that the stationary membrane density u_m^* remains bound from above in the limit $h \to \infty$

$$\lim_{h\to\infty} u_m^* < \bar{n}\, \frac{\ell_{\text{off}}^2}{\ell} = \bar{n}\, \frac{\sqrt{D_c \lambda}}{k_{\text{off}}} \,. \tag{56}$$

Strikingly, despite the absence of an explicit saturation term, there is an *emergent* saturation effect for the membrane concentration. In addition, this saturation effect is due to the combined effect of detachment and nucleotide exchange but completely independent of the attachment dynamics (f_{on}) that can be highly nonlinear/cooperative. We conclude that if reattachment to the membrane requires reactivation (which is generic for many protein classes), e.g. in the form of a nucleotide exchange, then the stationary flux onto the membrane, $f_{\text{on}}(u_m, \tilde{u}_T) = k_{\text{off}}\, u_m$ is limited to the value $\sqrt{D_c \lambda}$. As an ancillary remark, the emergent saturation provides an explanation for the surprising observation that models with simplified (unsaturated) recruitment term $\propto k_{dD} u_d u_{DT}$ (as the skeleton model used here) reproduces the dynamics *in vivo* as well as *in-vitro* with essentially the same kinetic parameters despite the fact that membrane densities *in-vitro* are two orders of magnitude higher than *in vivo*.

The saturation effect strictly requires the extended bulk dimension. To see this consider the analogous set of reaction equations with reduced bulk dimension (as described in the previous section III B 1)

$$\partial_t \bar{u}_D(t) = k_{\text{off}}\, u_m/h - \lambda \bar{u}_D \,, \tag{57a}$$

$$\partial_t \bar{u}_T(t) = -f_{\text{on}}(u_m, \bar{u}_T)/h + \lambda \bar{u}_D \tag{57b}$$

$$\partial_t u_m(t) = f_{\text{on}}(u_m, \bar{u}_T) - k_{\text{off}}\, u_m \,, \tag{57c}$$

where $\bar{u}_i(t) = \frac{1}{h}\int_0^h \mathrm{d}z\, u_i(z,t)$ denotes the spatial average over the cytosolic densities. From Eq. (57a) with the left hand side set to zero we obtain for the stationary states

$$u_m^* = h\, \frac{\lambda}{k_{\text{off}}}\, \bar{u}_D^* \,. \tag{58}$$

For any finite $\bar{u}_D^*$, there is obviously no saturation in the limit $h \to \infty$, and

$$\lim_{h\to\infty} u_m^* = \infty\,. \tag{59}$$

This clearly shows that due to the nucleotide exchange process the reduction of the bulk dimension is not a valid approximation for large bulk heights. If, however, the bulk height is small compared to the reactivation length scale ($h \ll \ell$), then the hyperbolic tangent can approximated as $\tanh(h/\ell) \approx h/\ell$. In this limit the reactive boundary conditions, Eq. (50a) and (50b), for the stationary bulk profiles reduce to

$$D_c \nabla_z u_D|_{z=0} = \lambda \tilde{u}_D^* h = k_{\text{off}} u_m^*\,, \tag{60a}$$

$$D_c \nabla_z u_T|_{z=0} = -\lambda \tilde{u}_D^* h = -f_{\text{on}}(u_m^*, u_T^*)\,, \tag{60b}$$

which is equivalent to the stationarity condition in the reduced system obtained from Eqs. (57a) and (57b) by setting the left hand sides to zero.
We conclude that nucleotide exchange prohibits reduction of the bulk dimension unless $h \ll \ell$. For the Min system studied *in-vitro* one has $h/\ell = \mathcal{O}(10^3)$ [11], i.e. one is actually in the opposite limit $h \gg \ell$ where bulk dynamics is essential. Neglecting nucleotide exchange or reducing the bulk dimension if the condition $h \ll \ell$ is not met would be seriously flawed as it misses the saturation of membrane attachment. In large (*in-vitro*) systems this either necessitates the inclusion of explicit *ad hoc* saturation terms that perturb the nonlinear dynamics and introduce additional parameters, or it leads to membrane densities that exceed the carrying capacities of a membrane (due to volume exclusion) by orders of magnitude. Both of these 'quick fixes' are unsuitable for a quantitative theoretical account for reaction-diffusion systems.

C. Reduction to 2D slice geometry

Since the bulk dimension cannot be eliminated a reduction of the spatial dimension can only be sought on the membrane. Let us assume cartesian coordinates (x, y, z) with the membrane at $z = 0$. Let us further assume a spiral wave pattern at the membrane with the spiral centre at $x = y = 0$. On any coordinate axis (either $y = 0$ or $x = 0$) we now find for any protein density u_i an approximately constant density profile in the direction orthogonal to the axis under consideration, i.e. $\nabla_y u_i|_{y=0} \approx 0$ or $\nabla_x u_i|_{x=0} \approx 0$. By focusing on such a section of the system we loose the ability to distinguish between spiral wave patterns, target wave patterns, and travelling wave patterns, but we also

reduce the reactive membrane to one dimension and the diffusive bulk to two dimensions. To study the mechanisms behind wave formation and coherence in general this is a very convenient reduction. Most importantly it allows us to run simulations on a time-scale of hours and days (2D) rather than weeks and months (3D). Therefore, we will perform the mechanistic analysis of wave dynamics in the 2D section and compare the results with a single representative 3D simulation that utilises the same parameters as the reduced 2D system. For now on we will refer to the reduced 2D system as the (x, z) frame, with the lateral dimension x and the extended bulk dimension z.

IV. LINEAR STABILITY ANALYSIS IN BOX GEOMETRY

The starting point of any linear stability analysis is the computation of a steady state around which the system can be linearised. For spatially extended systems this is typically a spatially uniform steady state. However, in the box geometry under consideration such a uniform steady state does not exist: While the steady state is spatially uniform along the membrane (in the lateral direction), nucleotide exchange in the bulk (longitudinal direction) induces density gradients characteristic for source-degradation processes; see also the discussion in the preceding section. Note that in general nonlinearities acting on non-uniform density profiles could seriously complicate the stability analysis due to mode-coupling. In the present case, however, the nonlinearities are restricted to the reactive boundary (membrane) such that the non-uniformity in the bulk (cytosol) has no direct effect on the nonlinear dynamics, i.e. it does not cause mode-coupling.

In the following we consider a 2D slice geometry as described above, with the lateral dimension x and the extended bulk (longitudinal) dimension z. A spatially uniform state at the membrane means that $\nabla_x u_i = 0$ for all protein densities. The stationary density profiles in the bulk are then given by (c.f. Sec. III B 2)

$$u_{DD}(z) = \tilde{u}^*_{DD} \frac{\cosh\left((h-z)/\ell\right)}{\cosh\left(h/\ell\right)}\,, \tag{61a}$$

$$u_{DT}(z) = \tilde{u}^*_{DT} + \tilde{u}^*_{DD}\left(1 - \frac{\cosh\left((h-z)/\ell\right)}{\cosh\left(h/\ell\right)}\right)\,, \tag{61b}$$

$$u_E(z) = \tilde{u}^*_E\,, \tag{61c}$$

where $\tilde{u}^*_i$ denote the spatially uniform stationary cytosolic densities at the membrane, and $\ell = \sqrt{D_c/\lambda}$ gives the penetration depth into the cytosol; note that the corresponding stationary profiles of the total mass densities, $u_E(z)$ and $u_D(z) = u_{DD}(z) + u_{DT}(z)$, are spatially uniform in the bulk. Upon inserting all these stationary bulk density profiles into the reactive boundary conditions at the membrane, Eqs. (31a)-(31c), one finds

$$\ell\, \tilde{u}^*_{DD}\, \tanh\left(h/\ell\right) = f_{DD}(u^*_{de})/\lambda\,, \tag{62a}$$

$$-\ell\, \tilde{u}^*_{DD}\, \tanh\left(h/\ell\right) = f_{DT}(\tilde{u}^*_{DT}, u^*_d)/\lambda\,, \tag{62b}$$

$$0 = f_E(\tilde{u}^*_E, u^*_d, u^*_{de})\,, \tag{62c}$$

which are complemented by the stationarity conditions for the membrane dynamics, Eq. (29d)-(29e),

$$0 = f_d(\tilde{u}^*_{DT}, \tilde{u}^*_E, u^*_d, u^*_{de})\,, \tag{63a}$$

$$0 = f_{de}(\tilde{u}^*_E, u^*_d, u^*_{de})\,. \tag{63b}$$

(As an aside we note that the above five equations determining the equilibria are not independent: $f_{de}=0$ is the same condition as $f_E=0$, and upon adding Eq. (63a) and Eq. (63b) one finds $f_{DD}+f_{DT}=0$, which is equivalent to $f_{de}=0=f_d$. Hence, there is no new information in the stationarity conditions on the membrane which is not already contained in the flux balance condition on the membrane.) Moreover, the stationary states have to satisfy global mass conservation

$$\overline{[\mathrm{MinD}]} = \tilde{u}^*_{DD} + \tilde{u}^*_{DT} + (u^*_d + u^*_{de})/h\,, \tag{64a}$$

$$\overline{[\mathrm{MinE}]} = \tilde{u}^*_E + u^*_{de}/h\,. \tag{64b}$$

In a linear stability analysis one considers the time evolution of small perturbations with respect to these stationary states, i.e. $u_i(x,z,t) = u^*_i(z) + \delta u_i(x,z,t)$ (where membrane densities lack the dependence on the z-coordinate). Expanding the dynamics of the small perturbations in terms of Fourier modes

$$\delta u_{DD}(x,z,t) = \sum_q e^{\sigma_q t}\cos(qx)\,\zeta_{DD}(z;q)\,, \tag{65a}$$

$$\delta u_{DT}(x,z,t) = \sum_q e^{\sigma_q t}\cos(qx)\,\zeta_{DT}(z;q)\,, \tag{65b}$$

$$\delta u_E(x,z,t) = \sum_q e^{\sigma_q t}\cos(qx)\,\zeta_E(z;q)\,, \tag{65c}$$

$$\delta u_d(x,t) = \sum_q e^{\sigma_q t}\cos(qx)\,\delta\tilde{u}^q_d\,, \tag{65d}$$

$$\delta u_{de}(x,t) = \sum_q e^{\sigma_q t}\cos(qx)\,\delta\tilde{u}^q_{de}\,, \tag{65e}$$

and inserting $u_i(x,z,t) = u^*_i(z) + \delta u_i(x,z,t)$ into the (linear) bulk diffusion equations (Eq. 29a-29c) and taking the boundary conditions (Eq. 31a-32c) into account, the corresponding bulk functions $\zeta_i(z;q)$ are obtained analytically

as

$$\zeta_{DD}(z;q) = \delta\tilde{u}^q_{DD}\ \frac{\cosh\left(\frac{h-z}{\ell_q(\lambda+\sigma_q)}\right)}{\cosh\left(\frac{h}{\ell_q(\lambda+\sigma_q)}\right)}, \tag{66a}$$

$$\zeta_{DT}(z;q) = (\delta\tilde{u}^q_{DT} + \delta\tilde{u}^q_{DD})\ \frac{\cosh\left(\frac{h-z}{\ell_q(\sigma_q)}\right)}{\cosh\left(\frac{h}{\ell_q(\sigma_q)}\right)} - \delta\tilde{u}^q_{DD}\ \frac{\cosh\left(\frac{h-z}{\ell_q(\lambda+\sigma_q)}\right)}{\cosh\left(\frac{h}{\ell_q(\lambda+\sigma_q)}\right)}, \tag{66b}$$

$$\zeta_{E}(z;q) = \delta\tilde{u}^q_{E}\ \frac{\cosh\left(\frac{h-z}{\ell_q(\sigma_q)}\right)}{\cosh\left(\frac{h}{\ell_q(\sigma_q)}\right)}, \tag{66c}$$

where we have defined

$$\ell_q(\chi_q) := \sqrt{\frac{D_c}{\chi_q + D_c q^2}}, \tag{67}$$

generalising the penetration depth ℓ to a wave vector dependent quantity, and $\delta\tilde{u}^q_i$ are Fourier coefficients that depend on the wavenumber q.
Using the shorthand notation for a term describing the coupling between the membrane concentrations and the density profiles in the bulk

$$\Gamma_q(\chi_q) = \frac{D_c}{\ell_q(\chi_q)}\ \tanh\left(\frac{h}{\ell_q(\chi_q)}\right), \tag{68}$$

and the first Taylor coefficient for the reaction terms

$$f^i_j = \left.\frac{\partial f_j(\mathbf{u})}{\partial u_i}\right|_{\mathbf{u}=\mathbf{u}^*}, \tag{69}$$

the linear system reads $\mathcal{L}_q\,\delta\tilde{\mathbf{u}}_q = 0$, for each $\delta\tilde{\mathbf{u}}_q = \left[\delta\tilde{u}^q_{DD}, \delta\tilde{u}^q_{DT}, \delta\tilde{u}^q_{E}, \delta\tilde{u}^q_{d}, \delta\tilde{u}^q_{de}\right]^T$, where $\mathcal{L}_q$ is given by

$$\mathcal{L}_q = \begin{bmatrix} f^{DD}_{DD}-\Gamma_q(\sigma_q+\lambda) & f^{DT}_{DD} & f^{E}_{DD} & f^{d}_{DD} & f^{de}_{DD} \\ f^{DD}_{DT}+\Gamma_q(\sigma_q+\lambda)-\Gamma_q(\sigma_q) & f^{DT}_{DT}-\Gamma_q(\sigma_q) & f^{E}_{DT} & f^{d}_{DT} & f^{de}_{DT} \\ f^{DD}_{E} & f^{DT}_{E} & f^{E}_{E}-\Gamma_q(\sigma_q) & f^{d}_{E} & f^{de}_{E} \\ f^{DD}_{d} & f^{DT}_{d} & f^{E}_{d} & f^{d}_{d}-\sigma_q-D_m q^2 & f^{de}_{d} \\ f^{DD}_{de} & f^{DT}_{de} & f^{E}_{de} & f^{d}_{de} & f^{de}_{de}-\sigma_q-D_m q^2 \end{bmatrix}. \tag{70}$$

The first three rows of $\mathcal{L}_q$ are the linearisation of the reactive boundaries Eq. (31a)-(31c), and the last two rows are the linearisation of the membrane dynamics Eq. (29d)-(29e).

The dispersion relation $\max \mathrm{Re}[\sigma_q]$ (i.e. the fastest growth rates of each wavenumber q) are then obtained as solutions of

$$\det \mathcal{L}_q = 0\,. \tag{71}$$

Since $\mathcal{L}_q$ is non-algebraic in σ_q, solutions can only be obtained numerically. For this purpose we use the iterative solver `FindRoot[]` provided by Wolfram Mathematica 9 to compute the data used in Fig. 2A,D and Fig. 4A,B in the main text.

V. NUMERICAL SIMULATION

All simulations have been performed with Comsol Multiphysics 4.4 that employs the finite element method. In all 2D simulations of the aforementioned (x, z) frame the system geometry is a rectangle with variable height h and fixed width $L = 500\mu m$. The boundaries $x = 0, L$ we employ periodic boundary conditions. We use a free triangular mesh with minimal mesh element size $\mathcal{M}_{\min} = 0.05\mu m$ at the membrane and a maximal mesh element size $\mathcal{M}_{\max} = 5\mu m$ in the bulk far away from the membrane. Close to the membrane the bulk mesh element size increases with a mesh growth rate r set to $r = 1.2$ (c.f. the documentation of Comsol Multiphysics for the details). All mesh sizes are chosen conservatively well below the smallest length scale of the observed pattern. Further reducing the mesh size has no effect on the simulation results. All simulations were performed using the direct PARDISO solver with relative tolerance manually set to 10^{-6} and default settings otherwise.

VI. EXTRACTING LOCAL EQUILIBRIA, AMPLITUDES AND CONTROL VARIABLES FROM NUMERICAL DATA

This chapter contains a description of the procedures we used to determine local equilibria, amplitudes and control variables from our numerical data.

A. Local membrane equilibria

In Section I we have introduced the 'Gedankenkonstrukt' (notional construct) of a local equilibrium for reaction-diffusion systems in a uniform d-dimensional reaction volume. Here we generalize this concept to situations where a reactive surface (membrane) is coupled to a bulk volume (cytosol).
Before giving a formal definition, let us take a step back and reiterate and expand on the main idea behind the local equilibrium concept. From the analysis of the planar 2-component reaction-diffusion system in Section I we have learned that any lateral instability (with unequal diffusion coefficients) induces a local change of total mass densities, and thereby shifts local equilibria. But what can be learned from the information about the local equilibria? One of the key advances brought about by the framework of nonlinear dynamics is the concept of *phase portraits*, which are geometric representation of the flow (system trajectories) in the phase space of a dynamical system. For well-mixed systems, already a calculation of the fixed points (equilibria) along with the surrounding flow field (linear stability) may often suffice to infer the global dynamics (attractors) of the system qualitatively. For instance, the dynamics in a system with one stable equilibrium will converge towards this stable state. In a system with two stable and one unstable equilibria, the unstable equilibrium will separate the basins of attraction of the two stable equilibria; as such the initial condition will fully determine the fate of the dynamics. If there is a single equilibrium which is oscillatory unstable (complex eigenvalues) the attractor approached by the dynamics is likely to be a limit cycle and the *structure of the flow field* (i.e. the topology of the associated vector field) that guides any dynamics will be that of a spiral with increasing amplitude (i.e. the distance to the unstable equilibrium). Of course, there are many more intricate cases that do not allow such a global a priori assessment of the flow flied in phase space (phase portrait). However, it is striking that a broad range of non-equilibrium phenomena can be reproduced and elucidated on the basis of such simple systems. Let us now illustrate how the notion of phase portraits is useful also for the investigation of spatially extended systems. One of the

most prominent classical examples, is the complex Ginzburg-Landau equation, which exhibits wave solutions as well as states of spatio-temporal chaos. In this model system the local flow field has the generic structure of a stable limit cycle close to supercritical Hopf bifurcation (Stuard-Landau oscillators). In the complex Ginzburg-Landau equation these local dynamics are coupled diffusively, however, the local flow field in phase space is spatially uniform and invariant with respect to the system dynamics (i.e. there is no movement of equilibria). If we now imagine the time-evolution of a spatially non-uniform state (e.g. a wave pattern) then all local dynamics will be guided by the flow field imposed by the Stuard-Landau oscillator. However, neighbouring points will be shifted in phase and diffusion will try to remove this difference. Therefore, the actual local trajectories of the spatially extended system will not be trajectories of the local dynamical system (Stuard-Landau oscillators) per se, and the stable limit cycle of the local dynamical system will never be reached (despite being the local attractor). We note this to emphasise that it is actually *not the local attractors which reflect the dynamics of the spatially extended system, but the flow fields they impose.* These flow fields can be inferred from a linear stability and bifurcation analysis of the local dynamical system.

With this in mind we can rephrase and specify the idea behind the notion of a local equilibrium: To infer local attractors from the observed spatiotemporal dynamics (in our case simulation data) in order to infer the structure of the local flow field (in local phase space) by computing the position, stability, and bifurcations of local equilibria as some control variables (local total densities) are varied.

Therefore, in the case of a reactive membrane coupled to a cytosolic volume, these local equilibria and attractors have to be defined such as to reflect the structure of the *instantaneous local flow field in local phase space* which guides the dynamics at a given membrane position $(x, y, z)|_{z=0}$ at time t. Consider a (two-dimensional) slice of the box geometry as described in Section III C and denote the membrane position by x. Since the reactive dynamics at the membrane is coupled to a cytosolic column of height h, one has to specify in the definition of local equilibria at the membrane (short: local membrane equilibria) how to account for the diffusive dynamics in the extended bulk direction. At first sight, one might argue that one should (for each membrane position x) integrate the instantaneous cytosolic densities over the whole cytosolic column $[0, h]$, and then compute the local equilibria (at position x) using the thereby

obtained total masses. Such a definition would, however, in general not be useful for understanding the local reaction dynamics at the membrane at a given time t as it includes proteins far away from the membrane that do not participate in the reactive dynamics at that given time. Those proteins only have a delayed effect since they need to diffuse to the membrane before they can participate in any reaction (in addition, these proteins would also spread laterally).

Aiming for an *instantaneous local flow field in local phase space* one needs a definition of local membrane equilibria that only depends on the protein densities at the membrane. This includes the cytosolic densities at the membrane $\{\tilde{u}_{DD}(x,t), \tilde{u}_{DT}(x,t), \tilde{u}_E(x,t)\}$, as well as the densities on the membrane $\{u_d(x,t), u_{de}(x,t)\}$. Imagine now a situation where at some time t the cytosolic column is in diffusive equilibrium with the membrane (and hence the bulk profiles are the stationary profiles corresponding to the given protein densities at the membrane, c.f. Section III B 2). Then, there would be no net protein flux to and from the membrane due to cytosolic diffusion, i.e. no effect of the diffusive dynamics in the cytosol on the membrane dynamics. In this case only a change of the densities at the membrane would induce dynamics in the cytosol. As a consequence, the structure of the flow field in local phase space would be completely determined by the densities at the membrane at time t and invariant with respect to diffusive dynamics in the cytosolic column. Moreover, the local values of the total mass densities controlling the ensuing equilibria and their stability would be those contained in the whole cytosolic column $[0, h]$.

All these statements would remain strictly valid as long as the bulk adiabatically follows the membrane dynamics (which in any realistic scenario is certainly not the case). However, for defining local membrane equilibria, it is key to realise that the local flow field which guides the local protein dynamics at the membrane is not determined by the globally conserved mass densities, but only by the local values of these mass densities right at the membrane. This suggests the following definition of a local membrane equilibrium: Given the protein densities at the membrane at some time t, one constructs the stationary density profiles in the bulk that correspond to these membrane densities; we call this an adiabatically extrapolated bulk. This ensures, as we have argued above, that the ensuing flow fields are independent of the diffusive cytosolic dynamics far away from the membrane at this particular time t. Hence, the local flow fields obtained from constructing the adiabatic bulk corresponding to a given set proteins densities at the membrane have precisely that property which one expects from a proper notion of local equilibrium: It reflects the

flow field of the nonlinear dynamics at the membrane at time t.
It is important to realise that the total mass computed with the adiabatic bulk does not necessarily coincide with the total mass in the actual system, it only reflects the total mass that affects the nonlinear dynamics at time t. As we will see below, for the model of the Min system considered in this article the average mass in the adiabatic bulk does coincide with the actual mass in the cytosol system. As such, all spatial averages of densities computed with the adiabatic bulk remain conserved.
Next we will present the detailed computation of local equilibria from the simulations of the model for the Min system. We denote all densities extracted from simulations by a superscript and positions and times by subscripts $u_i^{\mathrm{num}}(x,t)$. With the total cytosolic MinD density $u_D = u_{DD} + u_{DT}$ the stationary bulk dynamics are obtained by solving the stationary diffusion equation

$$0 = D_D \nabla_z^2 u_D \,, \tag{72a}$$

$$0 = D_E \nabla_z^2 u_E \,, \tag{72b}$$

subject to reflective boundary conditions at the surface $z = h$

$$D_D \nabla_z u_D|_{z=h} = 0 \,, \tag{73a}$$

$$D_E \nabla_z u_E|_{z=h} = 0 \,, \tag{73b}$$

and fixed (Dirichlet) boundary conditions at the membrane

$$\tilde{u}_D = u_D|_{z=0} = u_{DD}^{\mathrm{num}}(x,t) + u_{DT}^{\mathrm{num}}(x,t) \,, \tag{74a}$$

$$\tilde{u}_E = u_E|_{z=0} = u_E^{\mathrm{num}}(x,t) \,. \tag{74b}$$

Since the solutions to theses equations are simply constant in space we obtain for the local total densities, $[\mathrm{MinD}]_{x,t}^{\mathrm{num}}$ and $[\mathrm{MinE}]_{x,t}^{\mathrm{num}}$, extracted from the simulations

$$[\mathrm{MinD}]_{x,t}^{\mathrm{num}} = u_{DD}^{\mathrm{num}}(x,t) + u_{DT}^{\mathrm{num}}(x,t) + \left[u_d^{\mathrm{num}}(x,t) + u_{de}^{\mathrm{num}}(x,t)\right]/h \,, \tag{75}$$

$$[\mathrm{MinE}]_{x,t}^{\mathrm{num}} = u_E^{\mathrm{num}}(x,t) + u_{de}^{\mathrm{num}}(x,t)/h \,. \tag{76}$$

The local equilibria are then obtained as shown in Section IV with the local total densities

$$[\mathrm{MinD}]_{x,t}^{\mathrm{num}} = u_{DD}^{*\mathrm{num}} + u_{DT}^{*\mathrm{num}} + (u_d^{*\mathrm{num}} + u_{de}^{*\mathrm{num}})/h \tag{77}$$

$$[\mathrm{MinE}]_{x,t}^{\mathrm{num}} = u_E^{*\mathrm{num}} + u_{de}^{*\mathrm{num}}/h. \tag{78}$$

As discussed above, we note that due to the assumption of an adiabatic bulk the (lateral) spatial averages denoted by an overbar are not identical in general, i.e. $\overline{[\mathrm{MinD}]}^{\mathrm{num}}_{x,t} \neq \overline{[\mathrm{MinD}]}_x$ and $\overline{[\mathrm{MinE}]}^{\mathrm{num}}_{x,t} \neq \overline{[\mathrm{MinE}]}_x$. However, we find that the deviation is small and maximal in the turbulent state ($h = 20\mu m$):

$$\left(\overline{[\mathrm{MinD}]}^{\mathrm{num}}_{x,t} - \overline{[\mathrm{MinD}]}_x\right) / \overline{[\mathrm{MinD}]}_x \leq 0.01 \tag{79}$$

$$\left(\overline{[\mathrm{MinE}]}^{\mathrm{num}}_{x,t} - \overline{[\mathrm{MinE}]}_x\right) / \overline{[\mathrm{MinE}]}_x \leq 0.02. \tag{80}$$

These error bounds are one order of magnitude smaller for globally coherent traveling wave pattern observed at $h > 33\mu m$. The stability of local equilibria can be computed for the data extracted from simulations at any point x and time t as shown in Section IV by setting $q = 0$ and using $[\mathrm{MinD}]^{\mathrm{num}}_{x,t}$ and $[\mathrm{MinE}]^{\mathrm{num}}_{x,t}$ as total densities.

B. Control variables Σ and Δ

By our definition control variables are the local values of globally conserved quantities (total mass densities). We are mainly interested in the local change of these control variables relative to their globally conserved average. Hence, we normalise the total mass densities to the global averages

$$D_{x,t} = [\mathrm{MinD}]^{\mathrm{num}}_{x,t} / \overline{[\mathrm{MinD}]} \tag{81}$$

$$E_{x,t} = [\mathrm{MinE}]^{\mathrm{num}}_{x,t} / \overline{[\mathrm{MinE}]}. \tag{82}$$

Min protein oscillations are driven by the cyclic alternation between MinD dominance (accumulation at the membrane) and MinE dominance (depletion of the membrane). This dominance can only alternate by changing local densities. Therefore, the local ratio of MinE and MinD represents a natural control parameter for the dynamics, we define

$$\Delta_{x,t} = E_{x,t} / D_{x,t} \tag{83}$$

Since the cytosol is adiabatically slaved to the membrane dynamics on average, i.e.

$$\overline{[\mathrm{MinD}]}^{\mathrm{num}}_{x,t} \approx \overline{[\mathrm{MinD}]}_x, \tag{84}$$

$$\overline{[\mathrm{MinE}]}^{\mathrm{num}}_{x,t} \approx \overline{[\mathrm{MinE}]}_x, \tag{85}$$

the values of $\Delta_{x,t}$ remain centered around the ratio of the global average

$$\Delta_0 = \overline{E}_{x,t}/\overline{D}_{x,t}. \tag{86}$$

For the second control variable we choose the orthogonal coordinate which is a measure for the relative change of the joined total mass of MinD and MinE

$$\Sigma_{x,t} = \sqrt{\frac{1}{2}(E_{x,t}^2 + D_{x,t}^2)}, \tag{87}$$

and analogously the global average

$$\Sigma_0 = \sqrt{\frac{1}{2}(\overline{E}_{x,t}^2 + \overline{D}_{x,t}^2)}. \tag{88}$$

A representation of the coordinates in control space is shown in Supplementary Fig. 3.

C. Amplitudes

To simplify summation over components of the species MinD and MinE we define the index sets for MinD

$$\mathcal{D} = \{DD, DT, d, de\} \tag{89}$$

and for MinE

$$\mathcal{E} = \{E, de\}, \tag{90}$$

as well as the coefficient

$$\gamma_i = \begin{cases} 1/h^2 & \text{if } i \in \{d, de\} \text{ (surface densities)} \\ 1 & \text{if } i \in \{DD, DT, E\} \text{ (volume densities)} \end{cases} \tag{91}$$

to homogenise the dimensions.
We define the local amplitude of the pattern $A_{\text{pattern}}(x,t)$:

$$A_{\text{pattern}}^2(x,t) = \left(\frac{\sqrt{\sum_{i\in\mathcal{D}} \gamma_i \left(u_i^{\text{num}} - \bar{u}_i^{\text{num}}\right)^2}}{\sqrt{\sum_{i\in\mathcal{D}} \gamma_i \left(\bar{u}_i^{\text{num}}\right)^2}} \right)^2 + \left(\frac{\sqrt{\sum_{i\in\mathcal{E}} \gamma_i \left(u_i^{\text{num}} - \bar{u}_i^{\text{num}}\right)^2}}{\sqrt{\sum_{i\in\mathcal{E}} \gamma_i \left(\bar{u}_i^{\text{num}}\right)^2}} \right)^2 \tag{92}$$

the local distance from the local equilibrium $A_{\mathrm{stat}}(x,t)$:

$$A^2_{\mathrm{stat}}(x,t) = \left(\frac{\sqrt{\sum_{i\in\mathcal{D}} \gamma_i \left(u_i^{\mathrm{num}} - u_i^{*\mathrm{num}}\right)^2}}{\sqrt{\sum_{i\in\mathcal{D}} \gamma_i \left(u_i^{*\mathrm{num}}\right)^2}} \right)^2 + \left(\frac{\sqrt{\sum_{i\in\mathcal{E}} \gamma_i \left(u_i^{\mathrm{num}} - u_i^{*\mathrm{num}}\right)^2}}{\sqrt{\sum_{i\in\mathcal{E}} \gamma_i \left(u_i^{*\mathrm{num}}\right)^2}} \right)^2 \tag{93}$$

and the amplitude in control space $A_{\mathrm{control}}(x,t)$:

$$A^2_{\mathrm{control}}(x,t) = \left(\Sigma_{x,t} - 1\right)^2 + \left(\Delta_{x,t} - 1\right)^2 \ . \tag{94}$$

Note that $\Sigma_{x,t}$ and $\Delta_{x,t}$ are defined with respect to the normalised densities D and E.

VII. MAINTENANCE OF CHEMICAL TURBULENCE BELOW THE ONSET OF THE TURING INSTABILITY

To test whether a lateral instability of the spatially uniform state is required for the maintenance of chemical turbulence we modified the bulk equation of MinE (Eq. 29c) such that the total MinE density in the system slowly degrades

$$\partial_t u_E = D_c \nabla_c^2 u_E - \mu_- u_E \,. \tag{95}$$

The degradation rate μ_- is set such that the induced gradients of size $\ell_- = \sqrt{D_c/\mu_-}$ at the membrane are negligible, i.e. $h \ll \ell_-$ (c.f. section III B 2). As initial condition for the simulation with slow bulk degradation we import a numerical solution at a specific time after the system became tubulent. In this case we picked the time index $t = 1.7 \cdot 10^4\, s$. With this initial condition we then start a new simulation with bulk degradation, where we used the degradation rate $\mu_- = 1 \cdot 10^{-3}\, s^{-1}$. This choice ensures that the penetration depth is negligible, i.e. $h/\ell_- = 0.08$.
We ran this simulation for $1.7 \cdot 10^3\, s$ after which the total Min density and the MinE/MinD ratio reduced to the values $\Sigma = 0.96$ and $\Delta = 0.91$, respectively. Although these values were well below the critical values $(\Sigma, \Delta) = (1, 1)$ for the onset of the lateral instability (c.f. Fig. 2D in the main text), the turbulent state remained phenomenologically unaltered during the whole simulation time, c.f. Supplementary Fig. 4. This shows that the lateral instability is subcritical and that linear instability of the uniform state is not required for chemical turbulence. In other words: **The lateral instability is a route to chemical turbulence, but not the origin.**

VIII. POINT-TO-POINT CORRELATION KYMOGRAPHS

To visually inspect the spatiotemporal dynamics of pattern-forming systems kymographs of the particle densities are typically used. In the present case the system size is very large compared to the smallest intrinsic spatial structure of the pattern (e.g. nonlinear wave profiles), which makes kymographs of the densities ill-suited for visual inspection. We are mainly concerned with the distinction between turbulent phases of the dynamics, standing wave patterns, and travelling wave patterns. In particular, we are interested in transition between these phases. The structure of the pattern on the smallest length scales is secondary.

For an oscillatory system, the spatial correlations between histories at different points in space reveal information about the spatial coherence of the pattern. We will, therefore, compare the histories of membrane densities at specific time points t and compute the correlation of spatially nearby membrane signals. This will yield *point-to-point correlation kymographs* which are defined as follows: The spatial domain of length $L = 500\,\mu m$ is discretised into bins with a spatial resolution of $\Delta x = 0.2\,\mu m$; the position of these bins reads $x_i = i\,\Delta x$ with i an integer. For a given time t, we record at each position x_i the membrane signal (here the overall MinD membrane density $u_d^{\text{tot}} := u_d + u_{de}$)) over a time interval $T = 10\,s$ with a temporal resolution of $\Delta t = 1\,s$

$$m_i^T(t) = \left[u_d^{\text{tot}}(x_i, t-T),\ \ldots\ ,\ u_d^{\text{tot}}(x_i, t-\Delta t),\ u_d^{\text{tot}}(x_i, t)\right]. \tag{96}$$

We then, for each time point t, compute the Pearson correlation coefficients

$$\rho[m_i^T(t), m_{i\pm1}^T(t)] = \frac{\left\langle \left[m_i^T(t) - \left\langle m_i^T(t)\right\rangle\right] \cdot \left[m_{i\pm1}^T(t) - \left\langle m_{i\pm1}^T(t)\right\rangle\right]\right\rangle}{\sqrt{\left\langle \left[m_i^T(t) - \langle m_i^T(t)\rangle\right]^2\right\rangle}\sqrt{\left\langle \left[m_{i\pm1}^T(t) - \left\langle m_{i\pm1}^T\right\rangle(t)\right]^2\right\rangle}} \tag{97}$$

between membrane signals of neighbouring sites; here $\langle\cdot\rangle$ denotes the temporal mean, i.e. an average over the time sequence. Next, for each point x_i in space, we define what we term *local point-to-point correlation*

$$\rho_i^T(t) := \frac{1}{2}\Big(\,\rho[m_i^T(t), m_{i-1}^T(t) + \rho[m_i^T(t), m_{i+1}^T(t)]\,\Big), \tag{98}$$

where we assume periodic boundaries. This point-to-point correlations are then plotted as kymographs; see main text Figs. 3C, 5C, and Supplementary Fig. 9.

Since Δx is chosen much smaller that the characteristic length scales of the pattern, the point-to-point correlation will be typically high, i.e. $\rho_i^T \approx 1$. However, for any wave pattern with standing wave characteristic (which are at least

transiently maintained on the timescale T), there will be wave nodes where the local variation of the signal is small compared to the variation of signals in the vicinity of the node. Accordingly, at these points the point-to-point correlation will be very small, i.e. $\rho_k^T \approx 0$.
The point-to-point correlations function provides kymographs with a high contrast between spatial domains of high and low point-to-point correlations, and thereby gives high-resolution information on the spatiotemporal evolution of wave node positions and distances of wave nodes. For instance, standing wave patterns can be clearly identified by the uniform separation of spatially fixed wave nodes, c.f. main text Fig. 5 and Supplementary Fig. 9. Bands of travelling waves emitted from a source defect are identified as broad spatial domains of uniformly high point-to-point correlation which surrounds the two wave nodes of the source defect (single standing wave), c.f. main text Fig. 5. In the turbulent regime we observe spontaneous formations of wavefronts at (seemingly) random position, that drift in random directions with randomly varying velocities, and vanish spontaneously after random times, c.f. main text Fig. 3. A detailed analysis of the turbulent phase close to the transition to standing wave order will be made below in the following Supplementary section.

IX. TRANSITION FROM CHEMICAL TURBULENCE TO GLOBALLY COHERENT STANDING WAVES

In this section we provide the numerical evidence that the transition from chemical turbulence to coherent standing wave patterns is facilitated by the activation and interplay of two mutually commensurable modes induced by the lateral instability.

A. The defect control mode q_c

We start the discussion with the role of the *defect control mode* with wave vector q_c, which is the fastest growing mode within the band of linearly unstable modes. As described in the main text, its role is *the spatiotemporal coordination of local destabilisation, which results in the timed formation of finite sized and uniformly separated clusters of oscillatory unstable equilibria.*
To test this assertion we traced the temporal evolution of local stability in our numerical simulations: At every point x on the reactive membrane we extracted the local protein densities from the numerical data, and computed the stability of the respective local equilibria as described in the previous Sections VI A and IV of this Supplementary Material. Since we were primarily interested in their destabilisation we assigned a binary value to each local equilibrium, 0 for a stable equilibrium, and 1 for an unstable equilibrium. We extracted data from our simulations with a spatial resolution of $\Delta x = 0.4\,\mu m$ and a temporal resolution of $\Delta t = 1\,s$. We ran the simulations sufficiently long for the dynamics to enter a "stationary" phase, i.e. the spatiotemporal patterns to remain qualitatively unchanged for a sufficiently long time, here for about $\mathcal{O}(10^2)$-$\mathcal{O}(10^3)$ oscillation cycles (i.e. the spatial average of the local oscillation periods at each point in space x). From this "stationary" window we extracted the last $500s$ ($T = 500\,s$) corresponding to about $\mathcal{O}(10^1)$-$\mathcal{O}(10^2)$ local cycles. In this extracted window we computed the stability of local equilibria. Thereby we obtained, for every point x on our spatial grid, a binary sequence (string of 0s and 1s), $\mathbf{s}(x) = \{s_i(x)\}$, of length $T/\Delta t = 500$, encoding the time evolution of local stability change.
If the formation of defects is spatiotemporally coordinated, the local change of stability must be spatially correlated. To test defect coordination we, therefore, first computed the Pearson correlation coefficient $\rho(x_1, x_2) := \rho[\mathbf{s}(x_1), \mathbf{s}(x_2)]$ (c.f. Eq. (97)) for each pair of time sequences at space points x_1 and x_2 on our spatial grid. We then defined the spatial correlation function $C(r)$

characterising the local stability change,

$$C(r) = \overline{\rho(x_1, x_2)}|_{|x_1 - x_2| = r} \,, \tag{99}$$

where the average is taken over all pairs of space points (x_1, x_2) with given fixed distance $|x_1 - x_2| = r$. Since we were interested how the spatial correlation of the local equilibria's stability depends on the length scale $l_c = 2\pi/q_c$, set by the fastest growing mode q_c, we rescaled the spatial dimension by l_c and defined the dimensionless quantity $\tilde{r} := r/l_c$. To compare the spatial correlation for different system heights (control parameters) h we fitted an envelope $G(\tilde{r})$ to all rescaled correlations functions $C(\tilde{r})$,

$$G(\tilde{r}) = \left(1 + \tilde{r}/\tilde{\xi}\right)^{-2} \,, \tag{100}$$

where $\tilde{\xi} := \xi/l_c$ serves as a measure for the correlation length in units of l_c. The correlation functions with corresponding envelopes are shown for a large set of control parameters h in Supplementary Fig. 5. Please note that the wave length of the fastest growing mode, l_c, depends on the value of the control parameter, here the system height, $l_c = l_c(h)$.
From these data we make two key observations: (i) First, the correlation functions oscillate spatially with a period set by the wave length of the fastest growing mode, l_c. This shows that local destabilisation of equilibria is controlled by the fastest growing mode q_c. (ii) Second, the correlation length ξ is effectively zero for $h \leq 23\,\mu m$ (in the turbulent regime), and increases monotonically to finite values $\xi > l_c$ for $h \geq 24\,\mu m$, i.e. as soon as the first mode $q_r = 2q_c$ that is commensurable with q_c becomes part of the band of unstable modes and thereby active (Supplementary Fig. 6, c.f. main text Fig. 4D). This indicates that as soon as it becomes unstable the commensurable mode q_r plays a key role in maintaining controlled local destabilisations at distances l_c. We will discuss this role and its consequences for the spatiotemporal dynamics in the following section.

B. The mass redistribution mode q_r

In the main text we argued that the concurrence of the transition from chemical turbulence to standing waves with the activation of the commensurable mode q_r is *not* a coincidence, but that commensurability of q_r with the wave vector of the fastest growing mode q_c is in fact the mechanism underlying the emergence of order. Key to the argument was that the q_r-mode is responsible for mass

transport and determines the positions (distance from the source defect) where wavefronts are formed that are being send out by the source defects (which, in turn, are controlled by the q_c-mode). As a reminder: Source and sink defects can only be periodically formed at fixed positions if the mode responsible for mass transport is commensurable with the mode that coordinates defect distances (c.f. main text Fig. 4D and the corresponding section in the main text).

To consolidate this scenario, we inferred the characteristic distances of mass transport from the simulation data. Since mass transport is responsible for the destabilisation of local equilibria it must also be the cause for the redistribution of instability clusters (spatially connected sets of nearby unstable equilibria) from depleting source defects to nearby (propagating) wavefronts. Therefore, we can take the distance between instability clusters as a reliable and easyly accessible measure for the distance of mass transport.

Consider now a standing wave pattern (c.f. main text Fig. 4C,D), and let's take a closer look at the distances between instability clusters. From the wave profiles we infer three distinct distances between instability clusters (, c.f. Supplementary Figure 7):

(i) First, we observe short distances between shrinking instability clusters, corresponding to source defects, and instability clusters, belonging to wavefronts emitted by source defects. Let us denote this length scale as the source-wavefront (sw) distance d_{sw}. (ii) Second, we observe large, temporally increasing distances, $d_{\mathrm{w+}}$, that correspond to nearby wavefronts that originated from the same source and are propagating away from each other. These distances between instability clusters are found once the source is fully depleted, and all local equilibria at the source position become stable, such that no instability clusters are left between the wavefronts emitted by the source. As those wavefronts propagate away from each other, $d_{\mathrm{w+}}$ is bound from below by twice the distance between source and wavefront, $2d_{\mathrm{sw}} \leq d_{\mathrm{w+}}$. (iii) Third, we observe intermediate, temporally decreasing distances, $d_{\mathrm{w\text{-}}}$, that correspond to wavefronts emitted by neighbouring sources, and, therefore, propagate towards each other. This distance continuously shrinks until the instability clusters (wavefronts) merge. Since sources are separated at uniform distances l_c, this distance $d_{\mathrm{w\text{-}}}$ is bound from above by $d_{\mathrm{w\text{-}}} < l_c - 2d_{\mathrm{sw}}$.

To check whether these distances are characteristic length scales of the spatiotemporal dynamics in the standing wave regime, we computed the statistical distribution of the distances between instability clusters, d_{ic}. These distances were extracted from the same data as the spatial correlations in the previous section (i.e. stationary phases of the pattern, $T = 500\ s$, $\Delta t = 1\,s$). In the

standing wave regime ($24\ \mu m \leq h \leq 32\,\mu m$), all cluster distance distributions have a characteristic bimodal shape (Supplementary Fig. 7, c.f. main text Fig. 4D). Normalising the cluster distances d_{ic} to the respective length scale $l_r = 2\pi/q_r$, set by the commensurable mode q_r, shows that the first peak of the bimodal distribution exhibits a maximum around $l_r/2$, and extends to l_r, while the second peak of the distribution is bound from below by l_r.

From the foregoing observation of cluster distances in the standing wave profile we know that there are two bound distances, $d_{\mathrm{w+}}$ and $d_{\mathrm{w\text{-}}}$. The distance $d_{\mathrm{w\text{-}}}$, corresponding to merging wavefronts, is bound from above. Hence, these distances are entirely accumulated in the first peak of the distribution shown in Supplementary Fig. 7. On the other hand, the distance $d_{\mathrm{w+}}$ is bound from below since it corresponds to wavefronts propagating away from each other. Therefore, the distances $d_{\mathrm{w+}}$ must be entirely accumulated in the second peak of the cluster distribution. Moreover, since $d_{\mathrm{w+}}$ is bound from below by the distance of cluster redistribution d_{sw}, i.e. $2d_{\mathrm{sw}} \leq d_{\mathrm{w+}}$, our data reveals that this bound is set by l_r and we can identify $d_{\mathrm{sw}} \approx l_r/2$. In other words, the maximum of the first peak of the cluster distribution accumulates the source-wavefront distances d_{sw}, and this distance is set by the commensurable mass redistribution mode q_r in the standing wave regime.

Overall, the separation and sharpness of the two peaks in the cluster distance distribution can be seen as a measure for the precision with which the distance of mass transport (i.e. redistribution of instability clusters) is controlled. Upon comparing the instability cluster distance distributions of the standing wave regime and turbulent phase (e.g. at $h = 20\,\mu m$), the following features become apparent: In the turbulent phase (i) the distribution becomes much broader, (ii) the first peak gains weight and its maximum shifts towards zero, (iii) the separation between the two peaks becomes much weaker, and (iv) the alignment with the commensurable mode q_r is lost in the first peak. Hence, in the turbulent phase mass transport (redistribution of unstable clusters) takes place on a broad range of length scales. Strikingly, full separation between both peaks in the cluster distribution occurs between $h = 23\,\mu m$ and $h = 24\,\mu m$, i.e. right as the commensurable mode q_r becomes active (unstable).

Taken together, we conclude that mass transport (redistribution of instability clusters) is controlled by the active commensurable mode q_r, otherwise (when q_r is not active) there is no robust length scale of mass redistribution.

C. Commensurability and interaction of mass redistribution and defect coordination modes: Predictions

So far we have made the following key observations when the system height (control parameter) h is increased above a threshold value $h \approx 23.5\,\mu m$ where an unstable mode q_r emerges which is commensurable with the fastest growing mode $q_r = 2q_c$:

- Instead of the (turbulent) pattern we observe spatially coherent standing waves with a characteristic wavelength set by the fastest growing mode: $l_c = 2\pi/q_c$.
- Changes in the stability of local equilibria become spatially correlated, and the corresponding correlation length ξ increases monotonously with the system height (control parameter) h.
- The correlation function for the stability of local equilibria oscillates spatially with a period set by the fastest growing mode q_c.
- A fixed length scale $l_r/2$ for mass transport (redistribution of instability clusters) is established by the active (unstable) commensurable mode $q_r = 2q_c$.

In the main text we argued that these observations are caused by the concerted interplay between the two commensurable modes q_c and $q_r = 2q_c$: If source defects are synchronously formed at a uniform distance, and if the emission of mass by these source defects (wavefront formation) is symmetric and synchronised in all directions, then the positions of source and sink defects are invariant. Based on this *mode commensurability mechanism*, one can make predictions for the dynamics in the turbulent phase close to the transition to the standing wave phase, where defect coordination and mass transport are almost commensurable. These predictions can then be compared with our numerical data and provide a critical test for the proposed mode commensurability mechanism for the emergence of standing wave patterns.
Assuming that robust defect coordination and mass transport are indeed caused by the interaction of the commensurable modes q_c and q_r, what can we infer about the phenomenology at the transition? Let us perform the following "Gedankenexperiment" (thought experiment): Assume that the mode $q_{\max}$ at the outmost right of the band of unstable modes, i.e. the unstable mode with the shortest wavelength $l_{\min} = 2\pi/q_{\max}$, is almost commensurable

with the fastest growing mode q_c such that $2\pi/(l_{\min} - \delta) = 2q_c$ with some small $\delta > 0$.

Suppose that we align the troughs (the minima of the *defect control mode* which represent source defects where mass is redistributed from the minima to the maxima of the *mass redistribution mode*, c.f. main text Fig. 4D) of the modes q_c and $q_{\max}$ at some point in space. Henceforth, we will refer to this point as the *interface*); see Supp. Fig. 8 for an illustration. Then, at the right and left nearest neighbouring crests of the control mode (q_c), the mass redistribution mode ($q_{\max}$) has a phase shift of $+\delta$ and $-\delta$ with respect to the control mode, respectively. At the next neighbouring crests, this phase shift is $\pm\, 2\delta$, and it accumulates further as one moves away from the point of alignment (interface) until it reaches a full period $\pm 2\pi$ (phase slip) at some distance from the interface. Imagine now that an initial state given by a standing wave train of n wave nodes to the right and left to the interface respectively, and, for specificity, let's consider the left hand side of the interface. How does the concerted action of the control mode and the mass distribution mode now play out?

While the depleting mass sources, controlled by the q_c-mode, are still redistributed by the action of the mass redistribution mode $q_{\max}$, incommensurability between these modes implies that the left-right symmetry of mass redistribution is broken within each wave period of the control mode (c.f. Remark [12]). Wavefronts emitted by neighbouring sources do no longer merge (in a sink defect) in the exact center between the emitting sources, but at some off-center position which is half-way between the wavefronts at the crest of the mass-redistribution mode; for an illustration see again Supp. Fig. 8. We can expect that the phase shift between defect control and mass redistribution modes induces an increasing frustration with the distance from the interface that will at some point impede the concerted interplay between these two modes, and that this point will be reached well before the modes get out of phase at $n\delta = l_c/2$. As a consequence, the standing wave will be a finite wave packet with $k \ll l_c/(2\delta)$ nodes. After a half time period of the defect control mode the phase of the defect control mode will be shifted with respect to the mass redistribution mode by $\delta/2$ at the position of the first source defect left of the interface, $3\delta/2$ at the second source defect up to $(2k-1)\delta/2$ at the k-th defect to the left. Hence, in a band of k wave (space) periods the phase shift will have increased at each node by $\delta/2$ within a half time period (source-sink defect cycle), further increasing the frustration caused by the phase shift throughout the band of k waves. To maintain the wave form the positions of defects need to shift to the left – along with the controlling

mode q_c. The increased frustration can be removed entirely at one side of the interface (here the left side) by shifting the defect control mode $\delta/2$ to the left each half period. Assuming that the phase shift is small enough at the k-th node to maintain the standing wave pattern, a shift of the defect control mode by δ to the left per cycle would maintain a constant phase shift at each wave node, and thereby the pattern. However, this would also shift the position of the interface by $\sim 2l_{\min} \approx l_c$ to the left with each cycle, whereas the wave nodes are only shifted by $\sim \delta$ to the left with each cycle. Given that $\delta \ll l_c$ for weak incommensurability this suggests that with each cycle a wave node is lost at the right hand side of the pattern as it slips behind the interface whereas an additional wave node can be maintained at the left hand side, overall maintaining a band of k wave nodes.

Since we have, for specificity, assumed that mass distribution leads to realignment of the wave nodes for the control and mass distribution mode to the left of the interface, this concomitantly leads to an increasing misalignment to the right of the interface, as can be easily inferred from Supp. Fig. 8. The accumulating phase shift then quickly leads to phase slips at some constant distance from the interface. As the interface moves, these phase slips should, therefore, move alongside at a constant distance from the interface. In other words, while the wave train of k nodes to the left of the interface remains at some finite length is maintained, the pattern at the right of the interface is constantly broken up into smaller wave trains by those periodically generated phase slips.

Since the same arguments apply if we had assumed that the realignment of the wave combs happens to the right of the interface, one should observe interface propagation with the features of right and left propagating wave trains reversed. The choice between left and right will presumably depend on the history of the system.

Taken together, we predict – based on the hypothesis that order (global coherence) emerges due to commensurable mode interaction – the following precursor phenomena in the turbulent regime close below the threshold to the standing wave pattern regime:

(1) Alignment between the incommensurable wave modes q_r and q_c will lead to interfaces between left and right propagating wave trains. The speed of these interfaces v_I will be of the order of $v_I \approx l_c/\tau$, where τ denotes the period of one oscillation cycle. However, the above line of arguments suggests that the wave trains on both sides of the interface try to achieve alignment of the control modes to minimise the frustration caused by the phase shift on their respective sides. One may, therefore, expect that the

realignment to the side where the wave train is maintained is hampered by the realignment the wave trains on the other side try to achieve. Hence, the estimate of the interface speed, which took only one side of the interface into consideration, is likely to be an upper bound, i.e. $v_I \lessapprox l_c/\tau$.

(2) In addition, we can also estimate the speed of the propagating train of standing waves v_W to be of the order of $v_W \gtrapprox \delta/\tau$, which is the minimal phase shift per period required to maintain the wave pattern.

(3) The two points above imply that the speed of the interface is much faster than the speed of the wave train, $v_I \gg v_W$. This means that during each oscillation cycle the (rightmost) wave at the interface slips behind the interface, thereby, dropping out of the wave train. At the same time the phase shift left to the wave train is reduced, enabling an additional wave node to join the wave train.

(4) The maintenance of wave nodes in the wave train should be more stable close to the interface where the phase shift between defect control and mass redistribution mode is minimal.

(5) There will be a preferred formation of extended propagating wave packets close to one side of the interface, and turbulent-like dynamics at the other side. More precisely, the wave trains emerging on the other side of the interface are short because of phase slips induced by the moving interface. These phase slips should have a constant distance from the moving interface.

In the following section we will compare these predictions with the simulation data.

D. Commensurability and interaction of mass redistribution and defect coordination modes: Comparison with the simulation data

Supplementary Fig. 9 shows the point-to-point correlation kymograph for the case where q_c and $q_{\max}$ are weakly incommensurable ($\delta/l_c = 0.03$ for a control parameter $h = 23\,\mu m$) in the turbulent regime. Indeed, visual inspection of the kymograph does confirm our predictions: In the observed time window we find a standing wave train comprising a few ($\approx 5 \pm 2$) wave nodes drifting to the left. The right boundary of the wave packet marks a moving interface

to right moving wave trains. As predicted, the maintenance of drifting wave nodes is most stable (i.e. the position of the wave node changes continuously without any interruptions) close to the interface where the phase shifts δ have not given rise to a phase slip. As soon as phase slips occur (visible as irregular interruptions of wave nodes) the pattern become more turbulent , such that the left boundary of the standing wave train cannot be well defined. On the right hand side of the interface (the right boundary of the standing wave train), wave nodes mainly drift to the right, but are often interrupted and reformed at an approximately constant distance nearby the interface.
All these observations are fully consistent with the above predictions based on our idealised Gedankenexperiment. To test the predictions also quantitatively we extracted the speed of the interface v_I and the speed of few wave trains v_W from the kymograph in Supplementary Fig. 9. We estimated the local oscillation period $\tau \approx 16.67\, s$ by averaging over several local oscillation periods. For the speed of the interface we find $v_I \approx 0.42\, \mu m/s < l_c/\tau \approx 0.77\, \mu m/s$, which, given the idealised nature of our estimate is a surprisingly good agreement (note that we expected the actual interface speed to be slower due to the influence of counter-propagating waves). For the speed of wave trains v_W we find values in the range $0.026\, \mu m/s \; - \; 0.069\, \mu m/s$, which is also consistent with our estimate of the lower bound $v_W \gtrsim \delta/\tau \approx 0.023\, \mu m/s$. Hence, the spatial structure of the turbulent state closely below threshold is not only fully consistent with our *commensurability mechanism*, but it even enables us to infer qualitative and quantitative details of precursor phenomena close to the transition from the turbulent to the standing wave phase from the assumption that order emerges from the control of local stability by two commensurable modes.
We will next discuss the spatiotemporal dynamics for a control parameter value, $h = 24\, \mu m$, which is slightly above the threshold for the activation of the commensurable mode q_r. Visual inspection of the point-to-point correlation kymograph shows that wave nodes are now maintained (in time) throughout the whole spatial domain. Strikingly, we also observe considerable drift of wave nodes in some parts of the spatial domain, as well as local defects (phase slips) of the spatial structure. We can identify interfaces between right- and left-moving wave trains similar to those found in the turbulent regime (for the control parameter $h = 23\, \mu m$). In the particular time window shown in Supp. Fig. 9, there are several locations (interfaces) where the propagation direction of wave trains change. If this happens, the wave trains start to move apart from each other. The corresponding kymograph (Supp. Fig. 9) shows that the distance between the two wave nodes neighbouring the interface on

the left and right start to increase. However, according to our notion that the pattern (which is comprises all wave trains) is controlled by two global (extending through the whole spatial domain) modes q_c and q_r, c.f. Supp. Fig 8 and main text Fig 4D, the observed divergence of wave nodes cannot proceed. If we assume that the modes maintain alignment with the wave train in one direction (say with the right propagating wave train), then the phase difference with the wave train propagating in the other direction will increase, leading to a phase slip at some point. In this case both wave trains will merge following the phase slip and maintain the drift in one direction. Alternatively, if neither wave train achieves alignment with the control modes, the phase difference will increase for the wave trains propagating in both directions and both will undergo a phase slip defect at some point. In this case both wave trains will also merge following the phase slip. These two possibilities are exactly what we observe in the kymograph. For both cases we can summarise that the global dynamics (the pattern) follow the control modes (trying to achieve alignment with them).
Increasing the control parameter h even further ($h \geq 25\,\mu m$) shows that the propagation of wave trains is reduced and the point-to-point correlation kymographs show increasing global coherence, which is consistent with the increasing correlation length of local stability change (c.f. Supp. Fig. 6).

E. Commensurability and interaction of mass redistribution and defect coordination modes: Conclusion and Summary

One main finding of our article is that the relevant part of the pattern forming dynamics in mass-conserved reaction-diffusion systems is the redistribution of total mass by unstable modes activated in a lateral instability. We were able to show analytically that unstable modes always induce a redistribution of total mass for unequal diffusion constants. Hence, it remained to show that the redistribution of the total masses of the proteins comprising the biochemical network is the key process underlying pattern forming dynamics. Based on the assumption that mass redistribution is indeed the key process, we inferred that the concerted action of two mutually commensurable modes q_c and $q_r = 2q_c$ is responsible for the transition from chemical turbulence to long range coherent standing wave order. Indeed, the point where the commensurable mode $q_r = 2q_c$ becomes linearly unstable marks the threshold where the phenomenology of the spatiotemporal dynamics changes on a qualitative as well as a quantitative level, gaining characteristic features set by the length

scales l_c and l_r:

- The turbulent pattern becomes a standing wave pattern with wavelength approximately given by l_c.

- The change of local stability becomes spatially correlated and the corresponding correlation length increases with the control parameter h.

- The correlation function of local stability change oscillates on a length scale set by l_c which sets the distance separating source/sink defects.

- The redistribution of total mass occurs on a length scale set by $l_r/2$. This controls the positions where wavefronts emitted by the source defects are formed (c.f. main text Fig. 4).

In addition the proposed mechanism based on mutually commensurable modes controlling local stability enabled us to infer the precursor dynamics close to the transition from turbulence to standing wave order. In particular, we were able to predict and explain:

- Standing waves trains propagating at a finite velocity $v_w \gtrsim \delta/\tau$ in different directions.

- Moving domain interfaces (with speed $v_I \lesssim l_c/\tau$) separating the direction of wave-node propagation.

- A preferred formation of propagating wave trains close to the interface in one domain and turbulent dynamics (phase slips defects) in the other domain closely below the transition (weak incommensurability).

- Bands of propagating wave packets that tend to maintain a constant distance between wave nodes thereby showing short to intermediate range coherence closely beyond the transition in the standing wave regime (weak commensurability).

Taken together this presents a large set of independent evidence that strongly supports the conclusion that the relevant part of the pattern forming dynamics in mass-conserved reaction-diffusion systems is the redistribution of total mass by unstable modes activated in a lateral instability. We therefore summarise that **order emerges from the control of local stability**.

X. THE TRANSITION TO LOCAL OSCILLATIONS AND SIMILARITIES BETWEEN THE MIN SYSTEM AND THE CO–PT SYSTEM

A. The local oscillatory instability is subcritical

To further investigate the local dynamics at the transition to local instability we consider an isolated cytosolic column, i.e. a one-dimensional column of length h (representing the bulk height) with reactive boundary conditions (Eq. 31a-31c) at $z=0$ and no-flux boundary conditions at $z=h$ (Eq. 32a-32c). The parameters are identical to those given in Table 1 (for the laterally extended system), therefore, the steady state coincides with the uniform steady state in the spatially extended system. As described in Supplementary Section IV, we perform a linear stability analysis of the steady state by setting $q=0$ (the stability of the membrane point is equivalent to the stability of the extended membrane against uniform perturbations represented by the zero mode ($q=0$)). This reveals that the steady state of this system will become unstable for $h=h_{\mathrm{Loc}}\geq 36.3\mu m$ (Supplementary Fig. 10B, c.f. main text Fig. 4B). To test this stability analyis we performed simulations of the one-dimensional system. First we used the computed steady states u_i^* as initial conditions (c.f. Section IV), and perturbed the bulk profiles (Eq. 61) spatially with white noise,

$$u_i(z,0)=u_i^*(z)\ [1+0.02\Phi(z)]\ , \tag{101}$$

where $\Phi(z)$, at every point in space z, is drawn from a standard normal distribution (zero mean, and unit (1) variance). We kept the membrane densities unperturbed to minimise the perturbation of total mass (the bulk perturbation is zero on average, i.e. $\int_0^h \mathrm{d}z\ \Phi(z)\approx 0$). The simulations precisely confirmed the critical bulk height for the onset of autonomous oscillations, see Supplementary Fig. 10A. We also observed that the dynamics always enter a large amplitude limit cycle, regardless of the distance from the bifurcation at h_{Loc}. Since the amplitude does not vanish as the bifurcation is approached from above the bifurcation appears to be subcritical.

To consolidate the possible subcriticality of the bifurcation, we ran additional simulations for bulk heights below the bifurcation, $h<h_{\mathrm{Loc}}$, with initial conditions far from the steady state, specifically with all MinD on the membrane and all of MinE in the cytosol. Indeed, the simulations (Supplementary Fig. 10C) confirm that the large amplitude limit cycle exists before the steady state becomes unstable, and it can be reached for these particular initial conditions for $h\geq 35\,\mu m$. Hence, the dynamics indeed show clear signs of excitability. It is

worth pointing out that we did not find any stable limit cycles for $h = 33\,\mu m$, i.e. the value where the spatially extended system undergoes a chimera transition from standing to travelling waves. Intuitively, one might have been inclined to ascribe the formation of the maintained source emitting travelling waves to the existence of a large amplitude limit cycle which is then reached by the pattern forming dynamics at the location of the source. Our results indicate that this limit cycle does not exist (or cannot be reached easily , i.e. has a small basin of attraction) for $h = 33\,\mu m$ (and our choice of total densities of MinD and MinE) in the uniform state (which is equivalent to the point oscillator studied above). In turn, this implies that for the limit cycle to be created (made reachable) one has to change the total densities locally (here, by increasing the local MinE/MinD ratio Δ).

B. Are Min protein patterns *in-vitro* based on the same mechanism as patterns *in vivo*?

So far, Min protein patterns *in vivo* and *in-vitro* have been unanimously seen as an example for Turing patterns in a biological system. As a reminder for the reader: The mechanism for pattern formation found by Alan Turing, and now commonly referred to as Turing instability, is fundamentally based on the assumption that local dynamics (i.e. with lateral diffusion turned off) are in a stable chemical equilibrium. The astonishing discovery that Alan Turing made was that (lateral) diffusive coupling of these locally stable dynamics can lead to an instability that induces the formation of a non-uniform pattern form an initially uniform state. This is surprising and highly counterintuitive because diffusion is supposed to remove any concentration gradients and not induce them. *In vivo*, the assumption of a Turing mechanism for the Min protein dynamics appears to be justified. Theoretical models [8, 10] have shown that there is a critical cell length for the onset of pattern formation below which the system is uniform and stable. Furthermore, in almost two decades of experimental research on Min protein dynamics there has been (to the best of our knowledge) not a single report of *blinking* cells, i.e. cells that show uniform oscillations without any spatial heterogeneity (of course, this would biologically be undesired). However, in the case of *in-vitro* patterns, our analysis suggests that the Min protein patterns as observed experimentally (travelling waves and spirals) actually originate from local oscillatory dynamics. Therefore, the Min system *in-vitro* represents an example for an oscillatory medium and not a Turing mechanism. In the classical literature on pattern formation [1, 2, 13],

the field of oscillatory media is mostly seen as a class of pattern forming systems that are distinct from Turing systems. It is, therefore, particularly interesting that the Min proteins are able to generate patterns based on both mechanisms, only by a change of the system geometry (which is accompanied by a change of diffusion coefficients and total particle numbers). Investigating the transition between both mechanisms as control parameters are varied will be a very interesting future research project.

C. A mechanistic connection between the Min system and the CO–Pt system?

The heterogeneous catalysis of carbon monoxide oxidation (CO) on platinum (Pt) crystal lattices has been widely studied for its industrial application, and for its ability to form oscillatory patterns as spiral waves, standing waves, target patterns, and a broad range of irregular and chaotic wave phenomena [14–16]. At first glance, the structure of the reaction network appears to be very different from the Min system (and most other biological systems). Instead being based on the cycling between different states, the dynamics require a constant supply of CO and O_2 which is transferred into CO_2, without the reverse reaction taking place. However, the essential nonlinear process driving the CO oxidation is the catalytic action of the platinum lattice, which has a fixed and finite number of binding sites. The importance of this conservation law for the oscillatory dynamics has been nicely summarized by G. Eigenberger[17]:

> "The oscillation observed with the CO- and H_2-oxidation on platinum however often had the character of relaxation oscillations. This class of oscillations can be interpreted by the combination of one storage element with a switching device which changes the direction of the current to and from the storage."

Here storage denotes the dynamical reservoir of free binding sites, and the switching element the nonlinear kinetics selecting between predominant CO/O_2 adsorption and catalytic CO_2 desorption. It is important to note that this discussion addresses the (uniform/local) oscillation of the CO-Pt system, and not any aspect of pattern formation. To establish a clear conceptual connection to the *in-vitro* Min dynamics on the level of local oscillations, let us consider the dynamics of a point on the membrane in the oscillatory regime $h > h_{\mathrm{Loc}}$ (cf. main text Fig. 4B). In supplementary section VI A we have discussed that the calculation of the control variable (from which we infer local equilibria) is based on the adiabatic extrapolation of cytosolic protein densities near the membrane. This means, that only protein densities that participate in the nonlinear dynamics at time t contribute to the control variables; cytosolic densities far away from the membrane do not. We find that once the local equilibrium undergoes a oscillatory instability, the control variables become locally oscillatory and we can analyze the local oscillation in the control space framework (see Supp. Fig. 12). Note that this example emphasizes that the concept of local equilibrium refers to locality in space and time. Let us have a look at the trajectory of the local oscillation in its local control space. The trajectory is centered around the total mass in the system, i.e. as obtained from bulk integrations instead of adiabatic extrapolation. During the oscillation, mass is being shuffled to and from this cytosolic storage. Hence, we can therefore identify it as the storage in the sense of Eigenberger's interpretation. The amplitude in control space encodes the fraction of mass which is not adiabatically slaved to (does participate in) nonlinear dynamics at the membrane point. We can also identify three distinct regimes in control space along the Δ axis: For low Δ (MinD dominance) the cytosolic storage is full. The dynamics are driven by MinD/MinE accumulation on the membrane, which depletes the storage. For high Δ (MinE dominance) the storage is empty. The dynamics are driven by MinE-catalyzed detachment from the membrane, which refills the storage. In between these two regimes lies the domain of local instabilities, which we can interpret as a "switching device which changes the direction of the current to and from the storage." This control space picture reveals the interconnection between switching and storage: The position in control space, i.e. the momentary level of the storage, regulates the nonlinear dynamics to and from the storage. This highlights the major concept of our mass redistribution framework: The local dynamics (in space and time) are determined by the position of the control variables in control space.
There are several interesting conclusions to be drawn from the preceding discussion:

- The generalization of *in-vitro* Min protein dynamics within the mass redistribution framework strongly implies a fundamental mechanistic connection between the Min system and the CO-Pt system. This is particularly remarkable, as the connection only becomes evident through the realization that the Min system studied *in-vitro* is an oscillatory medium — in contrast to Min dynamics *in vivo* (cf. supplementary section X B). Note that this result also directly follows from the control space analysis, i.e. the characterization of local equilibria and their stability through control variable dynamics.

- The analysis of the local oscillation in its control space characterizes the local Min oscillation *in-vitro* as a relaxation oscillation in control space. The local oscillation is driven by the transfer of mass between the reactive membrane and a cytosolic storage (non-adiabatic bulk). On the one hand, this finding emphasizes that bulk dynamics must be explicitly considered in models of the *in-vitro* Min system (this question has been under considerable debate in the literature, see [18]). On the other hand, it suggests that the bulk coupling in the Min system mainly fulfils the role of a storage element, which is a generic part of relaxation oscillations as pointed out by Eigenberger [17]. Note that there is also coupling to a bulk (the gas phase) in the CO-Pt system. However, in contrast to the Min system the dynamics in the gas phase can be neglected. Instead the (slow) restructuring of the finite (conserved) number of lattice sites serves as the storage element in the CO-Pt system.

- The essential control space variable driving the local Min protein relaxation oscillation is the ratio Δ between MinE and MinD.

- Explicitly mass–conserved models of the CO-Pt system were, to the best of our knowledge, only studied in context of the uniform oscillation [16], but not in context of CO pattern formation. Our results show that Min protein dynamics are capable to generate very similar patterns as the CO-Pt system, including standing waves and spirals, as well as chemical turbulence. We explained these phenomena by lateral mass redistribution through unstable modes. This lateral mass redistribution requires different diffusion coefficients between the different components of a conserved species (cf. supplementary section I). In case of the CO-Pt system, the conserved species is the Pt lattice, its components are the occupation states (empty, CO occupied, O_2 occupied). Since CO is weakly bound to Pt (compared to O_2), it is usually considered as diffus-

ing component in classical models (cf. [14]), while O_2 is considered to be immobile. Therefore, the generic prerequisites for lateral mass redistribution are given, and an analysis of mass conserved CO-Pt models in our control space framework could shed new light on the principles and conditions underlying CO pattern formation on Pt surfaces.

XI. SUPPLEMENTARY FIGURES

A. Supplementary Figure 1: Lateral instabilities in mass–conserving two–component systems

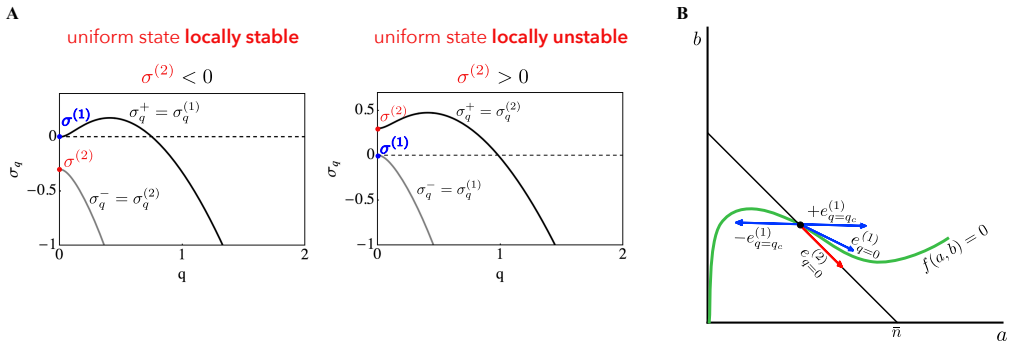

Supp. Fig. 1

A, Exemplary dispersion relations for the situation where the uniform state is locally stable ($\sigma^{(2)} < 0$) and the dispersion is governed by $\sigma_q^{(1)}$ (left), and the situation where the uniform state is locally unstable ($\sigma^{(2)} > 0$) such that this instability governs the dispersion relation. **B**, Phase-space illustration of the eigenvectors associated with unstable modes. The eigenvectors associated with uniform perturbations $q = 0$ parametrise the line of fixed points $e^{(1)}_{q=0}$ and the local phase space $e^{(2)}_{q=0}$respectively. The eigenvector of the fastest growing mode $e^{(1)}_{q=q_c}$ (assuming local stability, i.e. $\sigma^{(2)} < 0$) points away from the line of fixed points and from the local phase space of the uniform state $\bar{n}$, showing that the lateral instability induces a lateral redistribution of total density.

B. Supplementary Figure 2: Wave–pinning in the mass–redistribution framework

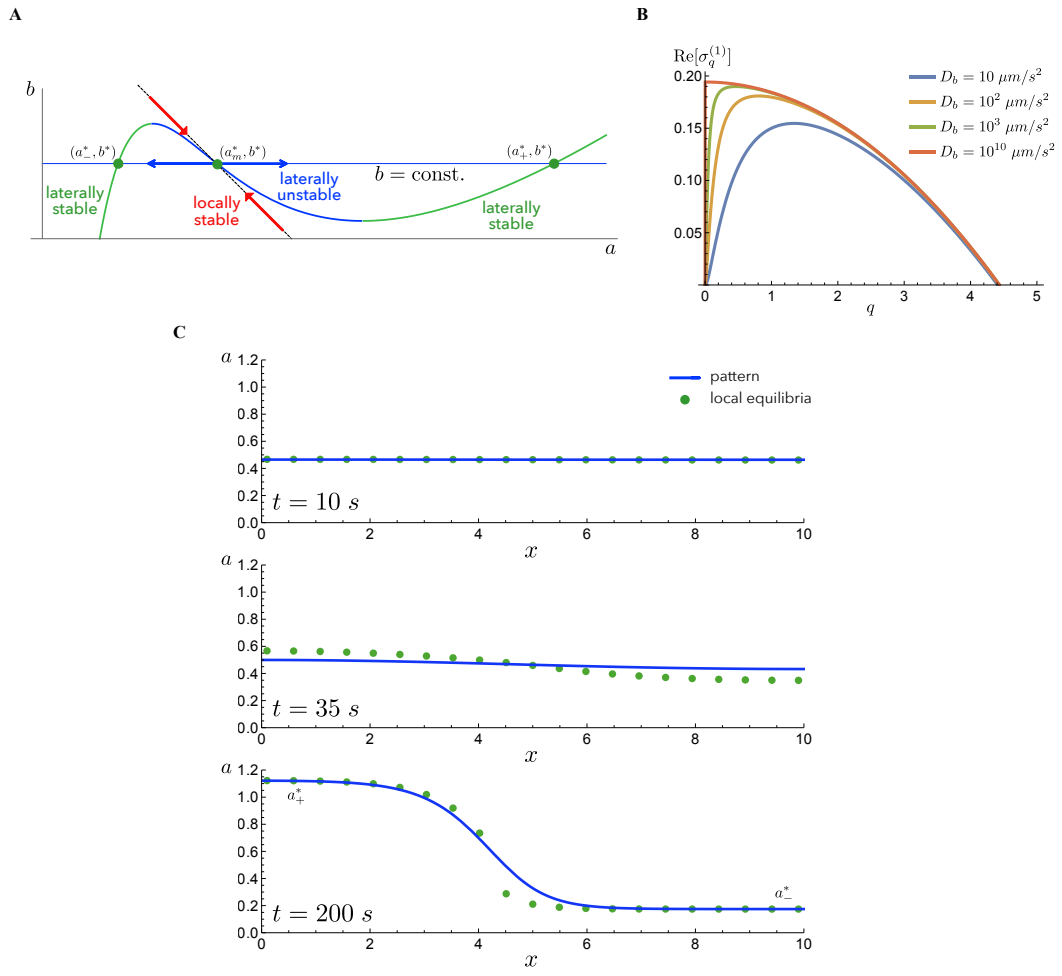

Supp. Fig. 2

A, Phase space illustration of the wave–pinning model (Eq. 18-20, cf. main text Fig 1B). For $D_b/D_a \gg 1$ ($D_b \to \infty$) the system is constrained to a subspace $b = \text{const.}$ (blue line). The curve shows the line of equilibria ($f(a, b) = 0$) and its intersections with the subspace of the pattern mark the local equilibria (a^*_-, b^*) and (a^*_+, b^*) used in the construction of the polarized state [3, 4]. The blue highlighted part of the nullcline marks the part where the uniform state is

laterally unstable (Turing instability). The flow induced by the lateral instability is depicted by the blue arrows. **B**, Dispersion relations for the wave–pinning model (Eq. 18-20, $\bar{n} = 2.35$) for various cytosolic diffusion constants D_b. The data clearly shows that as $D_b \to \infty$ the fastest growing mode approaches the zero mode $q = 0$ but $q = 0$ remains marginally stable ($\sigma^{(1)}_{q=0} = 0$) for any finite D_b. **C**, Snapshots from the simulation of the wave–pinning model (Eq. 18-20, $\bar{n} = 2.35$) staring with a weakly perturbed uniform steady state. It can be clearly seen that the lateral instability of the uniform state induces a dynamic displacement of local equilibria (green dots) which scaffold the spatiotemporal evolution of the observed pattern (here membrane species a). The final pattern ($t = 200\ s$) is a diffusive interface spanned between plateaus determined by the local equilibria a^*_- and a^*_+.

C. Supplementary Figure 3: Control space parametrization for the Min model

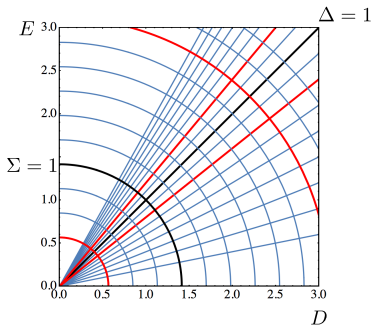

Supp. Fig. 3

For the Min model (cf. section III A) the control space is spanned by the (normalised) total densities of the conserved protein species MinD and MinE. With respect to this normalisation we consider coordinates given by the sum Σ and the ratio Δ of MinE and MinD. The highlighted area (red) shows the typical range in which the system is found in the simulations.

D. Supplementary Figure 4: Subcritical turbulence with cytosolic degradation

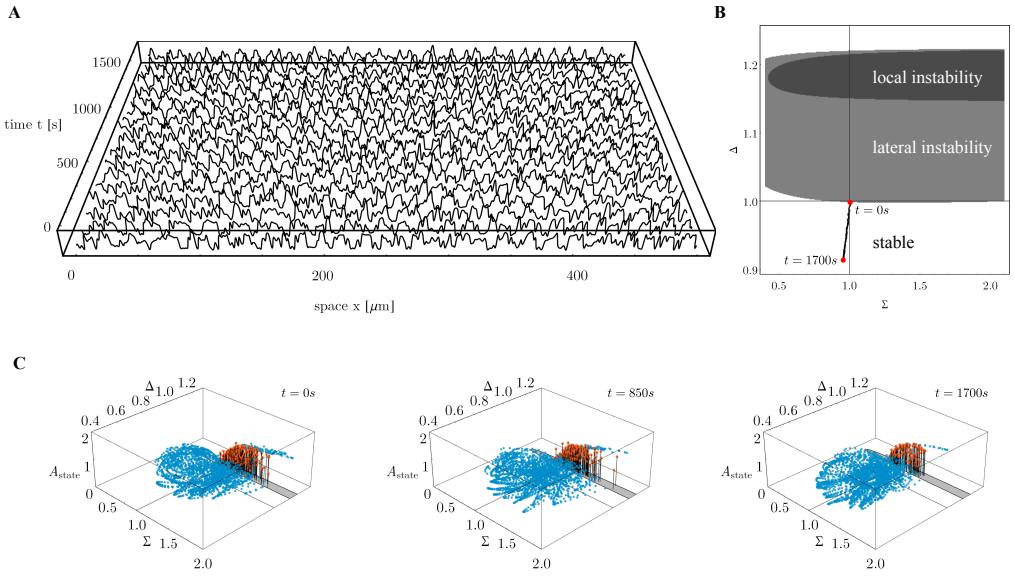

Supp. Fig. 4

Subcritical turbulence with cytosolic degradation. **A**, Phase diagram of the control space showing the area where the uniform steady state is unstable laterally (light grey) and locally (dark grey). The line connecting the red dots shows the time evolution of the total densities as the system moves from the laterally unstable domain ($t = 0s$) into the stable domain ($t = 1700s$). **B**, Wave profiles of the MinD densities on the membrane in the simulation with slow MinE degradation in the cytosol. The data shows that the patterns is maintained even if the uniform state is stable. Hence, a lateral instability is not required to maintain chemical turbulence. **C**, Distribution of the system in control space (c.f. main text Fig. 3) as the system moves in the regime where the uniform state is stable. The data shows that the local dynamics keep entering and leaving the unstable domain, thereby maintaining chemical turbulence.

E. Supplementary Figure 5: Spatial correlation of local destabilisation

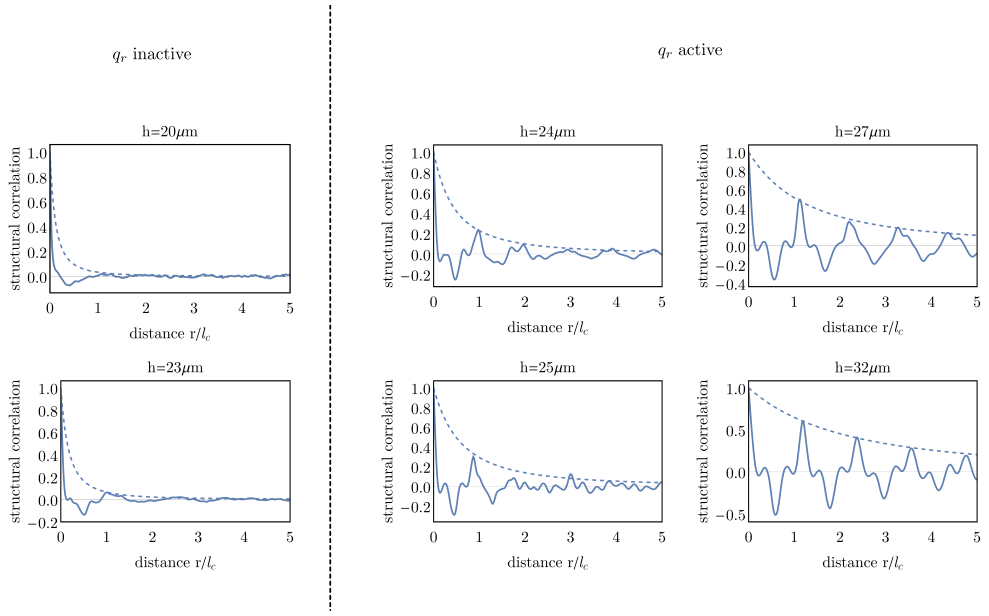

Supp. Fig. 5: Spatial correlation of local destabilisation.

Table of spatial correlation functions $C(r/l_c)$ (blue solid lines) for different values of the system height (control parameter) h, indicated in the graph, with the corresponding envelopes $G(r/l_c)$ (dashed lines). The figure is split into two panels, one where the commensurable mode $q_r = 2q_c$ is inactive (stable) [left], and the other where it is active (unstable) [right]. The data shows that the spatial correlation oscillates with a period set by the fastest growing mode $q_c = 2\pi/l_c$ close to the transition.

F. Supplementary Figure 6: Correlation length dependence on mode commensurability

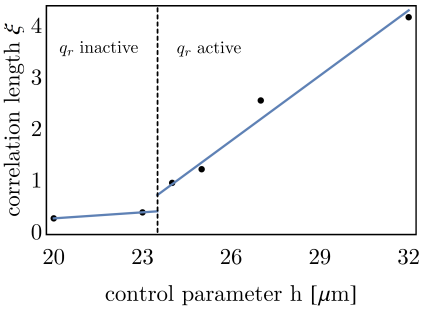

Supp. Fig. 6: Correlation length dependence on mode commensurability.

The correlation length ξ as a function of the control parameter h extracted from the envelope fits $G(r/l_c) = ((r/l_c)/\xi + 1)^{-2}$ in Supp. Fig. 5. The data shows a clear transition at the value of the control parameter $h = 23.5\mu m$ where the commensurable mode $q_r = 2q_c$ becomes active. Beyond the transition the spatial correlation increases monotonously (linear fit included for convenience).

G. Supplementary Figure 7: Cluster distance distributions

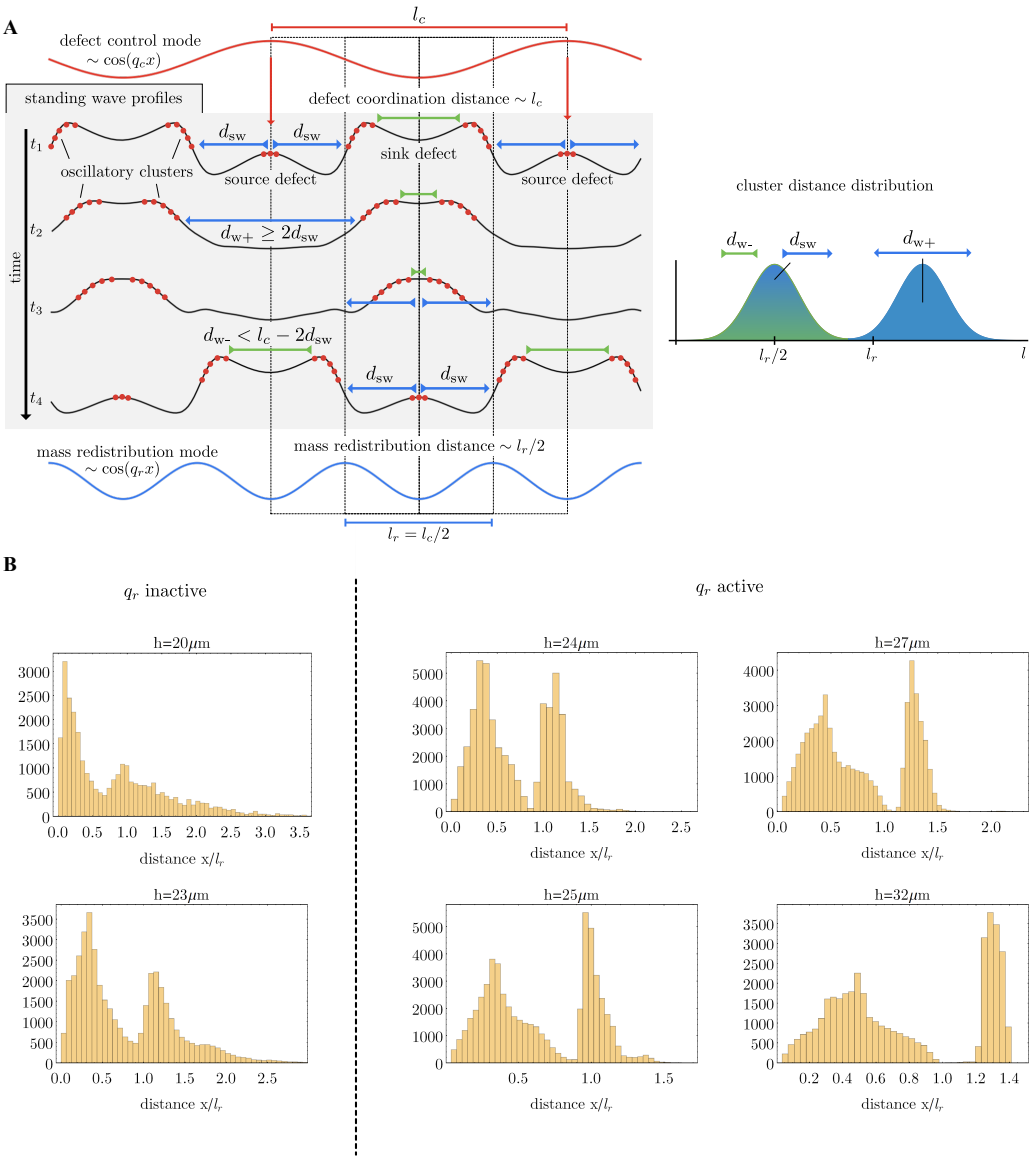

Supp. Fig. 7: Cluster distance distributions.

A, Reprint of main text Figure 4 D with the added definitions of cluster distance length scales d_{sw}, $d_{\mathrm{w+}}$, and $d_{\mathrm{w\text{-}}}$.
B, Histograms with the distance-distribution of local instability clusters for various values of the control parameter h. All distances are rescaled to the respective length scale set by the commensurable (mass redistribution) mode

$q_r = 2\pi/l_r$. The bimodal distribution shows a clear separation between both peaks for values of the control parameter $h > 23.5\mu m$ where the commensurable mode $q_r = 2q_c$ is active. In this regime the first peak aligns with the characteristic distance of mass redistribution $l_r/2$ mediated by the commensurable (mass redistribution) mode q_r, and the second peak becomes bound from below by l_r.

H. Supplementary Figure 8: Control mode alignment in the weakly incommensurable regime

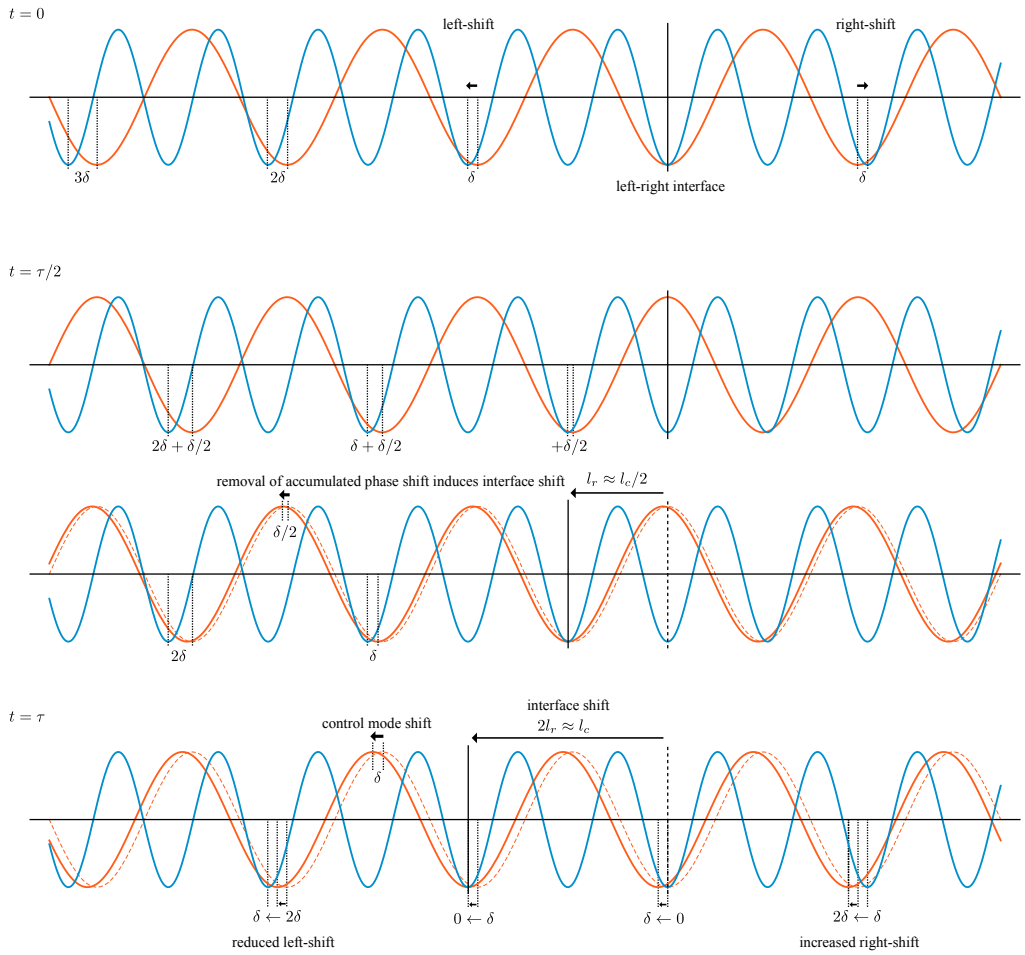

Supp. Fig. 8: Schematic of the precursor phenomenon

At $t = 0\ s$ we align the troughs of the weakly incommensurable control modes q_c (red) and $q_{\max}$ (blue) at some point in space. Right and left to this *interface* the weak incommensurability causes a phase shift of $+\delta$ and $-\delta$ of the mass redistribution mode ($q_{\max}$) with respect to the defect control mode (q_c), which increases by $\pm\delta$ with each wave node away from the interface. After a half temporal period this phase difference has increased by $\delta/2$ at each node to the right and the left, respectively. This increase increase can only be reduced

by shifting the defect control mode q_c (the unshifted modes are plotted with dashing for reference). However, as illustrated for $t = \tau$, while this will decrease the phase shift at one side, it will increase the phase shift at the other side. It will also lead to movement of the interface by one spatial period per oscillation cycle, $v_I \approx l_c/\tau$.

I. Supplementary Figure 9: Point-to-point correlation kymographs

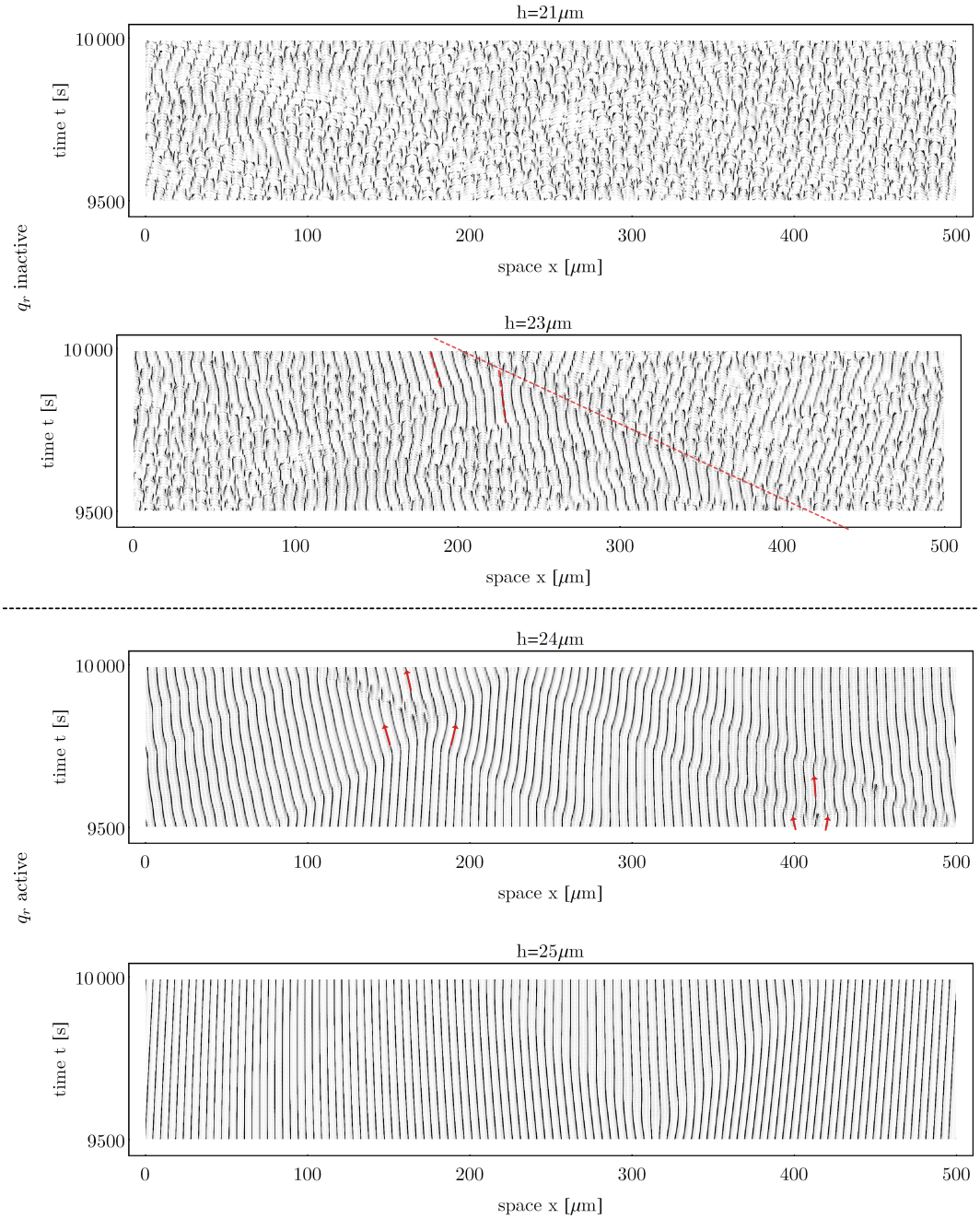

Supp. Fig. 9: Point-to-point correlation kymographs.

The kymographs show the point-to-point correlation as defined in the Supple-

mentary section VIII for increasing values of the control parameter h. The greyscale reflects the correlation of nearby membrane signals with light values corresponding to high correlation. We observe chemical turbulence in the regime where the commensurable mode q_r is inactive and the transition to standing wave patterns once q_r is activated (for $h > 23.5\mu m$). For $h = 23\mu m$ the mode with the smallest wavelength $q_{\max}$ is almost commensurable with the fastest growing mode q_c (phase difference $\delta/l_c = 0.03$, c.f. Supplementary section IX D). As expected we observe the formation of short bands of propagating wave trains (thick red lines) bounded by phase boundaries that separate predominant phase propagation direction (highlighted by the light red line).

J. Supplementary Figure 10: The Min point oscillator

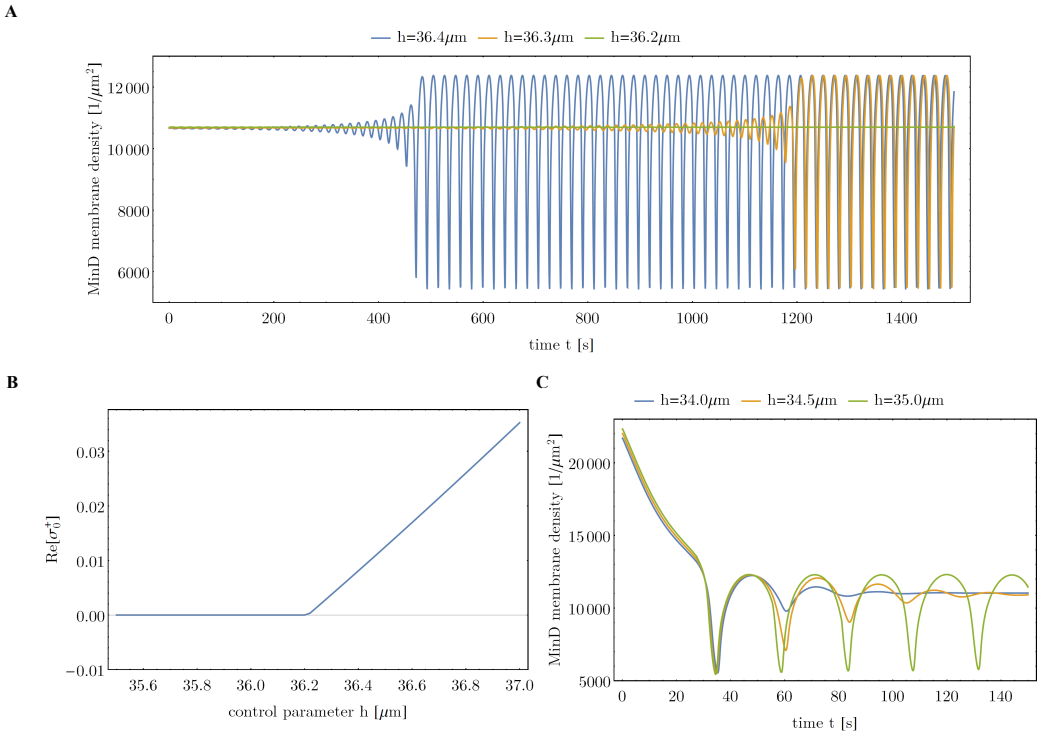

Supp. Fig. 10: The Min point oscillator.

A, Time evolution of membrane bound MinD ($u_d + u_{de}$) in a one dimensional system (bulk column with reactive boundary as membrane) starting with a initial condition in the vicinity of the steady state. The data show exponential growth for $h > 36.2\mu m$ as expected from the stability analysis in **B**. **B**, The growth rate $\mathrm{Re}[\sigma_0^+]$ shows the stability of the uniform steady state against uniform perturbations (in this case reflecting the stability of steady state in the 1 dimensional bulk column). **C** Time evolution of membrane bound MinD ($u_d + u_{de}$) in a one dimensional system (bulk column with reactive boundary as membrane) starting with an initial condition where MinD is on the membrane and MinE is in the cytosol. The data shows stable limit cycles even if the equilibrium of the system is stable.

K. Supplementary Figure 11: Supplementary data

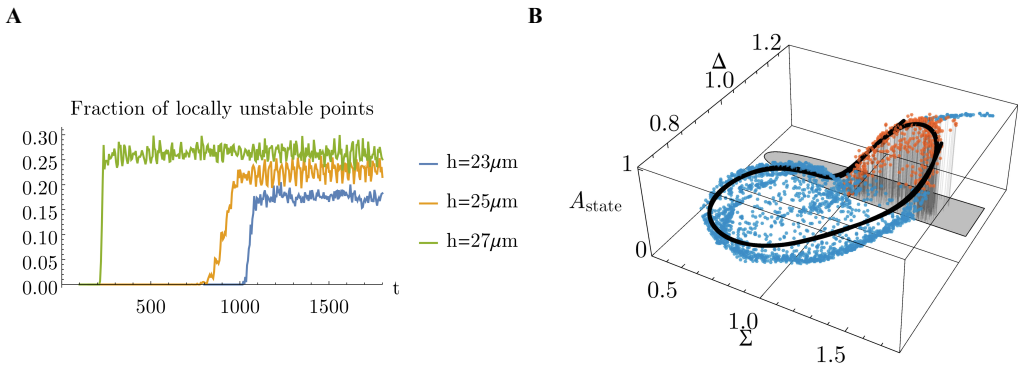

Supp. Fig. 11: Supplementary data.

A, Fraction of locally unstable equilibria extracted from simulation for increasing values of the control parameter h. The fraction of local instabilities increases with h and local destabilisation occurs sooner as the regime of local instability approaches the global average in control space (c.f. main text Fig. 2D and 4B). **B**, Distribution of the whole system in control space (Σ, Δ) and corresponding distances to local equilibria $A_{\text{state}}(x,t)$ (c.f. main text Fig. 3A) for $h = 25\mu m$ at $t = 625s$. With the onset of finite spatial correlation the distribution starts to contract towards a circle in control space (Σ, Δ). A single trajectory for a fixed spatial position ($x = 28\mu m$, $t = 600 \ldots 650s$) is highlighted in black.

L. Supplementary Figure 12: The local Min oscillation *in-vitro* in control space - an analogy to the CO-Pt relaxation oscillator

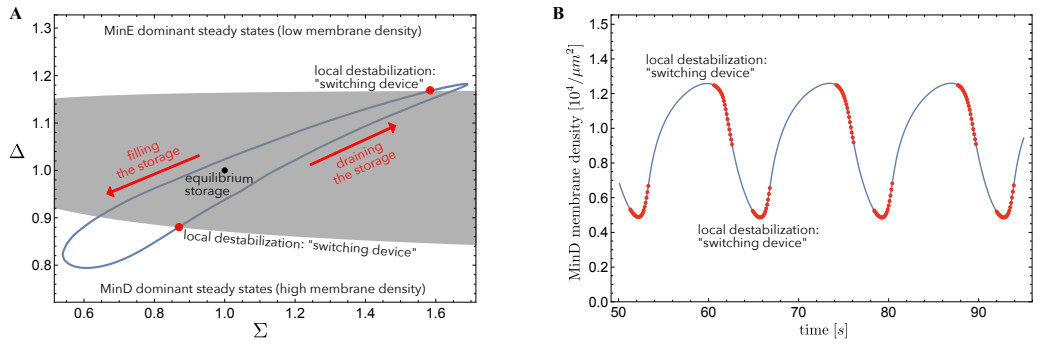

Supp. Fig. 12: The local Min oscillation *in-vitro* in control space.

A, The trajectory of an laterally isolated point (cf. Supp. Fig. 8) in control space ($h = 60\mu m$). The local equilibria are computed using the adiabatic extrapolation of the bulk state (cf. section VI A). The point $(1, 1)$ represents the average total density in the system. The data shows that the oscillation can be identified as a relaxation oscillation comprising a storage element and a switching device as heuristically described by G. Eigenberger for the CO-Pt system [17]. In the MinD and MinE dominant regimes the system approaches stable local equilibria with high and low membrane densities respectively. These regimes correspond to distinct values of the control variables. The dynamics of the control variables represent the periodic filling and draining of the cytosolic storage. The local destabilization acts as a "switching device" between draining and filling this storage. Hence, the non-adiabatic cytosol in the Min system has a similar role as the delayed restructuring of the platinum lattice in the CO-Pt system. **B**, The local oscillation of the MinD membrane densities for the data in Supp. Fig. 10A. The blue parts represent the sections of the trajectory where the local equilibria are stable. Local destabilization acts as switch (in the sense of Eigenberger) between accumulation and depletion of the membrane.

XII. MOVIE CAPTIONS

A. Movie 1: Onset of chemical turbulence

Top: Membrane profile of MinD during the transition from small amplitude standing waves to chemical turbulence for a control parameter (bulk height) $h = 20\mu m$. (Also, see main text Fig. 3B)
Bottom: Temporal evolution of the system's distribution in control space corresponding to the time step shown in the top wave profiles. (Also, see main text Fig. 3A)

B. Movie 2: Emergence of standing wave order

Top: Membrane profile of MinD at the onset of standing wave order for a control parameter (bulk height) $h = 25\mu m$. (Also, see main text Fig. 4C)
Bottom: Temporal evolution of the system's distribution in control space corresponding to the time step shown in the top wave profiles. (Also, see Supplementary Fig. 9B)

C. Movie 3: Spiral wave patterns in a 3d box geometry

Spatiotemporal dynamics of membrane bound MinD in the simulation of the full 3d box geometry for a control parameter (bulk height) $h = 100\mu m$.

D. Movie 4: Chimera transition from standing to travelling waves

Top: Membrane profile of MinD during the chimera transition from from standing to travelling waves (light grey highlighted area) for a control parameter (bulk height) $h = 33\mu m$. (Also, see main text Fig. 5B)
Bottom: Temporal evolution of the system's distribution in control space cor-

responding to the time step shown in the top wave profiles. (Also, see main text Fig. 5E) Data points corresponding to the spatial domain in the grey highlighted area (in the top wave profile) are plotted opaque to show the contraction of the distribution in control space to a well defined cycle.

---

[1] M. Cross and H. Greenside, *Pattern Formation and Dynamics in Nonequilibrium Systems* (Cambridge University Press, 2009).

[2] M. Cross and P. Hohenberg, Reviews of modern physics **65** (1993).

[3] Y. Mori, A. Jilkine, and L. Edelstein-Keshet, Biophysical journal **94**, 3684 (2008).

[4] Y. Mori, A. Jilkine, and L. Edelstein-Keshet, SIAM Journal on Applied Mathematics **71**, 1401 (2011).

[5] A. B. Goryachev and M. Leda, Molecular Biology of the Cell **28**, 370 (2017).

[6] P. K. Trong, E. M. Nicola, N. W. Goehring, K. V. Kumar, and S. W. Grill, New Journal of Physics **16** (2014).

[7] K. C. Huang, Y. Meir, and N. S. Wingreen, Proceedings of the National Academy of Sciences of the United States of America **100**, 12724 (2003).

[8] J. Halatek and E. Frey, Cell reports **1**, 741 (2012).

[9] F. Wu, B. G. C. van Schie, J. E. Keymer, and C. Dekker, Nature Nanotechnology (2015).

[10] F. Wu, J. Halatek, M. Reiter, E. Kingma, E. Frey, and C. Dekker, Molecular Systems Biology **12**, 642 (2016).

[11] M. Loose, E. Fischer-Friedrich, J. Ries, K. Kruse, and P. Schwille, Science (New York, N.Y.) **320**, 789 (2008).

[12] Remark: Since $q_{\max}$ has zero growth rate mass redistribution will be mediated by a mode $q \lessapprox q_{\max}$). for simplicity we will still refer to the mode as $q_{\max}$.

[13] Y. Kuramoto, *Chemical Oscillations, Waves and Turbulence* (Springer, Berlin,

1984).

[14] A. S. Mikhailov and K. Showalter, Physics Reports **425**, 79 (2006).

[15] M. Kim, M. Bertram, M. Pollmann, a. von Oertzen, a. S. Mikhailov, H. H. Rotermund, and G. Ertl, Science (New York, N.Y.) **292**, 1357 (2001).

[16] G. Eigenberger, Chemical Engineering Science **33**, 1263 (1978).

[17] G. Eigenberger, Chemical Engineering Science **33**, 1263 (1978).

[18] J. Halatek and E. Frey, Proceedings of the National Academy of Sciences **111** (2014), 10.1073/pnas.1220971111.

IX Geometrization of pattern formation: From quantitative models to the identification of self-organization mechanisms

This chapter is based on the following manuscript:

From quantitative models to geometrization of pattern formation mechanisms

by

F. Brauns†, J. Halatek†, and E. Frey

Department of Physics, Arnold Sommerfeld Center for Theoretical Physics and

Center for NanoScience, Ludwig-Maximilians-Universität München,

Theresienstraße 37, 80333 München, Germany

† equal contribution

Journal Reference:

in preparation for publication

Supplemental Material reproduced on pages 430 to 445.

From quantitative models to a geometrization of pattern formation mechanisms

Fridtjof Brauns†, Jacob Halatek†, and Erwin Frey*
Arnold Sommerfeld Center for Theoretical Physics (ASC) and Center for NanoScience (CeNS), Department of Physics, Ludwig-Maximilians-Universtiät München, Theresienstraße 37, 80333 München, Germany

† *these authors contributed equally to this work*

Abstract

The dynamics of any physical system are encoded in the (flow) structure of the system's phase space. All essential dynamics of a particular system are qualitatively contained in the phase portrait. Unfortunately, phase portraits can, in general, only be derived for low dimensional ODE systems. This strongly limits the applicability of the powerful geometric concepts with which the dynamics of a system can be inferred from the structure phase portraits. Here, we present a systematic theoretical framework to derive the phase portraits of quantitative reaction-diffusion models with mass-conserving interactions. This framework is based on the spatial decomposition of any system into local compartments. The phase space flows of isolated compartments are determined by the positions and stabilities of local equilibria. In turn, local equilibria are uniquely determined by the local amounts of the (globally conserved) total densities n of all protein species in these compartments. The essential effect of diffusive coupling between individual compartments is the lateral exchange of (globally conserved) total densities which changes the structure of the local phase spaces. Our key results is that the entire pattern forming process can be understood in terms of moving local equilibria, i.e. the dynamically changing structure of local phase spaces caused by lateral diffusive transport. As such, the phase portrait of the pattern forming system is obtained form the local phase spaces and the (linear) effect of diffusive coupling.

The geometrization lets us systematically extend a broad range of concepts from ODE theory (excitability, bifurcations, basins of attraction, nullclines) to pattern formation in mass-conserving reaction-diffusion systems. This, in turn, leads to a natural unification of existing pattern forming mechanisms, such as linear (e.g. Turing) instabilities and excitability. Furthermore, this geometrization approach reveals that the shape of the line of local equilibria (kinetic nullcline) is the central geometric object that universally classifies reaction-diffusion models on a mechanistic level. This classification is based on the topological equivalence classes of kinetic

nullclines, which is well-established for dynamical systems theory of ODEs.

To demonstrate the utility of our framework, we apply it to a quantitative model for Min protein patterns *in vivo*. The Min system regulates cell division in *E. Coli* through pole-to-pole oscillations. This lets the Min system appear mechanistically unique among biological systems with similar function (cell polarity), that are typically non-oscillatory. The systematic reduction of Min protein dynamics within our framework reveals that the underlying pattern forming process is intrinsically non-oscillatory and strictly equivalent to mechanisms underlying non-oscillatory polarity patterns in other biological system. MinD generates polarity through phase separation, whereas MinE takes the role of a control variable regulating the existence of polarized MinD patterns. Oscillations are facilitated by MinE redistribution and can be understood mechanistically as relaxation oscillations of the polarization direction.

Keywords: mass-conserving reaction–diffusion mechanism; pattern formation; geometrization; topological equivalence; self–organization; Min oscillations; timescale separation;

INTRODUCTION

Protein pattern formation is essential for spatial organization of many intracellular processes like cell division [1–4] , morphogenesis [5], and flagellum positioning [6]. The emergence of such function is a remarkable example for self-organization in real world systems: in the majority of cases any intracellular spatial structure arises endogenously as a consequence of the interactions between intracellular biomolecules.

Given this crucial role, it would certainly be desirable to generalize and unify self-organized pattern formation principles within a rigorous, quantitative theoretical framework. But is this a feasible goal? Pattern formation in reaction-diffusion system has been actively studied by the scientific community over the past six decades. A succinct review of this field would go beyond the scope of this introductory section. For the purpose of this article we can summarize that previous efforts to characterize and generalize pattern formation mechanisms were either based on a phenomenological analogy between observed patterns (e.g. amplitude equations, [7, 8]), or the effective molecular interactions (e.g. activator-inhibitor models, [9]). The amplitude equation formalism [7, 8] is a perturbative approach to study pattern formation in the *weakly nonlinear* regime. It provides a classification scheme based on the linear stability of the uniform state, and proposes that effective models (amplitude equations) represent each class, such as the (complex) Swift-Hohenberg equation [7, 8] or the (complex) Ginzburg-Landau equation [7, 8, 10]. The formalism distinguished between three different shapes of the dispersion relation, each of which can be oscillatory or non-oscillatory, giving rise to six distinct classes. This classification suggests that oscillatory and non-oscillatory instabilities comprise different pattern forming mechanisms. It is crucial to realize that this formalism is only applicable if the system is close to the onset of the linear instability (i.e. weakly nonlinear), and the bifurcation is supercritical (i.e. the amplitude of the pattern is small close to the instability). However, from an evolutionary perspective it seems implausible that a biological system is close to the instability that gives rise to its primary function (e.g. forming a pattern) in the first place — unless the system is excitable. In that case the biological system is natively in some stable (uniform) base state, and only switches promptly into a patterned state upon reception of some signal (external or internal perturbation with finite amplitude). This case, however, is at odds with the assumption of a supercritical bifurcation and rules out a perturbative approach. Hence, it is implausible that amplitude equations are applicable to biological systems.

Another widespread conceptual approach is that of Turing instabilities. In his

work [11], Turing used a reaction-diffusion model with two chemical components to show that such a system can undergo a lateral instability giving rise to pattern formation. His findings were later scrutinized by Segel and Jackson [12], and the underlying mechanism summarized as *short range activation and long range inhibition*. Employing this mechanism Gierer and Meinhardt [9] presented a class of *activator-inhibitor* models, and the activator-inhibitor mechanism and Turing mechanism are nowadays often used synonymously. This lead to the conception that in order to identify a pattern in a biological system as a *Turing pattern*, one *needs* to find the corresponding activator and inhibitor, cf. [13]. For systems with more than two components, as basically all biological systems are, the roles of activator and inhibitor are often heuristically assigned to "putative elements" of protein interaction networks [13]. This heuristic approach stems from the *motif paradigm*, where systems are represented by networks of the bio-molecular interactions, see e.g. [14]. However, the motif representation lacks any information about the parameters and diffusive coupling characterizing the (nonlinear) system. As such it is hardly surprising that motifs cannot be mapped uniquely to patterns, nor can patterns be uniquely mapped to motifs. For instance, the same interaction network for Min protein patterns can give rise to a multitude of different patterns, depending on system parameters[15–17], and the same pattern can be reproduce by a multitude of interaction networks [18, 19].

In these cases a strict identification with the *actual* activator-inhibitor mechanism as summarized by Segel and Jackson [12] is usually impossible, leaving the underlying mechanism elusive. However, there is no *a priori* reason that the activator-inhibitor mechanism should represent the general physical principle underlying Turing instabilities. Rather, the major issue appears to be that it is still unclear on which conceptual level the dynamics of self-organized pattern formation can be understood systematically in the physically most general terms. Addressing this issue is the goal of this article.

In physics the broadest and most general conceptual level to study dynamics is the level of *phase space* [20]. Each point in phase space represents a state of the system, and *flow* in phase space encodes the *dynamics of state* changes. For low dimensional ODE systems it is often possible to extrapolate the structure (topology) of the flow in a phase portrait from the properties (positions and stabilities) of the system's equilibria. This powerful geometric approach was fist introduced by Poincaré [20], and is now a centerpiece of Nonlinear Dynamics Theory [21, 22]. In the best case it provides full knowledge about the qualitative dynamics of a system without solving the underlying equations (which is often not possible in the fist place). One of the most use full concepts

from this geometric approach is *topological equivalence*, see e.g. [22]. Two systems are equivalent if their phase portraits can be continuously deformed into each other. To enable a systematic classification and unification of pattern forming mechanisms our aim is to develop an analogous concept for reaction-diffusion systems. A similar approach can be found in the theory of excitable media, where nullcline of the system are used to construct specific patterns (waves, pulses, fronts) based on the nullcline-structure [8, 22]. However, this framework strictly requires equal diffusion coefficients and a timescale separation of the reactive dynamics. As such, is not applicable to biological systems in general. Moreover, excitability strictly exclude all cases where the (uniform) base state of the system is laterally unstable, e.g. Turing unstable. A prominent example where excitability has been applied is cell polarity. Here the *wave–pinning* mechanism has been proposed as alternative to the Turing mechanisms [23, 24]. However, several commenters raised doubt that wave–pinning and Turing instabilities are indeed distinct mechanisms [18, 19, 25], but the exact connection remains unknown.

In this article we exploit the fact that protein dynamics are in general conformational state changes — the interactions driving the pattern forming process are mass-conserving. In a mass-conserving system the average *total densities* of all interacting protein species are *control parameters* for the pattern forming dynamics. It has recently been shown that pattern formation in mass-conserving systems is based on the lateral redistribution of the total densities [25]. Therefore, pattern formation can be understood by decomposing the system spatially into local (i.e. well-mixed) compartments containing variable amounts of *local total densities*, cf. [25]: The dynamically changing positions and stabilities of the *local chemical equilibria* of each compartment are uniquely determined by the local total densities, and any dynamical state of the system is scaffolded by these local equilibria. The *local phase spaces* of these compartments are low dimensional, and one can easily extrapolate the *local phase portrait*. The essential degrees of freedom of the pattern forming process are the total densities, spanning the *control space* of the system. In this article we combine the action of the local reactive dynamics with the diffusive dynamics to systematically construct phase portraits in the joint phase space spanned by the control space and the local phase spaces of the pattern forming system. This geometrization reveals general principles for lateral instability ("Turing instability") and lateral excitability and enables us to transfer the classification via topological equivalence to pattern forming systems. Further we find geometric criteria for the properties, bifurcations, and basins of attraction of stationary polarity patterns. While these results are discussed in context of

cell polarity models (e.g. wave–pinning [23]), the underlying principles are based on the properties of local equilibria alone, and are therefore independent of specific molecular interactions (e.g. as activator-inhibitor models [9]). The central geometric object classifying the pattern and the pattern forming process is the line of local equilibria (kinetic nullcline).

The key insight of the *mass-redistribution framework* is that pattern formation is a consequence of lateral redistribution of total densities. This suggests a systematic reduction scheme for multi-species reaction-diffusion models. Even if multiple protein species participate in the interactions, not all of them need to be necessarily redistributed to give rise to self-organized pattern formation. In any model, lateral redistribution of total densities can easily be turned off by setting the diffusion coefficients of entire protein species to zero. We use this idea to study a quantitative model for *in vivo* Min protein oscillations.

The biological function of Min proteins is to inhibit the assembly of the cell division machinery at the cell poles, thereby guiding assembly to mid-cell[1, 4, 26]. The Min system achieves this task by forming polarized patterns on the cell membrane that oscillate between both cell poles. In other biological systems cell division is ubiquitously regulated by non-oscillatory polarity patterns, and so far, there is no good explanation why it is mediated by oscillatory dynamics in *E. Coli*. Biochemically, Min protein dynamics are based on generic cooperative interactions similar to many non-oscillatory systems: The ATPase MinD drives the accumulation of itself and its AAP (ATPase activating protein) MinE on the membrane, while MinE drives itself and MinD off the membrane into the cytosol, cf. [26].

To gain a better understanding of the mechanism underlying Min protein dynamics we put the model to scrutiny by separating the effects of diffusive mass transport of MinD and MinE, respectively. Strikingly, this approach reveals that the fundamental mechanisms for pattern formation in the Min systems is only based on MinD transport and generically non-oscillatory. In fact, our approach reveals that the Min system is topologically equivalent to cell polarity system. MinE transport is not involved in pattern formation, but regulates the shape and existence of both possible polarized states. The oscillatory dynamics are induced by the periodic loss of MinD polarity in one cell half that forces the system to switch to the opposite polarized state. Through the employed reduction scheme we were further able to map the Min system to a generic relaxation oscillation dynamics. Hence, the separation of the Min system into its fundamental mechanisms rigorously reveals unambiguous analogies to other biological system. This shows that mass–conserved dynamics are a proper basis to generalize reaction-diffusion systems within a unified framework.

RESULTS PART I — TRANSFERRING ODE GEOMETRIZATION TO SPATIALLY EXTENDED SYSTEMS

In their simplest form, cell-polarization models involve a single protein species that can cycle between a cytosolic (c, fast diffusing) and a membrane bound (m, slowly diffusing) state via some nonlinear attachment–detachment kinetics $f(m, c)$. If geometry sensing is of no concern, the cell can be assumed as a one dimensional line of length L with reflective boundaries at $x = 0, L$. Accordingly the dynamics of the concentration profiles $m(x, t)$ and $c(x, t)$ are given by

$$\partial_t m = D_m \nabla_x^2 m + f(m, c), \tag{1}$$

$$\partial_t c = D_c \nabla_x^2 c - f(m, c), \tag{2}$$

where the global total density n_0

$$\int_0^L \mathrm{d}x \; m(x, t) + c(x, t) = L \cdot n_0 \tag{3}$$

is conserved. Our goal is to find the relevant concepts and principles that allow us to characterize pattern formation of systems of this form. In the literature, a characterization of pattern formation is usually sought by means of network/circuit diagrams representing the kinetic interactions $f(m, c)$. ODE geometrization is based on geometric structures (nullclines, fixed points, invariant manifolds) in the phase space of the dynamics, i.e. the space of the dynamic variables [8, 21, 22]. The dynamics due to kinetic interactions of two chemical states — with respective densities m and c — take place in (m, c)-phase space (see Fig. 1a). The kinetic interactions (conversion from m to c and vice versa) are balanced along the line of chemical equilibria $f(m, c) = 0$ (also called kinetic nullcline). When the kinetic interactions are not balanced, there will be a net *reactive flow* from one conformational state into the other, until a stable chemical equilibrium is restored. Since the kinetic interactions conserve mass, this reactive flow is restricted to the reactive phase space $m + c = n = \text{const}$. The total density (mass) n determines the position of the phase space and is thereby a parameter of the reactive flow (see Fig. 1a). In particular, the chemical equilibria are determined by

$$(m^*, c^*) : f(m^*, c^*) = 0 \text{ and } m^* + c^* = n, \tag{4}$$

i.e. the intersections of the line of chemical equilibria and the reactive phase space. This allows us to geometrically characterize the reactive flow (reactive phase portrait) using the reactive phase spaces and the line of chemical equilibria (kinetic nullcline).

By varying the total density — hence shifting the reactive phase space respectively — we can construct a diagram of the chemical equilibria in dependence of the total density (bifurcation structure, see Fig. 1b). As the reactive flow is directed towards stable chemical equilibria and away from unstable equilibria, the reactive phase portrait can be extrapolated from the properties (position and stability) of local equilibria. (cf. Fig. 1a). Moreover, in the vicinity of the line of equilibria $(m^*(n), c^*(n))$, the reactive flow can be approximated by the eigenvalue $\sigma_{\mathrm{loc}}(n)$ of the local equilibrium (linearization in local phase space):

$$f(m,c) \approx \sigma_{\mathrm{loc}}(n) \cdot \big(m - m^*(n)\big) = \sigma_{\mathrm{loc}}(n) \cdot \big(c - c^*(n)\big) \tag{5}$$

This equation concisely summarizes the two central elements of nonlinear ODE geometrization: fixed points (equilibria) and their linear stability. Together they can be used to approximate the structure of the flow field in phase space. We will later use that structure to understand the core self-organization principles of pattern formation in mass-conserving systems. But first we characterize stationary patterns in the mass-redistribution framework.

Stationary patterns lie in a flux-balance subspace of phase space

To extend the above geometrization approach of the kinetic interactions to a spatially extended system we have to understand the role of the diffusive coupling. Let us start our analysis of spatially extended systems by studying a stationary pattern profile obtained in numerical simulations of a pattern forming system of form Eqs. (1,2), e.g. the "wave–pinning" model by Mori et al. [23, 24].
Consider a steady state of Eqs. (1,2), i.e. a *stationary pattern* $\widetilde{m}(x)$, $\widetilde{c}(x)$ (see Fig. 2a) — solution to the PDE system

$$D_m \nabla_x^2 \widetilde{m} + f(\widetilde{m}, \widetilde{c}) = 0, \tag{6}$$

$$D_c \nabla_x^2 \widetilde{c} - f(\widetilde{m}, \widetilde{c}) = 0. \tag{7}$$

Comparing these equations with Eq. (4) reveals that the stationary pattern only deviates from reactive equilibria due to the local change of diffusive flux $D_m \nabla_x^2 \widetilde{m}(x)$ and $D_c \nabla_x^2 \widetilde{c}(x)$. Note that for any steady state (stationary pattern) the diffusive fluxes of m and c have to balance everywhere

$$D_m \nabla_x \widetilde{m}(x) = -D_c \nabla_x \widetilde{c}(x) \quad \forall x, \tag{8}$$

as obtained by adding both steady state Eqs. (6,7) and integrating over x. Integrating this pointwise *flux-balance* over the whole spatial domain yields that any stationary pattern fulfills the linear relation

$$D_m/D_c\widetilde{m}(x) + \widetilde{c}(x) = \eta_0 = \text{const.} \quad \forall x. \tag{9}$$

where η_0 is the integration constant. In the (m, c)-phase space any spatial density profile is a curve parametrized by x. Equation (9) implies that any stationary pattern confined to a linear subspace of the (m, c)-phase space (see Fig. 2b). We shall call this subspace the *flux-balance subspace*, since it represents the pointwise balance of diffusive fluxes in membrane and cytosol (Eq. (8)). The intercept η_0 is not *a priori* known. We will later see that a balance of reactive processes determines the value η_0 in dependence of global total density n_0 and system size L, i.e. $\eta_0 = \eta_0(n_0, L)$. The slope $-D_m/D_c$ of the flux-balance subspace is uniquely determined by the diffusion constants. Consequentially, whenever the diffusion constants D_m and D_c are unequal, the flux-balance subspace cannot coincide with any reactive phase space (which has slope -1). Hence, any stationary pattern (non-uniform $\widetilde{m}(x)$) must have a non-uniform total density profile $n_x = \widetilde{m}(x) + \widetilde{c}(x)$. Therefore, the *local total densities* n_x determine the *local (reactive) phase spaces of the spatially extended system, which we will next use to characterize the stationary pattern.*

Stationary patterns are scaffolded by local equilibria

We now will use this non-uniform total density profile n_x to find the relation between the stationary pattern and the kinetic nullcline. Consider the system spatially dissected into *local* compartments, an approach first put forward in [turbulence paper]. Within each compartment local kinetic interactions induce a reactive flow $f(m, c)$ that lies in the *local phase space* $m + c = n_x$ which is determined by the local mass n_x. The *local (chemical) equilibria*, where the kinetic interactions within a compartment balance, depend on the total density n_x in the compartment:

$$(m_x^*, c_x^*) : f(m_x^*, c_x^*) = 0 \text{ for } m_x^* + c_x^* = n_x. \tag{10}$$

Hence, given a mass distribution n_x we can calculate the local chemical equilibria (and their stability) within each compartment. These equilibria and their linear stability then serve as proxies for the local reactive flow (as in our discussion of the well-mixed system in the previous section; cf. Eq. (5)). The

compartmentalization extends the geometrization of the local kinetic interactions to the spatially extended system.
In summary, we have established three major geometric structures in (m, c)-phase space: First, the line of chemical equilibria $f(m, c) = 0$ along which the local kinetic interactions are balanced; second, the local phase spaces $m + c = n_x$ determined by the local total densities n_x — local equilibria (m_x^*, c_x^*) are intersections of the kinetic nullcline and the local phase space; third, the family of flux-balance subspaces, within which diffusive flows in membrane and cytosol balance each other. The flux-balance subspaces hence represent diffusive coupling, which is — as we shall see below — essential to understand pattern formation. As Eq. (9) shows, the *stationary* pattern state $(\widetilde{m}(x), \widetilde{c}(x))$ is embedded in a flux-balance subspace with a particular intercept η_0, which is determined by a balance of reactive processes as we will see later. Note that during the *dynamic* pattern formation process mass will be redistributed until the flux-balance is established (e.g. as the system becomes stationary).
A note on diffusion constants In the following we will only discuss the case $D_m \ll D_c$, so that we can neglect the non-constant term in Eq. (9) and approximate $\widetilde{c}(x) \approx c_0 = \eta_0(n, L)\ \forall x$. Importantly, c_0 is not a parameter: instead it is determined by the balance of reactive flows, as we will se later, and depends on the parameters n and L in addition to the kinetic rates. When considering not stationary states but dynamics, e.g. linear stability, both limits $D_m \to 0$ and $D_c \to \infty$ are pathological regarding the interpretation of the dispersion relation (cf. [19, 25]). In the Supplementary Material we show that all results of the following analysis can be simply extended to cases with arbitrary ratios $D_m/D_c > 1$. In essence, we can transform the phase space coordinates to coordinates that parametrize the dynamics within the flux-balance subspace, $\phi = m + D_m/D_c\, c$, and the respective orthogonal complement $\eta = c - D_m/D_c\, m$. All geometric relations which are below worked out in (m, c)-phase space for the case $D_m \ll D_c$ hold generally in (ϕ, η)-phase space for arbitrary diffusion constants.

The shape of the kinetic nullcline characterizes the stationary pattern

To understand the self-organization principle underlying pattern formation we need to understand the mechanism that induces mass redistribution. But first, we will discuss how qualitative properties of the stationary pattern (profiles) can be deduced from the geometrization.
Any stationary pattern must fulfill the stationarity condition Eq. (6) at every

point in space. We already discussed above that this condition contains two parts: the spatial change of diffusive flux and reactive flow. Both need to be balanced at every point in space. Flux-balance (Eq. (8)) ensures that if this balance is established for one diffusive component, it holds for all components. We can therefore restrict the discussion to the membrane density m alone. Let us start by considering points where the diffusive flux $D_m \nabla_x \widetilde{m}(x)$ does not vary between neighboring compartments, i.e. $\nabla_x^2 \widetilde{m}(x) = 0$. At these points the stationary pattern *must* coincide with a local equilibrium (cf. Eq (6)). In (m, c)-phase space, these points are marked by intersections of the flux-balance subspace with the kinetic nullcline. For a pattern composed of two plateaus, connected by a diffusive interface (see Fig. 2), there are three such intersection points: the plateaus (m_-, c_0) and (m_+, c_0), where the gradient of the density profiles vanish in extended regions — as well as the inflection point $m_0 = \widetilde{m}(x_0)$ where the the diffusive flux is locally constant:

$$x_0 : \nabla_x^2 \widetilde{m}(x_0) = 0 \;\Leftrightarrow\; f\big(\widetilde{m}(x_0), \widetilde{c}(x_0)\big) = 0 \tag{11}$$

The inflection point x_0 marks the center of the diffusive interface of a pattern. Due to the density gradient at the inflection point x_0, there will be a diffusive flux across x_0. This diffusive flux must be balanced by all reactive flows $f(m, c)$ on either side of the interface (illustrated by the red arrows and shaded areas in Fig. 2). Integrating Eq. (6) multiplied by the local flux $\partial_x m(x)$ from the boundaries to the interface x_0 yields the diffusive flux across the interface

$$D_m \nabla_x \widetilde{m}\big|_{x_0} = \int_0^{x_0} \mathrm{d}x\, f\big(\widetilde{m}(x), c_0\big) \tag{12}$$

$$= -\int_{x_0}^{L} \mathrm{d}x\, f\big(\widetilde{m}(x), c_0\big) \tag{13}$$

The reactive flow integrated over space (*reactive turnover*) on either side of the interface has to exactly balance the diffusive flux across it. This *flux–turnover balance* is the core physical criterium that determines the stationary pattern: The spatially non-uniform local equilibria *scaffold* the stationary pattern by means of "restoring forces" towards the (stable) local equilibria which maintain the pattern by balancing against the diffusive flux. In the vicinity of the local equilibria m_x^*, the reactive flow ("restoring force") can be approximated by the eigenvalue σ_x^{loc} of the local equilibrium (linearization in local phase space, cf. Eq. (5)):

$$f\big(m(x), c(x)\big) \approx \sigma_x^{\mathrm{loc}} \cdot \big(m(x) - m_x^*\big) \tag{14}$$

The shape of the nullcline determines how the local equilibria shift due to mass redistribution. Therefore we classify the possible patterns of two-component

systems based on the topological equivalence classes of kinetic nullcline and the flux-balance subspace (Fig. 3). First of all, plateaus are not necessary to obtain a stationary pattern. Instead, diffusive flux and reactive turnover can balance before the flow vanishes at local equilibria (Fig. 3a). This can happen, for instance, in a short system where only one discrete harmonic (eigen-)mode is unstable and the diffusive flux across the interface is confined to grow linearly with the pattern amplitude. The system assumes plateaus only where the local equilibria are reached in spatially extended parts of the system (regions), such that diffusive gradients have to vanish, cf. Eq. (6). When this happens only on one side of the interface (i.e. inflection point) only one plateau forms and the interface takes on the role of a peak (Fig. 3b). The turnover on the plateau side is bounded determining the peak amplitude via flux–turnover balance. When mass is added (i.e. n_0 increased) to a peak pattern, it cannot go into the cytosol, since this would shift the flux-balance subspace upwards breaking flux-turnover balance. Inescapably, the additional mass goes into the peak, which grows in hight and width, while the flux–balance subspace moves must move to lower c_0, to restore flux-turnover balance by increasing the turnover on the plateau side. Peak patterns are typically observed in cell-polarization systems such as the Cdc42 system of budding and fission yeast. Plateau patterns are formed when local equilibria are reached on both sides of the inflection point (Fig. 3c). Adding mass to such a system shifts the interface in space without significant change of amplitude and c_0. We will make use of this property later to analyze the bifurcations of plateau patterns with respect to the average total density n_0.

A mathematical trick allows us to formulate flux–turnover balance without knowledge of the explicit shape of the stationary profile $\widetilde{m}(x)$: If we multiply Eq. (6) by the local flux $\partial_x m(x)$ before integrating, we can reparametrize the integration to obtain

$$D_m/2 \left(\nabla_x \widetilde{m}\big|_{x_0}\right)^2 = \int_{\widetilde{m}(0)}^{m_0} \mathrm{d}m\, f(m, c_0) \tag{15}$$

$$= -\int_{m_0}^{\widetilde{m}(L)} \mathrm{d}m\, f(m, c_0), \tag{16}$$

which only depends on the boundary values $\widetilde{m}(0)$ and $\widetilde{m}(L)$ of the membrane density. This formulation of flux–turnover balance is useful to easily obtain quantitative properties (amplitude $|\widetilde{m}(L) - \widetilde{m}(0)|$ and interface slope $\widetilde{m}'(x_0) = \nabla_x \widetilde{m}|_{x_0}$) of stationary patterns without the need to perform full numerical simulations. In the case of plateau patterns, the boundary values of $\widetilde{m}(x)$ are given by the plateau densities which are marked by the intersections of flux-

balance subspace and kinetic nullcline. We will later use this to geometrically construct the bifurcation structure of plateau patterns.

Turing instability is a mass-redistribution instability

The thorough analysis of stationary polarity patterns provided us the tools and intuition to now finally turn to the *dynamic* mechanism of self-organized pattern formation. Essentially we need to understand how the system is driven into a nonuniform total density distribution governing a polarity pattern. As we will see, this redistribution can either occur endogenously due to lateral mass-redistribution instability of a uniform steady state or due to a strong external perturbation. These cases represent the two generic classes by which state changes of dynamical systems are characterized: linear instability and excitability.

Let us start with the first case, the response (linear stability) of a system in a spatially uniform chemical equilibrium (uniform steady state) to a small spatial perturbation of the membrane density $\delta m(x)$. This spatial perturbation will always perturb the total density distribution $n_x = n_0 + \delta n(x)$. Consequentially the local equilibria (m_x^*, c_x^*) will be shifted. This shift of local equilibria builds up spatial gradients in the cytosolic density $c(x) = c_0 + \delta c(x)$. Due to the fast cytosolic diffusion, gradients in the cytosolic density induce a flux $D_c \partial_x \delta c(x)$, which will redistribute total density. This the most central process of self-organized pattern formation: The direction of the cytosolic flux decides the fate of the further dynamics. If the slope of the kinetic nullcline is positive, compartments with more total density will have higher cytosolic density (see Fig. 4), so the flux will homogenize the non-uniform total density redistribution and the system returns to its uniform steady state. If however, the slope of the kinetic nullcline is negative, even more mass will be redistributed into compartments that have higher total density, further shifting the local equilibria and in turn increasing the diffusive flux. This cascade of shifting local equilibria and mass-redistribution via cytosolic flows will drive the system away from the uniform steady state and into a pattern state, which becomes stationary when flux–turnover balance is re-established.

We have revealed how the slope of the kinetic nullcline — a purely geometric criterion — determines the existence of mass-redistribution instability. This can be viewed as a topological equivalence class (see below for a *mechanical* system that has the same type of instability). In the case $D_m \ll D_c$, which we discussed above, a negative slope of the kinetic nullcline at the uniform

steady state ($(m^*(n_0), c^*(n_0))$) marks lateral instability. In the general case of arbitrary diffusion constants one has to compare the slope of the kinetic nullcline $\partial_m c^*|_{m^*}$ with the slope of the flux-balance subspace $-D_m/D_c$ and the criterion for mass-redistribution instability becomes $\partial_m c^*|_{m^*} < -D_m/D_c$ (see Supplementary Material). This geometric criterion implies that bifurcations where a uniform steady state changes its lateral stability are marked by changes of the geometric structure of the kinetic nullcline as it deforms under changes of the kinetic parameters.

The cascade of shifting local equilibria due to cytosolic diffusive transport is the general principle underlying the Turing instability. Form the physical point of view this instability was always considered at odds with the central physical property of diffusion, which is the removal of any gradients, seemingly the exact opposite of pattern formation. Here we clearly see that the fundamental physical principle underlying pattern formation is exactly the removal of gradients by lateral transport of total density.

Cytosolic diffusion facilitates mass redistribution and hence is the essential driver of lateral mass-redistribution instability, which is the generalization of Turing instability. Membrane diffusion on the other hand counteracts the growth of perturbation and acts against the reactive flow towards the shifted local equilibria. This also naturally explains why Turing instability, and mass-redistribution instabilities in general, are based on different diffusion coefficients. Yet, in contrast to the activator-inhibitor paradigm, no finite slow diffusion is required, the pattern forming process is entirely based on the lateral redistribution of the fast diffusing component.

The diffusive flux of the membrane component depends on the length scale of the perturbation. The minimal length scale where both processes exactly balance is determined by flux–turnover balance. By putting a the harmonic mode ansatz $m(x) = m_0 + \delta m \cos(\pi x/L)$ into the flux–turnover balance condition (12) we naturally obtain the minimal system length $L_{\min} = \pi\sqrt{D_m/f_m}$ for the length scale of neutral lateral (in-)stability (in the approximation $D_m \ll D_c$) . In the dispersion relation this length scale is marked by the right edge of the band of unstable modes $q_{\max} = \pi/L_{\min}$ (see Supplement Material for a detailed discussion of the dispersion relation in the context of mass redistribution instability and a comparison to the classical picture of short range activation and long range inhibition).

Subcritical patterns: lateral excitability and regional lateral instability

To address the question of excitability let us consider a system that exhibits plateau patterns when the length L is much larger than the interface width (e.g. the "wave–pinning" model used by Edelstein-Keshet et al., see Supplementary Material for details and the parameters used). As discussed above, the plateau values of $m(x)$ can be approximated by the local equilibria

$$m_\pm(c_0) : \; f(m_\pm, c_0) = 0 \tag{17}$$

The intercept c_0^∞ is then uniquely determined by the condition that the total reactive turnover has to vanish

$$c_0^\infty : \; \int_{m_-}^{m_+} \mathrm{d}m \, f(m, c_0^\infty) = 0. \tag{18}$$

Hence, plateau patterns are uniquely determined simply by global turnover balance (Eq. (18)), which determines the position of the flux-balance subspace c_0^∞ and thereby the plateau densities $m_\pm(c_0^\infty)$. Additionally, flux–turnover balance yields the interface properties (e.g. slope and width) via Eq. (15).
Using the uniquely determined flux-balance subspace position c_0^∞, we can now geometrically construct the range of average total densities n_0 for which stationary patterns exist. Two geometric conditions determine this range: First, the center of mass in (m, c)-phase space always lies in the 1-simplex $m+c = n_0$. Second, the center of mass has to lie in the flux-balance subspace determined by η_0^∞. In particular it can only lie in-between the plateau values $m_-(c_0^\infty)$ and $m_+(c_0^\infty)$ (see Fig. 5). Therefore, patterns exist only in the range

$$m_-(c_0^\infty) + c_0^\infty =: n_{\mathrm{exc}}^- < n_0 < n_{\mathrm{exc}}^+ := m_+(c_0^\infty) + c_0^\infty. \tag{19}$$

Note that these bounds on n_0 equal the total densities in the plateau regions of a system much longer than the interface width, where the reactive turnover saturates at the intersection points of flux-balance subspace and kinetic nullcline. Only if the average total density n_0 lies between these plateaus a polarized pattern can be formed.
As Fig. 5 clearly shows, patterns exist even if the uniform steady state is laterally stable. In fact, the possibility of a subcritical lateral Turing bifurcation has been suggested as cause for wave-pinning by Goryachev and Leda [18]. Other than in the vicinity of supercritical bifurcations, the pattern properties are apparently not determined by the lateral stability spectrum, i.e. dispersion relation, of the uniform steady state. This raises two questions: First, what

is the threshold (pattern) that separates basins of attraction of the uniform steady state and the polarized pattern? And second, what is the role of the lateral (mass-redistribution) instability for the properties of plateau patterns? To answer the first question, we need to find out what kind of (non-uniform) perturbation is necessary to drive a subcritical system from the uniform state into the polarized pattern. We learned that a non-uniform distribution of total density (local equilibria) is the core characteristic of stationary patterns. Hence, a perturbation that leads into a polarized pattern must redistribute mass in such a way, that the reactive turnover and diffusive flux induced by the perturbation drive the system away from the uniform state . The induced reactive turnover is the "driving force", whereas the diffusive flux acts as "restoring force". From the previous discussions we know that the diffusive flux balances the reactive flow locally proportional to $D_m\nabla_x^2\widetilde{m}(x)$ and $D_c\nabla_x^2\widetilde{c}(x)$, respectively (cf. Eq. (6) and (7)). Hence, the diffusive "restoring force" will only act in regions where the density gradients are not constant. This is clearly the case for plateau shaped perturbations. Let us therefore study the simplest spatial perturbation with that property: a step function which represents moving a "block" of mass (total density) from one end of the system to the other (see Fig. 6). Cytosolic perturbations quickly equilibrate back to a uniform profile, so we only consider a perturbation of the membrane density. The reactive flow induced by the perturbation in the plateau region must point away from the uniform state, and must be strong enough to dominate the diffusive flux of the membrane species induced at the "interface" of the plateau shaped perturbation. The reactive flow always points towards the stable local equilibria and thus switches its direction upon crossing the line of chemical equilibria. Crossing the kinetic nullcline in m-direction yields a lower bound for the threshold m_{th}. Strikingly, this simple criterion already provides a very good approximation for the excitability threshold in comparison to full numerical simulation (see Supplementary Figure 3). Again, as in the analysis of lateral mass-redistribution instability, we found that the kinetic nullcline, in particular its slope, provides the key information for understanding pattern formation dynamics.

Beyond bifurcations at $n_{\mathrm{exc}}^{\pm}$ where stationary patterns disappear, we find that perturbations can still lead to an excursion through a transient pattern, which mimics an actual stationary pattern, before returning to the uniform steady state. These excursions are typical for excitable systems in the vicinity of bifurcations where new attractors appear.

All results so far were based on the decomposition of spatially extended systems into isolated local compartments [25]. These compartments were assumed to

be so small that they can be considered well-mixed. That allowed us to apply the geometry ODE picture to the spatially extended system. Our discussion of plateaus and lateral excitability suggests an additional decomposition of the system on a coarser (regional) length scale where lateral coupling cannot be neglected *a priori*: the plateaus and the diffusive interface (shaded in gray) around the inflection point x_0. To study these regions individually, let us isolate the regions from each other by imposing no-flux boundary conditions. Note that this approach is analogous to the isolation of local compartments which leads to the notion of local equilibria. In the case of isolated regions lateral coupling cannot be neglected (inside each region) such that the local attractors are (in general) patterns and not points (equilibria). Just like in the case of local compartments these *regional attractors* are fully determined by the (average) total density contained in each region. The regional average densities can be estimated as $n_\pm \approx c_0 + m_\pm$ for the plateaus and $n_{\text{int}} \approx m_0 + c_0$ at the interface. The attractors of the plateau regions are simply uniform steady states. Importantly, note that the plateaus will always be laterally stable because the slope of the kinetic nullcline can only be positive at the respective intersections with the flux-balance subspace — hence, there cannot be anti-coarsening [compare e.g. "Self-replication of mesa patterns" [27], where plateaus are laterally unstable]. Conversely, the interface region is always laterally unstable. Since the plateau regions are isolated from the interface, the regional attractor of the interface is a harmonic profile. In other words: The interface is spanned and maintained by mass-redistribution instability. Because the reactive flow vanishes at the plateaus, the dominant contribution to the turnover comes from the interface region — flux-turnover balance has to be achieved within the interface region. We can estimate flux-turnover balance by linearizing around the inflection point, which is equivalent to linear stability analysis at $n = n_{\text{int}}$. The eigenmode fulfilling flux-turnover balance is $\cos(q_{\max}(n_{\text{int}})x)$, the right edge of the band of unstable modes. Hence, the interface width can be approximated by $L_{\text{int}} \approx \pi/q_{\max}(n_{\text{int}})$.

We conclude that *any* stationary pattern in mass-conserving two-component reaction–diffusion systems is inextricably linked with lateral instability, which maintains the diffusive interface. Just as the local equilibria scaffold the interface, we can think of the regional attractors as scaffold for the global pattern! The properties of the global pattern can be pieced together by (characteristically distinct) isolated regions (plateaus and interface). Intersections of flux-balance subspace and kinetic nullcline provide sharp characteristics in (m, c)-phase space: Plateaus are intersections where the slope of the kinetic nullcline is positive while interfaces extend around the point where the slope

is negative. The average total density in each of these regions determines the properties of the regional attractor. Regions are the natural extension of the compartmentalization approach, with regional attractors taking the place of local equilibria, and average total densities (in each region) the place of local total densities.

A mechanical analogy for Turing instability

Above we identified the core elements underlying lateral mass redistribution instability (e.g. Turing instability): shifting local equilibria that drive cascading redistribution of mass by the faster diffusing (here: cytosolic) species. The discussion of lateral excitability and regional attractors showed that this principle of shifting local equilibria by mass redistribution in central to all aspects of pattern formation. Due to the central role of this principle we would like to present a strikingly simple mechanical analogy for the lateral mass redistribution instability that captures all essential physical processes. To that end consider the mechanical system shown in Fig. 7 — a water-filled bucket resting on an overdamped spring. The amount (volume V) of water in the bucket determines the water level above ground $h^*(V)$ in (mechanical) equilibrium. Let us now ask a very simple question: How will the the equilibrium position h^* change if we either increase or decrease the water volume? The answer is simple: For sufficiently hard springs, the water level increases e.g. infinitely hard springs. For sufficiently soft springs however, the compression of the springs can overcompensate the increase of the water level within the bucket, such that the water level above ground decreases as more water is put in the bucket. Note that this is a simple mechanical example for a system where an equilibrium changes with mass contained in the system.
Now let us consider two identical bucket-on-spring systems: What happens when we couple both by connecting the buckets with a thin tube that allows water to slowly flow from one bucket to the other (Fig. 7b)? When a small amount of water is transferred from one bucket to the other, the equilibrium position of both buckets shift in opposite directions. The height difference of the water levels induces a pressure gradient which in turn leads to a flux through the tube. When the water level above ground $h^*(V)$ increases with the volume V in the bucket, this flux will equilibrate the water levels so that the system returns to a uniform equilibrium (left side in Fig. 7b). In the case of sufficiently soft springs ($k < k_c$), the water level above ground decreases with volume, inducing a flux into the bucket that already holds more water thereby

further increasing the difference of volumes. This self-amplifying flux drives the mass-redistribution instability, analogously to the lateral instability of a mass-conserving reaction–diffusion systems. The driver of lateral instability is the removal of gradients (hydrostatic pressure difference) by lateral transport of total density (water volume).
The mechanical analogy demonstrates the concept of topological equivalence: two distinct physical systems, a chemical one and a mechanical one, that share the same topological structure in phase space follow the same unifying principle of mass-redistribution instability. If we can establish such equivalence between mechanical and chemical systems, clearly we can establish it between different chemical systems alone.
In principle, the line of chemical equilibria is experimentally accessible since it can be studied using a single, isolated, and well-mixed reactor by externally controlling the available conserved quantity (e.g. particle number). Such experiments would allow probe and classify the core mechanism without knowledge of the molecular details (which are irrelevant for such a classification).

PART II — APPLICATION TO A QUANTITATIVE MULTI-SPECIES MODEL

Up to this point we have discussed our geometrization approach only for mass-conserving two component models. However, real biological pattern formation systems typically involve multiple protein *species* with many different conformal states (*components* of the kinetic interaction network). On the other hand, we learned that the essential process underlying pattern formation is the redistribution of total densities (though cytosolic diffusion). A pattern forming biological system contains as many total densities as there are individual (conserved) protein species participating in protein-protein interactions. While the diffusion coefficients of membrane-bound and cytosolic proteins are fixed, there is no *a priori* reason that the cytosolic redistribution of all protein species is *required* for pattern formation. This raises the following question: Can we systematically map a quantitative multi-species, multi-components model onto a core species governed by an effective two-component reaction diffusion system of the form Eqs. (1,2)? The key idea behind such a systematic approach is that mass redistribution of all species except for the core species can be set to a slower timescale without affecting the pattern qualitatively (topological equivalence).
In the following we demonstrate this approach for *in vivo* Min protein dynam-

ics which serve as a paradigmatic example for self-organized pattern formation in the literature [1, 4]. Min protein dynamics are based on the interactions between two (globally conserved) protein species: MinD and MinE. Physiologically this system exhibits pole-to-pole oscillations of the MinD and MinE total density profiles. Thus, superficially judging by phenomenology, the Min protein dynamics seem unrelated to stationary cell polarization. Before we proceed with the analysis of the model, let us first summarize the bimolecular basis of Min protein interactions (for a review, see [26]).

Quantitative model of Min oscillations

Cell division of *E. coli* is spatially organized by the reaction–diffusion dynamics of MinD and MinE: Cytosolic ATP-bound MinD dimerizes and binds to the membrane. It then recruits further MinD-ATP from the cytosol, as well as its ATPase-activating protein MinE. Together, MinD and MinE form membrane-bound MinDE complexes. Then, MinE stimulates MinD's ATPase activity, which initiates the disintegration of MinDE complexes and subsequent release of MinE and ADP-bound MinD into the cytosol. Reattachment of MinD is delayed by the requirement for nucleotide exchange (substitution of ATP for ADP). This biochemical reaction network, which we refer to as the skeleton network [15, 28], suffices to generate Min patterns *in vivo* [15–17] and *in vitro* [25], as has been confirmed by numerous experimental and theoretical studies. In it's full form the skeleton model comprises five interacting components [15, 28]: MinD-ATP (c_{DT}), MinD-ADP (c_{DD}), and MinE (c_{E}) in the cytosol, as well as MinD (m_{d}) and MinDE complexes (m_{de}) on the membrane (see Fig. 8b). The state changes (membrane attachment and detachment, complex formation and disintegration) of the proteins are accounted for by mass action law kinetics and conserve the total number of MinD and MinE proteins individually. Here, our goals is to reveal the mechanistic core principles underlying the *in vivo* pattern formation. So far, *in vivo* Min protein pattern formation has been studied in context of geometry adaption, i.e. the interdependence of pattern formation and cell geometry. In that regard, the cytosolic nucleotide exchange process has proven to be crucial. The main physical principle underlying pattern formation per se has so far been only identified as a oscillatory Turing instability. Form the preceding discussion we know that such a characterization is not very revealing without proper analysis in context of mass redistribution. For the *in vitro* variant of the model the analysis in the mass redistribution framework has proven to be highly interesting, revealing several

new concepts for pattern formation, see [25]. Hence, we now seek a systematic reduction scheme for the *in vivo* dynamics, based on the general property of mass conservation, which maps the quantitative model to a physically well defined, generic core model. In the following we present the main conceptual steps and ideas of this reduction. For the analytical details we refer the reader to the Supplementary Material.

Since we are interested in the pattern formation mechanism per se, and not in geometry adaption, the finite rate of nucleotide exchange in the cytosol is negligible. We can therefore eliminate the MinD-ADP (c_{DD}) from the dynamics in the limit of infinitely fast nucleotide exchange (see Supplementary Material for details).

For simplicity it is convenient to consider the model in a 2D rectangular box geometry (dimensions $L\times h$) with the membrane at one long edge and reflective boundaries at all other sides. The on–off dynamics are such that the cytosol quickly equilibrates in the direction normal to the membrane (in the following called vertical direction, see Supplementary Material). Under this condition the cytosol concentrations at the membrane ($y = 0$) can be approximated by the cytosol concentrations averaged over the vertical y-direction. Thereby the dynamics can be systematically reduced to effective dynamics on a line. Note that this reduction is only valid for the small system size *in vivo*, but not for large system sizes *in-vitro*, cf. [25, 29]. In the effective the 1D model, the diffusion constants only affect lateral diffusion in the cytosol and on the membrane, such that they now act as control parameters for the *lateral* mass transport alone (note that vertical bulk diffusion in an extended bulk geometry affects attachment, see Supplementary Material). The ensuing effective 1D model equations read

$$\partial_t c_{\mathrm{D}} = D_{\mathrm{D}}\nabla_x^2 c_{\mathrm{D}} - h^{-1}\left[(k_{\mathrm{D}} + k_{\mathrm{dD}} m_{\mathrm{d}})c_{\mathrm{D}} + k_{\mathrm{de}} m_{\mathrm{de}}\right]. \tag{20}$$

$$\partial_t c_{\mathrm{E}} = D_{\mathrm{E}}\nabla_x^2 c_{\mathrm{E}} - h^{-1}\left[k_{\mathrm{dE}} m_{\mathrm{d}} c_{\mathrm{E}} + k_{\mathrm{de}} m_{\mathrm{de}}\right], \tag{21}$$

$$\partial_t m_{\mathrm{d}} = D_{\mathrm{d}}\nabla_x^2 m_{\mathrm{d}} + (k_{\mathrm{D}} + k_{\mathrm{dD}} m_{\mathrm{d}})c_{\mathrm{D}} - k_{\mathrm{dE}} m_{\mathrm{d}} c_{\mathrm{E}}, \tag{22}$$

$$\partial_t m_{\mathrm{de}} = D_{\mathrm{de}}\nabla_x^2 m_{\mathrm{de}} + k_{\mathrm{dE}} m_{\mathrm{d}} c_{\mathrm{E}} - k_{\mathrm{de}} m_{\mathrm{de}}, \tag{23}$$

conserving of total MinD and MinE mass

$$\int_0^L \mathrm{d}x\ (h\cdot c_{\mathrm{D}} + m_{\mathrm{d}} + m_{\mathrm{de}}) = L\cdot n_{\mathrm{D}}, \tag{24}$$

$$\int_0^L \mathrm{d}x\ (h\cdot c_{\mathrm{E}} + m_{\mathrm{de}}) = L\cdot n_{\mathrm{E}}. \tag{25}$$

Note that c_D and c_E are the averaged cytosolic area densities while m_d and m_de are line densities on the membrane. All rate constants are identical to the original rate constants in the 2D box geometry at this point. For notational convenience we absorb the height h in the cytosolic concentrations $hc_\mathrm{D} \to \hat{c}_\mathrm{D}$, $hc_\mathrm{E} \to \hat{c}_\mathrm{E}$, and respectively rescale the attachment rates $k_\mathrm{D}/h \to \hat{k}_\mathrm{D}$, $k_\mathrm{dD}/h \to \hat{k}_\mathrm{dE}$, $k_\mathrm{dE}/h \to \hat{k}_\mathrm{dE}$. After this rescaling, the cytosolic component concentrations are also measured as line densities like the membrane concentrations. Because we will exclusively use the rescaled cytosolic densities and rate constants throughout the paper we suppress the hats to simplify notation.

Timescale separation of mass redistribution

For (well-mixed) systems described by ODEs, like metabolic networks or regulatory networks of genes and their promoters, one usually tries to dissect the interaction circuit into sub-circuits (so called motifs or modules) which can be analyzed independently (e.g. by separating timescales). For pattern formation, however, diffusive spatial coupling of the chemical components is an essential part of the dynamics. In previous work [25] it has been shown that diffusive redistribution of quantities conserved by the kinetic interactions are the essential degrees of freedom for spatially extended systems. In the preceding general analysis of mass-conserving two-component systems we have learned that the core mechanism of pattern formation is diffusive redistribution of the globally conserved total density (mass). Flux–turnover balance then determines the properties of the stationary pattern profile. This core mechanism is determined by how the chemical equilibria depend on the total density whereas molecular details of the interaction circuitry are irrelevant. Based on this insight, we seek a systematic reduction not on the level of interaction circuitry but on the level of diffusive redistribution of conserved quantities. In the Min system there are two protein species, MinD and MinE, each of whose copy number is conserved by their kinetic interactions. Separating the timescales of their diffusive transport will be our starting point to elucidate their bio-mechanistic role in the pattern formation dynamics.

Linear stability analysis

Preamble — characterizing the onset of lateral instability at the minimal system length Due to the reflective boundary conditions at $x = 0$ and $x = L$, only modes $\cos(q_k x)$ with $q_k = k\pi/L, k \in \mathbb{N}$ are compatible to a system of length L: the mode spectrum is discrete. Specifically, the system length imposes the smallest wavenumber (i.e. longest wavelength) $q_1 = \pi/L$ compatible with the reflective boundaries. Lateral instability only occurs if q_1 is smaller than the right edge of the (continuous) band of unstable modes $q_{\max} : \mathrm{Re}[\sigma(q_{\max})] = 0$. Hence, $q_{\max}$ determines the minimal system length $L_{\min} := \pi/q_{\max}$ at which the first compatible mode $\cos(q_1 x)$ becomes unstable. At the bifurcation point $L_{\min}$, the real part of the first mode growth rate vanishes ($\mathrm{Re}[\sigma(q_{\max})] = 0$). It can further be characterized by the imaginary part $\mathrm{Im}[\sigma(q_{\max})]$. If $\mathrm{Im}[\sigma(q_{\max})]$ is non-zero, the dynamics are oscillatory at the onset of instability (lateral Hopf bifurcation or oscillatory Turing instabilty), otherwise the onset dynamics are non-oscillatory. Also note that when there is no band of unstable modes in the continuous dispersion relation ($q_{\max} = 0$) there will be no pattern formation based on lateral instability for any system length.

Linear stability analysis reveals the regimes of pattern formation Mass redistribution of a protein species is facilitated by the diffusion of the individual components (i.e. conformal states, complex forms) belonging to that species. Hence, tuning the diffusion constants of all these components allows us to change the lateral redistribution of a species. In particular, note that when all diffusion constants belonging to one species are set to the same value, the total density of this species will not be redistributed in the flux balance subspace (since the flux balance subspace coincides with a local phase space where total density uniform and conserved).. By performing lateral linear stability analysis of uniform steady states (for identical diffusion coefficients of individual species) we can test if mass redistribution of a species is essential for lateral instability — and hence essential for pattern formation driven by mass redistribution. Thereby we can reveal the core mechanisms underlying Min protein dynamics.

MinD transport is essential for lateral instability Applying this idea to the Min protein system, we calculated the linear stability of the uniform steady state of (20) to (23) upon variation of the lateral diffusion of all the dynamical densities (D_{D}, D_{E}, D_{d} and D_{de}, see Fig. 8a, data for MinD diffusion not shown). It turns out, that the system is only laterally unstable if cytosolic MinD diffusion is much faster than diffusion of membrane bound MinD (already a hint, that MinD redistribution drives lateral instability as in the

two-component system). Furthermore, diffusion of cytosolic MinE may not to be much faster than diffusion of cytosolic MinD. We conclude that redistribution of MinD mass primarily drives lateral instability of the uniform Min protein steady sate. Next, let us turn to the role of MinE diffusion on the membrane and in the cytosol.

MinE transport can be set to a slower timescale In the diagram of lateral stability phases in dependence of D_{E} and D_{de} (Fig. 8a) we observe three regimes: Above some threshold value of D_{E}, the uniform state is always stable against lateral perturbations ($q_{\max} = 0$). The lateral instability becomes oscillatory ($\mathrm{Im}[\sigma(q_{\max})] \neq 0$) if cytosolic diffusion D_{E} of free MinE dominates over membrane diffusion D_{de} of MinDE complexes. This behavior extends down to arbitrarily small MinE diffusion constants. We therefore conclude that the essential dynamics of Min proteins is preserved in the limit of arbitrarily small MinE diffusion. Hence, MinE transport is not required for pattern formation — the lateral instability is a mass-redistribution instability of MinD alone and generically leads to non-oscillatory polarity patterns. The oscillatory nature of Min protein dynamics seems to be the result of Min redistribution. Hence, we can consider MinE redistribution on a slower timescale to study the principal mechanisms underlying the Min oscillations (the validity of this separation of timescales is corroborated by simulations and by reverting to physiological timescales after the core processes have been identified).

Effective dynamics under timescale separation

Before we proceed, we introduce the average MinE diffusion constant $d_{\mathrm{E}} := (D_{\mathrm{E}} + D_{\mathrm{de}})/2$. For small enough d_{E} (i.e. $d_{\mathrm{E}} \ll D_{\mathrm{d}}$ and $d_{\mathrm{E}} \ll L^2/\tau_{\mathrm{r}}$ where $\tau_{\mathrm{r}} \sim |\sigma_{\mathrm{loc}}|^{-1}$ is the typical timescale of the kinetic interactions (which can be estimated by the eigenvalue of the local equilibrium, see Supplementary Material), the total MinE density

$$\rho_{\mathrm{E}}(x) = c_{\mathrm{E}}(x) + m_{\mathrm{de}}(x) \tag{26}$$

can be considered to be stationary on the timescale of local reactive dynamics and MinD diffusion. As illustrated in Fig. 8b, the MinE density thus *parametrically influences* the fast MinD dynamics, which rapidly approaches its steady state profiles satisfying the reduced two-component system (see Supplementary

Material for derivation):

$$D_{\mathrm{D}}\nabla_x^2 c_{\mathrm{D}} - f_{\mathrm{eff}}(c_{\mathrm{D}}, m_{\mathrm{d}}; \rho_{\mathrm{E}}) = 0, \tag{27}$$

$$D_{\mathrm{d}}\nabla_x^2 m_{\mathrm{d}} + f_{\mathrm{eff}}(c_{\mathrm{D}}, m_{\mathrm{d}}; \rho_{\mathrm{E}}) = 0, \tag{28}$$

$$\int_0^L \mathrm{d}x\, [c_{\mathrm{D}} + m_{\mathrm{d}} + m_{\mathrm{de}}(m_{\mathrm{d}}; \rho_{\mathrm{E}})] = N_{\mathrm{D}}, \tag{29}$$

with the effective reaction kinetics f_{eff}, as well as the slaved MinE concentrations $c_{\mathrm{E}}(m_{\mathrm{d}}; \rho_{\mathrm{E}})$ and $m_{\mathrm{de}}(m_{\mathrm{d}}; \rho_{\mathrm{E}})$ given by

$$f_{\mathrm{eff}}(m_{\mathrm{d}}; \rho_{\mathrm{E}}) = (k_{\mathrm{D}} + k_{\mathrm{dD}} m_{\mathrm{d}}) c_{\mathrm{D}} - k_{\mathrm{de}} m_{\mathrm{de}}(m_{\mathrm{d}}; \rho_{\mathrm{E}}), \tag{30}$$

$$c_{\mathrm{E}}(m_{\mathrm{d}}; \rho_{\mathrm{E}}) = \frac{k_{\mathrm{de}}}{k_{\mathrm{dE}} m_{\mathrm{d}}}\, m_{\mathrm{de}}(m_{\mathrm{d}}; \rho_{\mathrm{E}}), \tag{31}$$

$$m_{\mathrm{de}}(m_{\mathrm{d}}; \rho_{\mathrm{E}}) = \rho_{\mathrm{E}}\, \frac{m_{\mathrm{d}}}{k_{\mathrm{de}}/k_{\mathrm{dE}} + m_{\mathrm{d}}}. \tag{32}$$

The first term of f_{eff} describes MinD attachment, which is independent of MinE. Detachment of MinD is catalyzed by the locally available MinE $\rho_{\mathrm{E}} = \rho_{\mathrm{E}}(x, \tau)$ (cf. Fig. 8b). Hence, the effective steady-state detachment rate is determined by Michaelis–Menten kinetics $k_{\mathrm{de}} m_{\mathrm{de}}(m_{\mathrm{d}}; \rho_{\mathrm{E}})$. The locally available MinE density is given by the MinE total density profile $\rho_{\mathrm{E}}(x, \tau)$ which is a function of x and varies on the slow (MinE redistribution) timescale τ. The kinetic nullcline of the effective kinetics f_{eff} has the shape shown in panels (a) and (b) of Fig. 3.

Due to the imposed timescale separation, the MinD quickly assumes its (quasi-) stationary patterns — solutions of the effective steady state equations (27, 28)). The densities of the MinE states $m_{\mathrm{de}}(m_{\mathrm{d}}; \rho_{\mathrm{E}})$ and $c_{\mathrm{E}}(m_{\mathrm{d}}; \rho_{\mathrm{E}})$ depend on the MinD membrane profile $m_{\mathrm{d}}(x)$ (see Eq. (32)). The resulting gradients of MinD-bound and free (cytosolic) MinE induce the redistribution of MinE when the diffusion constants of MinD-bound and free MinE differ. Introducing the parameter $\delta_{\mathrm{E}} := (D_{\mathrm{E}} - D_{\mathrm{de}})/(2d_{\mathrm{E}})$, representing the relative dominance of MinE diffusion constants, we obtain the purely diffusive dynamics on the slow (dimension-less) timescale $\tau = (d_{\mathrm{E}}/L^2)\, t$

$$\partial_\tau \rho_{\mathrm{E}} = \nabla_{x/L}\, j_{\mathrm{E}} = \nabla_{x/L}^2\, \rho_{\mathrm{E}} + \delta_{\mathrm{E}}\, \nabla_{x/L}^2 \big[c_{\mathrm{E}}(m_{\mathrm{d}}, \rho_{\mathrm{E}}) - m_{\mathrm{de}}(m_{\mathrm{d}}, \rho_{\mathrm{E}})\big], \tag{33}$$

$$\text{with} \quad \delta_{\mathrm{E}} := (D_{\mathrm{E}} - D_{\mathrm{de}})/(2d_{\mathrm{E}}).$$

Coupling to the MinD stationary profile $m_{\mathrm{d}}(x)$ via δ_{E} drives the MinE distribution away from the uniform distribution approached when $\delta_{\mathrm{E}} = 0$. Equations (30) and (33) express the mutual interdependence of MinD and MinE

dynamics: The steady state of each species is controlled by the density profile of the respective other species. The dynamics are the process of ongoing mutual adaption to these steady states as we will detail in the following.
We study the system close to the minimal length $L \gtrsim L_{\min}$, where only the first mode $\cos(\pi x/L)$ is laterally unstable and the stationary patterns are harmonic profiles which are well approximated by the first harmonic mode. We can therefore apply a projection of the spatial profiles to the first harmonic mode (Galerkin expansion, see Supplementary Material)

$$m_{\mathrm{d}}(x,t) \approx m_{\mathrm{d}}^0 + m_{\mathrm{d}}^1(t)\cos(\pi x/L),, \tag{34}$$

$$\rho_{\mathrm{E}}(x,\tau) \approx n_{\mathrm{E}} + \rho_{\mathrm{E}}^1(\tau)\cos(\pi x/L). \tag{35}$$

MinE is not an inhibitor

Let us point out an important consequence of the phase diagram structure (Fig. 9b) before we work out the stationary patterns of the effective MinD two-component system: Pattern formation in reaction–diffusion systems is usually explained using the activator–inhibitor paradigm *"short range activation and long range inhibition"*, see Gierer and Meinhardt [9], and Segel and Jackson [12]. A frequently used approach is to identify activator and inhibitor based on the biochemical interactions of the system components, e.g. see Kondo and Miura [13]. According to this approach one would naively identify MinE as an inhibitor in the Min system. However, to fulfill the role as an inhibitor ("long range inhibition") in the activator–inhibitor scheme it would need to diffuse sufficiently fast in the lateral direction for the dynamics to become Turing unstable. The phase diagram (Figure 8a) shows that this condition is clearly not fulfilled. Turing instability persists for arbitrarily small MinE diffusion. Hence, based on the quantitative model (20) to (23), we can conclude that the Min protein dynamics cannot be represented (not even effectively) by an activator–inhibitor system.

MinD steady states controlled by the MinE total density profile

The separation of the diffusive timescales on the level of conserved species (MinD and MinE) reduces the essential dynamics to a two-component system with mass–conservation and a slowly varying, spatially nonuniform control variable $\rho_{\mathrm{E}}(x,\tau)$. This two-component system, effectively modeling reaction–

diffusion dynamics of MinD, is topologically equivalent to the type of system we studied in Part I of this paper. We can therefore conclude that the core mechanism of MinD is polarization — thus linking it to other cell-polarity systems, e.g. see [18]. The Min system is distinct from these cell-polarity systems only due to the (secondary) control of the polarized MinD (steady) states by MinE.

To find out how the MinE total density profile $\rho_{\mathrm{E}}(x,\tau)$ controls the MinD stationary states, we numerically implemented the flux–turnover balance condition, making use of the first harmonic projection: For a short system — close to the onset length L_{min} — we can approximate the stationary pattern by a truncated harmonics expansion (see Eq. (34)). The expansion coefficients m_{d}^0 and m_{d}^1 are then determined by plugging the harmonic mode ansatz (34) into flux–turnover balance Eq. (12). As result, we obtain the stationary MinD patterns in dependence of the MinE total density profile amplitude $\rho_{\mathrm{E}}^1(\tau)$. This relation can be cast as a bifurcation diagram (see Fig. 9b) that depicts the dependence of the stationary MinD pattern on the MinE control profile.

Note: In a generic two-component system, the local total density is given by $n = m + c$, i.e. the local phase spaces are simplexes in the (m, c)-phase space. In the reduced system for the MinD dynamics (27-29) the MinDE complex concentration $m_{\mathrm{de}}^*(m_{\mathrm{d}};\rho_{\mathrm{E}})$ also contributes to the total MinD density $n_{\mathrm{D}} = m_{\mathrm{d}} + c_{\mathrm{D}} + m_{\mathrm{de}}^*(m_{\mathrm{d}};\rho_{\mathrm{E}})$. Hence the local phase spaces are nonlinearly deformed. The equations to calculate the local equilibria are adopted accordingly. Because the local phase spaces are still monotonously decreasing in c_{D} as m_{d} is increased, the slope of the kinetic nullcline still uniquely determines the lateral stability. Furthermore, the formulation of flux-turnover balance (12) only depends on the reactive flow $f(m_{\mathrm{d}}, c_{\mathrm{D}};\rho_{\mathrm{E}})$ and is hence unaffected by the deformation of the local phase spaces.

Redistribution of MinE drives periodic re-orientation of the polarized MinD pattern

Lateral transport of MinE total density is facilitated by diffusion of both free (cytosolic) MinE and its MinD-bound state (MinDE complexes on the membrane). Since free MinE is recruited to zones with high MinD concentration (polar zones), the flow of free MinE is intrinsically *co-polarizing*. MinDE complexes are formed in the polar zone and diffuse away from it. Their resulting flow is always *counter-polarizing* (see Fig. 10a). The balance of the co-polarizing flow of free MinE and the contra-polarizing flow of MinDE

complexes determines the steady state MinE profiles (see MinE nullclines in $(\rho_{\mathrm{E}}^1, m^1)$-phase space, Fig. 10b).

From the preceding analysis of pattern formation in two-component systems, we know that MinD polarized steady states are *scaffolded* by local equilibria. These equilibria are controlled by the local total density of MinD, whose (self-organized) lateral redistribution drives pattern formation. Because the effective local MinD dynamics are catalyzed by MinE (cf. Fig. 8a), MinE controls the reactive MinD dynamics locally. Specifically, the MinE total density profile $\rho_{\mathrm{E}}(x,\tau) \approx n_{\mathrm{E}} + \rho_{\mathrm{E}}^1(\tau)\cos(\pi x/L)$ controls the flux–turnover balance that maintains MinD polarity attractors (see Fig. 9a). While the MinD attractors are mirror symmetric for a uniform MinE distribution ($\rho_{\mathrm{E}}^1 = 0$), any (lateral) asymmetry in the MinE distribution breaks the symmetry between the two polarized MinD states. These two states are distinguished by their polarization relative to MinE, i.e. MinD can be co-polarized or counter-polarized with MinE. At critical MinE profile amplitudes $\pm\rho_{\mathrm{E}}^{1,\mathrm{crit}}$, MinD flux–turnover balance breaks down for the co-polarized MinD attractor, which vanishes in a (saddle node) bifurcation. At these *depolarization catastrophes* the MinD dynamics rapidly reorganizes into the respectively remaining counter-polarized attractor, i.e. the polarized MinD patter switches to the opposite pole. From there, MinE will start to co-polarize with MinD again and the cycle repeats itself thus constituting the essential pole-to-pole Min protein oscillation cycle shown in Fig. 10b. This oscillation cycle presents itself in its minimal, reduced form as a relaxation oscillator of MinD polarized steady states, controlled by redistribution of MinE mass. Hence, the lateral transport of (globally conserved) mass is found at the core of both (physically well defined) mechanisms — MinD polarity and control by MinE.

Strikingly, we find that the (self-organized) pattern forming mechanism underlying the oscillatory Turing instability of the skeleton model is not oscillatory: Oscillations are merely a consequence of the purely diffusive redistribution of the MinE total density, which passively follows the pattern forming process of MinD.

This relation of MinD driven polarization and oscillations due to control by MinE is also reflected in the structure of the dispersion relation. For $d_{\mathrm{E}} = 0$, there is no MinE redistribution, so the dispersion relation of the full system $\sigma(q)$ is given by the dispersion relation $\sigma_{\mathrm{D}}(q)$ of the effective MinD system alone. The right edge of the band of unstable modes $q_{\mathrm{max,D}}$ marks the onset of lateral instability in a confined system $L_{\mathrm{min,D}} = \pi/q_{\mathrm{max,D}}$. Because the effective MinD system is a mass-conserving two-component system, the eigenvalues in the band of unstable modes is purely real valued, in particular

$\mathrm{Im}[\sigma_{\mathrm{D}}(q_{\mathrm{max,D}})] = 0$. How does switching on slow MinE diffusion, $0 < d_{\mathrm{E}} \ll D_{\mathrm{d}}$, affect the dispersion relation? We performed a perturbation analysis of $\sigma(q)$ in the vicinity of $q_{\mathrm{max,D}}$ (see Supplementary Material). At the bifurcation point $q_{\mathrm{max,D}}$ we find

$$\sigma(q_{\mathrm{max,D}}) = \alpha \cdot \sqrt{-\delta_{\mathrm{E}} d_{\mathrm{E}}} + \mathcal{O}[d_{\mathrm{E}}/D_{\mathrm{d}}],$$

which implies that for $\delta_{\mathrm{E}} > 0$, the eigenvalue will become imaginary such that the onset dynamics become oscillatory with a frequency proportional to $\sqrt{\delta_{\mathrm{E}} d_{\mathrm{E}}}$. The pre-factor α is depends on the linearization Eqs. (30) and (33) encoding the cross-coupling between MinD and MinE dynamics.
In the vicinity of $q_{\mathrm{max,D}}$ we can write the dispersion relation as a perturbative expansion

$$\sigma(q) \approx \sigma_{\mathrm{D}}(q) + i\omega_{\mathrm{E}}, \tag{36}$$

$$\text{with } \omega_{\mathrm{E}} := \alpha\sqrt{\delta_{\mathrm{E}} d_{\mathrm{E}}} \tag{37}$$

illustrating that the dispersion relation can be split into a polarity term σ_{D} dependent on MinD redistribution and a control term $i\omega_{\mathrm{E}}$ dependent on MinD induced MinE redistribution. Using (36) the time evolution at onset has the form $\mathrm{e}^{\sigma_{\mathrm{D}} t}\cos(\omega_{\mathrm{E}} t)$ illustrating the respective roles of MinD and MinE in the dynamics.

DISCUSSION

In the introduction of this article we asked whether quantitative models for biochemical reaction–diffusion dynamics of proteins can be placed in a unifying framework revealing the general mechanisms underlying specific models. This would enable a classification of specific models by general mechanisms that follow from a systematic reduction of any reaction–diffusion system to a minimal functional core form.
A characterization of the general principles underlying the emergent dynamics of such a model based on the structure of its interaction network (motif) is not possible. Take the example of the skeleton model of Min protein dynamics: By changing the system parameters (kinetic rate constants, diffusion coefficients, system geometry, protein copy numbers) one encounters a broad range of phenomena *in vivo* (pole-to-pole oscillations, striped patterns, circular waves), and *in-vitro* (chemical turbulence, standing waves, travelling waves, spiral waves). Moreover, key characteristics of self-organized pattern formation such as multistability, geometry adaption, and intrinsic length scale selection can be turned

on and off by changing the parameters alone without altering the underlying interaction network (motif).

If not the motif, what does then encode the principal mechanism for pattern formation? Previous work revealed that pattern formation in mass-conserving reaction diffusion is based on shifting local equilibria by lateral diffusive transport of total density (*mass-redistribution framework*). In this article we further expanded this framework to extend the concept of *topological equivalence* to pattern forming systems. Two systems are topologically equivalent (and thereby members of the same mechanistic class) if their phases space flows can be continuously deformed into each other. The flow structure of a system's phase space is the most general characteristic of the system's dynamics. We found that the central geometric objects in phase space to characterize pattern formation are (i) the line of local equilibria (cf. control space [25]), (ii) the family of local (reactive) phase spaces, and (iii) the (diffusive) flux–balance subspace.

We found that this geometric characterization (in phase space) provides a fine grained classification of patterns and mechanisms, based on the shape of the kinetic nullcline. This classification takes into account the full phase space structure of the system far away from onset and supercriticality, and thereby goes beyond existing approaches based on Fourier modes and the shape of the dispersion relation (band of unstable modes). For stationary polarity patterns the geometrization reveals three distinct sub-classes based on regional properties (peaks, plateaus). Moreover, this approach reveals that the Turing instability and lateral excitability are two manifestations of the same (mass-redistribution) instability, further unifying pattern formation on a mechanistic level based on the shape of the line of local equilibria.

In in general terms the requirement for a mass-redistribution instability is an interaction network in which the (chemical) equilibrium density of the faster diffusing component decreases if the total density increases. This leads to a mass-redistribution cascade though cytosolic transport and a continual shifting of local equilibria that scaffold the pattern of the slowly diffusing component. In context of biological systems, the separation of diffusion coefficients is generic: membrane diffusion is typically orders of magnitude slower than cytosolic diffusion. Hence, any system based on membrane-cytosol cycling meets the basic requirements for pattern formation, and the only remaining (evolutionary) engineering task is the design of a protein-interaction network where cytosolic equilibrium densities decrease with increasing.

Form that perspective is not very surprising that our analysis of Min protein dynamics revealed that oscillatory Min protein patterns are based on the same

core mechanisms (mass-redistribution instability) as non-oscillatory models for cell polarity. The striking picture this analysis puts forward is that pattern formation in complex biochemical interactions networks can be understood by a decomposition into core mechanisms and control mechanisms. For pole-to-pole Min oscillations the core mechanism (MinD polarity by mass-redistribution instability) is controlled by diffusive MinE redistribution: the MinE total density profile *controls* the properties (shape, existence) of MinD polarity attractors. It would be very interesting to know if other multi-component multi-species pattern forming systems such as the CDC42 system in yeast [3], or the PAR system in *C. Elegans* [30] can be similarly decomposed into core and control modules.

In this article our analysis was focused on the core principle for pattern formation and the characteristic of polarity patterns. A main question in pattern formation theory is the selection of patterns, in particular the existence and selection of characteristic length scales. In the literature the term *Turing pattern* is closely tied to the existence of a characteristic length scale that is determined by the fastest growing mode. For systems close to a supercritical bifurcation the existence of a characteristic length scale is a given. However, in general the fastest growing mode does not determine the length scale of the pattern. Moreover, the coexistence of many stable patterns with different length scales is not uncommon [17, 31, 32]. The mechanistic origins of such multistability phenomena and pattern selection in general are still widely unclear for systems that are not in the vicinity of supercritical bifurcations (i.e. cannot be analyzed by amplitude equations, cf. Introduction). Expanding the toolset of the mass-redistribution framework to tackle these questions will be an interesting task down the road.

The main concept underlying the mass-redistribution framework is spatial compartmentalization followed by a phase space analysis of spatially isolated structures. We started the analysis with local equilibria of well-mixed compartments. Here we extended it to characteristic *regions* of patterns (interface, peak, and plateau). This decomposition was essential for the systematic analysis of pattern formation. As a next step it would interesting to naturally extend this conceptual approach to decompose patterns with multiple interfaces (finite wavelength) into elementary sections that represent polarized patterns considered in this article, and study the lateral coupling between these elementary sections to address questions such as coarsening, wave-length selection, multistability, and their relation to the band of unstable modes.

FIGURES

Figure 1

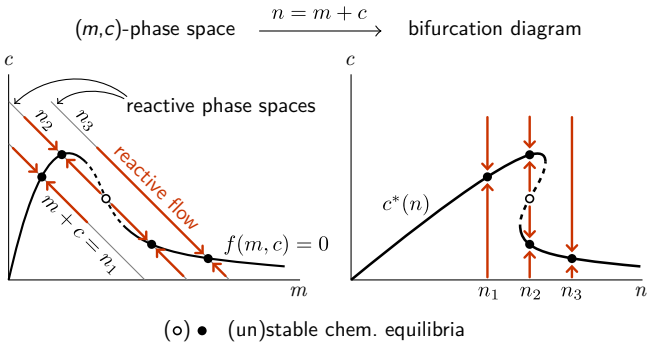

FIG. 1. The total density is a control parameter of mass-conserving reactions. The properties (number, position, and stability) of chemical equilibria depend on the total density (mass) in a well-mixed reactor.

(a) The conservation law is geometrically represented by 1-simplexes in phase space — each value of the total density corresponds to a unique 1-simplex. We will call these subspaces reactive phase spaces (local phases spaces in context of spatially extended systems). Kinetic interactions interconvert the conformal states of the proteins and hence change the densities of the components representing these conformal states. The changes in densities give rise to a flow in phase space which, due to mass conservation, is confined to the reactive phase space (1-simplex). Along the line of chemical equilibria the flow vanishes $f(m, c) = 0$. **(b)** Intersections of reactive phase spaces and the line of chemical equilibria allow us to read off the chemical equilibria in dependence of the total density n and plot the respective bifurcation diagram.

Figure 2

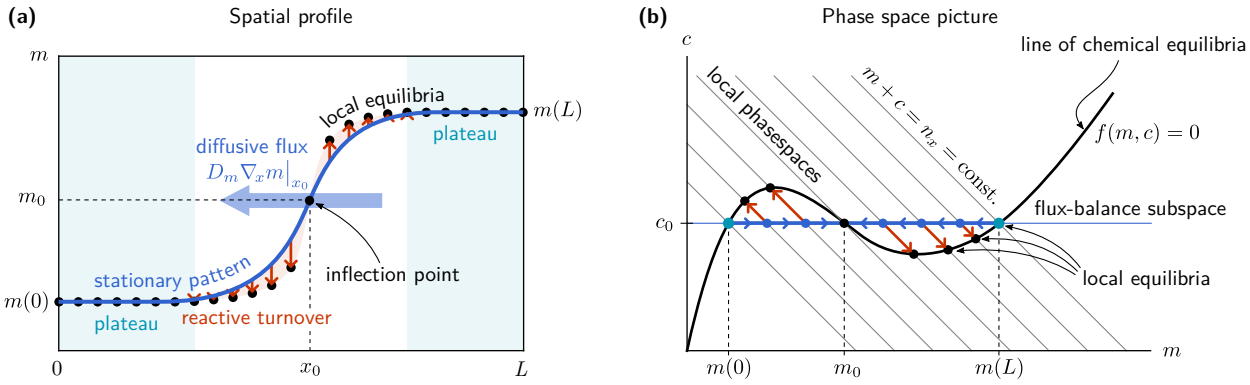

FIG. 2. Polarized states are determined by flux–turnover balance.

(a) Local chemical equilibria (black dots) scaffold the pattern profile due to the local reactive flow towards the local equilibria (red arrows). At x_0 the pattern intersects the kinetic nullcline $f(m(x_0), c_0) = 0$. In a steady state, the diffusive flux across the inflection point blue arrow exactly cancels the cumulative reactive turnover on either side of the inflection point (indicated by red shaded areas). (Remark: The parameters were chosen to exaggerate the local deviation from the local equilibria for visualization). **(b)** Plotting the distribution of the pattern (blue line) in phase space shows how mass redistribution shifts the local equilibria, giving rise to the pattern. The local reactive dynamics (red arrows) are restricted to the local phase spaces where total density is conserved locally. The intersections of the local phase spaces with the kinetic nullcline $f(m, c) = 0$ yields the local equilibria. Fast cytosolic diffusion restricts the stationary pattern to a line of nearly constant cytosolic concentration c_0 (flux balance subspace). Slow membrane diffusion (blue arrows) balances the reactive dynamics spreading the pattern.

Figure 3

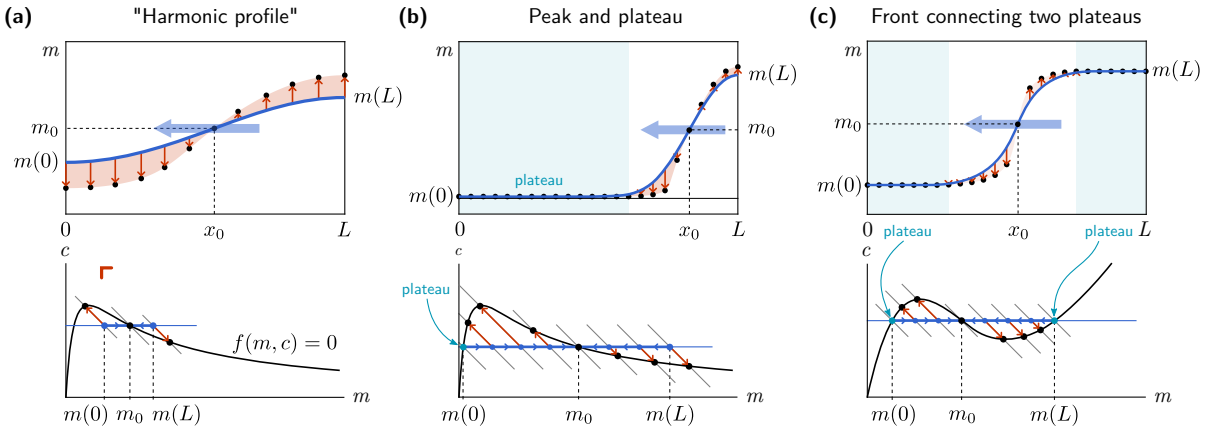

FIG. 3. Three possible types of polarized patterns, classified by the number of plateaus. Since the plateaus reveal themselves as intersections of flux-balance subspace and kinetic nullcline (in regions with positive slope) in phase space, the shape of the kinetic nullcline together with the ratio of diffusion constants (flux–balance subspace) determine the characteristic pattern type of a given two-component system.

(a) The harmonic profile type only occurs in short systems where the reactive turnover is balanced by the linearly growing diffusive flux at small amplitude (before any plateau is reached). **(b)** A peak connected to a single plateau forms when a local equilibrium is reached on one side of the inflection point. At this equilibrium, the flow vanishes so the turnover is bounded, which in turn determines the peak amplitude on the other side. **(c)** When local equilibria limit further amplitude growth on both sides of the inflection point two plateaus form. (Note that the number of arrows shown does not have a deeper meaning but is chosen for visualization purposes alone.)

Figure 4

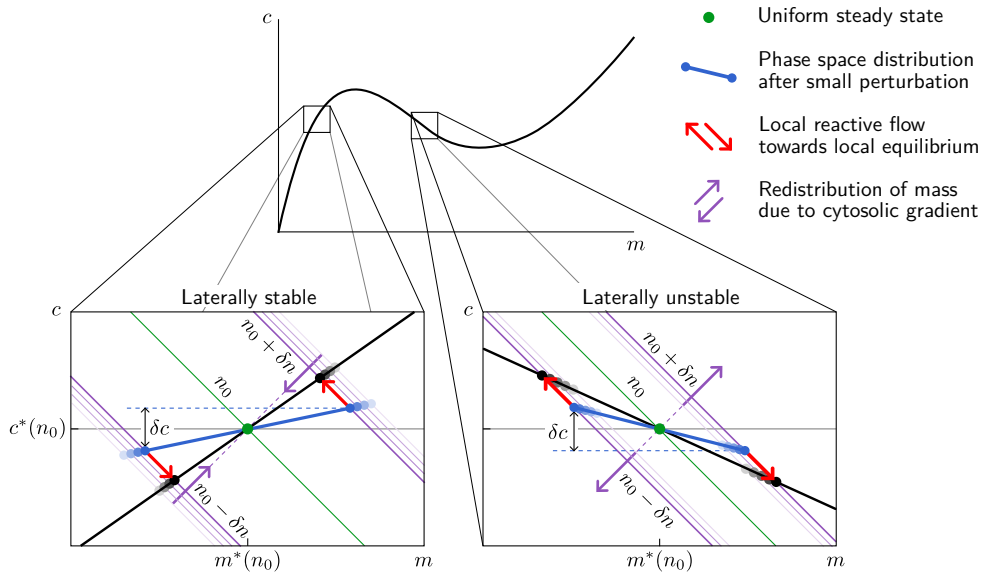

FIG. 4. Lateral (in-)stability is determined by the slope of the nullcline (black line). Consider a small perturbation of the uniform steady state $(m^*(n_0), c^*(n_0))$ (blue line) that redistributes mass $n_0 \pm \delta n$ and thereby shifts the local equilibria (black dots). The local reactive flow in the shifted local phase spaces (purple lines) drive the system locally towards these shifted equilibria (illustrated by red arrows). This, in turn, builds up a cytosolic gradient δc. Diffusive flow in the cytosol acts to remove this gradient by redistributing mass in the direction of the cytosolic gradient. If the slope of the nullcline is positive (bottom left), the cytosolic mass redistribution removes the gradient in total density δn (purple arrows), and both gradients (δc and δn) vanish as the system approaches n_0. In that case the system is laterally stable. If the slope of the nullcline is negative (bottom right), cytosolic densities are redistributed in the opposite directions, such that the total density gradient δn increases (purple arrows). This shifts the local equilibria away from the uniform steady state and thereby maintains a finite the cytosolic gradient. This cascade of shifting local phase spaces (mass redistribution) and a maintained cytosolic gradient drives lateral instability.

Figure 5

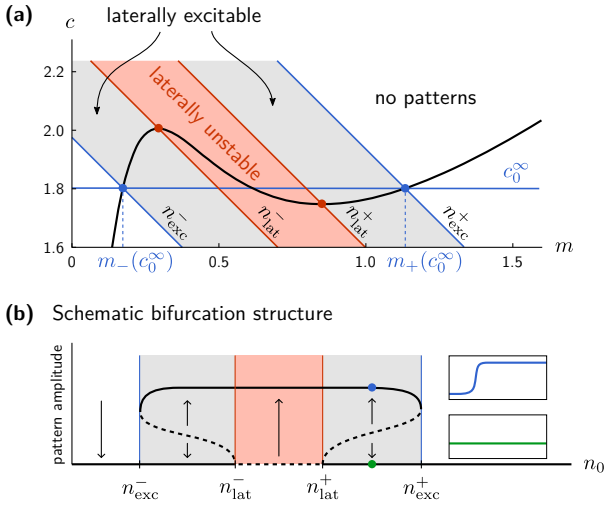

FIG. 5. Bifurcations of plateau patterns reveal themselves from the geometric properties of the line of chemical equilibria.

(a) Given some local kinetic interactions $f(m, c)$ (here shown for the "wave–pinning" model [23] and the diffusion constants (here $D_m = 0.01\,\mu\mathrm{m}^2\mathrm{s}^{-1}$ and $D_c = 0\,\mu\mathrm{m}^2\mathrm{s}^{-1}$ one can simply calculate the line of chemical equilibria $f(m, c) = 0$ (black line) and the position of the flux-balance subspace c_0^∞, determined by global turnover balance Eq. (18). These two geometric objects can then be used to obtain the properties and bifurcations of the plateau patterns: The uniform steady state is laterally unstable where the slope of the kinetic nullcline is smaller than the slope of the flux balance subspace $-D_m/D_c$ (red shaded area). The range of pattern existence extends beyond the range of lateral instability and is bounded by the total densities of the plateaus (Eq. (19)). These are determined by the intersections of the flux-balance subspace with the line of chemical equilibria (blue dots). **(b)** Schematic bifurcation structure (subcritical) of plateau patterns geometrically constructed from the the line of local equilibria and the flux-balance subspace we can construct.

Figure 6

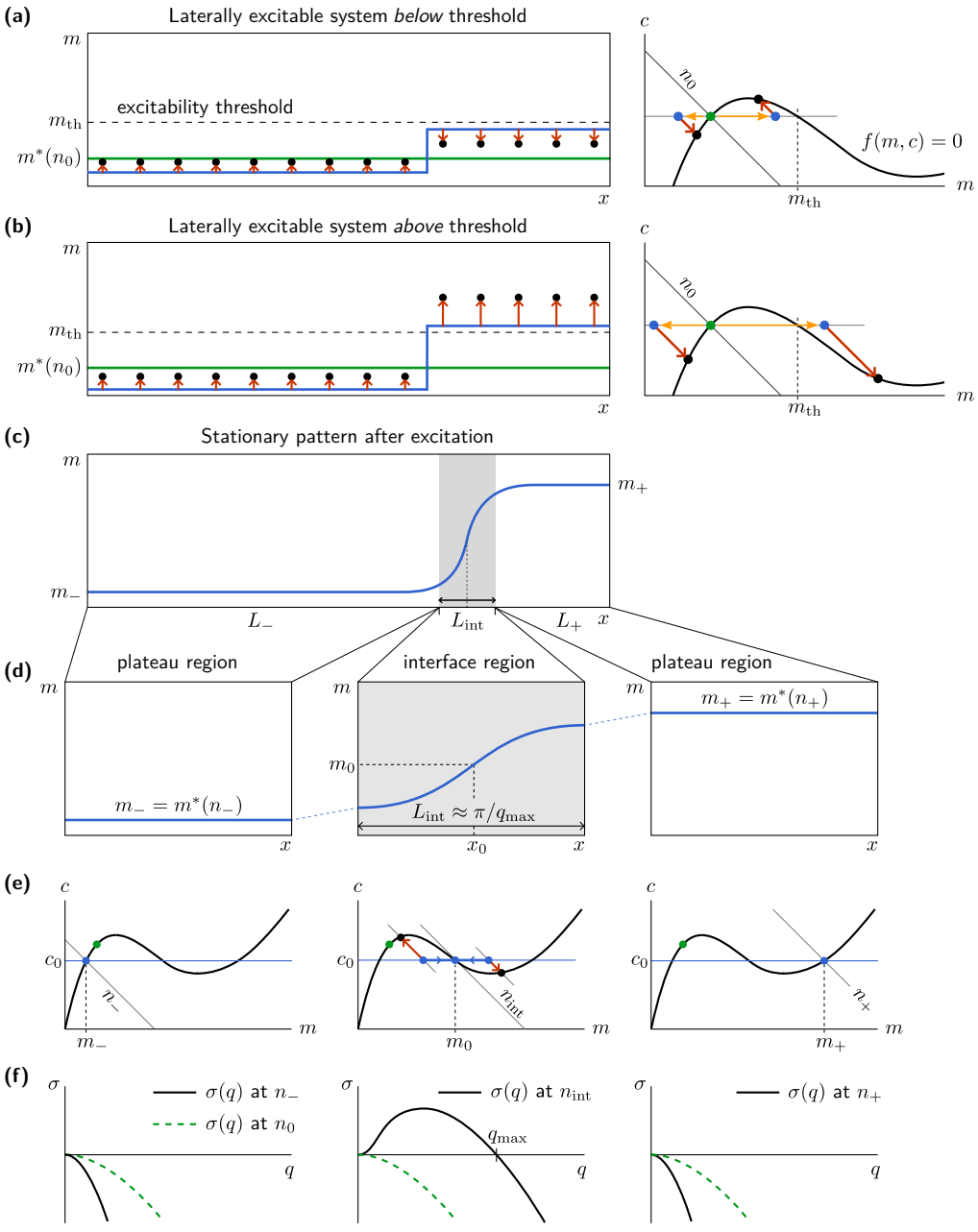

FIG. 6. Subcritical stationary patterns emerge from lateral excitability.

(a) After a small small perturbation (blue profile, yellow arrows in phase space), a laterally stable system returns to its uniform steady state (green

line). The high density region in the perturbation is below the threshold where the direction of reactive flow in (m, c)-phase space changes direction and thereby induces the cascade of lateral mass redistribution, i.e. a regional lateral instability. **(b)** A perturbation above that threshold induces to the mass-redistribution cascade (regional lateral instability) and the dynamics approach the polarized state (lateral excitability). Geometrically, the threshold can be read off the nullcline (intersection of the uniform cytosolic density with the kinetic nullcline). **(c)** The polarized pattern can be decomposed into three regions: two plateaus and a diffusive interface (shaded in gray) around the inflection point x_0. **(d)** We isolate these regions by imposing no-flux boundary conditions such that the dynamics in each of the regions approaches its regional attractor. **(e)** The local phase spaces corresponding to the respective average total densities (n_-, n_{int}, and n_+) in each region reveal the lateral stability properties of the regions. The plateaus are laterally stable regions — anti-coarsening is not possible. On the other hand, the interface region is always laterally unstable, even if the global system (uniform state n_0) is laterally stable. **(f)** Because the diffusive interface is spanned by lateral instability, we its properties can be estimated from the dispersion relation at n_{int}. In particular, the interface width L_{int} can be estimated by the rightmost root $q_{\max}$ of the dispersion relation: $L_{\text{int}} \approx \pi/q_{\max}$. The dashed lines show the dispersion relation for the spatially uniform state of the global system determined by n_0 (laterally stable).

Figure 7

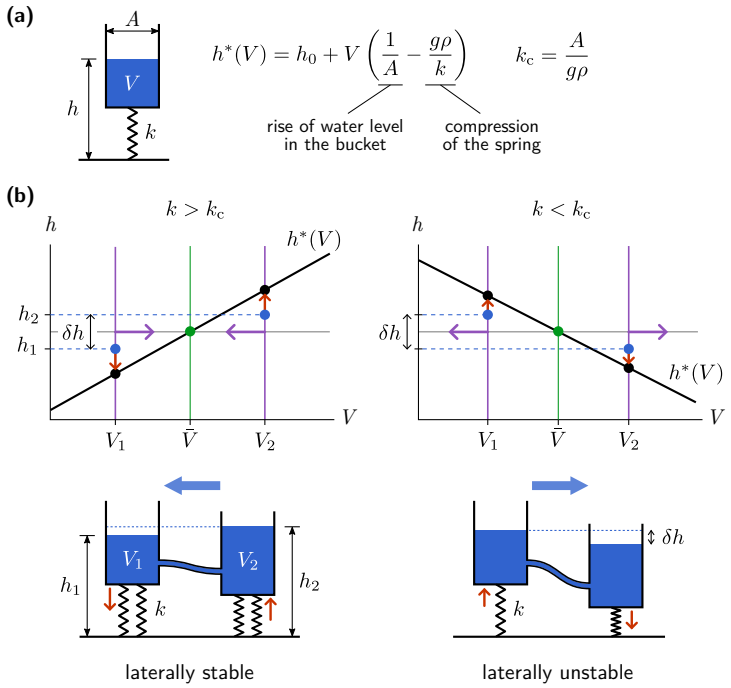

FIG. 7. A simple mechanical system exhibiting the key features necessary for a mass-redistribution instability.

(a) The (mechanical) equilibrium position of the water level h in a bucket with cross section area A, resting on an overdamped spring with spring constant k can either increase or decrease when water is added to the bucket. It increases when the the water level in the bucket V/A raises faster than the spring is compressed due to the added mass. When the spring is sufficiently soft, it will be compressed more than the water level in the bucket rises such that the water level measured from the ground will decrease. **(b)** The V-axis is the control space of the mechanical system. Plotting the equilibrium position $h^*(V)$ of the water level yields a line of equilibria that has positive (left) or negative (right) slope depending on the spring constant. Consider a system of two identical buckets connected by a thin tube, and perturbed by moving a small amount of water from one bucket to the other. Due to the shifting (mechanical) equilibrium positions of the buckets, a gradient in hydrostatic pressure $\sim \delta h$, is built up (red arrows). The phase spaces of each bucket (purple lines) shift (purple arrows) as water flows through the pipe to remove this gradient in

hydrostatic pressure. The slope of the line of equilibria determines whether the flow through the pipe induced by this gradient drives the system back to a uniform state or further away from it, analogously to the chemical system (cf. Fig. 4). For $k < k_c$, where the equilibrium position shifts downwards as the volume increases, the system is destabilized by a mass-redistribution instability, driven by water flow acting to equilibrate the water levels h_1 and h_2. Note that the chemical analog to the (V, h)-space is the (n, c)-space which is related to the (m, c)-phase space via the simple transformation $n = m + c$.

Figure 8

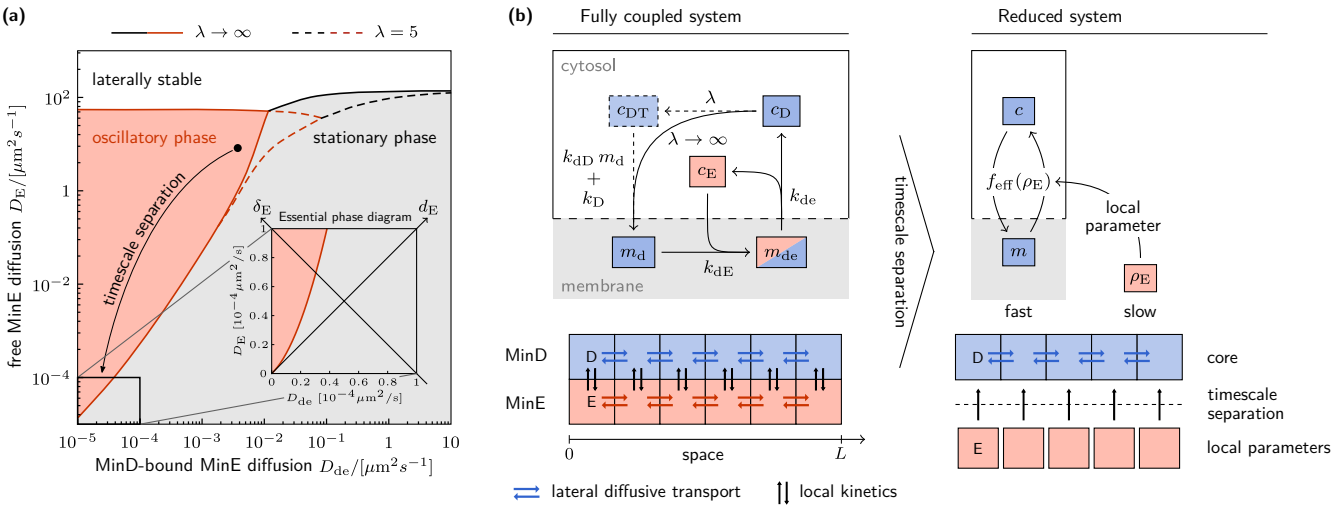

FIG. 8. Application of the mass-redistribution framework to applied to the Min system of *E. Coli*.

(a) We calculate linear stability of uniform steady states of the skeleton Min model under variation of the MinE diffusion constants. The structure of resulting diagram of linear stability phases extends smoothy to arbitrarily small diffusion of MinE. The transition between stationary and oscillatory behavior essentially depends on the relative dominance of the diffusion of free and MinD-bound MinE. We introduce the variables d_E and δ_E to encode the timescale separation and relative diffusive dominance (see inset). The phase diagram also shows that a finite nucleotide exchange rate does not change lateral stability significantly. **(b)** Lateral transport of conserved quantities is the essential dynamics in the mass-redistribution framework. In the Min system, there are two conserved quantities: the total densities of MinD and MinE, illustrated by the blue and red compartments. The structure of linear stability phases (cf. (a)) motivates us to set MinE transport on a slower timescale, $\tau = (d_E/L^2)\,t$, such that on the fast timescale only MinD mass is redistributed between compartments (reduced system on the right). This allows us to treat the local total MinE density as a local parameter on the fast timescale. here, we consider dynamics in the limit $\lambda \to \infty$, cf. (a), reducing the fast MinD dynamics to a two–component core system (m_d, c_D) for membrane-bound m_d and cytosolic c_D MinD.

Figure 9

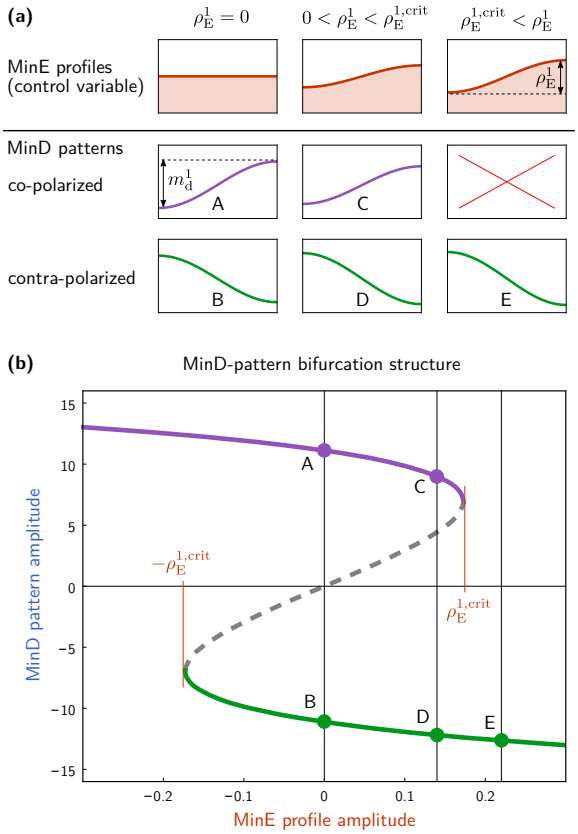

FIG. 9.

(a) Overview of the stationary MinD profiles controlled by the total density profile of MinE. The co-polarized state vanishes if the amplitude of the MinE profile exceeds a certain threshold $\rho_E^{1,crit}$. **(b)** Bifurcation structure of the MinD pattern amplitude with the MinE amplitude $\rho_E^1 > 0$ as parameter. For a uniform MinE profile ($\rho_E^1 = 0$), there are two mirror symmetric MinD attractors (A, B). Shifting the MinE density towards one of the poles $\rho_E^1 \neq 0$ breaks the mirror symmetry of the MinD attractors (C, D). When the MinE amplitude ρ_E^1 exceeds the critical amplitude $\pm\rho_E^{1,crit}$, the co-polarized MinD state vanishes in a (saddle-node) bifurcation because flux–turnover balance breaks down. Only the contra-polarized state (E) remains such that MinD polarity switches to the opposite pole.

Figure 10

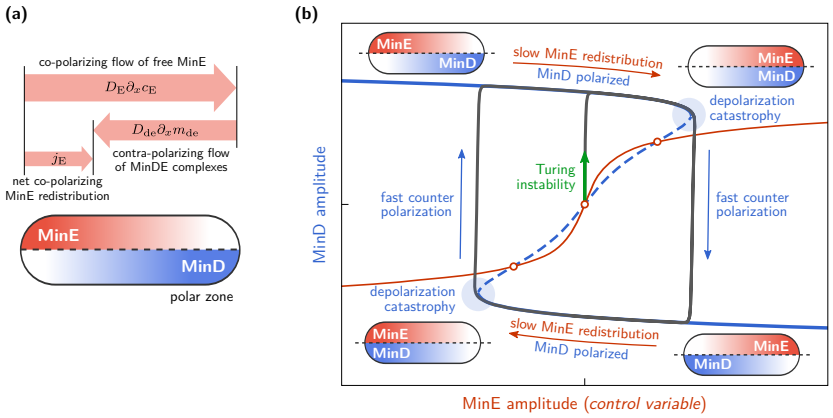

FIG. 10. The nonuniform MinD distribution (steady state of the fast polarization dynamics) induces diffusive fluxes of MinE.

(a) Visualization of the MinE flows: cytosolic MinE is recruited by MinD in the polar zone resulting in formation of MinDE complexes. This drives a flow of free MinE towards the polar zone (co-polarizing flow). The MinDE complexes diffusive out of the polar zone and respectively generate a MinE flow away from the polar zone (contra-polarizing flow). The sum of both flows determines the total MinE flow $j_E(\rho_E^1, m_d^1)$ for a given MinD and MinE density profiles (cf. Eq. (33)). **(b)** For the physiological parameter configuration of the wild type system (*in vivo* skeleton model) the MinE dynamics are intrinsically co-polarizing ($\delta_E \gg 0$) and oscillations are generically observed. In the phase space of the amplitudes, the Min oscillation cycle is revealed as a relaxation oscillator of the MinD polarization direction controlled by MinE redistribution. Out of the Turing unstable homogenous steady state(mass-redistribution instability), MinD rapidly polarizes and reaches a steady state. The nonuniform MinD distribution induces a MinE flux on the slow timescale. While MinE slowly redistributes, MinD stays slaved to its polarized steady state. The system moves along the branch of MinD steady states. When the MinE amplitude reaches a critical value, the co-polarized MinD steady state gets annihilated in a saddle-node bifurcation (depolarization catastrophe). The MinD pattern rapidly switches to the counter-polarized state. The MinE dynamics again drive the system towards the co-polarized states, eventually inducing another depolarization catastrophe. The ongoing repetition of this cycle constitutes the principal mechanism underlying pole-to-pole oscillations.

* frey@lmu.de

[1] D. M. Raskin and P. a. de Boer, Proceedings of the National Academy of Sciences of the United States of America **96**, 4971 (1999).

[2] L. Rothfield, A. Taghbalout, and Y.-L. Shih, Nature reviews. Microbiology **3**, 959 (2005).

[3] L. Merlini, O. Dudin, and S. G. Martin, Open biology **3**, 130008 (2013).

[4] S. Kretschmer and P. Schwille, Current Opinion in Cell Biology **38**, 52 (2016).

[5] P. Bourgine and A. Lesne, *Morphogenesis : origins of patterns and shapes* (Springer, 2011).

[6] B. Kazmierczak and D. Hendrixson, Molecular microbiology **88**, 655 (2013).

[7] M. Cross and P. Hohenberg, Reviews of modern physics **65** (1993).

[8] M. Cross and H. Greenside, *Pattern Formation and Dynamics in Nonequilibrium Systems* (Cambridge University Press, 2009).

[9] A. Gierer and H. Meinhardt, Kybernetik **12**, 30 (1972).

[10] V. García-Morales and K. Krischer, Contemporary Physics , 37 (2012).

[11] A. M. Turing, Philosophical Transactions of the Royal Society of London. Series B, Biological Sciences **237**, 37 (1952).

[12] L. a. Segel and J. L. Jackson, Journal of theoretical biology **37**, 545 (1972).

[13] S. Kondo and T. Miura, Science (New York, N.Y.) **329**, 1616 (2010).

[14] U. Alon, *An Introduction to Systems Biology* (Chapman & Hall, 2007).

[15] J. Halatek and E. Frey, Cell reports **1**, 741 (2012).

[16] F. Wu, B. G. C. van Schie, J. E. Keymer, and C. Dekker, Nature Nanotechnology (2015).

[17] F. Wu, J. Halatek, M. Reiter, E. Kingma, E. Frey, and C. Dekker, Molecular Systems Biology **12**, 642 (2016).

[18] A. B. Goryachev and M. Leda, Molecular Biology of the Cell **28**, 370 (2017).

[19] P. K. Trong, E. M. Nicola, N. W. Goehring, K. V. Kumar, and S. W. Grill, New Journal of Physics **16** (2014).

[20] H. Poincaré, Journal de Mathématiques Pures et Appliquées (1881).

[21] S. H. Strogatz, *Westview Press* (1994).

[22] E. M. Izhikevich, *Dynamical Systems in Neuroscience* (MIT Press, 2007).

[23] Y. Mori, A. Jilkine, and L. Edelstein-Keshet, Biophysical journal **94**, 3684 (2008).

[24] Y. Mori, A. Jilkine, and L. Edelstein-Keshet, SIAM Journal on Applied Mathematics **71**, 1401 (2011).

[25] J. Halatek and E. Frey, "Rethinking pattern formation in reaction-diffusion systems," (2017).

[26] J. Lutkenhaus, Annual review of biochemistry **76**, 539 (2007).

[27] T. Kolokolnikov, M. Ward, and J. Wei, Physica D: Nonlinear Phenomena **236**, 104 (2007).

[28] K. C. Huang, Y. Meir, and N. S. Wingreen, Proceedings of the National Academy of Sciences of the United States of America **100**, 12724 (2003).

[29] J. Halatek and E. Frey, Proceedings of the National Academy of Sciences **111** (2014), 10.1073/pnas.1220971111.

[30] N. W. Goehring, P. K. Trong, J. S. Bois, D. Chowdhury, E. M. Nicola, A. A. Hyman, and S. W. Grill, Science **334**, 1137 (2011), arXiv:arXiv:1011.1669v3.

[31] D. Iron, J. Wei, and M. Winter, Journal of Mathematical Biology **49**, 358 (2004).

[32] T. Kolokolnikov, M. J. Ward, and J. Wei, Studies in Applied Mathematics **115**, 21 (2005).

Supplementary Material

for

"From quantitative models to geometrization of pattern formation mechanisms"

Fridtjof Brauns†, Jacob HalatekBrauns†, Erwin Frey

---

1 2-Component system

1.1 Classical linear stability analysis

Linear stability analysis of spatially extended systems is performed by expanding a spatial perturbation in the eigenbasis of the diffusion operator (Laplacian) in the geometry of the system. In a line geometry with reflective boundary conditions at $x = 0, L$, the eigenfunctions are the discrete symmetric Fourier modes $\cos(n\pi x/L)$ with $n \in \mathbb{N}$. Linearization of the dynamics of a mass-conserving two-component system around a uniform steady state (m^*, c^*) yields the linear dynamics

$$\partial_t \begin{pmatrix} \delta m_q(t) \\ \delta c_q(t) \end{pmatrix} = J(q) \begin{pmatrix} \delta m_q(t) \\ \delta c_q(t) \end{pmatrix} \tag{1}$$

with the so called Jacobian

$$J(q) = \begin{pmatrix} -D_m q_n^2 + f_m & f_c \\ -f_m & -D_c q_n^2 - f_c \end{pmatrix}, \tag{2}$$

where we use the usual abbreviations $q_k = k\pi/L$ for the wavenumbers and $f_{m,c} = \partial_{m,c} f\big|_{(m^*,c^*)}$ for the linearized kinetics at the uniform steady state. The eigenvalues of the Jacobian yield the growth rates $\sigma_q^{(i)}$ of the respective eigenmodes such that a perturbation in the spatial eigenfunction $\cos(qx)$ evolves in time as

$$\begin{pmatrix} \delta m_q(t) \\ \delta c_q(t) \end{pmatrix} = \sum_{i=1,2} A_q^{(i)}\, \mathbf{e}_q^{(i)} \exp(\sigma_q^{(i)} t) \cos(qx), \tag{3}$$

with the eigenvectors $\mathbf{e}_q^{(i)}$ and the coefficients $A_q^{(i)}$ determined by projecting the initial condition into the eigenbasis $\mathbf{e}_q^{(i)} \cos(qx)$.

For every wavenumber q the Jacobian $J(q)$ has to eigenvalues (and associated eigenvectors), so the dispersion relation has two branches, as shown in Supp. Fig. 1. Only the fastest growing mode with the largest $\mathrm{Re}\,\sigma(q)$ is relevant for the dynamics since it exponentially outgrows slower modes. Special care has to be taken at the point $q = 0$ corresponding to a spatially uniform perturbation. The eigenvalues there are

$$\sigma_0^{(1)} = 0 \text{ and } \sigma_0^{(2)} = f_c - f_m. \tag{4}$$

with the respective eigenvectors

$$\mathbf{e}_0^{(1)} = (f_c, -f_m)^T \text{ and } \mathbf{e}_0^{(2)} = (1, -1)^T. \tag{5}$$

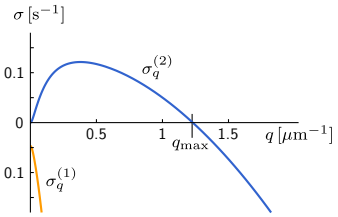

SUPP. FIG. 1. Typical dispersion relation of a mass-conserving two-component system in the laterally unstable regime.

Hence marginal perturbation breaks mass-conservation and moves the local equilibrium along the kinetic nullcline. Only the second eigenvalue $\sigma_0^{(i)}$ represents the stability of the an isolated local equilibrium within its local phase space where mass-conservation is fulfilled.

1.2 Linear stability analysis of mass-redistribution dynamics

In the main text we discussed the core processes underlying lateral instability: shifting local equilibria and mass redistribution due to cytosolic gradients. We now want to systematize this conceptual picture in mathematical framework of linear stability analysis. The natural choice of variables to study lateral instability in a mass conserving system are the local total density $n_x(t)$ shifting the local equilibria and $c(x,t)$ the fast diffusing species diffusively redistributing mass. Starting with the usual linearized dynamics Eq. (1), we add the second to the first row and to obtain the dynamics of the total density perturbation $\delta n_q(t) = m_q(t) + c_q(t)$. The respective *control space* Jacobian then reads

$$\tilde{J}(q) = \begin{pmatrix} -D_m q^2 & (D_m - D_c)q^2 \\ -f_m & -D_c q^2 - f_c \end{pmatrix}. \tag{6}$$

The first row of this Jacobian represents diffusive redistribution of total density, and thus the dynamics in control space.

To put the reactive dynamics into the context of shifting local equilibria, consider an alternative linearization of $f(m,c)$ in the vicinity of the equilibrium $\big(m^*(n), c^*(n)\big)$:

$$f(m,c) \approx \sigma_0(n) \cdot \big(m - m^*(n)\big) = \sigma_0(n) \cdot \big(c - c^*(n)\big), \tag{7}$$

where the eigenvalue of the equilibrium $\sigma_0(n) = f_c - f_m$ simply tells us how fast the local densities relax towards it. Because we study a small perturbation of uniform steady state, we also need to linearize this equation in the total density $n(x) = n_0 + \delta n(x,t)$. We obtain

$$f(n_0 + \delta n, c^* + \delta c) \approx \sigma_0(n_0) \cdot \big(\delta c - \delta n \gamma\big), \tag{8}$$

where $\gamma := \partial_n c^*|_{n_0}$ denotes the slope of the line of chemical equilibria in control space. Using this linearization we obtain the Jacobian

$$\tilde{J}(q) = \begin{pmatrix} -D_m q^2 & (D_m - D_c)q^2 \\ -\sigma_0 \gamma & -D_c q^2 + \sigma_0 \end{pmatrix}, \tag{9}$$

which is identical to Eq. (6) because $-\sigma_0\gamma = f_m$ as a straightforward calculation shows.

If the dispersion relation of a mass-conserving two-component system has a band of unstable modes, this band will always extend down to $q \to 0$. The derivative of the dispersion relation $\partial_{q^2}\sigma_q|_{q=0}$ is thus necessarily positive if there is a band of unstable modes. A simple calculation using shows

$$\partial_{q^2}\sigma_q|_{q=0} = -D_m\partial_n m^* - D_c\partial_n c^*,$$

where we used $\partial_n m^* + \partial_n c^* = 1$. The geometric criterion for onset of mass-redistribution is therefore

$$D_m\partial_n m^* + D_c\partial_n c^* < 0,$$

which is equivalent to

$$\partial_m c^* < -D_m/D_c \tag{10}$$

using the slope of the kinetic nullcline in (m, c)-phase space $\partial_m c^* = \partial_n c^*/\partial_n m^*$.

The control space representation of the reaction-diffusion system also allows us to geometrically construct the linearized flow field in control space, which is mathematically represented by the Jacobian (1.2) (see Supp. Fig. 2).

Moreover, the generalization to other physical systems is possible on the control space level. In the main text we presented the buckets-on-springs system, where the conserved quantity is the water volume, while redistribution is driven by height differences.

1.3 Flux-balance coordinate frame

As we established in the main text, every stationary pattern lies in a flux-balance subspace,

$$\widetilde{c}(x) - D_m/D_c\widetilde{m}(x) = \eta_0 \tag{11}$$

where the intercept η_0 is determined by a balance of reactive turnovers on both sides of the interface. The geometric relation between the flux-balance subspace and the kinetic nullcline $f(m, c) = 0$ underlies lateral instability, pattern properties and bifurcations. In the main text these relations are derived and illustrated in the limit $D_m \ll D_c$ where the

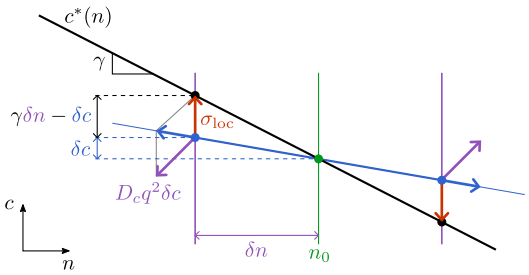

SUPP. FIG. 2. Using the kinetic nullcline in control space, we can construct the vector field generated by local reactive flow and diffusive flux which encodes lateral instability. The red arrow represents the local reactive flow towards the local equilibrium (black dot) on the line of local equilibria $c^*(n)$. This flow vector it only points in c-direction, i.e. does not change local total density. The purple arrow represents the diffusive flux due to the diffusive gradient $q^2\delta_c$. It is diagonal since the flux redistributes total density via transport of cytosolic density. The actual flow of the system is given by the sum of the reactive flow and the diffusive flux, represented by the blue arrow. This reaction-diffusion flow drives the dynamics in control space, spanning the control space distribution of the spatially extended system (blue line).

flux-balance subspace can be approximated by $c = c_0 = \text{const.}$. These results fully extend to arbitrary diffusion constants as we will show in the following.

We introduce new coordinates in (m, c)-phase space parametrizing the flux-balance subspace ϕ and its orthogonal complement η:

$$\phi = m + D_m/D_c\, c,\ \eta = c - D_m/D_c\, m. \tag{12}$$

In these coordinates, any flux-balance subspace is a line of constant η, such that the spatial structure of a stationary pattern is contained in $phi(x)$ alone. All results in the main text were derived in the limit $D_m \ll D_c$ where $\phi(x) \approx m(x)$ and $c(x) \approx c_0 = \eta_0$ such that the flux-balance subspace could be approximated to be a line of constant $c = c_0$ in (m, c)-phase space. Using (ϕ, η)-coordinates these results turn out to hold strictly for any ratio of diffusion constants. We just need to transform the kinetic nullcline $f(m, c) = 0$ into (ϕ, η)-coordinates. To that end we need the inverse transformation of (12) which read

$$m(\phi, \eta) = \frac{\phi - D\eta}{1 + D^2},\ c(\phi, \eta) = \frac{D\phi - \eta}{1 + D^2}, \tag{13}$$

where we introduced the relative unitless diffusion constant $D = D_m/D_c$.

Applying (12) and (13) we obtain

$$\tilde{f}(\phi,\eta) = f\big(m(\phi,\eta), c(\phi,\eta)\big) = f\left(\frac{\phi - D\eta}{1+D^2}, \frac{D\phi - \eta}{1+D^2}\right). \qquad (14)$$

Transforming the geometric criterion for lateral instability Eq. (10) yields the simple form

$$\partial_\phi \eta^*(\phi)\big|_{\phi^*} < 0.$$

1.4 Lateral excitability

What is the basin of attraction of plateau patterns in the subcritical regime, i.e. for $n^-_{\text{exc}} < n_0 < n^-_{\text{lat}}$ or $n^+_{\text{lat}} < n_0 < n^+_{\text{exc}}$ (cf. Fig. 5 in the main text)? We motivated a simple geometric criterion for the excitability threshold: the part of the kinetic nullcline with negative slope marks a threshold in (m, c)-phase space (cf. Fig. 6 in the main text). When a part of the system is shifted beyond this threshold (whereas the rest of the system has to shift in opposite direction due to mass conservation), the flow in phase space will increase the amplitude of the perturbation. If the reactive turnover due to the growing perturbation dominates over the cytosolic flux, the system will make an excursion and end up in a stationary pattern. Consider a perturbation where a "block" of membrane density is moved from the region $0 < x < L - w$ into the region $L - w < x < L$ via a step function perturbation (see Supp. Fig. 3a). Mass conservation relates the amplitude of the step function on the left a, with the amplitude on the right $a\frac{L-w}{w}$. The maximal amplitude of the perturbation on the left is limited by the uniform steady state, $a < \overline{m} = m^*(n_0)$. For such a perturbation, our simple geometric criterion predicts the excitability threshold to be

$$a_{\text{th}}(L - w)/w = m_{\text{th}}(n_0) \qquad (15)$$

where the amplitude on the right is equals the threshold $m_{\text{th}}(n_0)$ which is determined by the intersection with the kinetic nullcline (cf. Fig. 6 in the main text). Below the threshold, the system quickly returns to the uniform steady state. Above it, mass-redistribution drives the system further away from the uniform state and into a stationary pattern.

1.5 The "wave–pinning model"

In [3] Mori et al. introduce a model for cell polarity, which effectively describes proteins of a single species, that can cycle between membrane

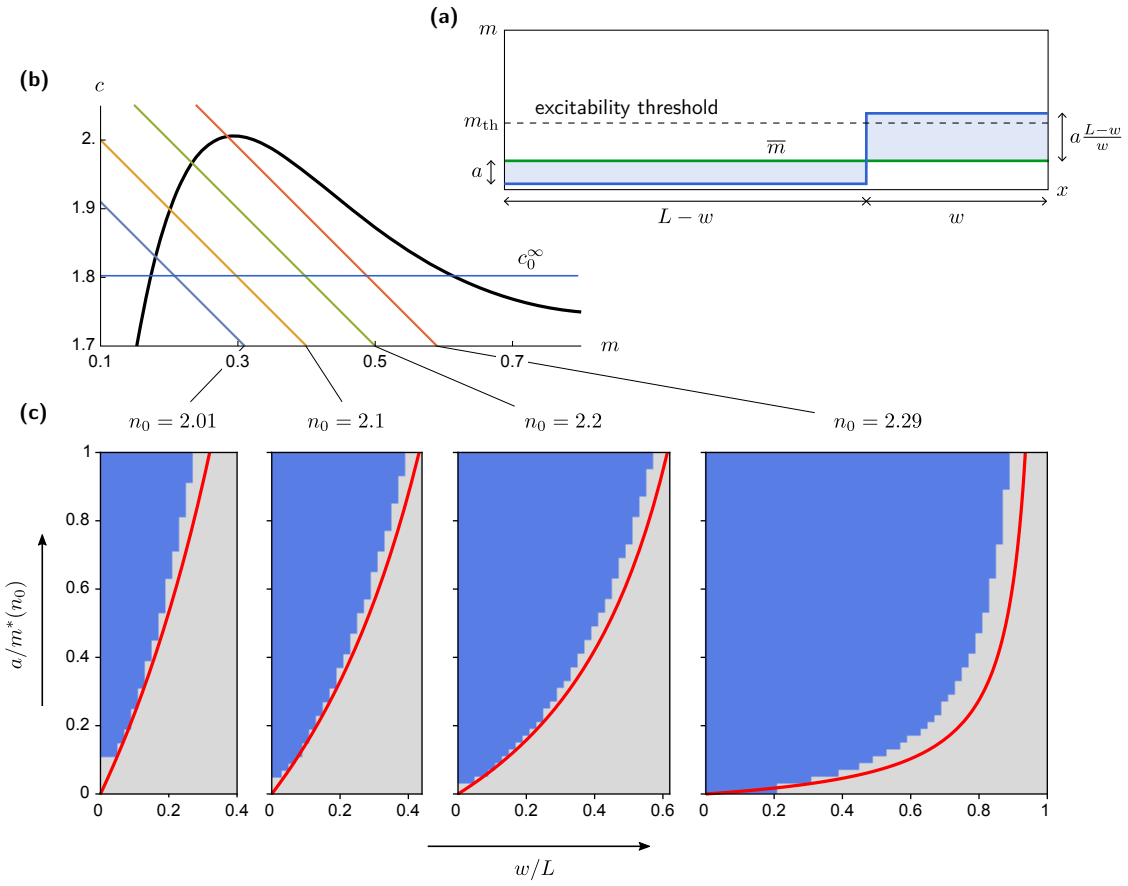

SUPP. FIG. 3. A simple geometric criterion predicts the excitability threshold of subcritical patterns. **(a)** We consider a simple step perturbation of a uniform steady state $\overline{m}$ that moves mass from the region $x < L - w$ into the region $x > L - w$. The perturbation amplitude on the left side of the step is determined (via mass conservation) by the perturbation amplitude a on the right which can be freely chosen in the range $0 < a < \overline{m}$. **(b,c)** To find the basins of attraction numerically, we ran simulations of the wave-pinning model initially perturbed as shown in (a) for different total densities and for different perturbation profiles, parametrized by w and a. The excitability threshold derived from the geometric criterion (red line) matches well with the basin of attraction boundary between stationary pattern (blue) and uniform state (gray). See Sec. 1.5 for the parameters.

and cytosol. To stay consistent with our notation, let us denote the respective densities by m and c (Edelstein-Keshet et al. use a and b). The reaction term reads

$$f(m,c) = \left(k_0 + \frac{\gamma m^2}{K^2 + m^2}\right) c - \delta m, \tag{16}$$

where the parameters in [Mori2008] are set to $k_0 = 0.067\,\mathrm{s}^{-1}$, $\gamma = 1\,\mathrm{s}^{-1}$, $\delta = 1\,\mathrm{s}^{-1}$ and $K = 1\,\mu\mathrm{m}^{-1}$. The system has a single chemical equilibrium for all total densities $n = m + c$.

For the diffusion constants $D_m = 0.01\,\mu\mathrm{m}^2\mathrm{s}^{-1}$, $D_c = 10\,\mu\mathrm{m}^2\mathrm{s}^{-1}$ the chemical equilibrium is laterally unstable in the range $2.30037\mu\mathrm{m}^{-1} < n_0 2.59822\,\mu\mathrm{m}^{-1}$. A representative dispersion relation for $n_0 = 2.35\mu\mathrm{m}^{-1}$ is shown in Supp. Fig. 1.

1.6 Discussion of wave–pinning

Redistribution of mass and shifting local equilibria are the general principles underlying pattern formation in mass conserving systems. For the case of a two component system, the mass redistribution framework generically leads to polarized patterns established by mass-redistribution and maintained by flux–turnover balance. Wave–pinning turns out out to be a special case of polarized patterns, in which, far away from the diffusive interface, the system is slaved to plateaus of local equilibria.

In the wave-pinning construction "bistability" (actually meaning "bistability in flux-balance subspace") is *assumed* a priori such that there is always slaving to plateaus of reactive equilibria far away. As the above discussion shows, wave–pinning is just a special case of polarized patterns. Neither "bistability" nor slaving to plateaus of reactive equilibria are necessary to obtain polarized steady states. Plateau patterns arise as a special case of a broader polarity mechanism based on redistribution of mass, scaffolding by local equilibria, and flux–turnover balance.

1.7 Comparison to domain walls bistable media

Domain walls in bistable media propagate when flux–turnover balance is broken, and hence there must be an advective flow. Pattern formation by mass redistribution is fundamentally different from bistable media because the local equilibria are shifted due to mass redistribution. The system with a stationary pattern can be locally monostable at every

point in space, because the *shifting* of local equilibria, which scaffold the pattern, is the essential pattern formation process. The interface of a stationary pattern is maintained by flux-turnover balance — *lateral* instability of the interface region prevents relaxation back to a uniform steady state. In contrast, interfaces in bistable media are maintained by local instability of the unstable fixed point inbetween t

2 Simplifying the Min model

2.1 Skeleton Min model in box geometry

The actual Min protein dynamics take place in the three dimensional geometry of the rod shaped cell. Both MinD and MinE can freely diffusive in the cytosol. MinD in its Active ATP-bound form can bind to the membrane where it recruits both more active MinD as well as MinE forming a membrane bound MinDE complex. In this complex, MinD is hydrolyzed (converting ATP to ADP) followed by dissociation of the complex, which releases both MinD and MinE into the cytosol. The freshly released MinD is ADP bound and can only bind the membrane again after nucleotide exchange. The interactions between MinD and MinE are illustrated by the reaction network Supp. Fig. 4 and can be mathematically modeled by mass action law.

The additional spatial dimension of the cytosolic domain is an essential aspect of the cellular geometry. Processes where proteins bind or detach from the membrane generate cytosolic fluxes orthogonal to the membrane. Since we are interested in the pattern formation mechanism per se, and not in geometry adaption we consider the simplest geometry capturing the coupling between cytosol and membrane: a rectangle of height h and length L representing the cytosol, with one of the horizontal edges representing the membrane. Robin boundary conditions at this edge couple the membrane to the cytosol, while all other edges have no-flux boundary conditions. The respective reaction-diffusion equations of the Min protein dynamics in this two-dimensional "box-geometry"

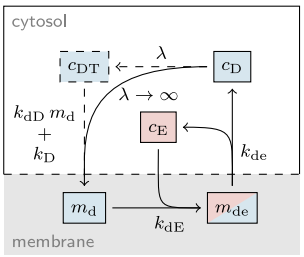

SUPP. FIG. 4. Interaction network of MinD and MinE. Finite nucleotide exchange can be neglected for the analysis of the elementary oscillation cycle.

read:

$$\partial_t c_{\mathrm{DD}}(x,y,t) = D_{\mathrm{D}}\nabla^2 c_{\mathrm{DD}}(x,y,t) - \lambda c_{\mathrm{DD}}(x,y,t), \tag{17}$$
$$\partial_t c_{\mathrm{DT}}(x,y,t) = D_{\mathrm{D}}\nabla^2 c_{\mathrm{DT}}(x,y,t) + \lambda c_{\mathrm{DD}}(x,y,t), \tag{18}$$
$$\partial_t c_{\mathrm{E}}(x,y,t) = D_{\mathrm{E}}\nabla^2 c_{\mathrm{E}}(x,y,t) c_{\mathrm{DD}}(x,y,t), \tag{19}$$
$$-D_{\mathrm{D}}\nabla_y c_{\mathrm{DD}}(x,y,t)|_{y=0} = k_{\mathrm{de}} m_{\mathrm{de}}(x,t), \tag{20}$$
$$-D_{\mathrm{D}}\nabla_y c_{\mathrm{DD}}(x,y,t)|_{y=0} = -(k_{\mathrm{D}} + k_{\mathrm{dD}} m_{\mathrm{d}}(x,t)) c_{\mathrm{DT}}(x,0,t), \tag{21}$$
$$-D_{\mathrm{E}}\nabla_y c_{\mathrm{E}}(x,y,t)|_{y=0} = -k_{\mathrm{dE}} m_{\mathrm{d}}(x,t) c_{\mathrm{E}}(x,0,t) + k_{\mathrm{de}} m_{\mathrm{de}}(x,t), \tag{22}$$
$$\partial_t m_{\mathrm{d}}(x,t) = D_{\mathrm{d}}\nabla_x^2 m_{\mathrm{d}}(x,t) + (k_{\mathrm{D}} + k_{\mathrm{dD}} m_{\mathrm{d}}(x,t)) c_{\mathrm{DT}}(x,0,t) \tag{23}$$
$$- k_{\mathrm{dE}} m_{\mathrm{d}}(x,t) c_{\mathrm{E}}(x,0,t), \tag{24}$$
$$\partial_t m_{\mathrm{de}}(x,t) = D_{\mathrm{de}}\nabla_x^2 m_{\mathrm{de}}(x,t) + k_{\mathrm{dE}} m_{\mathrm{d}}(x,t) c_{\mathrm{E}}(x,0,t) \tag{25}$$
$$- k_{\mathrm{de}} m_{\mathrm{de}}(x,t). \tag{26}$$

These dynamics conserve the total density of MinD and MinE respectively. We use the parameters from [1].

2.2 Cytosol averaging and fast nucleotide exchange

In [2], it has been shown that the extra cytosolic dimension can only be averaged out, if the height of the cytosol is much smaller than the penetration depth of the cytosolic gradients induced by the attachment dynamics $H \ll \sqrt{D_c/k_{\mathrm{on,max}}}$. *In vitro* the cytosol can not be averaged out and is essential for the observed dynamics. Here we are interested in the core pattern formation process *in vivo* where $h \approx 0.25\,\mu$m and the maximal membrane densities are much smaller than *in vitro*. Therefore we can reduce the geometry to a one-dimensional line using the averaging ansatz

$$\bar{c}(x,t) = \frac{1}{h}\int_0^h \mathrm{d}y\, c(x,y,t)$$

for the cytosolic components. In the following we suppress the overbar for the averaged cytosolic densities. The resulting model reads

$$\partial_t c_{\mathrm{DD}} = D_{\mathrm{D}}\nabla_x^2 c_{\mathrm{DD}} - \lambda c_{\mathrm{DD}} + h^{-1} k_{\mathrm{de}} m_{\mathrm{de}}, \tag{27}$$
$$\partial_t c_{\mathrm{DT}} = D_{\mathrm{D}}\nabla_x^2 c_{\mathrm{DT}} + \lambda c_{\mathrm{DD}} - h^{-1}(k_{\mathrm{D}} + k_{\mathrm{dD}} m_{\mathrm{d}}) c_{\mathrm{DT}}, \tag{28}$$
$$\partial_t c_{\mathrm{E}} = D_{\mathrm{E}}\nabla_x^2 c_{\mathrm{E}} - h^{-1}[k_{\mathrm{dE}} m_{\mathrm{d}} c_{\mathrm{E}} + k_{\mathrm{de}} m_{\mathrm{de}}], \tag{29}$$
$$\partial_t m_{\mathrm{d}} = D_{\mathrm{d}}\nabla_x^2 m_{\mathrm{d}} + (k_{\mathrm{D}} + k_{\mathrm{dD}} m_{\mathrm{d}}) c_{\mathrm{DT}} - k_{\mathrm{dE}} m_{\mathrm{d}} c_{\mathrm{E}}, \tag{30}$$
$$\partial_t m_{\mathrm{de}} = D_{\mathrm{de}}\nabla_x^2 m_{\mathrm{de}} + k_{\mathrm{dE}} m_{\mathrm{d}} c_{\mathrm{E}} - k_{\mathrm{de}} m_{\mathrm{de}}, \tag{31}$$

fulfilling the conservation of total MinD and MinE mass

$$\int_0^L \mathrm{d}x\,(c_{\mathrm{DD}} + c_{\mathrm{DT}} + m_{\mathrm{d}} + m_{\mathrm{de}}) = L \cdot n_{\mathrm{D}}, \tag{32}$$

$$\int_0^L \mathrm{d}x\,(c_{\mathrm{E}} + m_{\mathrm{de}}) = L \cdot n_{\mathrm{D}}. \tag{33}$$

Linear stability analysis shows that the linear stability regimes (stable, non-oscillatory unstable and oscillatory unstable) remain structurally invariant when the nucleotide exchange is instantaneous (i.e. $\lambda \to \infty$). In particular, in the regime where diffusive transport of MinE is set to a slower timescale ($d_{\mathrm{E}} \ll D_{\mathrm{d}}$), a finite nucleotide exchange rate is quantitatively negligible (see Fig. 8a in the main text). In the following analysis we will therefore use the reduced four-component system

$$\partial_t c_{\mathrm{D}} = D_{\mathrm{D}}\nabla_x^2 c_{\mathrm{D}} - h^{-1}\left[(k_{\mathrm{D}} + k_{\mathrm{dD}} m_{\mathrm{d}})c_{\mathrm{D}} + k_{\mathrm{de}} m_{\mathrm{de}}\right]. \tag{34}$$

$$\partial_t c_{\mathrm{E}} = D_{\mathrm{E}}\nabla_x^2 c_{\mathrm{E}} - h^{-1}\left[k_{\mathrm{dE}} m_{\mathrm{d}} c_{\mathrm{E}} + k_{\mathrm{de}} m_{\mathrm{de}}\right], \tag{35}$$

$$\partial_t m_{\mathrm{d}} = D_{\mathrm{d}}\nabla_x^2 m_{\mathrm{d}} + (k_{\mathrm{D}} + k_{\mathrm{dD}} m_{\mathrm{d}})c_{\mathrm{D}} - k_{\mathrm{dE}} m_{\mathrm{d}} c_{\mathrm{E}}, \tag{36}$$

$$\partial_t m_{\mathrm{de}} = D_{\mathrm{de}}\nabla_x^2 m_{\mathrm{de}} + k_{\mathrm{dE}} m_{\mathrm{d}} c_{\mathrm{E}} - k_{\mathrm{de}} m_{\mathrm{de}}, \tag{37}$$

which is obtained in the limit $\lambda \to \infty$ where $c_{\mathrm{DD}} \to 0$ and MinD can immediately reattach after detaching from the membrane.

For notational convenience we absorb the height h in the cytosolic concentrations $hc_{\mathrm{D}} \to \hat{c}_{\mathrm{D}}$, $hc_{\mathrm{E}} \to \hat{c}_{\mathrm{E}}$, and respectively rescale the attachment rates $k_{\mathrm{D}}/h \to \hat{k}_{\mathrm{D}}$, $k_{\mathrm{dD}}/h \to \hat{k}_{\mathrm{dE}}$, $k_{\mathrm{dE}}/h \to \hat{k}_{\mathrm{dE}}$. After this rescaling, the cytosolic component concentrations are also measured as line densities like the membrane concentrations. We suppress the hats to simplify notation.

3 Separation of diffusive transport timescales

Linear stability analysis shows, that the phase space structure of the *in vivo* Min system extends smoothly towards arbitrarily small MinE diffusion rates. This provides the motivation to impose a separation on the level of diffusive MinE transport. Adding Eqs. (35,37) we obtain the purely diffusive dynamics

$$\partial_t \rho_{\mathrm{E}} = D_{\mathrm{E}}\partial_x^2 \rho_{\mathrm{E}} + (D_{\mathrm{de}} - D_{\mathrm{E}})\nabla_x^2 m_{\mathrm{de}}. \tag{38}$$

of the total MinE density

$$\rho_{\mathrm{E}}(x) = c_{\mathrm{E}}(x) + m_{\mathrm{de}}(x). \tag{39}$$

If $D_{\mathrm{de}} = D_{\mathrm{E}}$, the above equation (38) reduces to $\partial_t \rho_{\mathrm{E}} = D_{\mathrm{E}} \partial_x^2 \rho_{\mathrm{E}}$. This means that for $D_{\mathrm{de}} = D_{\mathrm{E}}$ the MinE total density and will always approach a uniform distribution. Deviations from this uniform distribution of MinE are caused by relative dominance of the MinE diffusion rates. This inspires a transformation of these parameters:

$$\begin{array}{l} D_{\mathrm{E}} = d_{\mathrm{E}}(1+\delta_{\mathrm{E}}) \\ D_{\mathrm{de}} = d_{\mathrm{E}}(1-\delta_{\mathrm{E}}) \end{array} \quad \text{with} \quad \begin{array}{l} d_{\mathrm{E}} = (D_{\mathrm{E}} + D_{\mathrm{de}})/2 \\ \delta_{\mathrm{E}} = (D_{\mathrm{E}} - D_{\mathrm{de}})/(D_{\mathrm{E}} + D_{\mathrm{de}}) \end{array} \tag{40}$$

so that (38) becomes

$$\partial_\tau \rho_{\mathrm{E}}(x,\tau) = \nabla_x^2 \rho_{\mathrm{E}}(x,\tau) + \delta_{\mathrm{E}} \nabla_x^2 \big(c_{\mathrm{E}}(x) - m_{\mathrm{de}}(x) \big). \tag{41}$$

The timescale separation is now encoded in the parameter d_{E} with the respective slow time $\tau = (d_{\mathrm{E}}/L^2)t$.

On the fast timescale t, the MinE density profile $\rho_{\mathrm{E}}(x,\tau)$ is almost stationary and therefore has the role of a parameter. We want to find the steady states of the fast dynamics in dependence of this parameter. The dynamic variables on the fast timescale are the MinD components $m_{\mathrm{d}}(x)$, $c_{\mathrm{D}}(x)$. We denote their stationary (pattern) state by $\big(\widetilde{m}_{\mathrm{d}}(x), \widetilde{c}_{\mathrm{D}}(x)\big)$. Our goal is to find the MinD steady state profiles for a fixed MinE profile. The individual MinE densities c_{E} and m_{de} are then determined by the local equilibria of MinE for the given local MinE total density ρ_{E}

$$(m_{\mathrm{de}}^*, c_{\mathrm{E}}^*) : f_{\mathrm{E}}(m_{\mathrm{d}}, m_{\mathrm{de}}, c_{\mathrm{E}}) = 0 \;\&\; c_{\mathrm{E}} + m_{\mathrm{de}} = \rho_{\mathrm{E}}. \tag{42}$$

Solving this pair of equations simply yields

$$c_{\mathrm{E}}^*\big(\widetilde{m}_{\mathrm{d}}(x), \rho_{\mathrm{E}}(x,\tau)\big) = \frac{\rho_{\mathrm{E}}(x,\tau)}{1 + \frac{k_{\mathrm{dE}}}{k_{\mathrm{de}}} \widetilde{m}_{\mathrm{d}}(x)}, \tag{43}$$

$$m_{\mathrm{de}}^*\big(\widetilde{m}_{\mathrm{d}}(x), \rho_{\mathrm{E}}(x,\tau)\big) = \frac{\rho_{\mathrm{E}}(x,\tau)}{1 + \frac{k_{\mathrm{dE}}}{k_{\mathrm{de}}} \widetilde{m}_{\mathrm{d}}(x)} \cdot \frac{k_{\mathrm{dE}}}{k_{\mathrm{de}}} \widetilde{m}_{\mathrm{d}}(x), \tag{44}$$

for the local equilibria of MinE. These can then be plugged into (34) and (36) to obtain

$$D_{\mathrm{D}} \nabla_x^2 \widetilde{c}_{\mathrm{D}}(x) - f_{\mathrm{eff}}\big(\widetilde{m}_{\mathrm{d}}(x), \widetilde{c}_{\mathrm{D}}(x); \rho_{\mathrm{E}}(x,\tau)\big) = 0, \tag{45}$$

$$D_{\mathrm{d}} \nabla_x^2 \widetilde{m}_{\mathrm{d}}(x) + f_{\mathrm{eff}}\big(\widetilde{m}_{\mathrm{d}}(x), \widetilde{c}_{\mathrm{D}}(x); \rho_{\mathrm{E}}(x,\tau)\big) = 0, \tag{46}$$

$$\text{with} \quad \int_0^L \mathrm{d}x\, \widetilde{m}_{\mathrm{d}}(x) + \widetilde{c}_{\mathrm{D}}(x) + m_{\mathrm{de}}^*(\widetilde{m}_{\mathrm{d}}(x), \rho_{\mathrm{E}}(x)) = L \cdot n_{\mathrm{D}}, \tag{47}$$

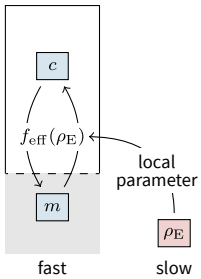

SUPP. FIG. 5. Effective MinD reaction scheme, with MinE entering as a local control parameter.

and the effective MinD reactive term

$$f_{\text{eff}}(m_{\text{d}}, c_{\text{D}}; \rho_{\text{E}}) = (k_{\text{D}} + k_{\text{dD}} m)c - \frac{k_{\text{dE}} m_{\text{d}} \rho_{\text{E}}}{1 + \frac{k_{\text{dE}} m_{\text{d}}}{k_{\text{de}}}}. \tag{48}$$

These equations define the steady states of a two–component mass–conserving reaction–diffusion system.

3.1 Galerkin expansion of flux–turnover balance

We study the Min system close to the onset of lateral instability, i.e. for $L \gtrsim L_{\text{min,D}}$, where $L_{\text{min,D}} = \pi/q_{\text{max,D}}$ is the right edge of the band unstable modes of the effective MinD system Eqs. (45,46). In such a short system, only the first harmonic mode $\cos(q_1 x)$, with $q_1 = \pi/L$, is unstable. The all higher harmonics $\cos(k\pi x/L)$ with $k \geq 2$ are strongly suppressed by diffusion. We can therefore apply a Galerkin expansion, expressing the approximate solution as a sum of harmonics and neglecting higher harmonics. The error due to that truncation lies in a subspace orthogonal to the approximate solution. In a short system, we can truncate after the first harmonic such that the Galerkin ansatz becomes particularly simple:

$$\widetilde{m}^1_{\text{d}}(x) = m^0_{\text{d}} + m^1_{\text{d}} \cos(q_1 x), \tag{49}$$

$$\widetilde{c}^1_{\text{D}}(x) = c^0_{\text{D}} - D_m/D_c m^1_{\text{d}} \cos(q_1 x), \tag{50}$$

where we used the flux-balance condition (11). Because the slaved component $m^*_{\text{de}}(m_{\text{d}}, \rho_{\text{E}})$ contributes to the total density of MinD (cf. Eq. (47)), the average total density in Galerkin approximation becomes

$$n_{\text{D}} = m^0_{\text{d}} + c^0_{\text{D}} + \frac{1}{L}\int_0^L \mathrm{d}x\, m^*_{\text{de}}\big(\widetilde{m}^1_{\text{d}}(x), n_{\text{E}} + \rho^1_{\text{E}} \cos(q_1 x)\big), \tag{51}$$

where we approximated the MinE profile as $\rho_{\text{E}}(x) \approx n_{\text{E}} + \rho^1_{\text{E}} \cos(q_1 x)$ in accordance with our Galerkin ansatz. The integral in (51) can be calculated analytically, e.g. using Mathematica.

To express flux-turnover balance in the Galerkin solution subspace (spanned by $(1, \cos(q_1 x))$ we need to project the reactive flow $f_{\text{eff}}(\widetilde{m}_{\text{d}}(x), \widetilde{c}_{\text{D}}(x); \rho_{\text{E}}(x))$ into this subspace

$$f_0 := \frac{1}{L}\int_0^L \mathrm{d}x\, f_{\text{eff}}\big(\widetilde{m}^1_{\text{d}}(x), \widetilde{c}^1_{\text{D}}(x); n_{\text{E}} + \rho^1_{\text{E}} \cos(q_1 x)\big)$$

$$f_1 := \frac{2}{L}\int_0^L \mathrm{d}x\, \cos(q_1 x) f_{\text{eff}}\big(\widetilde{m}^1_{\text{d}}(x), \widetilde{c}^1_{\text{D}}(x); n_{\text{E}} + \rho^1_{\text{E}} \cos(q_1 x)\big).$$

These integrals, similarly to the one in (51), can be calculated analytically. Flux-turnover balance

$$D_m \nabla_x \widetilde{m}\big|_{x_0} = \int_0^{x_0} \mathrm{d}x\, f_0 + f_1 \cos(q_1 x) \tag{52}$$

$$= -\int_{x_0}^{L} \mathrm{d}x\, f_0 + f_1 \cos(q_1 x) \tag{53}$$

then yields two conditions

$$f_0 = 0, \tag{54}$$

$$f_1 = -D_m \pi / L\, m_{\mathrm{d}}^1, \tag{55}$$

representing the conditions that (i) the total turnover must vanish, and (ii) turnover in either half-cell balances the flux across the interface $x_0 = L/2$. Together with the total density (51) these conditions determine the Galerkin solution $(m_{\mathrm{d}}^0, c_{\mathrm{D}}^0, m_{\mathrm{d}}^1)$ in dependence of the MinE profile amplitude ρ_{E}^1.

3.2 Lateral instability of the essential (control variable) dynamics

Above we have shown that the essential degrees of freedom of Min protein dynamics are the total densities of MinD and MinE. Their diffusive transport underlies both, polarization of MinD, driven by redistribution of MinD mass, as well as the oscillation of the MinD polarization direction, emerging due to redistribution of MinE mass. In the following we further corroborate this finding by showing that the lateral stability of a uniform steady state is fully determined by essential (mass-redistribution) dynamics.

Originally we performed linear stability analysis (of uniform steady states) of the full 4-component PDE system (34) to (37). Let us now study the linear stability of a system reduced to the essential degrees of freedom:

The core dynamics of MinD, without MinE transport ($d_{\mathrm{E}} = 0$), are an effective 2-component system (cf. Eqs. (45,46). Lateral instability of this core MinD system is driven by cascading mass-redistribution. This instability sets in at the minimal system length $L_{\mathrm{min,D}} = \pi / q_{\mathrm{max,D}}$ where the eigenvector $\mathbf{e}_{q_{\mathrm{max,D}}} \sim (D_c, -D_m)^{\mathrm{T}}$ in phase space coincides with the flux-balance subspace (for $D_m \ll D_c$ we can approximate

$\mathbf{e}_{q_{\max,\mathrm{D}}} \approx (1,0)^{\mathrm{T}}$). Therefore the amplitude dynamics of modes q close to $q_{\max,\mathrm{D}}$ can be projected onto the flux-balance subspace (coordinate $\phi = m - D_m/D_c c$, for simplicity we can approximate as $\phi = m$ as long as $D_m \ll D_c$), which captures the essential MinD mass redistribution that drives lateral instability. In that subspace the amplitude growth rate simply reads $\sigma_{\mathrm{D}}(q) = -D_\phi q^2 + f_\phi$. From this the maximal wavenumber can simply be read off as $q^2_{\max,\mathrm{D}} = f_\phi/D_\phi$.

How does switching on slow redistribution of MinE mass ($d_{\mathrm{E}} \ll D_{\mathrm{d}}$) influence the dynamics at onset of pattern formation $L \approx L_{\min,\mathrm{D}}$? Essentially we want to know how the coupling between MinD and MinE perturbs the eigenvalue $\sigma(q_{\max,\mathrm{D}})$ of the critical mode. From the above analysis of the Min oscillations, we learned that MinD polarized states are controlled by redistribution of MinE mass. We therefore replace the individual dynamics of the two MinE conformal states in the full system (34) to (37) by the effective dynamics of the total MinE density $\rho_{\mathrm{E}}(x,t)$ given by Eq. (41) (mathematically this approximation is justified by the separation of timescales; more abstractly put: we project the dynamics of the two MinE densities onto their slow invariant manifold). Using the abbreviation

$$g(m_{\mathrm{d}}, \rho_{\mathrm{E}}) = c_{\mathrm{E}}(m_{\mathrm{d}}, \rho_{\mathrm{E}}) - m_{\mathrm{de}}(m_{\mathrm{d}}, \rho_{\mathrm{E}}) = \rho_{\mathrm{E}}\, \frac{k_{\mathrm{de}} - k_{\mathrm{dE}} m_{\mathrm{d}}}{k_{\mathrm{de}} + k_{\mathrm{dE}} m_{\mathrm{d}}}$$

In the projection onto the essential (mass-redistribution) degrees of freedom, we obtain the effective Jacobian for the mode (harmonic) Fourier mode $\cos(qx)$

$$J_{\mathrm{eff}} = \begin{pmatrix} \sigma_{\mathrm{D}}(q) & f_{\rho_{\mathrm{E}}} \\ g_\phi(q) & g_{\rho_{\mathrm{E}}}(q) \end{pmatrix} = \begin{pmatrix} \sigma_{\mathrm{D}}(q) & f_{\rho_{\mathrm{E}}} \\ -d_{\mathrm{E}}\, \delta_{\mathrm{E}}\, q^2\, g_\phi & -d_{\mathrm{E}}\, q^2 (1 + \delta_{\mathrm{E}}\, g_{\rho_{\mathrm{E}}}) \end{pmatrix}, \quad (56)$$

where $f_{\rho_{\mathrm{E}}}$, g_ϕ and $g_{\rho_{\mathrm{E}}}$ are coupling coefficients between MinD and MinE total density dynamics linearized around the uniform steady state ($m_{\mathrm{d}}(x) = m^*_{\mathrm{d}}$, $\rho_{\mathrm{E}}(x) = n_{\mathrm{E}}$)

$$\begin{aligned} f_{\rho_{\mathrm{E}}} &= \partial_{\rho_{\mathrm{E}}} f\big|_* = -\frac{k_{\mathrm{de}} k_{\mathrm{dE}} m^*_{\mathrm{d}}}{k_{\mathrm{de}} + k_{\mathrm{dE}} m^*_{\mathrm{d}}}, \\ g_\phi &= \partial_\phi g\big|_* = -\frac{k_{\mathrm{de}} k_{\mathrm{dE}} n_{\mathrm{E}}}{(k_{\mathrm{de}} + k_{\mathrm{dE}} m^*_{\mathrm{d}})^2}, \\ g_{\rho_{\mathrm{E}}} &= \partial_{\rho_{\mathrm{E}}} g\big|_* = \frac{k_{\mathrm{de}} - k_{\mathrm{dE}} m^*_{\mathrm{d}}}{k_{\mathrm{de}} + k_{\mathrm{dE}} m^*_{\mathrm{d}}}. \end{aligned}$$

The eigenvalues of the effective Jacobian (56) yield linear stability of the system in the vicinity $q_{\max,\mathrm{D}}$ (in fact we can reproduce the full dispersion

relation and the phase diagram as long as $d_\mathrm{E} < D_\mathrm{d}$, so the mapping to the essential phase space only breaks down when MinE diffusion completely dominates over MinD diffusion. In this case there is no pattern formation at all because the lateral instability due to MinD mass redistribution is suppressed by fast MinE redistribution). In particular at the onset of lateral instability $q = q_{\max,\mathrm{D}}$ we find to leading order

$$\sigma(q_{\max,\mathrm{D}}) = \sqrt{-\delta_\mathrm{E}\, f_\phi g_\phi f_{\rho_\mathrm{E}}} \cdot [d_\mathrm{E}/D_\phi]^{1/2} + \mathcal{O}[d_\mathrm{E}/D_\phi].$$

Hence, if $\delta_\mathrm{E} > 0$ growth rate will become imaginary — the system will be oscillatory at onset ($L \approx L_{\min,\mathrm{D}}$). Using the growth rate $\sigma(q)$ we can write down the initial time evolution of the Fourier amplitude $\delta m_q(t)$:

$$\delta m_q(t) \approx \delta m_q(0) \cdot \exp\Big[\sigma_\mathrm{D}(q)\Big] \cdot \exp\Big[\sqrt{d_\mathrm{E}}\sqrt{g_\phi f_{\rho_\mathrm{E}}}\Big]$$

The first term represents lateral instability by redistribution of MinD mass while the second term arises from a secondary bifurcation due to redistribution of MinE mass on the slow timescale τ making the onset dynamics oscillatory if $\delta_\mathrm{E} > 0$. The oscillations are not intrinsic to the core mechanism of pattern formation (MinD polarization) but only arise due to coupling to MinE redistribution. Conversely, oscillatory instability can only arise under the precondition, that the reduced (2-component) MinD system is laterally unstable. Hence, the observed "oscillatory Turing instability" is not a mechanistically separate class of instability.

References

[1] Jacob Halatek and Erwin Frey. "Highly canalized MinD transfer and MinE sequestration explain the origin of robust MinCDE-protein dynamics." In: *Cell reports* 1.6 (June 2012), pp. 741–52.

[2] Jacob Halatek and Erwin Frey. "Rethinking pattern formation in reaction-diffusion systems". 2017.

[3] Yoichiro Mori, Alexandra Jilkine, and Leah Edelstein-Keshet. "Wave-pinning and cell polarity from a bistable reaction-diffusion system." In: *Biophysical journal* 94.9 (May 2008), pp. 3684–97.

X Geometry and mass-conservation: The switching paradigm and pattern robustness

This chapter is based on the following publication:

MinE conformational switching confers robustness on self-organized Min protein patterns

by

J. Denk[†,1,2], **S. Kretschmer**[†,2,3], **J. Halatek**[†,1], **C. Hartl**[1], **P. Schwille**[3], **and E. Frey**[1]

[1]Department of Physics, Arnold Sommerfeld Center for Theoretical Physics and Center for NanoScience, Ludwig-Maximilians-Universität München, Theresienstraße 37, 80333 München, Germany,

[2]Graduate School of Quantitative Biosciences, Ludwig-Maximilians-Universität München, Feodor-Lynen-Str. 25, 81337 München, Germany,

[3]Department of Cellular and Molecular Biophysics, Max-Planck-Institute of Biochemistry, Am Klopferspitz 18, D- 82152 Martinsried, Germany,

† equal contribution

Journal Reference:

***Proc. Natl. Acad. Sci. U.S.A.*, 201719801, 2018**

Supplemental Material reproduced on pages 468 to 488.

Mutually interlinked protein switches are essential for the robustness of protein patterns

Jonas Denk[1,*], Simon Kretschmer[2,*], Jacob Halatek[1,*], Caroline Hartl[1], Petra Schwille[2,†], and Erwin Frey[1,†]

[1]Arnold-Sommerfeld-Center for Theoretical Physics and Center for NanoScience, Ludwig-Maximilians-Universität München, Theresienstraße 37, D-80333 München, Germany.

[2]Max-Planck-Institute of Biochemistry, Am Klopferspitz 18, D-82152 Martinsried, Germany.

* These authors contributed equally.

† Correspondence to: schwille@biochem.mpg.de (P.S.), frey@lmu.de (E.F.).

Abstract:

Robust protein patterning is vital for many fundamental cellular processes. An established motif of intracellular pattern-forming networks is the self-organization of nucleoside triphosphatases (NTPases), which upon interaction with a cognate NTPase activating protein switch between an NTP-bound and nucleoside diphosphate (NDP)-bound form. In the Min system, a prototypical example for pattern formation during bacterial cell division, the adenosine triphosphatase (ATPase) MinD in turn triggers a conformational switch in its activating protein MinE from a latent to a reactive state, although the role of such mutual switching is unclear. By combining nonlinear dynamics analyses and *in vitro* reconstitution of mutant proteins, we show here that the MinD-dependent switch of MinE is essential for pattern formation in a broad and physiological range of protein concentrations. Our combined theoretical and experimental approach demonstrates that though simpler reaction networks can reproduce patterns, interlinking protein switches confers pattern robustness - a fundamental prerequisite for the evolvability of organisms.

Main Text

Correct and robust protein localization is vital for many fundamental cellular processes ranging from cell division [1] and chromosome segregation[2] to chemotaxis[3]. An intriguing question is to what extent these intrinsically complex processes can be reduced to their core principles and, in turn, what is the role of molecular details? An established motif of intracellular networks is the self-organization of P-loop NTPases, molecular switches that can exist in an active, NTP-bound and an inactive, NDP-bound form[4,5]. Transitions between these states are facilitated by an NTPase-activating protein, which is essential for protein pattern formation.

Among intracellular pattern-forming networks, the E. coli Min system is a particularly instructive example, and has become a paradigmatic model for both experimental6-10 and theoretical6,11-15 studies of protein pattern formation over the last 15 years. Here, ATP-bound MinD dimerizes and binds to the plasma membrane16,17. It then recruits further MinD-ATP, as well as its ATPase-activating protein MinE, which together form membrane-bound MinDE complexes16. MinE stimulates MinD's ATPase activity, thereby initiating disintegration of MinDE complexes and subsequent release of MinE and ADP-bound MinD into the cytosol16,18. Reattachment of MinD is delayed by the requirement for nucleotide exchange (substitution of ATP for ADP)12,17. This biochemical reaction network, which we refer to as the skeleton network (Fig. 1a), suffices to generate Min patterns, as has been confirmed by numerous experimental and theoretical studies8,11-14,16.

In particular, the latter suggest that the MinE-induced conversion of MinD from an ATP- to an ADP-bound state (Fig. 1b) is critical for efficient localization of the FtsZ ring to mid-cell[12], formation of multistable patterns, and adaptation to cell geometry [8]. However, all theoretical studies[11-15] also suggest that patterns can form only if MinE is less abundant than MinD, but this prediction is decisively refuted by reconstitution experiments, in which patterns emerge for MinE/MinD ratios ranging between 0.125 and 5[6,9,19-21]. This contradiction prompts a reconsideration of the

current perspective on the Min reaction network and raises the general question of how pattern-forming networks become robust against variations in protein concentrations.

Indeed, recent biochemical findings[22,23] suggest a possible extension of the skeleton network. In addition to the MinE-induced switch in MinD's nucleotide state, MinE itself is now believed to undergo a MinD-dependent conformational switch. According to this notion, upon encountering membrane-bound MinD, cytosolic MinE unmasks its buried MinD- and membrane-interaction regions, i.e. its anti-MinCD helix and membrane-targeting sequence (MTS), respectively (Fig. 1b). In this open conformation, MinE is assumed[22] to rapidly bind to membrane-bound MinD and stimulate its ATPase activity. In addition, after dissociation of the MinDE complex and release of MinD-ADP, MinE's MTS enables it to remain bound to the membrane, and the protein may reassociate with another membrane-bound MinD molecule or eventually return to the cytosol[7,22,23]. Upon detachment, open MinE quickly re-assumes its latent conformation with its MinD- and membrane-interaction regions buried (Fig. 1b). However, it is reasonable to assume that, after detachment, MinE persists in its reactive conformation for a short time before reverting to its latent state. In the reactive state, MinE could again be rapidly recruited to membrane-bound MinD. These two elements of MinE's conformational switch – the MinE-MinD interaction and the persistent membrane binding – could independently affect the formation of patterns. To analyze their respective impacts on pattern robustness to variations in the MinE/MinD ratio, we numerically studied the dynamics of reaction networks that exhibit either aspect of the switch by a linear stability analysis, and then tested the theoretical predictions by reconstituting the networks using suitable MinE mutants (see Methods and Supplementary Note 1, 2). We find that whereas persistent membrane binding does not affect the protein concentration range compatible with pattern formation, the MinE-MinD interaction switch of MinE is critical for patterns to emerge over a broad and physiological range of protein concentrations. Our study shows that interlinked protein switches are essential to

achieve robustness of patterns in intracellular reaction-diffusion networks, which are known to regulate many vital cellular processes.

Results

MinE-MinD interaction switch. First, we addressed the functional relevance of the MinD-induced exposure of MinE's buried MinD interaction region alone. For this, we extended the skeleton network to include both a latent, closed MinE conformation with low, and a reactive, open form with high recruitment rates to membrane-bound MinD, k_{dE}^{l} and k_{dE}^{r}, respectively (Fig. 1c). Upon recruitment of MinE, a membrane-bound MinDE complex is formed, in which MinE is assumed to remain in its reactive state. After disintegration of a MinDE complex, both partners are released into the cytosol. The timescale for reversion of reactive MinE to its latent conformation is taken to be 0.01s, the upper bound for a typical conformational switch[24].

Our analysis shows that in the physiologically relevant regime of low k_{dE}^{l} and high k_{dE}^{r}, patterns are formed over a broad range of MinE/MinD ratios, including those where MinE is present in excess (Fig. 2a, b). To test these predictions experimentally, we made use of the MinE L3E mutant, which is impaired in membrane interaction[22]. It should therefore be capable of undergoing the MinD-induced interaction switch, without staying attached to the membrane in the absence of MinD (see Supplementary Note 2). When reconstituted together with MinD on flat membranes, MinE L3E promoted pattern formation over a wide range of MinE/MinD ratios, just like wild-type MinE (Fig. 3). In agreement with our predictions (Fig. 2a, b), patterns formed even when MinE was present in excess over MinD (Fig. 3, 4).

These results suggest that MinE's ability to switch between high and low affinity for MinD is responsible for the robustness of Min protein patterns. If so, locking MinE in its reactive conformation should decrease the concentration range compatible with pattern formation. To test this prediction, we took advantage of the I24N mutation, which was previously shown to bypass the need for MinD to trigger MinE's

conformational switch ([22], Supplementary Note 2). Strikingly, introducing this mutation into either WT MinE or MinE L3E dramatically reduced the concentration range in which protein patterns formed (Fig. 3, 4). In agreement with our model predictions, patterns only prevailed in a very narrow range and only for MinE/MinD ratios far below 1 (Fig. 3, 4). In particular, MinE I24N forms patterns only outside the physiological concentration range [25], consistent with cell division defects described *in vivo*[22,26]. In summary, our analyses demonstrate that mutually interlinked protein switching is critical for the robustness of an exemplary pattern-forming system against variations in protein concentrations.

The relationship between the MinE/MinD ratio and the ability to generate patterns can be understood by considering the roles of the two proteins in the establishment of Min oscillations. Min oscillations are essentially characterized by alternating dominance of MinE and MinD[12,19]. In membrane regions depleted of Min proteins, cooperative binding of MinD first facilitates its accumulation on the membrane (MinD dominance). Then recruitment of MinE, and MinE-induced detachment of MinD, outpaces further MinD accumulation, and progressively depletes it from the membrane (MinE dominance). But MinE-induced detachment can only outpace MinD accumulation if the released MinE is recruited more rapidly to membrane-bound MinD than is MinD itself. Thus, the rate of recruitment of MinE must be higher than that of MinD. Since the skeleton network incorporates only a single, rapidly recruited MinE conformation, initial dominance of MinD accumulation is feasible only if [MinD] exceeds [MinE]. In contrast, if MinE can exist both in a latent and a reactive conformation, dominance of MinD over MinE becomes possible even if [MinE] exceeds [MinD]. This is because initially most MinE is in the latent form, whose recruitment rate is low (Fig. 2c). This would lead to accumulation of MinD on the membrane and Min dynamics would cease. However, after inducing ATP hydrolysis by MinD, MinE is released into the cytosol in its reactive conformation. As this state is short-lived, the reactive species is effectively restricted to a thin boundary layer close to the membrane (Fig. 2c), and will be preferentially recruited

(over cytosolic MinD) to membrane-bound MinD. This enables a transient dominance of MinE, which displaces MinD from the membrane. Remarkably, our theoretical analysis predicts an extended range of MinE/MinD ratios that support patterns even for very rapid MinE switching, i.e. when the layer of reactive MinE (~ 0.7 μm) is orders of magnitude thinner than the depth of the cytosol (~ 5,000 μm) (Supplementary Note 3).

Persistent MinE membrane binding. As MinE's conformational switch affects its affinity for both MinD and the membrane[22], we independently explored the impact of persistent MinE membrane binding mediated by its MTS (Fig. 1d, Supplementary Note 1, 4). This was previously shown to influence Min patterns[15,19,20,27,28], and was implied to be required for pattern formation [15], although the validity of the theoretical model[15] is controversial[29]. From our stability analysis (Supplementary Note 4, 5, Supplementary Figure 2, 3) in combination with our reconstitution experiments (Fig. 3, 4) we infer that persistent membrane binding is not required for pattern formation and, unlike the MinE-MinD switch, does not markedly affect the concentration range of *in vitro* Min patterns (Fig. 3, 4).

The skeleton network. In the MinE L3E/I24N double mutant, both membrane interactions and the MinE-MinD interaction switch are disabled, mimicking the MinE dynamics in the original skeleton network[12]. This mutant still self-organized into dynamic protein patterns, albeit only in a narrow range of MinE/MinD ratios (Fig. 3, 4), and – notably – only if [MinD] exceeds [MinE], in agreement with previous theoretical studies[11-14]. This result shows that, given a suitable choice of low MinE/MinD ratios, neither persistent membrane binding nor the MinE-MinD switch is required to generate patterns, and confirms the skeleton network as a valid and useful basis for the investigation of pattern-forming mechanisms in the Min system.

Discussion

In view of the ubiquity of structurally switchable proteins, including NTPases and possibly further NTPase-activating proteins[4,5], our study sheds new light on the role of alternative conformations in pattern formation and spatial regulation. Mutually interlinked switching enables self-regulation of the pattern-forming network by dynamically adapting its constituents' mode of action (Fig. 2c, 4). We propose that mutually interlinked switching is likely to be a general design principle which enhances the robustness of vital patterns to variations in protein concentrations in many biological reaction-diffusion systems. In particular, mutual switching of active and latent states has been reported for the widely conserved F1hF-F1hG circuit, which is essential for flagellar patterning[4]. It is also thought to play a major role in eukaryotic systems – for instance, in the process of cell polarization in budding yeast[30]. In the context of evolution, robustness of biochemical circuits is an important prerequisite for adaptability to environmental change[31].

Methods:

Mathematical Methods

Theoretical prediction of MinE to MinD ratios that permit the formation of patterns

Our theoretical analyses are based on different biochemical reaction circuits (networks) that incorporate either a MinE-MinD interaction switch or persistent MinE membrane binding. These networks extend a previous model[12,14] for the Min system, which accounts for the molecular interactions that are believed to be essential for Min protein dynamics (see Supplementary Methods), to include a MinE-MinD interaction switch and persistent MinE membrane binding, respectively, as additional features.

Reaction-diffusion network with a MinE-MinD interaction switch

Extension of the previously studied skeleton network[12,14] to include a MinE-MinD interaction switch leads to the following set of partial differential equations for the cytosolic concentrations of MinD-ATP, u_{DT}, MinD-ADP, u_{DD}, reactive MinE, $u_{E,r}$, and latent MinE, $u_{E,l}$, and the concentrations of membrane-bound MinD, u_d, and membrane-bound MinDE complexes, u_{de}.

$$
\begin{aligned}
\partial_t\, u_{DD} &= D_c {\nabla_{\mathrm{c}}}^2 u_{DD} - \lambda\, u_{DD},\\
\partial_t\, u_{DT} &= D_c {\nabla_{\mathrm{c}}}^2 u_{DT} + \lambda\, u_{DD},\\
\partial_t\, u_{E,r} &= D_c {\nabla_{\mathrm{c}}}^2 u_{E,r} - \mu\, u_{E,r},\\
\partial_t\, u_{E,l} &= D_c {\nabla_{\mathrm{c}}}^2 u_{E,l} + \mu\, u_{E,r},\\
\partial_t\, u_d &= D_m {\nabla_{\mathrm{m}}}^2 u_d + f_d\big(u_d, \tilde{u}_{DT}, \tilde{u}_{E,r}, \tilde{u}_{E,l}\big),\\
\partial_t\, u_{de} &= D_m {\nabla_{\mathrm{m}}}^2 u_{de} + f_{de}\big(u_{de}, u_d, \tilde{u}_{E,r}, \tilde{u}_{E,l}\big)\,.
\end{aligned}
$$

These equations are written in coordinate-free form, and the indices *c* or *m* signify that the corresponding Laplacian is acting in the cytosol or at the membrane, respectively. The chemical reactions on the membrane are given by the nonlinear functions

$$
\begin{aligned}
f_d\big(u_d, \tilde{u}_{DT}, \tilde{u}_{E,r}, \tilde{u}_{E,l}\big) &:= (k_D + k_{dD} u_d)\tilde{u}_{DT} - u_d\big(k_{dE}^l \tilde{u}_{Ec} + k_{dE}^r \tilde{u}_{Eo}\big),\\
f_{de}(u_{de}, u_d, \tilde{u}_{Eo}, \tilde{u}_{Ec}) &:= u_d(k_{dE}^c \tilde{u}_{Ec} + k_{dE}^o \tilde{u}_{Eo}) - k_{de} u_{de},
\end{aligned}
$$

where $\tilde{u}_i$ denotes the respective cytosolic densities immediately adjacent to the membrane. These equations are complemented by nonlinear reactive boundary conditions at the membrane surface:

$$
\begin{aligned}
D_c(\nabla_{\mathrm{n}} \mathrm{u}_{\mathrm{DD}})_m &= k_{de} u_{de},\\
D_c(\nabla_{\mathrm{n}} \mathrm{u}_{\mathrm{DT}})_m &= -(k_D + k_{dD} u_d)\tilde{u}_{DT},\\
D_c\big(\nabla_{\mathrm{n}} \mathrm{u}_{\mathrm{E,r}}\big)_m &= k_{de} u_{de} - k_{dE}^r u_d \tilde{u}_{E,r},\\
D_c\big(\nabla_{\mathrm{n}} \mathrm{u}_{\mathrm{E,l}}\big)_m &= -k_{dE}^l u_d \tilde{u}_{E,l}\,.
\end{aligned}
$$

Moreover, we use a no-flux boundary condition at all non-reactive surfaces. The above set of reaction-diffusion equations conserves the total protein number of MinD as well as MinE. For the in vitro experiments a simple box geometry is typically used, in which the reactive lipid bilayer (membrane) is located at the bottom of the box and the cytosol extends in the vertical direction. All other boundaries are reflective. Since the lateral extension of in vitro box geometries is typically very large ($\sim 10^3\ \mu m$) compared to the wavelength of the pattern ($\sim 10\ \mu m$), we perform our analyses in a box of length ($\sim 10^2\ \mu m$) and employ periodic boundary conditions. The height of the experimental box geometry is similarly very large ($\sim 10^3\ \mu m$), such that the dynamics perpendicular to the membrane must be taken into account[29].

Varying the MinE protein concentration for a fixed MinD protein concentration and a fixed set of reaction rates (see Supplementary Table 1), we numerically determined the linear stability of the stationary solutions (see Supplementary Note 1), and identified the regimes of MinE protein concentrations in which perturbations with respect to a steady state with uniform protein distribution on the membrane grow and patterns are predicted (Fig. 2b). The maximal MinE concentrations for a fixed MinD concentration of 1μM and different recruitment rates of reactive and latent MinE are plotted in Fig. 2a. We identified the regimes of MinE concentration where patterns are predicted by carrying out an extensive survey of different reaction rates, and obtained qualitatively similar results in all cases.

Reaction-diffusion network with persistent MinE membrane binding

In contrast to the biochemical reaction network with a MinE-MinD interaction switch, the network with persistent MinE membrane binding has only one MinE conformation with concentrationu_E; however, after disintegration of MinDE complexes and MinD detachment, MinE can now persist as a MinD-free, membrane-bound form with a concentration u_e. On the membrane, this ‘free’ MinE can either reassociate with membrane-bound MinD with a rate k_{ed} or disengage and return to the cytosol with a rate k_e. The ensuing reaction-diffusion equations read

$$\partial_t u_{DD} = D_c {\nabla_c}^2 u_{DD} - \lambda u_{DD} ,$$
$$\partial_t u_{DT} = D_c {\nabla_c}^2 u_{DT} + \lambda u_{DD} ,$$
$$\partial_t u_E = D_c {\nabla_c}^2 u_E ,$$
$$\partial_t u_d = D_m {\nabla_m}^2 u_d + f_d(u_d, u_e, \tilde{u}_{DT}, \tilde{u}_E) ,$$
$$\partial_t u_{de} = D_m {\nabla_m}^2 u_{de} + f_{de}(u_{de}, u_d, u_e, \tilde{u}_E) ,$$
$$\partial_t u_e = D_m {\nabla_m}^2 u_e + f_e(u_{de}, u_d, u_e) .$$

The chemical reactions on the membrane are now given by the nonlinear functions

$$f_d(u_d, u_e, \tilde{u}_{DT}, \tilde{u}_E) := (k_D + k_{dD} u_d)\tilde{u}_{DT} - u_d\left(k_{dE\tilde{u}_E} + k_{ed} u_e\right) ,$$
$$f_{de}(u_{de}, u_d, u_e, \tilde{u}_E) := u_d(k_{dE}\tilde{u}_E + k_{ed} u_e) - k_{de} u_{de} ,$$
$$f_e(u_{de}, u_d, u_e) := k_{de} u_{de} - u_d k_{ed} u_e - k_e u_e ,$$

with $\tilde{u}_i$ denoting the respective densities in the bulk, but in the immediate vicinity of the membrane. These equations are complemented by nonlinear reactive boundary conditions at the membrane surface:

$$D_c(\nabla_n u_{DD})_m = k_{de} u_{de} ,$$
$$D_c(\nabla_n u_{DT})_m = -(k_D + k_{dD} u_d)\tilde{u}_{DT} ,$$
$$D_c(\nabla_n u_E)_m = k_e u_e - k_{dE}\, u_d \tilde{u}_E ,$$

and a no-flux boundary condition at any non-reactive surfaces. In analogy to the reaction network with MinE-MinD interaction switch, we varied the MinE protein concentration for a fixed MinD concentration and fixed reaction rates (see Supplementary Table 2) and numerically determined the linear stability of the stationary solutions (see Supplementary Note 1). In this way, we identified the regimes of MinE protein concentrations where perturbations with respect to a steady state with uniform protein distribution on the membrane are predicted to grow and form patterns (Supplementary Fig. 2b). The maximal MinE concentration for a fixed

MinD concentration of 1 μM for different reassociation rates and MinE detachment rates is plotted in Supplementary Fig. 2a. We identified the regimes of MinE concentration in which stable pattern formation is predicted in the course of an extensive survey of different reaction rates, and obtained qualitatively similar results in all cases.

Experimental Methods

Protein purification

Expression and purification of His-MinD, His-eGFP-MinD as well as WT and mutant His-MinE were performed as described previously (*29, 6*).

Self-organization assays

Self-organization assays on flat supported lipid bilayers were performed essen- tially as described previously (*29, 6*). Briefly, SLBs composed of *E. coli* polar lipids (Avanti Polar Lipids, Alabaster, AL, USA) were prepared on glass as described in (*29*). Then, 1μM MinD incl. 20% eGFP-MinD, 2.5mM ATP (F. Hoffmann-La Roche AG, Basel, Switzerland) and MinE of varying concentration were added to Min buffer (25 mM Tris-HCl pH 7.5, 150mM KCl, 5mMMgCl2) in a total volume of 200 μL. The samples were then incubated for several hours to provide ample time for protein patterns to form. The concentration ranges compatible with pattern formation reported here were consistently observed in at least three independent experiments. For 0.3μM MinE L3E/I24N, patterns were observed in only 50% of experiments. We therefore categorized this concentration as being incapable of reliable pattern formation.

Microscopy and image processing

Fluorescence imaging was performed with a ZEISS LSM780 confocal laser scan- ning microscope equipped with a Zeiss C-Apochromat 40x/1.20 water-immersion objective (Carl Zeiss AG, Oberkochen, Germany). All images were processed using Fiji. As fluorescence intensities were low around the upper bounds in MinE concentration compatible with pattern formation, we adjusted the brightness and contrast levels to better visualize the transition. As, for consistency, the same

adjustments were equally made for all other images, the intensities in the micrographs corresponding to low MinE concentrations can be displayed outside the dynamic range.

Data availability: All relevant data are within the paper and its Supporting Information files.

References:

1 Kretschmer, S. & Schwille, P. Pattern formation on membranes and its role in bacterial cell division. *Curr Opin Cell Biol* **38**, 52-59, doi:10.1016/j.ceb.2016.02.005 (2016).

2 Schofield, W. B., Lim, H. C. & Jacobs-Wagner, C. Cell cycle coordination and regulation of bacterial chromosome segregation dynamics by polarly localized proteins. *EMBO J* **29**, 3068-3081, doi:10.1038/emboj.2010.207 (2010).

3 Sourjik, V. & Wingreen, N. S. Responding to chemical gradients: bacterial chemotaxis. *Curr Opin Cell Biol* **24**, 262-268, doi:10.1016/j.ceb.2011.11.008 (2012).

4 Bange, G. & Sinning, I. SIMIBI twins in protein targeting and localization. *Nat Struct Mol Biol* **20**, 776-780, doi:10.1038/nsmb.2605 (2013).

5 Leipe, D. D., Wolf, Y. I., Koonin, E. V. & Aravind, L. Classification and evolution of P-loop GTPases and related ATPases. *J Mol Biol* **317**, 41-72, doi:10.1006/jmbi.2001.5378 (2002).

6 Loose, M., Fischer-Friedrich, E., Ries, J., Kruse, K. & Schwille, P. Spatial regulators for bacterial cell division self-organize into surface waves in vitro. *Science* **320**, 789-792, doi:10.1126/science.1154413 (2008).

7 Vecchiarelli, A. G., Li, M., Mizuuchi, M. & Mizuuchi, K. Differential affinities of MinD and MinE to anionic phospholipid influence Min patterning dynamics in vitro. *Mol Microbiol* **93**, 453-463, doi:10.1111/mmi.12669 (2014).

8 Wu, F. *et al.* Multistability and dynamic transitions of intracellular Min protein patterns. *Mol Syst Biol* **12**, 873, doi:10.15252/msb.20156724 (2016).

9 Caspi, Y. & Dekker, C. Mapping out Min protein patterns in fully confined fluidic chambers. *Elife* **5**, doi:10.7554/eLife.19271 (2016).

10 Raskin, D. M. & de Boer, P. A. Rapid pole-to-pole oscillation of a protein required for directing division to the middle of Escherichia coli. *Proc Natl Acad Sci U S A* **96**, 4971-4976 (1999).

11 Fange, D. & Elf, J. Noise-induced Min phenotypes in E. coli. *PLoS Comput Biol* **2**, e80, doi:10.1371/journal.pcbi.0020080 (2006).

12 Halatek, J. & Frey, E. Highly canalized MinD transfer and MinE sequestration explain the origin of robust MinCDE-protein dynamics. *Cell Rep* **1**, 741-752, doi:10.1016/j.celrep.2012.04.005 (2012).

13 Howard, M., Rutenberg, A. D. & de Vet, S. Dynamic compartmentalization of bacteria: accurate division in E. coli. *Phys Rev Lett* **87**, 278102, doi:10.1103/PhysRevLett.87.278102 (2001).

14 Huang, K. C., Meir, Y. & Wingreen, N. S. Dynamic structures in Escherichia coli: spontaneous formation of MinE rings and MinD polar zones. *Proc Natl Acad Sci U S A* **100**, 12724-12728, doi:10.1073/pnas.2135445100 (2003).

15 Schweizer, J. *et al.* Geometry sensing by self-organized protein patterns. *Proc Natl Acad Sci U S A* **109**, 15283-15288, doi:10.1073/pnas.1206953109 (2012).

16 Hu, Z., Gogol, E. P. & Lutkenhaus, J. Dynamic assembly of MinD on phospholipid vesicles regulated by ATP and MinE. *Proc Natl Acad Sci U S A* **99**, 6761-6766, doi:10.1073/pnas.102059099 (2002).

17 Lutkenhaus, J. The ParA/MinD family puts things in their place. *Trends Microbiol* **20**, 411-418, doi:10.1016/j.tim.2012.05.002 (2012).

18 Hu, Z. & Lutkenhaus, J. Topological regulation of cell division in E. coli. spatiotemporal oscillation of MinD requires stimulation of its ATPase by MinE and phospholipid. *Mol Cell* **7**, 1337-1343 (2001).

19 Loose, M., Fischer-Friedrich, E., Herold, C., Kruse, K. & Schwille, P. Min protein patterns emerge from rapid rebinding and membrane interaction of MinE. *Nat Struct Mol Biol* **18**, 577-583, doi:10.1038/nsmb.2037 (2011).

20 Vecchiarelli, A. G. *et al.* Membrane-bound MinDE complex acts as a toggle switch that drives Min oscillation coupled to cytoplasmic depletion of MinD. *Proc Natl Acad Sci U S A* **113**, E1479-1488, doi:10.1073/pnas.1600644113 (2016).

21 Zieske, K. & Schwille, P. Reconstitution of self-organizing protein gradients as spatial cues in cell-free systems. *Elife* **3**, doi:10.7554/eLife.03949 (2014).

22 Park, K. T. *et al.* The Min oscillator uses MinD-dependent conformational changes in MinE to spatially regulate cytokinesis. *Cell* **146**, 396-407, doi:10.1016/j.cell.2011.06.042 (2011).

23 Park, K. T., Villar, M. T., Artigues, A. & Lutkenhaus, J. MinE conformational dynamics regulate membrane binding, MinD interaction, and Min oscillation. *Proc Natl Acad Sci U S A*, doi:10.1073/pnas.1707385114 (2017).

24 Shamir, M., Bar-On, Y., Phillips, R. & Milo, R. SnapShot: Timescales in Cell Biology. *Cell* **164**, 1302-1302 e1301, doi:10.1016/j.cell.2016.02.058 (2016).

25 Shih, Y. L., Fu, X., King, G. F., Le, T. & Rothfield, L. Division site placement in E.coli: mutations that prevent formation of the MinE ring lead to loss of the normal midcell arrest of growth of polar MinD membrane domains. *EMBO J* **21**, 3347-3357, doi:10.1093/emboj/cdf323 (2002).

26 Zheng, M. *et al.* Self-assembly of MinE on the membrane underlies formation of the MinE ring to sustain function of the Escherichia coli Min system. *J Biol Chem* **289**, 21252-21266, doi:10.1074/jbc.M114.571976 (2014).

27 Arjunan, S. N. & Tomita, M. A new multicompartmental reaction-diffusion modeling method links transient membrane attachment of E. coli MinE to E-ring formation. *Syst Synth Biol* **4**, 35-53, doi:10.1007/s11693-009-9047-2 (2010).

28 Kretschmer, S., Zieske, K. & Schwille, P. Large-scale modulation of reconstituted Min protein patterns and gradients by defined mutations in MinE's membrane targeting sequence. *PLoS One* **12**, e0179582, doi:10.1371/journal.pone.0179582 (2017).

29 Halatek, J. & Frey, E. Effective 2D model does not account for geometry sensing by self-organized proteins patterns. *Proc Natl Acad Sci U S A* **111**, E1817, doi:10.1073/pnas.1220971111 (2014).

30 Klunder, B., Freisinger, T., Wedlich-Soldner, R. & Frey, E. GDI-mediated cell polarization in yeast provides precise spatial and temporal control of Cdc42 signaling. *PLoS Comput Biol* **9**, e1003396, doi:10.1371/journal.pcbi.1003396 (2013).

31 Laan, L., Koschwanez, J. H. & Murray, A. W. Evolutionary adaptation after crippling cell polarization follows reproducible trajectories. *Elife* **4**, doi:10.7554/eLife.09638 (2015).

Acknowledgments: We thank Laeschkir Hassan, Fridtjof Brauns for discussions, and the MPI-B Core Facility for help with protein purification. E.F acknowledges support from the DFG via project B02 and P.S. via the project A09 within SFB 1032 and the German Excellence Initiatives via the 'NanoSystems Initiative Munich (NIM)'. J.D. and S.K. are supported by a DFG fellowship through the Graduate School of Quantitative Biosciences Munich (QBM).

Author contributions: J.H., J.D., S.K., P.S., and E.F. designed the research. J.D., J.H, C.H., and E.F. performed the mathematical analyses. S.K. and P.S. designed and carried out the experiments. J.D., S.K., J.H., P.S., and E.F. discussed and interpreted the results, and wrote the manuscript. All relevant data are within the paper and its Supporting Information files.

Competing financial interest: The authors declare no competing financial interest.

Figures

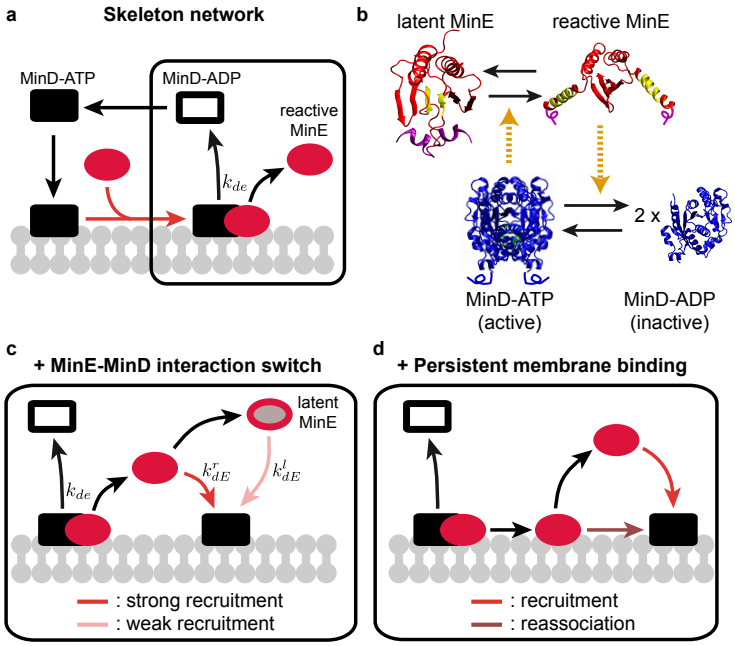

Figure 1. **MinE's conformational switch suggests distinct ways to form MinDE complexes.** (**a**) The skeleton model only accounts for one MinE conformation. (**b**) Scheme of interlinked MinDE protein switches: Whereas reactive MinE is known to trigger MinD's ATPase activity, membrane-bound (active) MinD induces a switch of MinE from a latent to a reactive state with inaccessible or exposed MinD interaction region (yellow) and membrane-targeting sequence (purple), respectively. (PDBs 1EVO, 2KXO and 3Q9L illustrate latent and reactive MinE and MinD, respectively). (**c**) The proposed extension to the skeleton network includes a MinE-MinD interaction switch for interconversion between latent and reactive states of MinE, which are weakly or strongly recruited to MinD with rates k^l_{dE} or k^r_{dE}, respectively. (**d**) Persistent MinE membrane binding allows MinDE complexes to form either by recruitment of cytosolic MinE or reassociation of membrane-bound MinE with membrane-bound MinD.

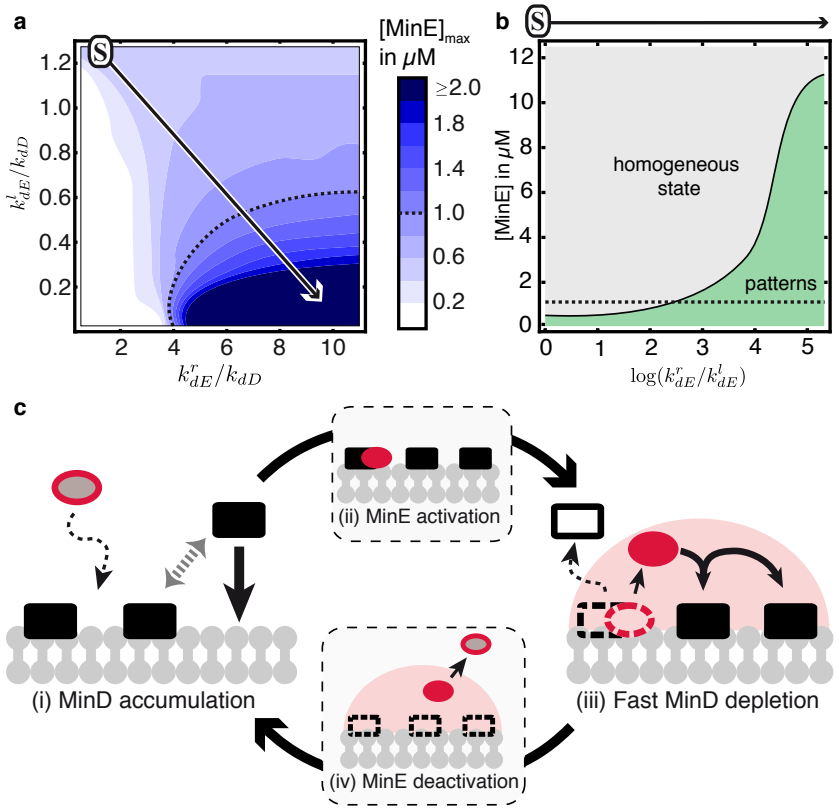

Figure 2. **The MinE-MinD interaction switch is essential for the robustness of Min patterns *in silico*.** (**a**) For high k_{dE}^{r} and low k_{dE}^{l} (compared to the MinD recruitment rate k_{dD}), linear stability analysis predicts an increase in the maximal MinE concentration compatible with patterns ($[\mathrm{MinE}]_{\max}$) relative to the skeleton network where $k_{dE}^{r} = k_{dE}^{l}$ (indicated by S). [MinD] is fixed at 1 μM. (**b**) Along the trajectory (I) in (**a**) the range of [MinE] compatible with patterns increases with k_{dE}^{r} / k_{dE}^{l}. (**c**) MinD-induced switching of MinE facilitates alternation of MinD accumulation and MinD depletion. For kinetic rates see Supplementary Tables 1, 2.

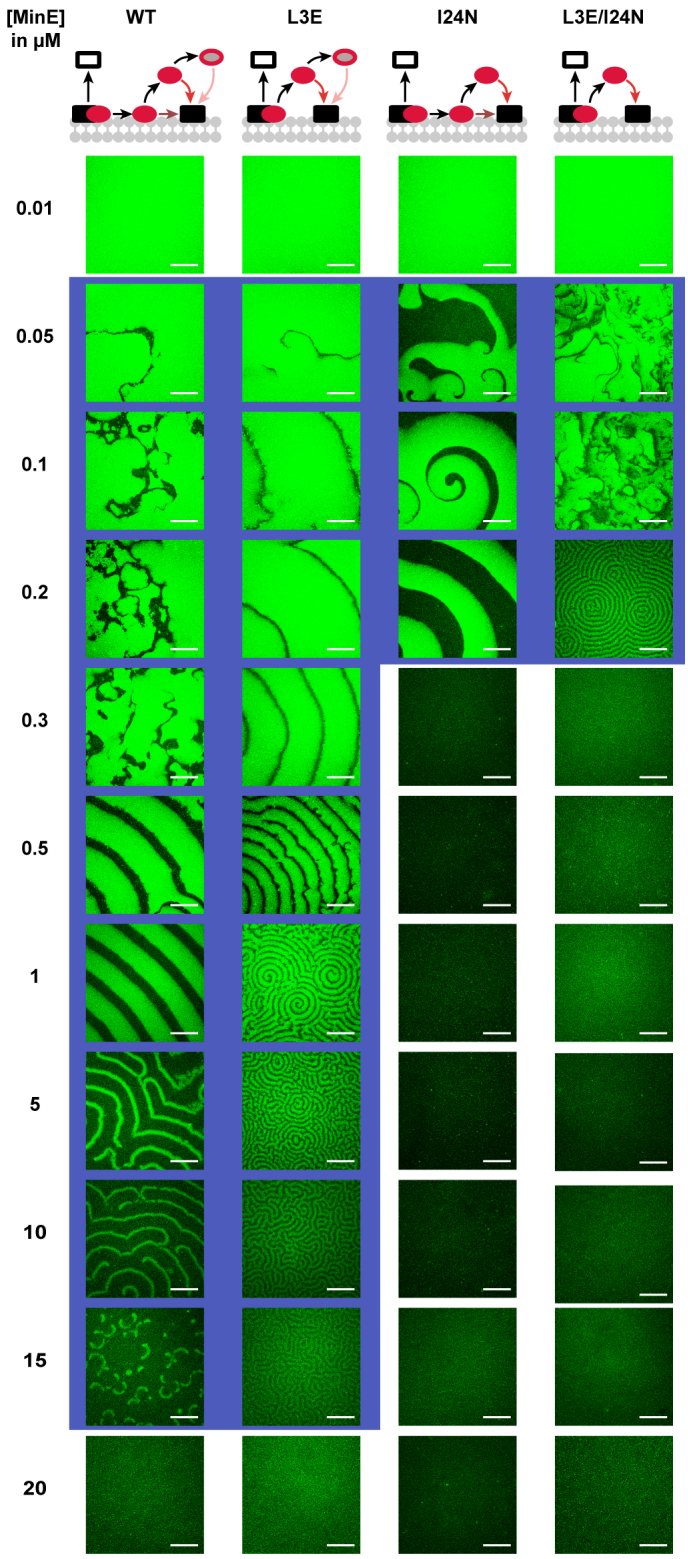

Figure 3. Impairment of MinE's MinE-MinD interaction switch dramatically decreases the robustness of Min protein patterns *in vitro*. Reconstitution assays were performed on flat supported lipid bilayers in the presence of 1 µM MinD with 20 % eGFP-MinD. The L3E mutation, which impairs MinE membrane binding, permits pattern formation over a similar range of MinE concentrations as WT MinE (purple background). In contrast, the I24N mutation, which locks MinE into its reactive conformation, dramatically decreases the maximal MinE concentration at which patterns can form. Scale bar: 50 µm.

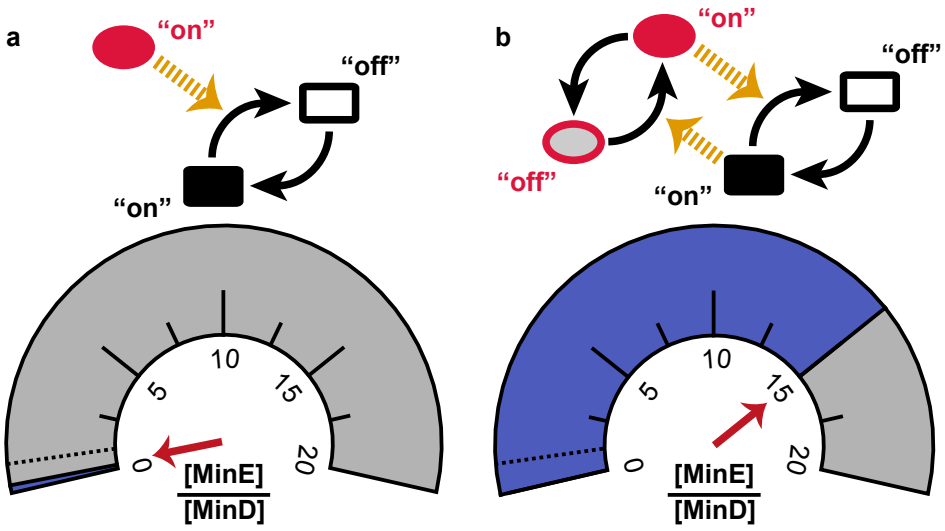

Figure 4. Mutually interlinked switching dramatically increases the robustness of protein pattern formation. (**a**) The MinE variants in which the MinE-MinD interaction switch is disabled (I24N and L3E/I24N) display patterns only within a narrow range (purple region) of MinE/MinD ratios below 1 (dotted line). (**b**) In contrast, variants that retain the interaction switch (WT and L3E) also form patterns even when MinE is present in great excess. The schematic networks highlight the roles of MinE and MinD in dynamically switching the activity of their respective interaction partner.

Mutually interlinked protein switches are essential for the robustness of protein patterns

Supplementary Information

J. Denk[1,*], S. Kretschmer[2,*], J. Halatek[1,*], C. Hartl[1], P. Schwille[2], and E. Frey[1]

[1]*Arnold Sommerfeld Center for Theoretical Physics and Center for NanoScience, Department of Physics, Ludwig-Maximilians-Universität München, Theresienstraße 37, D-80333 München, Germany*
[2]*Max-Planck-Institute of Biochemistry, Am Klopferspitz 18, D-82152 Martinsried, Germany*
[*]*These authors contributed equally*

Supplementary Note 1: Reaction-diffusion equations accounting for a MinD-dependent switch of MinE

Reaction-diffusion equations including a MinE-MinD interaction switch

We base our mathematical models on previous models[1–3] for the Min system that account for the molecular interactions that are taken to be essential for the Min protein dynamics. This model, which we referred to as *skeleton network* in the manuscript, includes the following set of biochemical reactions (Supplementary Figure 1a):

1. The attachment of MinD-ATP from the bulk, u_{DT}, to the membrane with rate constant k_D.

2. The recruitment of bulk MinD-ATP, u_{DT}, to the membrane by membrane bound MinD, u_d, with rate constant k_{dD}.

3. The formation of membrane bound MinDE complexes, u_{de}, through the recruitment of bulk MinE.

4. The disintegration and detachment of membrane bound MinDE complexes, u_{de}, into bulk MinD-ADP, u_{DD}, and bulk MinE with rate k_{de}.

5. The reactivation of bulk MinD-ADP, u_{DD}, by nucleotide exchange to MinD-ATP, u_{DT}, with rate λ.

To incorporate a MinE-MinD interaction switch of MinE we extend this skeleton network by the following reactions (Supplementary Figure 1b):

1. MinE exists in a latent and a reactive conformation, $u_{E,l}$ and $u_{E,r}$, respectively. The recruitment rates of latent and reactive MinE, k^l_{dE} and k^r_{dE}, respectively, can be different while the skeleton network is recovered for $k^r_{dE} = k^l_{dE}$, i.e. if there is only one MinE conformation.

2. recruitment of latent or reactive MinE leads to the formation of MinDE complexes, in which MinE exists in its reactive form. After disintegration and detachment of membrane-bound MinDE complexes bulk MinE persists in its reactive form for a very short time before it undergoes a conformational switch to latent MinE with a rate μ.

All components are able to diffuse in their respective domains (bulk or membrane). Since only the distinction between bulk and membrane diffusion is important for the dynamics, and since the diffusion coefficients with a domain (bulk

or membrane) are very similar for different proteins, we only distinguish between bulk and membrane diffusion with diffusion constants D_c for the bulk and D_m for the membrane, respectively.

In coordinate-free form (with index c or m denoting that an operator acts in the bulk or at the membrane, respectively) the ensuing system of partial differential equations for a model with MinE-MinD interaction switch reads:

$$\partial_t u_{DD} = D_c \nabla_c^2 u_{DD} - \lambda u_{DD}\,, \tag{1a}$$
$$\partial_t u_{DT} = D_c \nabla_c^2 u_{DT} + \lambda u_{DD}\,, \tag{1b}$$
$$\partial_t u_{E,r} = D_c \nabla_c^2 u_{E,r} - \mu u_{E,r}\,, \tag{1c}$$
$$\partial_t u_{E,l} = D_c \nabla_c^2 u_{E,l} + \mu u_{E,r}\,, \tag{1d}$$
$$\partial_t u_d = D_m \nabla_m^2 u_d + f_d(u_d, \tilde{u}_{DT}, \tilde{u}_{E,r}, \tilde{u}_{E,l}), \tag{1e}$$
$$\partial_t u_{de} = D_m \nabla_m^2 u_{de} + f_{de}(u_{de}, u_d, \tilde{u}_{E,r}, \tilde{u}_{E,l})\,, \tag{1f}$$

where the biochemical reactions on the membrane are given by the nonlinear functions

$$f_d(u_d, \tilde{u}_{DT}, \tilde{u}_{E,r}, \tilde{u}_{E,l}) := (k_D + k_{dD} u_d)\,\tilde{u}_{DT} - u_d\,(k_{dE}^l \tilde{u}_{E,l} + k_{dE}^r \tilde{u}_{E,r})\,, \tag{2a}$$
$$f_{de}(u_{de}, u_d, \tilde{u}_{E,r}, \tilde{u}_{E,l}) := u_d\,(k_{dE}^l \tilde{u}_{E,l} + k_{dE}^r \tilde{u}_{E,r}) - k_{de}\,u_{de}\,, \tag{2b}$$

with $\tilde{u}_i$ denoting the respective bulk densities right at the membrane. These equations are complemented by nonlinear reactive boundary conditions at the membrane surface stating that the biochemical reactions involving both membrane-bound and bulk proteins equal the diffusive flux onto $(-)$ and off $(+)$ the membrane (the index n denoting the outward normal vector at the boundary)

$$D_c \nabla_n u_{DD}\big|_m = k_{de}\,u_{de} =: f_{DD}\,, \tag{3a}$$
$$D_c \nabla_n u_{DT}\big|_m = -(k_D + k_{dD} u_d)\,\tilde{u}_{DT} =: f_{DT}\,, \tag{3b}$$
$$D_c \nabla_n u_{E,r}\big|_m = k_{de}\,u_{de} - k_{dE}^r\,u_d\,\tilde{u}_{E,r} =: f_{E,r}\,, \tag{3c}$$
$$D_c \nabla_n u_{E,l}\big|_m = -k_{dE}^l\,u_d\,\tilde{u}_{E,l} =: f_{E,l}\,, \tag{3d}$$

and no-flux boundary condition at any non-reactive surfaces (denoted by the index s)

$$D_c \nabla_n u_{DD}\big|_s = 0\,, \tag{4a}$$
$$D_c \nabla_n u_{DT}\big|_s = 0\,, \tag{4b}$$
$$D_c \nabla_n u_{E,r}\big|_s = 0\,. \tag{4c}$$
$$D_c \nabla_n u_{E,l}\big|_s = 0\,. \tag{4d}$$

The above set of reaction-diffusion equations locally conserve the total mass of MinD as well as MinE. This implies that the spatial averages, $\overline{[\mathrm{MinD}]}$ and $\overline{[\mathrm{MinE}]}$, of the total densities of MinD and MinE obey the relation

$$\overline{[\mathrm{MinD}]}\,\Omega = \int_\Omega \mathrm{d}c\ (u_{DD}+u_{DT}) + \int_{\delta\Omega} \mathrm{d}m\ (u_d+u_{de})\,, \tag{5a}$$

$$\overline{[\mathrm{MinE}]}\,\Omega = \int_\Omega \mathrm{d}c\ (u_{E,r}+u_{E,l}) + \int_{\delta\Omega} \mathrm{d}m\ u_{de}\,, \tag{5b}$$

where $\int_\Omega \mathrm{d}c$ and $\int_{\delta\Omega}\mathrm{d}m$ signify integration over the whole bulk volume Ω and membrane surface $\delta\Omega$, respectively. In order to study the robustness of patterns against variations in protein concentrations we performed extensive parameter scans in $\overline{[\mathrm{MinE}]}$ and $\overline{[\mathrm{MinD}]}$. We found that changing the total protein concentration $\overline{[\mathrm{MinE}]}+\overline{[\mathrm{MinD}]}$ only yields quantitative changes in the robustness. We therefore focused on varying $\overline{[\mathrm{MinE}]}$ while fixing $\overline{[\mathrm{MinD}]}$ to the experimental concentration of 1μM.

The advantage of such a general (coordinate-free) model definition is that it can be adjusted to any system geometry, allowing to consistently use the same model for different experimental setups. For the *in vitro* experiments a simple box geometry is typically used, where the lipid bilayer (membrane) is located at the bottom of the box and the bulk extends into the vertical direction. All other boundaries are reflective. Since the lateral extension of *in vitro* box geometries is typically very large $\mathscr{O}(10^3\mu m)$ compared to the wavelength of the patterns $\mathscr{O}(10\,\mu m)$, we perform our analyses in a two-dimensional box of length $L = 250\mu m$ and employ periodic boundary conditions on the two sides. The bottom of the box represents the membrane with reactive boundary conditions and we assume no-flux boundary conditions on the top of the box (Supplementary Figure 1c). The height h of the experimental box geometry is similarly very large $\mathscr{O}(10^3\mu m)$ such that the dynamics perpendicular to the membrane can, in principle, not be neglected[4].

Reaction-diffusion equations including persistent membrane binding of MinE

In addition to the biochemical reactions of the skeleton network, we included the following biochemical reactions to allow for persistent membrane binding of MinE (Supplementary Figure 1d):

1. MinE exists in only one conformation, u_E, and is recruited by membrane-bound MinD, u_d to the membrane with a rate k_{dE}, which leads to the forma-

tion of MinDE complexes, u_{de}. Membrane-bound MinDE complexes disintegrate with a rate k_{de} whereupon MinD-ADP detaches into the bulk and MinE remains membrane-bound.

2. Free, membrane-bound MinE, u_e, reassociates with membrane-bound MinD, u_d, with a rate k_{ed} or detaches from the membrane with a rate k_e.

In coordinate-free form (with index c or m denoting that an operator acts in the bulk or at the membrane, respectively) the ensuing system of partial differential equations for a model accounting for persistent membrane binding of MinE reads:

$$\partial_t u_{DD} = D_c \nabla_c^2 u_{DD} - \lambda u_{DD}\,, \tag{6a}$$
$$\partial_t u_{DT} = D_c \nabla_c^2 u_{DT} + \lambda u_{DD}\,, \tag{6b}$$
$$\partial_t u_E = D_c \nabla_c^2 u_E\,, \tag{6c}$$
$$\partial_t u_d = D_m \nabla_m^2 u_d + f_d(u_d, u_e, \tilde{u}_{DT}, \tilde{u}_E), \tag{6d}$$
$$\partial_t u_{de} = D_m \nabla_m^2 u_{de} + f_{de}(u_{de}, u_d, u_e, \tilde{u}_E)\,, \tag{6e}$$
$$\partial_t u_e = D_m \nabla_m^2 u_e + f_e(u_{de}, u_d, u_e)\,, \tag{6f}$$

where the biochemical reactions on the membrane are given by the nonlinear functions

$$f_d(u_d, u_e, \tilde{u}_{DT}, \tilde{u}_E) := (k_D + k_{dD} u_d)\,\tilde{u}_{DT} - u_d\,(k_{dE}\tilde{u}_E + k_{ed} u_e)\,, \tag{7a}$$
$$f_{de}(u_{de}, u_d, u_e, \tilde{u}_E) := u_d\,(k_{dE}\tilde{u}_E + k_{ed} u_e) - k_{de}\,u_{de}\,, \tag{7b}$$
$$f_e(u_{de}, u_d, u_e) := k_{de}\,u_{de} - u_d\,k_{ed} u_e - k_e u_e\,, \tag{7c}$$

with $\tilde{u}_i$ denoting the respective bulk densities right at the membrane. The reactive boundary conditions at the membrane surface read:

$$D_c \nabla_n u_{DD}|_m = k_{de}\,u_{de} =: f_{DD}\,, \tag{8a}$$
$$D_c \nabla_n u_{DT}|_m = -(k_D + k_{dD} u_d)\,\tilde{u}_{DT} =: f_{DT}\,, \tag{8b}$$
$$D_c \nabla_n u_E|_m = k_e\,u_e - k_{dE}\,u_d\,\tilde{u}_E =: f_E\,, \tag{8c}$$

and no-flux boundary condition at any non-reactive surfaces (denoted by the index s)

$$D_c \nabla_n u_{DD}|_s = 0\,, \tag{9a}$$
$$D_c \nabla_n u_{DT}|_s = 0\,, \tag{9b}$$
$$D_c \nabla_n u_E|_s = 0\,. \tag{9c}$$

The spatial averages, $\overline{[\mathrm{MinD}]}$ and $\overline{[\mathrm{MinE}]}$, of the total densities of MinD and MinE obey the relation

$$\overline{[\mathrm{MinD}]}\,\Omega = \int_{\Omega} \mathrm{d}c\ (u_{DD} + u_{DT}) + \int_{\delta\Omega} \mathrm{d}m\ (u_d + u_{de} + u_e)\,, \tag{10a}$$

$$\overline{[\mathrm{MinE}]}\,\Omega = \int_{\Omega} \mathrm{d}c\ u_E + \int_{\delta\Omega} \mathrm{d}m\ (u_{de} + u_e)\,, \tag{10b}$$

Again, to study the robustness of patterns against variations in protein concentrations we performed extensive parameter scans in $\overline{[\mathrm{MinE}]}$ and $\overline{[\mathrm{MinD}]}$ and then fixed $\overline{[\mathrm{MinD}]}$ to $1\mu\mathrm{M}$ while varying $\overline{[\mathrm{MinE}]}$.

Linear stability analysis in a box geometry

In order to make predictions about the stability of steady solutions, we performed linear stability analyses of the sets of equations (1)–(9). The starting point of a linear stability analysis is the computation of a steady state around which the system can be linearised. In the box geometry under consideration the steady state is spatially uniform along the membrane (in the lateral direction). Along the vertical direction, however, the nucleotide exchange and the MinE-MinD interaction switch in the bulk induce density gradients even for the steady state. Here, one considers the time evolution of small perturbations with respect to the resprective steady states. When the (exponential) growth rate of these perturbations is positive, these perturbations grow and will eventually lead to spatial or temporal patterns. In contrast, for negative growth rates perturbations decay and the system will eventually relax to a stable steady state, which is uniform on the membrane. Calculating the growth rates of small perturbations for different rate constants and protein concentrations thus yields the regimes in terms of these parameters where patterns are predicted or where uniform protein concentrations on the membrane prevail.

In the following we will focus on the linear stability analysis of the network inculding a MinE-MinD interaction switch. The stability analysis for the network with persistent MinE membrane binding is carried out analogously. In the following we consider a 2D slice geometry as described above, with the lateral dimension x and the extended bulk dimension z. A spatially uniform state at the membrane means that $\nabla_x u_i = 0$ for all protein densities. Using the network with a MinE-MinD interaction switch, eqs.(1),(3)–(4), the stationary density profiles in the bulk are then given by

$$u_{DD}(z) = \tilde{u}^*_{DD} \frac{\cosh\left((h-z)/\ell_D\right)}{\cosh\left(h/\ell_D\right)}, \tag{11a}$$

$$u_{DT}(z) = \tilde{u}^*_{DT} + \tilde{u}^*_{DD}\left(1 - \frac{\cosh\left((h-z)/\ell_D\right)}{\cosh\left(h/\ell_D\right)}\right), \tag{11b}$$

$$u_{E,r}(z) = \tilde{u}^*_{E,r} \frac{\cosh\left((h-z)/\ell_E\right)}{\cosh\left(h/\ell_E\right)}, \tag{11c}$$

$$u_{E,l}(z) = \tilde{u}^*_{E,l} + \tilde{u}^*_{E,r}\left(1 - \frac{\cosh\left((h-z)/\ell_E\right)}{\cosh\left(h/\ell_E\right)}\right), \tag{11d}$$

$$\tag{11e}$$

where $\tilde{u}^*_i$ denote the spatially uniform stationary bulk densities at the membrane, and $\ell_D = \sqrt{D_c/\lambda}$ and $\ell_E = \sqrt{D_c/\mu}$ give the penetration depth of respectively MinD-ADP and reactive MinE into the bulk; note that the corresponding stationary profiles

of the total mass densities, $u_E(z) = u_{E,r}(z) + u_{E,l}(z)$ and $u_D(z) = u_{DD}(z) + u_{DT}(z)$, are spatially uniform in the bulk. Upon inserting all these stationary bulk density profiles into the reactive boundary conditions at the membrane, (3), one finds

$$\ell_D\, \tilde{u}^*_{DD} \tanh(h/\ell_D) = f_{DD}(u^*_{de})/\lambda\,, \tag{12a}$$
$$-\ell_D\, \tilde{u}^*_{DD} \tanh(h/\ell_D) = f_{DT}(\tilde{u}^*_{DT}, u^*_d)/\lambda\,, \tag{12b}$$
$$\ell_E\, \tilde{u}^*_{E,r} \tanh(h/\ell_E) = f_{E,r}(u^*_{de}, u^*_d, \tilde{u}^*_{E,r})/\mu\,, \tag{12c}$$
$$-\ell_E\, \tilde{u}^*_{E,l} \tanh(h/\ell_E) = f_{E,r}(\tilde{u}^*_{E,l}, u^*_d)/\mu\,, \tag{12d}$$
$$\tag{12e}$$

which are complemented by the stationarity conditions for the membrane dynamics, Eq. (1d)-(1e),

$$0 = f_d(u_d, \tilde{u}_{DT}, \tilde{u}_{E,r}, \tilde{u}_{E,l})\,, \tag{13a}$$
$$0 = f_{de}(u_{de}, u_d, \tilde{u}_{E,r}, \tilde{u}_{E,l})\,. \tag{13b}$$

Moreover, the stationary states have to satisfy global mass conservation

$$\overline{[\mathrm{MinD}]} = \tilde{u}^*_{DD} + \tilde{u}^*_{DT} + (u^*_d + u^*_{de})/h\,, \tag{14a}$$
$$\overline{[\mathrm{MinE}]} = \tilde{u}^*_{E,r} + \tilde{u}^*_{E,l} + u^*_{de}/h\,. \tag{14b}$$

In a linear stability analysis one considers the time evolution of small perturbations with respect to these stationary states, i.e. $u_i(x,z,t) = u^*_i(z) + \delta u_i(x,z,t)$ (where membrane densities lack the dependence on the z-coordinate). Expanding the dynamics of the small perturbations in terms of Fourier modes

$$\delta u_{DD}(x,z,t) = \sum_q e^{\sigma_q t} \cos(qx)\, \zeta_{DD}(z;q)\,, \tag{15a}$$
$$\delta u_{DT}(x,z,t) = \sum_q e^{\sigma_q t} \cos(qx)\, \zeta_{DT}(z;q)\,, \tag{15b}$$
$$\delta u_{E,r}(x,z,t) = \sum_q e^{\sigma_q t} \cos(qx)\, \zeta_{Eo}(z;q)\,, \tag{15c}$$
$$\delta u_{E,l}(x,z,t) = \sum_q e^{\sigma_q t} \cos(qx)\, \zeta_{Ec}(z;q)\,, \tag{15d}$$
$$\delta u_d(x,t) = \sum_q e^{\sigma_q t} \cos(qx)\, \delta\tilde{u}^q_d\,, \tag{15e}$$
$$\delta u_{de}(x,t) = \sum_q e^{\sigma_q t} \cos(qx)\, \delta\tilde{u}^q_{de}\,, \tag{15f}$$

and inserting $u_i(x,z,t) = u^*_i(z) + \delta u_i(x,z,t)$ into the (linear) bulk diffusion equations

(Eq. 1a-1c) and taking the boundary conditions (Eq. 3a-4b) into account, the corresponding bulk functions $\zeta_i(z;q)$ are obtained analytically as

$$\zeta_{DD}(z;q) = \delta\tilde{u}^q_{DD}\ \frac{\cosh\left(\frac{h-z}{\ell_q(\lambda+\sigma_q)}\right)}{\cosh\left(\frac{h}{\ell_q(\lambda+\sigma_q)}\right)}, \tag{16a}$$

$$\zeta_{DT}(z;q) = (\delta\tilde{u}^q_{DT}+\delta\tilde{u}^q_{DD})\ \frac{\cosh\left(\frac{h-z}{\ell_q(\sigma_q)}\right)}{\cosh\left(\frac{h}{\ell_q(\sigma_q)}\right)} - \delta\tilde{u}^q_{DD}\ \frac{\cosh\left(\frac{h-z}{\ell_q(\lambda+\sigma_q)}\right)}{\cosh\left(\frac{h}{\ell_q(\lambda+\sigma_q)}\right)}, \tag{16b}$$

$$\zeta_{Eo}(z;q) = \delta\tilde{u}^q_{E,r}\ \frac{\cosh\left(\frac{h-z}{\ell_q(\mu+\sigma_q)}\right)}{\cosh\left(\frac{h}{\ell_q(\mu+\sigma_q)}\right)}, \tag{16c}$$

$$\zeta_{Ec}(z;q) = (\delta\tilde{u}^q_{E,r}+\delta\tilde{u}^q_{E,l})\ \frac{\cosh\left(\frac{h-z}{\ell_q(\sigma_q)}\right)}{\cosh\left(\frac{h}{\ell_q(\sigma_q)}\right)} - \delta\tilde{u}^q_{E,r}\ \frac{\cosh\left(\frac{h-z}{\ell_q(\mu+\sigma_q)}\right)}{\cosh\left(\frac{h}{\ell_q(\mu+\sigma_q)}\right)}, \tag{16d}$$

$$\tag{16e}$$

where we have defined

$$\ell_q(\chi_q) := \sqrt{\frac{D_c}{\chi_q + D_c q^2}}, \tag{17}$$

generalising the penetration depths ℓ_D and ℓ_E to wave vector dependent quantities, and $\delta\tilde{u}^q_i$ are Fourier coefficients that depend on the wavenumber q.

Using the shorthand notation for a term describing the coupling between the membrane concentrations and the density profiles in the bulk

$$\Gamma_q(\chi_q) = \frac{D_c}{\ell_q(\chi_q)}\tanh\left(\frac{h}{\ell_q(\chi_q)}\right), \tag{18}$$

and the first Taylor coefficient for the reaction terms

$$f^i_j = \left.\frac{\partial f_j(\mathbf{u})}{\partial u_i}\right|_{\mathbf{u}=\mathbf{u}^*}, \tag{19}$$

the linear system reads $\mathscr{L}_q\,\delta\tilde{\mathbf{u}}_q = 0$, for each $\delta\tilde{\mathbf{u}}_q = \left[\delta\tilde{u}^q_{DD}, \delta\tilde{u}^q_{DT}, \delta\tilde{u}^q_{E,r}, \delta\tilde{u}^q_{E,l}, \delta\tilde{u}^q_{d}, \delta\tilde{u}^q_{de}\right]^T$, where $\mathscr{L}_q$ is given by

$$\mathscr{L}_q = \begin{bmatrix} f_{DD}^{DD}-\Gamma_q(\sigma_q+\lambda) & f_{DD}^{DT} & f_{DD}^{Eo} \\ f_{DT}^{DD}+\Gamma_q(\sigma_q+\lambda)-\Gamma_q(\sigma_q) & f_{DT}^{DT}-\Gamma_q(\sigma_q) & f_{DT}^{Eo} \\ f_{Eo}^{DD} & f_{Eo}^{DT} & f_{Eo}^{Eo}-\Gamma_q(\sigma_q+\mu) \\ f_{Ec}^{DD} & f_{Ec}^{DT} & f_{Ec}^{Eo}+\Gamma_q(\sigma_q+\mu)-\Gamma_q(\sigma_q) \\ f_{d}^{DD} & f_{d}^{DT} & f_{d}^{Eo} \\ f_{de}^{DD} & f_{de}^{DT} & f_{de}^{Eo} \end{bmatrix}$$

$$\begin{bmatrix} f_{DD}^{Ec} & f_{DD}^{d} & f_{DD}^{de} \\ f_{DT}^{Ec} & f_{DT}^{d} & f_{DT}^{de} \\ f_{Eo}^{Ec} & f_{Eo}^{d} & f_{Eo}^{de} \\ f_{Ec}^{Ec}-\Gamma_q(\sigma_q) & f_{Ec}^{d} & f_{Ec}^{de} \\ f_{d}^{d}-\sigma_q-D_m q^2 & f_{d}^{de} & \\ f_{de}^{Ec} & f_{de}^{d} & f_{de}^{de}-\sigma_q-D_m q^2 \end{bmatrix} \tag{20}$$

The first four rows of $\mathscr{L}_q$ are the linearisation of the reactive boundaries Eq. (3), and the last two rows are the linearisation of the membrane dynamics Eq. (1d)-(1e).

The dispersion relation $\max \mathrm{Re}[\sigma_q]$ (i.e. the fastest growth rates of each wavenumber q) are then obtained as solutions of

$$\det \mathscr{L}_q = 0\,. \tag{21}$$

Since $\mathscr{L}_q$ is non-algebraic in σ_q, solutions can only be obtained numerically. For this purpose we use the iterative solver `FindRoot[]` provided by Wolfram Mathematica 11 to compute the data used in Fig. 2a,b,d, and e in the main text. Here, we tested the stability of perturbations of wavelengths in a range of approx. $5-250\mu m$ to cover the lengthscale of experimentally observed patterns.

The parameter values used in the linear stability analysis for the network with MinE-MinD interaction switch and persistent membrane binding of MinE are given in Supplementary Tables 1 and 2, respectively.

Supplementary Note 2: Relation of MinE mutant proteins to model extensions

Here, we discuss how the biochemical characteristics of the tested MinE variants (Fig. 3) relate to our reaction networks (Fig. 1).

WT MinE

As stated in the main text, MinE is recruited to membrane-bound MinD, whereupon it forms a MinDE complex in its reactive conformation. Upon stimulation of MinD's ATPase activity, disintegration of the complex and MinD detachment, MinE can stay attached to the membrane, a behavior termed persistent binding. In the persistently membrane-bound state, MinE can either reassociate with another MinD on the membrane or detach from the membrane and quickly revert to its latent state in the bulk phase. It can then again be recruited to membrane-bound MinD either in the short-lived reactive or, after conformational switching, in the latent state. Experiments[5–7] suggest that attachment of MinE to the membrane depends on prior interaction with membrane-bound MinD[5–7].

MinE L3E

The L3 residue lies on the hydrophobic face of MinE's amphipathic membrane targeting sequence[6,8] and is inserted into the lipid bilayer during membrane interaction[8]. Thus, substitution with a polar residue is expected to impair membrane binding. In agreement with this, *in vivo* experiments confirmed that this mutation perturbs membrane interaction[6]. In these experiments, the L3E mutation was introduced on top of the I25R or I24N mutation, both of which release the MTS and thereby bypass the need for MinD to enable MinE membrane attachment[6]. Such deliberate exposure of the MTS is a necessary step to test MinE membrane interaction independent of MinD binding. As the I24N mutation locks MinE in its reactive conformation with exposed MTS[6], this state also represents the conformation of MinE that would persist on the membrane after MinD detachment. As the L3E mutation disrupts membrane interaction of MinE I24N[6], we reason that it also abolishes persistent membrane interaction of MinE. In conclusion, these observations indicate that MinE L3E can neither bind to, nor persist on the membrane in the absence of MinD.

We note that Park et al.[6] suggested that the L3E mutation also interferes with MinE's sensing of MinD, i.e. the MinD-dependent conversion of MinE from the latent to the reactive state. However, there is no experimental evidence for this

notion, which was based on the observation that the L3E mutation resulted in a defect in cell division and colony growth *in vivo*[6]. In principle, it would be possible that the L3E mutation slows down recruitment of MinE to MinD. However, it is impossible that the mutant is completely deficient in binding to MinD, as this would impair its ability to form patterns and stimulate MinD's ATPase activity. In contrast, we observe pattern formation with the L3E mutant and even in a similar range as for WT MinE (Fig. 3).

In summary, the L3E mutation is a suitable means to impair persistent MinE membrane binding without disabling MinE's conformational switch. Therefore, it emulates our model extension with MinE-MinD interaction switch but without MinE membrane interaction.

MinE I24N

As noted above, the I24N mutation locks MinE in its membrane- and MinD-interactive conformation[6]. In this state, the $\beta 1$ strand of each MinE subunit in the dimer is converted to a contact helix that interacts with MinD in the membrane-bound MinDE complex[6]. The reactive state of MinE is expected to have a higher affinity to MinD than the latent form, which is incorporated as fast and slow recruitment in our model, respectively. Thus, locking MinE in the reactive conformation through the I24N mutation prevents switching to the latent form, resulting in an overall higher affinity and faster recruitment to membrane-bound MinD.

Besides modulating MinE's affinity to MinD, the I24N mutation also impacts MinE's ability to interact with the membrane[6]. Like the WT, MinE I24N would be expected to persist on the membrane even in the absence of MinD. In conclusion, the I24N mutation disrupts reversion of MinE from the reactive to the latent state, without disabling persistent MinE membrane binding.

We note that, due to its constitutively exposed MTS, MinE I24N is expected to have a higher effective membrane affinity than the WT. In particular, it can bind to the membrane independent of recruitment by MinD[6]. However, we argue that direct membrane binding is not responsible for the observed change in robustness for MinE I24N, as detailed below (see Supplementary Note 5).

MinE L3E/I24N

This double mutant combines the effects of the I24N and L3E mutations. Consequently, the mutant cannot undergo switching from the reactive to the latent form. Furthermore, even though the MTS is exposed, the L3E mutation prevents the mutant from binding the membrane directly or persistently[6]. Due to these deficiencies

in switching and membrane interaction, MinE L3E/I24N closely mimics the skeleton network[1,2] (Fig. 1a).

Supplementary Note 3: Thickness of reactive MinE layer

In the network with MinE-MinD interaction switch, after detachment of MinE from the membrane MinE remains in its reactive state until it quickly reassumes its latent form of low MinD binding affinity at a rate μ. Thus, the region in which reactive MinE exists is limited by the region it can diffuse through before it changes its conformation. The extension of this region into the bulk is given by the penetration depth of reactive MinE, $\ell_E = \sqrt{D_c/\mu}$, as defined in . For our analyses we assumed $D_c = 60\ \mu m^2 s^{-1}$ and $\mu = 100 s^{-1}$ such that $\ell_E = \sqrt{0.6}\mu m \approx 0.77\mu m$. The vertical extension of the box geometry used in our analyses is assumed to be $5000\mu m$ which is a good approximate of the bulk height in our *in vitro* experiments. This means that a bulk layer of reactive MinE that is three orders of magnitude thinner than the total bulk is sufficient to dramatically increase the robustness of patterns as shown in Fig. 2a,b in the main text.

Supplementary Note 4: Effect of persistent MinE membrane binding on the concentration range of pattern formation

To determine the impact of persistent membrane binding on the concentration range of pattern formation we studied a reaction network in which MinE remains on the membrane after detachment of MinD (see). Membrane-bound MinE can either detach at a rate k_e or reassociate at a rate $k_e d$ with membrane-bound MinD to form a new MinDE complex (Supplementary Figure 1d). We find that this model exhibits two qualitatively different regimes (Supplementary Figure 2), depending on whether reassociation with MinD or detachment of MinE is the faster process. If MinE detachment is dominant, the range of MinE/MinD ratios that allows pattern formation increases, as previously suggested[1] (Supplementary Figure 2b). Conversely, if reassociation is favoured, the maximal MinE/MinD ratio compatible with pattern formation decreases as the residence time of free MinE on the membrane is increased (Supplementary Figure 2c).

In analogy to the case with MinE-MinD interaction switch the change in robustness can be understood by considering the opposing roles of MinE and MinD in the establishment of Min oscillations. As detailed in the main text, for the skeleton network the alternation of MinD accumulation and MinE-dependent MinD depletion on the membrane requires the rate of MinE recruitment to be higher while MinD

has to be more abundant.

In our network with persistent MinE membrane binding we found that for 'slow' reassociation, i.e. when reassociation of membrane-bound MinE with membrane-bound MinD is slower than detachment of free MinE from the membrane, we found that the maximal MinE/MinD ratio compatible with pattern formation increases as the residence time of free MinE on the membrane is increased. As previously suggested[1], in this case, persistent membrane binding would partially sequester MinE on the membrane where it hardly contributes to the formation of MinDE complexes. This sequestration partially disables MinE in its action to deplete MinD on the membrane and thereby enables MinD accumulation for an increased MinE to MinD ratio (Supplementary Figure 2b).

For 'fast' reassociation, i.e. when reassociation of free membrane-bound MinE with membrane-bound MinD is faster than detachment of free MinE from the membrane, the maximal MinE/MinD ratio compatible with pattern formation decreases as the residence time of free MinE on the membrane is increased (the y-axis of Supplementary Figure 2a shows the minimal residence time of MinE on the membrane with persistent membrane binding $(1/k_{ed} + 1/k_e)$ as compared to the residence time without persistent membrane binding $(1/k_{ed})$). We argue, that for fast reassociation, the overall binding of free MinE to MinD on the membrane is amplified with respect to the skeleton network, which in turn favors depletion over accumulation of MinD on the membrane. As a consequence, initial MinD accumulation and subsequent patterns require lower MinE/MinD ratios than without persistent membrane binding (Supplementary Figure 2c).

These predictions can be tested with the MinE I24N mutant, which is capable of persistent membrane binding but defective in the MinE-MinD interaction switch as discussed above. As noted above, I24N mutant patterns only form in a very narrow range of MinE/MinD concentration ratios far below 1 (Fig. 3, 4). This demonstrates that, unlike the MinE-MinD switch, persistent MinE membrane binding cannot explain the robustness of *in vitro* Min patterns.

Supplementary Note 5: Direct membrane binding of the I24N mutant does not cause the poor robustness of patterns

After we theoretically studied persistent MinE membrane binding in the absence of a MinE-MinD interaction switch, we employed the MinE I24N mutant to experimentally test our theoretical predictions. The MinE I24N mutant is deficient in conformational switching while retaining the ability to independently bind to the membrane[6]. In addition to the persistent MinE membrane binding included in our

mathematical approach (6)–(9), MinE I24N is also able to directly bind to the membrane even in the absence of MinD due to its permanently exposed MinD binding reagion and membrane targeting sequence[6]. To rule out that the observed change in robustness for MinE I24N is due to direct membrane attachment of MinE, and not to the lack of a MinE-MinD interaction switch, we included an extra term in the equations (6)–(9) which enables direct attachment of MinE with a rate k_E. The terms f_E and f_e then read:

$$f_E := k_e u_e - k_{dE} u_d \tilde{u}_E - k_E \tilde{u}_E \tag{22}$$

$$f_e := k_E \tilde{u}_E + k_{de} u_{de} - u_d k_{ed} u_e - k_e u_e \,. \tag{23}$$

We performed a parameter scan in the MinE attachment rate k_E of MinE to the membrane. For low values of k_E the range of MinE/MinD ratios compatible with pattern formation only changes quantitatively (Supplementary Figure 3), i.e. it does not change the effect of an increase or decrease in the maximal MinE concentration compatible with patterns for slow or fast reassociation, respectively. In particular, for slow or fast reassociation, the respective increase or decrease of the maximal MinE/MinD ratio compatible with pattern formation is merely amplified. Only for very high k_E, when attachment of MinE is more than two orders of magnitude faster than attachment of MinD ($k_E \gtrsim 100 k_D$), the range of MinE/MinD where patterns are predicted decreases and shifts to lower MinE/MinD values for slow as well as fast reassociation. This is likely because for high k_E MinE is so abundant on the membrane that reassociation of free MinE and MinD on the membrane becomes more likely than MinE sequestration.

However, we note that the rate of the direct attachment of MinE is very likely of the same order of the MinD attachment rate or even smaller considering the approximately equal lengths of MinD's and MinE's amphipathic membrane targeting sequences[6,9]. Thus, direct membrane binding very likely only changes the effect of persistent membrane binding quantitively; however, it cannot yield a decrease in the range of predicted patterns, where persistent membrane binding alone would yield an increase of this range. Furthermore, the I24N/L3E double mutant, which lacks persistent as well as direct membrane binding, shows patterns in the same narrow range of protein concentrations as the I24N mutant. This demonstrates that the dramatic decrease of robustness of patterns is due to the lack of a MinE-MinD interaction switch and rules out direct MinE attachment as responsible for poor robustness.

Supplementary Tables

Parameter	Symbol	Value
MinD and MinE bulk diffusion	D_c	$60\,\mu m^2 s^{-1}$
MinD and MinDE membrane diffusion	D_m	$0.013\,\mu m^2 s^{-1}$
MinD mean total density	$\overline{[\mathrm{MinD}]}$	$638\,\mu m^{-3}$
MinD attachment rate constant	k_D	$0.065\,\mu m s^{-1}$
MinD recruitment rate constant	k_{dD}	$0.02\,\mu m^3 s^{-1}$
MinDE detachment rate	k_{de}	$0.34\,s^{-1}$
Nucleotide exchange rate	λ	$6\,s^{-1}$
Conformational switch of MinE	μ	$100\,s^{-1}$

Supplementary Table 1. Kinetic rate constants for the MinE-MinD interaction switch network. The values of the diffusion coefficients and protein densities are chosen in accordance with experimental data[7]. The kinetic rate constants are chosen within the order of magnitude of the values fitted to reproduce the *in vitro* phenomenology qualitatively and the wavelengths and -velocities quantitatively within the order of magnitude of the experimental data. In our analyses we performed extensive parameter scans in the recruitment rates k^r_{dE} and k^l_{dE} and the mean total MinE density $\overline{[\mathrm{MinE}]}$.

Parameter	Symbol	Value
MinD and MinE bulk diffusion	D_c	$60\,\mu m^2 s^{-1}$
MinD and MinDE membrane diffusion	D_m	$0.013\,\mu m^2 s^{-1}$
MinD mean total density	$\overline{[\mathrm{MinD}]}$	$638\,\mu m^{-3}$
MinD attachment rate constant	k_D	$0.065\,\mu m s^{-1}$
MinD recruitment rate constant	k_{dD}	$0.02\,\mu m^3 s^{-1}$
MinE recruitment rate constant	k_{dE}	$0.126\,\mu m^3 s^{-1}$
MinDE disintegration rate	k_{de}	$0.34\,s^{-1}$
Nucleotide exchange rate	λ	$6\,s^{-1}$

Supplementary Table 2. Kinetic rate constants for the network including persistent MinE membrane binding. All rates that appear in both studied networks, the one with a MinE-MinD interaction switch and the one with persistent MinE membrane binding, are chosen equal. To study the impact of persistent membrane binding on the robustness of patterns, we performed extensive scans in MinE's reassociation rate k_{ed} with MinD and its detachment rate k_e from the membrane and the mean total MinE density $\overline{[\mathrm{MinE}]}$.

Supplementary Figures

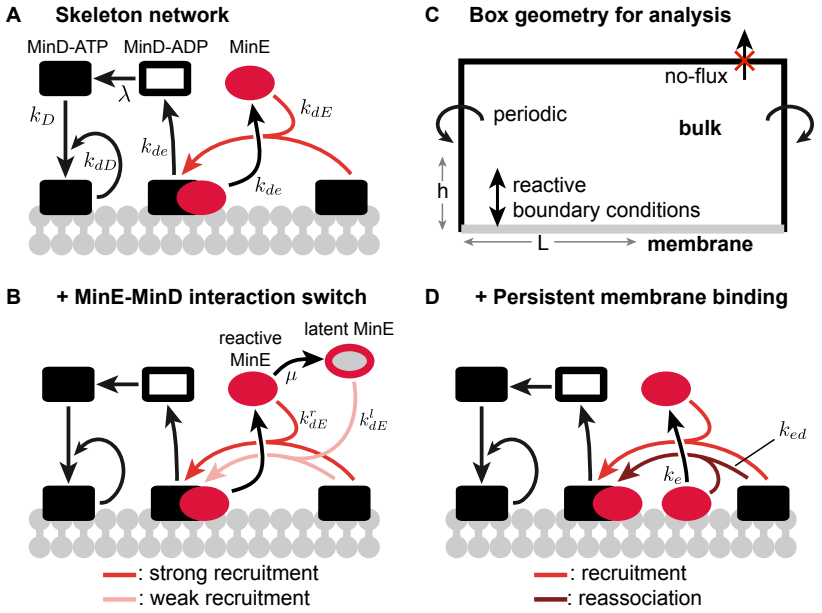

Supplementary Figure 1. Studied reaction networks. (**a**), In the previously studied skeleton network[1], MinD-ATP attaches to the membrane, where it recruits further MinD-ATP and MinE. Upon recruitment of MinE, MinE and membrane-bound MinD form a membrane-bound MinDE complex. MinE induces a switch of MinD to its ADP-bound form and thereby leads to MinDE disintegration and detachment of MinD-ADP and MinE into the cyctosol. There, MinD has to exchange ADP for ATP before it can attach to the membrane anew. The kinetic rates are indicated next to arrows of their respective reactions. (**b**), To emulate a MinE-MinD interaction switch, the respective reaction network includes a switch with rate μ from reactive MinE with a high recruitment rate k^r_{dE} to latent MinE with a low recruitment rate k^l_{dE}. (**c**), Since the lateral extension of patterns *in vitro* are typically very large compared to their wavelength, we assume a reduced box geometry. Here, the membrane is modeled as the bottom line. The perturbations in our linear stability analysis are given by planar waves extending along the membrane. (**d**), When MinE is able to persist on the membrane after MinD detachment, it can either reassociate with membrane-bound MinD at a rate k_{ed} or detach at a rate k_e.

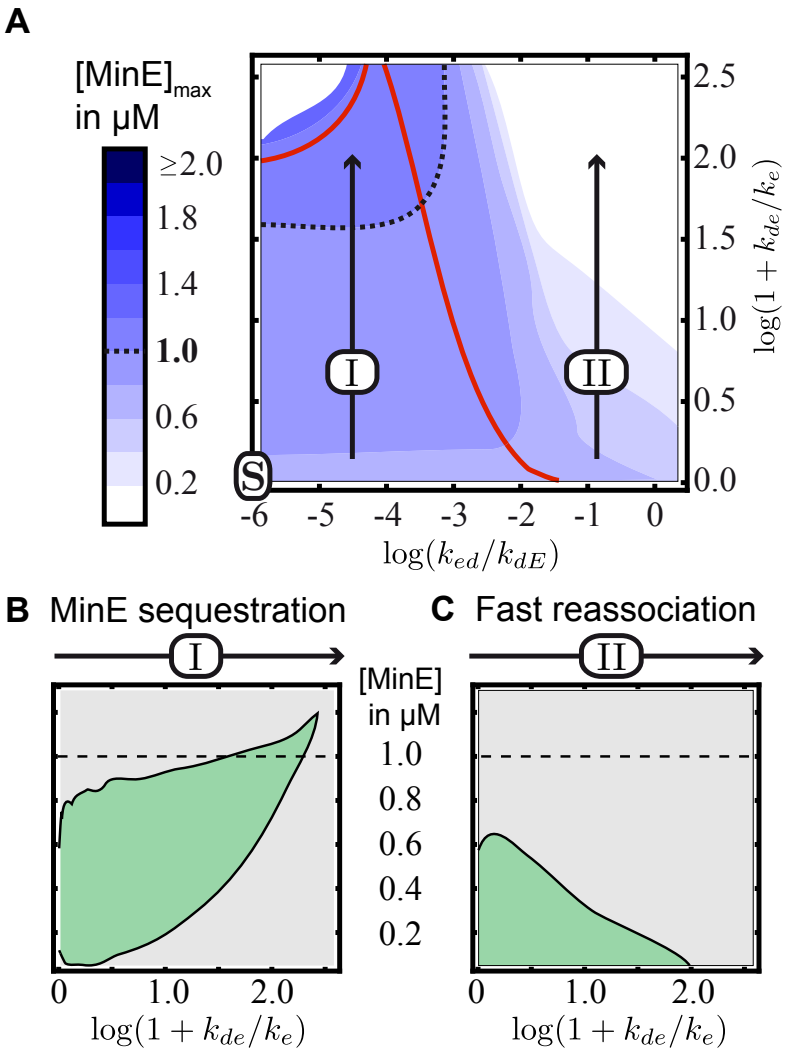

Supplementary Figure 2. Persistent membrane binding can modulate the range of pattern formation *in silico*. (**a**) Persistent MinE membrane binding can either increase or decrease $[MinE]_{\max}$, depending on whether detachment or reassociation is favored (inside or outside the red lines), respectively (red lines denote equal detachment and reassociation). The y-axis depicts the minimal persistence time of MinE (compared to the disintegration time $1/k_{de}$). (**b**), (**c**) Along the trajectories (I) and (II) in (**a**) the region of MinE concentrations compatible with patterns increases (**b**) and shifts to higher $[MinE]$ or decreases (**c**), when detachment or reassociation is favored, respectively.

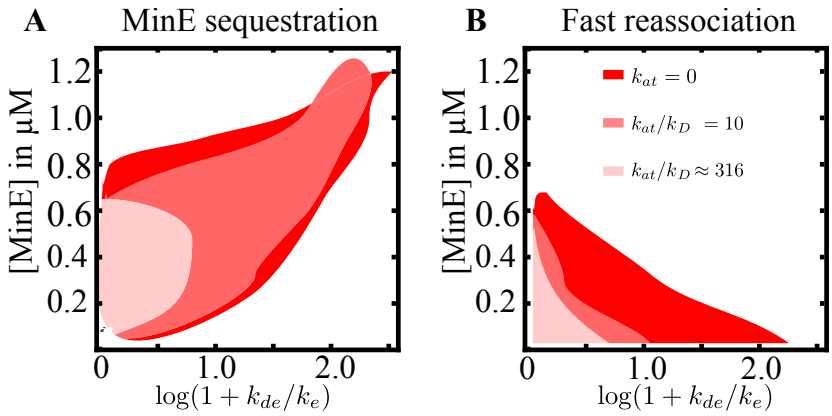

Supplementary Figure 3. Theory suggest that direct MinE attachment is not responsible for the the poor robustness of Min patterns. (**a**), For slow reassociation ($\log(k_{ed}/k_{dE}) \approx -4.5$) the region of MinE concentrations compatible with patterns (colored regions) is only changed qualitatively for unphysiologically high k_{at}. (**b**), For fast reassociation ($\log(k_{ed}/k_{dE}) \approx -1$), increasing k_{at} amplifies the decrease of the maximal MinE/MinD ratio compatible with pattern formation.

References

1. Halatek, J. & Frey, E. Highly canalized MinD transfer and MinE sequestration explain the origin of robust MinCDE-protein dynamics. *Cell reports* **1,** 741–52. ISSN: 2211-1247 (June 2012).
2. Huang, K. C., Meir, Y. & Wingreen, N. S. Dynamic structures in Escherichia coli: spontaneous formation of MinE rings and MinD polar zones. *Proceedings of the National Academy of Sciences of the United States of America* **100,** 12724–8. ISSN: 0027-8424 (Oct. 2003).
3. Wu, F. *et al.* Multistability and dynamic transitions of intracellular Min protein patterns. *Molecular Systems Biology* **12,** 642–653. ISSN: 1744-4292 (June 2016).
4. Halatek, J. & Frey, E. Effective 2D model does not account for geometry sensing by self-organized proteins patterns. *Proceedings of the National Academy of Sciences of the United States of America* **111,** E1817. ISSN: 1091-6490 (2014).
5. Hu, Z., Gogol, E. P. & Lutkenhaus, J. Dynamic assembly of MinD on phospholipid vesicles regulated by ATP and MinE (2002).
6. Park, K.-T. *et al.* The Min Oscillator Uses MinD-Dependent Conformational Changes in MinE to Spatially Regulate Cytokinesis. *Cell* **146,** 396–407. ISSN: 0092-8674 (2011).
7. Loose, M., Fischer-Friedrich, E., Herold, C., Kruse, K. & Schwille, P. Min protein patterns emerge from rapid rebinding and membrane interaction of MinE. *Nature structural & molecular biology* **18,** 577–83. ISSN: 1545-9985 (May 2011).
8. Shih, Y. L. *et al.* The N-terminal Amphipathic Helix of the topological specificity factor mine is associated with shaping membrane curvature. *PLoS ONE* **6.** ISSN: 19326203. doi:10.1371/journal.pone.0021425 (2011).
9. Szeto, T. H., Rowland, S. L., Rothfield, L. I. & King, G. F. Membrane localization of MinD is mediated by a C-terminal motif that is conserved across eubacteria, archaea, and chloroplasts. *Proceedings of the National Academy of Sciences of the United States of America* **99,** 15693–8. ISSN: 0027-8424 (Nov. 2002).

XI Geometry and mass-conservation: Why a rigorous account for the system geometry and total protein numbers is important

This chapter is based on the following publication:

Effective two-dimensional model does not account for geometry sensing by self-organized proteins patterns

by

J. Halatek and E. Frey

Department of Physics, Arnold Sommerfeld Center for Theoretical Physics and

Center for NanoScience, Ludwig-Maximilians-Universität München,

Theresienstraße 37, 80333 München, Germany

Journal Reference:

***Proc. Natl. Acad. Sci. U.S.A.* 111, 2014**

Supplemental Material reproduced on pages 494 to 525.

Effective two-dimensional model does not account for geometry sensing by self-organized proteins patterns

Jacob Halatek and Erwin Frey
Arnold-Sommerfeld-Center for Theoretical Physics and Center for NanoScience, Department of Physics, Ludwig-Maximilians-Universität München, Theresienstraße 37, D-80333 München, Germany

LETTER TO THE EDITOR

Subject article: Schweizer, J., Loose, M.,Bonny, M., Kruse, K., Mönch, I., and Schwille, P., Geometry sensing by self-organized protein patterns, *Proc. Natl. Acad. Sci. USA*, **109**, 15283-15288 (2012)

By means of a computational model analysis accompanying new intriguing experiments, Schweizer et al. [1] claim to show that MinE membrane binding is responsible for self-organized geometry sensing.

We investigated the simulation files provided by the authors and found that the model neither accounts for actual MinE membrane interactions nor for any observed MinDE protein patterns. It does not reproduce any of the computational data presented in the article [1]. For the published parameters, pattern formation is restricted to very small cytosol/membrane ratios. Cytosolic volume is not accounted for and total densities indicate an effective bulk height below $6\mu m$. We find that scaling the cytosolic dynamics by a small factor $\mathcal{O}(1)$ or increasing gold layer size eliminates the instability. Hence, the model configuration deviates from the experiment by orders of magnitude. In striking contradiction to the accompanying experiments and to the claim in the article, bulk volume has a severe effect on the computational model. The authors compensated for this system size dependence by adjusting intrinsic system parameters (MinE/MinD ratio) without mentioning it. Moreover, the adjusted parameters deviate from the experimental value while the published parameters do not.

Even with these adjustments the model relies on simulation artifacts to reproduce the experimental data. Alignment to the aspect ratio requires periodic boundaries at the gold layer. The alignment angle is controlled by cross-boundary coupling in horizontal and vertical directions. The aspect ratio of the patch has a negligible effect on alignment. Without periodic boundaries or for gold layers sizes as used in the experiment alignment ceases and waves become disordered blobs. This invalidates the model on a conceptual level.

The model is claimed to extend and supersede previous models by incorporating experimental evidence regarding MinE membrane interactions [3, 4]. We note that MinE membrane binding was already proposed and analyzed by Arjunan and Tomita [2]. Moreover, the model contradicts the experimental references in several aspects. Park et al. [4] have shown that unmasking the

anti-MinCD domains in $\mathrm{MinE}^{F7E/I24N}$ restores the wild type phenotype without membrane binding. In contrast, computational patterns are lost if MinE membrane binding is reduced and cannot be recovered by adjusting MinE recruitment. Hence, the model actually implies that MinE membrane binding is required for pattern formation in the first place and not for geometry sensing in particular as the paper claims. The ratio of MinE/MinD residence times quantifies the relative strength of MinE membrane binding. It has been quantified experimentally by Loose et al.[3]. The value in the computational model exceeds the experimental value by an order of magnitude. As a consequence MinDE waves contain about ten times more MinE than MinD, in contradiction to experiments [3, 5]. In particular, we note that the computational data in Figure 5C cannot be reproduced. We find a 16-fold increased MinE/MinD ratio, which represents a 23-fold deviation from the cited experiments [3].

We conclude that the computational model is invalid and any conclusions drawn from it are void.

[1] Schweizer, J., Loose, M.,Bonny, M., Kruse, K., Mönch, I., and Schwille, P., Geometry sensing by self-organized protein patterns. *Proc. Natl. Acad. Sci. USA* **109,** 15283-15288 (2012).

[2] Arjunan, S.N., and Tomita, M., A new multicompartmental reaction- diffusion modeling method links transient membrane attachment of E. coli MinE to E-ring formation. *Syst. Synth. Biol.* **4,** 25-53 (2009).

[3] Loose, M., Fischer-Friedrich, E., Herold, C., Kruse, K., and Schwille, P., Min protein patterns emerge from rapid rebinding and membrane interaction of MinE. *Nat. Struct. Mol. Biol.* **18,** 577-583 (2011).

[4] Park, K.-T., Wu, W., Battaile, K. P.,Lovell, S., Holyoak, T., and Lutkenhaus, J. The Min Oscillator Uses MinD-Dependent Conformational Changes in MinE to Spatially Regulate Cytokinesis. *Cell* **146,** 396-407 (2011).

[5] Loose, M., Fischer-Friedrich, E., Ries, J., Kruse, K., and Schwille, P. Spatial regulators for bacterial cell division self-organize into surface waves in vitro. *Science* **320,** 789-792 (2008).

Effective two-dimensional model does not account for geometry sensing by self-organized proteins patterns – Supplementary Document –

Jacob Halatek and Erwin Frey
Arnold-Sommerfeld-Center for Theoretical Physics and Center for NanoScience, Department of Physics, Ludwig-Maximilians-Universität München, Theresienstraße 37, D-80333 München, Germany

Subject article: Schweizer, J., Loose, M., Bonny, M., Kruse, K., Mönch, I., and Schwille, P., Geometry sensing by self-organized protein patterns, *Proc. Natl. Acad. Sci. USA*, **109**, 15283-15288 (2012)

CONTENTS

INTRODUCTION

Here we provide a thorough discussion of the model for Min protein dynamics proposed by Schweizer et al. [14]. The manuscript serves as supplementary document for our letter to the editor to appear in PNAS. Our analysis is based on the original COMSOL simulation files that were used for the publication. We show that all computational data in Schweizer et al. rely on exploitation of simulation artifacts and various unmentioned modifications of model parameters that strikingly contradict the experimental setup and experimental data. We find that the model neither accounts for MinE membrane interactions nor for any observed MinDE protein patterns. All conclusions drawn from the computational model are void. There is no evidence at all that persistent MinE membrane binding has any role in geometry sensing.

SUMMARY OF RESULTS AND CONCLUSIONS

- The authors do not use the same parameters that are given in the article but a lower MinE/MinD ratio that also deviates from the experimental value.

- With the experimental MinE/MinD ratio no patterns emerge. (cf. Figure 3)

- With the lower MinE/MinD value patterns emerge but do not resemble the experiments nor the computational data presented in the article. (cf. Figure 4/5)

- The quantitative data presented in Figure 5B/C/D in the paper cannot be reproduced by the proposed model (cf. Figure 7B and section).

- Alignment to the aspect ratio (Figure 5D in the paper) solely relies on self-coupling via the periodic boundaries in horizontal and vertical directions. (cf. Fig. 2/4/5)

- Alignment to curved membranes (Figures 5A/S7 in the paper) fails for gold layer sizes as used in the experiment. (cf. Figure 7D)

- Transient MinE membrane binding is an order of magnitude stronger than in the experiments. (cf. section)

- Adjusting MinE membrane binding to meet the experiment leads to loss of any patterns. (cf. section)
- The model assumes a very small bulk volume and is highly sensitive to volume effects in contrast to the experimental evidence and the claim in the paper. (cf. section)

We investigated the proposed model by means of linear stability analysis and numerical simulations. First, we note that the actual simulations provided to us by the authors use reduced MinE/MinD ratios ($C_{D0}/C_{E0} = 2.23$ and $C_{D0}/C_{E0} = 4.03$) that deviate from the experiments ([MinD]/[MinE]=1.6) and the published parameter values ($C_{D0}/C_{E0} = 1.56$). For the experimental/published values we find pattern formation to be restricted to very small ratios of gold layer to membrane, or equivalently bulk volume to membrane. The model does not account for cytosolic volume explicitly, but the choice of the total protein densities indicates an effective bulk height below $6\mu m$. We find that rescaling the effective bulk volume by a small factor $\mathcal{O}(1)$ or explicitly increasing gold layer size yields loss of instability. Hence, the model behavior described in the published simulations is limited to system sizes that deviate from the experiment by several orders of magnitude. Moreover, in striking contradiction to the accompanying experiments and to the claim in the article, bulk size does have severe effects on protein patterns. The authors have compensated for the effects of reservoir size by adjusting intrinsic system parameters (total protein densities). This was not mentioned in the published article. It should go without saying that the need to adjust genuinely intrinsic system properties to keep certain desired phenomena invariant to variations of system size clearly proves that those phenomena are not intrinsic to the system. This directly contradicts the main experimental findings the model claims to account for.

However, even with these adjustments in place the model relies on employing simulation artifacts to reproduce the published data. We find that alignment to the aspect ratio (Fig. 5D in the paper) strictly requires periodic boundary conditions at the outer boundary of the gold layer. These cross-boundary couplings in horizontal and vertical directions controls the alignment angle, while the aspect ratio of the patch has a negligible effect on alignment. Wave alignment ceases and waves become disordered propagating blobs if gold layer sizes are inclreased to match the experimental setup or if cross-boundary coupling is disabled by replacing periodic boundary conditions with no-flux conditions. Plainly put, for simulations to resemble the presented set of computational

data several distinct and independent artifacts and unphysical parameter adjustments have to be employed for each dataset individually. We were unable to determine the specific combinations of gold layer size, cross-boundary coupling, and total [MinE]/[MinD] density ratio, that yield the published data. Altogether, this invalidates the model on a conceptual level.

The model is claimed to extend and supersede all previous models by incorporating recent experimental evidence [6, 13] regarding MinE membrane interactions. We note that MinE membrane binding was already considered in the computational model by Arjunan and Tomita [1]. Furthermore, the model contradicts the cited experimental references [6, 13] in several implications regarding transient MinE membrane binding.
Park et al. [13] have shown that unmasking the anti-MinCD domains in $\mathrm{MinE}^{F7E/I24N}$ restores the wild type phenotype without membrane binding. We find that the model loses instability if the MinE membrane affinity is reduced. In contrast to the experiment the instability cannot be restored by any adjustment of the MinE recruitment rate (representing the unmasking of anti-MinCD domains). Hence, without any experimental support the model actually implies that MinE membrane binding is required for pattern formation in the first place. The claim that MinE membrane binding is supposed to be responsible for geometry sensing in particular is thereby unsubstantiated.
By means of the ratio of MinE/MinD residence times the relative strength of MinE membrane binding can be quantified. The individual residence times have been determined experimentally by Loose et al.[6]. We find that the value in the computational model exceeds the experimental value by one order of magnitude. While experiments show that the MinE membrane desity is always lower than the MinD density [6, 7], the waves in the computational model contain up to ten times more MinE than MinD. In particular, we note that the computational data in Figure 5C cannot be reproduced. The simulations yield a MinE/MinD density ratio which is increased up to 16-fold compared to the published computational data in Figure 5C. This represents a 23-fold deviation from the experiments cited alongside [6]. The fact that the model assumes wave propagation based on very high concentrations of membrane bound MinE not co-localized with MinD invalidates the model on a qualitative level in addition to the various aforementioned quantitative discrepancies. We conclude that the model neither accounts for MinE membrane interactions nor for any observed MinDE protein patterns. Therefore, all conclusions drawn from the computational model are void.

SIMULATIONS

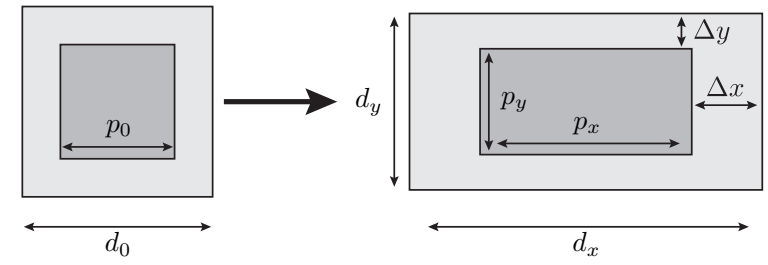

$$d_x = s_x d_0,\ p_x = s'_x p_0$$
$$d_y = s_y d_0,\ p_y = s'_y p_0$$

$$\text{aspect ratio: } a = \frac{p_y}{p_x}$$
$$\text{gold/membrane ratio: } g = \frac{d_x d_y - p_x p_y}{p_x p_y}$$

FIG. 1. Model geometry and scaling operations.

Model files and definitions

Since we were unable to reproduce the published results we asked the authors, following PNAS journal policies, to provide us with the full set of model files that were used to produce the data in the paper and accompanying supplement. The files we received are listed in Table 1 with the corresponding parameter configurations. In contrast to the value given in the paper ($C_{E0} = 1.9 \cdot 10^3/\mu m^2$) the MinE density is set to $C_{E0} = 1.3 \cdot 10^3/\mu m^2$ in all simulations except the one for the L-shaped membrane patch (c.f. Fig 5 in the paper), where it is set to $C_{E0} = 0.72 \cdot 10^3/\mu m^2$. We did not receive an explanation or justification for the use of two different parameter values. Because the modification creates a conflict with the [MinD]/[MinE] ratio in the experiment[10], we will consider both cases in the investigation of the computational model. Table 1 lists the protein densities, and the ratios of gold layer and membrane area used in the simulations. One notices that the gold layer area is always smaller or of comparable size as the membrane area but never very large as the experiments suggest. It is largest for the L-shape simulation where the MinE density is smallest. We further note that the boundary conditions are periodic. In combination with the small gold layer size a coupling of patch dynamics across the periodic boundaries appears likely. This will be

considered below in the context of wave alignment to rectangular membrane patches. The aspect ratio in the corresponding model file is preset to $a = 0.5$. The geometry is constructed by applying scaling operations on two squares with sides d_0 and p_0. The scaling operations are defined in Figure 1. All simulations of rectangular patches with altered aspect ratio or increased gold layer size are derived from this model file. For all simulations we have computed the solutions for $1.6 \cdot 10^4 s$ from onset and compared the results with the solution at $1.2 \cdot 10^4 s$ to ensure that the system reached a steady state. In simulations with increased gold layer sizes we have coarsened the gold layer mesh with increasing distance from the membrane patch. In these cases the mesh size in the gold layer was increased up to 5-fold of the value of the membrane mesh. We have carefully verified that this does not affect the patch dynamics by comparing the results with the simulations that employ a constant mesh size in the gold layer that corresponds to the membrane mesh. In particular, we have compared the onset of pattern formation (first $1000s$) for original and coarse gold layer mesh. In addition we have verified that the final pattern after $1.6 \cdot 10^4 s$ does not change if the simulation is continued for $1000s$ with a constant mesh in the gold layer that equals the membrane mesh.

Simulations with $C_{E0} = 1.9 \cdot 10^3/\mu m^2$ ([MinD]/[MinE] = 1.53)

In all following simulations the total MinE density is set to $C_{E0} = 1.9 \cdot 10^3/\mu m^2$ unless noted otherwise.

Alignment to rectangular membrane patches

The simulation file corresponding to Figure 5D in the original paper (AspectRatio_Paper.mph) produces the reported alignment to the diagonal for the preset aspect ratio $a = 0.5$ (c.f. Figure 2A). We started out increasing the size of the surrounding gold layer ($2d_0$, $g = 5.25$) and found that the system settles in an homogeneous stable state (Figure 2B). This implies that pattern formation requires a very small gold layer to membrane ratio. Next, we went to investigate wave coupling across periodic boundaries and the impact on wave alignment in the original model simulations. To eliminate any possible coupling across periodic boundaries we replaced the periodic condition by a no-flux condition. As a result waves ceased to align to the diagonal in contrast to the data in the original paper. Instead we observed a disordered pattern

filename	C_{D0} $[\mu m^{-2}]$	C_{E0} $[\mu m^{-2}]$	g
AspectRatio_Paper.mph	2.9	1.3	0.56
circle_S7.mph	2.9	1.3	4.13
CouplingD15_S11.mph	2.9	1.3	0.38
CouplingD50_S11.mph	2.9	1.3	0.38
L_shape_Paper.mph	2.9	0.72	6.68
largeGaps_S10.mph	2.9	1.3	1.67
LargePatch_S09.mph	2.9	1.3	0.35
note_S7.mph	2.9	1.3	4.14
serpentine_S7.mph	2.9	1.3	4.16
smallGaps_S10.mph	2.9	1.3	0.61
smallPatch_S9.mph	2.9	1.3	0.86

TABLE I. Comsol Multiphysics simulation files provided by the authors. We list the preset values for the total MinD and MinE densities, C_{D0} and C_{E0}, as well as the gold/membrane ratio g (Fig. 1).

of oscillatory blots without any apparent alignment but with preference for the edges and center of the patch (Figure 2C). This leads us to the conclusion that the alignment observed in the simulation must result from the coupling across periodic boundaries. To shed light on this matter we changed the aspect ratio of the surrounding gold layer, leaving the aspect ratio and size of the membrane patch unaltered. Increasing either the horizontal (x) or vertical (y) width of the gold layer by a factor 1.5 or more resulted in a stable homogeneous state without any pattern on the membrane patches. Increasing the width merely by a factor 1.25 led to a standing wave pattern aligned to the major axis of the patch (Figure 2D). This complex change in dynamics due to a small perturbation of the surrounding geometry strongly indicates that the ratio of gold layer area to membrane area as well as the anisotropic coupling across boundaries mainly regulate the formation and selection of patterns on the rectangular membrane patches. Since the alignment angle is regulated by the aspect ratio of the patch in the experiment one might expect a similar result in the simulation. The paper clearly states that the model accounts

for these experimental findings. In our attempts to reproduce this claim we rescaled the membrane patch along with the surrounding gold layer in order to obtain a membrane patch and gold layer with an aspect ratio of 0.2. For this case the paper reports alignment of waves to the long axis in the experiment as well as in the simulation. In contrast, we find that waves start at the edges of the patch and align to the diagonals in the initial phase. After $1.6 \cdot 10^4 s$ the system consists of a mixture of disordered waves and imperfect drifting spirals with no alignment to a specific axis (Figure 2E). Again, slightly increasing the size of surrounding gold layer leads to a complete loss of any patterns and a spatially uniform density. Increasing the vertical width by a factor 1.25 leads to a pattern of standing nodes attached to the edges of the long axis with odd symmetry with respect to the short axis (Figure 2F). Increasing the horizontal width instead leads to domains forming consecutively in the upper and lower half of the patch (Figure 2G).
To conclude, we find that the published data (Figure 5D in the paper) cannot be recovered. Waves do not align to the aspect ratio of the membrane patch. On the contrary, alignment arises as pure result of the cross-boundary coupling, and only if the surrounding gold layer area is very small compared to the patch size. Hence, alignment is not intrinsic to the membrane geometry as the authors claim but, in fact, the exact opposite: there is no intrinsic alignment (i.e. independent of cross-boundary coupling) to the membrane geometry at all. This point is further emphasized by the simulation that the authors used to investigate decoupling of patters due to increased patch distance (large_gaps_S10.mph). In contrast to the published data (Figure S10B in the paper), we find that the system settles in a homogeneous stationary state (Figure 3A) for the published parameter set.

Alignment to curved membrane patches

The second quantitative dataset provided by the computational analysis in the paper concerns the alignment of Min protein waves to curved membrane patches. In the simulation files the membrane patches are embedded in rectangular domains representing surrounding gold layer. The preset ratio of gold layer area to membrane area g can be found in Table 1. Again, we ran all simulations with the total MinE and MinD concentrations as published in the paper and found that the system settled in a stable homogeneous state (Figure 3A-C). It is obvious that a rectangular domain surrounding curved patches cannot be made arbitrarily small to yield dynamical instabilities. Therefore,

other parameters need to be changed to trigger any pattern formation process and enable comparison with the published results. To reproduce the published results the initial MinE density has been reduced by the authors to $C_{E0} = 1.3 \cdot 10^3/\mu m^2$ ([MinD]/[MinE] = 2.23) in all simulations except the one for the L-shape simulation, in which case the initial MinE concentration had been set to $C_{E0} = 0.72 \cdot 10^3/\mu m^2$, i.e. [MinD]/[MinE] = 4.03. This does not come as a surprise, given that the sensitivity of Min protein patterns to [MinD]/[MinE] ratios is well documented in the literature [3–5, 9]. Nonetheless, the necessity to change this parameter in this particular case directly contradicts the accompanying experiments the model strives to account for. To gather insight into the reported model dynamics we repeated the simulations with the reduced total MinE density that was preset in the simulations files. The results are discussed in the next section.

Simulations with $C_{E0} = 1.3 \cdot 10^3/\mu m^2$ ([MinD]/[MinE] = 2.23)

In all following simulations the total MinE density is set to $C_{E0} = 1.3 \cdot 10^3/\mu m^2$ unless noted otherwise.

Alignment to rectangular membrane patches

Running the simulation of rectangular patches with the preset MinE concentration $C_{E0} = 1.3 \cdot 10^3/\mu m^2$ yields target patterns forming approximately at the center of one of the long edges. The target waves propagate along the short axis (Figure 4A) and the pattern remains disordered. Increasing the size of surrounding gold layer first stabilizes the target pattern and yields clean target waves centered at the edge of the long axis for $2d_0$ (Figure 4B). However, further increase of the gold layer size leads to a destabilization of the target pattern and we observe disordered propagating blots for $5d_0$ (Figure 4C) and disordered standing waves/blots for $10d_0$ (Figure 4D). These waves and blots are typically attached to the inner boundaries of the patch and tend to form and propagate rather chaotically within the patch domain. As none of these patterns resembles the reported data from the paper we investigated the effect of cross-boundary coupling. Increasing the width of the gold layer in either direction yields waves roughly aligned to the diagonal (Figure 4E/F). Leaving the gold layer unaltered but replacing the periodic boundary conditions with no-flux boundary conditions yields disordered waves and blots that are aligned

to the long axis (Figure 4G). Once more, the results indicate that the reported alignment to the diagonal requires careful tuning of the cross-boundary coupling and gold layer size.

To investigate the effect of the patch geometry we repeated the simulations for different aspect ratios of the membrane patch. Rescaling the whole system to obtain a membrane patch with aspect ratio 0.2 yields counter-propagating waves aligned to the diagonal and originating at two diagonally opposed corners (Figure 5A). Note that the paper reports alignment to the long axis for this aspect ratio in the experiment and corresponding simulations. Increasing the horizontal width of the gold layer yields diagonally aligned waves originating from horizontally opposed corners (Figure 5B). We find that the alignment to the long axis requires increasing the vertical width of the rescaled gold layer (Figure 5C). In this case wave originate from all four corners of the patch, and waves originating from vertically opposed corners merge to align to the long axis. However, the pattern is symmetric as counter-propagating waves annihilate each other. As in the previously discussed simulations for patches with aspect ratio $a = 0.5$ we find disordered waves and blots attached to the membrane edges if the area of the gold layer is increased uniformly (Figure 5D). Similar results are obtained for membrane patches with aspect ratio 1 (Figure 5E/F). Hence, any realistically sized gold layer where cross-boundary coupling can be excluded results in a disordered state that does not resemble the experimental or computational data from the paper.

As the experimental data for large membrane patches indicates a much broader distribution of alignment angles one might suspect that the failure of the model originates from the choice of patch size. In particular, the experiments imply that misalignment occurs if the patch is much larger than the wavelength of the patterns. Therefore, we investigated the model dynamics for large gold layers and smaller patches with constant aspect ratio. We find that reducing the patch size to $0.75p_0$ and $0.5p_0$ results in a pure standing wave pattern aligned to the long axis for aspect ratios $a = 0.5$ (Figure 6A/B) and $a = 0.2$ (Figure 6C/D). Hence, the patch size is not the cause for the disordered waves and failed alignment.

We conclude that a commensurable alignment can only be achieved by exploiting cross-boundary coupling effects and tuning the total MinE density. For instance, to recover alignment to the long axis one needs to employ an anisotropic rescaling of the cross-boundary coupling in y-direction and reduce the MinE density. This demonstrates that the [MinE]/[MinD] ratio sensitively regulates the alignment angle in presence of active cross-boundary coupling. Moreover, reducing the total MinE density entails that the dynamical insta-

bility is not lost when the gold layer is increased. This enables us to study the alignment to curved membrane patches in the following section.

Alignment to curved membrane patches

As mentioned above the MinE concentration in the L-shape model file provided by the authors is preset to $C_{E0} = 0.72 \cdot 10^3/\mu m^2$ while it is set to $C_{E0} = 1.3 \cdot 10^3/\mu m^2$ in all other model files (cf. Table 1). For the sake of a systematic study we adjusted the MinE concentration to match all other simulations. With an otherwise unaltered model file we find that wave trains align to the patch as reported in the paper after about $10^4 s$ (Figure 7A). While the phenomenology is quite similar, i.e. waves are aligned to the long rectangular sections then turn into the kink and realign afterwards, neither wave velocities nor [MinE]/[MinD] ratios along the patch match the data from the paper. The paper reports velocities in the range $1.3\mu m/s - 3.2\mu m/s$ (on the rectangular section and at the outer edge of the curve) while we find waves with velocities in the range $0.8\mu m/s - 2.2\mu m/s$. This shows that the data in the paper is not recovered with the current parameters. The ability of waves to realign is ascribed to the dynamics that locally increase the [MinE]/[MinD] ratio (and thereby the wave velocity) at the outer part of the curve. This mechanism for geometry sensing is ascribed to MinE membrane binding, quoting the paper:

> "When we plotted the ratio between the activator MinE and the membrane-bound ATPase MinD along the travel path of the membrane, we found that this ratio is significantly higher at the outer part compared to the inner part of the wave, thereby accelerating the detachment of the proteins from the membrane (23) (Fig. 5C). [...] Importantly, we could only reproduce this behavior when we considered transient binding of MinE to the membrane in our model."

In this context the authors cite their previous work [6] where the local [MinE]/[MinD] ratio within a wave had been quantified. These previous experiments revealed that the [MinE]/[MinD] membrane density ratio peaks at the rear of the wave. The maximal [MinE]/[MinD] ratio is about 0.9 and it marks the point where the protein flux off the membrane is maximized and drives wave propagation. For the computational model the authors report a [MinE]/[MinD] ratio about 1.33 at the outer part vs. 1.15 at the inner part, (cf. Figure 5C in the paper).

We find that the simulations yield a local [MinE]/[MinD] ratio about 21 at the outer part of the curve and 15 at the inner part (Figure 7B). This represents a striking 16-fold deviation from the simulation data in the paper and a 23-fold deviation from the experimental data the authors cite in this particular context to support the model. We have also plotted the mean profile of the [MinE]/[MinD] density ratio on the patch in Figure 7C. Time-integration was performed over 950s which is the period of the envelope modulating the amplitude of the protein waves [2]. As expected the mean [MinE]/[MinD] profile shows a maximum at the outer part of the curve and a minimum at the inside. The mean [MinE]/[MinD] density ratio takes values between 3.6 and 9.5 throughout the patch. Comparison of the wave profile for MinE and MinD densities and [MinE]/[MinD] ratios from the rectangular section of the L-shaped patches with experimental data published by the authors (see supplementary figure 1 in [6]) reveals a similar quantitative inconsistency, cf. Figure 8. We note that these results are equally recovered if the simulations are performed with a further reduced total MinE concentration ($C_{E0} = 0.72 \cdot 10^3/\mu m^2$) that was preset in the model file we received from the authors. The most notable difference was that alignment was already established after about $1000s$ with $C_{E0} = 0.72 \cdot 10^3/\mu m^2$, hence, one order of magnitude earlier than with $C_{E0} = 1.3 \cdot 10^3/\mu m^2$. The origin of the quantitative discrepancies between [MinE]/[MinD] membrane density ratios in the published dataset and the simulations remains elusive. It appears to be intrinsic to the model as it relies on very strong MinE membrane binding. This will be discussed in the next section.

Before we go into that, we address the question if waves are sustained for realistically large gold layers as the experiments dictate. We note that the variation of the cytosolic protein densities is already very small at the system boundary (well below 1%). Still, when the surrounding gold layer is increased ($g = 72$) waves become disordered and cease to align (Figure 7D). This observation is consistent with the previous simulations of rectangular patches (cf. Figure 4C/D and 5D/F). This observation emphasizes that coupling across the periodic boundary and the gold/membrane ratio g are two distinct aspects of the geometry affecting the model dynamics. The irregular waves found for the increased gold layer do not span the patch width but are attached to the interior edges. Also, waves do not align and realign after passing through the curve. Apparently, transient MinE membrane binding does not facilitate the local increase of the [MinE]/[MinD] ratio at the outer part of the curve (Figure 7E/F) any more. To conclude: For simulations to resemble the data depicted in the paper, both, the total MinE density as well as the size of the

surrounding gold layer need to be fine tuned. While this procedure already conflicts with the experiments in the first place, the simulations one recovers deviate from the published experimental and computational data by one order of magnitude in the very quantity that is argued to be key for the phenomenon of geometry sensing that the computational analysis tries to explain.

INCOMPATIBILITY OF MODEL ASSUMPTIONS AND EXPERIMENTAL DATA

So far we have established by means of numerical simulations that the model does not account for any experimental observation in the paper. Clearly, this conflicts with the final conclusion reached by the authors in the paper's abstract:

> "Using a computational model we quantitatively analyzed our experimental findings and identified persistent binding of MinE to the membrane as requirement for the Min system to sense geometry. Our results give insight into the interplay between geometrical confinement and biochemical patterns emerging from a nonlinear reaction-diffusion system."

The molecular basis of the model is set by the authors' previous experimental work [6] and the work by Park et al. [13]. The main intention is to address the role of MinE membrane binding by means of the computational analysis, quoting from the paper:

> "Recently, two reports have shown that MinE persists at the MinD-membrane surface after activation of the MinD ATPase (23, 30). Although persistent binding of MinE appears to be important for its ability to completely remove MinD from the membrane (23), its possible role for the ability of the Min system to organize the interior of the cell has so far not been addressed. Our model extends previous models by incorporating that MinE transiently interacts with the membrane during the activation of MinD. This description gives a unified account of all currently known stable Min-protein patterns in vivo and in vitro as will be discussed in detail elsewhere."

The final statement is proven false by the results from the previous sections. In this context the question arises whether the model can be used for an

assessment of MinE membrane binding at all. The research by Park et al. [13] strongly suggests that MinE membrane interactions take place. We want to emphasize that we do not question these experimental findings in any way. On the contrary we find these results very helpful to understand the molecular basis of MinE protein dynamics as reflected in our own research [3].
In this section we show that the model conflicts with the available experimental evidence in it's molecular basis. Our analysis will show that the model operates in a kinetic regime that contradicts the experimental data. As such, the model is invalid as a theory for MinE membrane interactions. No conclusions about MinE membrane interaction can be drawn from it. To establish a mutual basis in terminology we start by describing how the proposed model introduces MinE membrane interactions. We discuss the distinct molecular processes the model is based on and compare the qualitative and quantitative implications with experimental data. We limit the comparison to experimental research papers that are explicitly cited in the paper to motivate the model. In the last part we will address the role of particle numbers, bulk-membrane ratio, and the validity of an effective 2D modeling.

The role of MinE membrane interactions

The model assumes that cytosolic MinE is able to sense membrane bound MinD-ATP and form a MinDE complex upon recruitment. These two steps are introduced and quantified by the MinE recruitment rate $\omega_E = 5 \cdot 10^{-4} \mu m^2/s$. Upon MinDE complex formation, MinE stimulates MinD ATPase activity which leads to the detachment of MinD-ATP (nucleotide exchange is neglected in the model) from the membrane. The stimulation of MinD ATPase with MinD detachment is quantified by the sum of detachment rates $\omega_{de} \equiv \omega_{de,c} + \omega_{de,m} = 0.88 s^{-1}$. Persistent MinE binding is introduced by enabling the MinE dimer bound in a MinDE complex to directly interact with the membrane. Upon stimulation of MinD ATPase activity MinE remains bound to the membrane with a certain probability $p_m = \omega_{de,m}/\omega_{de} = 0.91$ or detaches instantly along with MinD with probability $p_c = 1 - p_m = \omega_{de,c}/\omega_{de} = 0.09$. Of course, within the notion of a deterministic model p_m and p_c can be interpreted as fraction of MinE concentration that remains membrane bound or becomes cytosolic upon stimulation of MinD ATPase activity, respectively. The strength of the MinE-membrane bond is characterized by the MinE detachment rate $\omega_e = 0.08 s^{-1}$. The parameter $\omega_{ed} = 2.5 \cdot 10^{-3} \mu m^2/s$ quantifies MinE-MinD reassociation at the membrane. All these parameters can be

tuned individually to study the model dynamics. However, no experimental data exists to support any particular parameter choice. Moreover, mutations studies (e.g. regarding the MTS of MinE) are unlikely to affect only one corresponding model parameter alone. To constrain MinE membrane binding and MinE-MinD interactions in the model we will take the experimentally determined Min protein residence times into account. This enables us to establish a direct relation between quantitative experimental data and the corresponding model parameters.

Residence times of Min proteins in vitro

The residence $< \tau_D >$ and $< \tau_E >$ times of MinD and MinE along the protein wave have been quantified by the authors in previous experiments [6]. The experiments revealed that MinE remains longer in a membrane bound state than MinD which indicates transient MinE membrane binding. While the individual residence times increase from front to rear of the wave, the ratio of residence times $\Delta\tau =< \tau_E > / < \tau_D >$ appears to be constant throughout the wave ($\Delta\tau_{\text{exp}} \approx 1.31$). Therefore, we can use the ratio of residence times as characteristic parameter to quantify transient MinE membrane interaction in context of any specific model.
The mean residence time of MinD $< \tau_D >$ is given by the time it takes cytosolic or membrane-bound MinE to sense and attach to a membrane-bound MinD, and the time MinE needs to drive MinD off the membrane. Hence,

$$< \tau_D >= (\omega_E c_E + \omega_{ed} c_e)^{-1} + \omega_{de}^{-1}. \tag{1}$$

For the mean MinE residence time $< \tau_E >$ one has to consider the conditional branches whether MinE detaches alongside MinD (with probability p_c) or remains on the membrane (with probability $p_m = 1 - p_c$), and whether membrane-bound MinE detaches from the membrane (with probability $q_c = \omega_e/(\omega_e + \omega_{ed} c_d)$) or reassociates with MinD (with probability $q_m = 1 - q_c$):

$$< \tau_E >= p_c \omega_{de,c}^{-1} + p_m(\omega_{de,m}^{-1} + q_c \omega_e^{-1} + q_m((\omega_{ed} c_d)^{-1} + < \tau_E >)). \tag{2}$$

After a few algebraic manipulations one obtains an expression for the mean MinE residence time

$$< \tau_E >= \frac{2(\omega_{de,m} + \omega_{ed} c_d + \omega_e)}{\omega_{de,c} \omega_{ed} c_d + \omega_{de} \omega_e}, \tag{3}$$

and for the ratio of the residence times $\Delta\tau$

$$\Delta\tau = \frac{2\omega_{de}(\omega_{de,m} + \omega_{ed}c_d + \omega_e)(\omega_{ed}c_e + \omega_E c_E)}{(\omega_{de,c}\omega_{ed}c_d + \omega_{de}\omega_e)(\omega_{de} + \omega_{ed}c_e + \omega_E c_E)}. \tag{4}$$

By comparison with the experiment ($\Delta\tau_{\text{exp}} \approx 1.31$) we obtain an expression relating all processes that characterize MinE interaction with the membrane to interactions with MinD. Due to the explicit dependency on the protein concentration c_d, c_e, and c_E numerical simulations or additional approximations are required for further progression. We note that for the specific parameter choice in the present model $\Delta\tau$ becomes independent of c_d. The reason is that both exit processes for MinE occur on the same time scale, i.e. $\omega_{de,c} = \omega_e$, such that $< \tau_E > \to 2/\omega_e$ and

$$\Delta\tau \to \frac{1}{p_c} \cdot \frac{2(\omega_{ed}c_e + \omega_E c_E)}{\omega_{de} + \omega_{ed}c_e + \omega_E c_E}. \tag{5}$$

To obtain a first estimate we approximate the missing values for the protein concentrations by the stationary solution that represents the mean concentrations in linear approximation. For the parameters provided in the paper we find $\Delta\tau \approx 14.7$, hence an 11-fold deviation from the experimental value $\Delta\tau_{\text{exp}} \approx 1.31$. We conclude that the model's assumption regarding MinE dynamics (in terms of parameter choice) clearly conflicts with experimental data. It represent the underlying molecular processes. In the following section we will investigate the model's linear stability upon varying the MinE dynamics.

Linear Stability for varying MinE dynamics

The research by Park et al. [13] indicates that membrane associated MinE has an increased MinE-MinD interaction rate due to an exposed contact helix compared to the stable conformation in solution where the contact helix is buried in the dimeric interface. It is our understanding that this is the main idea which defines *persistent binding* [6] and *tarzan of the jungle* [13] models. To keep these mechanisms unaltered while trying to reduce the relative residence times we focus on the isolated effect of MinE membrane interactions. The membrane affinity of MinE can be expressed by $p_m = 1 - p_c$ alone. Tuning this parameter enables a smooth reduction of the relative residence time $\Delta\tau$ without altering the reassociation process with MinD. By decreasing the MinE membrane affinity we find that the dynamical instability is lost for $p_m < 0.72$ at $\Delta\tau = 3.9$, c.f. Figure 9A. Releasing the constraint $\omega_{de,c} = \omega_e$

and increasing ω_e to weaken MinE membrane binding similarly leads to loss of dynamical instability for $\omega_e > 0.65$ at $\Delta\tau = 4.5$, c.f. Figure 9B. We draw two conclusions from these results. First, tweaking the MinE membrane affinity alone proves to be insufficient to recover consistency with the experimental data. It appears that the problems are at least inherent to the parameter configuration as a whole (in particular, the MinE-MinD interactions) such that the model requires a broad reinvestigation in it's vast parameter space.[11] Second, the fact that the model requires at least 72% of MinE remaining membrane bound after stimulating MinD ATPase activity implies that strong membrane interactions are a key requirement for pattern formation in the proposed model. Translated into an experimental test a hypothetical MinE mutant with slightly reduced membrane binding affinity but otherwise unaltered protein-protein interactions should lack any Min oscillations. In that case one would expect to observe the corresponding phenotypes (filamentous cells and minicells). However, we couldn't find any experimental evidence that supports this major model prediction. In Park et al. [13] four mutations of the MinE MTS ($minE^{L3E}$, $minE^{F7E}$, $minE^{L4E}$, $minE^{F6E}$) are investigated, quoting [13]:

> "Surprisingly, the strains containing $minE^{L3E}$ and $minE^{F7E}$ were extremely filamentous and could not form colonies on plates with arabinose (Figure 4B and data not shown), indicating that MinE function was absent. In contrast, strains containing $minE^{L4E}$ and $minE^{F6E}$ formed colonies normally on plates with arabinose, but the morphologies of the cells were heterogeneous in length with some minicells. The average cell length of an exponential culture of the strain with $minE^{WT}$ was $2.84 \pm 0.89\mu m$ compared to $4.68 \pm 2.48\mu m$ for the strain lacking Min function. The strains containing $minE^{F6E}$ and $minE^{L4E}$ had average cell lengths of $3.81 \pm 2.67\mu m$ and $2.95 \pm 1.37\mu m$, respectively ($N \sim 250$ for each). In summary, each of the four charge substitution mutations eliminated membrane binding of the MinE^{I25R} mutant. However, two of the mutations, $minE^{L3E}$ and $minE^{F7E}$, completely eliminated the ability of MinE to counteract MinC/MinD, whereas the other two, $minE^{L4E}$ and $minE^{F6E}$, did not, although they did reduce the ability of MinE to spatially regulate division as evidenced by the increases in the average cell length and the standard deviation."

Hence, removing MinE membrane binding affects the performance of the Min system rather than disabling it's function altogether. As discussed in our

previous work [3], altering Min protein recruitment rates (which represent the sensing step discussed before) has significant impact on midcell localization by pole-to-pole oscillations. Therefore, the observed filamentous phenotypes in Park et al. [13] might be explained by an altered Min oscillation with reduced midcell localization precision due to weakened MinE-MinD interactions. The explanation offered by Park et al. [13] appears to agree with this line of thought, quoting [13]:

> " [...] two of the MinE mutants we described above, MinE^{F7E} and MinE^{L3E}, were unable to rescue cells from expression of MinC/MinD (Figure 4B). This was surprising because these residues lie beyond the putative interacting helix. We reasoned that these residues could play a role in sensing MinD and therefore might have a defect in MinD-MinE interaction similar to that of the MinD^{M193L} mutant. If so, the *minE*^{I24N} mutation should suppress these mutations. As shown in Figure 2D, the double mutant MinE$^{F7E/I24N}$ rescued cells from expression of MinC/MinD, demonstrating that the *minE*^{I24N} mutation is an intragenic suppressor of *minE*^{F7E}. It also suppressed *minE*^{3LE} [*sic*] (data not shown)."

This picture is also consistent with the earlier experimental results by Ma et al. [8] which showed that MinE^{I25R} lacks the ability to sense MinD. In turn, this leads to the loss of Min-oscillations and results in the filamentous phenotype. The fact that *minE*^{L4E}, *minE*^{F6E}, and MinE$^{F7E/I24N}$ seems to retain the function of the Min system, while lacking the ability to bind to the membrane clearly implies that not membrane binding itself but the effect it has on MinD sensing enables proper Min oscillations. For *minE*^{L4E} and *minE*^{F6E} the specific effect on MinD sensing cannot be deduced from the experimental data. This impedes an unequivocal comparison with the model. However, this is not the case for MinE$^{F7E/I24N}$. MinE^{I24N} shows significantly increased MinD sensing ability through unmasking of the anti-MinCD domains (β1 strands) which are buried in the dimeric interface in WT MinE. So, on one hand MinE$^{F7E/I24N}$ lacks the ability to interact with the membrane, such that membrane binding effects can be excluded. On the other hand the unmasked anti-MinCD domains enable it to interact with MinD as if it were in it's membrane bound conformation. As the experiment indicates that this mutation restores proper function of the Min system this scenario can be directly translated into a test of the model dynamics: We incorporate the corresponding modification by preventing MinE to bind to the membrane $\omega_{de,m} = 0/s$, $\omega_{de,c} = 0.88/s$ and setting

the recruitment rate ω_E for cytosolic MinE equal to the reassociation rate ω_{ed} of former membrane bound MinE species, i.e. $\omega_E = \omega_{ed} = 2.5 \cdot 10^{-3} \mu m^2/s$. The experimental observation implies that the dynamical instability should be restored. In contrast, the linear stability analysis reveals no instabilities in this kinetic configuration, cf. Figure 9C.[12] Moreover, we find that without MinE membrane binding the instability cannot be restored by changing the MinE recruitment rate. Therefore, not the modified MinE-MinD interaction but MinE membrane binding is the crucial component in the model. Assuming that the $\text{MinE}^{F7E/I24N}$ mutant most likely restores pole-to-pole Min oscillations (hence, geometry sensing) without requiring membrane binding further questions the claim that MinE membrane binding is responsible for geometry sensing, we conclude that the experiments by Park et al. [13] disprove the proposed model. We stress that a loss of dynamical instability without MinE membrane binding does not imply that MinE membrane bindings is required or responsible for geometry sensing in any way. The demonstration is given by the model simulations above: There one observes pattern formation based on dynamical instabilities but no geometry sensing.

Total particle numbers, bulk-membrane ratio, and effective 2D modeling

In this last section we focus on questions about volume effects, spacial dimensions, and effective system size. A main claim of the theoretical investigation in the paper is that

> " [...] Min protein waves sense the geometry of the flat, two-dimensional membrane, rather than the three-dimensional space of the cell or the curvature of the membrane. "

Certainly, there is no doubt that the available experimental data offers such a conjecture as waves are found for various system/bulk heights and the gold layer size does not seem to have any impact beyond enabling and disabling patch-to-patch coupling. However, in light of the numerical investigation above this statement raises the question why the size of the space above the membrane should not matter while additional space around the membrane (in form of the surrounding gold layer) has significant impact on the model dynamics. Increasing gold layer size leads to loss of patterns for the experimental [MinE]/[MinD] ratio and impedes wave alignment (i.e. geometry sensing phenomena) for fine tuned [MinE]/[MinD] ratios. This indicates that bulk size (via bulk/membrane ratio) affects wave dynamics. Furthermore, our investigation

showed that alignment to rectangular membrane patches solely emanates from cross-boundary coupling effects. This directly contradicts the model-based claim that "*Min proteins waves sense the geometry of the flat, two-dimensional membrane*". The foundation of this conclusion appear inscrutable to us. The authors state in the supplementary document to the paper that they "*have checked on specific examples that the same phenomena [...] can also be observed in the full three-dimensional description*". Obviously this requires an explicit mapping between the full 3D dynamics and the effective 2D reduction. However, no such mapping is provided in the model definition. Inspection of the model parameters reveals that the cytosolic protein concentrations are treated as surface densities: $C_{D0} = 2.9{\cdot}10^3 \mu m^{-2}$ and $C_{E0} = 1.9{\cdot}10^3 \mu m^{-2}$. This indicates an underlying bulk integration. The protein concentrations in the experiment are $c_D = 0.8\mu M \approx 481.8 \mu m^{-3}$ MinD and $c_E = 0.5\mu M \approx 301.1 \mu m^{-3}$ MinE. Comparison with the model parameters implies integration of $6\mu m$ bulk, i.e. $C_{D0/E0} \approx 6 c_{D/E}$. The paper does not provide the experimental bulk height explicitly, however, it is stated that the bulk height is very large, quoting [14]:

> "Although the space above the membrane was not limited in our experiments, the proteins were located only in a small layer above the membrane during pattern formation."

The corresponding figure (Figure S1 in the supplement of the paper) clearly shows that the experimental bulk height is much larger than $6\mu m$, and previous in vitro experiments were performed with a total bulk height about $h = 5 \cdot 10^3 \mu m$ [7]. Regarding particle numbers the model accounts for a system that is three orders of magnitude smaller than the typical experimental setup.
Without any notion of bulk volume in the model definition we are left with ad hoc approximations that maintain the mathematical structure of the model. The bulk dynamics in normal direction to the membrane can be eliminated via integration or averaging to yield a 2D reaction-diffusion system. In the first case we increase the total densities of MinD (C_{D0}) and MinE (C_{E0}) keeping the ratio constant. In the second case we keep the total densities of MinD and MinE fixed and introduce a scaling factor h between between membrane and bulk dynamics, i.e.

$$\partial_t c_B = D_B \nabla^2 c_B + \frac{1}{h} f_B \tag{6}$$

where c_B denotes any bulk species with membrane reactions given by f_B. Note that in this case bulk densities are (mean) volume densities and not surface densities as the reported parameters suggest. Using the effective system size as parameter we find that dynamical instabilities are rapidly lost in both approximation (Figure 9E/F). This proves that the model's dynamics are actually

highly sensitive to volume effects in contrast to the authors' claim in the paper. We further note that these findings are supported by the fact that patterns vanish if the gold layer size is increased.
We conclude that the model cannot account for experimental system sizes. Moreover there is no explicit notion of bulk volume and no relation to the full three-dimensional dynamics. Increasing the effective system size leads to loss of any pattern forming instabilities which directly contradicts the claim that three dimensional dynamics do not affect pattern formation.

FIGURES AND REFERENCES

[1] A. Arjunan and M. Tomita. A new multicompartmental reaction-diffusion modeling method links transient membrane attachment of E. coli MinE to E-ring formation. *Syst. Synth. Biol.*, 4:35–53, 2009.

[2] M. Cross and H. Greenside. *Pattern Formation an Dynamics in Nonequilibrium Systems*. Cambridge University Press, 2009.

[3] J. Halatek and E. Frey. Highly Canalized MinD Transfer and MinE Sequestration Explain the Origin of Robust MinCDE-Protein Dynamics. *Cell Reports*, 1(6):741–752, June 2012.

[4] K. C. Huang. Dynamic structures in Escherichia coli: Spontaneous formation of MinE rings and MinD polar zones. *Proc. Natl. Acad. Sci. USA*, 100(22):12724–12728, Oct. 2003.

[5] R. A. Kerr, H. Levine, T. J. Sejnowski, and W.-J. Rappel. Division accuracy in a stochastic model of Min oscillations in Escherichia coli. *Proc. Natl. Acad. Sci. USA*, 103(2):347–352, 2006.

[6] M. Loose, E. Fischer-Friedrich, C. Herold, K. Kruse, and P. Schwille. Min protein patterns emerge from rapid rebinding and membrane interaction of MinE. *Nat. Struct. Mol. Biol.*, 18(5):577–583, 2011.

[7] M. Loose, E. Fischer-Friedrich, J. Ries, K. Kruse, and P. Schwille. Spatial Regulators for Bacterial Cell Division Self-Organize into Surface Waves in Vitro. *Science*, 320(5877):789–792, May 2008.

[8] L. Ma, G. King, and L. Rothfield. Mapping the MinE site involved in interaction with the MinD division site selection protein of Escherichia coli. *J. Bacteriol.*, 185(16):4948–4955, 2003.

[9] G. Meacci and K. Kruse. Min-oscillations in Escherichia coli induced by inter-

actions of membrane-bound proteins. *Phys. Biol.*, 2(2):89–97, 2005.

[10] In the experiment a [MinD]/[MinE] ratio of 1.6 is maintained ($0.8\mu M$ MinD, $0.5\mu M$ MinE). The original parameters agree with that ($2.9/1.9 \approx 1.53$), but the modified parameter do not ($2.9/1.3 \approx 2.23$ and $2.9/0.72 \approx 4.03$).

[11] We note that reducing the MinE-MinD interaction parameters ω_E and ω_{ed} leads to loss of instability as well.

[12] Figure 9D shows the same data as Figure 9C but with the hydrolysis rate ω_{de} reduced by 50%. This corresponds to the measurement of reduced MinD ATPase activity stimulation by MinE^{I24N}-h* in the experiment by Park et al. [13].

[13] K.-T. Park, W. Wu, K. P. Battaile, S. Lovell, T. Holyoak, and J. Lutkenhaus. The Min Oscillator Uses MinD-Dependent Conformational Changes in MinE to Spatially Regulate Cytokinesis. *Cell*, 146(3):396–407, 2011.

[14] J. Schweizer, M. Loose, M. Bonny, K. Kruse, I. Mönch, and P. Schwille. Geometry sensing by self-organized protein patterns. *Proc. Natl. Acad. Sci. USA*, 109(38):15283–15288, Sept. 2012.

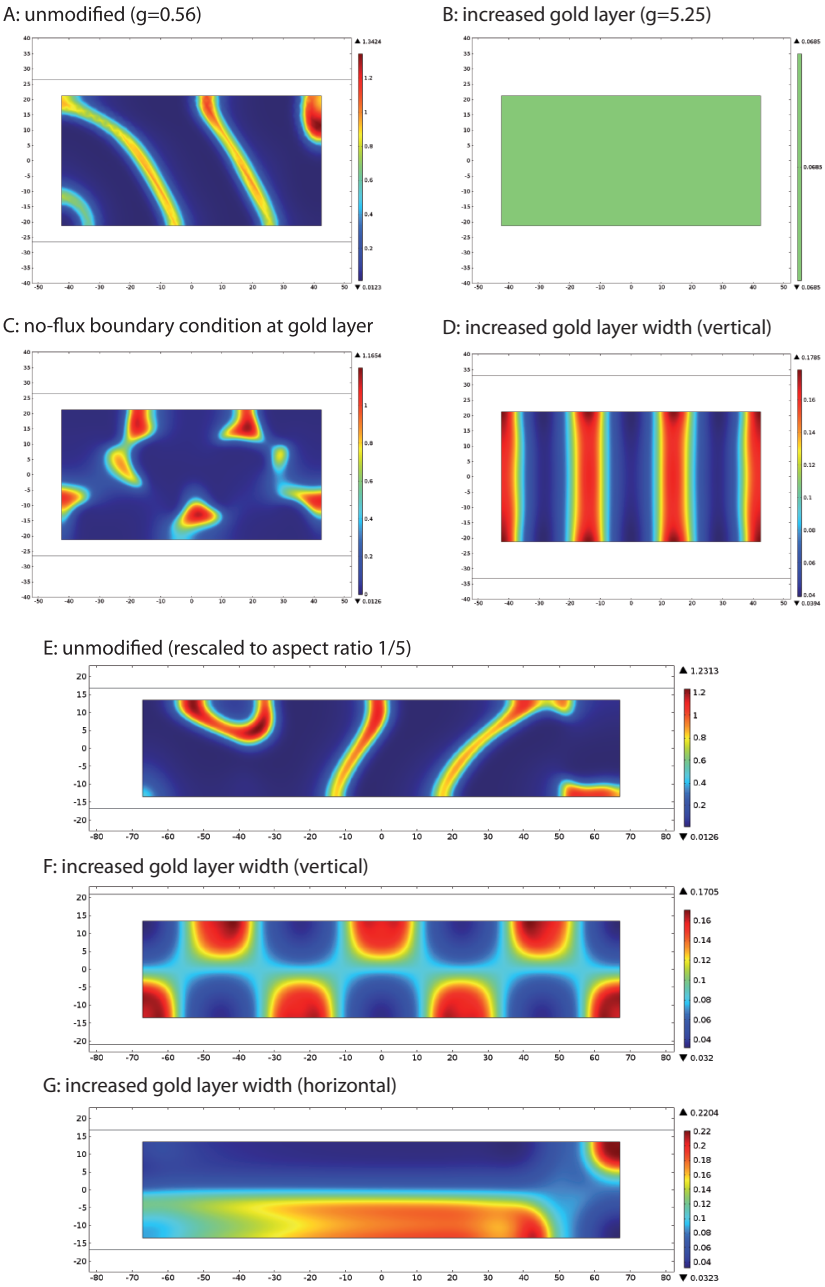

FIG. 2. Dynamics on rectangular patches for $C_{E0} = 1.9 \cdot 10^3/\mu m^2$ as published in the paper. All simulations are based on the file AspectRatio_Paper.mph

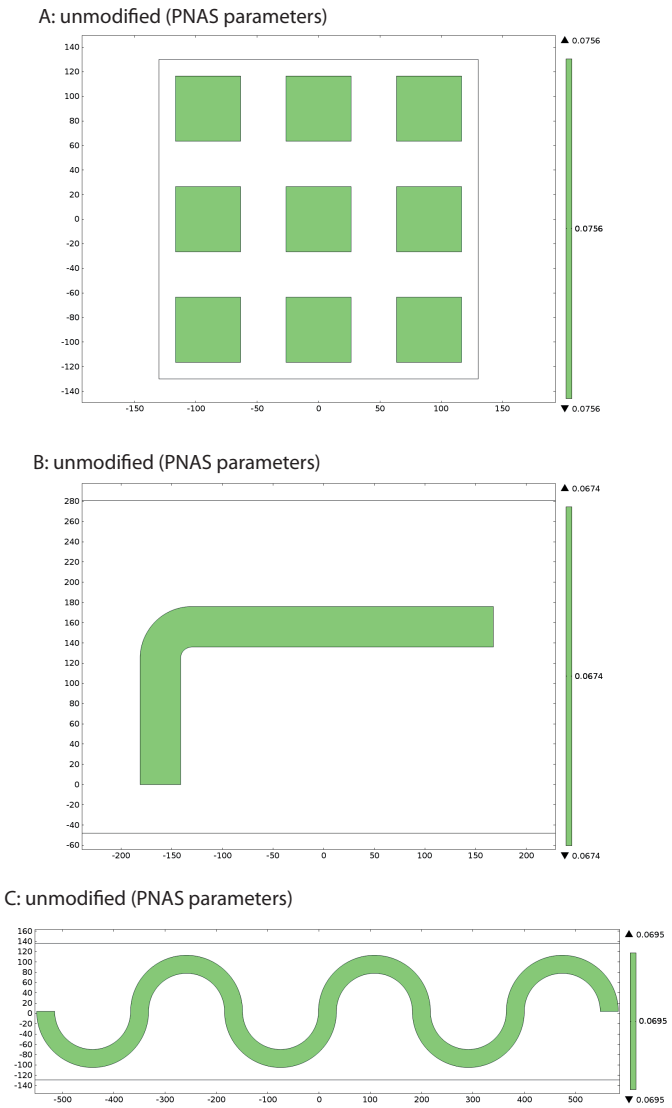

FIG. 3. Absence of patterns on quadratic and curved patches for $C_{E0} = 1.9{\cdot}10^3/\mu m^2$ as published in the paper.

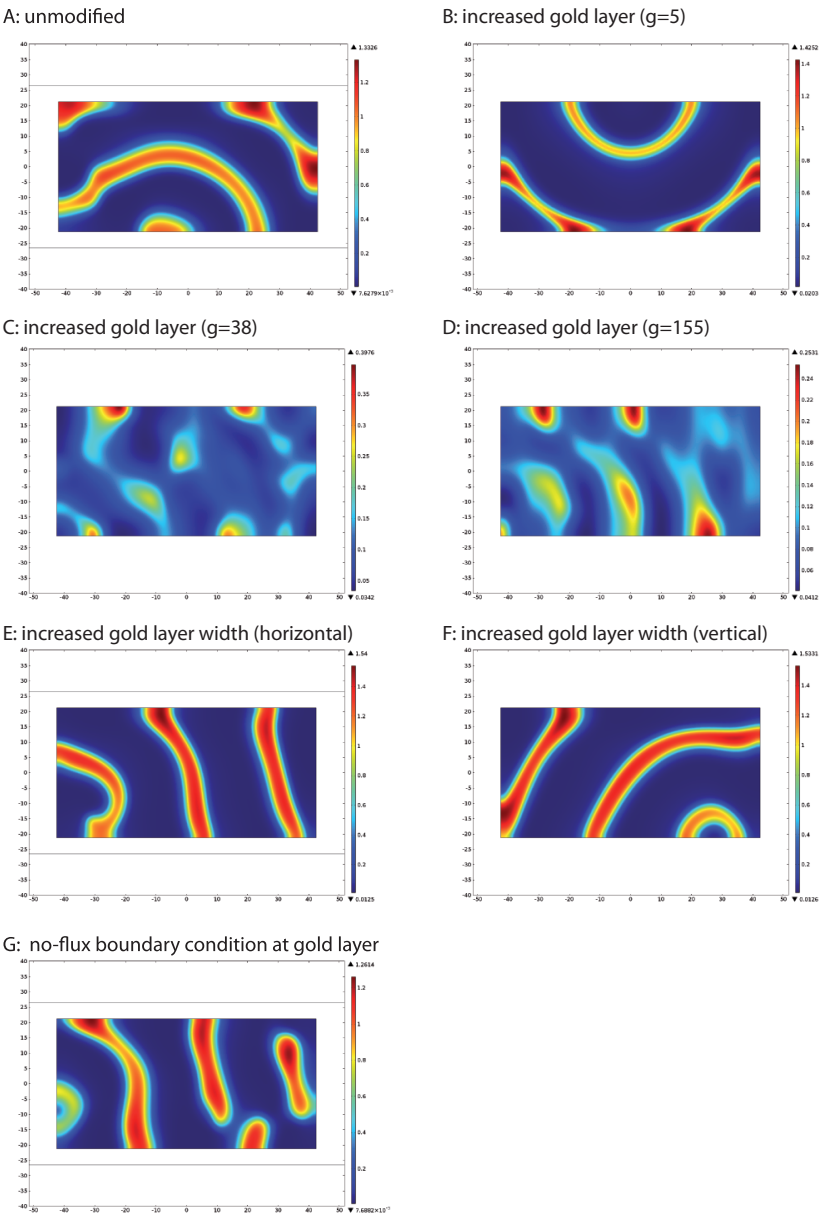

FIG. 4. Dynamics on rectangular patches for $C_{E0} = 1.3 \cdot 10^3/\mu m^2$ as preset in the simulation files. All simulations are based on the file AspectRatio_Paper.mph

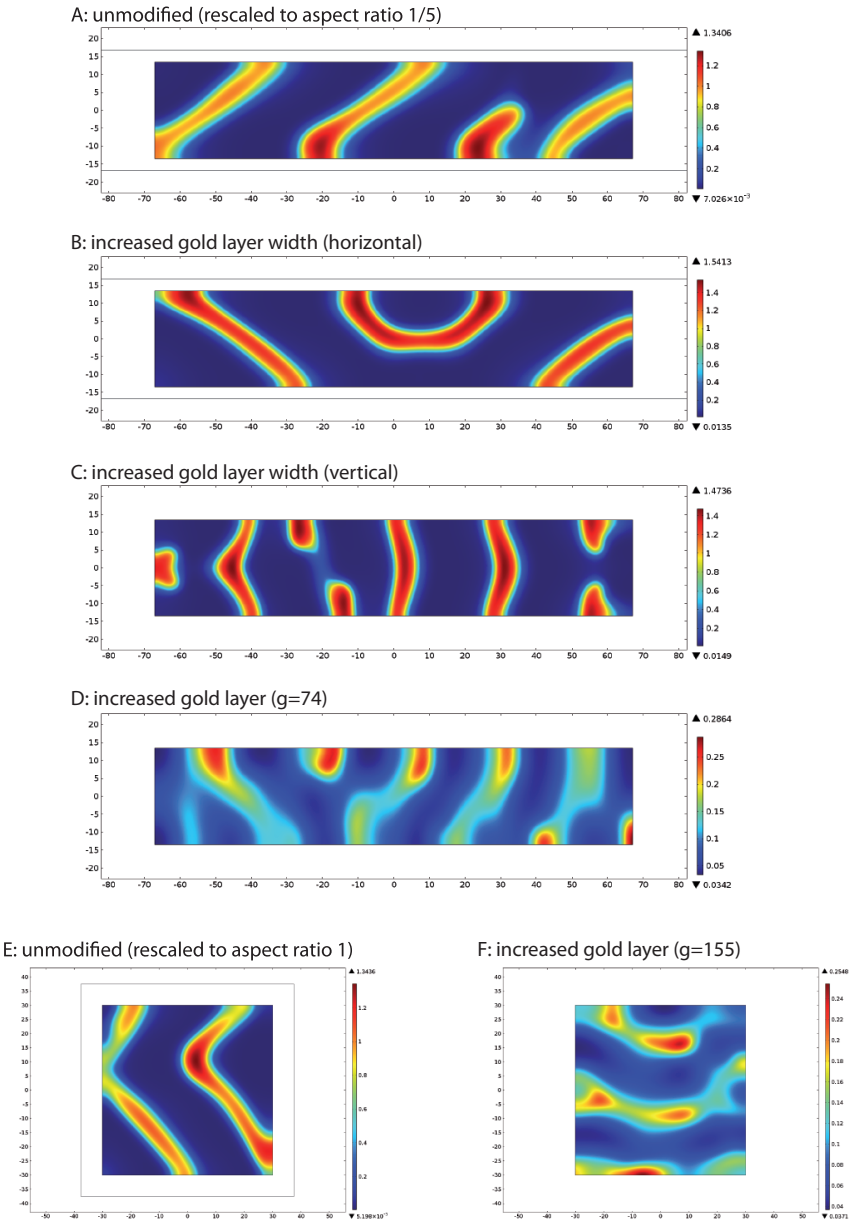

FIG. 5. Dynamics on rectangular patches for $C_{E0} = 1.3 \cdot 10^3/\mu m^2$ as preset in the simulation files. All simulations are based on the file AspectRatio_Paper.mph

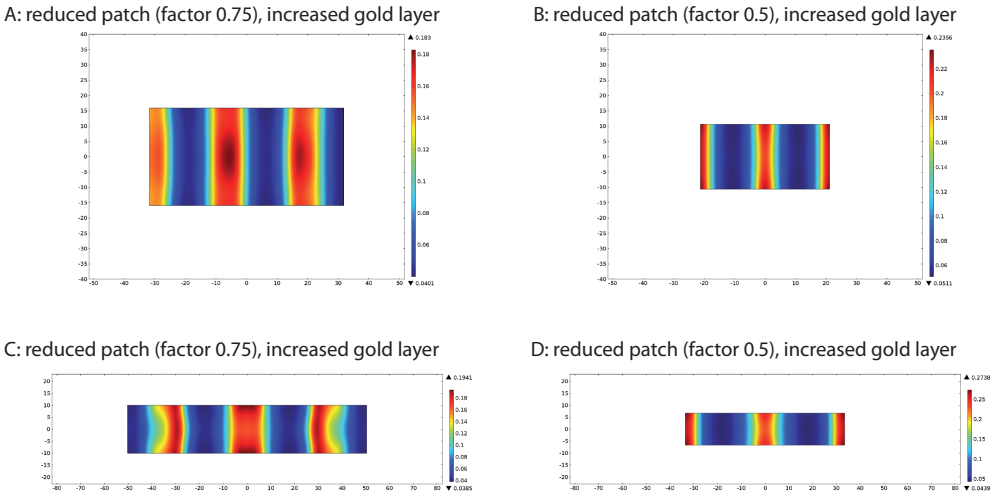

FIG. 6. Dynamics on smaller rectangular patches for $C_{E0} = 1.3 \cdot 10^3/\mu m^2$. All simulations are based on the file AspectRatio_Paper.mph

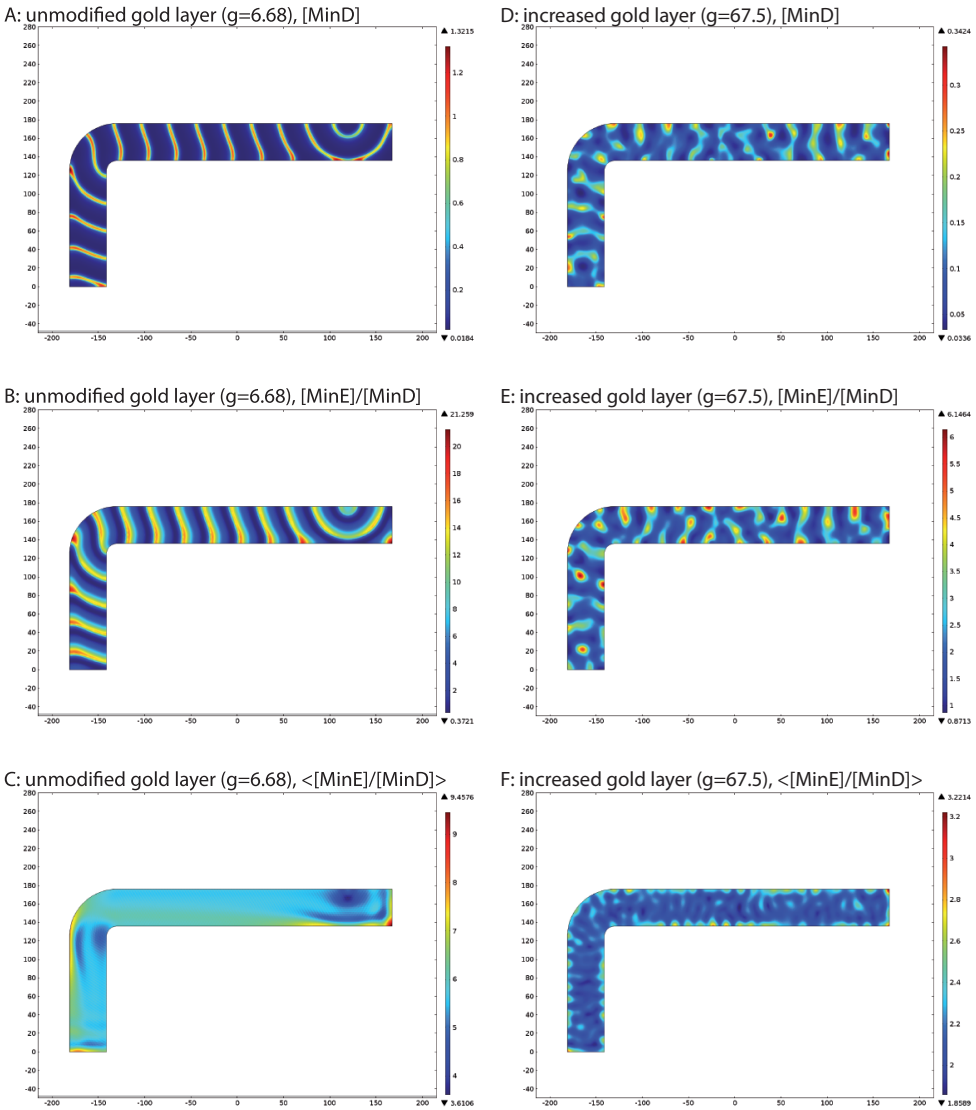

FIG. 7. Dynamics on L-shaped patches for $C_{E0} = 1.3 \cdot 10^3/\mu m^2$. All simulations are based on the file L_shape_Paper.mph

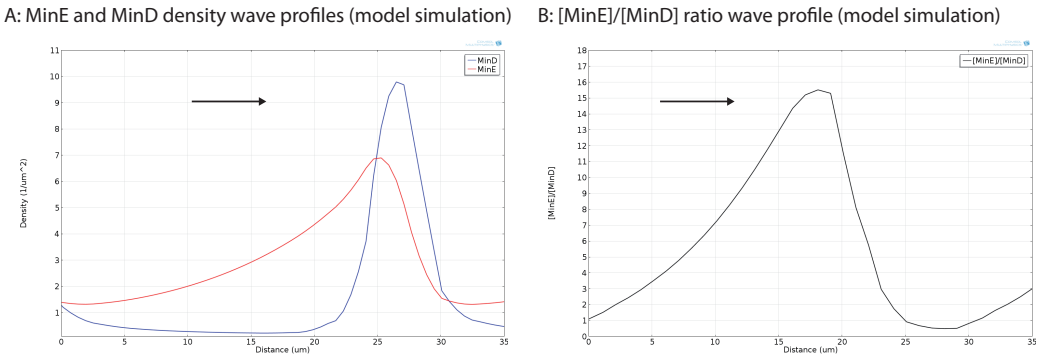

FIG. 8. Computational data of protein density profiles and [MinE]/[MinD] ratios along a wave in the L-shape simulation.

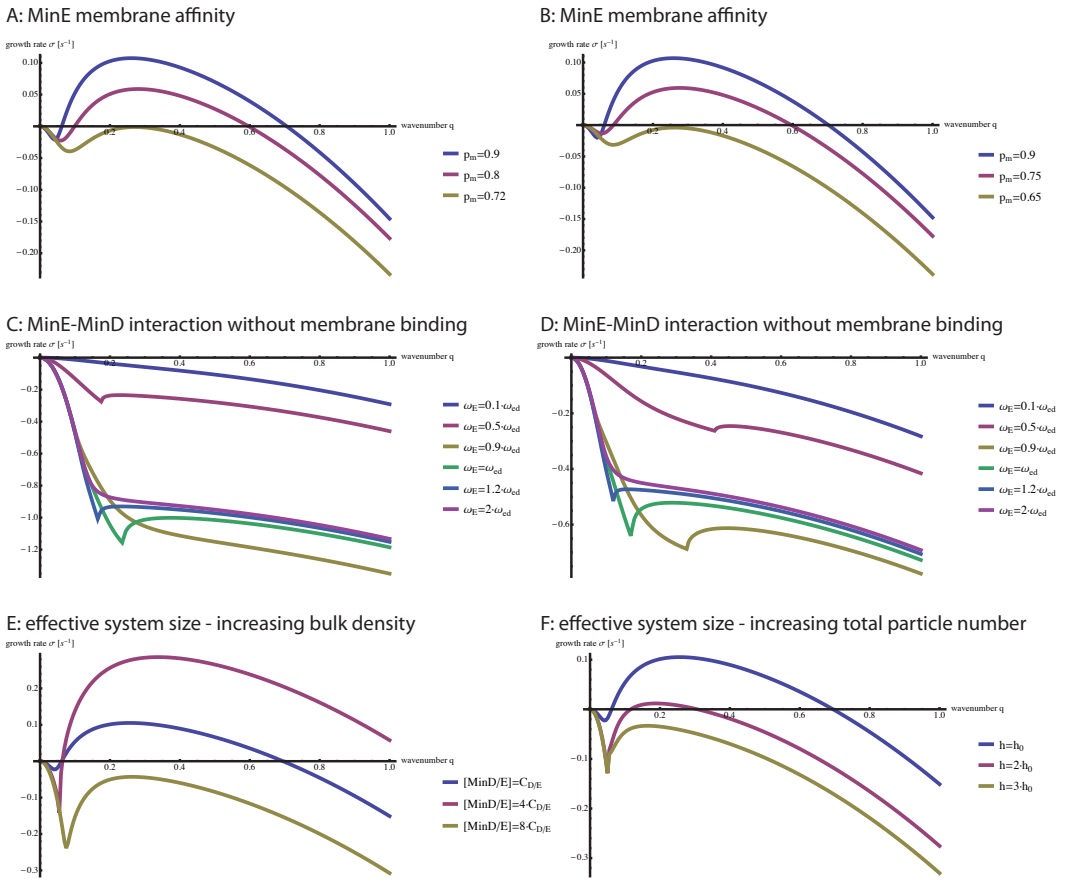

FIG. 9. Dispersion relations for varying MinE-MinD interactions and effective system sizes showing loss of instabilities.

Acknowledgements

First, I want to express my gratitude to Erwin Frey. I am deeply grateful for the extraordinary support and freedom you gave me from the very beginning and at every stage of this long project. I greatly enjoyed the countless discussions we had on all topics. I always appreciated you enthusiasm for our research, and your unbroken positive attitude even in the more difficult situations. I find it hard to imagine a nicer, more productive and intellectually stimulating working environment than your group.

I also want to express my gratitude to Fridtjof Brauns. Without your extraordinary commitment the *mass-redistribution framework* wouldn't be where it is now. It was a joy to observe how it shifted from my project to our project. It was a pleasure working with you, and I am very curious what will follow. Thank you for all your feedback and support! Along the same lines I thank Jonas Denk and Dominik Thalmeier for the many interesting discussion we had on Nonlinear Dynamics and the Min System. I greatly benefitted from these discussions!

I had the pleasure to work with many excellent researchers on a broad range of projects. I would like to thank Raphaela Geßele for picking up the PAR project an bringing it to fruition. I thank Laeschkir Hassan for contributing his incredible expertise with finite element simulations to the project, and for working his magic to speedup Comsol. I also thank my experimental collaborators Fabai Wu and Simon Kretschmer for doing such outstanding work on the Min system which really advanced my understanding of the dynamics. Furthermore, I would like to thank Cees Dekker. It was a great experience collaborating with you and your group.

I would also like to thank all members of the MaRD seminar: Silke Bergeler, Fridtjof Brauns, Jonas Denk, Florian Gartner, Raphaela Geßele, Laeschkir Hassan, Tobias Hermann, Lorenz Huber, Bernhard Lohner, Korbinian Pöpel, and Manon Wigbers. Thanks for taking the time, for your great contributions, and all the valuable input! During my thesis I had the pleasure to work with many formidable students: Michael Hartmann, Caroline Hartl, Thomas Fehm, and Tim Meinhardt. I learned a lot from you! I also thank Marianne Bauer, Jonas Cremer, Patrick Hillenbrand, Ben Klünder, Hannes Knebel, Jan-Timm Kuhr, Matthias Lechner, Anna Melbinger, Johannes Nübler, Matthias Rank, Louis Reese, Emanuel Reithmann, Steffen Rulands, Filipe Tostevin, Christoph Weber, Markus Weber, Cornelius Weig, Karl Wienand, and Thomas Franosch, Uli Gerland, as well as Chase Broedersz. I enjoyed the many discussions, and in particular, the trips to Antholz.

Zu guter Letzt möchte ich meinen Eltern, meinen Geschwistern Julia und Robert, und meiner Frau Tetyana für ihre grenzenlose Unterstützung danken. Tetyana, danke, dass du mir in den Endzügen dieser Arbeit den Rücken freigehalten hast!